europhysics
conference
abstracts

14 th European Conference on

Controlled Fusion and Plasma Physics

Madrid, 22 - 26 June 1987

Editors: F. Engelmann, J. L. Alvarez Rivas

Contributed Papers
Part I

Published by: European Physical Society

Series Editor: Prof. S. Methfessel, Bochum

Managing Editor: G. Thomas, Geneva

VOLUME
11 D
PART I

14 th European Conference on

CONTROLLED FUSION
AND PLASMA PHYSICS

Madrid, 22-26 June 1987

XIV
FUSION
MADRID
1987

Contributed Papers, Part I
Editors: F. Engelmann, J.L. Alvarez Rivas

VOLUME 11D

EUROPHYSICS CONFERENCE ABSTRACTS is published by the
European Physical Society, 1987

The 14th European Conference on Controlled Fusion and Plasma Physics was held in Madrid, Spain from 22 to 26 June 1987. It was organized by Centro de Investigaciones Energéticas Medioambientales y Tecnológicas (CIEMAT), Madrid, Spain on behalf of the Plasma Division of the European Physical Society (EPS).

The following topics for poster sessions were taken into consideration:

A. Tokamaks
B. Stellarators
C. Alternative Magnetic Confinement Systems
D. Inertial Confinement
E. Plasma Edge Physics
F. Plasma Heating and Current Drive
G. Tokamak and Basic Fusion Plasma Theory
H. Diagnostics

The orally presented contributed papers were grouped into four sessions covering:

Confinement and Heating in Toroidal Plasmas
Plasma Edge Physics
Inertial Confinement

The Conference Programme included 18 invited lectures, 19 orally presented contributed papers and more than 400 papers presented in poster sessions. In addition, an evening lecture on the Status of Fusion Research was given by R.S. Pease.

The contributed papers of this 3-volume publication are photographically reduced in size from the originals provided by the authors.

Programme Commitee/Paper Selection Committee

F. Engelmann (Chairman), FOM (The Netherlands), NET (German Fed. Rep.)
J.L. Alvarez Rivas, CIEMAT (Spain)
K. Appert, CRPP (Switzerland)
R. Behrisch, IPP (German Fed. Republic)
G. Briffod, CEN (France)
A. Gibson, JET (United Kingdom)
M. Key, Chilton Lab. (United Kingdom)
D.D. Ryutov, Inst. Novosibirsk (USSR)

The invited papers will be published by Pergamon Press in the journal "Plasma Physics and Controlled Fusion" and sent free of charge to each registered participant.

TABLE OF CONTENTS

TITLE LIST

A. Tokamaks

E. Plasma Edge Physics

G. Tokamak and Basic Fusion Plasma Theory

H. Diagnostics

A

TOKAMAKS

TRANSPORT IN TOKAMAK EDGE PLASMAS

H.P. Furth

Princeton University, Plasma Physics Laboratory

1. Architectural Optimization

Toroidal-confinement experiments prior to the mid-60's were characterized by Bohm diffusion[1] [$D = cT_e/16\,eB \sim 6 \times 10^3\, T_e$ (eV)/B(kΓ) cm^2/sec; $\chi_{Bohm} \sim 3\,D$] or worse.[2] In the US, the search for improved confinement took the direction of architectural optimization. The levitron[3] (Fig. 1a) offered axisymmetry and high shear, along with stability against current-driven modes. The spherator[4] (Fig. 1b) added minimum-average-B stability, and/or the ability to localize trapped particles in a region of favorable ∇B_t, on the small-R side of the plasma. Experimentally, confinement was found to improve with rising[5] n/J, (up to $\nu_{the}/\nu_s \sim 10^3$) and with rising[6] T_e (up to a collisionality $\nu_{ce}/\omega_{be} \sim 1$). For higher T_e, transport was found to increase according to a Bohmlike scaling[6,7]

$$\chi_e = (G/30)\,\chi_{Bohm} = G\ 600\ T_e/B\ \ (cm^2/sec)\ , \tag{1}$$

where architectural features determine G:

1. Configuration 1a has the highest fluctuation levels and the worst confinement.

2. The best confinement, corresponding to $G \sim 1/3$, is obtained in configuration 1c when $B_t \lesssim B_p \sim B$ -- even though configuration 1b has better theoretical minimum-average-B properties.

3. In configuration 1c, reduction of B_t/B_p weakens the shear and removes the magnetic well, yielding $G \to B_p/B_t$ in the range $B_t \ll B_p \lesssim B$.

4. In the "tokamak limit" $B_p \ll B_t \lesssim B$, which implies particle trapping of the form 1b, the reduction in shear gives $G \to B_t/B_p$.

On the basis of (4), one would expect tokamaks to follow a Bohmlike scaling

$$\chi^*_B \sim 600\ T_e/B_p\ (cm^2/sec)\ . \tag{2}$$

In applying Eq. (2), one should note, however, that it is not based on direct local measurements of χ_e, but on measurements of the gross τ_{Ee}, together with the assumption of no strong extraneous spatial dependences of χ_e.

2. Edge Effects

In the edge region of a representative large tokamak,[8] where $B_p \sim 5$ kΓ, $T_e \sim 300$ eV and $\chi_e \sim 3 \times 10^4$ cm^2/sec, the magnitude given by Eq. (2) is about right -- but the observed radial dependence is quite different, with χ_e increasing strongly towards the limiter. Remarkably,

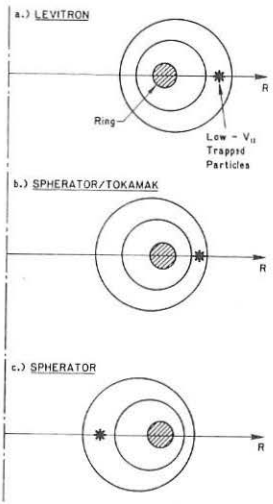

Fig. 1

A family of axisymmetric toroidal-confinement configurations.

the plasma core region is characterized by $\chi_e \lesssim 10^2 \chi^*_B$. In other words, a plasma configuration of the type $B_p \ll B_t$, which is known to be architecturally inferior, nonetheless exhibits greatly superior confinement. The clear implication is that non-architectural features must play a dominant role in determining the quality of plasma confinement.

Since both plasma fluctuations and transport increase so strongly towards the edge of the tokamak plasma, it is natural to suppose that surface effects may be the main source of trouble (analogous to fluid flow through a rough pipe[9]). There is also a general experimental observation that tokamak $T_e(r)$-profiles are rigid against modification by local heating (or cooling) and tend to be fairly well determined by the edge value of d log T_e/dr, within the Δ'-constraints set by the MHD safety factors q(o) and q(a). These observations suggest a model of the tokamak where transport on the plasma interior adjusts itself for the maintenance of certain profile shapes (i.e., architectural self-optimization), while "edge transport coefficients" at some radius $r_{edge} = a - \delta r$ control the global energy confinement time.[10]

If profile consistency is invoked to give $T_{edge} \propto (\delta r/L)\, T(o)$, and Eq. (2) is used to estimate the magnitude of χ_{edge}, one arrives at a fair approximation of experimental τ_E-values. Noting that the total plasma energy is proportional to $n(o)\, T(o)\, L^3$, while the heat outflow through r_{edge} is proportional to

$$L^2\, n_{edge}\, \chi_{edge}\, \nabla T_{edge} \propto n_{edge}\, \delta r\, T_e^2(o)/B_p,$$

one finds

$$\tau_E \propto n(o)\, L^3\, B_p\, T^{-1}(o)\, (n_{edge}\, \delta r)^{-1}. \qquad (3)$$

This equation can be made to approximate the neo-Alcator formula by assuming that $\delta r \propto n_{edge}^{-1}$ (as in the case of neutral-gas penetration) and noting that for ohmic heating, B_p/T is roughly constant. This model for δr conforms with the prejudice that "atomic effects" may be damaging to confinement.[11] A main reason for the historic advance of the tokamak relative to other toroidal experiments of the 60's (including the spheromak, which had superior architecture) may have been its ability to banish edge-related problems -- such as "atomic effects" -- to a relatively thin surface layer.

3. Bohm and Goldston

For sufficiently high density (small δr), one might expect the favorable τ_E-dependence of Eq. (3) to saturate, so that

$$\tau_E \propto B_p L^2/T(o) \quad [n(o)L/n_{edge}\,\delta r], \tag{4}$$

with the term in brackets depending on the gross profile,[10] rather than the magnitude of n. In terms of the heating power P_H, the Bohmlike scaling of Eq. (4) corresponds to

$$\chi^*_B \propto P_H^{1/2} L^{-1/2} B_p^{-1/2} n^{-1/2}, \tag{5}$$

which does not differ drastically from the Goldston formula[12]

$$\chi_G \propto P_H^{1/2} L^{-1/2} B_p^{-1}. \tag{6}$$

There seems to be a certain historical parallel between the reigns of Bohm and Goldston scaling. During the first part of the 1960's, Bohm scaling was so commonly found in stellarator experiments that it came to be regarded as a "universal" lower limit on anomalous transport. Before long, however, toroidal-confinement experiments in multipoles[13] and levitron/spherators[3-5] demonstrated that architectural improvements could reduce transport well below the simple Bohm rate, and the T-3 tokamak[14] discovered the possibility of large non-architectural improvement factors. In hindsight, it seems that the Bohm formula really gave a kind of upper limit on anomalous transport, peculiar to MHD-stable plasmas with little shielding against edge effects and with such small values of average B_p/B_t (typically $<10^{-2}$) that Eq. (2) would have prescribed worse confinement than the Bohm formula.

During the latter part of the 1980's, when strong auxiliary heating began to be available, tokamak confinement appeared to deteriorate sharply relative to ohmic heating. The accumulating evidence pointed to the presence of a "universal" τ_E-scaling[12] proportional to a factor $I/P_H^{1/2}$ (or B_p/T) that had remained concealed in the ohmic-heating regime, where P_H and I are tied together. During subsequent years, substantial improvements in confinement have once more emerged, even within the architectural constraints of tokamak geometry.[15,16] At first, the tokamak enhanced-confinement regimes were simply characterized as giving some numerical multiple of Goldston low-mode confinement, but present evidence suggests that the scaling of confinement in these regimes may be altogether different -- with the adverse dependence of τ_E on P_H being much weaker or even entirely absent.

The recent advances relative to the Goldston low-mode scaling provide strong additional evidence that anomalous transport is stimulated by surface phenomena. Surprisingly large improvements in the global τ_E arise from techniques that might be expected to affect only the outer plasma edge: introduction of a poloidal-field separatrix with strong shear in its immediate vicinity; minimization of plasma density in the edge region relative to the core; alteration of the edge plasma potential by various means, including beam-driven rotation.

The "universality" of the Goldston scaling, like that of the Bohm scaling, seems to consist in setting an upper limit for anomalous transport. In the case of Goldston scaling, this limit governs tokamak plasmas with sufficient edge-shielding and B_p/B_t to do much better than Bohm, but with a lack of special edge-control features.

References

1. Hinnov, E., Bishop, A.S. (1966). Phys. Fluids, 9, 195.
2. Butt, E.P., et al., (1966), Plasma Phys. and Cont. Nucl. Fusion Research, II, 751.
3. Birdsall, D.H., et al., (1966). Plasma Phys. and Cont. Nucl. Fusion Research, II, 291.
4. Yoshikawa, S. (1973). Nucl. Fusion, 13, 433.
5. Alcock, M.W., et al., (1976). Plasma Phys. and Cont. Nucl. Fusion Research, II, 305.
6. Okabayashi, M. (1973). Phys. Fluids, 16, 2339.
7. Ejima, S., Okabayashi, M., (1975). Phys. Fluids, 18, 904.
8. Bell, M.G., et al., (1986). Plasma Phys. and Cont. Fusion, 26 1329.
9. Analogy pointed out by B.B. Kodomtsev.
10. Furth, H.P., (1986). Plasma Phys. and Cont. Fusion, 28, 1305.
11. Furth, H.P., (1986). IAEA (INTOR-Related) Specialists Meeting on Confinement in Tokamaks with Intense Heating, Kyoto, Japan, November 21-22, 1986, 351.
12. Goldston, R.J., (1984). Plasma Phys. and Cont. Fusion, 26, 37.
13. Ohkawa, T., et al., (1966). Plasma Phys. and Cont. Nucl. Fusion Research, II, 531. Also, Kerst, D.W., et al., (1965). Phys. Rev. Lett., 15, 396.
14. Artsimovich, L.A., et al., (1969). Plasma Phys. and Cont. Nucl. Fusion Research, I, 157.
15. Wagner, F., et al., (1982). Phys. Rev. Lett., 49, 1408.
16. Hawryluk, R.J., et al. Proc. 11th Int. Conf. on Plasma Phys. and Cont. Nucl. Fusion Research, Kyoto, Japan (November 1986).

STUDIES OF H-MODE IN THE LIMITER DISCHARGES ON JFT-2M TOKAMAK

H.Matsumoto, A.Funahashi, M.Hasegawa*, K.Hoshino, S.Kasai, H.Kawashima, T.Kawakami,T.Matoba,T.Matsuda,Y.Miura,M.Mori,K.Odajima,H.Ogawa,T.Ogawa, H.Ohtsuka,S.Sengoku,T.Shoji,N.Suzuki,H.Tamai,Y.Uesugi,T.Yamauchi,T.Yamamoto A.Honda, I.Ishibori, Y.Kashiwa, M.Kazawa, K.Kikuchi, Y.Matsuzaki, K.Ohuchi, H.Okano, E.Sato, T.Shibuya, T.Shiina, K.Suzuki, T.Tani and K.Yokoyama

Japan Atomic Energy Research Institute, Tokai,Naka, Ibaraki, Japan
* on leave from Mitsubishi Electric Co., Tokyo, Japan

ABSTRACT An enhanced confinement mode, H-mode, was observed on JFT-2M during NBI or ICRF heating under the material limiter discharge conditions within a wide range of plasma parameter regime. Operational regime and confinement characteristics of this H-mode were studied.

1.INTRODUCTION

On JFT-2M, an enhanced confinement mode, H-mode can be observed in both limiter and open divertor[1,2] configurations. With the limiter case, a duration of the H-mode is shorter and the rate of improvement in energy confinement is smaller than the divertor H-mode case. However there are no essential differences in the nature of the phenomena between them. We also observe H-mode by NBI heating or by ICRF heating which is mainly a electron heating through Landau damping of the mode converted wave[3]. In the limiter operation, there are more freedom in the plasma shaping parameters compared with the divertor case. In this study, this operational regime of the H-mode in the limiter configuration will be surveyed. In this study, our definition of H-mode includes all the transition phenomena, no matter how small the improvement of the energy confinement is. Since, the study of this transition phenomena should be very important to understand the physics of the enhanced confinement.

2.EXPERIMENTAL CONDITIONS AND OPERATIONAL REGIME OF LIMITER H-MODE

The vacuum vessel of JFT-2M has a D shaped cross section with a minor radius of 0.415 m in the horizontal and 0.595 m in the vertical direction. Carbon fixed limiters are installed on the inner side wall in six toroidal positions. Almost toroidally continuos carbon divertor plates are mounted on the bottom and the top of the vessel. We also have movable carbon limiters from the top and from the side. Magnetic flux surfaces of the plasma in the typical H-mode case are shown in the Fig.1. In this case the outermost plasma surface is decided by the inner fixed limiter, although the top and bottom tips of the plasma are almost touching to the divertor plates. Time evolutions of plasma parameters in this shot are shown in Fig.2. Vertically measured line averaged electron density are shown in the top box. The upper trace is measured at R=1.24 m and the lower trace is at R=1.1 m whereas the plasma center is usually at R=1.28 - 1.29 m. The second box from the top is the stored energy from the diamagnetic measurement. Total radiation loss, loop voltage, H_α/D_α emission intensity, and the neutral beam injected power are shown from the third to the bottom. With the sudden depression of the H_α/D_α emission, electron density, the radiation loss and the stored energy all start increasing rapidly.

Especially, the line averaged electron density in the outer region increases more quickly than the central cord density, and shows the broadening of the density profile. This H-mode is terminated suddenly, and electron density or the radiation loss start decreasing sharply. In this shot,H-mode phase is repeated twice. Central electron temperature measured by soft x-ray pulse hight analyzer, and the ion temperature measured by the charge exchange neutrals do not increase during the H-mode.

There are several experimental requirements for the transition. The first is the inside limiter operation. With less than 2 cm of the gap between the outer limiter and the plasma surface, we have never seen the transition. Insertion of the movable limiter from the top does not hinder the transition, even when it is touching the plasma. A contact of the plasma with the inner wall limiter is not a necessary condition. We still observe the transition when the plasma outermost surface is decided by the top or the bottom carbon divertor plates.

The second is the threshold values in the additional heating power and the electron density. The transition happens above the certain threshold power and the electron density. These threshold values have dependences on the plasma parameters. The threshold density is also dependent on the additional heating power. Figure 3 shows the operational regime of H-mode in the neutral beam heating power and the line averaged electron density. The minimum electron density needed for the transition decreases with the increase of the NB heating power. With the increase of the electron density, deposition power to the periphery increases in NBI heating case. However, the same dependence of the threshold power on the electron density can be seen with the ICRF heating case where the power deposition profile should not change as much as NBI heating.

The threshold power is also dependent on the safety factor q_ψ as shown in Fig.4. The solid line is the boundary of H-mode and L-mode data points with $1.21 < B_T < 1.26$ T, and the dashed line with $275 < I_P < 295$ kA. The nature of humps between $q_\psi = 4$ and 5 is not very clear. In the single null divertor case, these humps are not seen and the both lines agrees well. Plasma shaping parameters are also important for the transition phenomena. The solid line in Fig. 5 shows the dependence of the threshold power on the ellipticity κ. It becomes high when the plasma comes close to the circular shape, $\kappa = 1$. It also slightly increases when it become strongly noncircular. However, when κ and δ is high (typically $\kappa > 1.4$, and $\delta > 0.6$) the outermost plasma surface is decided by the upper or the lower divertor plate. Then,the configuration is very close to that of the double null divertor, and the duration of the H-mode becomes much longer than the case when plasma is only limited by the inner limiter. Typically the duration of H-mode is 50-70 ms in low κ case, and it is sometimes limited by the heating pulse (close to 200 ms)in high κ case. In JFT-2M, κ and the triangularity δ can not be changed independently,and κ changes almost in proportion to δ. This proportionality can be changed by changing the poloidal field coil configuration. Keeping κ within 1.37 and 1.45, δ was changed from 0.24 to 0.5 with $3.3 < q < 3.8$. Within this range, the threshold power was constant and was around 350 kW.

Other conditions are the cleanliness of the plasma and the ion species. Titanium gettering reduces the threshold power. For example, it was reduced from 1.3 MW to 0.9MW in ICRF heating case by the gettering.

In NBI heating case, the H-mode threshold power of hydrogen plasma is more than two times as high as that of deuterium plasma.

3.CONFINEMENT CHARACTERISTICS OF LIMITER H-MODE

During the H-mode phase, density pedestal is always clearly formed, and the improvement of the particle confinement is quite certain. However the improvement of the energy confinement is not always clear, and the formation of electron temperature pedestal is sometimes very weak. Also the central temperatures do not increase appreciably during the transition. In Fig.5, dependence of the maximum global energy confinement time during the H-mode on the ellipticity κ with the plasma current around 250 kA, and the NBI heating power of 700 kW is also shown. Here, the global energy confinement time is defined by $\tau_E^G = W / (P_{tot} - dW/dt)$, where W is the plasma stored energy determined from the diamagnetic measurement, and P_{tot} is the sum of the ohmic and the additional heating power. Kaye-Goldston L-mode confinement times[4] which well represent JFT-2M NBI L-mode confinement are plotted by open circles for the comparison. When the κ is close to unity, improvement of energy confinement is very small. The rate of improvement increases in proportion to κ up to κ=1.3 and it decreases at higher κ.

Density dependence of the energy confinement can be seen in Fig.6, where $280 < I_p < 300$ kA, and $3 < q_\psi < 3.5$. Ohmic values are represented by the solid line. Closed circles show the H-mode value and the open circles are of L-mode. In both cases, the total heating power was from 870 kW to 940 kW. In H-mode case, τ_E^G continues to increase with the electron density, and finally becomes as comparable as the ohmic value in the high density region. However the global energy confinement time decreases with the increase of the heating power as the L-mode case shown in Fig.7.
Closed circles show the H-mode confinement time and the open circles show the L-mode data. For the comparison, Kaye-Goldston confinement times are represented by the dashed line. Below 800 kW, incremental confinement time τ_{inc} defined by $\tau_{inc} = d W / d P_{tot}$ is almost twice as large as that of L-mode which is around 15 ms. Above 900 kW, the incremental energy confinement time of H-mode become as low as the L-mode value. It seems that the gain of the stored energy by the transition is almost constant in high power region. This may suggest that the merit of the H-mode in JFT-2M limiter operation case is just the addition of the pedestal part due to the improvement of the particle confinement in that region.

4.CONCLUSION

On JFT-2M, H-mode was observed in a wide operational regime, κ = 1.03 to 1.55, δ = 0 to 0.57, and q_ψ=2.4 to 5.5 by NBI heating or by ICRF heating. When κ is close to 1, the improvement of energy confinement during H-mode is small and the threshold power for the transition is large. The global energy cofinement time improves about 30 % during H-mode. However it decreases with the total heating power as L-mode.

REFERENCES

[1] S.Sengoku, et al., submitted to Phys. Rev. Letter
[2] N.Suzuki, et al., "Characteristics of the H-mode in divertor configuration on JFT-2M tokamak" to be presented in this conference.
[3] H.Matsumoto, et al., "H-mode phenomena during ICRF heating on JFT-2M" to be published in Nuclear Fusion
[4] S.M.Kaye, R.J.Goldston, Nuclear Fusion 25(1985)69

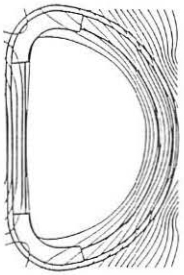

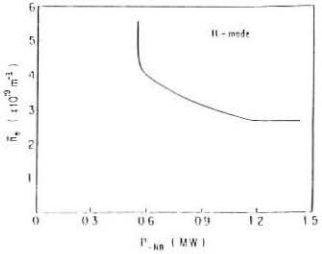

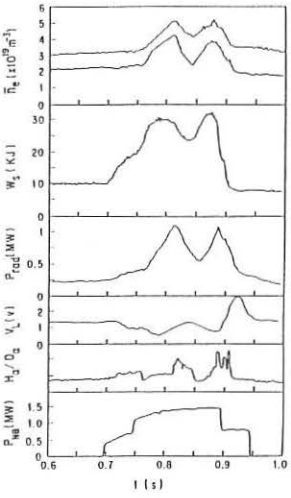

Fig. 2

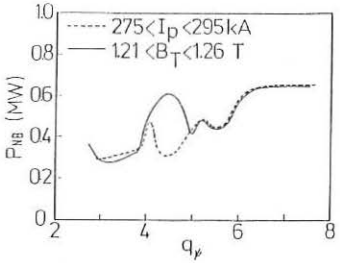

Fig. 4

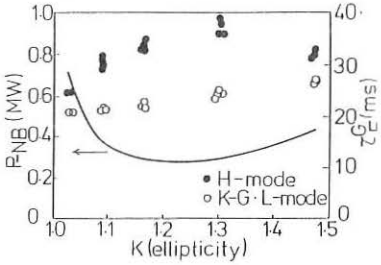

Fig. 5

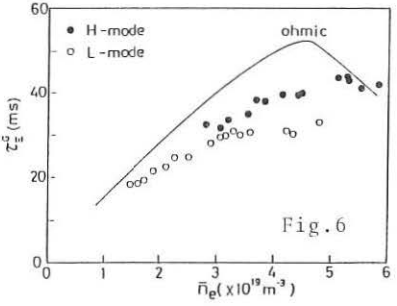

Fig. 6

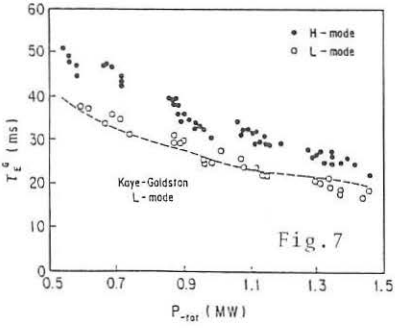

Fig. 7

H-MODE INVESTIGATIONS IN DIII-D

M. Shimada[a], K.H. Burrell, S. Ejima, D.P. Schissel, S. Allen[b], N.H. Brooks, G. Bramson, R.W. Callis, T.N. Carlstrom, A.P. Colleraine, D. Content[c], J.C. DeBoo, H. Fukumoto[d], P. Gohil, R.J. Groebner, D.N. Hill[b], R.-M. Hong, N. Hosogane[a], C.L. Hsieh, G.L. Jackson, G.L. Jahns, R. James[b], G. Janeschitz[e], A.G. Kellman, J. Kim, S. Kinoshita[d], L.L. Lao, P. Lee, J.M. Lohr, P. Lomas[f], J.L. Luxon, M.A. Mahdavi, C.P. Moeller, H. Nakamura[a], N. Ohyabu, T.H. Osborne, D. Overskei, M. Mayberry, S. Perkins[b], M. Perry[c], P.I. Petersen, T.W. Petrie, J.C. Phillips, W. Pickles[b], R. Prater, M. Rensink[b], J.T. Scoville, R.P. Seraydarian, T. Simonen[b], B.W. Sleaford, R.T. Snider, B. Stallard[b], R.D. Stambaugh, R.D. Stav, H.E. St.John, R. Stockdale, E.J. Strait, T. Taylor, J.F. Tooker, Y. Uesugi[a], R. Wood[b] and S. Yamaguchi[g]

(GA Technologies Inc., P.O. Box 85608, San Diego, Calif. 92138 USA)

[a]Japan Atomic Energy Research Institute; [b]Lawrence Livermore National Laboratory; [c]John J. Hopkins University; [d]Hitachi, Ltd.; [e]Max Planck Institut für Plasmaphysik, Garching, Fed. Rep. of Germany; [f]JET Joint Undertaking. [g]Mitsubishi Electric Corp.

INTRODUCTION

DIII-D is a large tokamak (major radius $R = 1.67m$, minor radius $a = 0.67m$), capable of producing vertically elongated limiter and divertor plasmas with high plasma current at modest toroidal field ($B_T = 2.2T$ on axis). To date, maximum plasma currents achieved are 3.0 MA in limiter plasmas (elongation in excess of 2.0), 2.0 MA in divertor plasmas (elongation 1.9). The DIII-D divertor is a reactor-compatible open divertor design, with no separate divertor chamber and no coils in vacuum. The divertor plates are two toroidal bands of carbon tiles on the bottom of the vacuum vessel. Deuterium plasmas are heated by hydrogen neutral beams (75 keV, coinjection only) and electron cyclotron heating /1/. Power levels to date are 6 MW (beam) and 1.0 MW (ECH).

PHENOMENOLOGY OF H-MODE DISCHARGES

Neutral beam heated divertor discharges in DIII-D /2/ have shown a clear transition to the H-mode (Fig. 1) which occurs after a 50-100 ms long L-mode phase. At this point, D_α radiation drops precipitously, density increases and energy confinement time improves significantly. Edge Localized Modes (ELM) limit total energy content in some discharges. During ELM-free phases, continuous rise in density and central electron and ion temperatures for periods up to 0.3 sec were observed, limited only by beam pulse length.

H-MODE THRESHOLD

The H-mode transition has a threshold in density and beam power (Fig. 2). At I_p =1 MA B_T = 2.1T, density threshold must exceed 2×10^{19} m^{-3} and power threshold is about 2.8 MW. Below the density threshold, the discharges are not sawtoothing, whereas all the shots above the density threshold have sawteeth before the beam. Therefore, the presence of sawteeth before the beam injection might be one of the prerequisites of L-H transition. In the discharges documented in Ref. 2, the ion ∇B drift was toward the divertor x-point. Discharges with inverted B_T shown in Fig. 2 are L-mode, although they have density and input power well above the threshold values with the normal B_T direction. This agrees qualitatively with ASDEX experimental results /3/ and the theoretical prediction by Hinton /4/. These discharges do have sawteeth before the beam injection, and the levels of D_α emission from the inside separatrix hit point were lower by a factor of 2 - 5 with reversed B_T, whereas levels of D_α from outside hit point did not change by reversing B_T.

EDGE LOCALIZED MODES

Repetitive bursts during the H-mode expel energy and particles from the main plasma. There are giant bursts like those indicated in Fig. 1 and also much smaller, more frequent mini-bursts. The giant bursts are observed in D_α/H_α signals, SX emission, VUV line intensities,

diamagnetic loop signals and line average density. Diamagnetic loop signals and infrared camera measurements of the divertor plate indicate that 10-20% of plasma energy is lost to the divertor during the ELM burst. Many minibursts appear in discharges with low beam power. Radiation from impurity ions saturates quickly for discharges with mini-bursts. During the burst-free phase, continuous increase in impurity radiation was observed. For H-mode discharges with mini-bursts, precursor fluctuations were observed in the magnetic probe signals located on the large major radius side of the torus. The toroidal mode number was identified as $n \approx 6$, and the mode was rotating toroidally in the direction opposite to the plasma current. The infrared camera measurements /7/ indicate that the heat pulse hits the outside separatrix 0.5–0.6 msec earlier than the inside separatrix, which suggests that the burst originates from the large major radius side.

PARTICLE RECYCLING

Particle recycling flux measured by D_α photodiode array is plotted in Fig. 3 versus line average density of the main plasma for ohmic, L and H cases. In H-mode cases, values away from the bursts are plotted. This figure shows that the particle recycling flux increases non-linearly with an increase of density for ohmic and L-mode cases, and only small increase during H-mode. L-mode recycling levels are enhanced over ohmic values by a factor of two, and H-mode recycling levels are reduced by a factor of 5-10 from L-mode levels. Particle recycling flux at the divertor is a weak function of input power and toroidal field. Wall recycling flux is lower by a factor of ≈ 30 than divertor recycling flux, and the ratio does not vary strongly with ohmic, L and H cases.

ENERGY CONFINEMENT SCALING /5/

As discussed previously, the confinement characteristics of H-mode discharges are strongly influenced by the presence of ELM's. The interval between ELM's (50 msec to 300 msec for giant ELM's and 10 msec for mini-ELM's) is so short that the discharge tends not to reach steady state before the next ELM. Furthermore, the beam pulse length available for this study (0.3 – 0.4 sec) was not long enough for ELM-free H-mode discharges to reach steady state. Therefore, for the ELM-free transport study, the dW/dt corrections were important. The confinement times with and without the dW/dt correction are shown in Fig. 4, plotted against total input power. For the discharges with input power marginally above the threshold, the discharges are dominated by many mini-ELM's so that the dW/dt correction is small. Energy confinement in H-mode discharges show a factor of three improvement over Kaye-Goldston L-mode confinement scaling /6/ (with dW/dt correction: without dW/dt correction, improvement is factor of two). Up to 6 MW of neutral beam power available, the H-mode discharges show no apparent deterioration of energy confinement. In Fig. 5, energy confinement time is shown as a function of line average density of the main plasma. Again, τ_E values with and without the dW/dt corrections are shown. Neither of these values show a strong change for the density range investigated. H-mode τ_E also shows little variation with B_T (Fig. 6). τ_E scaling with plasma current is being investigated. With high power long pulse beam sources (14 MW, 3 sec), confinement studies of ELM-free transport without a large influence from ELM's, as well as effects of radiation loss will be possible in the near future.

ACKNOWLEDGEMENT

This work was supported by the U.S. Department of Energy Contract DE-AC03-84ER51044.

REFERENCES

/1/ R. Prater, *et al.* this conference.

/2/ J. Luxon, *et al.*, Proc. of 11^{th} Intl. Conf. on Plasma Phys. and Cont. Nucl. Fusion Res., Kyoto, Japan, 13-20 November 1986, IAEA-CN-47/A-III-3.

/3/ F. Wagner, *et al.*, *Nucl. Fusion*, **25** (1985) 1490.

/4/ F. Hinton, *Nucl. Fusion*, **25** (1985) 1457.

/5/ K. H. Burrell, *et al.*, to be published in *Phys. Rev. Lett.*
/6/ S. M. Kaye, *et al.*, *Nucl. Fusion*, **25**, 65 (1985).
/7/ D. N. Hill, *et al.*, to be published in *Nucl. Fusion*.

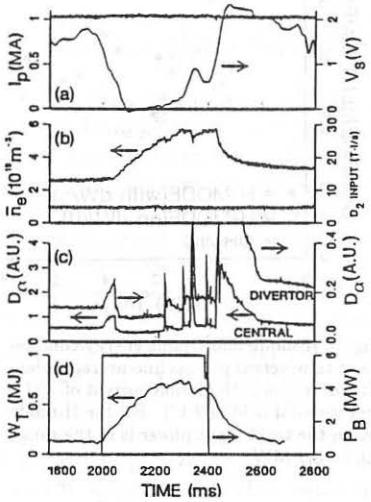

Fig. 1. (a) I_p and loop voltage at the plasma surface, (b) line-averaged density and deuterium gas injection rate, (c) D_α radiation along a horizontal chord through the plasma midplane and along a chord viewing the divertor region, (d) neutral beam power and plasma stored energy.

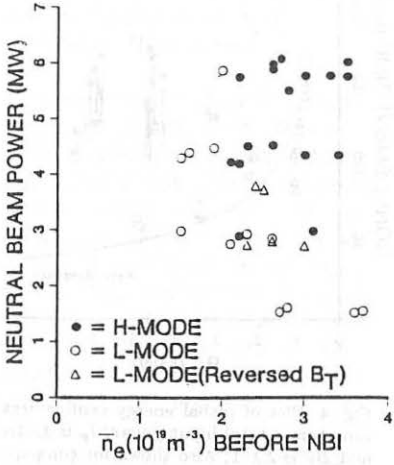

Fig. 2. Plot showing the region of parameter space where the H-mode exists. The density plotted is the plasma line-averaged density just before the neutral beams are turned on. Most of the cases are for the ion ∇B drift towards the divertor X-point. Those marked reversed B_T have the opposite polarity of the toroidal field, which means that the ion ∇B drift is away from the divertor X-point. Plasma current for all cases shown is 1 MA; the magnitude of the toroidal field is 2.1 T.

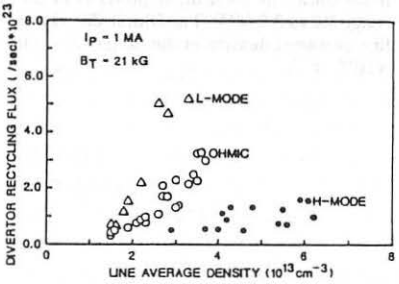

Fig. 3. Plot of particle recycling flux at the divertor versus line-average density of the main plasma. Particle recycling flux was measured by D_α photodiode array looking at the divertor region.

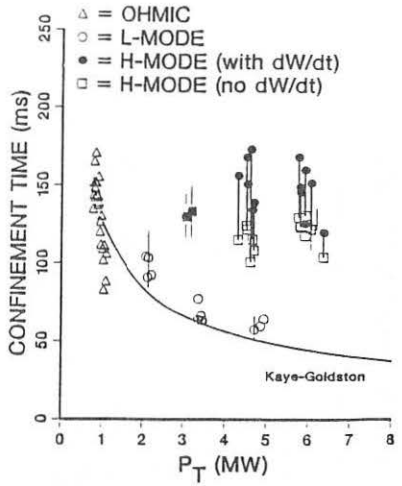

Fig. 4. Plot of global energy confinement time versus total input power, I_p is 1 MA and B_T is 2.1 T; Also shown for comparison with the L-mode data is the prediction of the Kaye-Goldston scaling law /6/.

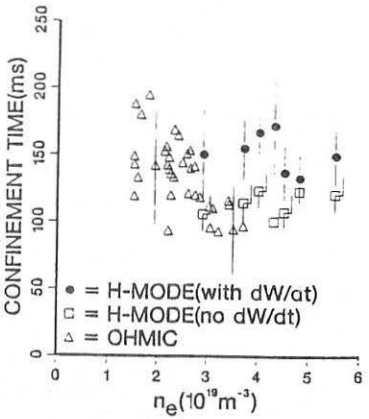

Fig. 5. H-mode and Ohmic energy confinement time versus plasma line-averaged density for a case with plasma current of 1 MA and toroidal field of 2.1 T. For the H-mode cases, the total input power is in the range 4.5 to 5.0 MW.

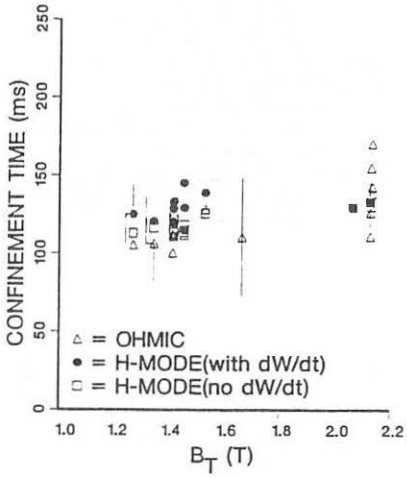

Fig. 6. H-mode and Ohmic energy confinement time versus toroidal field for a case with plasma current of 1 MA. For the H-mode data, the total input power is in the range 3.0 to 3.3 MW. The Ohmic data have line averaged density in the range 2.6 – 3.0 $\times 10^{19}$ m^{-3}.

STABILITY OF THE TOKAMAK IN THE q(o) < 1 REGIME*.

J. Manickam, C. Z. Cheng, P. H. Rutherford, W. Stodiek and A. M. M. Todd†
Princeton Plasma Physics Laboratory, Princeton, New Jersey, U. S. A.

Tokamak operation in the q(o) < 1, regime would provide several advantages: i) it would allow higher plasma current, thus providing improved confinement ; ii) it would promote stabilization of the external kink mode by permitting increased shear associated with central peaking of the j(r) profile; iii) it would provide for enhanced <ß> limits to the ballooning mode by reducing both q(o) and q(a); and iv) it would enhance the maximum ohmic heating power. However this regime is generally considered to be inaccessible due to various MHD instabilities. Principal amongst these is the resisitive m=1, n=1 mode associated with "sawteeth". Other instabilities of concern include the ideal internal kink, Mercier and ballooning modes. Several techniques are known to exist which can provide stability against the latter set of instabilities. The suppression of the resistive m=1 mode has been more problematic. Recent studies [1,2] have shown that feedback stabilization by rf heating and/or current drive is a viable technique for islands of modest size. Further, experimental evidence, corroborated by theoretical analysis [3], now exists for the existence of current profiles with q(0) substantially below unity (≈ 0.65) through many cycles of (weak) sawtooth activity. It is in this context that we consider the MHD stability, both ideal and resistive of tokamak plasmas in the q(o) < 1 regime.

Ideal-MHD stability at q(o) < 1

The ideal-MHD stability of a conventional INTOR-like D-shaped tokamak (ellipticity = 1.6, triangularity = 0.3 , R/a = 3.2) with q(o) = 0.6 and q(a) = 1.8 has been examined using a code that adjusts the pressure gradient locally to provide marginal stability against the Mercier or ballooning mode, depending on which one is more restrictive. The profile in the region near the axis is determined by the Mercier criterion and further out the ballooning mode sets the limit on the gradient (see Fig. 1). It is interesting to note that even in the region where the Mercier criterion dictates the limit on the gradient, a finite pressure gradient can be supported. This is due to the shear stabilization as well as the triangularity, which is also responsible for stabilizing the internal kink mode. The overall (stable) <ß> value is 10.0%, which exceed the Troyon-Gruber limit [$<ß>_T$% = 3.5 I(MA) / a(m)B(T)] by a factor of 1.35. The n=1 external kink mode, dominated by an m=2 component, requires a conducting wall at r_w/a = 1.15, and would otherwise be strongly unstable.

It should be noted that this requirement of a nearby conducting wall is imposed by the low q(a) rather than the low q(o), and is shared by many other designs which have q(o) > 1, and low q(a).

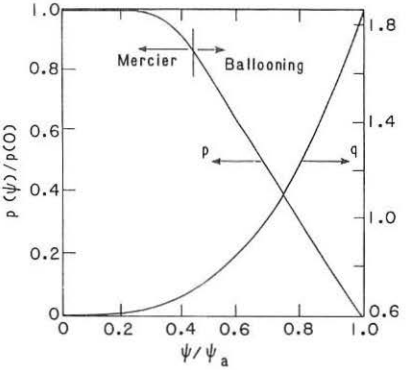

Fig. 1. Profiles of p and q versus poloidal flux, ψ, for a D-shaped tokamak, R/a = 3.2, κ = 1.6, δ = 0.3 , that is marginally stable to localized pressure-driven modes with q(o)=0.6 and q(a)=1.8. The ß values is 10% and exceeds the "Troyon limit", by a factor of 1.35.

Resistive stability at q(o) < 1

Tokamaks with q(o) < 1 generally exhibit sawtooth activity associated with a strongly-growing m = 1 resistive mode in the central region of the plasma. The successful suppression of this mode and the associated sawteeth would have substantial benefits for tokamak performance as outlined above. However, even if it is suppressed, and possibly as a consequence, higher order modes (m/n = 4/5, 3/4, 2/3 ...) with resonant surfaces in the plasma may be destabilized. We start first by addressing these modes. These modes have been studied in the cylindrical low-beta approximation and also with toroidal and finite-beta effects included. The principal mechanism for stabilizing the resistive modes is to reduce the gradient near the rational surface. This is demonstrated in Figure 2, which shows a profile which has

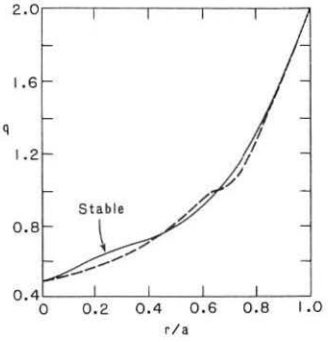

Fig. 2 q(r) profile (solid curve) optimized to be stable to all m/n resistive modes, with the exception of the 1/1, in cylindrical geometry . The broken curve shows a nearby profile unstable to m/n = 2/3 and 3/5.

been optimized to be stable to all the resistive modes, with the exception of the 1/1 in a cylindrical low beta tokamak. The sensitivity to the profile is indicated by the nearby profile (broken curve) which is unstable to the 2/3 and 3/5 modes. We note that this stabilization was achieved without a nearby conducting shell. Optimized profiles with q(o) = 0.5 and q(1) as low as 1.1 have also been obtained. As indicated earlier the 1/1 remains unstable in the cylindrical limit regardless of the profile modification. To stabilize this mode, we must invoke the aid of toroidal coupling. When the aspect-ratio is sufficiently low, then a suitable flattening of the current-profile expressed through a flattening of the q-profile can achieve stabilization of the 1/1 resistive mode. This is consistent with experimental observation as indicated in Figure 3, which shows a TEXTOR-like profile with q(o) = 0.66 and q(a) = 1.96. The substantial plateau near the q = 1 surface is responsible for stabilizing the 1/1 mode.

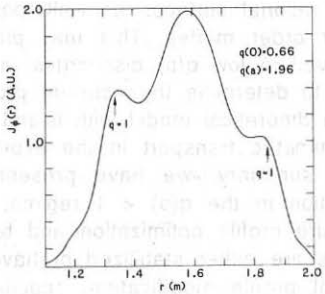

Fig. 3 TEXTOR-like J(r) profile which has been modified to stabilize the 1/1 mode. The difference between the theoretical model and the measured profile lies well within the experimental error bars.

The significance of toroidicity is observed in Figure 4, which shows the poloidal harmonic components of the radial field B_r. The substantial

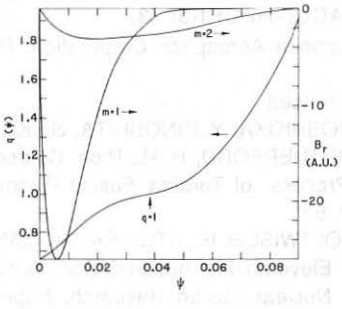

Fig. 4. Fourier decomposition of the resistive n=1 tearing mode. The m=1 component dominates, but a substantial m=2 is observed. Superposed is the q-profile showing the flattening of the q-profile near the q=1 surface. Note, that the shear is reduced but is not zero. q(o) = 0.66 and q(a) = 1.96.

contribution of the m=2 enhances the stabilization achieved through flattening q(r). We also note here that the gradient is reduced but not to zero. When the aspect-ratio is increased keeping the gradient fixed, we observe that the relative contribution of the m=2 decreases, and the 1/1 is destabilized. As the aspect-ratio is increased the shear at the rational surface must be reduced further to achieve stability. This sets a limit on the largest aspect-ratio at which complete stabilization can be achieved. Beyond that, we find that while instability persists, $r_s\Delta'$, the usual measure of tearing mode growth, remains small, opening the possibility of feedback stabilization through rf heating and/or current drive in the island. In reality, we must allow for all the possible modes to exist, and any scheme for stabilizing them must stabilize all of them simultaneously. As indicated earlier the 1/1 mode is the dominant resistive mode when $q(o) < 1$, and requires a substantial plateau near the $q = 1$, surface to stabilize it. This necessarily modifies the gradients at the other rational surfaces as well, possibly destabilizing the previous stable higher order modes. This may play a role in the sawtooth oscillations observed in low q(o) discharges, and may also provide a mechanism for MHD to determine the current profile, if we equate the profile flattening in the theoretical model with island growth and saturation and subsequent axisymmetric transport in the experiment.

In summary, we have presented the possibility of stable tokamak operation in the $q(o) < 1$ regime, where ideal modes are stabilized by pressure profile optimization and by a nearby conducting shell. Resistive modes are either stabilized or have their growth-rate sharply reduced by current profile modification, specifically through flattening q(r). Residual instabilities may be susceptible to feedback control, allowing for the possibility of tokamak operation in a "sawtooth-suppressed regime".

*Work supported by U.S. Department of Energy Contract No. DE-AC02-76-CHI-3073.

†Grumman Aerospace Corporation, Plainsboro, New Jersey, U.S.A.

References

[1] YOSHIOKA, Y.,KINOSHITA, S., KOBAYASHI, T., Nucl. Fusion 24 (1984) 565.

[2] RUTHERFORD, P. H., Proc. Course and Workshop on Basic Physical Process of Toroidal Fusion Plasma (Varenna, 1985), CEC, EUR 10418 EN, P. 531

[3] SOLTWISCH, H., STODIEK, W., MANICKAM, J., SCHLUETER, J., IAEA Eleventh International Conference on Plasma Physics and Controlled Nuclear Fusion Research, Paper CN-47/a-v-1-3 (Kyoto, 1986).

NEUTRAL BEAM AND EDGE FUELLING EFFECTS IN JET DISCHARGES

T T C Jones, E Thompson, A Gondhalekar, P J Lomas, P D Morgan, J O'Rourke, D Stork.

JET Joint Undertaking, Abingdon, UK.

1. INTRODUCTION

Understanding recycling is of considerable importance for Neutral Beam Heating (NBH) since there is strong additional edge fuelling from the limiter. Significant density increase is also observed during RF heating [1]. Density control during NBH depends on the ability of the limiter to pump (recycling coefficient $R < 1$) and low recycling may also help in obtaining favourable edge plasma conditions necessary for good energy confinement. The density behaviour of high power ($\lesssim 10$ MW) NBH JET plasmas has been compared with the predictions of a simple model describing the beam fuelling, and recycling at the various graphite surfaces of the machine (conventional outer limiters, inner wall and X-point protection tiles). The comparison supports the validity of the model, and the consequences for the material properties are described. Since, in principle, it should be possible to derive the parameters of the model rigorously from particle transport within graphite (and in the plasma) the results may provide a useful constraint for the more materials-oriented recycling modelling in tokamaks currently in progress, e.g. [2,3].

2. DENSITY BUILD UP WITH NBH FOR OUTER LIMITER DISCHARGES

Figure 1 shows the typical behaviour of volume averaged electron density $\langle n_e \rangle$, edge recycling fluxes ϕ_L and ϕ_W at the limiter and vessel wall respectively (from H_α measurements), and recycling coefficient R for an outer limiter NBH plasma. Figure 1 defines the asymptotic beam fuelling efficiency ε; the gas and beam fluxes ϕ_g and ϕ_b are also shown. The principal features are: (i) recycling takes place mainly at the limiter; (ii) there is a transient increase in recycling flux on application of NBH ($R>1$) resulting in an initial beam fuelling efficiency >1; (iii) an asymptotic fuelling efficiency $\varepsilon < 1$ which implies R must tend to a value < 1, but since $\phi_b \ll \phi_L$ the asymptotic value of R must remain close to 1. The behaviour suggested applying a model based on dynamic equilibrium between the plasma particles and particles retained on the limiter for some finite time before being re-emitted. The initial transient influx from the limiter can be explained by a disturbance of equilibrium established prior to application of NBH, towards a new equilibrium favouring the plasma. Ignoring losses, the equations describing this exchange can be written:

$$\dot{N}_p = -\alpha(1-r)N_p + \beta N_s + \phi_b \qquad (1)$$

$$N_s + N_p = N_o + \phi_b t$$

where N_p = plasma electron content; N_s = H + D content of limiter surfaces

$N_o = (N_s + N_p)\ (t=0)$; ϕ_b = beam atom flux;

$\alpha^{-1} = \tau_p$ = plasma particle confinement time;

$\beta^{-1} = \tau_s$ = limiter surface residence time;

r = limiter surface prompt reflection coefficient.

The solution of (1) subject to the boundary condition $N_p(t=0) = N_p^o$ is:

$$N_p = N_p^o + \Delta N_p^\infty\ (1-\exp -t/\tau) + \varepsilon\phi_b t \qquad (2)$$

where $\varepsilon = \beta/(\beta + \alpha\ (1-r))$; $\tau = 1/(\beta + \alpha\ (1-r))$;

and $\Delta N_p^\infty = \varepsilon N_o + \alpha(1-r)\phi_b/(\alpha(1-r) + \beta)^2 - N_p^o$

The function (2) was fitted to the experimentally measured N_p for many outer limiter discharges and hence best-fit values for $\alpha(1-r)$ and β obtained. The fits were generally very good (eg. fig 2). The total recycling flux can be written:

$$\phi_R = \alpha r N_p + \beta N_s \qquad (3)$$

The first term is the prompt reflected flux and the second the re-emitted particle flux. The initial increase in ϕ_L as measured (eg. fig 1) is not instantaneous at t=0, but typically has a rise time of ~ 200 ms; if power flux into the scrape-off layer is responsible for enhanced re-emittance, the finite beam slowing down time (~ 100 ms) has to be taken into account. The fitted values of τ are typically ~ 0.8 s and during the main transient characterized by τ, ϕ_L always 'turns over' as the density ie. the second time derivatives of N_p and ϕ_L are of the same sign. It can be proved using (3) that necessary and sufficient conditions for the latter are that $\alpha r > \beta$ and $r > \varepsilon$. Figure 3 shows plots of $\tau_p^* = 1/\alpha(1-r)$ and $\tau_s = 1/\beta$ versus ε obtained by fitting (2) to the measured $N_p(t)$. The asymptote for τ_p^* as $\varepsilon \to 1$ supports the fact that $r > \varepsilon$, as expected. Also, when r was calculated using values of τ_p from the standard global particle balance equation, using $\tau_p^* = \tau_p/(1-r)$, it was again found that $r > \varepsilon$. Thus the variations in ε are largely explained by changes in r.

3. DENSITY RISE AT ONSET OF H-MODE

Equation (2) well describes the density increase observed at the onset at t = 0 of the H-mode [4]. The initial fuelling rate is typically ~ 2-3 times ϕ_b, asymptotically approaching a value of $\varepsilon \leq 1$. Here, the initial increase is considered to be due to an instantaneous increase in τ_p, and ϕ_R measured at the X-point tiles instantaneously drops, consistent with the drop in the reflected flux $\alpha r N_p$ [5].

4. DENSITY CONTROL USING He CONDITIONED INNER LIMITER

The foregoing discussion assumes that the limiters are 100% saturated, i.e. all the strongly binding traps (~ 4 eV) are occupied. Such strongly bound H or D atoms can only be displaced by incident ions and the displaced atoms repopulate all available traps, including those of lower binding energies, on a statistical basis. A model based on this process [6] predicts an inversely temperature dependent saturation H + D content

N_{SAT} for graphite; at saturation for each incident ion exactly one H or D atom is promoted from the trapped population (N_T) to a weaker trap from which thermal detrapping is possible, and adds to the mobile, diffusing population (N_{free}). Assuming the build-up to saturation is approximately exponential with total fluence the probability of an incident ion adding to N_T is:

$$P_{trap} = 1 - N_T/N_{SAT} = 1 - (N_s - N_{free})/N_{SAT} \quad (4)$$

and a modified set of particle balance equations may be written:

$$\begin{aligned} \dot{N}_p &= \alpha(1-r)N_p + \beta N_{free} + \phi_b \\ N_s &= N_T^o + N_{free}^o + \phi_b t - N_p \\ \dot{N}_{free} &= \alpha(1-r)N_p(1-P_{trap}) - \beta N_{free} \end{aligned} \quad (5)$$

where N_T^o, N_{free}^o refer to $t = 0$

Integrating equations (5) shows that (i) for sufficiently depleted surfaces ($N_T^o/N_{SAT} < 1$) the asymptotic beam fuelling efficiency $\varepsilon \to 0$; (ii) $\dot{N}_p/\phi_b > 1$ for small t, depending on the value of N_{free}^o established by the target plasma; (iii) for 100% saturation ($N_T^o/N_{SAT} = 1$) this model reduces to that described in section 1. These features are observed in the density behaviour of NBH discharges run on the inner wall tiles after He discharge conditioning, and in L-mode X-point discharges (figure 4).

5. CONCLUSIONS

The density rise observed with NBH and at the onset of the H-mode can be satisfactorily described using a simple particle balance model. The fitted parameters show that H or D atoms retained on graphite plasma limiters have a characteristic residence time ≥ 1 s. The magnitude of the density increase is largely dependent on the transient influx from the limiter, and not simply on the beam fuelling rate. Density control can be obtained by sufficient depletion of the H + D content of the limiters and other surfaces interacting with the plasma, e.g. by He discharge conditioning. This method has been successfully employed in JET for the inner wall tiles which present a larger area and operate cooler than the outer limiters.

REFERENCES

[1] M Bures et al, contributed paper, this conference.

[2] J Ehrenberg, S A Cohen, L deKock et al, contributed paper, this conference.

[3] D Heifetz, private communication.

[4] A Tanga, XI IAEA Conference on Plasma Physics and Controlled Nuclear Fusion Research, Kyoto, Japan, 1986.

[5] P D Morgan and J O'Rourke, this conference.

[6] D K Brice, B L Doyle and W R Wampler, J.Nucl.Mater. 111/112 p.598.

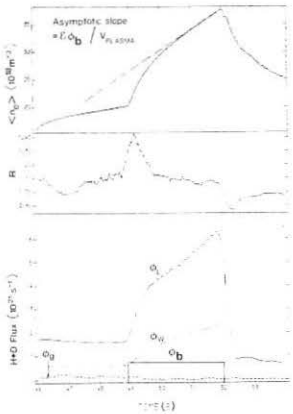

Figure 1 Input fluxes and evolution of plasma density for 5.2 MW H° injection into a 4 MA, 3.4 T D plasma, and definition of asymptotic beam fuelling efficiency ε, where V_{PLASMA} = plasma volume.

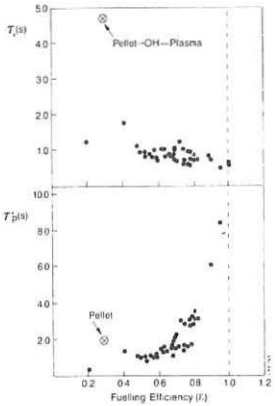

Figure 3 Dependence of best fit values of τ_p^* and τ_s on ε for outer limiter NBH discharges, plus one pellet injection case, calculated setting ϕ_b = 0 in (2) and assuming α,β,r do not change after the pellet.

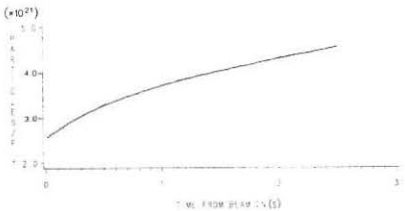

Figure 2 Time evolution of measured plasma electron content during NBH with function (2) fitted for an outer limiter discharge.

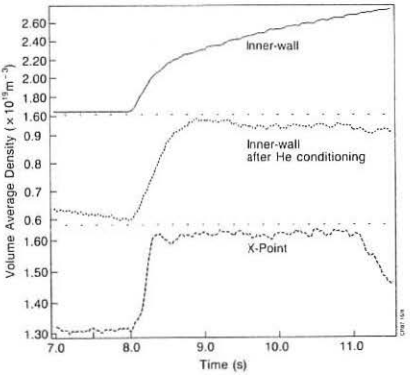

Figure 4 Density response for an unconditioned inner wall, He discharge conditioned inner wall, and double null separatrix plasma on application of NBH at t = 8.0 s in each case.

TRANSIENT STABILIZATION OF SAWTEETH BY ADDITIONAL HEATING IN JET

D J Campbell, D V Bartlett, V P Bhatnagar[1], M Bures, G A Cottrell, P A Duperrex[2], C D Challis, J G Cordey, A W Edwards, C Gormezano, C W Gowers, R S Granetz, J H Hamnen[3], T Hellsten, J Jacquinot, E Lazzaro, P J Lomas, N Lopes Cardozo[4], P Mantica[5], J A Snipes, D F H Start, D Stork, P E Stott, P R Thomas, E Thompson, K Thomsen, G Tonetti[2] and J A Wesson

JET JOINT UNDERTAKING, ABINGDON, OXON OX14 3EA, UK.
[1] EUR-EB Association, LPP-ERM/KMS, B-1040 Brussels, Belgium.
[2] CRPP/EPRL, 21 Avenue des Bains, CH1007 Lausanne, Switzerland.
[3] Swedish Energy Research Commission, S-10072 Stockholm, Sweden.
[4] FOM Instituut voor Plasmafysica, 3430 Be Nieuwegein, The Netherlands.
[5] EURATOM-CNR Fusion Association, Milan, Italy.

1 Introduction

During additional heating in JET, sawtooth activity normally dominates the evolution of the plasma core, limiting plasma temperature and density. However, in some experiments with auxiliary powers of above 5 MW (ICRH plus NBI, ICRH alone, or NBI alone), the plasma undergoes a transition to a new regime in which the sawtooth instability is suppressed for periods of up to 1.6 s and the level of long wavelength coherent mhd activity is very low. The long quiescent period (3-5 energy replacement times) allows plasma transport and confinement to be studied in a regime free from mixing due to sawteeth, and permits an evaluation of the possible benefits of sawtooth stabilization for near-ignition conditions.

2 Experimental Observations

Experiments with additional heating have been carried out in JET at total power levels of up to 19 MW, using an NBI system capable of delivering up to 10 MW of 80 keV deuterons into the torus, and an ICRH system which has injected up to 8 MW into the plasma [1]. The experiments reported here utilised NBI co-injection and on-axis ICRF resonance heating. Under such conditions, the sawtooth and mhd activity exhibit two distinct types of behaviour. In the more usual [2,3], the sawtooth period increases by a factor of 2-3 relative to the ohmic phase of the discharge, ie up to ~0.5 s, and the relative modulation $T_e(max)/T_e(min)$ increases to ~2 compared to 1.1-1.2 during ohmic heating. A variety of mhd activity accompanies the sawteeth.

The second, newly observed and significantly different type of behaviour is illustrated in fig 1. The rise of the 'sawtooth' beginning at 9.6 s exhibits weak mhd activity. In a number of cases, a small partial sawtooth also occurs. However, after 300-400 ms the mhd activity becomes quiescent ($\tilde{B}_\theta/B_\theta \leq 5.10^{-6}$). In many cases both the density and stored plasma energy rise continuously until the sawtooth collapse occurs, although the central electron temperature saturates. This saturation lasts for ~0.7 s (and can last for up to 1.4 s), during which no low m,n number mhd activity is

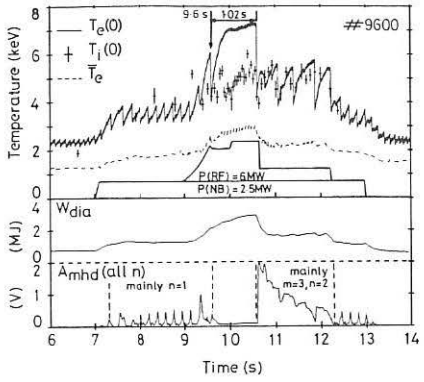

Fig 1: Evolution of a JET discharge in which sawtooth stabilization occurred.

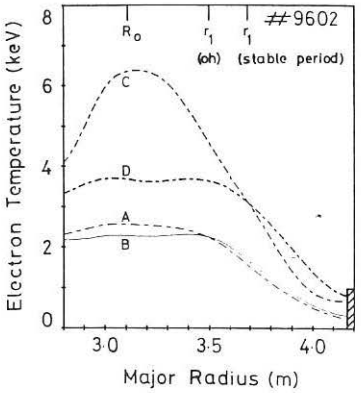

Fig 2: Electron temperature profiles before (A) and after (B) an ohmic sawtooth, and before (C) and after (D) the collapse terminating a stable period such as that in Fig 1.

observed by ECE, soft X-ray diagnostics, or magnetic pick-up coils. Throughout this period, therefore, the m=1 mode appears to be stabilized. A significant consequence is that the global energy confinement time can improve by up to 20% relative to the normal sawtoothing regime.

The stable period is terminated by an m=n=1 instability which exhibits the dynamics of the normal sawtooth collapse in JET [4], but, in addition, an m=3,n=2 mode is often destabilized, as shown in fig 1. This may be due to changes in the current profile during the stable period which could lead to a steep current gradient at the q=3/2 surface at the sawtooth collapse (note that the edge value of q remains virtually constant). The observed expansion of the sawtooth inversion radius r_1, from ~40 cm during the normal sawtoothing regime to 50-60 cm at the collapse terminating the quiescent period, provides further evidence for changes in the current profile during this time. Fig 2 illustrates the expansion of the inversion radius as observed in the electron temperature profiles. More precise measurements with an ECE polychromator and soft X-ray tomography confirm this result. In discharges where the (3,2) mode is quenched during the auxiliary heating phase, or is not excited, subsequent long stable periods can occur (up to 1.6 s in duration). However, a mode with n=1 (usually m=2) may also be destabilized [5]. In these cases, the mode locks after ~50 ms, leading to a significant deterioration in central temperatures, and a degradation of ~25% in global energy confinement time.

The quiescent regime has been obtained under a wide range of conditions in JET (I_p=2-5 MA, B_φ=2-3.4 T, q_ψ=3.4-6, $\bar{n}_e$=1.5-4.$10^{19}m^{-3}$), but no crucial parameter has yet been identified. The regime occurs in plasmas limited on

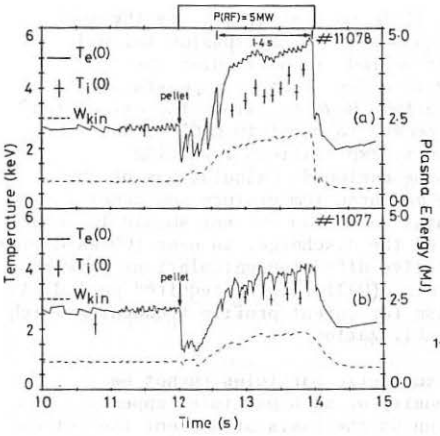

Fig 3: (a) Sawtooth stabilization following pellet injection.
(b) Similar discharge with 'locked' n=1 mode. Note lower stored energy.

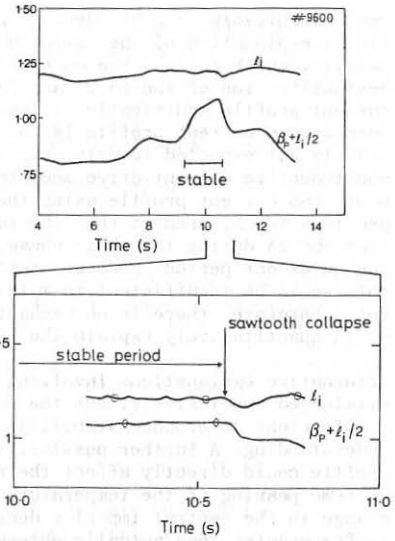

Fig 4: Behaviour of l_i and $\beta_p+l_i/2$ during a discharge in which stabilization occurred.

the outer limiter, the torus inner wall, or by a magnetic separatrix. It was first observed during combined heating (NBI plus ICRH), but has subsequently been attained with ICRH alone, in $He^3(H)$, D(H), and $D(He^3)$ minority heating schemes, and with NBI alone. Sawtooth stabilization has also been observed following pellet injection into ICRF heated discharges, and such a case is shown in fig 3a. Significantly, in similar discharges where stabilization did not occur (fig 3b) a locked n=1 mode was observed accompanied by substantially degraded confinement.

3 Analysis

Detailed measurements of the current profile j(r) in ASDEX have shown that sawtooth stabilization by lower hybrid current drive is due to a broadening of the current profile which raises q(0) above 1 [6]. We have investigated the evolution of j(r) during the quiescent period in JET by analysis of magnetic measurements using the JET equilibrium codes [7]. While the analysis indicates that q(0) lies in the range 0.9-1.0 during this time, the systematic uncertainty (~20%) in the derived value of q(0) makes it impossible to determine unambiguously whether q(0) is above or below 1. The most significant result obtained is that the plasma inductance l_i remains constant, or decreases slightly (fig 4), indicating that j(r) is not peaking, in spite of the strong peaking of T_e.

The good agreement between observations of the sawtooth collapse in JET [4], and the predictions of an ideal instability model [8] suggests that a

mechanism involving a broadening of j(r), so that q(0)>1, is the most likely explanation of the sawtooth suppression. The substantial mhd activity which follows the quiescent period, in particular the destabilization of the (3,2) and (2,1) modes, further suggests that a current profile modification is occuring. However, since the calculated beam-driven current profile is too peaked to maintain q(0)>1, and since ICRH is not expected to drive currents, explanations involving non-inductive current drive seem to be excluded. Calculations of the bootstrap current profile using the measured temperature and density profiles in JET predict that the total bootstrap current should increase, from ~50 kA during the ohmic phase of the discharge, to over 100 kA during the quiescent period. However, resistive diffusion calculations show that this would be insufficient to maintain q(0)>1 for the required period. As yet, therefore, there is no mechanism for curent profile broadening which would quantitatively explain the stabilization.

Alternative explanations involving energetic particles cannot be eliminated conclusively, but the density of such particles appears insufficient to produce stabilization on the basis of current theoretical understanding. A further possibility is that a change in the impurity profile could directly affect the rate of current diffusion. However, the extreme peaking of the temperature profile would necessitate a substantial change in the central impurity density of, perhaps, a factor of 3, which is far greater than actually observed.

The most significant aspect of these results is that it may be possible to suppress sawteeth without active stabilization measures. However, the present transient stabilization, can be followed by a deterioration of the plasma behaviour at the sawtooth collapse. A further important point is that the long stable period (3-5 energy confinement times) allows potential advantages of full sawtooth stabilization to be evaluated. It is found that the energy confinement time can be 15-20% higher than in the normal sawtoothing regime, but this appears to be the result of allowing the plasma to approach equilibrium rather than an improvement in transport. The major advantage is expected to be a significant enhancement of the D-T fusion yield which, in the near-ignition regime, is approximately proportional to $n_i^2 T_i^2$. Our calculations predict a substantial gain in fusion power production if the appropriate profiles can be achieved.

4 References

[1] P H Rebut et al, Proc 11th Int Conf on Plasma Phys and Contr Fus Res, Kyoto, Japan, 1986.
[2] D J Campbell et al, ibid.
[3] R D Gill et al, Proc 13th EPS Conf, Schliersee, W Germany, 1986, 1 21.
[4] A W Edwards et al, Phys Rev Lett, 57 210 (1986).
[5] J A Snipes et al, this Conference.
[6] K McCormick et al, Phys Rev Lett, 58 491 (1987).
[7] D J Campbell et al, JET Preprint JET-P(86)46 (to be published).
[8] J A Wesson, Plasma Phys Contr Fus **28(1A)** 243 (1986).

DENSITY PERTURBATIONS AT RATIONAL q–SURFACES FOLLOWING PELLET INJECTION IN JET

A. Weller[(a)], A. D. Cheetham, A. W. Edwards, R. D. Gill,
A. Gondhalekar, R. S. Granetz, J. Snipes, and J. Wesson
JET Joint Undertaking, Abingdon, Oxon OX14 3EA, United Kingdom

[(a)] *Permanent address : EURATOM-IPP Association, Garching, W. Germany*

Introduction – The ablation of pellets injected in JET [1] produces a pronounced resonance effect at rational q – values of 1 and 3/2. After ablation, $m = 1, n = 1$ and $m = 3, n = 2$ structures are observed as compact snake-like perturbations [2] by the soft x-ray cameras. The "snake" oscillation is caused by a rotating localised region of higher density, which can persist for $\geq 2\ s$. The observed effect can be used to measure the dynamic behaviour of the $q = 1$ and $q = 3/2$ surfaces. In particular, new information on the evolution of the q – profile during sawtooth collapses is obtained. The characteristics of these perturbations, their relationship to rational q – surfaces, and possible explanations for the existence of the "snake" are presented.

Observation of the snake oscillation – Two soft x-ray cameras[3,4] containing 100 detectors view the plasma with a spatial resolution of $\approx 7\ cm$ in orthogonal directions at the same toroidal position as the D_2 pellet injector. Pellets of 2.2×10^{21} or 4.5×10^{21} atoms are injected in the horizontal plane into ohmically heated JET plasmas ($2 \leq B_T(T) \leq 3$, $3 \leq I_p(MA) \leq 3.6$) with velocities of $\sim 1\ km/s$. Their penetration and ablation is deduced by observing the intense bremsstrahlung emission from interactions of plasma electrons with pellet particles, using the vertically mounted soft x-ray camera (fig. 1).

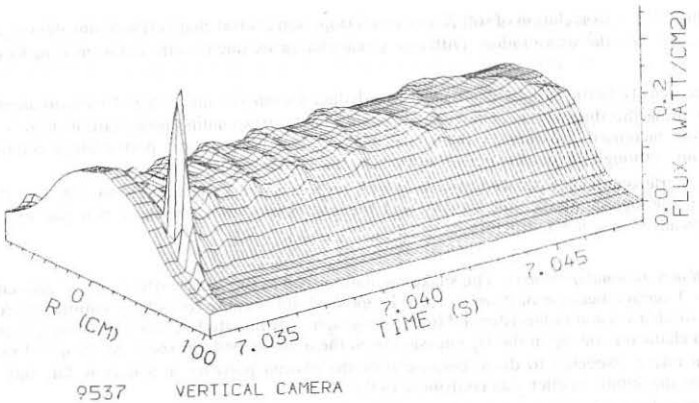

Fig. 1 : Soft X–ray flux (vertical camera, 140 μm Be – filter) around the time of pellet injection showing the initial peak from ablation and the subsequent "snake" oscillation.

Immediately after pellet ablation, the x-ray emission decreases due to the cooling of the plasma. The most striking remaining effect is the observation of a snake-like modulation superimposed on a

symmetric emission profile. The snake is caused by the rotation of a small region of plasma with usually enhanced x-ray emission. The dimensions of this region and its position in the plasma can be accurately determined both directly from the experimental data, and also by tomographic reconstruction techniques. A typical snake has dimensions of of ~ 15 *cm* (FWHM) in radial and of ~ 25 *cm* in poloidal direction.

Plasma parameters in the snake region – The temperature and density in the snake region are determined from an ECE polychrometer and a 2 *mm* microwave transmission interferometer (fig. 2).

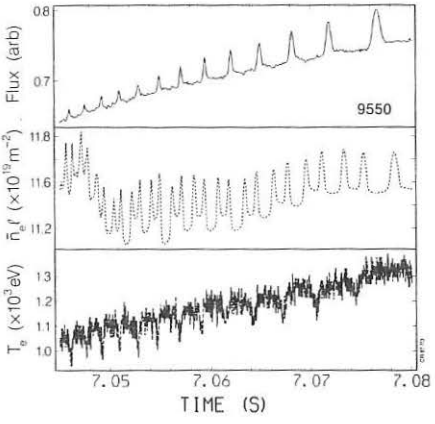

Fig. 2 : Correlation of soft X-ray signal (top, non central channel) with line density and T_e at the snake radius. Different signal phases are due to different measuring locations.

Large density perturbations $\delta n_e/n_e \lesssim 1$ are deduced from the line integral measurements of the density using the dimensions of the snake region. The corresponding temperature drop is smaller, indicating increased pressure in the snake region. The temperature perturbation reduces after ~ 100 *ms*, although the density perturbation remains unchanged.

The interferometer is displaced toroidally with respect to the x-ray cameras by 135° and the phase between the signals of the line density and the soft X-ray emission show that the snake has a topologically $m = 1, n = 1$ structure.

Relation to rational q-values – The snake oscillation seen in fig. 1 is clearly an effect associated with the $q = 1$ surface because of its $m = 1, n = 1$ topology and because its radial location coincides with the sawtooth inversion radius (derived from tomographically inverted signals). Moreover, at this same radius a characteristic dip in the D_α emission from the ablating pellet is seen. At the $q = 1$ radius the ablation rate is expected to drop, because only the plasma particles in a narrow flux tube, which intersects the ablating pellet, can contribute to the ablation.

Another observation is that the snake oscillation is more frequently seen, when the pellet is injected just before a sawtooth collapse. At this time the $q = 1$ radius has probably grown to its maximum value and the $q = 1$ surface is more easily accessible to the injected pellet, as shown later.

Occasionally, in addition to the snake at $q = 1$, a perturbation of higher symmetry is also seen. Analysis of the complicated soft X-ray signal patterns reveal a $m = 3, n = 2$ structure. A clear correlation with $m = 3$, $n = 2$ magnetic signals is also found, and the location of the perturbation coincides with the calculated position of $q = 3/2$.

Lifetime of the snake – The local density enhancement at $q = 1$ can persist for $\geqslant 2\ s$ without a significant decay or spreading during that time. This is even seen after several sawteeth which leave the structure unaffected. Fig. 3 shows the snake modulation during two 100 *ms* time intervals of the same discharge. Generally, the rotation slows down after some 100 *ms* and the snake is locked between sawtooth collapes (fig. 3 b, ~ 0.9 *s* after pellet ablation). During the sawtooth collapse a rotation is initiated for a short time.

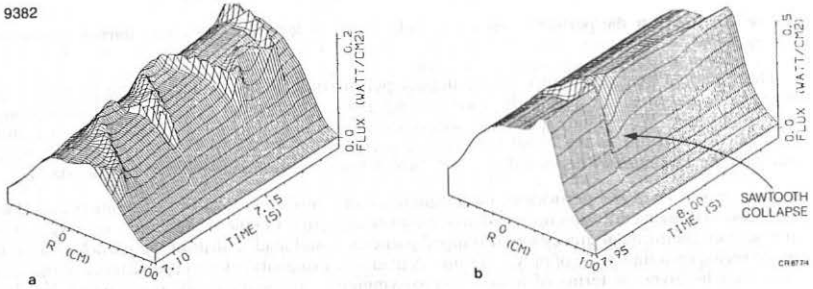

Fig. 3 : X – ray emission (vertical camera) showing a long lasting snake. In the later phase (b) the oscillation has locked. The sawtooth does not change the snake.

The long lifetime of the snake can be used to make a continuous determination of the position of $q = 1$. In particular, a large rapid inward shift of the $q = 1$ radius is seen during the sawtooth collapse phase followed by a slow expansion of the $q = 1$ surface after the collapse (fig. 4).

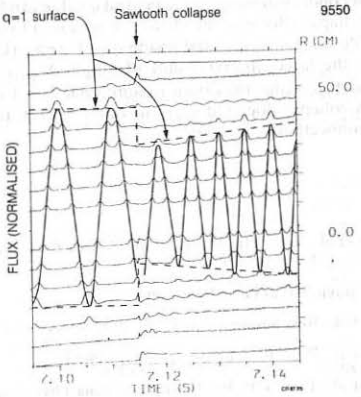

Fig. 4 : X – ray signals during a sawtooth crash, which shows the inward shift of $q = 1$ derived from the snake oscillation.

Discussion – In the case of an axisymmetric equilibrium, perturbations of temperature δT and density δn are expected to spread out poloidally by collisional diffusion along the magnetic field lines. Around $q = 1$, the spreading times scale like :

$$t_{spread} \sim \frac{1}{(1-q)^2}$$

Given the plasma parameters in the "snake" region, these values are found to be

$$t_{spread} \sim 100\ \mu s \text{ for } \delta T \quad \text{and} \quad t_{spread} \sim 10\ ms \text{ for } \delta n$$

These are times for the perturbations to fall below a 10 % level outside a very narrow region with $|1-q| < 10^{-2}$.

The observed long persistence of the density perturbation therefore implies the *formation of a magnetic island* at $q = 1$ due to the local cooling and the associated current perturbation along a helical flux tube. We estimate that a magnetic island of several centimeters width would grow within a time of $\sim 100\ \mu s$ due to the initial temperature perturbation $\delta T/T \geq 0.2$. During this time ablated particles are continuously deposited at $q = 1$, which later are confined effectively in the island.

The *persistence* of the particles in the magnetic island, however, is difficult to understand. First, neoclassical (banana diffusion regime) particle confinement times in the snake region are only $\sim 0.3\ s$; and second, the toroidal precession of trapped particles would lead to drift of the particles out of the snake region on a time scale of only $\sim 15\ ms$. A plausible explanation for the persistence of the snake may then be given in terms of a new non-axisymmetric stationary equilibrium, which has been accessed by the pellet injection. The higher density in the snake region could be maintained by inward convection, in a similar but not understood manner to the inward convection of particles in the bulk of the tokamak plasma.

Another observation is that the temperature perturbations become very small after $\sim 100\ ms$. However, calculations show, that an *island* with the dimensions of the snake can be *maintained* by $\delta T/T \approx 10^{-2} - 10^{-1}$, which is too small to be detected. The required current perturbation could also be produced by a local change of Z_{eff} due to the electric potential associated with the locally enhanced deuteron pressure.

The observed effect gives information about the q – *profile* : First, the radial position of $q = 1$ (and $q = 3/2$) are derived, and secondly estimates of the central q value can be made from the radial shift of $q = 1$ during a sawtooth collapse. Because the change in q caused by sawteeth in JET is $\Delta q \sim 0.02$ only[5], a smooth q – profile has to be very flat inside $q = 1$ with $q(0) \sim 0.97$ before the sawtooth crash in order to produce the large observed shift of $r_{q=1}$ ($\Delta r_{q=1}/r_{q=1} = -1/3$, fig. 4). For the discussion of sawtooth models it is also important to note, that $q = 1$ exists throughout the sawtooth cycle, and that a sawtooth collapse does not seem to cause a large rearrangement of the magnetic topology (eg. complete reconnection at $q = 1$).

References

[1] A. Gondhalekar et al., Proc. 11th Int. Conf. on Plasma Phys. and Contr. Nucl. Fusion Research, Kyoto, IAEA-CN-47/I-I-6, (1986)

[2] A. Weller et al., submitted to Phys. Rev. Lett.

[3] A.W. Edwards et al., Rev. Sci. Instrum. 57 (8), 2142 (1986)

[4] A.W. Edwards et al., Phys. Rev. Lett. 57 (2), 210 (1986)

[5] D.J. Campbell et al., Proc. 11th Int. Conf. on Plasma Phys. and Contr. Nucl. Fusion Research, Kyoto, IAEA-CN-47/A-VII-5, (1986)

[6] J.A. Wesson et al., Proc. 11th Int. Conf. on Plasma Phys. and Contr. Nucl. Fusion Research, Kyoto, IAEA-CN-47/E-I-1-1, (1986)

PELLET INJECTION EXPERIMENTS ON THE TFR TOKAMAK

TFR-Group (presented by H.W. DRAWIN)
Association EURATOM-CEA
Département de Recherches sur la Fusion Contrôlée
Centre d'Etudes Nucléaires de Cadarache
13108 Saint Paul Lez Durance CEDEX/FRANCE

ABSTRACT :

The essential results of the pellet injection experiments carried out on the TFR Tokamak from 1983 until the shut-down of the machine in June 1986, are summarized. Hydrogen and deuterium pellets, occasionally doped with neon, were injected into ohmically and also additionally NB and ECR heated plasmas. Direct observation of the pellet trajectories yields insight in the properties of the ablation clouds. Measurements of the bulk plasma show a rapid temperature evolution during and just after the ablation process. The electron density changes radially on a much longer time scale. Transport simulations in particular for multi-pellet injection leads to the conclusion that the transport coefficients for the density transport are not drastically modified during the density relaxation phase.

THE PELLET INJECTORS

The pellets were injected pneumatically using either a single-shot extrusion device built by the RISØ National Laboratory or a multi-pellet injector (6 pellets at maximum) developed by the SBT, CEA Grenoble. In both cases, the average number of atoms was $N_p \simeq 8.10^{18}$-$1.5.10^{19}$ per pellet, the velocity range was $v_p \simeq 600$ - 700 m/s. Injection was radially into the TFR plasmas (major radius $R_o = 98$ cm, minor plasma radius $a = 18$ - 20 cm, toroidal induction $B_\phi = 1.9$ to 4.8 T, plasma currents $I_p = 100$ - 300 kA). The plasma density was increased by 25 - 50 % by one pellet.

THE ABLATION CLOUDS, PELLET PENETRATION

The pellet trajectories were viewed under an oblique angle with respect to the injection plane, and independently by a photomultiplier equipped with an interference filter (H_α,H_β) and connected to a rapid acquisition device.

Injection into ohmically heated plasmas : Pellets were injected into pure ohmically heated plasmas under very different conditions. The photographies show very different ablation features depending on the plasma parameters [1].

Above some critical value of n_e and T_e, the visible part of the pellet trajectory degenerates into a sequence of alternating bright and dark zones corresponding to maxima and minima of the photomultiplier signal. One observes nearly straight lines extending toroidally with a weak poloidal inclination, lines crossing each other under angles up to 18 degrees [1,2], small crescents or a kind of ellipse [3]. The trajectories are always bent in the electron current direction.

Reversal of the toroidal magnetic field direction reverses the weak poloidal inclination of the striations. Assuming the striations to extend along the actual magnetic field lines has allowed to determine the safety factor q(r) as a function of radius [4] from "well-behaved" ablation clouds.

From the Stark-broadened deuterium lines follow a time-averaged electron density of $\sim 10^{17}$ cm^{-3} and L.T.E. temperatures ranging from 1.6 eV to appr. 20 eV. These values are in broad agreement with the neutral shielding model [1,4].

Injection into neutral-beam-heated plasmas : The experiments were made at moderate plasma densities (line density $n_e l \simeq 2.10^{15}$ cm^{-2}, $I_p \simeq 205$ kA at $B_\phi = 4.7$ T, ohmic power 230 kW). The neutral beam power injected into the plasma was 250 kW. There was practically no difference in the ablation between the ohmic and NB heated plasmas. As the pellets penetrate only until a radius of $\simeq 12 - 13$ cm whereas the fast neutrals are captured and slowed down within $r \leq 8$ cm, there is no direct interaction between pellet and beam-originating particles. This also holds for larger radii where the beam particle density is extremely low.

Injection into electron-cyclotron resonance (ECR)-heated plasmas : A drastic change of the ablation process is seen during ECR heating [3]. In almost all cases the pellets were ablated in the very outer part of the plasma of mean density $\bar{n}_e \simeq 1.2.10^{13}$ cm^{-3}. The striations disappeared, a broad ablation cloud extends toroidally over the whole observable region ($\simeq 25$ cm toroidally). The H_β emission shows a sharp maximum without any particular structure. For further details see Ref. [3].

FAST EVOLUTION OF PLASMA PARAMETERS

A common feature of pellet injection experiments is the very fast drop of T_e and a very fast evolution of the radial T_e profile. This response of the bulk plasma to single pellet injection has been studied for standard TFR ohmic discharges ($B_\phi = 4$ T, $I_p \simeq 180$kA, $\bar{n}_e \simeq 4.10^{13}$ cm^{-3}) together with magnetic activity and small scale fluctuations.

1. Electron temperature : The time-dependent temperature profile $T_e(r,t)$ was obtained from ECE measurements at 6 different plasma radii. The temperature decrease occurs simultaneously at all radii, although the pellet reaches only after an ablation time of appr. 120 µs the radius r = 11 cm corresponding to a penetration depth of $L_p \simeq 8$ cm. A cold front (CF) propagates towards the center with increasing velocity which finally exceeds the pellet velocity. Therefore, cooling of a given magnetic surface must be due to radial heat transport rather than due to deposition of cold matter. The temperature decrease stops abruptly at all radii at the end of the ablation process. There exist cases for which the quasi-instantaneous temperature drop ends at the q = 1 surface. Inside the q = 1 surface the temperature decrease is slower and lasts between 200 and 500 µs. It

seems that the q = 1 surface acts as a thermal barrier. Temperature differences as large as 300 eV have been observed between radii inside and outside the q = 1 surface during more than 100 μs. The $T_e(r,t)$ profile recovers almost its self-similar initial shape within a fraction of a millisecond following pellet injection. The absolute values, however, increase on a longer time scale (see below).

2. Ion temperature : The ion temperature first decreases and than rises to values higher than the pre-injection temperatures because equipartitioning between electrons and ions is better due to the higher density after pellet injection. Insufficient time resolution did not allow conclusions concerning an eventual fast ion temperature transport.

3. Electron density : The time-dependent electron density profiles $n_e(r,t)$ are obtained from Abel inversion of HCN laser interferometric data along 8 chords. Limited time resolution (~ 400 μs) did not allow conclusions concerning an eventual fast matter transport during and immediately after pellet injection.

4. Magnetic and electron density fluctuations : The fluctuations $\tilde{\delta B}/B_\theta$ of the poloidal magnetic induction B_θ (poloidal mode numbers m = 2,3 ; toroidal mode numbers n = 1,2) have been measured by means of Mirnov coils. Short bursts of m = 2,3 oscillations are seen during pellet injection. The m = 1, n = 1 oscillation (island at q = 1) has been observed using X-ray detectors viewing along 32 chords. The fast temperature drop during injection is also seen on the soft X-rays and exhibits a large m = 1 oscillation on chords viewing the q = 1 region. When the m = 1, n = 1 oscillation (island at q = 1) is already seen before pellet injection it continues without perturbation after pellet injection. The m = 1 oscillation has a frequency close to but different from the m = 2 oscillation. This behaviour is different from the one after minor disruptions (without pellet injection) for which the m = 2 mode is always phase locked to the m = 1 oscillation. The strong similarity of the fast heat transport during minor disruptions and during pellet injection suggests that the same physical effect (the global fast heat transport) can be triggered by different phenomena. For further details, see Ref. [1].

Electron density fluctuations $\tilde{\delta n}$ have been measured using active microwave (λ = 2.2 mm) and CO_2 infra-red laser (λ = 10.6 μm) diffusion techniques. During and some 50 μs after pellet ablation the scatterred power (proportional to $(\tilde{\delta n})^2$) increases by a factor of ten. The signals appear as a series of bursts similar to the H_α (H_β) signals. However, at present no correlation has been found between the two types of signals, neither in time nor in amplitude. The scattered signals resemble those observed during minor disruptions, however in the latter case the scattered power is roughly three times smaller.

SLOW EVOLUTION OF PLASMA PARAMETERS ; TRANSPORT SIMULATIONS FOR MULTI-PELLET INJECTION

After the ablation has finished and the (self-similar) temperature profile been recovered a much slower evolution of all plasma parameters occurs on a time scale of some milliseconds to tens of milliseconds. After single pellet injection, the initial temperature values T_e are reestablished after appr. 5 to 10 ms. Since matter is only deposited in the outer part of the discharge ($r > 8$ cm) the $n_e(r,t)$ profile is hollow at the end of the ablation-process and stays hollow during a few milliseconds.

Successive injection of 4 pellets in time intervals of appr. 40 ms (standard case) yields moderate central peaking of $n_e(o)$ which increases with the n° of injected pellet. In one (special) case peaking is more pronounced. Sawtooth activity is in all cases weak before and remains in general weak after pellet injection. The evolution of $n_e(r,t)$ has been simulated by means of the transport code Makokot, for details see Ref. [6].

It seems that the stronger peaking in the "special case" is not only a consequence of a modification of the transport coefficients but rather due to either a deeper pellet penetration or to matter deposition in a plasma whose central particle confinement time is higher immediatly after deposition of a pellet.

AKNOWLEDGEMENT

We thank the ECRH-team of the FOM-Instituut voor Plasmafysica "Rijnhuizen", The Netherlands, for the ECR-heating during our pellet injection experiments.

REFERENCES

[1] TFR Group, "Pellet Injection Experiments on the TFR Tokamak", Report EUR-CEA-FC- 1321, Cadarache, February 1987

[2] TFR Group, Proc. 13th European Conf. on Contr. Fusion and Plasma Heating, Schliersee (FRG), 14-18 April 1986, Vol. 10C, part I, pp. 200-204, European Physic. Society.

[3] TFR Group, Contributed Paper 0326A, 14th European Conf. on Contr. Fusion and Plasma Phys., Madrid/Spain, 22-26 June, 1987

[4] TFR Group, Europhys. Lett. 2 (1986) 267

[5] Park,P.B.,Turnbull, R.J., Foster,C.A.,Nucl.Fusion 17 (1977) 539

[6] TFR Group, Contributed paper 0298A, Conference as in Ref. [3].

Pellet Injection with Improved Confinement in ASDEX

V. Mertens, M. Kaufmann, K. Büchl, G. Fussmann, O. Gehre, K. Graßie, O. Gruber, G. Haas, G. Janeschitz, M. Kornherr, K. Lackner, R.S. Lang, K.F. Mast, K. McCormick, J. Neuhauser, H. Niedermeyer, W. Sandmann, D. Zasche, H.P. Zehrfeld

Max-Planck Institut für Plasmaphysik, EURATOM Association
D-8046 Garching, Fed. Rep. of Germany

Z.A. Pietrzyk, University of Washington, Seattle, Wash., USA

Introduction :

An intensive campaign to study the consequences of repetitive pellet injection was carried out on ASDEX. It was possible to improve by pellet injection considerably the plasma confinement compared to earlier investigations /1/. In addition we could advance considerably the understanding of the relevant mechanisms. The dominant difference between the earlier and the recent experiments was different recycling in the plasma boundary and the divertor. While the earlier campaign aimed at low-recycling pellet injection (LRP) to study the genuine pellet fuelling, the second campaign aimed at an improvement of the density limit.

Experimental parameter :

The investigation concentrated on ohmically heated doulble null discharges in deuterium but discharges with additional neutral beam heating are considered as well. The ASDEX device was run typically at $B_t = 2.2$ tesla, $I_p = 380$ kA, $q_a = 2.7$. The density range was extended from $\overline{n_e} = 0.1 \times 10^{20}$ m^{-3} to $\overline{n_e} = 1.2 \times 10^{20}$ m^{-3}. The pellets with about 4.5×10^{19} deuterium atoms each were accelerated by a centrifuge to a velocity of 620 $\frac{\mathrm{m}}{\mathrm{s}}$ /2/ and yield penetration depths of roughly half the plasma radius. Normally up to 20 pellets were injected with a repetition rate of 30 ms. In typical cases of good confinement ASDEX was carbonized.

In a first campaign discharges were performed to demonstrate the potential of very low recycling at the plasma boundary by combining divertor operation and pellet fuelling. The pellet injection started at low density. Only a poor density build-up could be attained under these conditions. Figure 1 shows the successful density build-up in a typical high-recycling pellet injection (HRP) discharge beyond the gas puff (GP) density limit. The flat electron density profile starts to peak strongly with pellet injection whereas the temperature drops somewhat but the profile stays nearly self-similar.

The increase of the energy content and the improvement of the averaged energy confinement time is clearly seen in fig. 1; $\tau_E = 1.9 \times W_e/(P_{OH} - 1.9\dot{W}_e)$. W_e : energy content of the electrons; P_{OH} : ohmic heating power without correction for radiation.

In the pure GP phase the radiation profile is strongly peaked at the edge. During and after pellet injection when sawtooth activity is reduced the central radiation increases exponentially to a value comparable to the local power input without indication of saturation. Spectroscopic observation indicates Fe and/or Ti to be responsible for the rise of central radiation. Often nearly stationary density phases up to 230 ms duration could be observed after the last pellet. This phase is characterized by a very peaked pressure profile coinciding with a relatively flat temperature profile. The final breakdown seems therefore correlated to a violation of the ballooning criterion in the plasma centre. HRP discharges with neutral beam injection below $\sim$ 1 MW behave like ohmically heated discharges. The unsuccessful density build-up at higher neutral injection power seems to be correlated with a more peaked electron temperature profile and a specific MHD-activity triggered by the pellet.

Improved energy confinement with pellet injection was always correlated to a successful density build-up. The improvement of τ_E in HRP discharges compared to standard ohmically heated GP discharges by about a factor of 2 is demonstrated in fig. 2. The increase of τ_E starts with the first pellet and the enhancement lasts for times long compared with τ_E . The data may suggest that the pellets remove the reason for the τ_E roll-over because the peaked density profile in HRP discharges seems to establish a new type of discharge. This improvement of τ_E might be explained either by a local heat transport model or the profile consistency model of Furth /3/.

Discharges with proper edge conditioning (HRP) show distinct changes in bulk plasma particle transport with pellet injection. The observed peaking of the density profile can not be attributed to central deposition of pellets because the penetration depth is approximately half the minor radius and the peaking lasts up to 230 ms after the last pellet. Assuming that the particle transport i.e. the electron flux Γ may be interpreted by a diffusive and convective driving term with a diffusion coefficient D and an inward velocity V,

$$\Gamma(r) = -D(r) \times n'(r) - V(r) \times n(r),$$

nearly stationary phases are analyzed neglecting particle sources. Figure 3 shows typical electron density profiles and deduced ratios $\frac{V}{D}$ before and after pellet injection. In the inner two-thirds of the minor radius $\frac{V}{D}$ has increased by a factor of about 3 or more demonstrating the change in particle transport. During density build-up the following transport coefficients fit the observed electron flux in the inner region :

$$D(r) = 0.1 \text{ m}^2/\text{s} \quad \text{and} \quad V(r) = 1 \times \frac{r}{a} \text{ m/s}$$

(a: minor radius)

Reduced sawtooth activity and the correlated decreased outward flow of particles during a sawtooth disruption - compared to GP discharges - seems also to be a condition for the profile peaking. GP discharges without sawteeth show a similar peaking /4/. A macroscopic vertical electric field of the order of 10 V/m might explain an enlarged inward velocity. Calculation of the neoclassical current profiles show a small but significant increase of q on axis which reflects the increase of the collisionality with pellet injection.

In typical GP discharges there is a strict relation between the bulk plasma density and the edge density $n_s = 0.3 \times \overline{n_e}$. n_s is the density at the separatrix and $\overline{n_e}$ is the line-averaged bulk density /5/. The relative exponential density decay length in the scrape-off layer is practically independent of $\overline{n_e}$. In LRP discharges the particle density in the boundary exhibits large variation during pellet injection because the divertor walls are far from saturation and the neutral flux density in the divertor is low. This lack of saturation leads to a continuous outflow of the injected particles as seen in fig. 4a . In HRP discharges the high neutral flux density prevent loss of particles. The edge density stays nearly constant during the build-up of bulk density (fig. 4b) and the very small modulation of the edge density during pellet cycle indicate that the particle density in the boundary seems to be in equilibrium with the bulk density and the recycling. While the edge density behaviour is similar to GP discharges the ratio $n_s/\overline{n_e}$ decreases from its standard GP value consistent with the peaking of the bulk profile.

References :

/1/ G. Vlases et al, Proc. 12th Europ. Conf. on Contr. Fusion and Plasma Physics, Budapest 1985, 1 (1985) 78

/2/ W. Amenda, R.S. Lang, Proc. 13th Symp. on Fusion Technology, Varese 1984, 243

/3/ M. Kaufmann et al, Nucl. Fusion, to be published

/4/ F. Wagner et al, Proc. Invited Papers, 13th European Conf. on Contr. Fusion and Plasma Heating, Schliersee 1986, vol 28 9A, 1225

/5/ K. McCormick et al, J. Nucl. Mater., 145-147 (1987), 215

Figure Captions :

1 : The electron particle content N_e and the energy content W_e are shown together with the global energy confinement time τ_E as function of time. The density and temperature profile development can be seen from the $\frac{n_e(0)}{\overline{n_e}}$ and the $\frac{T_e(0)}{T_e(a/2)}$ traces.

2 : Energy confinement time τ_E as function of the line averaged density $\overline{n_e}$ for LRP, HRP and standard ASDEX GP discharges. All discharges are with ohmic heating only.

3 : The ratio of the inward drift velocity to the particle diffusion coefficient $\frac{V}{D} = \frac{n_e'}{n_e}$ together with density profiles (*dotted lines*) is given before (a) and after pellet injection (b).

4 : Electron density profiles at the plasma boundary for LRP (a) and HRP (b) discharges. In case (a) one pellet cycle is shown. The profile steepens by the pellet and flattens afterwords again. R_S : radius of the separatrix, t_p : pellet injection time.

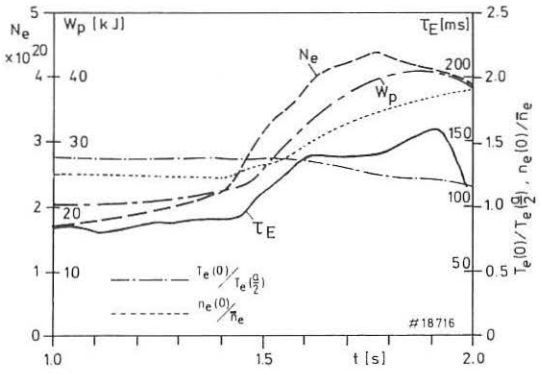

Fig. 1

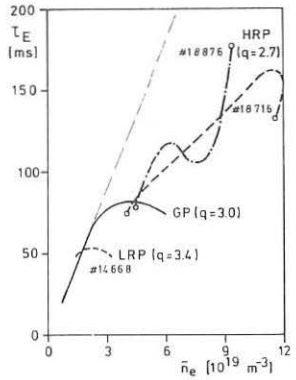

Fig. 2

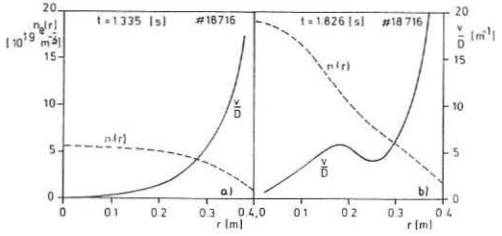

Fig. 3

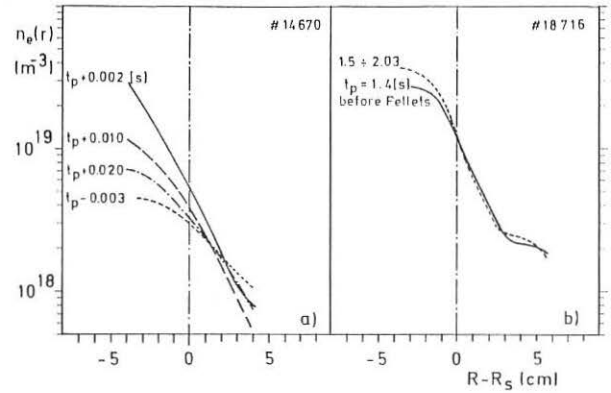

Fig. 4

ELECTRON TEMPERATURE PROFILES IN HIGH POWER NEUTRAL BEAM HEATED TFTR PLASMAS

G. Taylor, B. Grek, F.J. Stauffer*, R.J. Goldston, E.D. Fredrickson,
R.M. Wieland and M.C. Zarnstorff.
Princeton Plasma Physics Laboratory, Princeton N.J. 08544, USA
*University of Maryland, College Park, Maryland, USA

Introduction

In 1986, the maximum neutral beam injection (NBI) power in TFTR was increased to 20MW, with three beams co-parallel and one counter-parallel to I_p [1]. TFTR was operated over a wide range of plasma parameters; $2.5<q_{cyl}<10$, and $2\times10^{19}<\overline{n_e}<7\times10^{19}m^{-3}$. Databases have been constructed with over 600 measured electron temperature profiles from multi-point TV Thomson scattering (TVTS) which span much of this parameter space. We have also examined electron temperature profile shapes from electron cyclotron emission (ECE) at the fundamental ordinary mode and second harmonic extraordinary mode for a subset of these discharges.

In the light of recent work [2,3] on "profile consistency" (or "resiliency") we have analysed these temperature profiles in the range $0.3<(r/a)<0.9$ to determine if a profile shape exists which is insensitive to q_{cyl} and beam heating profile.

Analysis of Electron Temperature Profile Shape

Three techniques have been employed to map TVTS and ECE $T_e(R)$ data to a normalized radial coordinate, $T_e(r/a)$. In all cases, the ECE profiles are first mapped from frequency space to physical space, taking into account the effects of the plasma diamagnetism and poloidal field [4], using a code based on the measured β_p^{dia} and Λ. After smoothing $T_e(R)$ with $\delta r\approx a/10$, we then map to $T_e(r/a)$. In the first, "simple-one-sided" mapping $T_e(R)$ is mapped to $T_e(\rho)$ where $\rho = (R - R_o)/(R_{max} - R_o)$ [5]. R_o is the position of the magnetic axis as determined from the peak of the T_e data and R_{max} is the major radius at the outer edge of the plasma, as determined from magnetics. In the second, "slice-and-stack" method, $T_e(R)$ is sliced on isotherms to produce a 2r versus T_e dependence; $T_e(r/a)$ is then generated by inverting this dependence.(This technique cannot be used with second harmonic ECE due to harmonic overlap.) No account is taken of the slight ellipticity ($\approx$ -10%) observed at the surface of TFTR plasmas at the highest values of $\beta_p\approx2$ and $\Lambda\approx3$. A third,

"flux-surface-integral" approach was also employed where a simple algorithm for the separation between two shifted, circular cross-section, toroidal flux surfaces was derived. For two such toroidal flux surfaces with major and minor radii (R_1, a_1) and (R_2, a_2), the average separation, $<\Delta r>$ is approximately given by : $<\Delta r> = (a_2 - a_1) - (a_1/2)(1 - (R_2/R_1))$ and $T_e(r/a) = \int(\Delta T_e/<\Delta r>)dr$, where ΔT_e is the temperature increment between isotherms. We have examined 40 profiles using these three different mapping algorithms, and both ECE and TVTS $T_e(R)$ measurements. These profiles were chosen to span the full available range in q_{cyl}, β_p, n_e and beam power. We find the "slice-and-stack" and "flux-surface-integral" methods yield similar results. However the "simple-one-sided" method can disagree by as much as 30% on $T_e(r/a)$.

Comparison of Diagnostic Measurements

At the highest central temperatures (T_{eo}), we find that the central ECE measurements exceed the TVTS measurements to a degree which is outside the range of experimental error. The extraordinary mode second harmonic and ordinary mode fundamental ECE measurements begin to diverge from TVTS data when the TVTS T_{eo}>4 keV and >6keV, respectively. For example, when T_{eo} from TVTS reaches 6.5 keV, the extraordinary mode second harmonic result is typically 8.5 keV . Soft X-ray pulse height analysis measurements agree fairly well with the TVTS results. Since optical depths in the core exceed 70 for the second harmonic extraordinary mode and outside the plasma core (r/a>0.3) ECE and TVTS results generally agree well, it is difficult to explain these observations as being simply due to suprathermals. These disagreements are currently under study.

Results

The electron temperature profile shape in low q_{cyl} NBI discharges is flattened in the core by sawteeth, and we believe convection losses associated with cold electron deposition may be the cause of the flattening in the core of high q_{cyl} NBI plasmas. At the highest β_p's obtained, $\approx$2, the calculated Shafranov shift and the distance of T_{eo} from the center of the plasma is >30 cm. These effects are clearly seen in figure 1, where TVTS $T_e(R)$ shapes seem to violate any concept of "consistency" or "resiliency". However, figure 2 shows the result of remapping the profiles of figure 1 to $T_e(r/a)$ with the "flux-surface-integral" method, and normalizing the temperatures to T_e at r/a=0.5. These four discharges appear to have very similar $T_e(r/a)$ profiles away from the core. (TVTS data is typically subject to random measurement errors of 5-10% with the largest errors occuring in the low density region well away from the core.)

In figure 3 a slice-and-stack remapping of TVTS data reveals a weak dependence of profile shape on q_{cyl}. Here two sets of profiles were averaged with $7<q_{cyl}<8$ and $2.5<q_{cyl}<3.5$, the data are plotted on a semi-log plot to emphasize variations of the profile in the region $0.3<(r/a)<0.9$. NBI powers for these discharges were greater than 8MW. The error bars indicate the standard deviation of the data set. There is a slight tendency of the low q_{cyl} plasmas to be broader, with $T_e(0.4a)/T_e(0.8a)$ approximately 10% smaller in the lower q_{cyl} cases. In order to study the effect of heating profiles on the $T_e(R)$ profile, we overlay in figure 4 profile shapes from L-mode discharges at I_p = 1.4 and 2.2 MA, with $P_{inj}>8$ MW, sorted by density. In the higher density dataset, the beam heating profile is modestly hollow in the center, with 1/3 of the central beam heating power density of the lower density discharges, but the electron temperature profiles show at most a 5% difference. Although there was some indication on individual profiles of a dependence on β_p or the fraction of NBI power co-parallel to I_p a statistical study with the full database did not reveal any systematic dependencies.

Conclusions

We have found that a "slice-and-stack" method for mapping $T_e(R)$ from TVTS and ECE data to flux surfaces provides a reliable measurement of $T_e(r/a)$, with results similar to a more sophisticated "flux-surface-integral" method. We have studied over 600 temperature profiles for NBI discharges which span a broad range in q_{cyl} and heating power profiles. There is a systematic trend towards slightly broader profiles at lower q_{cyl}, with $T_e(0.4a)/T_e(0.8a)$ approximately 10% higher at $q_{cyl}\approx 3$ than at $q_{cyl}\approx 7.5$. $T_e(r/a)$, in the region $0.3<r/a<0.9$ is found to be remarkably insensitive to heating profiles going from peaked on axis, to hollow.

Acknowledgement This work was supported by DoE contract #DE-AC02-76-CH03073.

References

[1] R. Hawryluk et al., Eleventh Intl. Conf. on Plasma Phys. and Contr. Fus. Res. (IAEA, Kyoto 1986) IAEA-CN-47/A-I-3.

[2] R.J. Goldston, et al., Eleventh Intl. Conf. on Plasma Phys. and Contr. Fus. Res. (IAEA, Kyoto 1986) IAEA-CN-47/A-II-1.

[3] D.A. Boyd, et al., Eleventh Intl. Conf on Plasma Phys. and Contr. Fus. Res. (IAEA, Kyoto 1986) IAEA-CN-47/AVI4.

[4] W.H.M. Clark, Plasma Phys. **25** (1983) 1501.

[5] A. Taroni and F. Tiboni, Proc. 13th EPS Conf. (Schliersee 1986) **10c**, 160.

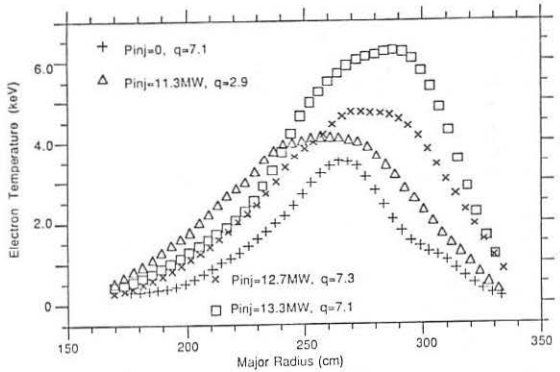

Figure 1: Electron temperature profiles for several different plasma conditions.

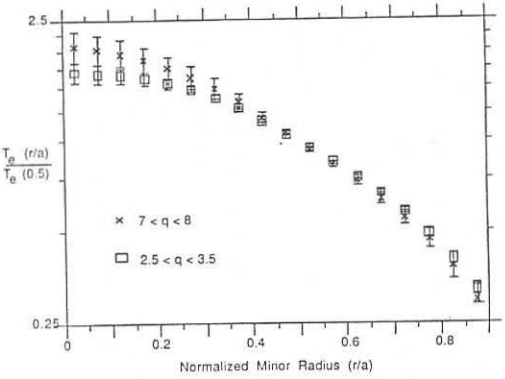

Figure 3 Comparison of two sets of plasma profiles with 7<q<8 and 2.5<q<3.5. Heating Power > 8 MW

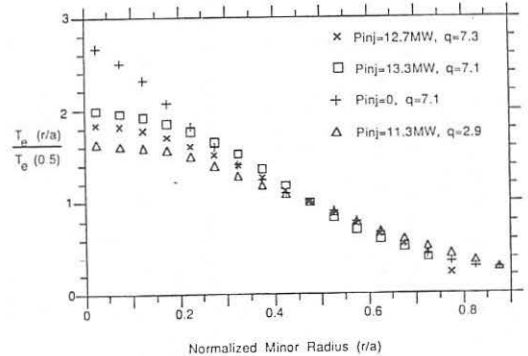

Figure 2 Flux surface integral remapping of the four profiles in figure 1 to (r/a)

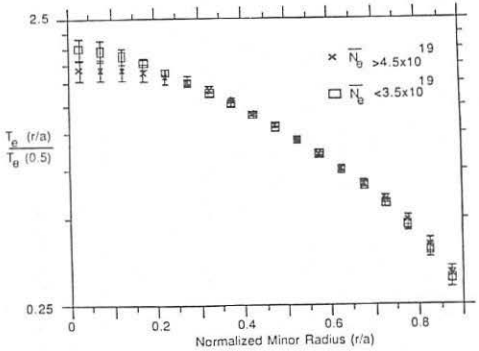

Figure 4 Two sets of re-mapped profile data for high and low density L-mode. Heating Power > 8 MW

STUDY OF IMPURITY ACCUMULATION IN THE ASDEX TOKAMAK

G. Fussmann, G. Janeschitz and G. Becker, H.S. Bosch, H. Brocken,
A. Carlson, A. Eberhagen, G. Dodel[1], H.-U. Fahrbach, O. Gehre,
J. Gernhardt, G. v.Gierke, E. Glock, O. Gruber, G. Haas, W. Herrmann,
J. Hofmann, A. Izvozchikov[2], E. Holzhauer[1], K. Hübner[3], F. Karger,
M. Kaufmann, O. Klüber, M. Kornherr, K. Lackner, M. Lenoci, G. Lisitano,
H.M. Mayer, F. Mast, K. McCormick, D. Meisel, V. Mertens, E.R. Müller,
H. Murmann, J. Neuhauser, H. Niedermeyer, A. Pietrzyk[4], W. Poschenrieder,
H. Rapp, A. Rudy, F. Schneider, C. Setzensack, G. Siller, E. Speth,
F. Söldner, K. Steinmetz, K.-H. Steuer, N. Tsois[5], S. Ugniewski[6],
O. Vollmer, F. Wagner, D. Zasche

Max-Planck-Institut für Plasmaphysik,
EURATOM Association, Garching, FRG

Abstract: The internal disruptions are found to play an important role in preventing impurity accumulation. We describe several situations where strong peaking of metallic impurities in the plasma center is observed after suppression of the sawtooth activity.

I. Introduction

The possibility of high level impurity accumulation in tokamaks and stellarators was already recognized in the early days of these devices. From a theoretical point of view the principle mechanisms leading to accumulation became quite evident: The frictional forces between impurity (z) and background ions (i) should result in radial ambipolar interchange fluxes ($z\Gamma_z=-\Gamma_i$), such that the high Z impurities are rapidly driven towards the plasma center.
In the experiments, on the other hand, such a dramatic accumulation was generally not observed. During the last years, however, a number of observations showed clear evidence that, at least under certain conditions, strong impurity accumulation can occur /1, 2/, and in the following we will discuss the various observations made on ASDEX.

II. Impurity accumulation and counteracting mechanisms

Impurity accumulation was observed in ASDEX for the first time during the quiescent H-phase achieved by NI heating. As reported in /3/ these discharges collapse because of tremendous radiation losses in the plasma center. The quiescent H-mode differs from the normal one by the lack of bursts caused by edge localized modes (ELMs). It was originally assumed that accumulation can be prevented in the normal H-phase due to counterating mechanisms being correlated with the ELMs. A more detailed analysis, however, revealed that also in this case a quite similar accumulation of metallic impurities takes place /4/. The main difference between normal and quiescent H-phase is found in the Fe-impurity concentration (and hence the Fe influxes) during the preceding L-phase. This concentration is typically three times higher for the quiescent case.

[1] University of Stuttgart; [2] Ioffe Institute; [3] University of Heidelberg; [4] University of Washington, Seattle, USA; [5] N.R.C.N.S. "Democritos", Athens, Greece; [6] Inst. for Nuclear Research, Swierk, Poland;

It is still unclear whether during the H-mode the ELMs effectively improve the screening efficiency of the plasma or if they are rather an indication of low metallic influxes.
Comparing ASDEX with other tokamaks /2/, we have to realize that in our experiments sawteeth do not occur during the H-phase. Therefore, the above accumulation is presumably more pronounced in ASDEX since the counteracting effect of the internal disruption is missing. The dispersing effect of sawteeth (st) has already been shown in a number of investigations /1, 5/. In ASDEX we have studied this effect by means of: a) current ramp-up to increasing plateaus, b) Kr gas puffing, c) pellet injection.
In addition, we have investigated sawtooth initiation during the early current build-up phase. Frequently, the first sawtooth is a very pronounced event (the so-called "Ereignis", further discussed in /6/). By comparison with discharges where the sawteeth grow continuously from noise level, some information on the transport induced by sawteeth can be obtained. Such a comparison is shown in Fig. 1. It is seen that the discharge exhibiting the "Ereignis" shows a substantial increase in the central soft X-ray (SX) intensities prior to the st-crash. After the crash, the SX-signal (dominated by Fe) approaches rapidly the trace of the reference shot. We also note that there is practically no effect to be seen on other spectroscopic signals (FeXVI, OVIII) emitted from outside half the minor radius. Taking further into account that central temperatures differ only by $\lesssim 1\%$ in the two cases, we conclude: Sawteeth expell in short pulses impurities out of the central region but do not lead to a net loss of particles from the plasma volume.
The effect of sawtooth suppression by current ramp-up has been described in /7/. Here it suffices to repeat the essential findings: Firstly, the procedure is not successful in any case. Depending on small changes of some unknown parameters, st may be suppressed or sustain with marked amplitude for the residual part (~2s) of the discharge. In case of suppression, only two changes are observed: 1) the n_e-profile is becoming more peaked, and 2) the central radiation losses are considerably increased (~ factor 10 for $q_a \leq 3$) and become comparable to the input power of ~0.2 W/cm^3, although the Z_{eff} determined by resistivity is as low as ≤ 1.5. Moreover, inspite of the high radiation losses, both the total energy content and the central energy density remain unchanged in comparison with the st case. Thus, a concomitant substantial reduction of the thermal conductivity is to be inferred.

Similar effects can be observed by applying Kr-puffing as demonstrated in Fig. 2. Shot #19691 is a discharge following a shot into which Kr had been blown. The SX-rays (as well as Kr-lines of highly ionized ions) are seen to increase monotonously. As to be seen from the st-amplitude $A=(\bar{n}_e - \langle \bar{n}_e \rangle)/\langle \bar{n}_e \rangle$ (with $\langle \bar{n}_e \rangle$ being the averaged line-density) plotted on top of Fig.2, there are no sawteeth developped in this discharge. The following shot had even less Kr and this time st occur after t=0.72 s. The reduction in the central soft X-rays is evident (whereas the non-central OVIII-radiation is nearly uneffected).
As mentioned above, another method for st-suppression is the injection of pellets with the centrifuge system. This has been done in ohmic discharges and also under carbonized conditions during counter-NI heating (see Ref. /8/ for more detail). The salient features to be observed during the post pellet phase, when the st activity is reduced or even quenched are as de-

scribed before: Peaking of the n_e-profile, accumulation of metal impurities and improvement of energy confinement.
In the following, we concentrate on the accumulation aspects of two discharges with P_{NI}=0.45 MW (#20032) and 0.9 MW (#20033) counter NI (t=0.9 - 1.5s) into which 5 pellets have been injected (t=1.1 - 1.3s). In Fig. 3 we show the SX-signal of the second shot. The times of pellet injection are to be recognized from the $\bar{n}_e$ -trace depicted on top of Fig. 3. After the last pellet the sawteeth vanish (with one large exception) and the SX and TiXX intensities (λ=256 Å, peaking approximately at r=10 cm) are seen to rise exponentially. In Fig. 4 we compare the SX and TiXX radiation on log-scale for the two cited discharges. Each of the two signals is seen to rise very similar with a multiplier of ~2 for the shot with doubled NI power. This proportionality to P_{NI} is also found from bolometer array measurements yielding very peaked profiles with central radiation losses as high as 0.5 and 0.9 W/cm^3 for the two discharges. Despite these large losses the central T_e drop is only about 10 % ($T_{e,max}$≈1.4 keV). Assuming Ti being the most abundant metallic impurity in these discharges (Fe being strongly reduced by carbonization) we need a central density of $n_{Ti}(0)/n_e(0)$≈1 - 2%. Invoking the collision parameter $\alpha=Z^2 n_z/n_i>4$, we conclude that the interaction of the impurity ions among themselves is much larger than with the background ions - a situation imposing greatest difficulties in theory. However, the parallel development of the signals shown in Fig. 4 demonstrates that nonlinear impurity transport processes, with the possibility of enhanced impurity accumulation on account of the high impurity density (as discussed in /2/), are probably unimportant.

III. Transport simulation

Our observations suggest the following ansatz for the impurity fluxes:

$$\Gamma_z(r,t) = \Gamma_s(r,t) + \Gamma_{an}(r) + \Gamma_{neo}(z,r)$$

with

$$\Gamma_s = \sum_k A_k P(t-t_k)\, V_s(r) n_z$$
$$\Gamma_{an} = -D_{an}(r)\, n'_z - v_{in}(r) n_z$$
$$\Gamma_{neo} = -D_i(r) n_z + Z(r) D(r) [n_i'/n_i - (o.5+1/Z) T_i'/T_i]$$

Γ_s represents the expelling effect of the sawteeth with P(t) being a pulse like-function Γ_{an} describes the underlying anomalous transport which is assumed equal for all particles, and finally Γ_{neo} is the neoclassical term /9/ (notation: '=∂/∂r).
We have simulated our experimental results using an impurity transport code applying measured $T_e(r,t)$ and $n_e(r,t)$. Particular emphasis has been devoted to the accumulation phase of #20033. In Fig. 3 we have included our results for the SX and TiXX chord integrals. All sawteeth were modelled in the same way: $\Gamma_{s,k}=V_{so}\exp\{-[(t-t_k)/\tau]^2\}(r/r_o)\exp(-r/r_o)^2$ with r_o=15 cm, τ=1ms, V_{so}= 1 000 cm/s. Most remarkably, these pulses control the peaking of the profiles very effectively at the beginning when the repetition time is still high. Assuming D_{an}=500 cm^2/s, V_{in}= 70 r/a cm/s, the peaking of the n_e-profiles could be roughly simulated by treating hydrogen in the code. Finally, in order to attain at least approximately the strong Ti peaking observed from the radiation profiles, we had to double the neoclassical drift term and dropping the outward T_i'/T_i term therein.

References
/1/ R.C. Isler, Nucl. Fusion, 24, 1599 (1984)
/2/ K. Ida, et al., Phys. Rev. Lett., 58, 2, 116-119 (1987)
/3/ M. Keilhacker et al., Proceedings of the 10th Int. Conf. on Plasma Physics and Contr. Nucl. Fus. Research, London 1984, Vol. I, p. 71
/4/ E.R. Müller, IPP III/112 (1986) to be published in Nucl. Fusion)
/5/ TFR Group, Nucl. Fus. Lett. 25, 8, 981-986 (1985)
/6/ O. Gehre, this conference
/7/ F. Wagner, to be published in Nuclear Fusion
/8a/ V. Mertens, and /8b/ F. Mast this conference
/9/ S.P. Hirshman, Phys. Fluids, 19, 1, 155-158 (1975)

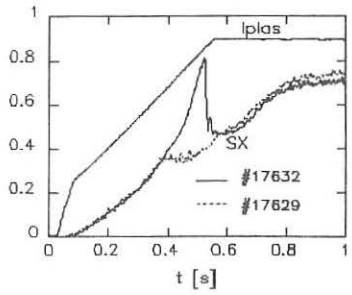

Fig.1: Soft X-ray emission in two discharges with different sawtooth initiation.

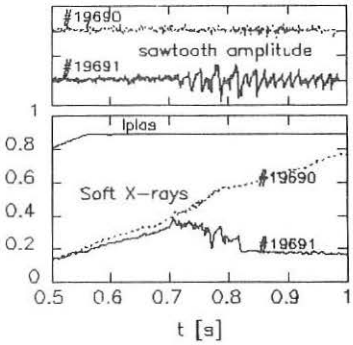

Fig.2: Increase of central SX radiation due to sawtooth suppression by means of Kr puffing.

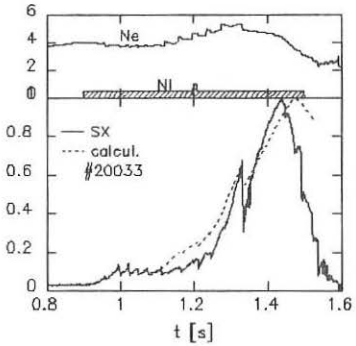

Fig.3: Impurity accumulation in case of pellet injection during the (counter) NI phase. ($\bar{n}_e$ in units of 10^{13} cm^{-3})

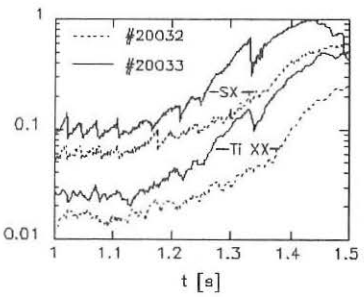

Fig.4: Development of SX and TiXX radiation, demonstrating the similarity of Ti accumulation in shots with different Ti influxes.

Pressure Profile Consistency in ASDEX Discharges

O. Gruber and G. Becker, H.S. Bosch, H. Brocken, A. Carlson, A. Eberhagen, G. Dodel[1], H.-U. Fahrbach, G. Fussmann, O. Gehre, J. Gernhardt, G. v.Gierke, E. Glock, G. Haas, W. Herrmann, J. Hofmann, A. Izvozchikov[2], E. Holzhauer[1], K. Hübner[3], G. Janeschitz, F. Karger, M. Kaufmann, O. Klüber, M. Kornherr, K. Lackner, M. Lenoci, G. Lisitano, F. Mast, H.M. Mayer, K. McCormick, D. Meisel, V. Mertens, E.R. Müller, H. Murmann, J. Neuhauser, H. Niedermeyer, A. Pietrzyk[4], W. Poschenrieder, H. Rapp, A. Rudyj, F. Schneider, C. Setzensack, G. Siller, E. Speth, F. Söldner, K. Steinmetz, K.-H. Steuer, N. Tsois[5], S. Ugniewski[6], O. Vollmer, F. Wagner, D. Zasche,

Max-Planck-Institut für Plasmaphysik
EURATOM Association, Garching, FRG

1. Introduction

Ohmically (OH) and additionally heated "L-mode" Tokamak discharges exhibit an electron temperature T_e profile invariance against changes in power deposition profiles and plasma density and are only influenced by the safety factor q_a. This has led to the concept of "profile consistency" where the local transport coefficients are not only a function of local plasma parameters but might also depend on non-local processes adjusting the T_e profiles. At present, there exists no coinvincing model for this profile consistency, first introduced by B. Coppi to describe the current density behaviour and the connected T_e profiles of Ohmic heated plasmas. But if the thermal transport is governed, for instance, by electromagnetic modes, not only the current density should show a canonical profile, but also the pressure (p) gradient profiles. Moreover, these profiles can adjust after changes of the heating deposition much faster than the current density, and any deviation from the canonical profile might then result in an additional heat transport which can be expected to act complementory on ion and electrons.

According to Kadomtsev /1/, a pressure profile consistency arises from the existence of relaxed states with thermal and poloidal field minimized subject to a single (constant current) or two constraints (constant current and helicity of the magnetic field). With such a strong principle the resulting pressure and current density profiles depend on the ratio q_a/q_o only and, depending on the constraint, are finite or zero, respectively, at the plasma boundary r=a. Profiles for both cases approach each other at high q_a/q_o. In this paper we examine the total pressure profile shapes in all phases of ASDEX discharges (OH, L and H mode) and compare them with the T_e profiles.

2. T_e and pressure profiles in OH and L mode discharges

There is no commonly agreed format of the T_e profile normalization showing an invariance for different operating conditions. With increasing order of

[1] University of Stuttgart; [2] Ioffe Institute; [3] University of Heidelberg; [4] University of Washington, Seattle, USA; [5] N.R.C.N.S. "Democritos", Athens, Greece; [6] Inst. for Nuclear Research, Swierk, Poland;

the profile consistency quality, the possibilities proposed are: $T(0)/\langle T\rangle$, $T(r)/T(a/2)$ or $\ln(T(r)/T(a/2))$ and $1/T\cdot dT/dr$. Using the normalizaiton $T(r)/T(a/2)$ ASDEX T_e-profiles coincide within the error bars and discharge to discharge variations outside the q=1 surfaces ($r_{q=1}\approx a/q_a$) for all OH- and L-mode discharge conditions as is shown in Fig. 1 (Thomson scattering measurements). Data from discharges are used for which transport analyses with the TRANSP code have been carried out including stationary and unstationary discharge phases and the following parameter variations: I_p=300÷440 kA, $\bar{n}_e$=1÷11·$10^{19}m^{-3}$; $P_h\leq 3.8$ MW; strong on- and off-axis heating deposition profiles /2/ and pellet refuelled discharges /3/.
For different q_a-values deviations can be seen at radii $r<r_{q=1}$, but differences exist also in the confinement zone between q=1 and q=2 (which is roughly at $r_{q=2}=a/\sqrt{q_a/2}$). This is more clearly demonstrated in Fig. 2 showing for the same discharges the radial profiles of the upper and lower bounds of the normalized T_e scale length r_{Te} given by the inverse logarithmic derivative $r_{Te}/a = -(T_e/dT_e/dr)/a$. Part of the q_a-dependence is certainly due to the T_e-flattening inside the sawtooth region. At fixed q_a there is a weak T_e profile response to changes in the heating profile yielding broader profiles, i.e. higher r_{Te}, with increasing off-axis heat deposition. The latter is obtained by using a lower energy/nucleon of the injected fast neutrals or an increasing density (beam deposition at larger radii, broader resistivity profile due to higher collisionality and reduced $T_e(0)$).

The total kinetic pressure profiles are obtained by using the TRANSP analyses code. Input data are the $n_e(r,t)$ and $T_e(r,t)$ profiles measured by a 16-spatial channel multi-pulse Thomson scattering system and supplemented by a HCN-laser interferometer and ECE diagnostic (4 channels both), the bolometrically measured profiles of the radiation losses and global parameters like the loop voltage V_L, I_p, $\beta_{p\perp}$ from diamagnetic flux measurements and $\beta_{p_\parallel}+l_i/2$ as deduced from poloidal fields and fluxes. Lacking a measurement of the full ion temperature T_i profiles for all discharges we assume a spatially constant enhancement factor α of about 2 to 3 of the ion heat diffusivity χ_i over the neoclassical value as calculated by Chang and Hinton, checking the resulting T_i profiles for their compatibility with the available neutron production and T_i measurements (passive and active CX diagnostic, Doppler broadening of impurity lines). The calculated kinetic pressures include also the contributions due to the anisotropic fast beam ions (using Monte Carlo calculations for the deposition and slowing-down of the beam particles) and are in good agreement with the magnetically measured ones. Fig. 3 shows the pressure scale length r_p for the discharges of Fig. 1 and 2 exhibiting a somewhat stronger separation of the two q_a data sets, which are not in disagreement with the Kadomtsev p(a)=0 pressure profiles. The influence of the χ_i assumption was estimated by taking α-values between 1 and 5, yielding r_p variations below 10%.

3. H-mode profiles

The invariance of the pressure profiles is even more impressive if we look at their time development during single discharges as is shown for a β-limit discharge in Fig. 4. Fig. 4a demonstrates the strong T_e profile variation at the L/H mode transition where the T_e profile flattens in the

center (higher r_{Te}) and develops shoulders towards the boundary. After reaching β_{max} the T_e profiles flatten even more in the center due to increasing central radiation losses /4, 5/. As also the density profiles form shoulders in the H-mode, the electron pressure (p_e) profiles do the same (see Fig. 4b) but are by far not comparable to the second class of Kadomtsev-profiles with $p(a)\neq 0$ which would have nearly constant r_p for $0.5a<r<a$. Contrary to p_e, the total pressure profile is nearly time independent. In this discharge, the fast ions contribute up to 40 % of the pressure and a comparable amount to the pressure gradient and the ion temperature is well above T_e. The universality of the p profile shape is also demonstrated by comparing H-mode discharges both with H^0 and D^0 injection, i.e. different deposition profiles (see Fig. 5). The disappearance of the q_a-dependence might be partly caused by the lack of sawteeth.

4. Conclusions

The total pressure profiles of ASDEX discharges exhibit a canonical shape which is preserved also in the H-mode contrary to a changing T_e profile shape. There exists one exception namely the high confinement pellet refuelled discharges revealing a steeper pressure gradient and smaller scale lengths /3/. For instances in a q_a=2.5 ohmic pellet discharge the r_p/a profile is about at the lower bound of the gas fuelled discharges shown in Fig. 3. This might be related to the process limiting the pressure shape yielding a lower bound for the r_p profile which is nearly reached in these pellet discharges. It is interesting that only in the pellet discharges n_i-values below 1 are observed over a large part of the plasma column.

References

/1/ B. Kadomtsev, IAEA-Meeting on Confinement in Tokamaks with Intense Heating, (Nov. 1986), Kyoto

/2/ O. Gruber, et al., Proc. 13th Europ. Conf. on Contr. Fusion and Plasma Heating, Schliersee 1986, Europhys. Conf. Abstr. 10C Part I (1986) 248.

/3/ G. Vlases, O. Gruber, M. Kaufmann, et al., Nucl. Fusion, 27 (1987) 351
M. Kaufmann, et al., to be published in Nucl. Fusion

/4/ O. Gruber, et al., Proc. 11th Conf. on Plasma Phys. and Contr. Nucl. Fus. Research, Kyoto, 1986

/5/ O. Gruber, et al., Proc. 12th Europ. Conf. on Contr. Fusion and Plasma Physics, Budapest 1985. Europhys. Conf. Abstr. 9F, Part I(1985) 18

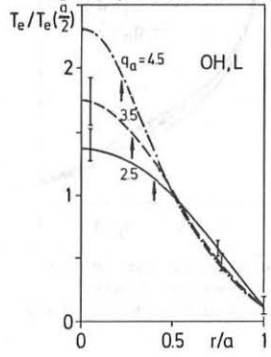

Fig.1: Averaged T_e profiles normalized to $T_e(a/2)$ vs. flux surface radius r in ohmic and L-mode discharges at q_a= 2.5±0.1, and q_a=3.5 ± 0.2, and for a comparison discharge at q_a=4.5.

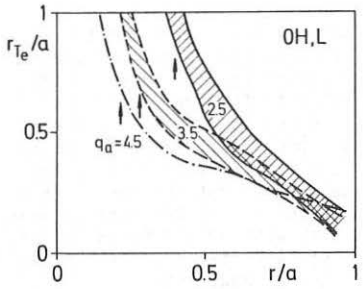

Fig.2: Radial profiles of the upper and lower bounds of the T_e scale length $r_{Te}=-T_e/dT_e/dr)$ normalized to a for the discharges used in Fig. 1 (OH, L-mode).

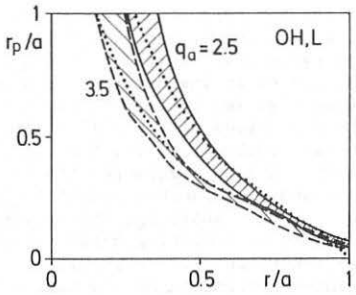

Fig.3: Radial profiles of the upper and lower bounds of the normalized presure scale length r_p/a (OH, L-mode). The dotted lines are the Kadomtsev pressure profiles with p(a)=0 for q_a=2.5 and 3.5.

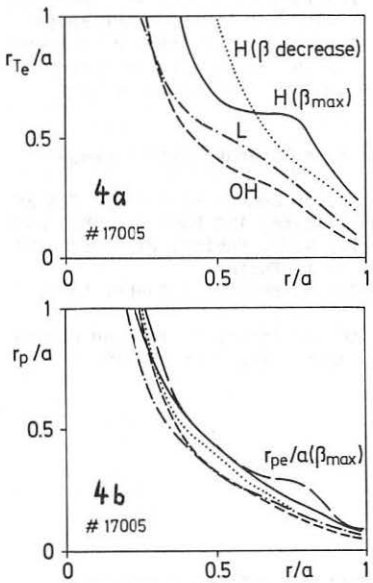

Fig.4: Radial profiles of the normalized T_e and p scale lengths for a beam heated ASDEX discharge (q_a=3.7) in different discharge phases (OH, L, H-mode).

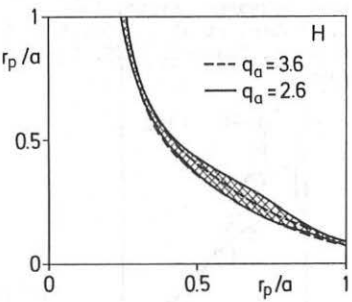

Fig.5: Radial profiles of the bounds of the normalized pressure scale length for beam-heated H mode discharges.

BEAM-PLASMA FUSION YIELD IN ROTATING TOKAMAK PLASMAS

W.G.F. Core, P. van Belle, G. Sadler

JET Joint Undertaking, Abingdon, Oxon., OX14 3EA, UK

1. Introduction

In the neutral injection heating of tokamak plasmas, fast ions are initially injected as neutrals, which after ionisation, slow down on the background plasma to thermal energy. During this relaxation process, the fast ions, in addition to heating the plasma directly, can undergo thermonuclear reactions, and even in the case of balanced injection, impart momentum to the system. This input of momentum gives rise to plasma rotation preferentially in the toroidal direction, and for uni-directional injection, velocities in excess of the sound speed have been predicted [1]. These bulk plasma rotational velocities may have important consequences for the beam heating efficiency, the thermonuclear reactivity of the system, and in the interpretation of the measured fusion yields.

In this paper we first consider the effect of bulk plasma toroidal rotation on the beam-plasma reactivity rates, and in particular, the thermonuclear power amplification factor Q of systems close to ignition [2]. Then the modification to the fusion charged particle birth profiles due to the combined effects of rotation and orbit trajectory is examined. Finally, results of calculations done using actual measured plasma parameters for the JET D→D injection experiments in which large rotational velocities have been observed are compared with the measured neutron fluxes.

2. Preliminary Considerations

Some obvious points regarding the injected ions as viewed in the laboratory and plasma frames are worth mentioning. Fast ions deposited in passing orbits moving in a co-rotational direction in the laboratory frame will in the rotating plasma frame suffer an apparent reduction in energy, and conversely, passing ions moving in a counter-rotational direction will have their energy increased. Accordingly, the fast ion slowing down time and consequently their density is then either reduced or increased. The transformation of particle velocity v, and pitch variable ξ ($=v_{\parallel}/v$), from the laboratory to the plasma frame $(v,\xi)\rightarrow(v_R,\xi_R)$ is: $v_R^2=v^2-2v\xi v_{\parallel o}+v_{\parallel o}^2$, $\xi_R=(v\xi-v_{\parallel o})/v_R$, where $v_{\parallel o}$ is the component of the bulk plasma ion velocity along the magnetic field. If, under this transformation, orbit distortions are small, and $f(v,\xi)\rightarrow f(v_R,\xi_R)$, where $f(v,\xi)$ is the flux surface averaged fast ion distribution function, then the relaxation of the injected ions can be most conveniently described by the Fokker-Planck equation,

$$\frac{\partial f}{\partial t} = C(f) + S, \qquad \ldots (1)$$

where C(f) is the usual Coulomb scattering operator valid in the velocity range $v_i \ll v \ll v_e$, where now v_i, v, and v_e are the thermal ion, fast ion, and electron velocities in the plasma frame respectively. S is the number of

fast ions produced per unit phase space volume per second with initial velocity v_o on a particular magnetic surface.

The thermonuclear reactivity $\langle\sigma v\rangle$ is then

$$\langle\sigma v\rangle = 4\pi \int_0^\infty v^2 dv\, a_o(v)\, (\sigma v),$$

where (σv) is the reaction rate for fast ions interacting with a warm Maxwellian target plasma, and a solution to Eq.(1) has been obtained in the form of an expansion in Legendre polynomials P_n, viz $f(v,\xi) = \Sigma a_n(v) P_n(\xi)$. Similarly, the "figure of merit", or amplification factor for such a system is defined by

$$Q = \frac{\langle\sigma v\rangle Y}{\bar{S}\, E_o},$$

where Y is the total fusion energy release per reaction, $\bar{S}$ is the number of fast ion produced per unit volume per sec., and E_o is the injection energy.

Using these model simplifications the effects under consideration here can now be examined by invoking the well developed techniques appropriate to the study of injection into stationary plasma systems [3].

3. Effect of Rotation on Local $\langle\sigma v\rangle$ and Q-Factor

For this purpose, and in view of its importance in achieving ignition in present and future tokamaks, we consider the beam-plasma system T(D,n)^{4}He, and in particular the two limiting cases of co-and counter-rotational injection. In the former, and for the range of injection energies $E_o < 120$keV, the rotation of the plasma gives rise to a reduction in the beam-target interaction energy, leading to a reduced reactivity rate and Q-value. In the latter, an increase in the fusion yield will occur. For fast ions in trapped orbits, and due to the increase in thermonuclear cross section with energy, there will be a net gain in yield for these particles.

The results for typical values of electron temperature and injection energies are shown in Figs.2,3. The asymmetry in $\langle\sigma v\rangle$ and Q are clearly indicated. Unbalanced injection leads to a decay in the neutron production during the heating phase. For 80keV deuterium injection into a $T_e = T_i = 10$keV, $n_e = 3\times10^{13}$cm^{-3} tritium plasma rotating with velocity $v_\phi \simeq 0.5C_s$, where C_s is the ion sound speed, a decay in the neutron production due to the fast ions in passing orbits of 10% is predicted. However, this loss in neutron production will be partially compensated by the trapped ion contribution. This point will be discussed in the next section.

4. Modifications to the Fusion Product Birth Profiles

As previously mentioned, for trapped beam ions, the effect of plasma rotation leads for this class of particle, to a net gain in the thermonuclear reactivity and local Q of the system. Since the fraction of fast ions in trapped orbits increases with distance from the toroidal axis, the occurrence of hollow fusion yield profiles in beam-plasma configurations where the fast ion deposition is broad is then expected.

In order to examine this situation we again consider the aforementioned system of 80keV deuterium injection into the $T_e=T_i=$ 10keV, $n_e=3\times10^{13}cm^{-3}$ tritium plasma rotating at various toroidal velocities. In addition we assume a small aspect ratio ($\varepsilon=r/R_o<<1$) cylindrical plasma with minor radius a = 1.25m, major radius R_o = 2.96m, and a flat fast ion deposition profile. The effective fusion reaction rate $\langle\sigma v\rangle \approx \langle\sigma v\rangle_+ + \sqrt{2\varepsilon}(\langle\sigma v\rangle_- - \langle\sigma v\rangle_+)/2$, where the subscripts (+,-) are the calculated, Fig.1, co- and counter-rotation reaction rates respectively. The results of these calculations are shown in Fig.3. It is to be noted that everywhere within the plasma volume the reactivity is reduced. This reduction, which is typically 10% when $v_\phi = C_s$, is greatest on or near the toroidal axis where the fraction of fast ions in trapped orbits is least. However, current large tokamaks (JET, TFTR) have measured $v_\phi < C_s$.

5. Comparison with Measured Neutron Yields during D→D Injection Heating Experiments

We consider #8902 of the current JET database. The decay of the neutron production during the neutral beam heating phase, represented by the bold straight line, is shown in Fig.4. The plasma rotational velocity was observed to be $v_\phi = 1.5\times10^7 cms^{-1}$ after 2 seconds of beam heating alone. for these particular plasma parameters of $T_e=$ 3.63keV, $n_e=2\times10^{13}cm^{-3}$, injection energy $E_o=$ 65keV, and assuming that the principle contribution to the measured neutron yield is from the centre of the discharge, where the fast ions are in passing orbits we obtain $\Delta\langle\sigma v\rangle/\langle\sigma v\rangle \approx 6\%$. However, Fig.4 gives, for constant deuterium density, $\Delta\langle\sigma v\rangle/\langle\sigma v\rangle = 9\%$. This discrepancy between measurement and theoretical prediction is probably due to the uncertainty in deuterium density.

6. Concluding Remarks

The build-up of toroidal momentum during uni-directional neutral injection heating of tokamak plasmas leads to:

i) A reduction in the beam-plasma reactivity and local thermonuclear Q-value.

ii) For the T(D,n)^{4}He system considered this reduction which is greatest at the centre of the discharge is typically 10% for rotation velocities at or near the ion sound speed.

iii) The effect of plasma rotation on fusion reactivity rates can be reduced by increasing the fraction of fast ions in trapped orbits which will be the case during ICRF heating of the beam ions.

iv) Finally, it is worth mentioning that measurements of plasma rotational velocities in current large tokamaks (JET, TFTR) are less than the ion sound speed.

Results of calculations done using actual measured plasma parameters for the JET D→D experiments in which large rotational velocities have been observed are in reasonably good agreement. The possibility of deducing the plasma rotational velocity from the neutron yield measurements should not be excluded.

References

[1] CALLEN, J.D., CLARKE, J.F. Bull. Am. Phys. Soc., 16 (1971).

[2] DAWSON, J.M., FURTH, H.P., TENNEY, F.H. Phys. Rev. Letts., 26 (1971).

[3] CORDEY, J.G., CORE, W.G.F. Phys. of Fluids 17 (1974).

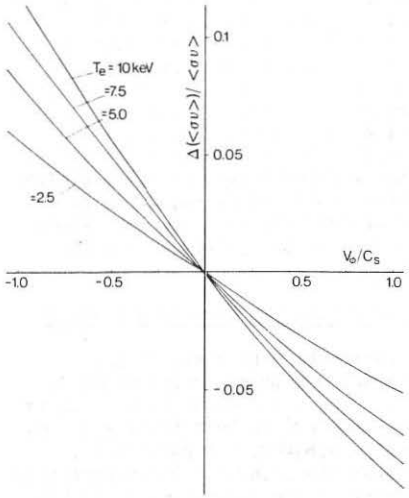

Fig. 1: The effect of rotation on the reactivity rate of fast ions injected in the co- ($v_\phi/c_s > 0$) and counter-rotation ($v_\phi/c_s < 0$) directions are shown.

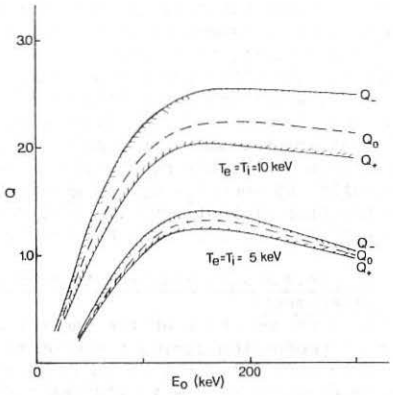

Fig. 2: The local thermonuclear amplification factor Q as a function of deuteron injection energy. Q_+ is the value for counter-rotation and Q_- for co-rotation. Electron density $n_e = 3 \times 10^{13} cm^{-3}$, $v_\phi \simeq 0.5 c_s$, Y=17.6MeV.

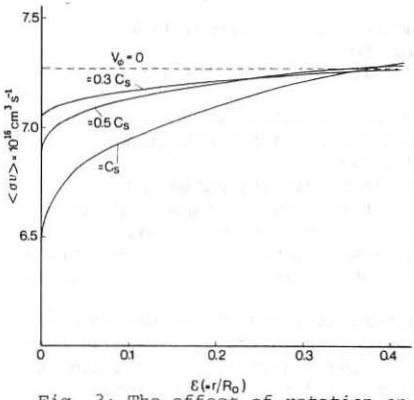

Fig. 3: The effect of rotation on the fusion yield profile is shown. Rotation leads to a reduction in the reactivity which is greatest on or near the toroidal axis where the fraction of fast ions in trapped orbits is least.

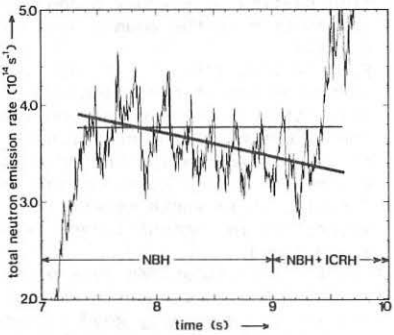

Fig. 4: #8902, D→D injection. The measured neutron yield during the beam heating phase is shown. E_o = 65keV, $n_e = 2 \times 10^{13} cm^{-3}$, T_e=3.6keV.

REDUCTION IN TFTR FUSION REACTION RATE BY UNBALANCED BEAM INJECTION AND ROTATION

H.W. Hendel, D.L. Jassby, M.L. Bitter, G. Taylor

Plasma Physics Laboratory, Princeton University
Princeton, NJ 08544 USA

Abstract. In TFTR plasmas at low to moderate density, the highest fusion energy gain Q_{dd} (D-D fusion power/injected power P_b) is obtained with nearly balanced co- & counter neutral-beam injection. For a given P_b, significantly unbalanced injection reduces Q_{dd} because the accompanying plasma rotation reduces the beam-target fusion reactivity and the fast-ion slowing-down time, the beam-beam reaction rate is reduced, and $\langle T_e \rangle$ and $\langle T_i \rangle$ decrease from their maximum values.

Introduction. Neutral-beam injection (NBI) into tokamak plasmas can be an efficient heating method, but it may also supply torque to the plasma, resulting in bulk-plasma rotation. This rotation in the direction of the beams decreases the relative energy of the beam ions and thermal ions, thereby reducing the beam-target fusion reactivity. Rotation also shortens the slowing-down time of the beam ions into the thermal distribution, resulting in a further reduction of the fusion probability per beam ion [1]. However, in previous tokamak experiments the measured rotation velocity was generally small, $\lesssim 1 \times 10^5$ m/s [2]. Thus simultaneous co and counter injection (defined relative to the plasma current direction) showed only modest advantages in fusion neutron source strength, S, over unidirectional (ie, solely co- or counter-) injection, for the same total beam power, P_b [3]. Counter-injection also seemed to generate a higher impurity level in the plasma than did co-injection. Based on such results, the present generation of large tokamaks was equipped with either co-injection only, or with substantially greater amounts of co than counter power.

TFTR Experimental Conditions. In TFTR during 1985, the neutral beam power was entirely co-injected [1]. During 1986 up to 6 MW counter and up to 14 MW co-injected power were used [4], so that balanced injection (Pco = Pctr) at up to 12 MW of total beam power could be studied. The plasma and fusion parameters could be compared with unbalanced co-only injection at similar total P_b. At the largest P_b, rotational velocity up to 10^6 m/s was measured from the Doppler shift of the Fe XXV resonance line [4,5].

S was measured with a set of seven ^{235}U and ^{238}U fission detectors, which have been calibrated 5 times over a period of 2.5 years, using D-D and D-T neutron generators located inside the TFTR vacuum vessel [1].

Measurements of Q_{dd}. Measurements of S and fusion power gain Q_{dd} (D-D fusion power/injected beam power) have been made over a wide range of densities n, plasma current I_p = 0.6 to 2.2 MA, P_b = 0 to 20 MW, beam energy up to 100 keV, and various proportions of co and counter beam power. Figure 1(a) shows the measured S with D beam injection into D plasmas as a function of I_p, over most of the range of P_b. In TFTR,

higher I_p results in higher n, even with well-conditioned limiter surfaces. S and Q_{dd} maximize at $I_p \simeq 1$ MA, which is associated with low initial target density. Figure 1(b) shows the electron temperature T_e vs P_b, indicating a general trend similar to that of the S behavior. The beam-target (S_{bt}) and beam-beam (S_{bb}) reaction rates [6] increase strongly with the beam slowing-down time, which is proportional to $(T_e)^p/n$, where $p \simeq 1$ for the present conditions [1]. Thus one of the reasons that S (and Q_{dd}) maximize at I_p near 1 MA is the maximum in T_e and (importantly for S_{bb}) the relatively low n that pertain to this I_p.

Figure 2 shows Q_{dd} vs P_b near the optimum $I_p = 1$ MA, both for unidirectional and bidirectional (co+counter) injection. At a given P_b, there is a distinctly higher Q_{dd} for bidirectional injection, compared with unidirectional injection. This result is due to 3 effects: (1) Plasma rotation is much smaller under balanced conditions than for unidirectional injection. (2) Beam-beam reactions are greatly enhanced with bidirectional injection. (3) At higher P_b, bidirectional injection gives rise to the so-called "supershot" conditions, which generate better confinement and therefore higher T_e and T_i [7]. Simulations using the SNAP [8] and TRANSP [9] codes that include these effects predict values of S in generally good agreement with the experimental values.

The improved Q_{dd} for bidirectional injection is observed at I_p up to about 1.4 MA. However, for still higher I_p, which is associated with higher density, unidirectional injection produces results similar to those of bidirectional injection at the same total P_b. This result is due to the facts that, at high density, plasma rotation is negligible, $S_{bb} \propto 1/n^2$ is small, and the enhanced-confinement "supershot" regime has not been accessible to date under high-n, high-I_p conditions. Hence little is gained by using balanced injection at high density.

Figure 3 shows the behavior of Q_{dd} as a function of the power balance parameter, defined as BAL = (Pco - Pctr)/P_b, for the optimal range of I_p. As evident from both Figs. 2 and 3, $Q_{dd} = S/P_b$ with bidirectional injection exceeds Q_{dd} with co-injection alone by a factor up to 4.8, and with ctr-injection alone by a factor up to 12. The smallest Q-values occur at BAL = ±1 because: (1) The largest torque and rotational velocity, v_ϕ, occur at BAL = 1, with smaller but still substantial v_ϕ at BAL = -1 for the same P_b. (2) The beam-beam reaction rate is relatively small with unidirectional injection. (3) For a given P_b, the highest T_e and T_i occur at BAL ~ 0.1. The enhanced-confinement "supershot" conditions are inaccessible with completely unbalanced injection. (It is not clear whether the magnitude of rotation affects the ability to obtain supershot conditions. v_ϕ is still significant at BAL = 0.1, where Q_{dd} is maximum.)

Computer Simulations. The contributions of various physical phenomena to the increase in S in going from unidirectional injection to nearly balanced injection have been investigated with computer simulations. The measurements of S near the end of the beam pulse have been compared with results calculated by the SNAP time-independent radial profile analysis code [8], which accounts for rotation and the 3 sources of fusion

reactions. For "supershot" conditions, agreement of the code predictions with experimental S is rather good, with a typical discrepancy ~ 25%, which is within the experimental and modeling uncertainties. The code results show that, near the end of the NBI pulse, S_{bt}/S is generally close to 0.55, but there is considerable variation in S_{bb}/S_{tn} from one set of plasma and beam conditions to another.

Table 1 shows the variation of the S_{ij} values for 2 shots with BAL=0 and BAL=1, both for I_p = 0.9 MA, total P_b = 10.4 MW and Z_{eff} ~ 4. The balanced case has 2.8 times the Q_{dd} of the BAL=1 case (a smaller factor than usual), and the S calculated by SNAP is in reasonable agreement with the measured value in both cases. If rotation is eliminated in the SNAP simulation for the BAL=1 case, S_{bt} increases by a factor of 1.65, S_{bb} increases by a factor of 4, and total S and Q_{dd} increase by a factor of 1.8. (The large increase in S_{bb} is due mainly to a substantial increase in beam-ion slowing-down time when rotation = 0.) The remaining factor of 1.5 difference in the Q's between the BAL = 0 case and the BAL = 1 case without rotation is due to a further increase in S_{bb} with bidirectional injection, and to the 20% higher T_e and somewhat broader T_e profile obtained when BAL ~ 0.1 [4,7]. Other pairs of shots show significantly larger S_{tn}/S at BAL=0, which in those cases is due to a substantial increase in T_i with balanced injection [4,7].

This work was supported by the U.S. Dept. of Energy. We acknowledge useful discussions with H.H. Towner and M.C. Zarnstorff.

References

[1] H. W. Hendel, et al., J. Fusion Energy 5 (1986) 231.
[2] S. Suckewer, et al., Phys. Rev. Lett. 43 (1979) 207; R. C. Isler, et al., Nucl. Fusion 23 (1983) 1017.
[3] J.D. Strachan, et al., Nucl. Fusion 21 (1981) 67.
[4] R.J. Hawryluk, et al., in 11th Intern. Conf. Plasma Physics and Contr. Nucl. Fusion Res. (Kyoto, Japan, 1986), Paper No. A-I-3; GOLDSTON, R.J., et al., ibid., Paper No. A-II-1.
[5] M. Bitter et al., Phys. Rev. A 32 (1985) 3011.
[6] D.L. Jassby, Nucl. Fusion 17 (1977) 309.
[7] J.D. Strachan, et al., Phys. Rev. Lett. 58 (1987) 1004.
[8] H.H. Towner, et al., Bull. Am. Phys. Soc. 28 (1983) 1252 and Bull. Am. Phys. Soc. 31 (1986) 1610.
[9] R.J. Goldston, D.C. McCune, H.H. Towner, J. Comp. Phys. 43 (1981) 61.

Table 1.
Variation of Neutron Source Strength with Injection Mode and Rotation

Shot #	Case	Rotat. (m/s)	$T_e(0)$ (keV)	SNAP Calculations (10^{15} n/s) Sbb	Sbt	Stn	Total S	Expt. S (10^{15} n/s)
25915	BAL=0	0	5.6	1.57	2.60	0.67	4.84	4.50
25916	BAL=1	5.2×10^5	4.7	0.25	1.22	0.48	1.95	1.65
25916	BAL=1	0	4.7	1.16	2.00	0.38	3.54	1.65

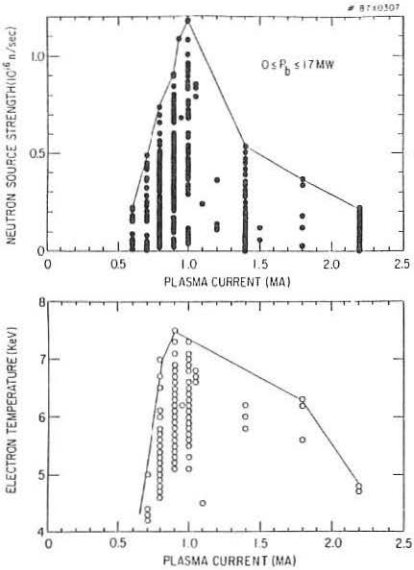

Fig. 1 Neutron source strength and central electron temperature vs. plasma current. $T_e(0)$ is determined from electron cyclotron emission.

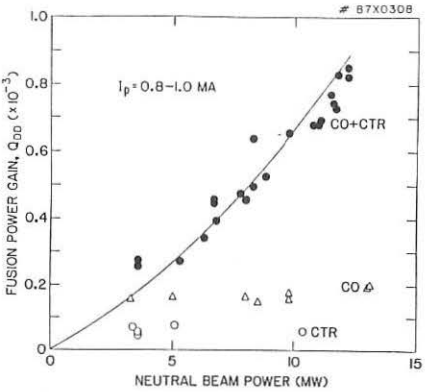

Fig. 2 D-D fusion power gain vs. beam power, for bi-directional injection and unidirectional injection.

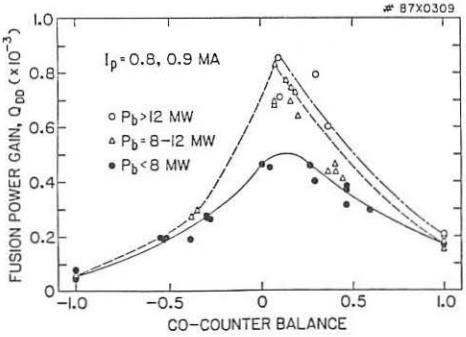

Fig. 3 D-D fusion power gain vs. NBI balance parameter = (Pco - Pctr) /P_b.

ENERGY AND PARTICLE CONFINEMENTS OF COMBINED HEATING DISCHARGES IN JT-60

S. Tsuji and JT-60 Team
Naka Fusion Research Establishment
Japan Atomic Energy Research Institute
Naka-machi, Naka-gun, Ibaraki 311-02, Japan

Introduction: Combined heating with NB and LHCD (current drive by lower hybrid range of frequency waves) produces an improvement in energy confinement, while NB heating alone suffers degradation with power/1,2/. This mode of operation may have possibility to decouple current profile from electron temperature profile and to be free of a constraint on energy confinement by "profile consistency".

JT-60 is equipped with three units of LH system with total generator power of 24 MW. One unit of the LH system is designed for current drive and the other two for heating experiments/3/. We tried to extend the improved confinement regime to higher plasma current and/or higher electron density with the help of LH power of the heating units in 1987. The effect of combined heating was explored applying the LH power up to 6 MW. Consequently suppression of internal MHD modes by LHCD was found to be essential to get the improved energy confinement.

Global particle confinement time was examined in relation to the degradation and improvement in energy confinement by beam heating and by the combined heating with LHCD, respectively.

Improved Energy Confinement by LHCD + NB: The incremental energy confinement time τ_E^{inc} ($\equiv \Delta W_s / P_{add}$) evaluated from magnetics is plotted against $\beta_p + \ell_i/2$ just before beam injections into LHCD plasmas in Fig. 1. When the LH wave reduced $\beta_p + \ell_i/2$, the incremental energy confinement time increased up to 90 ms. Since the variation of $\beta_p + \ell_i/2$ mostly reflects the change in internal inductance, target plasmas with broader current profiles tend to have better energy confinement. As the plasma current increases, the improvement curve shifts to left-hand side since q_{eff} decreases.

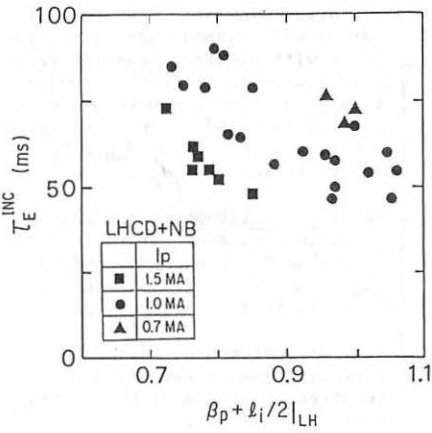

Fig. 1: Incremental energy confinement time of LHCD + NB as a function of $\beta_p + \ell_i/2$ just before beam injections.

The improvement in energy confinement is well correlated with the suppression of internal MHD modes. While beam injections often excite internal m=1 oscillations and enhance sawteeth, the combined heating with LHCD suppresses the m=1 oscillation as shown in Fig. 2. In this case, a mild MHD mode at outer radius was excited after switching off the LH power. Figure 3 indicates that there is anti-correlation between τ_E^{inc} and central soft X-ray fluctuations, which include the m=1

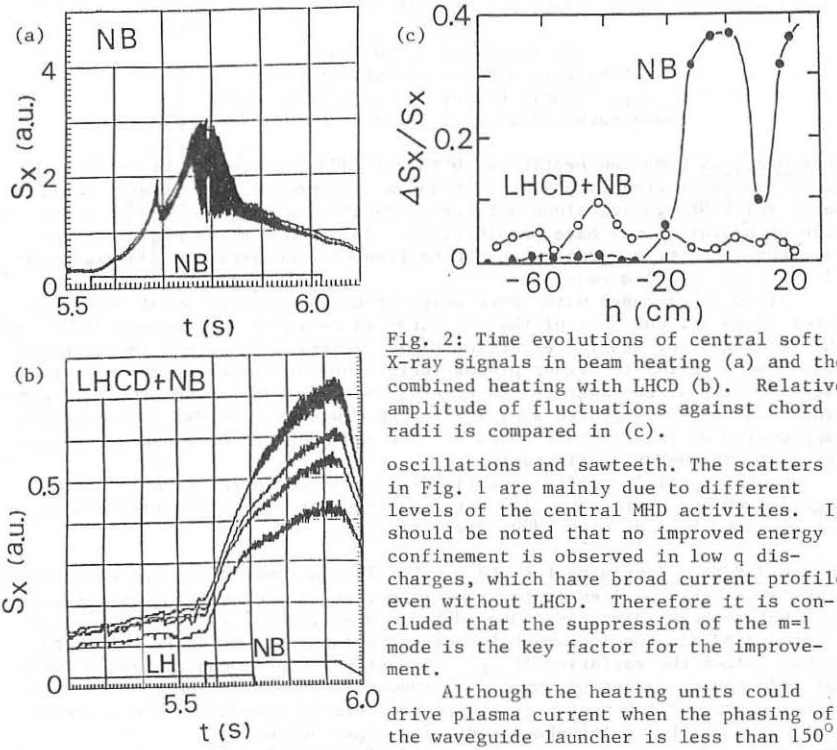

Fig. 2: Time evolutions of central soft X-ray signals in beam heating (a) and the combined heating with LHCD (b). Relative amplitude of fluctuations against chord radii is compared in (c).

oscillations and sawteeth. The scatters in Fig. 1 are mainly due to different levels of the central MHD activities. It should be noted that no improved energy confinement is observed in low q discharges, which have broad current profile even without LHCD. Therefore it is concluded that the suppression of the m=1 mode is the key factor for the improvement.

Although the heating units could drive plasma current when the phasing of the waveguide launcher is less than 150°, they were not so effective in reducing ℓ_i of target plasmas. Hence significant improvement was observed in few discharges with plasma current of 1.5 MA or with electron density higher than $1.2\times10^{19}m^{-3}$. Further conditioning of the launchers and more careful gas feed is required since a figure of merits of $P_{LH}/\bar{n}_e I_p$ counts to reduce $\ell_i/2$/.

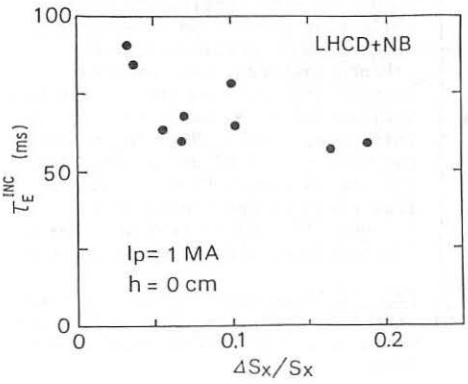

Fig. 3: Incremental energy confinement time of LHCD + NB against relative amplitude of the central soft X-ray signal.

Particle Confinement: Global particle confinement time is evaluated basing on H_α measurements /4/ assuming toroidal symmetry, which is believed to be a good

approximation in divertor discharges. Figure 4(a) shows the particle confinement time as a function of line averaged electron density. LHCD plasmas have longer particle confinement time with lower recycling coefficient. Although τ_p of OH plasmas is about 0.15 s at low electron density, it drops sharply around $n_e \sim 3\times10^{19}m^{-3}$, where energy confinement time begins to saturate departing from neo-Alcator scaling in JT-60/5/. Electron density profile becomes very flat at higher density and the recycling coefficient approaches to unity. Thus τ_p has strong correlation with peakedness of electron density profile as plotted in Fig. 4(b).

Beam heated plasmas have shorter particle confinement time than ohmically heated plasmas by a factor of about one third when compared with the same peakedness. Data points with $n_e(0)/\langle n_e\rangle \sim 1.25$ are collected in Fig. 5 to see the dependence of τ_p on heating power. The result indicates that the particle confinement time decreases with nearly inverse square root of heating power similarly to the energy confinement time. Considering that beam fueling is deep inside the plasma compared with gas fueling, the deterioration in particle confinement should be severer than it appears to be.

There is no apparent difference between LHCD + NB and NB in terms of τ_p. Regrettably we cannot estimate τ_p of He discharges, by which most of the good energy confinement data were obtained. Among the data points in Fig. 4, improvement was only observed when $\tau_p > 0.08$ s. The discharges with improved energy confinement have peaked electron density profile including He shots.

Discussion: Both in ohmically and beam heated plasmas, the degradation in

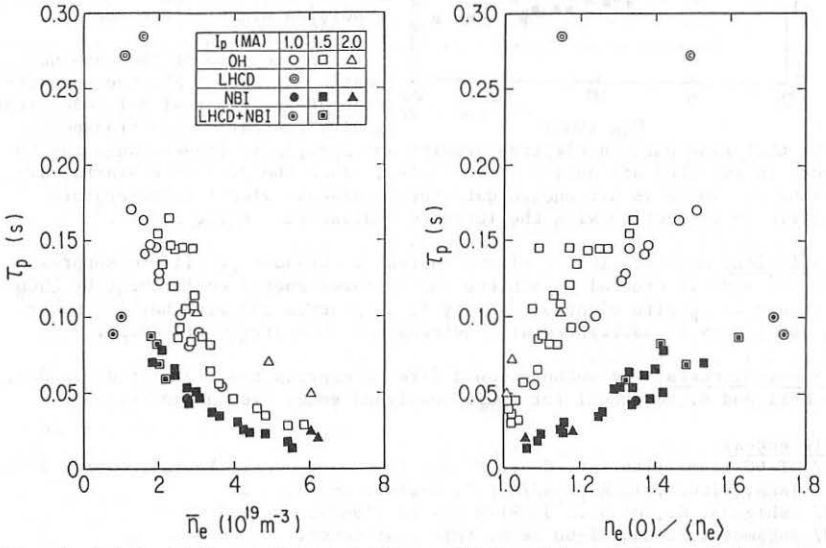

Fig. 4: (a) Particle confinement time against line averaged electron density. (b) Particle confinement time against electron density peakedness.

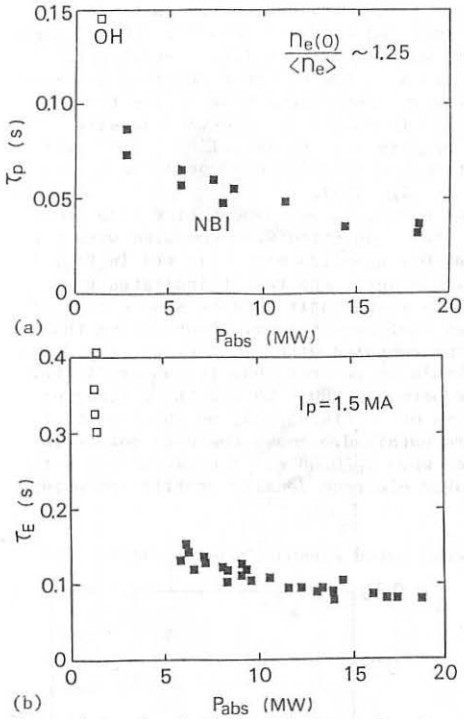

Fig. 5: (a) Particle confinement time as a function of heating power with nearly the same electron density peakedness.
(b) Energy confinement time against heating power for 1.5 MA hydrogen discharges.

particle confinement is associated with that in energy confinement. While particle confinement is not directly connected with energy confinement, it determines boundary conditions. When τ_p is less than 0.05 s, convective loss dominates at the boundary in addition to enhanced charge exchange loss, resulting in low boundary temperature. Actually the electron temperature at 3~6 cm inner from the separatrix surface measured by Thomson scattering is almost constant around 500 ev even when beam power is doubled from 7 MW to 14 MW. If there is the constraint of profile consistency, the boundary condition might affect energy confinement.

In the case of the combined heating of LHCD + NB, the suppression of the internal m=1 mode might modify central plasma transport. Note that rise both in electron density and $\beta_p+\ell_i/2$ is impeded when the LH power is switched off during a beam pulse, since the discharge starts saw-toothing. There is not enough data set to discuss electron temperature profile in connection with the improved confinement at the moment.

Conclusion: Modification of plasma current to broader profile to suppress the m=1 mode is crucial to achieve the improved energy confinement by LHCD. Decrease in τ_p with electron density in OH plasmas and with heating power in NB plasmas is associated with degradation in energy confinement.

Acknowledgements: The authors would like to express their gratitude to Drs. S. Mori and K. Tomabechi for their continued encouragement and support.

References:

/1/ JT-60 Team, 11th Int. Conf. Plasma Phys. and Contl. Fusion, Kyoto, 1986, IAEA, Vienna, IAEA-CN-47/A-I-1, A-II-2. K-I-2.
/2/ Ushigusa, K., et al., JAERI-M 87-012 (1987).
/3/ Sakamoto, K. and JT-60 Team, this conference.
/4/ Yamada, K., et al., to be published in Nucl. Fusion.
/5/ Hirayama, T., et al., JAERI-M 87-029 (1987).

CONFINEMENT OF OHMICALLY HEATED PLASMA

F. Alladio, F. De Marco, L. Pieroni

Associazione EURATOM-ENEA sulla Fusione, Centro Ricerche Energia Frascati, C.P. 65 - 00044 Frascati, Rome, Italy

INTRODUCTION

Ohmically heated tokamaks have recently attracted renewed interest because of the complexities of auxiliary heating systems and the degradation of confinement in L regimes. Moreover [1,2] it has been found in JET and TFTR that the ignition parameter $n_i(o)\ T_i(o)\ \tau_E$ is quite similar in both purely ohmic plasmas and those with large additional power.

Paradoxically this fact has produced two opposite trends to reach ignition: one toward very high field compact tokamaks (HFT), such as Ignitor and Ignitex [3,4], the other toward very large devices [5].

With respect to HFTs valuable information can be derived from existing high field devices such as FT and Alcator C.

In FT a detailed study of ohmic confinement was performed both with the global power balance and with the heat pulse propagation method [6]. The two methods are in good agreement with each other and also confirm our previously published data [7]. The global confinement τ_E turns out to be lower than that calculated with Neo Alcator - TFTR scaling (NAT), i.e., $\tau_E(s) = 7\times10^{-22}\ \bar{n}R^2aq_L$. This is shown in Fig. 1 by FT data for $B_T > 4T$.

This result led us to make a comparison with published data on ohmic confinement from other experiments and to attempt an assessment on this subject.

METHOD OF INVESTIGATION

We perform this assessment comparing global confinement times τ_E with NAT.

This method is open to the following criticisms:

a) There is some debate as to whether τ_E is a meaningful parameter. If, for example, confinement is determined by profile consistency plus edge conditions, τ_E does not depend essentially on the characteristics of the main plasma.

b) There is a large degree of arbitrariness in choosing a scaling law.

Regarding point a), due to the heat pulse propagation results, we believe that, at least in ohmic discharges, τ_E is a meaningful parameter and depends on bulk plasma parameters.

Concerning point b), we decided to compare the experimental results with NAT for the following reasons:

1) There is a growing consensus on the R^2a factor which is also derived by a number of theoretical models [8].
2) FT shows a $\tau_E \propto I^{-1}$ dependence (Fig. 1). In addition most of the machines show $\tau_E \propto_E q^{\alpha}$ with $0.5 \leq \alpha \leq 1$.

It results that the actual values for τ_E derived from NAT are in satisfactory agreement with the experimental ones obtained in a number of

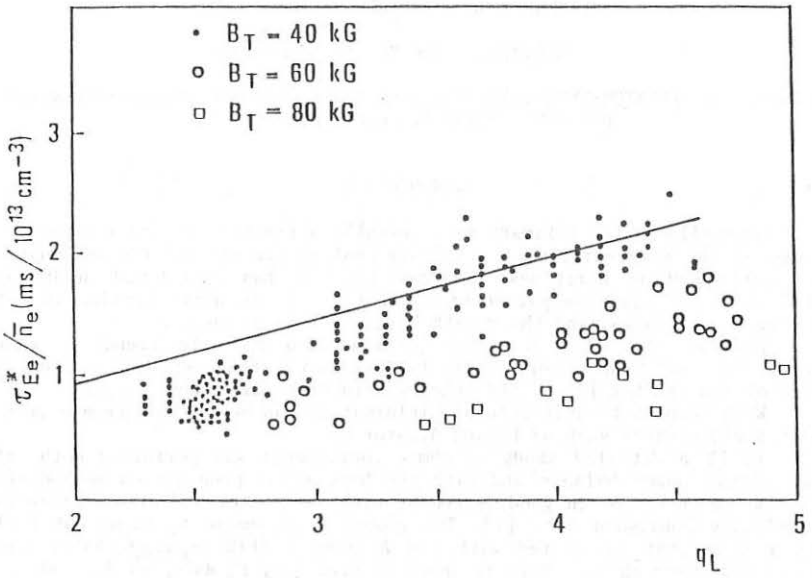

Fig. 1: FT electron energy replacement time ($\tau^*_{Ee} \sim \tau_E/2$) normalized to line average intensity vs q_L at different values of toroidal field. The full line represents the Neo Alcator TFTR scaling.

low or medium field tokamaks. On the other hand HFTs appear to have confinement results below those predicted by NAT. It must be noted that the analysis refers to experimental points away from density saturation, runaway regimes and strong transient conditions.

RESULTS OF THE ANALYSIS

Figures 2 and 3 show the experimental energy confinement times vs $\bar{n}R^2aq$ for the labelled devices. Among the large experimental devices, results of ohmic confinement in JT-60 are not represented since the density saturation occurs at very low linear average density and the density profiles, especially in divertor discharges, are very flat and cannot be assimilated to a parabolic shape as in all the other tokamaks [9].

Alcator C results refer to discharges at $7.5 \leq B_T \leq 8.5$ T [10] and $3.5 \leq q_L \leq 4.5$, while those of Alcator A [11] refer to $B_T = 6$ T and $0.16 \leq I_p \leq 0.18$ MA.

The trend of ohmic energy confinement in HFTs (Fig. 3) shows a lower value with respect to NAT scaling.

In Table I some characteristics of HFTs and low field large tokamaks are indicated.

It is to be noted that the main difference, apart of course from the

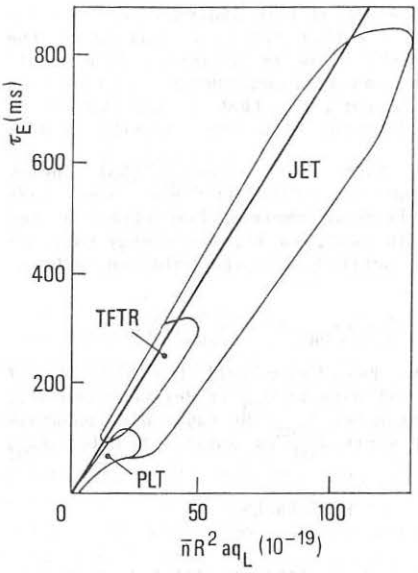

Fig.2: Range of experimental energy confinement times in ohmic discharges vs $\bar{n}R^2aq_L$ for PLT, TFTR and JET. The full line represents the Neo Alcator TFTR scaling.

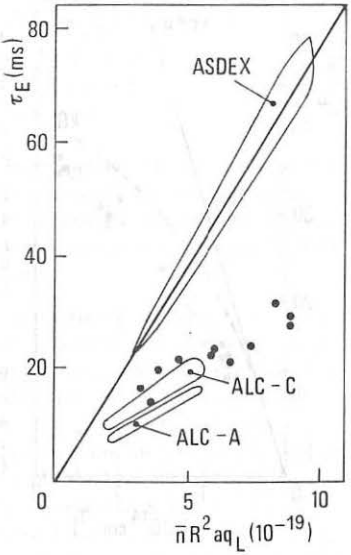

Fig. 3: Range of experimental energy confinement times in ohmic discharges vs $\bar{n}R^2aq_L$ for ASDEX, Alcator C, Alcator A. The points represent data for FT at 6 T. The full line represents the Neo Alcator TFTR scaling.

TABLE I

	P_{OH}(MW)	Vol(m^3)	P_{OH}/V(W/cm^3)	P_{AUX}(MW)	P_{TOT}/V(W/cm^3)
FT	1	0.6	1.7	0.5	2.5
ALC A	0.35	0.1	3.5		
ALC C	1	0.34	3	2	> 5
ASDEX	0.4	5.2	$8x10^{-2}$	< 5	< 1
TFTR	2	32	$6x10^{-2}$	20	0.6
JET	3	150	$2x10^{-2}$	30	0.2

size of the device, is in the power density that is obtained in all HFTs with respect to the low medium field devices, even when the maximum additional power is taken into account.

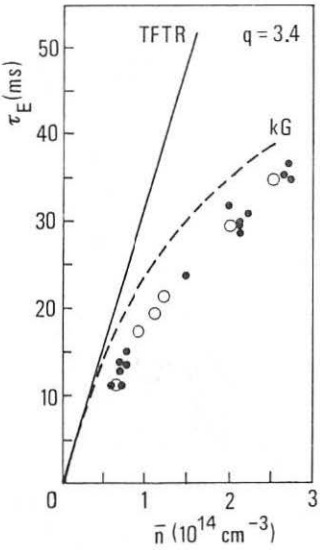

Fig.4: FT experimental confinement time vs $\bar{n}$ at $B_T = 6$ T and $q_L \sim 3.4$. The full line represents the Neo Alcator TFTR scaling. The dotted line represents the Goldston combination between "ohmic" confinement time and τ_{aux} with P_{OH} substituting P_{TOT} in the Kaye-Goldston scaling law for L mode regime.

The result of this analysis seems to indicate that either the size scaling of the quoted scaling law is different from a 1^3 dependence (an $1^{3.5}$ dependence could explain the difference), or that a degradation of ohmic confinement with power density is present.

This last fact suggests that energy confinement in tokamaks has the same features both in ohmic and auxiliary heated plasmas. In fact, in FT, the energy confinement time derived from the Goldston combination, i.e.

$$(\tau_E)^{-2} = (\tau_{OH})^{-2} + (\tau_{aux})^{-2}$$

represents reasonably well the behavior of experimental data if τ_{OH} is derived from NAT, and assuming for τ_{aux} the Kaye-Goldston scaling [12] where P_{OH} is substituted for P_{TOT} (Fig. 4).

REFERENCES

[1] THE JET Team, IAEA-CN-47/A-I-2, 11th Int. Conf. on Plasma Physics and Controll. Nuclear Fusion Research, (Kyoto 1986).

[2] R.J.Hawryluk and TFTR Group, IAEA-CN-47-/A-I-3, 11th Int. Conf. on Plasma Physics and Controll. Nuclear Fusion Research, (Kyoto 1986).

[3] B. Coppi, Comments Plasma Phys. Controll. Fusion 3, 47 (1977).

[4] Basic Design Report for the Fusion Ignition Experiment (IGNITEX) - Center for Fusion Engineering (University of Texas, Austin) March 1987.

[5] P.H. Rebut and the JET Team, 14th Symposium on Fusion Technology, (Avignone 1986).

[6] F. Alladio et al., paper No 0396, this Conference.

[7] F. Alladio et al., Nucl. Fusion 22, 479 (1982).

[8] W.M. Tang, Nucl. Fusion 26, 1605 (1986).

[9] M. Nagami and JT-60 Team, IAEA-CN-47/A-II-2, 11th International Conference on Plasma Physics and Controlled Nuclear Fusion Research, (Kyoto 1986).

[10] K.I. Thomassen, LLL-PROP-00202, Lawrence Livermore National Laboratory Rep. July (1986).

[11] M. Gaudreau, et al., Phys. Rev. Lett. 39, 1266 (1977).

[12] S.M. Kaye and R.J. Goldston, Nucl. Fusion 25, 65 (1985).

MEAUSUREMENTS OF TOROIDAL ROTATION ON TFTR

S. D. Scott, M. Bitter, H. Hsuan, K. W. Hill,
R. J. Goldston, S. von Goeler, M. Zarnstorff
Princeton Plasma Physics Laboratory

Abstract Toroidal rotation measurements during a beam power scan at constant final density on TFTR show a offset-linear increase in rotation speed with increasing power. Rotation measurements during edge and central beam heating experiments suggest that momentum transport is governed by a diffusive mechanism and that momentum diffusivity is considerably larger during central heating.

To supplement a large database survey of rotation speed during neutral beam injection in TFTR[1], we consider a dedicated scan in which only the beam power was varied from zero to 5.6 MW. Beam power from two co-tangential beamlines was injected for 500 ms into the current flattop of a 2.2 MA, 4.7 T plasma resting on the outer blade limiter at R = 2.58 m, a = 0.82 m. The pre-injection density ($\overline{n}_e$ = 4.2 to 3.2 $\times$ $10^{19}\mathrm{m}^{-3}$) was adjusted to provide nearly the same density at the end of injection ($\overline{n}_e$ = 4.3 to 4.9$\times 10^{19}\mathrm{m}^{-3}$) for all shots. The plasma heating and confinement scaling derived from this scan has been discussed by Murakami et al. [2]. As shown in Fig. 1, the global energy confinement time decreased with beam power according to $\tau_\mathrm{E} \propto P_b^{-0.6}$ or by an offset linear form, $\tau_\mathrm{E} = \alpha + \beta/P_\mathrm{heat}$, with the incremental confinement time, α, equal to 100 ms.

Figure 2 shows the central rotation speed versus time measured from the Doppler shift of Ti XXI Kα line radiation for several representative shots in the scan. Analysis of the velocity time history just following beam turn-on (first 60 ms) shows that the product of the pre-injection plasma density and the initial velocity time derivative increases linearly with beam power, confirming that deposited torque increases proportionately to incident beam power. As observed on PDX [3], the exponential decay-time for central velocity following beam turn-off (500 ms, decreasing to 325 ms at higher power) is substantially larger than the steady-state momentum confinement time. The maximum velocity attained during neutral injection increases in an offset-linear fashion to the applied power or torque, $v_\phi(\mathrm{m/s}) = 3.0 \times 10^4 + 2.35 \times 10^4 \times P_b(\mathrm{MW})$, or $v_\phi(\mathrm{m/s}) = 3.0 \times 10^4 + 4.7 \times 10^{23} \times T(\mathrm{N \cdot m})/\overline{n}_e(\mathrm{m}^{-3})$, where T is the incident beam torque. The velocity can be fit equally well by a power-law form, $v_\phi \propto (\mathrm{T}/\overline{n}_e)^{0.74\pm0.12}$.

To derive quantatative estimates of the global momentum confinement time from the central rotation speed measurements, we solve the global angular momentum balance, $\frac{\partial L}{\partial t} = T_\mathrm{a}(t) - \frac{L}{\tau_\phi}$, where L is the total angular momentum stored in the plasma, τ_ϕ is a global momentum time, and $T_\mathrm{a}(t)$ is the beam torque delivered to the thermal plasma. This equation is solved assuming (1) A fixed radial profile for $v_\phi(r) \propto (1 - (r/a)^2)^{0.5}$; (2) Equal rotation speeds for all ions; (3) No beam-ion losses; and (4) Deposited torque calculated numerically using standard Fokker-Planck operators for slowing-down and pitch-angle scattering. Figure 1 shows the global momentum confinement times derived from this analysis that are consistent with the

measured central rotation speeds. The inferred τ_ϕ decreases modestly with increasing torque ($\tau_\phi = 123 \rightarrow 95$ ms at high power) and is substantially less than the global energy confinement time. The assumed profile shape is broader than measured by Burrell et al. [6] in D-III limiter discharges (which were slightly more peaked than parabolic) but it matches the early rise of $v_\phi(t)$ just following beam turn-on better than a parabolic profile. The experimental values for τ_ϕ are considerably larger than rough theoretical estimates based on neoclassical viscosity [4,5] ($\tau_\phi \propto R^2 Z_{eff} B_T / T_i$), using Z_{eff} values measured from visible bremsstrahlung and central ion temperatures derived from Doppler broadening of Ti XXI Kα line radiation, which lie in the range $\tau_\phi(\text{theory}) = 30 - 45$ ms. The measured central rotation speeds would be consistent with $\tau_\phi(\text{theory})$ only for rather peaked radial profiles of velocity, $v_\phi \propto (1 - (r/a)^2)^4$.

Goldston et al. [7] compare the plasma heating obtained with edge-weighted and centrally-weighted neutral injection by injecting beams that either miss the magnetic axis or that pass through the plasma core in a slightly reduced-bore plasma with $R = 2.36\text{m}, a = 0.70\text{m}, I_p = 1.2\text{MA}, B_T = 4.6\text{T}, \bar{n}_e(\text{OH}) = 2.6 \times 10^{19}\text{m}^{-3}$, and $P_b \simeq 2.3\text{MW}$. The beams were modulated in three 100 ms pulses separated by 100 ms off-periods. Differences in time response of the observed *central* rotation speed in these experiments allow us to identify the dominant momentum transport process as diffusive or non-diffusive, and to determine the relative magnitude of momentum transport during edge and central heating. The central rotation speed during centrally-weighted heating shows a clear modulation which is correlated with the beam timing (Fig. 3a). By contrast, the rotation speed during edge-heating rises more or less monotonically throughout the entire 500 ms of modulated beam injection to a final speed approximately 2/3 of the speed attained with central-heating. This is the qualitative behavior one would expect if momentum transport were predominantly diffusive in character, allowing an inverted rotation speed profile ($v_\phi(\text{edge}) > v_\phi(\text{central})$) to relax to a flatter profile during the beam-off periods. To quantify this observation, we compare the mean central rotation speed to the results of a 1-D transport simulation.

The transport simulation [8] solves the momentum balance equation [9],

$$mnR\frac{\partial}{\partial t}v_\phi + mRv_\phi\frac{\partial n}{\partial t} = T_a(r,t) + \frac{1}{r}\frac{\partial}{\partial r}(rRmn\chi_\phi\frac{\partial}{\partial r}v_\phi) - \frac{mnRv_\phi}{\tau_{\phi cx}} - \frac{1}{r}\frac{\partial}{\partial r}(mrRv_\phi\Gamma_p) \quad (1)$$

where $T_a(r,t)$ is the deposited beam torque density, $\Gamma_p(r,t)$ is the ion flux, $\tau_{\phi cx}(r)$ is the charge-exchange loss time for toroidal momentum, and $\chi_\phi(r)$ is the momentum diffusivity. The deposited torque is calculated from collisional slowing-down and pitch-angle scattering of the energetic beam ions, plus a small contribution ($O(\epsilon)$) due to first-orbit effects [9]. For computational efficiency, the particle flux is calculated crudely through the continuity equation ($\partial n/\partial t + \nabla \cdot n = \text{sources}$), using only beam ionization as a particle source.[1] Simulations were performed for $\chi_\phi(r) = \text{constant}$ and for $\chi_\phi(r) = \text{constant} \cdot (1 + 2r/a)$, where the magnitude of the constant was chosen

[1]This treatment obviously underestimates convective transport at the plasma edge where ionization by wall neutrals is a significant source of ions, but it captures an essential process in that it cancels

to best reproduce the measured velocity time history. Fig. 3b shows the calculated velocity time history for edge-heating, using $\chi_\phi = 3.0\ \mathrm{m}^2/\mathrm{s}$. It confirms that a diffusive transport mechanism gives rise to a monotonically increasing or very gently modulated central velocity. The agreement between measured and calculated velocity is excellent, with the exception of the calculated bulge following final beam turn-off that is not present in the measurements. Similarly, the simulation for central heating (Fig. 3a) reproduces the modulated velocity observed in that experiment, using $\chi_\phi = 7.0\ \mathrm{m}^2/\mathrm{s}$. Thus, momentum transport appears to be considerably faster when the beam heating is centrally weighted, similar to the behavior of energy transport. This conclusion is not altered if a radially-dependent form of χ_ϕ is utilized; rotation during edge-heating is adequately fit by $\chi_\phi(r) = 1.4(1 + 2r/a)\mathrm{m}^2/\mathrm{s}$, while rotation during central heating is fit by $\chi_\phi(r) = 3.1(1 + 2r/a)\mathrm{m}^2/\mathrm{s}$.

We remark that the *inward* diffusion of momentum implied by the edge-heating experiment is inconsisent with the recent gyroviscous model of momentum damping [4], which without further development appears to allow for only an outward-directed flow of momentum. Inward diffusion of momentum is also inconsistent with local damping mechanisms such as ripple-damping. Also, even without measurements of radial profiles of rotation speed, the edge-heating experiments establish some bounds on the radial dependence of $\chi_\phi(r)$. The momentum diffusivity cannot be too strongly peaked near the plasma edge, because an excessively edge-weighted $\chi_\phi(r)$ causes the deposited torque to dissipate to the wall before it can diffuse to the plasma center. Thus, profiles of $\chi_\phi(r)$ more peaked than $\chi_\phi(r) \propto (1+2r/a)$ are unable to reproduce the measured central rotation speed, irrespective of the *magnitude* of χ_ϕ. Small multipliers on the magnitude of χ_ϕ generate large edge rotation speeds, but then the time scale for diffusion of the edge momentum to the plasma center exceeds the duration of beam injection, and thus the calculated *central* velocity remains smaller than the observed value.

This work was supported by U.S. DOE contract No. DE-AC02-76-CHO-3073.

References

[1] M. Bitter et al., these proceedings.
[2] M. Murakami et al., Plasma Physics and Controlled Fusion **28** (1986), p. 17-27.
[3] K. Brau et al., Nucl. Fusion **23** (1983) p. 1643.
[4] W. M. Stacey, D. J. Sigmar, Phys. Fluids **28** (1985) 2800.
[5] W. M. Stacey, C. M. Ryu, M. A. Malik, Nucl. Fusion **26** (1986) p. 293.
[6] K. H. Burrell et al., GA-A18679 (1986). Submitted to Nucl. Fusion.
[7] R. J. Goldston et al., these proceedings.
[8] M. Bitter et al., PPPL-2357 (1986). Submitted to Nucl. Fusion.
[9] R. J. Goldston, Proceedings of Course and Workshop: Basic Physical Processes of Toroidal Fusion Plasmas (Varenna, 1985), p. 165.

---

the $\partial n/\partial t$ term in Eq. 1 following beam turn-off, which would otherwise lead to an unphysical global increase in velocity (neglecting momentum diffusion) as the density falls.

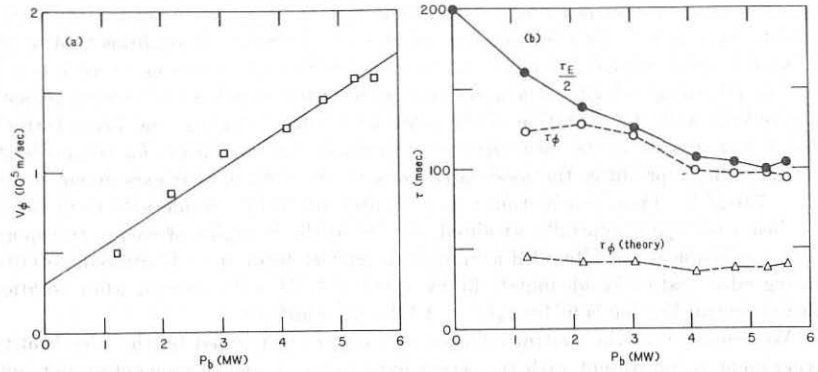

Fig.1. (a) Central rotation speed versus power. (b) Energy and momentum confinement time in beam power scan, and theoretical momentum damping time (gyroviscosity).

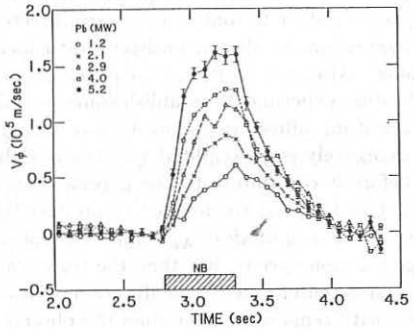

Fig.2. Time history of central rotation speed during the beam power scan.

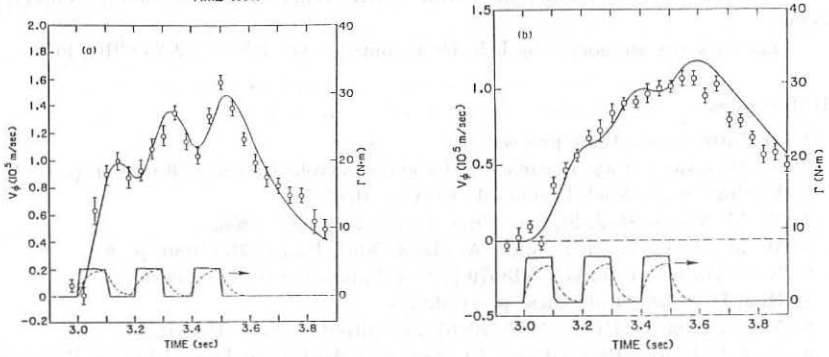

Fig.3. (a) Measured rotation speed during central heating and 1-D transport simulation. Lower curves show incident (solid) and absorbed (dotted) beam torque. (b) Rotation speed and simulation during edge-heating.

LOCKED n=1 MODES IN JET

J A Snipes, D J Campbell, P S Haynes*,
T C Hender*, M Hugon, N Lopes Cardozo@, F C Schuller

JET Joint Undertaking, Abingdon, Oxon, OX14 3EA, UK

*(UKAEA/Euratom Fusion Assn)Culham Laboratory, Abingdon, Oxon, OX14 3DB, UK
@Association Euratom-FOM, FOM-Instituut voor Plasmafysica, Rijnhuizen, Nieuwegein, The Netherlands

Introduction MHD oscillations in JET are often observed to slow down as they grow and lock when the amplitude exceeds $\tilde{b}_\theta$(wall) $\sim$ 10 G, then continue to grow to large amplitude ($\tilde{b}_r/B_\theta$(wall) $\sim 0.6 - 1.2 \times 10^{-2}$). Such locked modes occur before all density limit disruptions and most current rise disruptions and can also develop after pellet injection, as well as after 'monster' [1] sawteeth and remain at a large amplitude throughout the discharge. They have a dominant toroidal mode number of n=1 and poloidal mode numbers of m=2, 3, or 4. These large amplitude modes can have profound effects on the plasma affecting sawteeth, the electron temperature profile, plasma rotation, particle losses and in some cases may be responsible for a decrease in the plasma stored energy.

Calculations with two MHD codes [2,3] indicate that interaction of the growing oscillating mode with a resistive wall or a small ($\sim$ 10 G at the wall) external field asymmetry may be responsible for mode locking.

Detection of Locked Modes Integrating the difference of signals from saddle coils about the outer midplane from the same signals 180° apart toroidally measures the odd n component of the radial field perturbations in the plasma. Two of these predominantly n=1 signals, at toroidal angles of 45° and 135° (relative to Octant 1) provide the sin and cos components of the mode so that the amplitude and phase of the locked mode can be determined.

Location of Locked Mode O and X Points Under most conditions, the mode locks in the same position and remains in that position throughout the discharge. Figure 1 shows a view of Octant 3 (ϕ = 90°) of JET for the standard locked mode position as calculated by an MHD code [2]. The X point of the m=2, n=1 mode lies in the midplane. This corresponds to having the 45° locked mode signal negative and equal and opposite to the 135° signal. In some cases, especially after the plasma current and toroidal field were reversed for counter injection operation, the mode locks in other locations or changes phase after it has locked, suggesting that if a field asymmetry is responsible, it changes with conditions.

Pre-disruptive Locked Modes Oscillating growing MHD precursors with predominantly m=2, n=1 (or sometimes m=3) are observed before most disruptions. The frequency of oscillation usually lies between 200 Hz and 1 kHz, but increases with NB power to > 5 kHz. The oscillations may last for only a few msec or for as long as 200 msec before the mode locks. When locking occurs, the tangential field amplitude at the wall is 4 - 20 G and the radial field is 0.25 - 1.5 G. After locking, the mode grows to an amplitude of $\tilde{b}_r/B_\theta$(wall) $\sim 0.6 - 1.2 \times 10^{-2}$ just before disruption. The

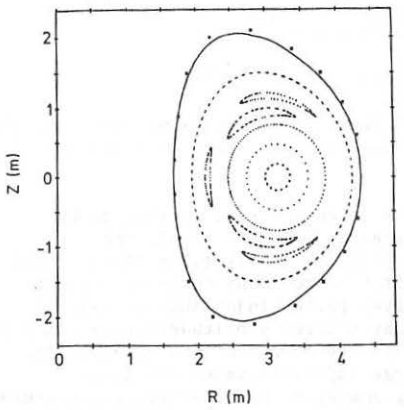

Figure 1. Simulation of locked mode just before disruption ($\tilde{b}_\theta/B_\theta = 1\%$).

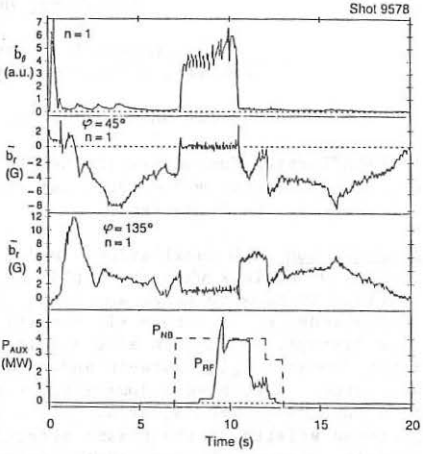

Figure 2. Early locked mode unlocks during NB, then locks again after a sawtooth collapse.

duration of the locked mode phase before disruption is normally about 100 msec, but can be shorter than 10 msec at very low q or longer than 1.5 sec at intermediate or high q. At very low q, the usual precursor oscillations are absent leaving only a rapidly growing n=1 displacement about 20 msec before the disruption.

Current Rise Locked Modes Locked modes often develop during the current rise even as early as 400 msec into the discharge reaching an amplitude of $\tilde{b}_r/B_\theta$ (wall) $\sim 2 - 6 \times 10^{-3}$. Depending on the evolution of $q_\psi(a)$, the locked mode can decay after 0.5 - 2 sec, continue to grow until disruption, or persist throughout the length of the discharge. It is observed that the chance of having a disruption following a current rise locked mode is greatly enhanced when $q_\psi(a)$ lies between 3 and 4.. By modifying the evolution of $q_\psi(a)$ through changing the plasma aperture, the current rise rate, the toroidal field, or indirectly through changing the density, current rise locked modes can be reduced in amplitude or even eliminated. Skin current effects may play a role in mode locking during the current rise. Figure 2 shows a locked mode that begins in the current rise, then unlocks with the NB and oscillates for several seconds before it locks again after a sawtooth collapse and remains locked throughout the remainder of the discharge. The top trace is a rectified and smoothed n=1 combination of poloidal field pick-up coils. The second and third signals are the locked mode monitor signals. Poloidal analysis of the mode structure of current rise locked modes indicates that the dominant mode number can be at least as high as m=4, n=1. It is possible that the driving mode is still m=2, n=1 through toroidal mode coupling.

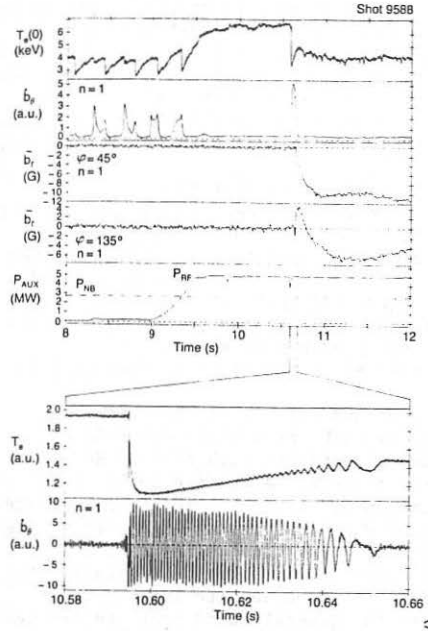

Figure 3. Mode locking occurs after a monster sawtooth during combined ICRH and NB heating. The expanded T_e signal looks just inside the sawtooth inversion radius.

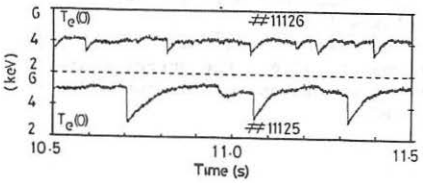

Figure 5. Effects of locked modes on sawteeth. The top trace is during a locked mode, while the bottom trace has no locked mode.

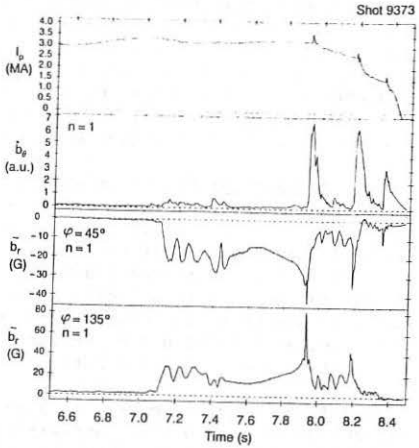

Figure 4. Pellet injection (7.0 sec) induces a locked mode that leads to a disruption.

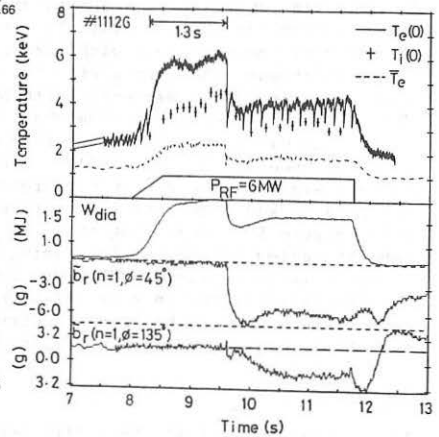

Figure 6. Reduction in diamagnetic stored energy during a locked mode after an ICRH only monster sawtooth.

Locked Modes After Monster Sawteeth Figure 3 shows a locked mode induced by a monster sawtooth collapse during combined ICRH and NB heating. The expanded time traces show the mode locking on both the ECE and n=1 poloidal pick-up coil combination signals. Normally, after a combined heated monster sawtooth there is a large ($\tilde{b}_\theta / B_\theta \sim 7 \times 10^{-4}$) oscillating m=3, n=2 mode that persists for several seconds [1], but when the oscillating mode locks, the m=2, n=1 can be dominant and oscillate for only 60 msec before locking.

Locked Modes After Pellet Injection In many cases, just after the injection of a pellet there arises a large locked mode that can persist for several seconds or result in a disruption. Figure 4 shows such a pellet induced locked mode that eventually leads to a disruption. The pellet was fired at 7.0 sec into the discharge. The density decays much more rapidly if the pellet induces a locked mode, suggesting that such large MHD modes can increase particle losses. The 'snake' oscillations [4] often observed after pellet injection can persist in the presence or absence of oscillating and locked MHD activity observed on the magnetic diagnostics.

Discussion Large MHD modes can have profound effects on the plasma. Figures 3 and 5 show that sawteeth during such large modes are reduced in amplitude by more than a factor of two and saturate much faster. Before density limit disruptions, the electron temperature profile about the q_ψ=2 surface is rapidly flattened over a region of 10-15 cm just after the mode locks [1]. The spatial distribution of the neutral influx due to recycling can also be affected during large MHD modes near the density limit.

A very prominent effect of locked modes is that they can actually stop the observed central plasma ion toroidal rotation despite intense input momentum from the NB [5]. This follows the general trend that the central ion velocity compares well with that calculated from the frequency of edge MHD oscillations. The strong effects on sawteeth and the central plasma rotation suggest that magnetic perturbations measured at the wall can affect the center of the plasma when they reach sufficient amplitude.

In some cases, particularly after monster sawteeth, the onset of a large MHD mode ($\tilde{b}_r/B_\theta \sim 2.4 \times 10^{-3}$) coincides with a 20 - 25% drop in the stored energy (Figure 6). In the previous shot, which was similar but without a locked mode, the temperature reached 5.5 keV at the sawtooth peaks (Figure 5), suggesting that the large MHD mode may have kept the temperature low perhaps by increasing plasma losses.

Since large amplitude MHD modes can affect the plasma momentum, particle balance, and in some cases, appear to affect the energy content their effects need to be better understood and taken into account when these basic plasma properties are analyzed.

References

[1] D J Campbell, et al, Proc 11th Int Conf on Plasma Physics and Contr Nucl Fusion Research, (Kyoto, 1986).
[2] T C Hender, D C Robinson, and J A Snipes, Proc 11th Int Conf on Plasma Physics and Contr Nucl Fusion Research, (Kyoto, 1986).
[3] M F Nave and J A Wesson, this conference.
[4] A Weller, et al, this conference.
[5] D Stork, et al, this conference.

SAWTOOTH PERIOD AND THE POSSIBLE EVIDENCES OF A MAGNETIC TRIGGER FOR THE SAWTOOTH CRASH IN THE OHMIC DISCHARGES OF FT

F. Alladio, G. Bardotti, R. Bartiromo, M. Bassan, G. Bracco, F. Bombarda, G. Buceti, P. Buratti, E. Caiaffa, R. Cesario, F. Crisanti, R. De Angelis, F. De Marco, M. De Pretis, D. Frigione, R. Giannella, M. Grolli, S. Mancuso, M. Marinucci, G. Mazzitelli, F. Orsitto, V. Pericoli-Ridolfini, L. Pieroni, S. Podda, G.B. Righetti, D. Santi, S.E. Segre, A.A. Tuccillo, O. Tudisco, G. Vlad, V. Zanza

Associazione EURATOM-ENEA sulla Fusione, Centro Ricerche Energia Frascati, C.P. 65 - 00044 Frascati, Rome (Italy)

CHARACTERISTICS OF THE SAWTOOTH RELAXATION

An extensive study of the sawtooth period and of the MHD activity connected with the sawtooth crash has been performed in the deuterium ohmic plasmas of FT at a toroidal field B_T= 6 T. The sawtooth inversion radius r_s, as desumed by the SXR emission Abel inverted using the Cormack method [1] (with m=0 poloidal number), scales with the safety factor at the edge q_L as: $r_s/a = 1/q_L$ (where a is the minor radius of the plasma) (Fig. 1). Such dependence, already observed in other machines [2], is well verified in the whole range of discharges considered, with $2.5 < q_L < 4.5$. The empirical scaling of the sawtooth period is found to be $\tau_R(ms)=3.9\ \bar{n}_e^{1/2}$ (with the electron density $\bar{n}_e$ in units of $10^{20}/m^3$), without any significant dependence on q_L. The central sawtooth electron temperature modulation, as measured by electron cyclotron emission (ECE) ranges between 3% and 15% in all these shots, with a scaling that is not far away from $\Delta T_e(0)/T_e(0) \sim 1/n_e\ q_L^{5/2}$.

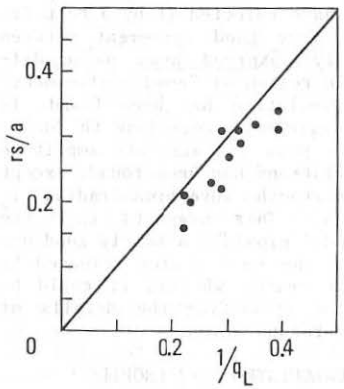

Fig. 1: Inversion radius as desumed by the Abel inverted SXR emission (using the Cormack method with m=0) vs $1/q_L$.

THE SAWTOOTH TRANSPORT SIMULATION CODE

A full transport simulation code [3] which solves the system of coupled non-linear diffusive equations for the electron temperature $\tilde{T}_e$ and poloidal field $\tilde{B}_\theta$ perturbations has been used in order to simulate the sawtooth activity. We use the boundary conditions of $\tilde{T}_e(a,t)=\tilde{B}_\theta(a,t)= 0$ and as initial conditions the perturbations of the quantities $\tilde{T}_e$ and $\tilde{B}_\theta$ as predicted by the Kadomtsev reconnection model [4]. Electron thermal conduction as desumed by the (steady state) power balance [5] and neoclassical electric conductivity have been used. In performing the power balance, purely neoclassical ion losses [6] have been assumed: this figure is

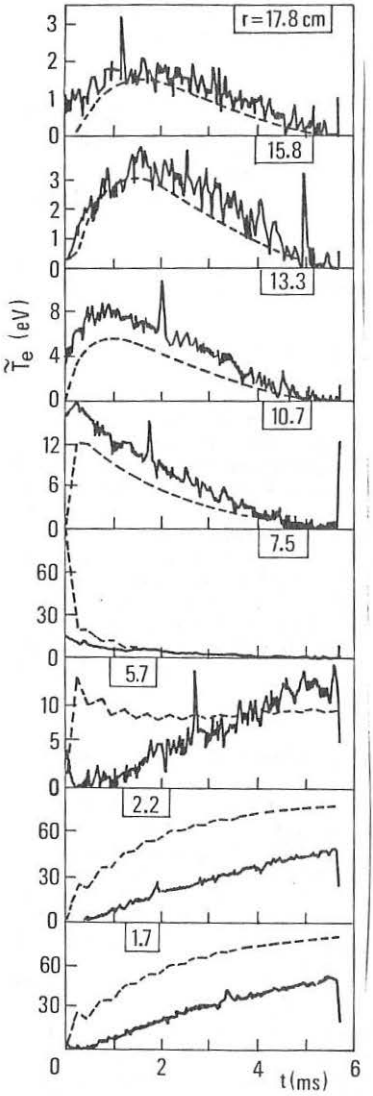

Fig. 2: $\tilde{T}_e(r,t)$ versus time for different radii as measured by ECE (solid lines) and calculated by the diffusive code (dashed lines). Discharge parameters are: q_L=2.55, $\bar{n}_e$=1.88x10^{20} m^{-3}, r_S~7.4 cm.

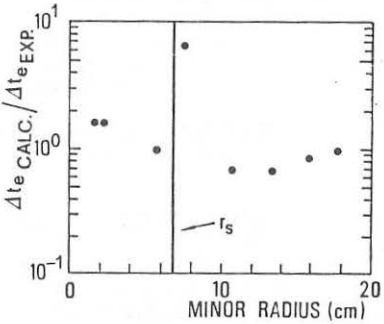

Fig. 3: Ratio between the calculated electron temperature fluctuation and the observed one versus the minor radius, for the same discharge of Fig. 2.

compatible with $T_e(0)$ and $T_i(0)$ measurements in the centre. In the region $0<r\lesssim r_s$ the value of the electron thermal conductivity can not be desumed by the power balance: we have selected it by a best fit of $\tilde{T}_e(0,t)$. Very good agreement between experimentally observed heat pulse diffusion in the region of "good confinement" $1\lesssim q\lesssim 2$ and simulation has been found. In particular, agreement regarding the delay of the pulse peak and absolute amplitude of the oscillations has been found, except near the sawtooth inversion radius r_s (Figs 2 and 3). This suggests that the Kadomtsev model provides a fairly good description of the heat source released by the sawtooth crash, whereas it could be inadequate in accounting the details of the magnetic reconnection.

THE CALCULATED q(r) PROFILE

In the central region of the plasma ($r\lesssim r_s$) the calculation predicts hollow q(r) profiles: just after the Kadomtsev reconnection the q in the centre is calculated to rise above unity. Then the q profile evolves in a non-monotic

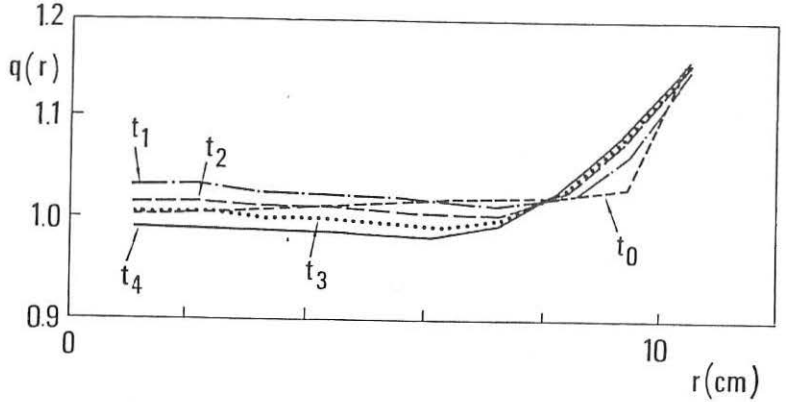

Fig. 4: Typical behavior of the q(r,t) profile: t_o= just after the crash; $t_1=\tau_R/4$; $t_2=\tau_R/2$; $t_3=3/4\tau_R$; $t_4=\tau_R$, just before the crash.

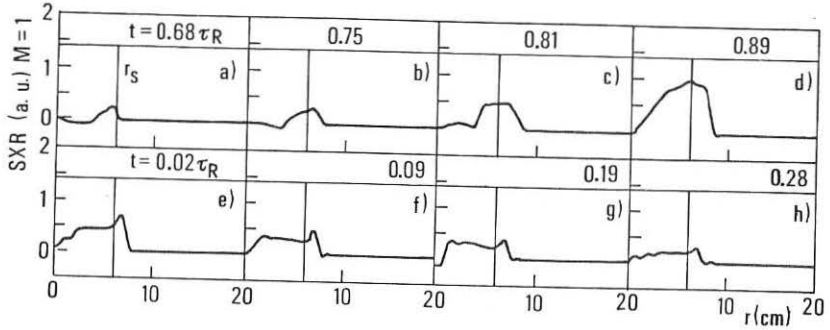

Fig. 5: Abel inverted amplitude of the MHD activity (using the Cormack method with m=1) versus radius for different times before the sawtooth crash a) b) c) d) and after e) f) g) h). Discharge parameters are: q_L=3.13, $n_e=0.80\cdot10^{20}$ m^{-3}, τ_R=3.5 ms.

profile with an off-axis minimum (Fig. 4). In a time $t\sim(0.6\div0.7)\tau_R$ the off-axis minimum falls below unity and two q=1 resonant radii appear: the external one is almost fixed in time, the innermost is calculated to move towards the centre and to reach it in a time that is very near to the sawtooth repetition time for all the discharges. However the calculated values of q in the central region are always very close to unity $|q-1|\sim0.02$.

THE MHD ACTIVITY ASSOCIATED WITH THE SAWTOOTH

This picture is supported by the observation of an m=1 MHD precursor activity phase of the sawtooth ($t\sim(0.7\div0.8)\tau_R$) on the SXR signals. The amplitude of the m=1 Cormak inverted signals reveal that the observed before the end of the rising time reaching the centre just before the and that its radial extension increases in mode starts near the inversion radius r_s crash (Fig. 5). This suggests the possibility of a magnetic trigger condition [7] q(0)=1 for the sawtooth crash.

A preliminary analysis of the linear stability of such hollow q(r) profiles with a complete MHD resistive toroidal code [8] has shown that a radial displacement eigenfunction localized between the two q=1 resonances is obtained, as far as a resistive mode is excited. This happens for values of the magnetic Lundquist number $S\lesssim10^7$, comparable with those obtained in FT.

As far as an ideal mode is excited (e.g. rising the value of S or increasing the pressure gradient) a two steps radial displacement eigenfunction appears with the discontinuities localized around the two q=1 resonant surfaces, the amplitude being higher in the centre, as expected by an analytic minimisation of δW for two q=1 radii [9]. Thus the experimental evidence of the localized MHD activity in FT seems to be in agreement with the onset of a resistive m=1 mode. In almost all the discharges an m=1 successor MHD activity (Fig. 5) is also observed which is radially flat between the centre and r_s, persisting up to $t\sim0.3\ \tau_R$. Again such behavior suggests that the details of the magnetic reconnection are not well described by the Kadomtsev model.

ACKNOWLEDGMENT

The authors are indebted with Drs T.C. Hender, J. Hastie and D. Robinson for providing the access to the toroidal stability code FAR and fruitful discussions.

REFERENCES

[1] A.M. Cormark, J. Appl. Phys. 34, 2722 (1963) and 35, 2908 (1964)
[2] R.J. Goldston, Plasma Phys. Controll. Fusion 26, 87 (1984)
[3] F. Alladio, G. Mazzitelli, A.A. Tuccillo, G. Vlad, 12th European Conference on Controlled Fusion and Plasma Physics, Budapest (1985) Part. I, p. 138.
[4] B.B. Kadomtsev, Sov. J. of Plasma Phys. 1, 389 (1975).
[5] F. Alladio et al., paper No 0396A this Conference.
[6] C.S. Chang, F.L. Hinton, Phys. Fluids 25, 1493 (1982).
[7] J. Wesson, Plasma Phys. 28, 1A, 243 (1986).
[8] T.C. Hender, private communication.
[9] J. Hastie, private communication.

SAWTOOTH HEAT PULSE DIFFUSION IN THE FRASCATI TOKAMAK

F. Alladio, G. Bardotti, R. Bartiromo, M. Bassan, G. Bracco, F. Bombarda, G. Buceti, P. Buratti, E. Caiaffa, R. Cesario, F. Crisanti, R. De Angelis, F. De Marco, M. De Pretis, D. Frigione, R. Giannella, M. Grolli, S. Mancuso, M. Marinucci, G. Mazzitelli, F. Orsitto, V. Pericoli-Ridolfini, L. Pieroni, S. Podda, G.B. Righetti, D. Santi, S.E. Segre, A.A. Tuccillo, O. Tudisco, G. Vlad, V. Zanza

Associazione EURATOM-ENEA sulla Fusione, Centro Ricerche Energia Frascati, C.P. 65 - 00044 Frascati, Rome (Italy)

1. THE OPERATION PARAMETERS

The sawtooth heat pulse diffusion has been systematically studied in the FT ohmic discharges in deuterium plasmas at a toroidal field B_T = 6 T. The operating Hugill-Murakami diagram [1] has been explored in the range $2.4 < q_L < 4.5$; $1.0 \bar{n}_e R/B_T < 3.7 \cdot 10^{19}$ Wb^{-1} (Fig. 1).

The electron temperature profiles $T_e(r)$, as measured by a single shot multi-point Thomson scattering system are shown in Fig. 2, the profile for each series being ordered in the figure according to its Hugill-Murakami parameters. The fits to the profiles shown in Fig. 2 have been obtained compelling the q=1 resonance to correspond to the SXR inversion radius r_s [2].

Also marked in Fig. 2 are the q=1 and q=2 resonant radii, that bound the so called confinement region of the discharge, and the shaded area below each profile corresponds to the radial extent over which the sawtooth heat pulse diffusion is observed; such region corresponds in all cases to the inflection of the $T_e(r)$ profile.

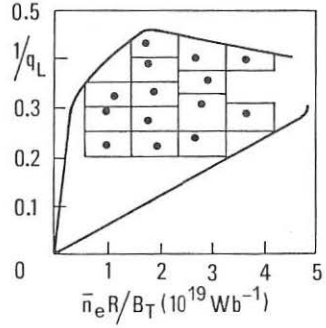

Fig. 1: Hugill plot of sawtooth ing discharges parameters studied in this paper.

2. χ_{ePB} FROM THE POWER BALANCE

In order to derive the electron thermal conductivity χ_{ePB} a power balance in steady state must be performed [3], taking into account the local ohmic power input calculated from $T_e(r)$, the measured radiation loss, the computed charge exchange loss, and the electron-ion power exchange. The latter comes from the solution of the ion power balance equation, with neoclassical thermal transport assumed in the Chang-Hinton form [4] with a neoclassical multiplier α=1 (the available data of $T_e(0)$-$T_i(0)$ are not in conflict with $1<\alpha<3$). The electron equation is solved for the heat conduction loss $P_{\chi e}$ and the resulting $\chi_{ePB} = \int P_{\chi e}\, dv/4\pi^2 r R n_e \nabla T_e$ can be estimated. Three examples of radial

behavior of χ_{ePB} for a low density, a high density and a low q_L discharge are shown in Fig. 3.

3. χ_{eHP} FROM THE SAWTOOTH HEAT PULSE DELAY

The average $\bar{\chi}_{eHP}$ in the plasma region through which the temperature perturbation diffuses can be directly deduced from the radial observation of the time elapsed $t_p(r)$ until the heat pulse induced by the sawtooth activity reaches its maximum amplitude. This method can be summarized by the formula [5]

$$\Delta t_p = \Delta r^2 / 9\bar{\chi}_{eHP} \qquad (1)$$

In Figure 4 $\bar{\chi}_{eHP}$ as deduced from electron cyclotron emission is compared to χ_{ePB}, the cylindrical volume average of χ_{ePB} in the heat pulse observation region [5]. For all q_L values and $n_e R/B_T$ values, one can summarize the result as $1 < \bar{\chi}_{eHP}/\bar{\chi}_{ePB} \lesssim 2$.

In order to check this result a more complete comparison of the $2\omega_{ce}$ emission measured electron temperature fluctuations has been performed with a diffusion-reconnection code. The detailed comparison is presented in the companion paper [2] in this Conference and confirms that a single electron thermal conductivity $\chi_e(r)$ determines both the steady state $T_e(r)$ profiles and rules as well the transient modifi cations of such profiles (as far as the sawtooth induced perturbations are considered).

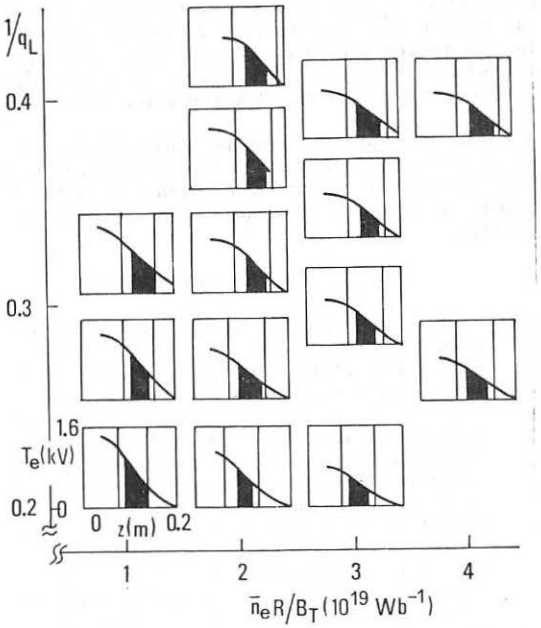

Fig. 2: Electron temperature profiles ordered in the Hugill-Murakami diagram.

4. INFERENCE ON THE ION THERMAL TRANSPORT

The electron energy confinement time can be written as

$$\tau_{Ee} = k a_T^2 / \bar{\chi}_{eHP} \qquad (2)$$

where a_T is the effective discharge radius obtained extrapolating linearly at the $T_e(r)$ inflection toward the edge of the discharge.

On the other hand, as the radial profile of the total energy confinement time τ_E is quite constant over the radius, the comparison should re

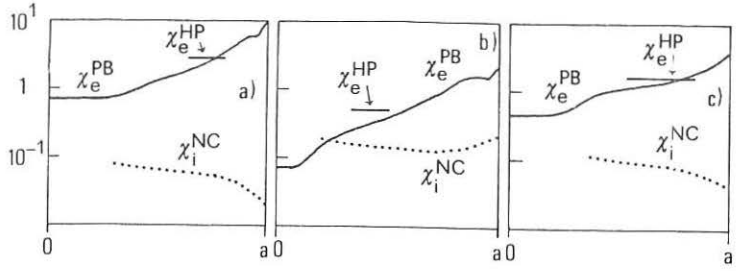

Fig. 3: Radial behavior of the thermal conductivity χ_{ePB} (r) as desumed from the power balance for a) low density discharge, b) high density discharge, c) low-c_L discharge.

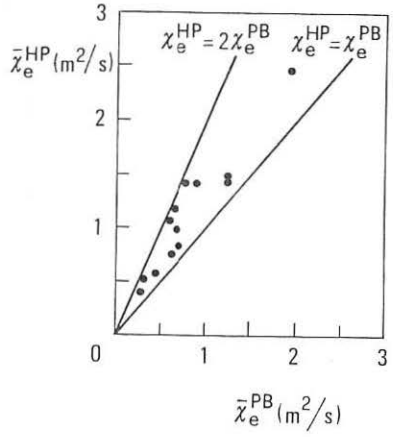

Fig. 4:Comparison between $\bar{\chi}_{eHP}$ as deduced from sawtooth diffusion and $\bar{\chi}_{ePB}$ deduced from power balance.

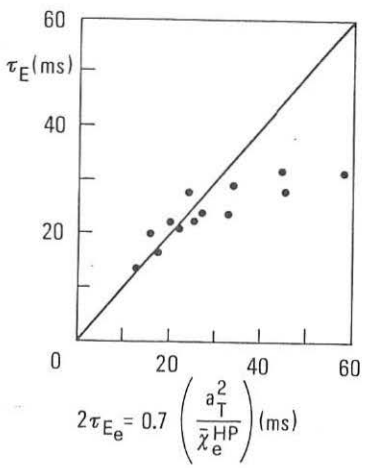

Fig. 5:Plot of total energy confinement time τ_E (from profile measurements) versus $2\tau_{Ee} = 0.7(a_T^2/\bar{\chi}_{eHP})$ (from sawtooth diffusion).

veal whether the electron thermal transport dominates the plasma energy balance in the confinement region or whether the ion thermal conduction plays in this region any significant role. Considering, as in all the present cases, approximately equal total thermal energy in the electron and ion species one gets the link with the ion energy confinement time τ_{Ei}, as:

$$2/\tau_E = 1/\tau_{Ee} + 1/\tau_{Ei} \qquad (3)$$

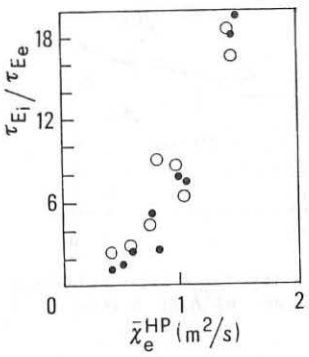

Fig. 6:Ratio of ion energy confinement time and electron energy confinement time as deduced from sawtooth diffusion (•) and from power balance with neoclassical ion thermal-conductivity (○).

So, if the ions do not play a significant role in the energy transport, $\tau_E = 2k(a_T^2/\bar{\chi}_{eHP})$. If, instead, the ions play a significant role, the deviation of the dependence of τ_E on $(a_T^2/\bar{\chi}_{eHP})$ from a linear one should give the ratio

$$\tau_{Ee}/\tau_{Ei} = 2ka_T^2/\bar{\chi}_{eHP}\ \tau_E - 1 \qquad (4)$$

Figure 5 shows that at large values of τ_{Ee} the ion effect seems quite relevant (with k=0.35 to fit reasonably well the linear portion of the data in expression (2)).

Figure 6 compares the estimates of τ_{Ei}/τ_{Ee} coming from equation (4) applied to the data of Fig. 5 with the value of τ_{EiNC}/τ_{Ee} as deduced from the power balance. A first observation is that the comparison in Fig. 6 seems to indicate that the ion thermal transport in the confinement region has roughly neoclassical values $\chi_i \sim (1\div2)\ \chi_{iNC}$. A second observation is that already at 3/4 of the high density limit (see Fig. 1) Fig. 6 seems to suggest that the ion thermal transport is almost equal to the electron thermal transport.

REFERENCES

[1] F. Alladio et al., Nucl. Fusion 26, 11 (1986)
[2] F. Alladio et al., paper No 0397A this Conference
[3] F. Alladio et al., Nucl. Fusion 22, 479 (1982)
[4] C.S. Chang, F.L. Hinton, Phys. Fluids 25, 1493 (1982)
[5] E.D. Fredrickson et al., Nucl. Fusion 26, 849 (1986)

MAGNETIC FLUCTUATIONS AND THEIR CORRELATION WITH DENSITY FLUCTUATIONS IN TEXT*

K. W. Gentle, Y. J. Kim, Ch. P. Ritz, and T. L. Rhodes
Fusion Research Center
The University of Texas at Austin
Austin, Texas 78712

Introduction

Magnetic fluctuations and turbulence are of particular interest in tokamaks as a possible mechanism for anomalous transport in the plasma interior and as an elucidator of the mechanisms of edge turbulence. Although there is good evidence implicating magnetic turbulence with degradation of confinement in some high-beta, beam-heated plasmas,[1,2] the situation for ohmic discharges is not resolved. Extensive observations of magnetic fluctuations on TEXT,[3] a tokamak with $R = 1m$, $a = 0.26m$, and operated with $1.5 \leq B_T < 3T$, $100 \leq I_p \leq 400$ kA, and $1 \times 10^{19} \leq n \leq 8 \times 10^{19}/m^3$, illustrate the complexity of the phenomena. A ubiquitous spectrum of magnetic turbulence can be observed from outside the plasma extending to several hundred kiloHertz. The spectrum extends from coherent, discrete modes of $m = 2$ or 3 through a broad turbulent range which includes both moderate-m components ($m \leq 10$) from the interior and high-m components ($m \leq 40$) which are associated with the electrostatic edge turbulence. The spectral properties (frequency, wavenumber, coherency) of these components will be described, as well as their association with transport. The first measurement of $k_\parallel$ for edge turbulence will be described.

Experimental Technique

The magnetic fluctuations are measured with small loops inside a thin stainless steel jacket. Their sensitivity extends to 1 MHz and $k < 3\text{cm}^{-1}$ ($m < 80$); they may be placed as close as 1 cm to the limiter radius. Ordinary Langmuir probes penetrating just inside the limiter radius are used to measure the properties of the electrostatic edge turbulence. Conventional FFT techniques are used to obtain frequency spectra, but more modern, powerful statistical techniques[4] are used to extract the coherency and phase as a function of frequency for signal pairs.

Characteristics of Magnetic Turbulence

A typical power spectrum for $\dot{B}$ is shown in Fig. 1. The largest power is in discrete (narrow-band) low-frequency modes found to be $m = 2 - 4$. Above that, the spectrum is featureless and monotonically decreasing. (The apparent peak sometimes appearing near 100 kHz is significant, but the power curve for $\tilde{B}$, obtained by dividing by ω^2, never has maxima.) The spectra extend to a few hundred kiloHertz, but

* Work supported by the U. S. Department of Energy.

with negligible power in the higher frequencies. Even excluding the discrete modes, significant magnetic turbulence does not extend much beyond 100 kHz. The signals have the properties expected: they are primarily radial and poloidal with at most a small toroidal component, radial and poloidal components at one point are highly correlated and 90° apart in phase, and a single component at points separated only in minor radius maintains perfect correlation and no phase difference.

To test for a gross correlation of magnetic turbulence with energy transport, a survey of $\tilde{B}_{\rm rms}$, excluding the discrete modes, over discharge parameters was compiled. (For this survey, the coil was kept 0.03m behind the limiter, but the values of $\tilde{B}$ were extrapolated to the limiter radius from the measured radial dependence, although the correction was never large.) The magnetic turbulence shows a strong dependence on q and little on density, whereas energy confinement scales with density over this range and has little q dependence. There is no simple or direct relation between measured magnetic turbulence and energy confinement time for these ohmic discharges.

To obtain information on the $k_\perp$ or m spectrum of the turbulence, an array of coils with poloidal separations of 6°, 20°, and 27° at the same toroidal angle was 0.03m outside the limiter radius. The coherency and phase difference as a function of frequency for a typical discharge are shown in Fig. 2. The low-frequency components are highly coherent and correspond to $m = 3 - 7$ as labelled. At higher frequencies, the coherence decreases rapidly with poloidal angle. The lack of coherency merely implies a range of m present at each frequency. From the slope of the phase with frequency, an average dispersion relation can be obtained. For the data shown, these are approximately linear, consistent with phase velocities in the range of $6 - 12 \times 10^3 m/s$. These results are generally compatible with a model of various (m, n) modes on rational surfaces which appear with a frequency driven by poloidal rotation. The rotation cannot be rigid-body, however, for that would not produce a spread in m-values for a given frequency. A similar result emerges from comparison of two loops separated both poloidally and toroidally.

Relation Between Magnetic and Density Fluctuations

To determine if some portion of the magnetic turbulence were associated with edge electrostatic turbulence, correlations between magnetic and Langmuir probes were sought. Significant correlations were found only if the Langmuir probe were inside the limiter radius, the magnetic probe were near the limiter, and the two were on nearly the same field line. Representative data are shown in Fig. 3 for probes with a toroidal separation of 90° and $q_{\rm res} = 3$. Both coherence and phase are shown. The properties of the electrostatic turbulence, in both spectra and coherence, are well established.[5] The phase angle between density and magnetic field is determined by numerous instrumental and physical effects, but if the difference is the same for all m, the frequency dependence of the phase difference will arise solely from the frequency dependence of the component of k along the path between the probes. The condition of constant phase implies $k = 0$ along the path for that q. Since this

occurs at a q different from that for which the two probes are on a field line, $k_\parallel \neq 0$. The phase dependences at the various q shown are all consistent with $k_\parallel/k_\perp = .01$. At a frequency of 100 kHz, where $m \simeq 40$, $\lambda_\parallel \simeq 4m$. For the edge electrostatic turbulence, the parallel wavelength is remarkably short.

Although the coherence between density and magnetic field is significantly large, it never comprises the largest part of the magnetic turbulence at any frequency, and it is a small portion of the total magnetic power. This probably explains why the effect has not been previously reported. However, these measurements clearly establish that the edge electrostatic turbulence has a physically significant magnetic component. (One would never expect complete coherence between density and magnetic field because the density measurement is local and has a short radial coherence length, whereas the magnetic field is an integral over current perturbations at all radii.)

Conclusions

Magnetic fluctuations arise from several processes. High-m turbulence arises in association with edge electrostatic turbulence, whereas lower-m effects are associated with MHD effects from further into the interior. This has the direct consequence of implicating resistivity-gradient driven modes (or similar modes with current perturbations) as the mechanism responsible for edge turbulence as opposed to drift or density-gradient driven modes with no such effects. It has the indirect consequence of complicating any analysis based on the radial dependence of the magnetic signal outside the limiter, which would generally be r^{-m}. Given the combination of processes and m-values present, one can only conclude that near the limiter, both low-m and high-m from the edge will be seen, whereas well outside the limiter, only the low-m would be detectable. High-m turbulence from the interior, if present, would never be detectable outside the plasma. The edge electrostatic modes of high-m are certainly associated with particle transport at the edge. They have many of the properties of resistivity-gradient driven modes, but have rather large m values and surprisingly large k for such modes.[6]

The magnetic turbulence of lower m-values arising from the interior does not have a clear association with transport or confinement. The observed amplitudes are certainly not sufficient to produce significant flux through stochastic magnetic transport. Whether high-m turbulence in the interior is responsible for anomalous transport cannot be determined from external measurements.

1. B. A. Carreras, et al., Phys. Rev. Lett. **50**, 503 (1983).
2. N. Ohyabar, et al., Phys. Rev. Lett. **58**, 120 (1987).
3. R. V. Bravenec, et al., Plasma Phys. and Controlled Fusion **27**, 1335 (1985).
4. E. J. Powers, Nucl. Fusion **14**, 794 (1974).
5. Ch. P. Ritz, et al., J. Nuclear Mat. **145–147**, 241 (1987).
6. P. W. Terry, et al., Phys. Fluids **29**, 2501 (1986).

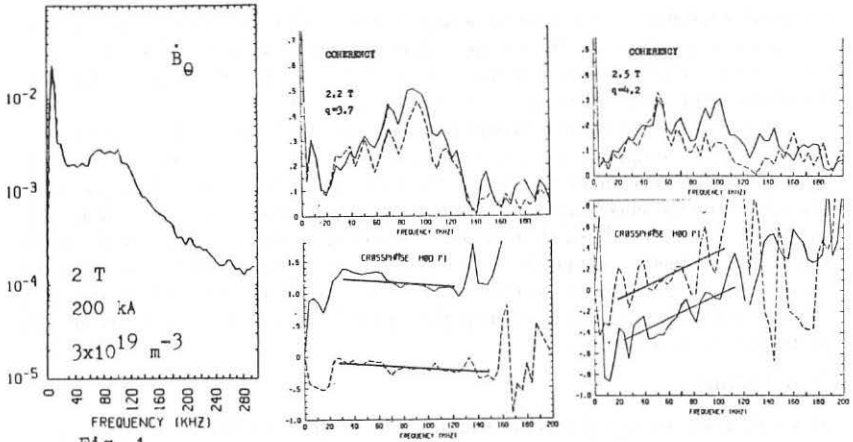

Fig. 1

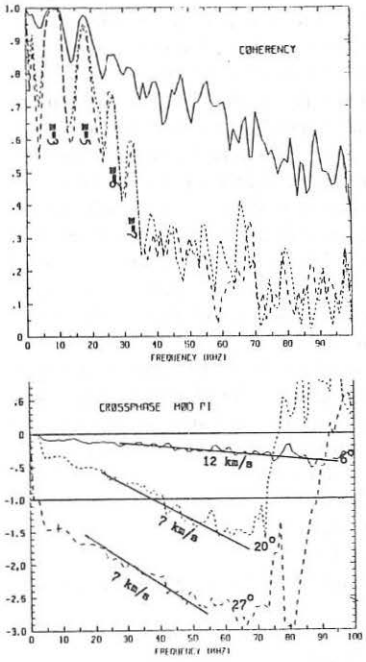

Fig. 2 Conditions as Fig. 1

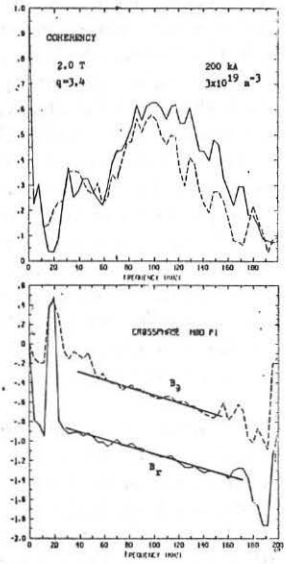

Fig. 3

SAWTOOTH OSCILLATION: MECHANISMS AND STABILIZATION

W. Park, K. McGuire, D. A. Monticello, W. Morris
Plasma Physics Laboratory, Princeton University
P.O. Box 451, Princeton, NJ, USA

SAWTOOTH MECHANISMS

Different types of sawteeth observed on TFTR have been studied. Most of them can be described by using reconnection models. Sawtooth oscillations can be classified as "slow" or "fast" by the time scale of the crash, or as "simple" or "compound" by the structure of their diagnostic signals. The simple slow crash sawteeth which are the "classical sawteeth" examined years ago, agree very well with the usual Kadomtsev type reconnection model in simulation studies. The crash time in a reconnection model is the full reconnection time $\tau_{cr}=\Delta\Psi/\dot{\Psi}$, where $\Delta\Psi$ is the total helical flux inside the q=1 surface, and $\dot{\Psi}$ the reconnection rate. From the modified Sweet-Parker scaling[1], $\dot{\Psi}\sim F^{3/4}\eta^{1/2}$ where F is the driving energy of the ideal nonlinear instability, and η the resistivity. Since $\Delta\Psi\sim\Delta q=1-q_o$, we obtain $\tau_{cr}\sim(\Delta q/F^{3/4})\eta^{-1/2}$. Using a procedure in Ref.1, one can then estimate τ_{cr} to be on the order of msec for a typical low β TFTR equilibrium with $q_o=0.97$, which agrees with the slow crash time. (It is noted that slow crashes as well as fast crashes are driven by an ideal mode. A typical low β tokamak equilibrium with $q_o<1$ is linearly unstable to the m=1 resistive mode but stable to the ideal mode. However the ideal mode gets destabilized nonlinearly, in most cases. When this does not happen as in the case of the nonlinear m=2 mode, the reconnection time is on the extremely slow skin time which is on the order of seconds.[1] Any reconnection process faster than the skin time needs a singular current sheet maintained as a result of an ideal mode.)

The fast crash of a sawtooth could occur in three different ways:

1) When F is large and Δq small with combined enhancement of factor 10 in the above τ_{cr} formula, a fast crash time of ~100μsec can occur. This condition can be satisfied when the driving pressure is large and the shear small. In such a case, the reconnection process proceeds with a crescent shaped hot core as shown in Fig.1 (Ψ contours). This shape is similar to the results reported by the JET group (but given a different interpretation using a non-reconnection picture).[2]

2) The equilibrium can be somewhat similar to the slow crash case and

the reconnection is triggered (the first trigger) by the current sheet formed due to a nonlinear ideal instability as usual. If this current sheet develops strong microinstabilities (the second trigger) which enhance η by a factor of 100, then the crash time will be shortened by a factor of 10. Such a sudden speed up of crash process can be found in some of TFTR shots as shown in Fig.2(c). This figure shows an example of a slow and a fast crash, and an example of a sudden transition between a slow and fast crash. (The anomalous η for this process may also come from the electron viscosity due to stochastic field line in the x-line region.)

3) It is still possible that a Petschek type reconnection($\dot{\Psi} \sim \tau_A^{-1}$) may occur under certain conditions, although numerical simulations have not yet found such a case. The crash time then will be as fast as ~10μsec.

As the shear inside the q=1 surface becomes even lower and the temperature profile before the crash becomes relatively more peaked, the reconnection model gives a hollow temperature profile after the crash. This causes multiple q=1 surfaces to form off axis, and compound sawteeth can occur in the simulation. Fig.3 shows contours of helical flux Ψ during the main crash process of a compound sawtooth. One unique character we can discern from this picture is that the crash occurs in two distinctive steps of similar time scales. The hot core become a semi-hot core after the first full reconnection step, and then this semi-hot core disappears during the next full reconnection step. It should be possible to check this two step crash in the experiment if the time resolution of the measurement during the crash is good enough or a slow crash compound sawtooth can be found.

SAWTOOTH STABILIZATION

Most types of sawteeth manifest themselves as a fast local drop of electron temperature and flattening of the q-profile. Since it is local, the adverse effect of sawteeth are usually not critical in present-day tokamaks. However, as plasma beta and shaping factor increase as in the proposed CIT device, a sawtooth crash will also generate large stochastic regions thus becoming more dangerous. A method for sawtooth stabilization has been found theoretically.[3] The basic nonlinear stabilizing effect comes from the increased plasma pressure in the m=1 magnetic island. The stability condition is

$$\Delta\beta_p > 8\varepsilon_{q=1}^{-1}(\Delta q)^2 ,$$

where $\Delta\beta_p$ represents the enhanced pressure in the island, and $\Delta q = 1 - q_o$,

and $\varepsilon_{q=1}$ is the inverse aspect ratio at the q=1 surface. This stabilizing effect can explain the saturation of sawteeth observed in lower-hybrid wave-driven experiments in PLT, where the ECE signals showed that the island was heated effectively. This stabilizing effect could also explain the "snake" phenomenon seen in JET experiments, which has a helical high pressure structure lasting for seconds. The confinement of this local high pressure region suggests that this region is a magnetic island, and that a saturated equilibrium has been reached due to the high pressure in the island. To intentionally generate such a snake, one would inject a pellet near q=1 surface. This will cause a local depression of current density to form a magnetic island. The high pressure in the island then can stabilize the helical structure to last on the time scale of particle confinement in the island.

*This work supported by U.S. DoE Contract No. DE-AC02-76-CHO-3073.

References

[1]W. Park, D. Monticello, and R. white, phys.Fluids 27, 137 (1984).
[2]A.W. Edwards, et al., Phys. Rev. Lett. 57, 210 (1986).
[3]W. Park, D. A. Monticello, and T. K. Chu, Phys.Fluids 30, 285 (1987).

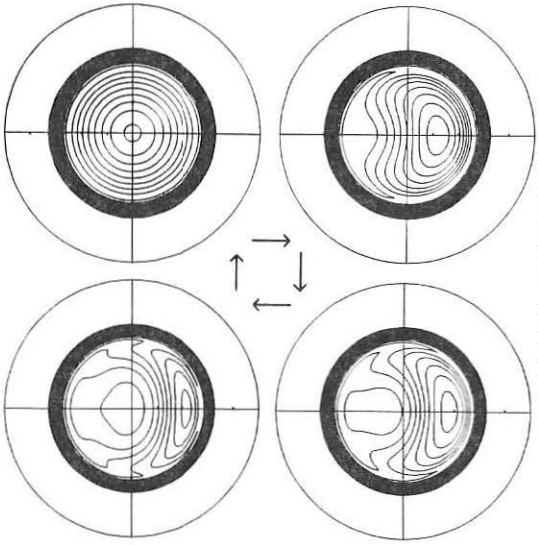

Fig. 1. Helical flux Ψ contours during a fast reconnection process. The hot core is crescent shaped in this case, where the β_p difference between the q=1 surface and the center is 0.2, and Δq=0.03.

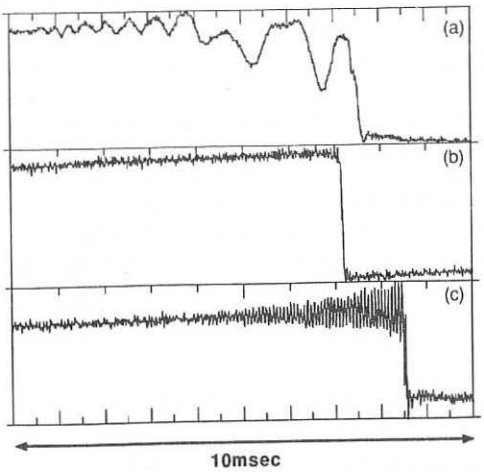

Fig 2. TFTR soft x-ray data from the central channel for; (a) a slow crash, (b) a fast crash and (c) a sudden transition between a slow and fast crash. All three disharges have neutral beam heating; (a) 9.5MW with 5.5MW in the counter direction; (b) 6.5MW co-only and (c) 7MW co-only. Hence (b) and (c) rotate faster than (a) because of the more unbalanced neutral beam injection.

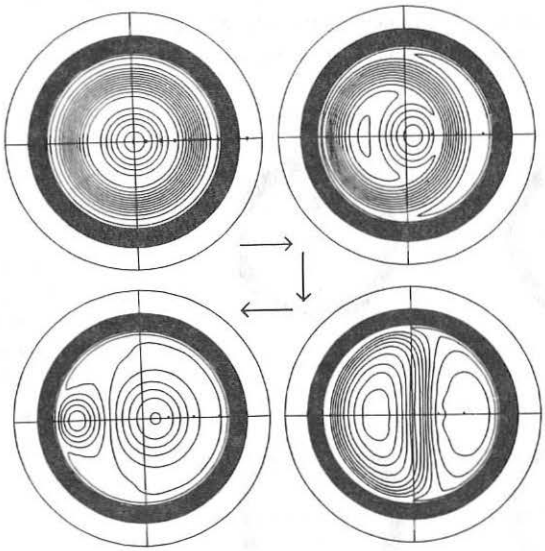

Fig. 3. Helical flux Ψ contours during the main crash process of a compound sawtooth. Two q=1 surfaces are present in this example. The crash occurs in two distinctive steps of similar time scale, which could be detected in experiment in principle.

PARTICLE TRANSPORT IN SAWTEETH

D. Zasche, V. Mertens, O. Gehre, M. Kaufmann, H. Röhr, K.-H. Steuer, G. Becker, H.B. Bosch, H. Brocken, A. Carlson, A. Eberhagen, G. Dodel[1], H.U. Fahrbach,G. Fußmann, J. Gernhardt, G. v.Gierke, E. Glock, O. Gruber, G. Haas, W. Hermann, J. Hofmann, A. Izvozchikov[2], E. Holzhauer[1], K. Hübner[3], G. Janeschitz, F. Karger, O. Klüber, M. Kornherr, K. Lackner, M. Lenoci, G. Lisitano, F. Mast, H.M. Meyer, K. McCormick, D. Meisel, E.R. Müller, H. Murmann, J. Neuhauser, H. Niedermeyer, A. Pietrzyk[4], W. Poschenrieder, H. Rapp, A. Rudyj, F. Schneider, C. Setzensack, G. Siller, E. Speth, F. Söldner, K. Steinmetz, S. Ugniewski[5], O. Vollmer, F. Wagner

Max-Planck Institute für Plasmaphysik,
EURATOM Association, D-8046 Garching, Fed. Rep. of Germany

[1]University of Stuttgart, [2]Ioffe Institute, [3]University of Heidelberg,
[4]University of Washington, Seattle, USA, [5]Inst. for Nuclear Research, Swierk, Poland

Summary

The particle transport in ASDEX discharges with sawtooth oscillations is investigated on time scales comparable to and smaller than the sawtooth period. The net particle flux is calculated using time dependent electron density measurements both from 16-point Thomson scattering [1,2] and 4-chord FIR interferometer [3] diagnostics. The inward flux during the sawtooth build-up phase at $\bar{n}_e \approx 5 \cdot 10^{19} m^{-3}$ is found to be of the order $10^{19} m^{-2} s^{-1}$ around the radius of the q=1 surface and extends considerably to the outside. This relatively large inward flux is balanced by disruptive outward particle transport during the sawtooth collapse phases, resulting in a quasi-stationary flat denstiy profile.

Method

At ASDEX there is no direct measurement of the particle flux in the bulk plasma. The electron density, however, is measured. It is related to the radial electron flux by the continuity equation

$$\dot{n}(r,t) + \frac{1}{r}\frac{\partial}{\partial_r}(r \cdot \Gamma(r,t)) = S(r,t)$$

(Γ: radial electron flux, $\dot{n}$: electron density change, S: electron sources, r: minor radius)

The radial particle flux ($n_i \approx n_e$) is then

$$\Gamma(r,t) = \frac{1}{r}\int_o^r r'[S(r',t) - \dot{n}(r',t)]dr'$$

With the density n(r,t) known, the flux is then

$$\Gamma(r,t) = -\frac{1}{r}\int_o^r r'\dot{n}(r',t)dr'$$

Density profiles are derived from YAG (laser Thomson scattering) measurements and HCN (laser interferometric) measurements. The YAG data are available for 16 points with minor radius from 0.055 ...0.39 m every 0.017 s, with a resolution $\Delta_{YAG} \approx 5 \cdot 10^{18} m^{-3}$. HCN data (line integrated densities) are available for 4 horizontal chords with minor radius 0, +0.21, -0.21, -0.30 m every 0.001 s, with a resolution $\Delta n_{HCN} \approx 2 \cdot 10^{17} m^{-3}$. Although the density profiles from the 16 direct YAG measurements are more detailed, and hence better suited for flux calculations than profiles from the 4 inverted line integrals, the higher sensitivity and sampling rate of the HCN density profiles make them better suited for investigations of small and fast density changes characteristic for sawtooth oscillations. To find out whether the inverted HCN line integrals result in the same flux profiles as the direct YAG measurements do, both kinds of evaluation were done for a neutral beam-heated discharge, where the sawteeth are large enough to show up on the YAG density data. Since the sawtooth period in ASDEX discharges is of the order of a few times $10^{-2}s$, there are generally not enough YAG measurements between two consecutive sawtooth collapses to allow a direct flux calculation. Therefore, during the stationary phase of the discharge, i.e. when the density profile does not change significantly over many sawteeth, the YAG profiles are reordered in time according to their phase within a sawtooth. In this way an average sawtooth is reconstructed with enough sample profiles for calculation of the sawtooth build-up flux. The resulting flux profile is shown in Fig. 1a. The maximum inward flux is about $1 \cdot 10^{19} m^{-2} s^{-1}$.

For a cross-check the flux profile was calculated from the HCN measurements that were reordered in the same manner as the YAG profiles, and then straightforwardly from consecutive HCN profiles during one sawtooth (Fig. 1b and c). The YAG flux agrees well with the HCN fluxes, although the HCN profiles themselves do not match exactly the YAG profiles. The flux values found should be higher than the real flux, because the assumption of zero particle sources is not true for neutral beam heated discharges (10^{20} ions/s injected for $P_{NBI} \approx 10^6 W$), but the error introduced is systematic and the same in both YAG and HCN measurements.

The good agreement lends confidence to the calculation of sawtooth build-up fluxes from HCN data alone in an ohmic discharge with sawteeth too small to be detected in the YAG data. In this case, the plasma is source-free. The inward flux is found to be on the order of $\approx 10^{19} m^{-2} s$ around the radius of the q=1 surface and extends considerably to the outside (see fig. 2).

Conclusions

Since the density profile is generally quasi-stationary in the presence of sawteeth, we must conclude that the inward flux is compensated for by the violent, disruptive particle transport in the opposite direction which takes place in the sawtooth collapses. This ensures that the net particle flux, averaged over times long compared to the sawtooth period, is zero, and the density profile remains unchanged as long as the sawteeth continue.

The inward flux seen during the sawtooth build-up phases is not marginal. A simple estimate shows that the observed inward flux could double the central density within 0.1 ... 0.2 s, if there were no opposing mechanism. There are indeed some cases, when the balancing effect of the sawtooth collapses is obviously absent. This is found, for example, in the early stages of a discharge, before sawteeth have started [5], or during successful pellet refuelling [6]. The observed peaking of the density profile in these cases is of a magnitude that is compatible with the profile peaking during the sawtooth build-up.

References

/1/ H. Röhr, K.-H. Steuer, et al., Nucl. Fusion 22, (1982) 1099.

/2/ H. Röhr, K.-H. Steuer, H. Murmann, D. Meisel, IPP internal report, IPP III/121, in print.

/3/ O. Gehre, Int. Journal of Infrared and Millimeter Waves, Vol. 5 (1984), 369.

/4/ V. Mertens, private communication.

/5/ O. Gehre, V. Mertens, M. Kornherr, E.R. Müller, this conference.

/6/ V. Mertens, M. Kaufmann, et al., this conference.

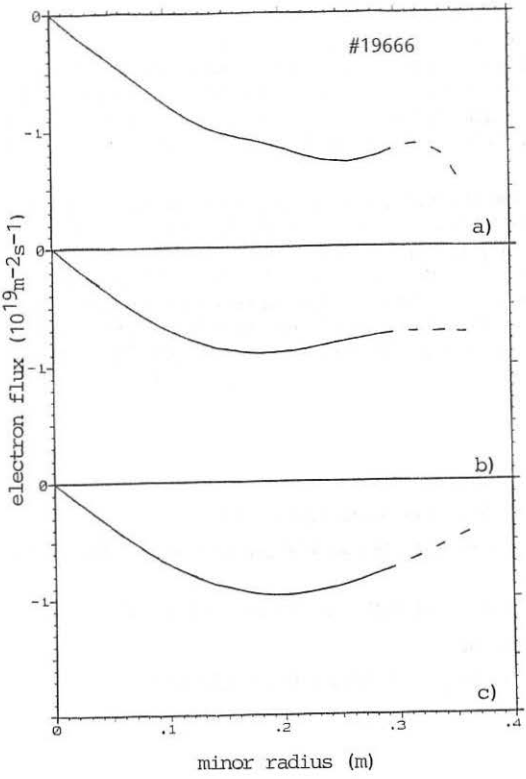

Fig.1: Inward flux during sawtooth build-up in neutral beam heated discharge

a) calculated from YAG data, re-ordered, average over 7 sawteeth

b) from HCN data, re-ordered, average over 7 sawteeth

c) from HCN data, consecutive samples, single sawtooth

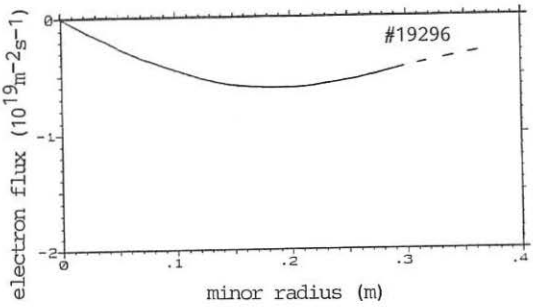

Fig.2: Inward flux during sawtooth build-up in ohmic discharge

HCN data, average over 5 sawteeth

FLUCTUATIONS AND CONFINEMENT IN JET

P A Duperrex[+], P Cripwell[x], A W Edwards, R D Gill, R S Granetz, A Hubbard[x], M Malacarne, G Matthews[*], F Simonet[l], J Snipes, A Weller[o]

JET Joint Undertaking, Abingdon, Oxfordshire, OX14 3EA, UK
On attachment from: [+] CRPP, Lausanne, Switzerland,
[x] Imperial College, London, UK
[*] Culham Laboratory, Abingdon, Oxfordshire, UK
[l] CEA, Cadarache, France
[o] IPP, Garching, FRG

ABSTRACT

Fluctuation measurements in JET are presented and their correlation with the confinement is discussed for limiter and X-point discharges.

I INTRODUCTION

Measurement of turbulence in tokamak is motivated by the fact that anomalous transport is often attributed to micro-instabilities. The results presented here concern fluctuations analysis in JET using different diagnostics: edge located pick-up coils for poloidal magnetic fluctuations ($\tilde{b}_\theta$), diodes for fluctuations of soft X-ray and visible light emission, a reflectometer for density fluctuations and Langmuir probes for electrostatic fluctuations.

II LIMITER DISCHARGES

Magnetic pick-up coils in JET detect the usual Mirnov activity (f ~ 0.3 → 7 kHz) [1], events linked with the internal disruption (the so-called gong [2]) and fluctuations [3]. The signal is either recorded with relatively fast ADC (sampling frequency: 40 kHz) or monitored by 8 hardware band-pass filters (from 5 to 56 kHz). The amplitude decreases with frequency: $\tilde{b}_\theta \propto f^{-1.5 \pm 0.5}$ above 2 kHz. The total normalised amplitude is typically: $\tilde{b}_\theta / B_\theta \sim 10^{-4} - 10^{-5}$. Cross correlation techniques have been used to determine the spatial characteristics of these fluctuations. Two different types of activity can be observed in the frequency range 0 to 20 kHz. The first, dominant at frequencies up to 10 kHz, is observed to propagate in the electron diagmagnetic drift velocity direction (also with Neutral Beam Injection). On the contrary, the second type (dominant from 10 kHz) appears to be stationary even during NBI with n=1 and m equal to the outermost integral q_ψ value. Both types are strongly correlated along a direction parallel to the equilibrium magnetic field ($\underline{B}_o$) (fig. 1). The corresponding correlation length is larger than the major radius (R). The phase shift between 2 magnetic probes along this direction is very close to zero for all frequencies indicating $\underline{k} \cdot \underline{B}_o \sim 0$ for the broadband spectrum.

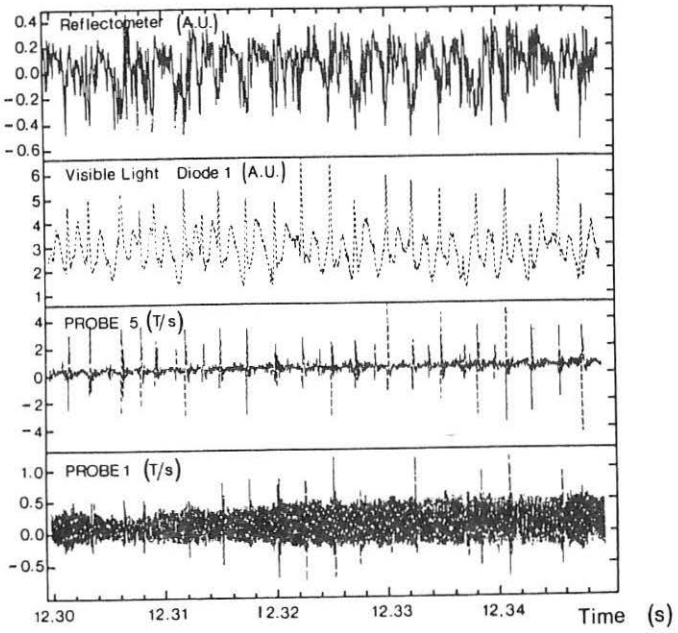

Fig. 3: "spike" activity at the edge during the L phase prior to an H mode transition. # 10850

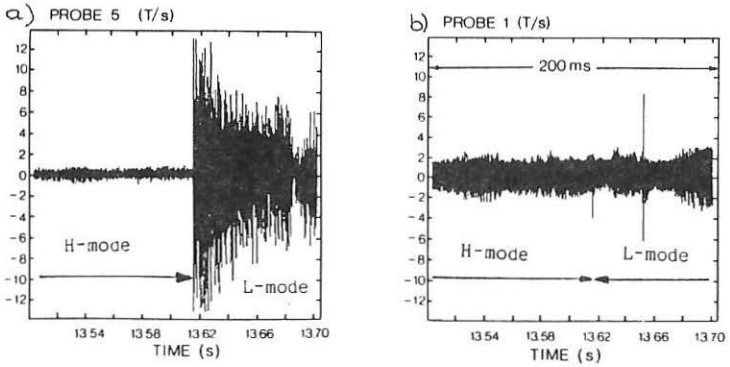

Fig. 4: Magnetic signals at the H-L transition. # 10789
a) probe 5 near the X-point for which edge fluctuations signal dominates.
b) probe 1 behind the limiters, dominated by coherent oscillations resonant deeper inside the plasma.

The $\tilde{b}_\theta$ level depends strongly on the plasma-probe distance and increases when additional heating is applied. This enhancement is observed for all pick-up coils and therefore is not due to a simple shift of the plasma. It also increases with I_p and decreases with B_T though it is not possible to determine if it is a genuine enhancement or is due to the closer location of the resonant layer at lower $q_\psi(a)$. However, taking these effects into account by multiplying $\tilde{b}_\theta$ by $q_\psi(a)$ (or B_T/B_p) the normalised level is shown in Fig. 2 (for f = 40 kHz in this example) to increase with τ_E^{-1} (τ_E = energy confinement time).

Fluctuations from visible light emission were measured by 2 arrays of soft X-ray diodes without foils. Tomographic reconstruction confirms that the measured emission is essentially located at the plasma edge. Cross-correlation analysis shows the presence of high m wave numbers. In the frequency range 15-20 kHz the measured m numbers are about 25 - 35 and for the frequency range 40-60 kHz the corresponding m numbers are m ~ 70-100.

Density fluctuations have been measured with a reflectometer. Coherent oscillations are sometimes seen which correlate well with the magnetic signals. However no correlation between broadband density and magnetic fluctuations has yet been found. Langmuir probes in the scrape-off layer can also detect fluctuations in the range 0 to 20 kHz. Preliminary results indicate that the correlation length is shorter than the distance (10 cm) between the 2 probes. No correlation has been obtained either with the magnetic or the reflectometer data as far as the broadband spectrum is concerned.

III FLUCTUATIONS DURING X-POINT DISCHARGES

During X-point discharges, visible light fluctuations are seen to correlate with the first type of magnetic activity (the propagating type) measured with a coil which is near the X-point and very close to the plasma for this configuration, whereas the n=1 low m magnetic standing fluctuations do not have any visible counterpart.

A new type of edge activity in JET has also been observed. Perturbations appear to dominate in the phase preceding the transition from a low confinement regime (L-mode) to a high confinement regime (H-mode) (fig. 3): regular spikes are observed on the magnetic, reflectometry (when probing the edge density) and visible light emission signals. They are correlated with a sudden flattening of the soft X-ray emission at the edge. The repetition frequency of these spikes is slowed down by sawtooth disruptions, one of which often marks the final transition to the H-mode. In contrast H-L transitions (which are preceded by a large increase of edge radiation) are characterised by a sudden burst of broadband (turbulent) activity with $m \gtrsim 6\text{-}8$ and $n \gtrsim 1$, (fig 4a). Coherent oscillations resonant on surfaces deeper inside the plasma are apparently unaffected by the transitions (fig 4b). The X-ray emission drops at the edge and H_α radiation from the single X-point region shows a

large increase; very often spikes reappear after this initial burst. During the H-mode, edge turbulent fluctuations are still present, though at a much lower level.

IV DISCUSSION AND CONCLUSION

Turbulence up to 50 kHz has been observed with different diagnostics. Magnetic fluctuations have a very long correlation length ($\geq$ R). This could confirm that the magnetic connection length is of the order of ~ qR.

No correlation has yet been found between the broad-band fluctuations of the different diagnostics for limiter discharges. During X-point discharges the light emission exhibits some correlation with a magnetic coil near the X-point for which edge fluctuations dominate the signal. The enhancement of $\tilde{b}_\theta$ during additional heating proportionally to τ_E^{-1} points out a possible link between $\tilde{b}_\theta$ and the anomalous transport. Edge perturbations appear to play an important role in the physics of the high confinement regime (H-mode).

REFERENCES

[1] Snipes J et al: EPS Schliersee 1986, Vol I, p152.
[2] Duperrex P A, Keller R, Malacarne M, Pochelon A: EPS Budapest 1985, Vol I, p126.
[3] Malacarne M, Duperrex P A: JET Report JET-P(86)31.

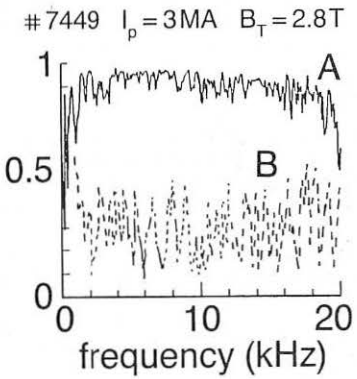

Fig. 1: Coherence spectrum between 2 magnetic coils A) along $\underline{B}_o$, B) across $\underline{B}_o$.

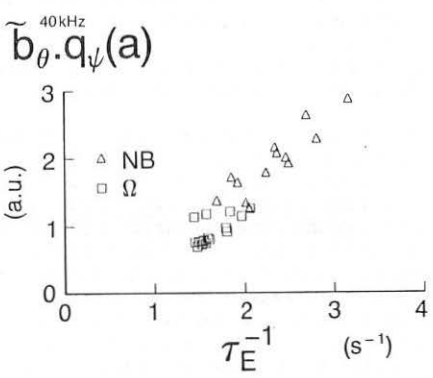

Fig. 2: Normalised level $\tilde{b}_\theta$ (at 40 kHz) versus τ_E^{-1}. Ip = 2, 3, 4 MA, B_T = 2.5, 2.8, 3.4 T.

SIMULATION OF TRANSIENTS IN JET BY MEANS OF PREDICTIVE TRANSPORT CODES

A. Taroni and F. Tibone

JET Joint Undertaking, Abingdon, Oxon., OX14 3EA, UK

Introduction

An empirical electron heat conduction coefficient χ_e constraining the electron temperature profile to asymptotically reach observed "consistent profiles" was proposed in [1]. In this paper we summarise the results of simulations of several JET discharges in a variety of situations. The cases considered are felt to be particularly significant and to constitute a much more demanding test for a transport model than standard steady state or slowly evolving cases. They allow to assess clearly merits and limitations of our model that has to be modified in order to take into account fast time scale phenomena such as the heat pulse propagation after a sawtooth crash.

Computational Results

We have used the expression for the electron heat diffusivity first derived in [1]:

$$\chi_{ePC}(r) = F(r) \cdot \frac{\int_0^r [P_{in}(r) - P_{out}(r)]\, r dr}{n_e(r)\, T_e(r)}$$

where $P_{in}(P_{out})$ represents all of the source (sink) terms in the electron energy balance, while F(r) is a shape factor which determines the detailed shape of the exponential temperature profile that will be reached in steady-state (e.g. for a Gaussian profile $T_e(r) = T_{eo}\exp(-\alpha_T r^2/a^2)$ one will have $F(r) = a^2/(2\alpha_T r^2)$).

This model has been used to simulate, by means of a 1½D predictive transport code, the following plasma regimes experimentally observed in JET.

Localised off-axis heating experiments - RF heating experiments have been performed in JET by shifting the minority resonance layer position away from the plasma centre. Ray tracing calculations predict that heating occurs in a narrow radial range ($\Delta r \sim 20$cm), and that electron heating is largely dominant in the H-minority cases we have studied [2].

During off-axis heating, the shape of the electron temperature profile remains essentially unchanged, with its magnitude increased (Fig.1).

While the Ohmic profile can be reproduced acceptably using various different models (Fig.1a), we find that during RF heating one has to prescribe $\chi_e(RF) > \chi_e(OH)$ in the external region, while $\chi_e(RF) < \chi_e(OH)$ in the inner core, where no auxiliary power is deposited (Fig.1b). This behaviour is a natural outcome of the definition of χ_{ePC}.

The result is similar to that reported in [3] for TFTR edge heating experiments with neutral beam injection.

"Monster" sawtooth evolution - The "monster" sawtooth regime, with up to 1.5 sec long sawtooth-free intervals, offers an opportunity to study the evolution of the central portion of the electron temperature profile towards a steady-state configuration without the effect of sawtoothing.

In JET, such transition is observed to occur on a relatively fast time scale (0.2-0.3sec), and is characterised by a sudden saturation of the central temperature (Fig.2).

When trying to simulate this behaviour, we find that a transport model is needed that predicts a strong increase of heat diffusion when T_e gets close to the steady-state, "limit" profile.

One way of doing this is provided by χ_{ePC}, by virtue of its implicit profile constraint (Fig. 2).

Heat pulse propagation - Full transport code simulations where the Kadomtsev model is used to simulate sawteeth (with the sawtooth period prescribed from experiment) give realistic predictions as to the sawtooth amplitude and to the size of the "mixing" region, and can therefore also be used to follow the time evolution of the computed sawtooth-induced heat pulses.

We have compared computed and measured results for one representative discharge for which heat pulse propagation measurements were available during both the Ohmic and a strong auxiliary heating (P_{tot}> 10MW) phase. During the latter, computed and measured times required for the heat pulse to reach the boundary region are in reasonable agreement. For the Ohmic plasma the experimental time is about three times faster. Here, it does not seem to be possible to make the agreement any better by using a purely diffusive model, if this is bound to reproduce the global confinement and the steady-state temperature profile.

One effective way of tackling the problem seems to be the introduction of a substantial "heat pinch" along the lines suggested in [4,5]. We have added to the electron thermal flux q_e an inward term linear in the minor radius. Thus one has:

$$q_e = - n_e \chi_{ePC} \nabla T + q_{avv} - rh.$$

Here q_{avv} is the usual convective term and h is a constant such that the total heat pinch related source in the plasma volume V_p is $\int_{V_p} hdV \approx (1-2)P_{OH}$. Notice that one can interpret rh/χ_{ePC} as a "critical gradient" [6,7].

This modification of the model, as shown in Fig.3, actually provides the required speeding up of heat pulses, while leaving the global confinement unchanged. The effect is small during the auxiliary heated phase, and does not change the previous picture significantly there.

Discussion and Conclusions

Results obtained so far show the following:

- The tendency of T_e profiles to relax in steady state to the same shape independent of the power deposition profiles is consistent with an empirical electron heat diffusion coefficient increasing locally with the power deposited inside a given radius. This dependence of χ_{ePC} and its local inverse dependence on n_e and T_e also provide an automatic improvement of the confinement in the central region of the plasma when off axis auxiliary heating is applied, as experimentally observed. However, this does not imply that the electron heat flux must really be dependent on non

Figure Captions

Fig 1: Experimental and computed T_e-profiles plotted versus a normalised flux surface coordinate ρ for a JET discharge with off- axis RF heating (#8961, B_t=2.5Tm I_p=2.5MA, $\langle n_e \rangle_{OH}=1.7\cdot10^{19}m^{-3}$, $\langle n_e \rangle_{RF}=2.2\cdot10^{19}m^{-3}$, P_{RF}=4.8MW). Figure 1a refers to the ohmic phase, Fig 1b to the RF-heated phase. Full circles represent the experimental profiles. The computed ones are obtained using χ_e(Alcator-Intor) [solid lines] and χ_{ePC} [dotted lines]. During RF heating, the power deposition profile is peaked around ρ = 0.6 with a width $\Delta\rho$ = 0.1. χ_{eAI} is increased in order to reproduce the degradation in global confinement, by 50% over the whole plasma cross-section.

Fig 2: Results of the simulation of the time evolution of T_{eo}^{EXP} during a monster sawtooth (solid curve) with χ_{ePC} (dotted curve) and χ_{eAI} (dashed curve). In both computations the experimental confinement time is reproduced.

Fig 3: Heat pulse propagation as computed without (dashed) and with (solid line) a heat pinch term included in the electron energy balance, as discussed in the text.
The plasma is ohmically heated, and $\int hdV$ ~ 3.5MW. The experimental time for the heat pulse to travel from ρ = 0.4 to ρ = 0.7 is 30 msec.

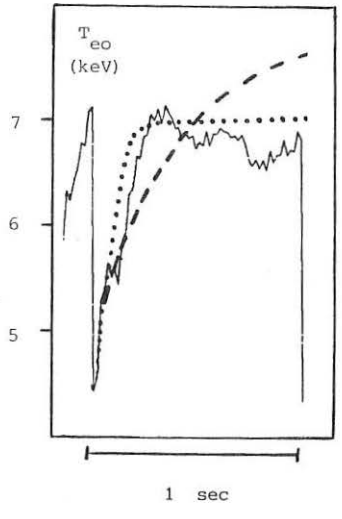

Figure 3

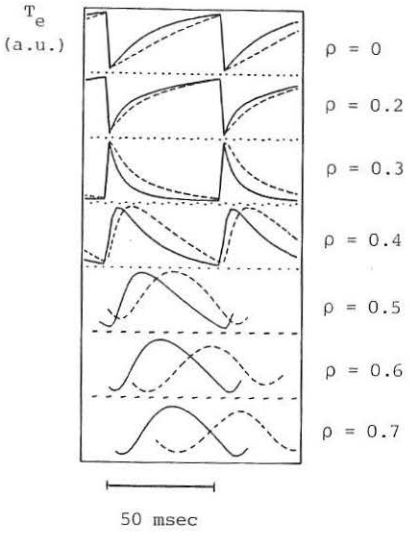

Figure 4

local quantities. Most probably, it simply shows that one must look for a plausible physical mechanism that can provide effects equivalent to the ones produced by χ_{ePC} in our computations. We notice that a coefficient χ_e with a suitable non linear dependence on ∇T_e and other local quantities could in practice produce steady-state results non distinguishable from those obtained with χ_{ePC} [8].

- Results with χ_{ePC} based on Gaussian or other exponential profiles are sensitive to the value of T_e at the boundary of the region where χ_{ePC} is applied [1]. Thus the scaling of the electron energy content is strongly coupled to the power handling capability of the plasma boundary region. However this is not the only possible way to "normalise" χ_{ePC}. An alternative way is to provide the required normalisation through a proper internal microinstability, as proposed in [9]. The same microinstability should provide the correct radial dependence of χ_e, which remains unexplained in [9].
- χ_{ePC} seems to be consistent with the time evolution of the central value of T_e in "monster" sawteeth.
- The main features of the heat pulse propagation following a sawtooth crash cannot be simulated by a transport model including χ_{ePC} alone. A simple modification of the transport model including a so-called "heat pinch" does allow simulation of heat pulse diffusion. However the "heat pinch" prescription, while having some theoretical basis in the critical gradient approach [7], is far from being uniquely defined at present.

References

[1] A. Taroni, F. Tibone, Proc. 13th EPS Conference (1986) 10c, p.160.
[2] V.P. Bhatnagar et al, Proc. 13th EPS Conference (1986) 10c, p.193.
[3] R.J. Goldston et al, Proc. 13th EPS Conference (1986) 10c, p.41.
[4] N. Lopez-Cardozo, B. Tubbing, JET-R(87)01 to be published in Nucl. Fus.
[5] J.D. Callen et al, JET-P(87)10, to be published in Nuclear Fusion.
[6] P.H. Rebut, M. Brusati, Pl. Phys. Contr. Fus. 28 (1986) 113.
[7] P.H. Rebut et al, This conference.
[8] A. Taroni, F. Tibone, JET-IR(87)02.
[9] W.M. Tang, Nucl. Fus. 26 (1986) 1605.

Fig. 1a

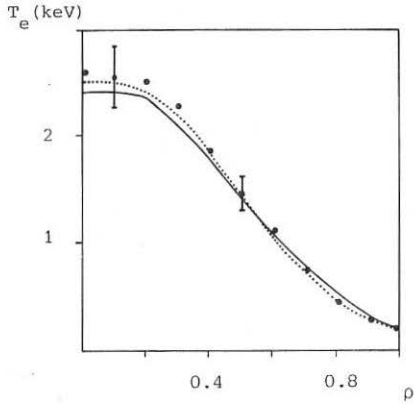

Fig. 1b

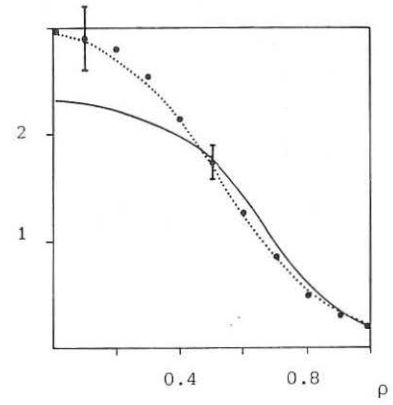

COMPARISON BETWEEN MODEL CALCULATIONS AND EXPERIMENTAL OBSERVATIONS OF INJECTED IMPURITY ION PROFILES IN THE DITE TOKAMAK

N C Hawkes, N J Peacock, R Barnsley*, S J Fielding,
J Hugill and P C Johnson

Culham Laboratory, Abingdon, Oxon, OX14 3DB, UK
(UKAEA/Euratom Fusion Association)

* Department of Physics, University of Leicester, Leicester, UK.

Introduction

We have observed a long impurity confinement mode in DITE when operating with high density helium plasmas at low rates of change of density [1, 2]. Typical results are shown in figure 1a for aluminium injected by laser ablation. For discharges with near constant density ($|\partial n_e/\partial t| < 2\times10^{19} m^{-3}.s^{-1}$) the confinement time, τ, increases with density. In contrast, discharges with rising density ($\partial n_e/\partial t = 10\text{-}20\times10^{19} m^{-3}.s^{-1}$) depart from this trend at $n_e > 4.5\times10^{19} m^{-3}$ with $I_p = 100$kA and $n_e > 6\times10^{19} m^{-3}$ at $I_p = 150$kA. For these conditions, τ falls with increasing density. Energy confinement and other global parameters of the discharge are apparently not influenced by these changes.

Time Dependence

The time histories of emission lines (Al XII $1s^2$-1s2p 7.757Å and Al XIII 1s-2p 7.176Å) are measured with a Bragg rotor spectrometer [3] and compared with the results of a transport code developed for ASDEX and JET [4], where the impurity flux Γ_k (of species k) is given by the equation:

$$\Gamma_k = -D \operatorname{grad} n_k - 2S \frac{Dr}{a^2} n_k, \qquad (1)$$

where n_k is the impurity density, r the radial coordinate, a the limiter radius, D the diffusion coefficient and S a dimensionless parameter representing the magnitude of the inwards convection. The code accepts the measured temperature and density profiles and calculates chordal emission intensity by the van-Regemorter prescription. The values of D and S are adjusted to achieve the best fit to the measured rise and fall characteristics of the Al XII and Al XIII emission lines.

The procedure is to vary D and S simultaneously so as to match the measured decay time making use of the approximation [5],

$$\tau = 0.173 \frac{a^2}{D} \exp(-0.34S) \qquad (2)$$

while at the same time achieving as close a match as possible to the detailed rise time behaviour of the experimental line emission. Probable errors are estimated from the sensitivity of the fit to changes in S and D, the results of this procedure are shown in figs 1b and 1c. In general the values S and D can be determined within 0.5 and 0.05 (20% over most of the range) respectively. Figures 2a and 2b illustrate the quality of agreement often found in this fitting procedure. The results indicate

that changes in τ are accounted for predominantly by changes in S. The predictions of the code are in agreement with the ratio of the experimental intensities from Al XII and XIII at particular values of S and D. This gives us confidence in our adopted T_e profile, the Al XII/Al XIII line intensities being particularly sensitive to $T_e(r)$. The model fails, however, to predict the abundances of aluminium ions in the discharge. These should increase as S is increased whereas in experiments there is no change in aluminium abundance in long and short confinement regimes. This is consistent, however, with the idea that the observed changes are due to changes in central confinement and that the amount of aluminium entering the discharge is strongly dependent on the plasma edge physics, which is not altered between long and short confinement regimes. It should be noted that in all cases the estimated fraction of aluminium that actually appears in the plasma is of order 1% of the total ablated off the target.

Observations of Al XI (2s-2p, 550Å) emission made with a grazing incidence diffraction grating instrument are in agreement with the model predictions of the time dependence of emission for the decay phase (figure 2c). The rise time of Al XI emission is faster than that of Al XII or XIII, due to its greater emitting shell radius and lower ionisation energy. The grating instrument time response is slower than the Bragg instrument due to a lower light throughput so a detailed comparison of the risetime with the model is not possible. A comparison of the magnitude of the emission of Al XI with the model is not possible since the instrument is not calibrated at this wavelength.

In a series of discharges with aluminium injection into a density plateau followed by a strong gas puff the discharge is made to change from a long to short confinement mode. At the transition to short confinement, aluminium held in the core of the plasma is released as the impurity profile broadens and the Al X line intensity is seen to increase, transiently to be followed by diffusion losses from the plasma as a whole (figure 3).

Spatial Profiles

The Bragg spectrometer is capable of spatially scanning the plasma allowing Abel inversion of the chordal line brightness. The spatial form of these Abel inverted profiles was compared to the model predictions and close agreement found (figure 4a). The major influence on the width of the spatial profiles is, however, the temperature profile. In the discharges produced with the long to short confinement transition the model predicts a rapid readjustment of profile halfwidth by 0.44cm. Such a change ought to be just detectable in the experimental data (figure 4b), even above fluctuations in the Abel inverted profiles, but is not observed. A possible explanation for this lies in small changes in the temperature profile as the confinement changes. The outer chords of the uninverted spatial profile, where signal levels are around 1% of axial, do show a marked increase in the shorter confinement phase. This is expected on the basis of our model, but quantitative interpretation is impossible due to the sensitivity of this emission to immeasurably small changes in the temperature profile, as well as to the gross changes in confinement.

Conclusions

Injected aluminium impurity confinement in DITE in a helium plasma is well modelled by an anomalous transport equation of the form of equation 1 where D is approximately $0.3 m^2 s^{-1}$ and S varies from 1 to 6 depending upon confinement regime.

References

[1] Allen J et al. Paper A-IV-4, Proc. 11th Int. Conf. on Plasma Phys. and Cont. Nuc. Fusion. Kyoto, November 1986.
[2] Barnsley R, et al. Submitted to Phys. Rev. Lett (1986).
[3] Barnsley R, et al. Rev. Sci. Instrum., 57 (1986) 2159.
[4] Behringer K H, et al. Nuclear Fusion., 26, 6 (1986) 751.
[5] Fussman G., IPP Garching Laboratory Rep. III/105 (1985).

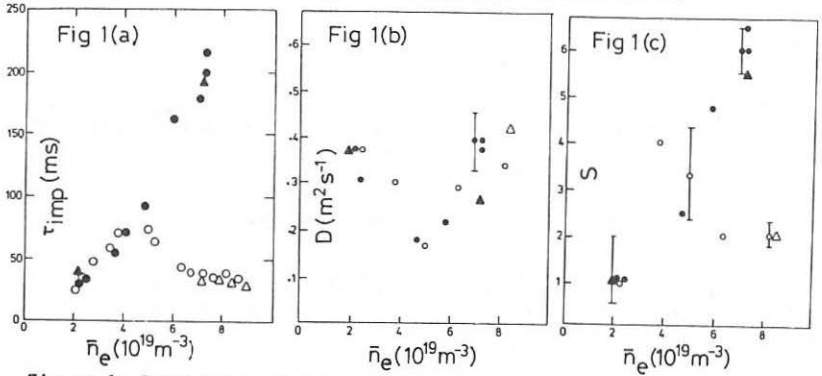

Figure 1: Dependence of (a) injected aluminium impurity confinement time τ, (b) diffusion coefficient D, and (C) pinch term S, upon density. Filled symbols are with constant density, open symbols: density rising with time at 10 - 20 x $10^{19} m^{-3} s^{-1}$. Circles are Al XII, triangles Al XIII. Plasma current is 100kA.

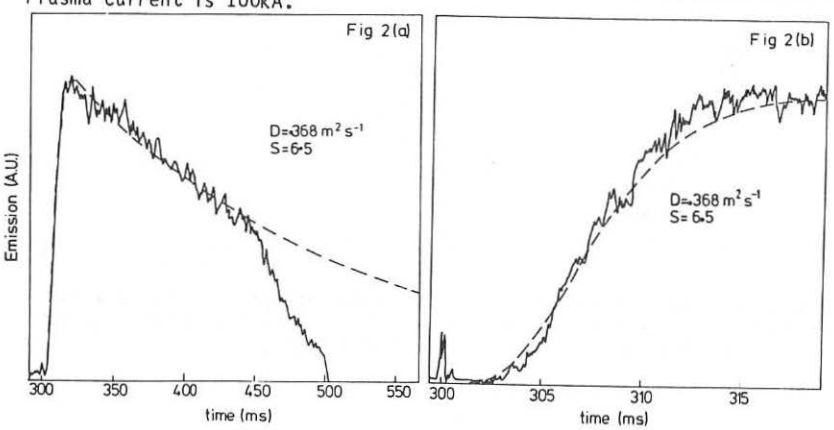

Figure 2: Example of fit of model predictions (dashed lines) to experimental data (solid lines) for (a)Al XII, (c)Al XI and (b)blow-up of rise portion of Al XII. Data taken from a long confinement shot: #29865.

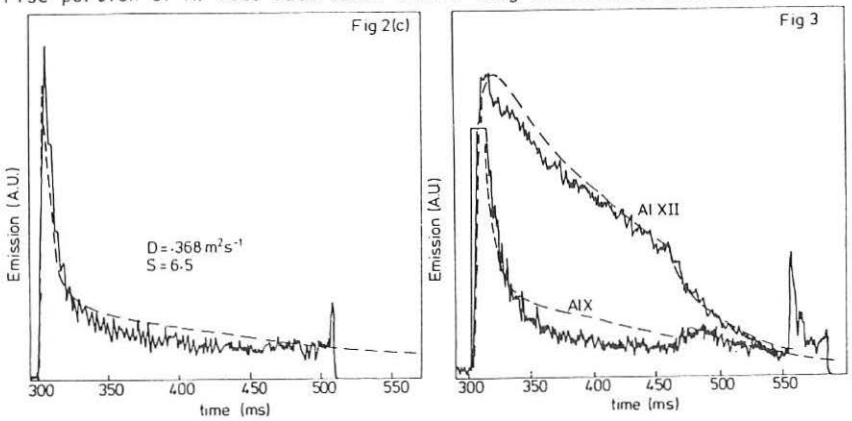

Figure 3: Example of a shot (# 29940) where the confinement was changed from long to short at 460ms by gas puffing. After the transition an increase in Al X is seen as aluminium is released from the core and subsequently a decay as it escapes from the plasma. Dashed line shows model predictions with D = $0.3 m^2 s^{-1}$ and S = 5.5 in the long and 2.5 in the short confinement regimes.

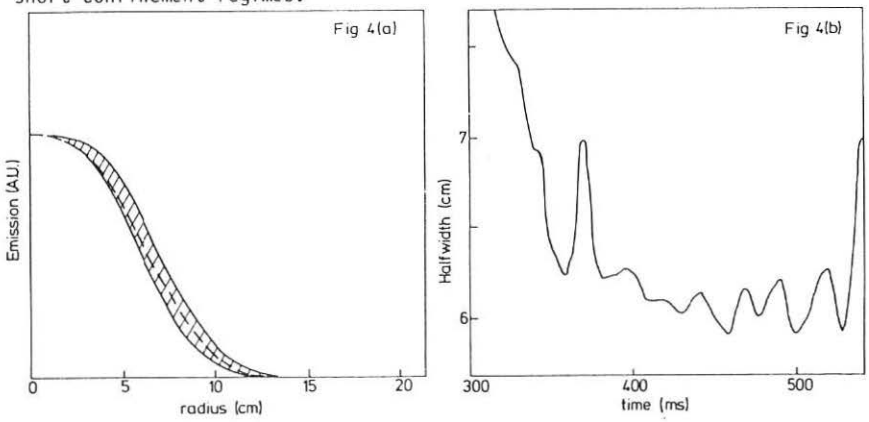

Figure 4: (a) Comparison of model predicted Al XII emission profile (dashed) with experimental observations (after Abel inversion - hatched area). (b) Time dependence of measured half width.

TRANSPORT ANALYSIS OF TEXTOR DISCHARGES WITH RF-HEATING

A. Nicolai, P. Börner
Institut für Plasmaphysik, KFA-Jülich, Association EURATOM-KFA

R. Koch, D. Van Eester[1]
Plasma Physics Laboratory, ERM-KMS, Association EURATOM-BELGIAN STATE

1. Introduction

Tokomak plasma diagnostics yield data sets ("level I data") from which - among other important quantities concerning e.g. the current density, the neutral gas and the impurities - the radial profiles of the plasma parameters ("level II data") may be derived. We concentrate here on the transport analysis which resorts to the radial profiles and the power deposition due to ohmic and additional heating and yields the diffusion coefficient, the electron- and ion heatdiffusivities, D, χ_e and χ_i respectively ("level III data") and consequently the local and global power balances. Essential prerequisites for this are the computation of the deposition profiles due to RF-heating and the numerical method yielding the transport coefficients.

2. Power deposition due to RF-heating.

To estimate the deposition profiles the eikonal expansion of the the wave equation is used as in geometric optics /1/. The resulting hyperbolic equation for the phase is solved by the method of characteristics, i.e. by tracing rays in the threedimensional tokamak geometry thereby employing the dispersion relation of the warm plasma /1/. The rays are started at a surface surrounding the antenna, as indicated in Fig.1; the power allotted to each ray is proportional to the respective surface element and to the Poynting flux, i.e. the square of the antenna current, which has its maximum at the high field side (HFS) of TEXTOR (Fig.1). In Fig.1 all rays have been launched with the same initial power; as a consequence the majority is started at HFS. All rays are started on the magnetosonic branch; the ones coming from HFS reach the confluent layer and are converted to ion Bernstein waves /2/.Due to a strong increase of the parallel wavevector component ($k_{||}$), resulting from its self-consistent evolution along a ray in the total tokamak magnetic field, these waves normally transfer their power to the electrons via Laundau damping. However, for some rays only minor increments of $k_{||}$ occur in the central hot region allowing most of the power to escape towards the edge;this power can be efficiently absorbed by harmonic damping of the impurity ions (at $f = f_{O6+}$ in Fig 1; f_{O6+} denotes the cyclotron frequency of O^{6+}). The rays started at the low field side mainly heat the minority species (protons) during many transits between the confluent

[1] EEC grantee at the Institut für Plasmaphysik, KFA Jülich

layer and the cutoff at the boundary. The deposition profiles of ref./2/ are approximated by spline fits; the power deposited in the impurity ions is assumed to be transferred to the electrons. Fig 2 shows the resulting profiles for the electrons (broken line) and for the ions (full line). The peak in the elctron absorption at large radius is partly due to impurity heating.

3. Transport analysis

The aim of the transport analysis is to calculate the transport coefficients and thus to obtain the local and global power balances. The computational tool is an extended version of an 1 1/2 d code /3/ in which a feedback loop connecting the transportcoefficients and the measured profiles is used. During an artificial time evolution which is started - as in predictive calculations /3/ - from prescribed intial profiles, this feedback effects corrections of the $\chi_e -$, $\chi_i -$ and D - profiles at each time step such that in stationary limit the experimental profiles are reproduced approximately. One advantage of this procedure, as compared to a direct inversion, is that the code can be run partly also in the predictive mode, i.e. that it can reconstruct missing data e.g. concerning the impurity- and the neutral gas transport from model assumptions; another is that unrealistic (negative) coefficients are avoided which might otherwise arise because of incompatible profile data. The initial coefficients are those of the empirical ALCATOR-model /3/ in which the diffusion coefficient is given by $D_{ALC} = 1.25*10^{17}/(cm^3\, n_e)\ cm^2/\mathrm{sec}$. To obtain the corrections for χ_e, χ_i and D, the system of transport equations is evolved with respect to time thereby requiring the computed profiles $H_i(\rho)$ to converge within prescribed accuracy limits to experimental ones ($E_i(\rho)$); i = 1 stands for T_e, i = 2 for T_i and i = 3 for the density n. The method described below effects that the accuracy limits agree with the experimental error bars. As long as the deviation between the profiles $E_i(\rho)$ and $H_i(\rho)$ are to large, particle- and power source are applied which reflect the mismatch between the experimental and the simulated data; they read

$$P_i(\rho) = P_{o_i} \left[\Theta_b(F_i(\rho)-H_i(\rho)) - \Theta_b(H_i(\rho)-G_i(\rho)) \right] \qquad (1)$$

P_{o_i} is a constant source density for power (i = 1,2) or particles (i = 3); this density can be prescribed almost arbitrarily; its upper limit is given by the maximum allowable stiffness of the the transport equations. The auxiliary profiles $G_i(\rho)$ and $F_i(\rho)$ enclose $E_i(\rho)$; the difference G_i-F_i is of the order of the error bars and thus determines the accuracy of the procedure. $\Theta_b(x)$ is the smoothed step functions with transition width b. If inserted directly into the transport equations, the source densities $P_i(\rho)$ would tend to shift the computed profiles $H_i(\rho)$ between F_i and G_i . However, to obtain the equivalent change of e.g. the electron heat diffusivity, $\Delta\chi_e$, the respective source density is to be transformed into a conductive source density reading

$$\frac{1}{\rho}\frac{d}{d\rho}\left(\rho < |\vec{\nabla\rho}|^2 > \left\{\Delta\chi_e n \frac{\partial T_e}{\partial\rho}\right\}\right) = \{P_1\} \qquad (2)$$

Similar equations hold for ΔD and $\Delta\chi_i$. $< |\vec{\nabla\rho}|^2 >$ is a metric quantity accounting for the shape of the flux surfaces /3/. On the corrected diffusion coefficient upper and lower bounds given by $0.1\, D_{ALC} < D < 10\, D_{ALC}$ are imposed. Analogous relations are used for χ_e and χ_i. These constraints may sometimes prevent the simulation profiles to reach the experimental ones but the calculations (sect. 4) show that this margin is in general sufficient. Finally we note that as in predictive calculations the Engelhardt-inward flow term /3/ is applied to reproduce experimental density profiles.

4. Results

The calculations resort to the data of shot Nr. 19161, which is characterized by the plasma current $I_p = 480kA$ (flat top value) a line averaged density reaching $4.7 \times 10^{13} cm^{-3}$ during the RF-pulse and the total RF-power deposited in the plasma P_{RF} = 1.94 MW. Fig.3 shows the plasma parameters during the flat top of the RF-puls between 1000 ms and 1400 ms. The maximum electron and ion temperatures are 1140 eV and 1000 eV respectively. The maximum electron density is $6.3 \times 10^{13} cm^{-3}$ and the density profile is approximated by a fourth order parabola. The maximum of T_e follows from ECE - and the profile shape from current density measurements thereby presupposing neoclassical resistivity. The profile parameters of T_i are the same as those for T_e except for the maximum taken from neutron yield. The transport coefficients computed from the profiles in Fig.3 are displayed in Fig.4 (full line) together with those of the ohmic heating phase (broken line). In this phase the maximum values of T_e, T_i and n_e are 870 eV, 740 eV and $5.4 \times 10^{13} cm^{-3}$ respectively. Fig.4 demonstrates the ability of the plasma to adjust the transport coefficients to the deposition /4/. In case of RF-heating χ_e at r = 0.9a is around 4 times larger than χ_e in the ohmic heating phase at the same radius; at the plasma center, however, χ_e is during the ohmic heating phase larger than during the RF-phase because the ohmic heating power density peaks at the plasma center. Due to the assumed inward flow term the diffusion coefficient has its maximum value at the plasma center as well so that the particles deposited there are removed. However, the diffusion coefficient turns out to be limited by the upper bound mentioned before. In spite of this the computed density profile is still flat. The electron and ion power balances which resort also to the deposition profiles of Fig.2 as an essential input, reveal that the dominant unloading process is heat conduction (87%). Radiation (6%), convection (5%) and charge exchange (2%) are less important.

References

1 V.P.Bhatnagar, R.Koch, P.Geilfus, R.Kirkpatrick, R.R.Weynants, Nucl. Fus. 24 (1984) 955

2 R.R.Weynants, D.Van Eester, V.P.Bhatnagar, R.Koch, Proc.of the 13th Europ. Conf. on Contr. Fus. and Plas. Heat., Schliersee, Vol II (1986) 33

3 A.Nicolai, D.Reiter, Proc. of the 11th Europ. Conf. on Contr. Fus. and Plas. Phys. Aachen, Vol. II, 295 (1983)

4 Wagner et al., Phys. Rev. Lett. Vol. 56 (1986) 2187

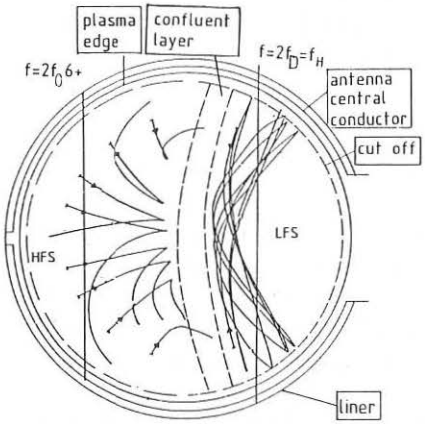

Fig.1

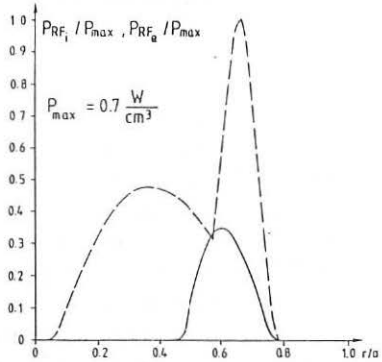

Fig.2

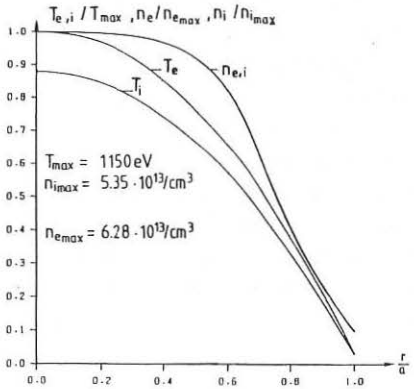

Fig.3

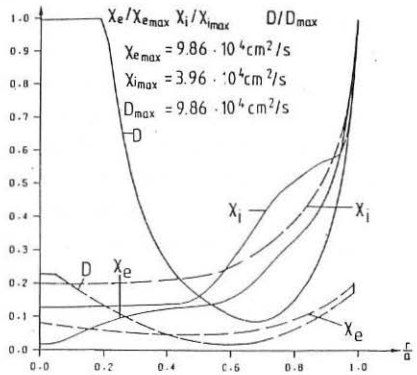

Fig.4

IMPURITY BEHAVIOUR IN X-POINT PLASMAS ON JET

B Denne, K Behringer, A Boileau, G Fussmann+, M v Hellermann, L Horton, J Ramette*, B Saoutic*, M F Stamp and G Tallents

JET Joint Undertaking, Abingdon, OX14 3EA, UK
+ IPP-Garching, D-8046, FRG
* EURATOM-CEA Association, CEN Cadarache, France

INTRODUCTION

The magnetic separatrix (X-point) configuration has been successfully established in JET /1/. Spectroscopic diagnostics (XUV, VUV, visible and Charge Exchange Recombination Spectroscopy (CXRS)) have been used for studying impurity behaviour in these discharges.

The main impurities in JET plasmas are carbon (from carbon limiters and protection plates) and oxygen. Metals (nickel and chromium from Inconel walls and antenna screens) generally contribute little to Z_{eff} and radiated power. Typical impurity concentrations (in % of the electron density, n_e) are /2/: 2-4% C, ≈1% O, and 0.02%, or less, metals. During the period in which most of the X-point operation was carried out, the oxygen concentration in the plasma was, however, somewhat higher (≈2%) due to occasional leaks.

X-POINT PLASMAS WITH OHMIC HEATING

During ohmic X-point operation, the carbon concentration was observed to be only 1-2% n_e, a reduction compared to similar limiter discharges, implying that less carbon was produced at the X-point graphite target plates than at the limiters. Metal concentrations were reduced, too, although the plates were most likely covered by wall material. During previous operation with Inconel target plates no increase was observed in metal concentrations in the plasma when changing from carbon inner-wall to X-point operation. These observations indicate a low plasma temperature (≈20 eV) in front of the plates, resulting in a low sputtering yield. The oxygen concentration, oxygen most likely originating from the vessel walls, was 1-2% n_e, similar to limiter plasmas for the same plasma conditions. As a result, for given $\bar{n}_e$, Z_{eff} was somewhat lower in X-point as compared to limiter plasmas (see Fig.1). The total power radiated, P_{rad}, was ≈40% of the input power at the lowest electron densities, increasing with n_e and approaching 100% at $\bar{n}_e \approx 2\times10^{19}$ m^{-3}. This includes the power radiated from the X-point region which was 30-40% of the total power radiated in all cases.

ADDITIONAL HEATING (L-MODE)

During additional heating a modest increase in n_e was observed. With Neutral Beam Injection (NBI) both carbon and metal concentrations were higher than in the ohmic case, which is consistent with an observed increase in the edge electron temperature, although the metals might also have originated from CX sputtering. The C/O ratio increased during NBI, in contrast to what was observed in limiter plasmas, where oxygen was the dominant impurity during NBI at high $\bar{n}_e$. Somewhat higher Z_{eff}-values were found in X-point plasmas with additional heating - the general

falling trend with increasing n_e, observed in ohmic cases, being maintained. During Ion Cyclotron Resonance Heating (ICRH) and combined heating, increased levels of screen material (Ni and Cr) were found in the plasma as in the limiter cases /2/. The total power radiated from the bulk of the plasma was typically ~25% of the total input power.

H-MODE

During H-mode, n_e increased steeply (Fig.2). The electron density profile was quite flat. Langmuir-probe data /3/ showed that n_e in the scrape-off layer was approximately constant throughout the duration of the H-mode despite ~3x increase in bulk density. The electron temperature profile became broader and the edge temperature was high (a few 100 eV). Radiation emitted from peripheral carbon and oxygen ions (C III - C V and O IV - O VII lines) was essentially unchanged (or even decreased) after the L→H transition, whereas C VI and O VIII radiation, emitted from radial locations further in, increased, reflecting the increasing bulk electron density. The behaviour of the lowly-ionised C and O is consistent with the observed change in edge parameters, and results in less total radiation per ion for these light impurities. After the H-mode was established, the total power radiated from the bulk plasma increased approximately as $\bar{n}_e^2$ /4/, except when ICRF was applied, in which case it increased more steeply due to some metal contribution. Eventually the radiation losses lead to the termination of the H-mode. No ASDEX-type edge-localised-modes (ELM's) (see e.g./5/) were observed, probably because of the high radiation levels.

The bulk particle confinement increased by a factor ~3 /6/ in the L→H transition. The impurity confinement increased similarly. For carbon the improved confinement can be seen in Fig.2: the carbon concentration is essentially constant, or increases slightly in the H-mode, although the carbon influx (represented by the C III-line brightness) remains unchanged with respect to the hydrogen flux, ϕ_H (carbon production yield $\phi_C/\phi_H \approx 5\%$). Towards the end of the H-mode the impurity confinement deteriorated as τ_E (deduced from the decay of the nickel concentration). There is no indication of impurity accumulation in the neoclassical sense. Analysis of several metal ionisation stages as well as the soft X-ray emission profiles and bolometer profiles show that the metal density profile is not peaked. The absence of impurity accumulation might be explained by the presence of sawteeth in the H-mode discharges.

The bolometer profiles are hollow with a broad radiating shell /4/. Transport code modelling for carbon and oxygen reproduces the measured peak radiated power, but the measured radiating shell extends further in radially than predicted by the code. This discrepancy is presently not understood.

During the H-mode, Z_{eff} did not decrease as normal at high $\bar{n}_e$ (see Fig.1), but remained similar to the lower-$\bar{n}_e$ values of 3-4. The high Z_{eff} values could be accounted for by the measured central concentrations of light impurities. The C/O ratio during H-mode was 1-2:1. An observed increase in metal density can be explained either by sputtering by CX neutrals or by the increased edge temperature. The metal concentration is rather independent of n_e for H-mode plasmas which contrasts with the falling trend with increasing $\bar{n}_e$ seen in all other types of discharges.

However, the metal concentration is still low: its contribution to Z_{eff} is ≤0.2, and ≤10% of P_{rad} is due to metals according to transport code calculations. For the discharge shown in Fig.2, e.g., the metal concentration at the end of the H-mode was 0.002%.

SUMMARY AND CONCLUSIONS

In ohmic X-point plasmas Z_{eff} is reduced somewhat compared to similar limiter discharges as a result of lower carbon and metal concentrations. This indicates a low plasma temperature in front of the neutraliser plates.

In additionally heated, L-mode, X-point plasmas, carbon and metal concentrations are higher, consistent with the observed increase in edge temperature. ICRH and combined heating results in higher levels of screen material (Ni and Cr) in the plasma like in the limiter cases.

During H-mode, particle confinement improves by a factor of ~3; impurity confinement improves similarly. No impurity accumulation, in the neoclassical sense, has been observed.

During H-mode, Z_{eff} does not decrease as normal with higher $\bar{n}_e$, but remains at values of 3-4, typical of lower-$\bar{n}_e$ plasmas. Measured carbon and oxygen concentrations (from CXRS) can account for the measured bulk radiated power and Z_{eff}, metals contributing only little.

No ASDEX-type ELM's have been observed. ELM's could allow control of the plasma density and impurity contamination. It might be possible to achieve longer H-modes in JET by reducing the impurity content of the plasma, in order to obtain ELM's, or to provide some efficient density pumping mechanism.

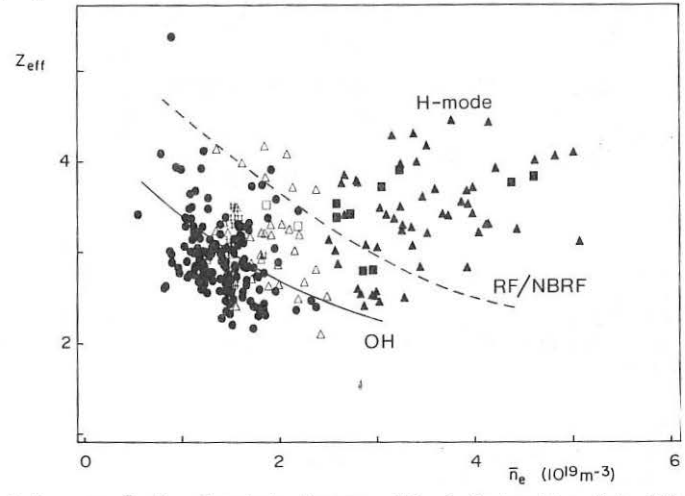

FIG.1 Z_{eff} vs $\bar{n}_e$ for X-point plasmas with ohmic heating (●), NB-heating (Δ) and combined heating (□) (filled symbols denoting H-mode). For comparison the typical behaviour of limiter plasmas with ohmic heating (——) and with RF/combined heating (----) are shown.

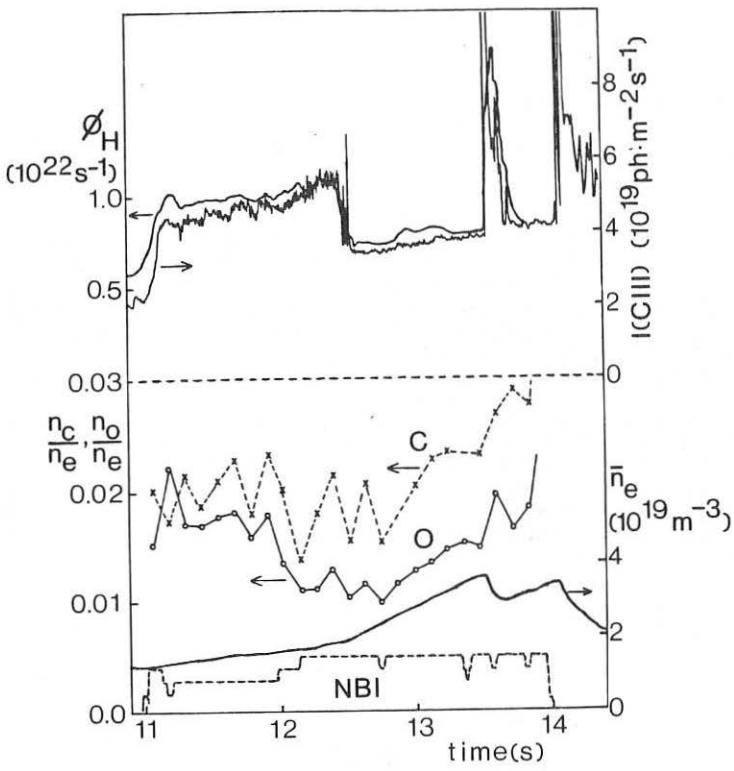

FIG.2. Behaviour of line average electron density ($\bar{n}_e$), carbon and oxygen concentrations (from CXRS), hydrogen flux (ϕ_H), and carbon influx, represented by the brightness of a C III-line (vertical viewing) during L- and H-mode in a NB-heated (5MW) X-point discharge. The L→H transition takes place at ~12.5 s.

REFERENCES

[1] Keilhacker, M, et al, (this conference)
[2] Behringer, K et al, IAEA, Kyoto 1986
[3] Tagle, A J (private communication)
[4] Jäckel, H, et al (this conference)
[5] Keilhacker, M, et al, Plasma Phys.and Contr.Fusion 26, 49(1984)
[6] Morgan, P D and O'Rourke, J J, (this conference)

CONFINEMENT OF IMPURITIES INJECTED BY LASER BLOW OFF IN THE TJ-1 TOKAMAK

B. Zurro, F. Mompean, C. Pardo, S. Clement and TJ-1 Group

Association Euratom/Ciemat. 28040 Madrid, Spain.

INTRODUCTION

Confinement studies of impurities introduced in the plasma by either laser blow off or pellet injection have been performed during the last years in several devices (1) (2) and (3). A non generally accepted picture emerges from these results, that justifies additional work.

In ohmically heated tokamak discharges, many of the experimental confinement time data can be fitted by the Alcator scaling (1); plasma expells the particles independently of their charge and mass, while the type of background ions determines the particle transport. A slight decrease in the impurity confinement with increasing toroidal field has also been found. No clear dependence with plasma density has been reported, except close to the density limit where long confinement times have been observed (2) (3).

In this paper the confinement of iron injected by laser desorption in the TJ-1 tokamak has been studied as a function of the plasma density and of the toroidal field. This experiment has been performed in a lower range of toroidal fields than in previous experiments.

EXPERIMENTAL

The laser ablation technique was used to inject iron into ohmically heated discharges in the TJ-1, a small tokamak (major radius 30 cm, minor radius 9,5 cm), operated at CIEMAT, at toroidal fields between .8 and 1.5 T and plasma currents between 35 and 45 KA. The stainless steel vacuum chamber, conditioned by Taylor discharge cleaning, is the only limiter. Hydrogen is puffed in the discharge with a piezoelectric valve started at a base

pressure of 2.10^{-4} torr. A Q switched ruby laser, delivering pulses of 2 J in 30 ns. was focalized on an 1 μm iron film deposited on a pyrex plate. A vacuum manipulator permits a fine orientation of the plate within an auxiliary chamber, maintained at a pressure of 10^{-7} torr. and coupled to the tokamak through a 75 cm long tube, perpendicular to the torus axis and contained in the equatorial plane. The alignement of the whole system was initially made using an He-Ne laser, and subsequently optimized by monitoring the FeI emission at 3581Å, both at the injection point and at the plasma edge.

Impurity injection takes place once the plasma current reaches its plateau value. The time behaviour of the injected iron in the hot plasma core has been monitored with a pyroelectric detector and a vacuum ultraviolet monochromator provided with a channelectron, both collimated along the central chord. The decay time of the perturbations in the signatures of both detectors is then used to deduce the impurity confinement time.

RESULTS AND DISCUSSION

Wooton et al (4) have shown that the confinement time for energy and particles is dependent on the wall condition and on the radiation losses. All the measurements presented here have been performed under well controlled conditions as indicated by the stationary value of Zeff.

The deperdence of τ_I on the toroidal field has been studied at values of .8, 1., 1.2 and 1.5 T, at a fixed line averaged electron density of 2.5×10^{13} cm^{-3}. Fig. 1 shows the results obtained, the -

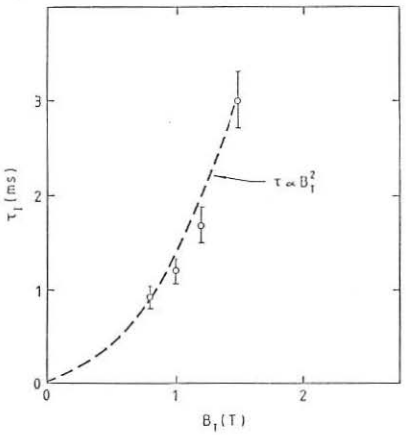

FIGURE 1

Variation of the iron confinement time with toroidal field

dashed line corresponding to a parabolic dependence. The observed increase in τ_I is that predicted by the neoclassical theory (4), contrasting with the results obtained at higher toroidal fields in other tokamaks (1), (6) where the confinement time decreases as the toroidal field increases. In Table 1 we compare our experimental confinement times for iron with the values calculated from the Alcator scaling, and from the neoclassical expression due to Rozhanskii (4). Note that Alcator scaling fails to give account for the observed dependence on B_T, while Rozhanskii expression predicts fairly well the data trend and the numerical values.

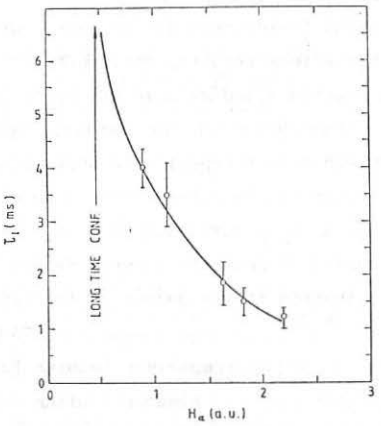

FIGURE 2

Variation of the iron confinement time with the puffing level

This latter expression was applied to the TJ-1 case assuming parabolic profiles for the density and temperature and the Artsimovich ion temperature. The dependence of with the plasma density has been studied varying the amount of gas puffed into the chamber. The density was quantified with an H_α monitor coupled to the same toroidal sector than the piezoelectric valve. The confinement time is plotted versus the H_α signal in Fig. 2. At very low density, actually without puffing any additional gas into the discharge, the pyroelectric detector and the VUV spectrometer data show the same behaviour, a long confinement time, that disrupts the discharge in few milliseconds. This point is represented by an arrow in Fig. 2. With increasing plasma density, the iron is expelled faster. This behaviour is not predicted neither by the Alcator Scaling nor by the Rozhanskii theory.

The observed variation of the confinement time with B_T is that one would

expect form a simple picture of the plasma. However, it has not been observed for impurities in other tokamaks. It must be remarked that the impurity experiments in the literature have been carried out at higher toroidal fields than in our case. Our measurements are not in contradiction with previous results, they rather suggest that τ_I improves with increasing B_T, reaches a saturation and tends to decrease at higher toroidal fields. This dependence on the density has not been observed, for impurities, although recent experiments show similar results for τ_p (7). In TJ-1, this behaviour can be interpreted as an effect due to the plasma collisionality, though a Z_{eff} variation with n_e or an electric field effect cannot be discarded as possible causes. We are indebted to Dr. J. Tagle (JET) for his contribution to the design of the experiment.

TABLE 1

Comparison between TJ-1 confinement times,
Alcator scaling and Rozhanskii theory

B_T(T)	I_p(KA)	q_a	τ_I^{EXP} (ms)	τ_I^{ROZ}	τ_I^{ALC}
1.5	46	4.9	$3.0\pm.5$	2.0	3.7
1.0	35	4.4	$1.2\pm.1$	1.2	5.7
0.8	37	3.2	$0.9\pm.1$	0.8	4.1

REFERENCES

(1) Marmar, E.S., Rice, J.E., Terry J.L., Seguin, F.H., Nucl. Fusion 22, 1567 (1982).

(2) Bagdasarov, A.A., et al., 12th European Conference on Controlled Fusion. Budapest Paper Ao Th 1710M (1985).

(3) Isler, R.C., Rowan, W.L. and Hodge, W.L., Phys. Rev. Lett. 55, 2413 (1985).

(4) Wooton, A.J., Bush, C.E., Edmonds, P.H., Howe, H.C., Lazarus, E.A. Ma, H., Murakami, M., Neilson, G.H., Nucl. Fusion 25, 4, 479 (1985).

(5) Rozhanskii, V.A., Sov. J. Plasma Phys. 6, 4, 465 (1980).

(6) Isler R.C., Nucl. Fusion 24, 12, 1599 (1984).

(7) JT-60 team, Proc. 11th., Int. Conf., Kyoto, 1986.
Paper IAEA-CN-47/A-II-2.

IMPURITY TRANSPORT DURING RESONANT MAGNETIC PERTURBATION EXPERIMENTS IN THE TEXAS EXPERIMENTAL TOKAMAK *

William L. Rowan, Roger D. Durst, S.-P. Fan+, J. C. Forster++,
A. G. Meigs, S. C. McCool, P. E. Phillips, B. Richards, P. M. Schoch++,
James C. Wiley, A. J. Wootton, X.-H. Yu+++, and S.-B. Zheng+++
The Fusion Research Center, The University of Texas at Austin
Austin, TX 78712, U.S.A.

J. S. deGrassie, T. E. Evans, and G. L. Jackson
GA Technologies
San Diego, CA 92138, U.S.A.

INTRODUCTION

A resonant magnetic perturbation applied in the TEXT edge reduces the central impurity concentration by modifying the edge impurity transport and by reducing the impurity source. Generated by a toroidally discrete set of poloidal coils, the radial component of the perturbative field, δB_r, is small with respect to the toroidal field, B_ϕ, and decreases approximately exponentially from the plasma surface toward the center. δB_r has a principal component which is resonant with a magnetic flux surface near the plasma edge and additional sideband components that are resonant with neighboring surfaces[1]. Computation of the total magnetic field[2] (for example, figure 1) suggests that as the perturbation is increased, islands form at each surface resonant with the principal component or a sideband, increase in width, and eventually overlap inducing ergodicity in the region of overlap.

EXPERIMENTAL RESULTS

The perturbation is applied to a TEXT[3] discharge with a resonant surface (m/n=7/2 or 7/3 for this coil set) sufficiently close to the plasma surface that $\delta B_r/B_\phi \approx 10^{-3}$. For $\rho(=r/a) < 0.8$, $T_e(r)$ and $n_e(r)$ are unaffected by the perturbation so there is no reason to expect that the perturbation modifies either central electron energy transport or central particle transport. In response to the perturbation, the emission from all central impurties is reduced by the same factor, and the reduction occurs on an impurity transport time scale (figure 2). In addition, the central impurity confinement time as determined from the temporal behavior of injected impurities is not changed. Since it is thus unlikely that central impurity transport is affected by the perturbation, the central impurity reduction must follow from changes in edge processes, either in transport or in the impurity source.

The perturbation causes a substantial modification in some edge impurity distributions. On a time scale comparable to that of the perturbation, light impurity ion concentrations for $\rho < 0.95$ tend to decrease while for larger radii they tend to increase. Some edge impurity distributions develop well-localized, strong increases near the field line

---

*Supported by U. S. DOE Contract DE-AC05-78ET-53043
+IPP, Hefei, PRC
++RPI, Troy, NY 12181, USA
+++IPP, Chinese Academy of Sciences, Beijing, PRC

X-points for induced islands (figure 3), but their shapes are otherwise unaltered. The strength of the distribution perturbation increases as δB_r increases, and those impurity ion distributions which are most perturbed are also the most localized radially. Thus far, this distribution phenomenon is the most robust indication for the presence of a poloidally varying perturbation.

The edge electron temperature, the edge radial electric field, E_r, and the edge particle transport are all substantially affected by the perturbation. T_e is reduced in the range $0.8<\rho<1.0$ suggesting that the impurity variations are at least partially due to changes in source. The inward-directed E_r is substantially reduced over the perturbed region. Edge particle transport is increased for a limited range of δB_r thus demonstrating that the perturbation can affect at least this aspect of transport.

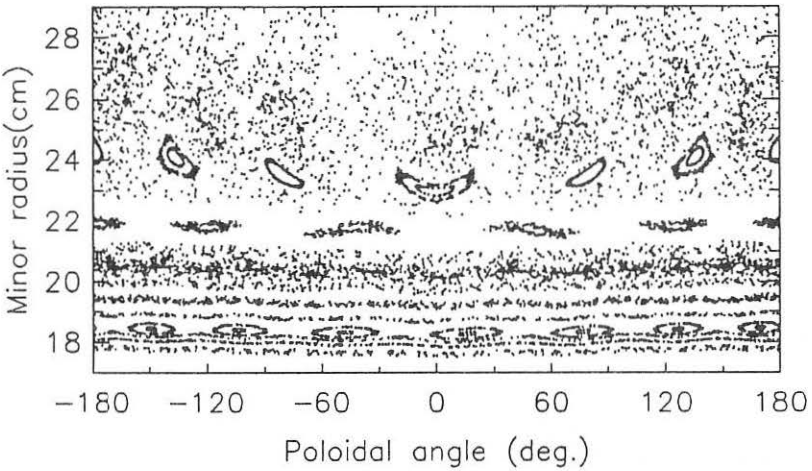

Figure 1. A Poincare plot showing the intersection of perturbed field lines with a poloidal cross section. For this case, the m/n=7/2 perturbation produces both islands and ergodic regions for r>18 cm ($\rho > 0.7$), but its effect does not penetrate nearer the center.

DISCUSSION

While the supporting data (ϕ and T_e, for example) indicate that both edge transport and source contribute to the reduction of the central impurity concentration, simple inspection of the observations does not conclusively select one over the other. One dimensional impurity transport simulation[4] does suggest the most likely mechanism. The simulation is limited to the edge plasma since there is no experimental evidence for transport variation for $\rho < 0.8$ and since computations (for example, figure 1) predict that the effects of the perturbation are limited to $\rho > 0.7$. In the simulation, the effect of reducing the impurity source is to reduce the concentration for every edge impurity

ionization stage on an impurity transport time scale. This clearly disagrees with observations for the edge impurities. The effect of a well localized transport feature, as might be expected for an island[5] is in good qualitative agreement both with time scales for changes and with the increase of some impurity ionization stage concentrations and decrease for others. With a broader stochastic feature[6] ($\propto (\delta B_r/B\phi)^2$) extending over the entire perturbed plasma region, the simulation predicts the observed changes in impurity concentration, but also suggests that equilibrium is established over a time scale that is longer than observed. Radially limited stochastic layers might be a more realistic description for the type of stochasticity present in this experiment.

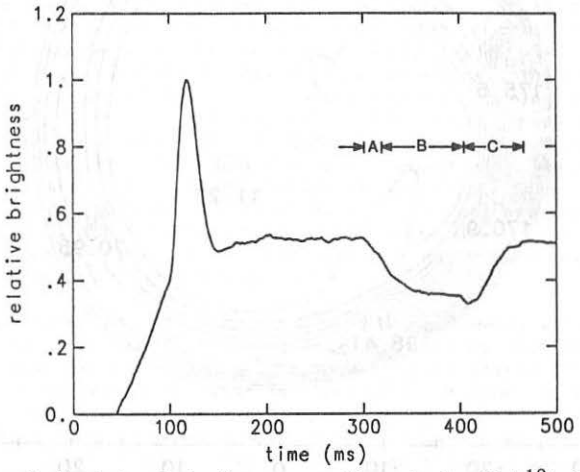

Figure 2. Typical emission from a central impurity ion (Fe^{+19}). In the interval (A), the perturbation is increasing and the impurity emission begins to decrease on a transport time scale. Over (B), the perturbation is constant. In interval (C), the perturbation decreases to zero, and the impurity emission responds by returning to the preperturbation level.

CONCLUSION

The resonant magnetic perturbation reduces central impurity concentration without affecting central transport. The reduction is caused by direct modification of the edge transport and by indirect modification of the impurity source via changes in the edge T_e. Impurity reduction is a significant result, but its usefulness -- the degree to which it can be optimized as a plasma purification tool in fusion applications or exploited as a means for better physical understanding of plasma processes -- depends on identification of the cause. Here, the major perturbative effect seems to be the production of a well localized transport feature. An island is most likely, but an ergodic layer more localized than that used in the simulation is also a candidate. This experiment confirms predictions[7] that a resonant magnetic perturbation can be used to control impurities although the specific mechanism is not yet fully understood.

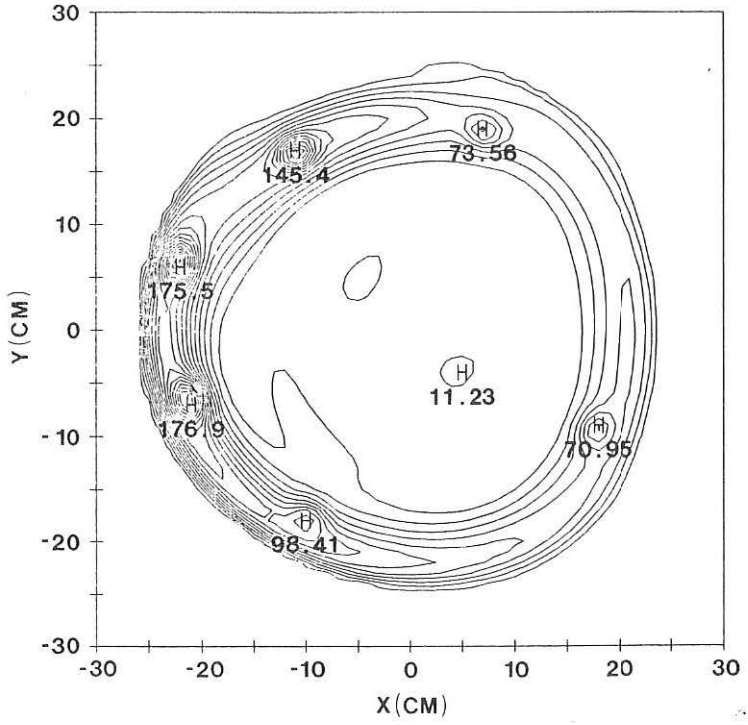

Figure 3. Tomographic reconstruction of the emission contours for a C^{+3} spectral line. This poloidal cross section demonstrates enhancement of emission near the X-points for interior islands. The field line configuration predicted is that of figure 1.

REFERENCES

1. N. Ohyabu, J. S. deGrassie, N. Brooks, T. Taylor, et al., Nuclear Fusion 25,1684(1985).
2. T. J. Martin and J. B. Taylor, Pl. Phys. and Contr. Fusion 26, 321(1984).
3. K. W. Gentle, Nucl. Tech/Fusion 1, 479(1981).
4. J. C. Wiley, W. H. Miner, Jr., and D. W. Ross , Paper 1D8, Sherwood Controlled Fusion Theory Conference, SanDiego, CA(1987).
5. Y. N. Pyatov and A. A. Shiskin, Nuclear Fusion 19, 831(1979).
6. J. Y. Hsu, R. W. Harvey, and S. K. Wong, Phys. Fluids 24, 2216(1981).
7. A. Samain, A. Grosman, and W. Feneberg, Journal of Nuclear Materials 111 & 112, 408(1982).

IMPURITY PENETRATION INTO A ROTATING PLASMA -- THEORY AND EXPERIMENT

K.L. Wong, C.Z. Cheng, B. Stratton, A. Ramsey

Princeton University, Plasma Physics Laboratory
Princeton, New Jersey 08544 USA

ABSTRACT

Guiding center orbits of impurity ions in a rotating tokamak plasma are calculated for TFTR parameters. The calculation is carried out in a coordinate system which rotates with the plasma. It is found that the centrifugal force and the Coriolis force play a dominant role; as a result, the banana width can be significantly larger when the plasma is rotating at high speed due to neutral beam injection. The banana width is approximately proportional to the rotational speed and inversely proportional to the plasma current. The orbit characteristics are sensitive to the direction of injection. In the case of co-beam injection, freshly ionized impurity ions, essentially stationary in the laboratory frame, are counter-rotating in the plasma frame. Thus, their first banana orbits move outward in minor radius and are much enhanced in width. This makes it difficult for the impurity ions to penetrate through the plasma edge. This calculation offers a qualitative explanation for the experimental data from PLT and TFTR.

It was found in PLT[1] impurity injection experiments with neutral beam heating that the impurity line-radiation profiles and their temporal evolution are not sensitive to the direction of plasma rotation. This apparently disagrees with existing theory.[2,3] However, a given injected amount of impurity results in a factor of two to three less impurity concentration in the co-beam case. Similar behavior was observed in TFTR recently. Figure 1 shows the 127.8Å MoXXXII line intensity evolution after molybdenum was injected into a rotating TFTR plasma. The amount of injection was kept to a minimum so that the increase in total radiated power from the injected impurity was negligible. During counter-beam injection, the line intensity was more than a factor of two stronger than during co-beam injection. In this paper, we attempt to explain this from the orbits of the impurity ions.

Let us assume that each magnetic surface in the plasma rotates as a rigid shell about the axis of symmetry with angular velocity ω which can vary among different magnetic surfaces. ω usually peaks at the plasma center with values $\lesssim 3 \times 10^5$ rad/sec for TFTR experiments. In order to avoid complications associated with moving magnetic field lines, we carry out the orbit calculation in a coordinate system which rotates with the plasma. The equation of motion for an impurity ion is

$$m \frac{d\vec{v}}{dt} = q (\vec{E} + \vec{v} \times \vec{B}) - 2m \vec{\omega} \times \vec{v} - m \vec{\omega} \times [\vec{\omega} \times (\vec{R}_o + \vec{r})] . \qquad (1)$$

The last two terms on the right hand side are the Coriolis force and the centrifugal force, respectively. The centrifugal force pushes the plasma

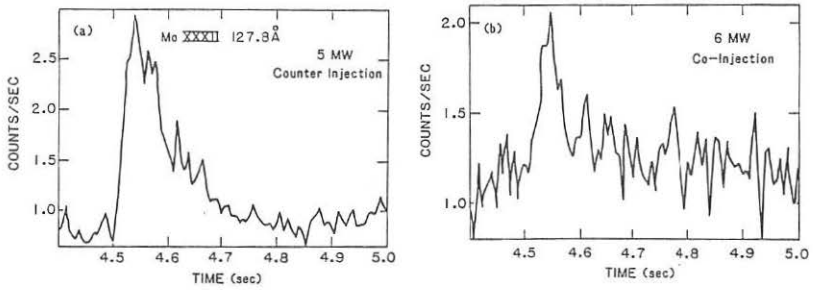

Fig. 1 Evolution of the 127.8Å line intensity from MoXXXII after molybdenum injection into TFTR at 4.5 sec. (a) 5 MW of counter-beam power (b) 6 MW of co-beam power. I_p = 900 kA for both cases.

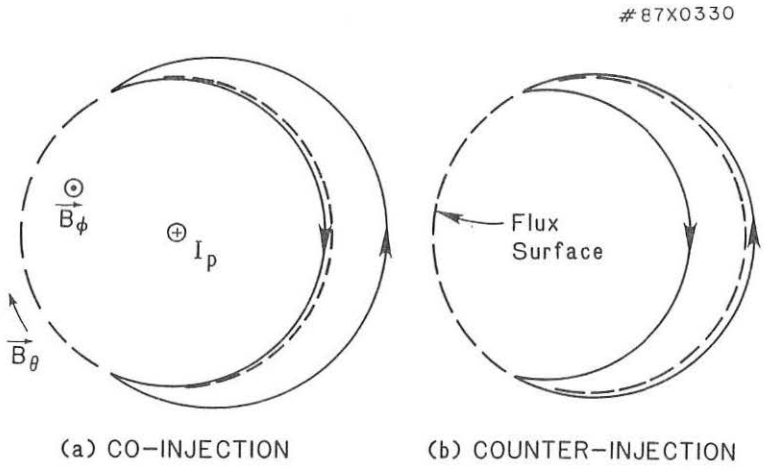

Fig. 2 Schematic drawing for a banana orbit of an impurity ion in a plasma with (a) co-beam injection, (b) counter-beam injection. For $\omega = 8 \times 10^4$ rad/sec, I_p = 1 MA, a 1 keV Fe^{XVI} ion trapped between $\theta = \pm 2$ radians has a banana width of 5 cm.

ions towards the large major-radius side and causes an electrostatic potential to build up:[4]

$$\Phi = \frac{m_i}{e} \frac{T_e}{T_i + Z_i T_e} \frac{\omega^2}{2} (R^2 - \langle R^2 \rangle) \qquad (2)$$

where $\langle\ \rangle$ denotes averaging over the magnetic surface. Putting $\vec{E} = -\nabla\Phi$ and solving Eq. (1) with the guiding center approximation, we obtain the guiding center drift velocity in the rotating frame:

$$\vec{W}_\perp = \frac{\mu}{qB^2}\left(1 + \frac{2\,V_\parallel^2}{V_\perp^2}\right) \vec{B} \times \nabla\vec{B} + \frac{\vec{E} \times \vec{B}}{B^2}$$

$$- \frac{2m\,(\vec{\omega} \times \vec{V}) \times \vec{B}}{q\,B^2} - \frac{m[\vec{\omega} \times (\vec{\omega} \times \vec{R})] \times \vec{B}}{q\,B^2}\ , \qquad (3)$$

where $\mu = 1/2\ mV_\perp^2/B$ is the magnetic moment. The first term is the drift velocity due to magnetic field gradient and field line curvature, and the other three terms are the consequence of plasma rotation. For TFTR parameters, the first term is small compared with the other terms and we find that the banana widths of impurity ions can be several times larger in a rotating plasma. The orbits are obtained by integrating Eq. (3) together with the parallel component of Eq. (1). For simplicity, we assume circular concentric magnetic surfaces and Fig. 2 schematically shows the banana orbits for the two directions of plasma rotation. In the co-injection case, the orbit shifts towards the plasma edge, and in the counter-injection case, the orbit shifts towards the plasma center.

In order to explain the impurity injection experiment, let us consider a neutral impurity atom near the plasma edge. Since the atom is almost stationary in the laboratory frame, it will be a passing particle in a rotating plasma after it is ionized and collisions will scatter the particle into a banana orbit. In the case of co-beam injection, the impurity ion stationary in the laboratory frame is counter rotating in the plasma frame; the first banana orbit moves outward in minor radius, and it can be scraped off by the limiter as shown in Fig. 3a. In the counter injection case, the first banana orbit moves away from the liniter and inboard in minor radius and therefore has a better chance to penetrate into the plasma interior. Numerical particle simulation based on this orbit theory is being carried out. Pitch-angle scattering and energy equilibration with the bulk plasma are included. Preliminary results show that it is indeed true that more impurity ions can penetrate into the interior of a plasma with counter-injection, in qualitative agreement with experimental observations.

ACKNOWLEDGMENT

This work is supported by United States Department of Energy Contract No. DE-AC02-76-CHO-3073.

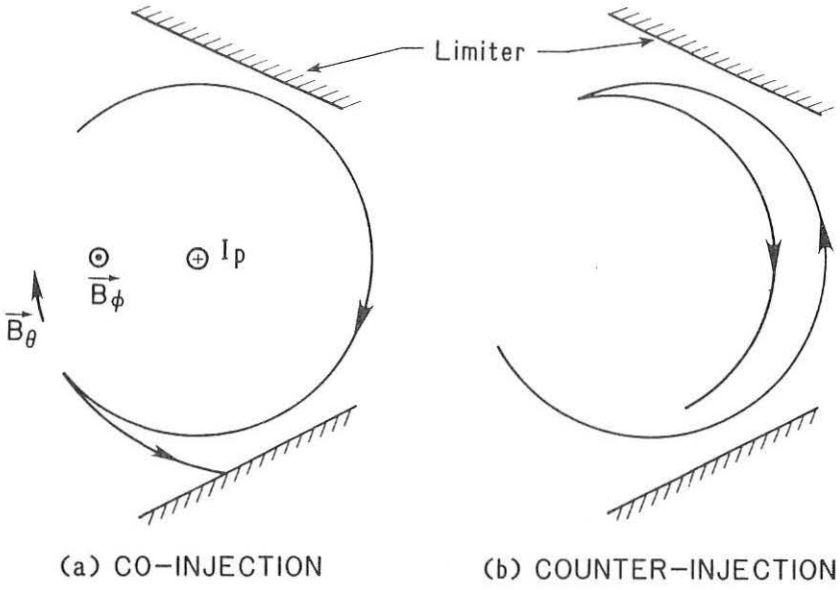

Fig. 3 First banana orbit of a freshly ionized impurity ion in a plasma with (a) co-beam injection, (b) counter-beam injection.

REFERENCES

[1] S. Suckewer et al., Nucl. Fusion 24, 815 (1984).
[2] W.M. Stacey, D.J. Sigmar, Nucl. Fusion 19, 1665 (1979).
[3] K.H. Burrell, T. Ohkawa, S.K. Wong, Phys. Rev. Lett. 47, 51 (1981).
[4] F.L. Hinton and S.K. Wong, Phys. Fluids 28, 3082 (1985).

STUDY OF OHMIC, LOWER HYBRID AND ELECTRON CYCLOTRON REGIMES IN T-7 TOKAMAK

V.V.Alikaev, A.A.Borshchegovskij, V.V.Chistyakov, A.N.Chudnovskij, M.M.Dremin, Yu.A.Gorelov, V.I.Il'in, D.P.Ivanov, N.V.Ivanov, A.M. Kakurin, P.P.Khvostenko, A.Ya.Kislov, V.A.Kochin, P.E.Kovrov, Yu.S.Maksimov, A.F.Shcherbak, Yu.A.Sokolov, A.M.Stefanovskij, N.L. Vasin, V.V.Volkov

I.V.Kurchatov Institute of Atomic Energy, Moscow, USSR

J.Datlov, V.Kopecky, P.Magula, J.Stockel, F.Zacek

Czechoslovak academy of sciences institute of plasma physics, Prague, Czechoslovakia

The experiments on the study of Ohmic, lower hybrid current drive and electron cyclotron resonance heating regimes have been continued on T-7.

In the Ohmic regimes of the discharge with various currents and toroidal fields an evolution of the plasma density and temperature profiles at variation of $\bar{n}_e$ has been measured. The comparison between the discharges with the same $\bar{n}e/I$ but with various q_L has been done. A particular attention in the discussion of the results is given to the profiles formed in the discharges with the limiting $\bar{n}e/I$ and in the discharges close to them. The main dependences of plasma parameters in these regimes are formulated.

The study of MHD-plasma instability with respect to the m=2, at its spontaneous development and under the quadrupole magnetic field produced with a special coil, has been done. The m=2 magnetic island width has been measured with the synchronous detection of the sygnal from the scanning sensor of soft X-ray radiation with respect to the sygnal from Mirnov probes. The studies have been done in the Ohmic and LH-regimes.

In the experiments on current drive simultaneously with the LH-power, the power from two gyrotrons, operating at different frequencies, was launched into the plasma. One of the gyrotrons generated the power at the ECR-frequency, at the plasma column axis. The frequency of the second gyrotron was chosen from the condition of Cherenkov resonance for fast electrons in the beam produced by the LH-waves. The main attention in the experiments has been given to the problem of current drive efficiency and to the study of heating of the electron component.

The experiments were carried out at the following LH and ECR parameters: power launched in the LH-range (900 MHz) was 500 kW, total power of two gyrotrons was 600 kW, their frequencies were 63 GHz and 81 GHz

FLUCTUATION INDUCED TRANSPORT STUDIES IN TEXT WITH AN HIBP.

P.M. Schoch, J.C. Forster, R.L. Hickok, and A.J. Wootton*

Rensselaer Polytechnic Institute, Troy, NY 12180; *Fusion Research Center, The University of Texas at Austin, Austin, TX 78712. USA.

INTRODUCTION

Simultaneous measurements of the turbulent fluctuations in both n and Φ have been obtained on the TEXT tokamak with a heavy ion beam probe(1). These measurements show that in the plasma interior $\tilde{\Phi}/kT_e$ is greater than $\tilde{n}/n$. The measurements also permit the evaluation of the $S(k,\omega)$ spectra and the local particle flux due to the electrostatic fluctuations as a function of radius. The total flux is estimated by assuming poloidal and toroidal symmetry and integrating over the magnetic surface. The results are compared to the total particle flux evaluated from both Lyman alpha measurements of neutral hydrogen and from Langmuir probe measurements(2).

EXPERIMENTAL RESULTS

A 500 keV Cs^+ ion beam HIBP was used to study the turbulent fluctuation spectra in TEXT. The ohmicaly heated plasma discharge conditions were B_t = 2.0 T, I_p = 200 kA and $n_e = 3 \times 10^{19} m^{-3}$. For these operating conditions, measurements could be obtained over the range $0.6 < r/a < 1.1$. The bandwidth for both the density fluctuations, $\tilde{n}$, and potential fluctuations, $\tilde{\Phi}$, was 500 kHz. Separation between the two simultaneous sample points varied with the radial location of the measurements but was of the order of 2 cm. The orientation of the separation could be varied from strictly poloidal to strictly radial but only one fixed orientation was available at a given plasma location. Signal to noise ratios in excess of 100:1 have been obtained for $\tilde{n}$ but for $\tilde{\Phi}$ the typical value was 3:1.

Typical auto power spectra for $\tilde{n}/n$ and $\tilde{\Phi}$ are shown in Fig. 1a for data from one sample volume. The system is sensitive to poloidal wavenumbers (k_Θ) values up to 10 cm^{-1}, and the spike in the $\tilde{\Phi}$ spectra below 50kHz is due to MHD effects. Fig.1b shows the coherance, (γ), and phase difference, (α),between $\tilde{n}$ and $\tilde{\Phi}$. The phase is nearly constant with a value of $-\pi/4$ and the coherance is greater than 0.4 for 50kHz to 400kHz. A plot of $\tilde{n}/n$ and $\tilde{\Phi}/kT_e$ as a function of radius is shown in Fig. 2. The plotted points are rms values for frequencies above 50kHz so as to avoid MHD effects. A typical value for $\tilde{\Phi}$ is 10 volts. For all radii except r/a= .88 $\tilde{n}/n$ is greater than $\tilde{\Phi}/kT_e$, which is in disagreement with the simple Boltzman condition. $\tilde{n}/n$ and $\tilde{\Phi}$ have the same spectral shape in the frequency range of 50kHz to 150kHz, (these are the frequencies which contribute to turbulent transport), so the disagreement with the Boltzman condition occurs over this entire frequency range.

The coherence and phase between simultaneous measurements of $\tilde{n}/n$ at two separate points in the plasma are shown in Fig. 3. The $\tilde{\Phi}$ measurements showed the same phase shift as the $\tilde{n}/n$ in the spectral range of 50kHz to 150kHz, showing that the $\tilde{n}$ and $\tilde{\Phi}$ have the same k values. For this particular measurement r/a was equal to 0.9 and the separation between the two points was 1.5 cm in the poloidal direction. The 2π phase shift at 120 kHz indicates spatial aliasing (half the wavelength becomes equal to the sample point separation). The well defined phase shift permits evaluation of k_Θ and yields an experimental dispersion relation of ω/k= constant. It also indicates that the poloidal correlation length is greater than 1.5 cm. Similar measurements with a radial separation between the two points shows very small coherence, indicating that the radial correlation length is measureably smaller than the poloidal correlation length, in agreement with Langmuir probe measurements in the outer region of the plasma.

The two point measurements indicate that the fluctuations are propagating in the electron diamagnetic drift direction. The associated poloidal electric field is $k_\Theta\Phi$ and the radial E x B flux (which is in the outward direction) is given by

$$\Gamma_l = \langle \tilde{n}\, \tilde{v} \rangle = (1/B) k_\Theta \tilde{n}\, \tilde{\Phi}\, \gamma \sin\alpha$$

where α in the phase angle between the density and potential fluctuations. Γ_l is the local particle flux: assuming poloidal and toroidal symmetry it is possible to estimate the total outward particle flux (Γ) due to the turbulent fluctuations. This is shown in Fig. 4 as a function of plasma radius. The HIBP measures a nonzero flux of 1-4 x $10^{18} m^{-2} s^{-1}$ at r/a=0.65. Also shown is the total particle flux,derived from spectroscopic H_α measurements. To within experimental error the fluxes are in agreement over the radial range measured with the HIBP. At larger radii the results can be compared to Langmuir probe measurements.

Thus the measured electrostatic turbulance accounts for the total particle flux for r/a>0.6. The convective energy flow to the limiter ($\int 5/2 k T_e \Gamma ds$), is ~140kw for this discharge. Charge exchange and radiated power measurements by bolometry accounts for ~125kw. Combine these account for all but 55kw of the 320 kw ohmic heating input power for this discharge.

CONCLUSIONS

Simultaneous $\tilde{n}$-$\tilde{\Phi}$ measurements on TEXT have shown that $\tilde{\Phi}/kTe$ is approximately 2 times larger than $\tilde{n}/n$ over most of the plasma radius, for all frequencies in the 50khz to150khz range. The poloidal correlation length is larger than the radial correlation length and the dominate direction of propagetion in in the electron diamagnetic drift direction. The net outward particle flux from electrostatic fluctuations (for r/a>0.6) is equal to the total flux to within experimental errors, and for this discharge convective energy loss is significantly greater than conductive. Additional measurements are needed to evaluate the validity of the assumed poloidal and toroidal symmetry.

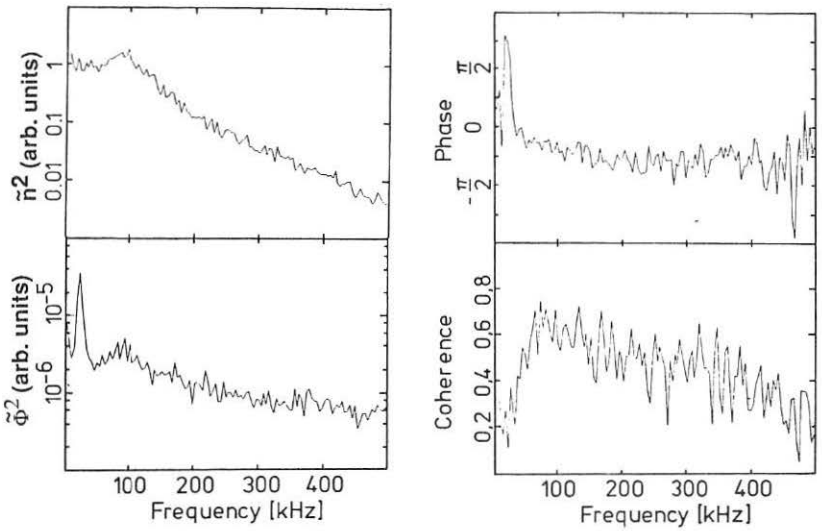

Fig. 1a Autopower spectra for $\tilde{n}$ and $\tilde{\Phi}$ at r/a=0.9, 1b phase and coherance of cross correlation of $\tilde{n}$ and $\tilde{\Phi}$.

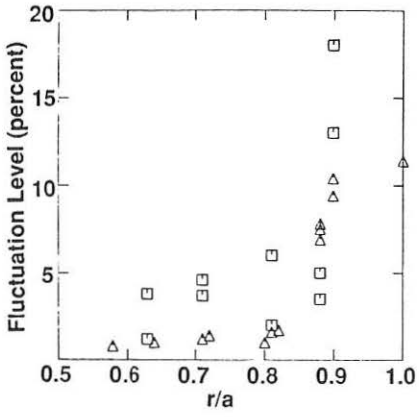

Fig. 2 Normalized fluctuations levels, boxes are $\tilde{\Phi}/kT_e$ and triangles are $\tilde{n}/n$. Spectra are integrated from 50kHz to 500kHz to elimanate MHD effects. The density point at r/a=1.0 has substantial power in the 0 to 50khz range which is not included in this measurement.

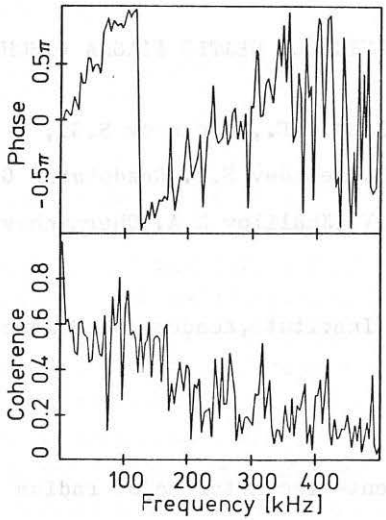

Fig. 3 Phase and coherance between two spatial points, note the spatial aliasing at 120kHz.

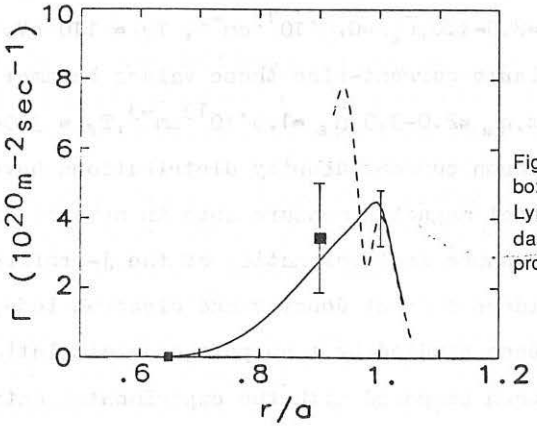

Fig. 4 Measured particle flux, boxes are HIBP, solid line is from Lyman α measurements, and dashed line is from Langmuir probes.

1) F.M. Bieniosek, P.L. Colstock, K.A. Connor, R.L. Hickok, S.P. Kuo, R.A.Dandl, Rev. Sci. Instrum. 51, 206 (1980).

2) W.L.Rowan, C.C.Klepper, Ch.P.Ritz, R.D.Bengtson, K.W.Gentle, P.E.Phillips, T.L.Rhodes, B.Richards, A.J.Wootton, "Global Particle Confinement in the Texas Experimental Tokamak," accepted for publication in Nucl. Fusion (1987).

FAST CURRENT-RISE STUDIES ON THE TUMAN-3 TOKAMAK DURING STATIONARY STAGE OF OHMICALLY HEATED PLASMA DISCHARGE

Askinasi L.G.,Bogdanova N.E.,Golant V.E.,Goncharov S.G., Gryasnevich M.P.,Izvozchikov A.B.,Lebedev S.V.,Razdobarin G.T., Rozhdestvenskij V.V.,Sakharov N.V.,Khalilov M.A.,Chernyshev F.V., Shahovetz K.G.

A.F.Ioffe Physical-Technical Institute,Academy of Science, Leningrad, USSR

ABSTRACT

The experiments on fast current-rise after major radius compression have been performed /1/.Initial plasma parameters were: I_p = 40 kA,R =62 cm,q_a =2.5-4.0,$\bar{n}_e$ =0.8·10^{13}cm^{-3}, T_i = 110 eV. After compression and plasma current-rise these values became: I_p = 100-120 kA,R =53 cm,q_a =2.0-3.5,$\bar{n}_e$ =1.5·10^{13}cm^{-3},T_e = 350-500 eV,T_i =130-200 eV.Plasma current density distributions have been obtained from external magnetic measurements in several discharges.Preliminary data shows fast relaxation of the j-profiles. Time behaviour of the plasma current density and electron temperature profiles have been studied by transport code simulations. Numerical results have been compared with the experimental data. Magnetic islands on the plasma periphery seems to be responsible for MHD-activity spikes during current-rise period.Fast increase of T has been observed in the regime with low q values.

1.Bender S.E.,Golant V.E.,Gornostaev S.V.et al.XI Eur.Conf. on Contr.Fusion and Plas.Phys.,Aachen,1983,v.1,p.111.

14 European Conference on Controlled Fusion
and Plasma Physics

NUMERICAL SIMULATION OF DISCHARGES IN TOKAMAK ON THE BASIS OF A SELF-CONSISTENT MODEL FOR ANOMALOUS TRANSPORT PROCESSES

Parail V.V., Tarasyan K.N.
I.V.Kurchatov Institute of Atomic Energy, Moscow, USSR

A self-consistent model of energy and particle balance in tokamak in both Ohmic and auxiliary-high power-heating regimes on the basis of an analysis of stokhastic processes in the transport of charged particles at their interaction with the vigorously-non-linear electromagnetic fluctuations has been built. It is considered that an anomalous transport in Ohmic regimes is mainly related with the stokhastic diffusion of banana electrons in the regular convective cells, resulting in a well-known relationship for the electron diffusivity coefficient: $\chi_e = \frac{c\,\epsilon}{\omega_{Be}} \frac{\partial T_e}{q \cdot R} \cdot \mathcal{E}$. The inclusion of an auxiliary-high power-heating results in a destabilization of the drift-type cells, when an inequality $\nabla n_e/n_e \neq \frac{1}{2}\,\nabla T_e/T_e$ is satisfied. The presence of a finite life time for the cells results in the emergence of anomalous heat fluxes for both electron and ion components as well as in the plasma diffusion, as a whole, with a characteristic transport coefficient $\chi_{e,i} \sim \frac{c T_e}{e B_\varphi} \sqrt{\frac{T_e}{M}} \left| \frac{\partial n_e}{n_e} - \frac{1}{2} \frac{\partial T_e}{T_e} \right|$ The proposed set of equations for the energy and particle balance has been integrated numerically. The results of calculations have shown that the proposed model allows to describe both the Ohmic discharges and the discharges with auxiliary-high power-heating on T-10, D-III, TFTR, including the super shots, by the same approach. This model gives a good agreement with the results of dynamic experiments on heat pulse propagation.

ELECTRON DENSITY PROFILES IN NEUTRAL BEAM HEATED PLASMAS

Grek B., Park H., Goldston R.J., Johnson D.W. , Mansfield D.K., Schivell J.
Princeton University Plasma Physics Laboratory, Princeton N.J., 08544, USA

INTRODUCTION

In this paper we present data on electron density profiles measured with a 76 spatial channel Thomson scattering system and a 10 channel infrared interferometer during neutral beam heating experiments on TFTR. For the data presented here the carbon tiled inner wall was used as the plasma limiter. Depending on operating conditions the electron density profiles exhibited a variety of shapes, as well asymmetries with respect to the electron temperature profiles. Differences between the line integrals of the Thomson scattering density data and the interferometer data are interpreted as being caused by cold plasma located between the last closed magnetic flux surface of the plasma and the vacuum vessel walls. All the profiles shown here were taken near the end of the neutral beam pulse, so as to be as near steady state as possible.

Electron density profiles on TFTR during neutral beam heating fall into two general categories. The first is a generally broad density profile which is characteristic of the L-mode operation with significantly reduced energy confinement compared with purely ohmically heated discharges. The second category consists of peaked profiles which are observed at lower plasma currents (.8 to 1.1 MA), in a well conditioned machine, with confinement times much greater than given by traditional L-mode scalings. Although a continuum of electron density profiles between these categories has been observed depending on vacuum vessel conditioning and machine operation, we will consider these two regimes independently.

L-MODE REGIME

Electron density profiles characteristic of this mode of operation, for two different densities, are shown in Fig. 1. For reference purposes density profiles of ohmic discharges, for similar density ranges, are also shown. As can be seen the beam heated plasmas differ in overall profile shape as well as edge characteristics from the ohmically heated ones. The ohmic plasmas have a generally parabolic shape that goes to a density that is usually of the order of $10^{13}/cm^3$ or less at the wall. The second derivative of the density with the minor radius is negative everywhere. Depending on the form and magnitude of the pinch velocity assumed, particle diffusivities from 10^3 to 10^4 cm^2/sec are calculated from this ohmic plasma over the bulk of the profile (using particle source terms as calculated by the SNAP code). The higher density beam plasma has a much higher edge density at the inner wall that is the limiter, and also has very steep density gradients at the outer edge. The lower density beam shot was obtained with a well conditioned inner wall, whereas the higher density discharge was generated before wall conditioning. Comparison of the two profiles show that the major difference between them is an apparent pedestal of about

FIGURE-1

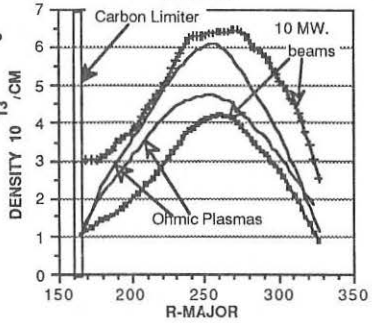

Electron density profiles with and without neutral beam heating in plasmas with currents of 1.4 MA., toroidal magnetic fields of 4.8T.

$2x10^{13}/cm^3$. Very high density gradients are therefore generated at the plasma edge for this mode of operation. Particle diffusivities for the beam shots are of the order of 10^4 cm^2/sec, over most of the inner plasma. It is also of interest to note that the interior density gradients are nearly identical in these two shots, since the major difference between these two beam shots is a pedestal in the density. The second derivative of the density with respect the minor radius is generally positive on the inside of the plasma and negative on the outside. Since purely radial diffusive flow cannot account for this, one might assume that poloidal flows must exist in the plasma.

Line integrals of the Thomson scattering data were calculated assuming that flux surfaces are shifted circles with constant electron temperatures, but with densities that have a poloidally varying component with a cosine dependence on the poloidal angle. The ratio of line integrals of the Thomson scattering data thus obtained and the interferometer data are shown in Fig. 2. As is evident from the figure a significant contribution of cold plasma to the interferometer signal must be assumed at the plasma periphery. This plasma is either outside the range of temperatures that is detectable by the Thomson scattering system (<30 e.V.) and/or is located out of the machine mid-plane. Taking account of geometry of the TFTR inner limiter implies that a cold plasma with a density in excess of $10^{14}/cm^3$ must exist near the inner edge for the high density case. For the lower density beam heated case and for ohmic plasmas, a cold edge plasma with a density in the range of $10^{13}/cm^3$ is sufficient to account for the differences between the Thomson line integrals and the interferometer data.

The above general characteristics do not seem to change with either beam power or beam orientation. Fig 3 shows density profiles obtained in somewhat smaller plasmas using beams (about 2.5 MW.) that were more perpendicular in order to penetrate deeper into the plasma (tangency radii of 1.9m) or for beams that were more tangential with the outside of the plasma (tangency radii of 2.75m), so as to heat and fuel the outside.[1] Although the calculated particle source terms were considerably different in the two cases, particularly in the plasma center, the two density profiles are remarkably similar.

FIGURE-2

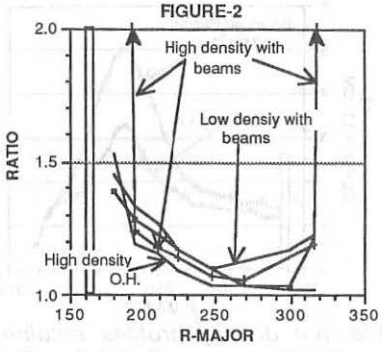

Ratio of interferometer density line integrals to Thomson scattering density line integrals vs major radial positions of interferometer

FIGURE-3

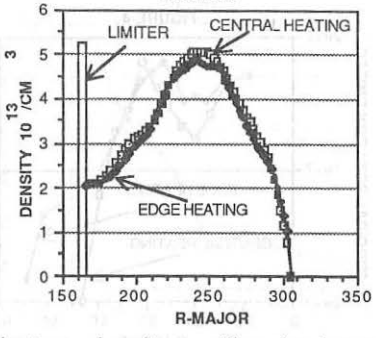

Electron density profiles for beam heated plasmas with edge heating (tangency R=1.9m) and central heating (tangency R=2.75m). Plama current of 1.1MA. Fields of 4.9T

The two density profiles do however show some differences in asymmetry with respect to the temperature profile. The edge heating case has a higher outward asymmetry at the outer plasma edge. If this density asymmetries are interpreted in terms of a toroidal rotation,[3] and assuming that the ion temperature profile is the same as the electron temperature profile (with a central ion temperature as calculated by SNAP), the toroidal rotation profiles shown in Fig. 4 are obtained.

SUPERSHOT MODE

Electron density profiles characteristic of this mode of operation are shown in Fig. 5. The profiles in this mode differs in two major respects from those in the L-mode.[2] First the density profile is highly peaked, with negative second derivatives over the bulk of the discharge. A larger part of the density difference is now supported in the bulk of the plasma. Peak to edge density differences of up to $6x10^{13}/cm^3$ have been observed to be supported by the interior of the plasma, with edge pedestals of about $1.5x10^{13}/cm^3$ or less. Second, the character of the cold edge plasma is different. The ratio of the line integrated density from Thomson scattering to that from the interferometer is generally close to one over the full profile, and deviates from unity only near the inner wall. This implies that a colder plasma region exists primarily near the inner wall with line averaged densities of significantly less than $10^{13}/cm^3$. The main difference between the two profiles shown in Fig. 5 is the neutral beam orientation. The central densities for the case of near balanced beam injection are considreably higher than those obtained for the all co-injection cases. The peak electron temperatures obtained with balanced injection are often greater than 6 KeV. whereas the peak electron temperatures for the co-injection case is of the order of 4.5 KeV.

Another difference between the two discharges shown in Fig. 5 becomes apparent when the density asymmetry with respect to the temperature is examined. This is shown in Fig. 6 where the normalized density asymmetry [(outer density-inner density)/(mean density)] at a given temperature is plotted vs. minor radius. As is characteristic of all disharges limited by the inner wall, the density is significantly higher on the inner side of the plasma for large minor ra-

FIGURE-4

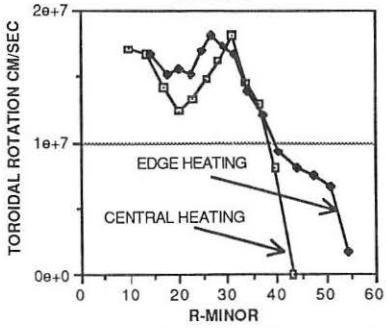

Toroidal velocity rotation profile calculated from the density asymmetries for the edge and central heating cases of Fig. 3.

FIGURE-5

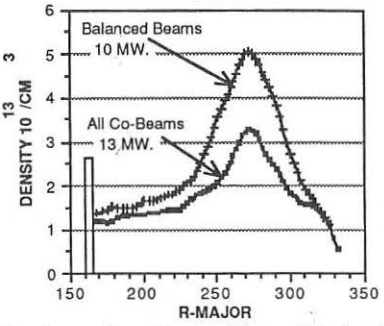

Electron density profiles obtained with all co-beam injection and balanced beam injection. The plasma current was 0.9MA. and the toroidal magnetic field 5.1T.

dii. The slight negative asymmetry, that is present over the central regions of the profile, for the balanced beam injection cases is also often seen in ohmic discharges. If the positive density asymmetry over the remainder of the discharge, for the co-injection case, is interpreted as being caused by a toroidal rotation,[3] the toroidal rotation profile shown in Fig. 7 is obtained. If the difference in asymmetry between the co-injection case and the balanced injection case is used to calculate a toroidal rotation velocity the rotation profiles obtained are considerably broader. The central rotation velocities thus calculated are usually comparable to those obtained from doppler shifts of impurity lines although significant differences are sometimes observed.It is expected that in these case other mechanisms such as poloidal rotation or convective flows might be active.

CONCLUSIONS

There are two general type of density profiles observed on TFTR. The first is a generally broad profile with a significant fraction of the density supported by the plasma edges where a cold plasma blanket exists. These profiles are usually associated with reduced energy confinement times. The second type is a much more peaked density profile with the bulk of the plasma supporting the density differences. This latter type of discharge also has a more tenuous edge plasma blanket than the L-mode plasmas. Finally the density asymmetries observed on TFTR are generally small and are usually comparable to those expected from toroidal plasma rotation, except near the plasma periphery where large negative asymmetries exist.

ACKNOWLEDGEMENTS

The authors thank the TFTR physics staff, operations staff and the beam group for their particiaption in these experiments. This work was supported under U.S. DoE Contract #DE-AC02-76-CH03073.

REFERENCES

1. Strachan J.D., et al, Phys. Rev. Lett., 58, 1004 (1987)
2. Goldston R.J., et al, Controlled Fusion and Plasma Heating, 13th European Conference (1986) 148, Schierse, F.R.G.
3. Semenzato S., et al, LRP 258/85, Ecole Polytechnique Federale de Lausanne

FIGURE-6

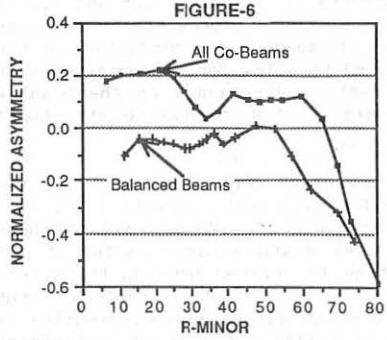

Normalized density asymmetry ((outer density-inner density)/ mean-density) vs minor radius for the data in Fig. 5.

FIGURE-7

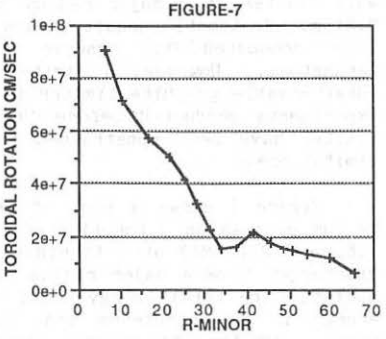

Rotation velocities obtained from the the data in Fig.6 (co-injection) assuming purely toroidal rotation. The central velocity obtained is near the acoustic velocity.

RECENT CONFINEMENT STUDIES OF OHMICALLY-HEATED HELIUM PLASMAS

P.C. Efthimion, D.W. Johnson, N.L. Bretz, M. Bitter, C.E. Bush, B. Grek, K.W. Hill, R.J. Goldston, H. Park, A.T. Ramsey, B.C. Stratton, F.J. Stauffer[a], Y. Takase[b], G. Taylor and R.M. Wieland

Princeton University Plasma Physics Laboratory, Princeton, NJ 08544 USA

ABSTRACT

A series of density scans at different currents for helium plasmas has been completed to study the energy confinement in the linear and saturated regimes of ohmic heating. The linear regime characteristics are identical to those obtained previously for deuterium plasmas. In the saturated regime confinement becomes essentially independent of density and current.

A set of recent confinement experiments of ohmically-heated plasmas on TFTR have focused upon gas fueled helium discharges. Helium plasmas are particularly useful because high electron density discharges are easily achieved in TFTR. A maximum line average electron density of $9 \times 10^{19} m^{-3}$ was reached for 2.2 MA full-size a = 0.81 m minor radius plasmas. Equally important, line-average densities as low as $1 \times 10^{19} m^{-3}$ were obtained. This large density range enabled both the linear and saturated regimes of ohmic confinement to be studied for a single species in TFTR. The limited density range for deuterium plasmas on TFTR is not sufficient to study the saturated regime for these full-size plasmas.

The majority of the helium plasmas were formed on the graphite inner-wall limiter at a major radius of R = 2.46 m and a minor radius of a = 0.81 m. Systematic density scans at currents of 1.0, 1.4, 1.8 and 2.2 MA were conducted to observe the confinement dependence on these parameters. However, a limited number of scans were conducted on the outer movable graphite limiter (R = 2.57 m) to allow for a comparison with experiments conducted before 1986. Recently, discharges on the movable limiter have been constrained to currents of 1.4 MA due to structural limitations.

Figure 1 shows a plot of the total energy confinement time of the helium plasmas as a function of density for different currents (1.0, 1.4, 1.8, and 2.2. MA) at a toroidal magnetic field of 4.78 T. All of these discharges have a major radius of R = 2.46 m and a minor radius of a = 0.81 m. The total energy confinement time is defined here as the stored energy in the electrons and ions divided by the ohmic heating input power. For this figure the ion energy content was calculated assuming 1x neoclassical ion transport [1]. There is a linear regime of confinement at each current that obeys the scaling of the previous deuterium plasma results of $\tau \propto \bar{n}_e q_c$ [2]. The lines in the figure are the actual TFTR

[a]Permanent address: University of Maryland, College Park, MD
[b]Permanent address: MIT, Plasma Fusion Center, Cambridge, MA

scaling $\tau = 6.5 \times 10^{-22} \bar{n}_E R^2 a q_a$ which is the best fit to the previous TFTR deuterium data [2]. At these low densities of plasma operation, the impurity content is very high, resulting in a low helium ion content. This point will be later illustrated in Fig. 2. These same characteristics were exhibited in previous experiments for deuterium plasmas. In the saturated regime, the current dependence essentially disappears and the saturated confinement time is approximately 0.33 s on the inner wall graphite limiter. Note that there is no indication of the confinement time decreasing with density, as observed in some experiments [3]. The density disruption limit at each current coincides with the observation of MARFE behavior.

The central ion temperatures for some of the discharges were measured by Doppler broadening of impurity nickel K_α lines. These temperatures are found to be consistent with 0-6 times neoclassical ion transport (χ_i^{neo}), and using them to determine multipliers on χ_i^{neo} would change the resultant global confinement times by 5% or less. With the assumption that the enhancement in the ion transport determined by the central electron and ion temperatures is modelled as a fixed multiplicative factor applied to neoclassical ion conduction across the entire profile, the ion and electron conductivities (χ_e and χ_i) are calculated at a radius of 0.66 of the plasma minor radius. At this radius, the net input power is not obscured by edge radiation, or sawtooth effects as in the plasmas core, and the temperature gradient is accurately measured. The calculations show that χ_i/χ_e is in the range of 0.1 - 0.75 with the ratio at 0.75 when the multiplier is near 6. However, for the electron conduction to depend inversely with density in the saturated regime, this multiplier must be in the range of 15-20. Therefore, if we model $\chi_i = \propto \chi_i^{neo}$ the power loss is still dominated by the electrons. However, we cannot exclude models in which ion transport dominates in the outer region because of a strongly radially rising $\chi_i(r)$.

There is a large variation in the Z_{eff} of these plasmas in going from low to high density (Fig. 2). The Z_{eff} was determined primarily by the visible bremsstrahlung measurements, but there were some measurements from the horizontal X-ray pulse height analyzer. The very large Z_{eff} at low density is a concern in the confinement studies because of the low helium ion content. At densities of $\bar{n}_e > 6 \times 10^{19} m^{-3}$, Z_{eff} approaches 2. Furthermore, there is a linear current and inverse density dependency in the Z_{eff} at low density, which has been observed previously in TFTR [2].

In 1985 helium discharges were studied on the outer movable limiter (I_p = 1.8 MA and B = 4.71 T), and it is interesting to compare those results with the recent ones (1987). The data indicates that the 1985 plasmas have 25-30% more stored energy, due to higher electron temperatures although the Z_{eff}, determined from the visible bremsstrahlung, and the ohmic input power are the same. A comparison of electron temperature profiles from Thomson scattering and electron cyclotron emission show that the laser temperature was 10-12% higher than the electron cyclotron emission measurement in 1985, while the two measurements agree to within 5% for recent helium plasmas. A calculation of the total energy confinement times with either electron temperature

measurement, could only produce less than a 10% variation in the confinement time value. Z_{eff} deduced from neoclassical resistivity agreed well with the measured Z_{eff} from visible bremsstrahlung for the 1985 data, while in the recent data the neoclassical and Spitzer Z_{eff}'s bracket the visible bremsstrahlung value as is often the case in TFTR. While there are significant variations in diagnostic calibrations, resulting in a 10-12% uncertainty in τ_E, the differences in the saturated confinement times appear to be real. In addition, the peaking factor of the temperature profile are slightly different ($\langle T_e \rangle / T_e(0)$ = 0.46 for R = 2.57 M and 0.4 for R = 2.46 M) and may be due to small differences in R. The current and magnetic field scans to study the peaking factor do not explain the variation in the factor in going from the inner to the outer wall limiter.

To help clarify the differences in the saturated confinement data for the movable and axisymmetric inner wall bumper limiter, a comparison of confinement on the inner and outer limiters was recently completed at a current of I_p = 1.4 MA and a toroidal field of B = 4.0 T (Fig. 3). The data shows the saturation levels are similar. However, the temperature peaking factors are slightly different ($\langle T_e \rangle / T_e(0)$ = 0.35 for R = 2.57 m and 0.3 for R = 2.46 m) - a result observed in the 1985 data.

In conclusion, helium discharges offer a convenient means of examining the saturated confinement regime for ohmically-heated plasmas in TFTR. There is no indication of a turning over of the confinement times or a current dependence in the saturated regime. Based on measurements of the central ion temperature, we deduce that ion transport can be a significant part of the overall power balance, but if we assume $\chi_i = \alpha \chi_i^{neo}$, the χ_e does not vary as n_e^{-1} in the saturated regime. Differences in the saturated confinement level for data in 1985 and recent data cannot be completely explained by diagnostic uncertainties. In the linear regime, the confinement results are identical to those previously reported for deuterium TFTR plasmas. Further experiments will continue to examine the effect of the toroidal field, gas programming, and limiter conditioning on the saturation level. Modelling the data with different electron and ion transport models is also planned.

This work was supported by U.S. DOE Contract No. DE-AC02-CHO-3073.

REFERENCES

1. Chang, C.S. and Hinton, F.L., Phys. Fluids 25, 1493 (1982).

2. Efthimion, P.C., Bretz, N.L., Bell, M.G., Bitter, M., Blanchard, W.R., et al., in Plasma Physics and Controlled Nuclear Fusion Research (Proc. 10th Int. Conf. London, 1984) IAEA, Vienna (1984) paper A-I-2.

3. Ejima, S., Nucl. Fusion 22, 1627 (1982).

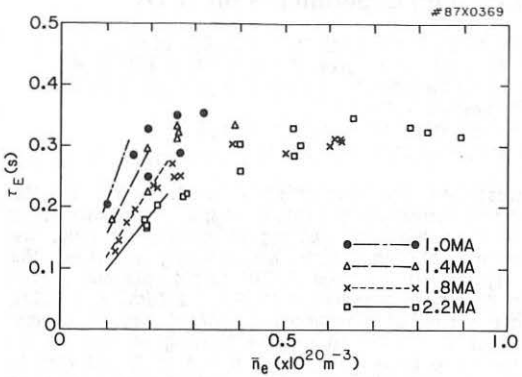

Fig. 1 Total energy confinement time, τ_e, as a function of density. Both linear and saturated regimes are present. The four lines are the previous TFTR ohmic scaling as a function of density for the four currents.

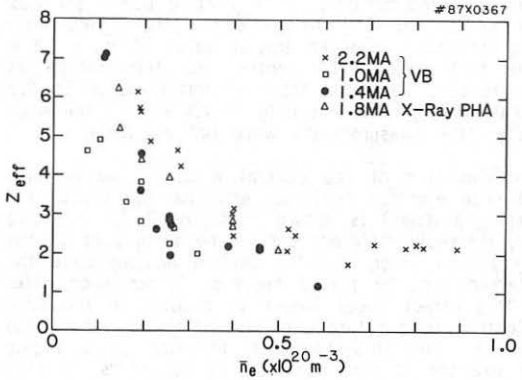

Fig. 2 Z_{eff} from X-ray PHA and visible bremsstrahlung as a function of density for the currents 1.0, 1.4, 1.8, and 2.2 MA.

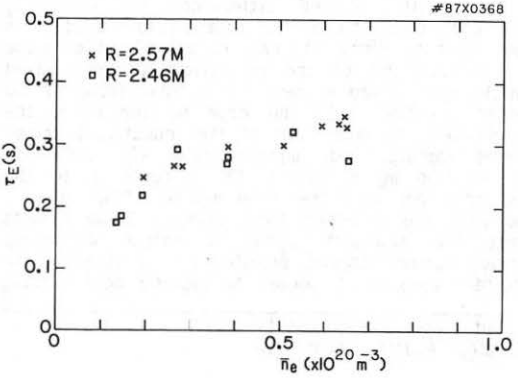

Fig. 3 Recent comparison of confinement on the inner (R=2.46 m) and outer (R=2.57 m) limiter at a current of 1.4 MA.

Edge and Center Heating Experiments on TFTR

R.J. Goldston, Y. Takase*, D.C. McCune, M.G. Bell, M. Bitter, C.E. Bush, P.H. Diamond+, P.C. Efthimion, E.D. Fredrickson, B. Grek, H. Hendel, K.W. Hill, D.W. Johnson, D. Mansfield, K. McGuire, E. Nieschmidt, H. Park, M.H. Redi, J. Schivell, S. Sesnic, G. Taylor
Plasma Physics Laboratory, Princeton University
P.O. Box 451, Princeton, N.J. 08544

Introduction In order to investigate the mechanism(s) contributing to the apparent resiliency of the electron temperature profile shape in tokamaks, in the face of perturbing forces such as auxiliary heating or current-ramping, we have performed a series of experiments in which we strongly modified the neutral-beam heating profiles applied to a fixed TFTR target plasma. The experiments were carried out in deuterium plasmas with R_0 = 2.36m, a = 0.7m, B_T = 4.9T, and I_p = 1.2MA. In one series of discharges 2.8MW of neutral beams were aimed at a tangency radius of R = 1.9m to provide heating of the plasma center, and in a second series the same beam power was aimed at R = 2.75m to heat the outer region of the plasma predominantly. The heating power profiles for these two conditions are shown in figure 1. At the end of the 0.5sec beam pulse, the electron density had increased from an initial value of n_e = 2.6 x $10^{19}/m^3$ to 3.4 x $10^{19}/m^3$ in both cases. The central ion temperature as measured by x-ray crystal spectroscopy increased from an initial value of 2.2 keV up to 3.5 keV in the central heating case, but only to 2.9 keV in the edge heating case. Ion temperature profile measurements were not available.

Sawtooth Behavior The time evolution of the central electron temperature, as measured by fundamental O-mode electron cyclotron emission (calibrated for these shots to Thomson scattering profiles) is shown in figure 2 for the two cases. The sawtooth behavior is markedly different during the early part of the beam pulse, but becomes more similar later. For the central heating case the sawtooth amplitude becomes larger and the period becomes longer soon after the beam power is applied. This effect takes longer to develop in the edge heating case. Because the electron temperature profiles differ by very little in the two cases (see figure 3), and this sawtooth behavior is a highly reproducible phenomenon, (for example it also occurred in the shots reported in ref. [2].) it seems possible that the difference is associated with beam-driven currents, rather than with detailed differences in resistivity profiles. In the central heating case calculations, the total current profile is unaffected by the beam-driven current, since it has essentially the same profile as the ohmic current. However 8% of the inductively driven current within r = 0.4a is replaced with beam-driven current on a time scale of 50 msec, at the beginning of beam injection. In the edge heating case, the beam-driven current is located off-axis, so only 1.5% of the inductively driven current within 0.4a is replaced rapidly, and approximately 400 msec is required for that core current to drop by a further 3% in response to the off-axis current drive. This is consistent with the more modest effect of injection on the sawteeth, and with the observed time delay. These results suggest, albeit indirectly, that the sawtooth cycle is rather delicately controlled by the inductively-driven current density profile, and is sensitive to the presence of beam-driven current because it serves to replace destabilizing inductively-driven current.

* M.I.T. Plasma Fusion Center, Cambridge, Massachusetts USA
+ U.T.A. Institute for Fusion Studies, Austin, Texas USA

The direct electron heat transport across r = 0.2m (just outside the q = 1 surface) due to the sawteeth, determined from fast time resolution ECE off-axis measurements, was found to be small ($\leq$ 40 kW for both cases) compared to 250 kW (edge heating) and 400 kW (central heating) of electron conduction losses (assuming χ_i neoclassical). The sawtooth transport at r = 0.35m is completely negligible.

Transport Analysis The electron power balance in these discharges was also analyzed using the TRANSP code. A sawtooth model keyed to the measured sawtooth times was used to account for the observed direct sawtooth transport in the electron power balance, and to impose ion sawtooth transport in the calculation of $T_i(r,t)$. Anomalous ion thermal transport due to η_i modes was included in some calculations, using $\chi_i(\eta_i)$ as derived by Lee and Diamond [1]. A cubic threshold function which gradually "turns on" $\chi_i(\eta_i)$ was used. This function initiates $\chi_i(\eta_i)$ at η_i = 1.5 and reaches full strength at η_i = 2.5. Steepening the threshold function so that it reached full strength at η_i = 2 yielded very similar results.

In figure 4, $\chi_e(r)$ deduced assuming $\chi_i = \chi_i^{neo}$ is shown by the dashed lines, for central and edge heating. For central heating, $\chi_e(r)$ is everywhere enhanced beyond its ohmic counterpart. For edge heating, $\chi_e(r)$ is comparable to (or even lower than) ohmic values in the plasma core, but is significantly enhanced in the outer half-radius. In order to test the robustness of the result that the transport coefficients are different in the two cases, the calculated $\chi_e(r,t)$ from the TRANSP analysis of a central heating case was used as input for another run of TRANSP, operated in a mode to predict $T_e(r,t)$ based on $\chi_e(r,t)$, using edge heating beams. The result was that edge heating, given the same $\chi_e(r,t)$ as deduced for central heating (and with χ_i neoclassical), caused no central electron temperature rise at all, but did induce a significant broadening of the electron temperature profile. Since the experimental observation is that T_{e0} rises with edge heating, and that the electron temperature profile shape if anything shrinks slightly (figure 3), we deduce that there must be real differences in the transport mechanisms in these two cases. On the other hand, the major difference need not be in the electron channel, as pointed out in our previous work [3]. The calculated central ion temperature agrees well with the measured value in the case of edge heating, but is much higher (4.5 keV vs. 3.6 keV) in the case of central heating. This suggests that anomalous ion thermal transport may play a role, and η_i modes are a natural candidate for this situation where, on the basis of neoclassical ion thermal transport, we calculate much more peaked $T_i(r)$ profiles with central than with edge heating. $\chi_e(r)$ calculated assuming $\chi_i = \chi_i^{neo} + \chi_i(\eta_i)$ is shown by the solid lines in figure 4. (In the low density ohmic phase of this discharge including η_i effects is unimportant for the electron power balance.) $\chi_e(r)$ is now more similar for the edge and central heating experiments, and the calculated $T_i(0)$ agrees well with the measured value. Inclusion of $\chi_i(\eta_i)$ had no effect on χ_e in the core region of the edge heating case, because the hollow heating profile did not drive η_i past threshold in this region.

It is interesting to note that the nonlinear dependence of $\chi_i(\eta_i)$ on η_i, and its large absolute value beyond threshold, ensures that approximate marginal stability (i.e. $\eta_i \approx \eta_i^{crit}$) is maintained in these calculations over most of the profile, in the presence of strong central ion heating. An exception to this occurs near the edge, where the temperature dependence of $\chi_i(\eta_i) \propto T_i^{3/2}$ allows η_i to significantly exceed threshold. As a result the marginal stability "link" from the plasma surface to the core confinement

region is broken. However recent theoretical studies [3] indicate that a proper treatment of the effects of $n \neq 0$ radial eigenmodes will further enhance the absolute value of $\chi_i(\eta_i)$ (particularly near the edge) thus broadening the extent of marginally stable plasma. This may help to explain the strongly enhanced transport in the outer regions of the plasma seen in figure 4, as well as the apparent strong sensitivity of tokamak energy confinement in general to edge recycling conditions and particle confinement. Preliminary calculations using $\chi_i(\eta_i)$ from [3] show a strong sensitivity of core ion temperature to the assumed edge ion temperature and neutral recycling conditions. A task which remains is to test if other predictions of η_i-driven transport, particularly particle flows and electron thermal diffusivity, can be correlated quantitatively with experimental observations. The remaining difference in χ_e seen in figure 4 may itself be correlated with η_i-driven turbulence. The issue of momentum diffusion in these edge and center heated plasmas is addressed in the paper by Scott et al., at this conference [4]. Another topic of possible importance is the role of beam ions in the stability of η_i modes, and any beam ion radial transport caused by them.

Conclusions Central and edge heated TFTR plasmas were analyzed using the transport analysis code TRANSP. When the effects of anomalous ion transport due to η_i modes were included, the agreement between measured and predicted $T_i(0)$ with central heating was significantly improved. Moreover the observed resiliency of the measured electron temperature profile in the face of very different heating profiles could then at least in part be explained by a theoretically predicted marginal stability mechanism in the ion channel. Finally, the differences in sawtooth behavior between edge and central heating suggest the possibility that the sawtooth cycle is sensitively controlled by the inductively-driven current density in the inner region of the plasma, and is not sensitive to beam-driven current, except insofar as it replaces destabilizing inductively-driven current.

Acknowledgment
This work supported by DoE contract #DE-AC02-76-CHO-3072

References
[1] G.S. Lee and P.H. Diamond, Phys. Fluids 29, 3291 (1986).
[2] R.J. Goldston et al., Procedings of the European Physical Society (1986)
[3] P.W. Terry, P.H. Diamond, Sherwood Conference (1987).
[4] S. Scott et all, this conference.

Figure Captions
1. Beam and ohmic heating profiles in edge and central heating cases.
2. Time evolution of central electron temperature for edge and central heating. T_e offset by -0.5 keV for edge heating case, to separate traces.
3. Electron temperature profiles for edge and central heating, as well as ohmic target plasma. Note that the auxiliary-heated plasmas have 30% higher n_e than the ohmic plasma.
4. Electron thermal diffusivity deduced in ohmic phase, and for edge and central heating. Dashed lines correspond to assuming neoclassical ion thermal transport, while solid line indicate inclusion of $\chi_i(\eta_i)$. For each line type the higher curve corresponds to central heating, and the lower curve corresponds to edge heating.

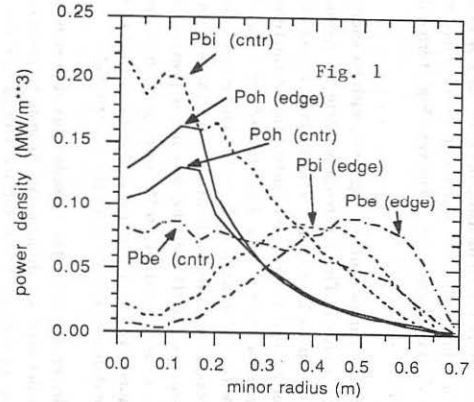
Fig. 1
Pbi (cntr)
Poh (edge)
Poh (cntr)
Pbi (edge)
Pbe (edge)
Pbe (cntr)
power density (MW/m**3)
minor radius (m)

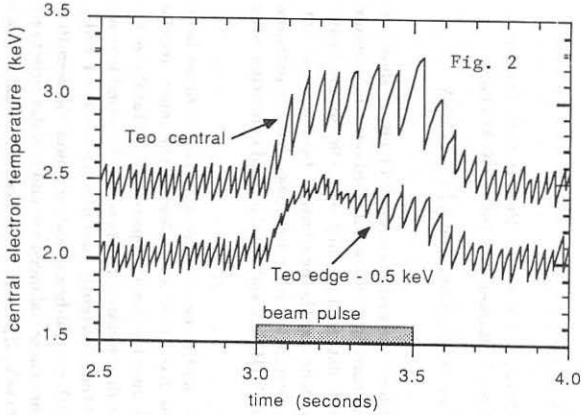
Fig. 2
Teo central
Teo edge - 0.5 keV
beam pulse
central electron temperature (keV)
time (seconds)

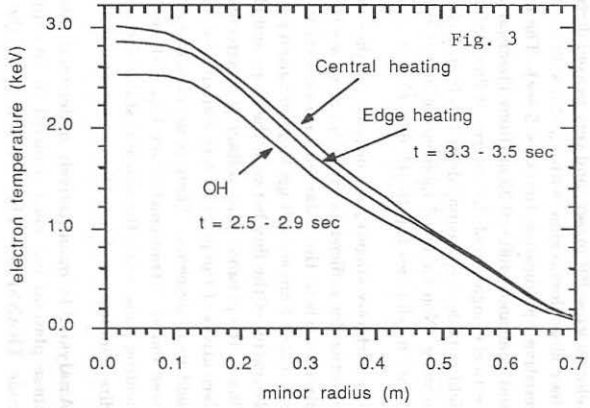
Fig. 3
Central heating
Edge heating
t = 3.3 - 3.5 sec
OH
t = 2.5 - 2.9 sec
electron temperature (keV)
minor radius (m)

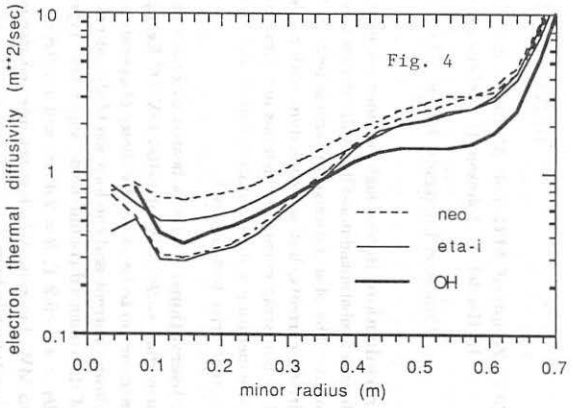
Fig. 4
neo
eta-i
OH
electron thermal diffusivity (m**2/sec)
minor radius (m)

DRIVEN CURRENTS IN TFTR

M.C. Zarnstorff, M.G. Bell, M. Bitter, R.J. Goldston, B. Grek, R.J. Hawryluk, G. Hammett, H. Hendel, D. Johnson, D. McCune, H. Park, A. Ramsey, G. Taylor, R. Wieland

Princeton University, Plasma Physics Laboratory, Princeton NJ 08544 USA

Introduction: Recent high-confinement neutral-beam heated plasmas in TFTR [1] show evidence of substantial non-Ohmically-driven toroidal current, even for balanced beam momentum input. The observations are inconsistent with calculations including only Ohmic and beam-driven currents, but are consistent with models including the neoclassical bootstrap current. The bootstrap current, which has not previously been detected in tokamaks, has the potential for generating a steady-state tokamak and driving MHD instabilities[2,3], and enhancing other current drive techniques[4].

Observations: TFTR is heated by one counter- and three co-tangential neutral-beam lines, providing $\sim$ 20 MW of $\sim$100 keV D^0 for up to 2 seconds, and allowing the input angular momentum to be varied by choice of operating beams. Feedback loops control and stabilize the plasma current and the location of the outermost flux surface. The plasmas discussed here are of the enhanced confinement "supershot" type obtained recently, and have $I_P = 0.8 - 1.1$ MA, $B_T = 4.8 - 5.2$ T, $R = 2.45$ m, and $a = 0.8$ m. With neutral-beam heating power P_B from 10 to 15 MW, but relatively low net injected momentum (near balanced co- and counter-injection), they typically have $T_e(0) \sim 6$ keV, $T_i(0) = 15 - 20$ keV, $Z_{eff} = 2 - 4$, moderate toroidal rotation velocity $v_\phi \sim 10^5$ m/sec, and very peaked density profiles $n_e(0)/\overline{n}_e \sim 2.5$. These plasmas are in the collisionless regime with $\nu_{*i} < 5 \times 10^{-3}$, $\nu_{*e} < 10^{-1}$ at the half-radius, and have very long resistive equilibration times ($\sim$ 5 sec). The measured diamagnetic $\beta_{P\perp} \sim 2$, $\beta_{Peq} + l_i/2 \sim 3$, and Shafranov shift$\sim$ 0.35 m (from Thomson scattering density and temperature profiles). The vertical elongation of the outermost flux surface (as inferred from measurements of the poloidal field outside the plasma) decreases from 1.05 in the Ohmic phase to $\sim$ 0.9 at the end of beam heating. Non-balanced momentum injection into similar plasmas produces very high toroidal rotation velocities (up to 10^6 m/sec), but lower $n_e(0)$, $T_e(0)$, and $T_i(0)$.

The surface-voltage V_{sur} is negative for these plasmas during beam heating, even with balanced injection for sufficiently large β_P, as shown in Figs. 1 and 2. This has remained true for recent plasmas where the balanced beam-injection lasted up to 2 seconds. The surface voltage is calculated from six voltage loops arranged poloidally about the plasma, correcting for the time derivative of the flux between the loops and the plasma and the time derivative of the toroidal flux in the plasma. This voltage is in agreement with that calculated from the numerical time derivatives of the poloidal flux contained in the plasma, as inferred from the external poloidal field measurements. There is no evidence of disruptive MHD activity, which has previously been found to transiently force $V_{sur} < 0$. Since I_p is held constant, in the later portion of the heating pulse when the shape is stable the continued expulsion of poloidal flux ($V_{sur} < 0$) is a direct indication of non-Ohmic currents, from the diffusion equation for the electric field.

Analysis: To quantitatively understand these driven currents, the poloidal flux diffusion in these plasmas has been modeled by the time-dependent $1\frac{1}{2}$ dimensional transport analysis code TRANSP[5]. The code calculates the time evolution of the surface voltage for vari-

ous assumptions of plasma transport and driven currents, using measured time-dependent plasma parameters. The T_e and n_e profiles are measured at two times in each discharge by a seventy-six point Thomson scattering system. The T_e profile is also measured by first-harmonic electron-cyclotron-emission radiometry, and the n_e profile by an array of infrared interferometers. Central and near-central values of T_i and v_ϕ are measured spectroscopically, using Doppler-broadening of Fe XXV, and Fe XXIV lines. Z_{eff} is determined by tangential measurements of visible bremsstrahlung emission and radial x-ray spectroscopy. Z_{eff} is assumed to be uniform for most of the calculations. The analyses presented assume that the flux surfaces are circular, though subjected to the Shafranov shift. The effects of the measured flux surface deformation are currently being analyzed. The measured profiles of n_e and T_e are mapped onto the calculated flux surfaces by shifting the respective iso-contours to the flux surfaces with the same minor diameter. This shift is typically < 10 cm, indicating good agreement between the calculated and experimental flux surfaces.

Neutral-beam deposition, orbiting, and thermalization is simulated by a Monte-Carlo technique[6]. The T_i profile is not measured, but is calculated from the ion energy-balance equation, assuming neoclassical[7] ion heat conduction, classical electron-ion temperature equilibration, and a $\frac{5}{2}\Gamma T$ convective heat flow. The cross-field particle flow Γ is calculated from the continuity equation, the measured density and Z_{eff}, and the calculated beam and neutral particle source rates. For an assumed global ion particle confinement time τ_p of 0.15 sec, consistent with limiter D_α measurements for similar plasmas, the beam-particle-source is larger than the wall source inside $\frac{2}{3}a$. In the ion power-balance calculation, the ion convective power loss is dominant inside $\frac{3}{4}a$, and is larger than the the neoclassical conductive loss by a factor of ~ 30 inside $\frac{2}{3}a$. This analysis has been restricted to plasmas with near-balanced momentum injection, avoiding the complications[8] introduced by the large rotation velocities obtained with unbalanced injection. For near-balanced injection, these simulations are in good agreement with the measured central impurity temperatures, the measured neutron flux, and magnetic measurements of stored energy.

V_{sur} for the pre-beam Ohmic plasma is lower than the value calculated using the other measurements and neoclassical theory[9], but not as low as predicted using Spitzer resistivity (without trapped particle corrections). To account for this, the conductivity has been increased by a factor of 1.5 to match the pre-beam V_{sur}. Calculations with the standard conductivity, or an initially parabolic Z_{eff} profile to match V_{sur} do not show significant differences during the beam-heating phase. The electron shielding of the beam-ion current is calculated including trapped particle effects[9], increasing the calculated net beam-driven current. The calculated shielding of the beam-driven current is small, due to the strength of the electron trapping and relatively large Z_{eff}. Uncertainties in Z_{eff} do not significantly affect the calculated net beam-driven current, due to the electron trapping. The neoclassical bootstrap current calculation[9] includes the effects of impurity ions and finite aspect ratio, but does not include the unthermalized beam ions. The calculated bootstrap current has a relatively large uncertainty, due to its sensitivity to the unmeasured Z_{eff} and T_i profiles.

Results: As shown in Fig. 3, the measured V_{sur} is well matched during the beam-heating pulse when the model includes both the neoclassical bootstrap current and the beam driven current, but does not agree without the bootstrap current. This is the case for all eight plasmas

analyzed in detail. The disagreement between the experimental V_{sur} and all the models for the first 0.2 seconds of beam heating may be due to the initially rapid flux surface shape change, which is currently not included in the analysis. The calculated beam-driven-current is non-zero, even for near-balanced injection, due to the orientation of the counter-injected beams being closer to perpendicular to the magnetic field than for the co-injected beams. The sum of the calculated beam (~250 kA) and bootstrap (~ 350 kA) currents does not exceed the total current in the discharge (850 kA). The negative surface voltage is due to the broadening of the current profile by the bootstrap current while the total current remains constant. The toroidal voltage remains positive on axis. The calculations also indicate that during the 0.7 sec heating pulse, the surface voltage is only sensitive to changes in the current in the outer 0.3 m of the plasma, due to the high electrical conductivity.

No satisfactory alternate explanations of these observations, not involving the bootstrap current, have been found. In particular, variation of the value of Z_{eff}, or its profile, does not significantly increase the amount of beam-driven current, due to the calculated lack of significant electron shielding current. To replace the calculated broad-profile bootstrap current, whose evolution matches the observed surface voltage, by beam-driven current would require that some 70% of the calculated beam-driven current flow in the outer 0.3 m. Since the beam-driven current is dominated by fast ions that have not slowed down or pitch-angle scattered significantly, such a spatial rearrangement of the beam-driven current by fast-ion transport is incompatible with the observed plasma heating and $d(d,n)He^3$ neutron emission. The surface voltage can be roughly matched, without the bootstrap current, by assuming that the atomic cross-sections used in the calculation of beam deposition (primarily impact ionization and charge exchange with impurities[10]) are too small in the 50 keV/nucleon region by a factor of 3 to 5, well outside the accepted range[11].

Summary: Substantial non-Ohmic currents have been found in high-β_P neutral-beam-heated TFTR plasmas, even for near-balanced injection. Modelling of the plasma V_{sur} requires inclusion of the neoclassical bootstrap current.

We are grateful for discussions with J.D. Callen, H.P. Furth, D. Meade, P. Rutherford, and J.D. Strachan. This work was supported by the US DOE, contract number DE-AC02-76-CHO-3073.

References

[1] STRACHAN, J. D. et al., Phys. Rev. Lett. **58** (1987) 1004.
[2] BICKERTON, R. J. et al., Nature (London) Phys. Sci. **229** (1971) 110.
[3] BOOZER, A. H., Phys. Fluids **29** (1986) 4123.
[4] FISCH, N. J., Rev. Mod. Phys. **59** (1987) 175.
[5] HAWRYLUK, R. J., in *Proc. Course and Workshop, 1979* (Varenna, 1980) p. 19.
[6] GOLDSTON, R. J. et al., J. Comp. Phys. **43** (1981) 61.
[7] CHANG, C. S. and HINTON, F. L., Phys. Fluids **29** (1986) 3314.
[8] GOLDSTON, R. J., in *Proc. Course and Workshop, 1985* (Varenna, 1986) p. 165.
[9] HIRSHMAN, S. P. and SIGMAR, D. J., Nucl. Fusion **21** (1981) 1079.
[10] OLSON, R. E. et al., Phys. Rev. Lett. **41** (1978) 163.
[11] PHANEUF, R. A. et al., Technical Report 6090, ORNL (1987).

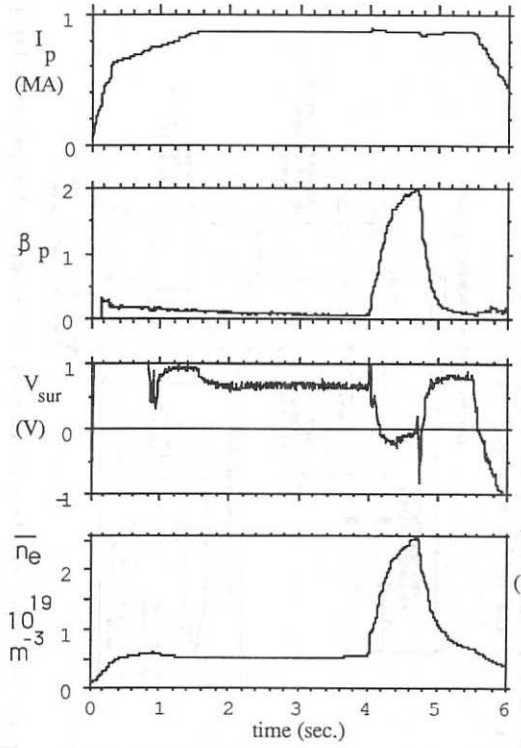

Figure 1: Typical time dependence of I_p, β_p, V_{sur}, and $\overline{n}_e$.

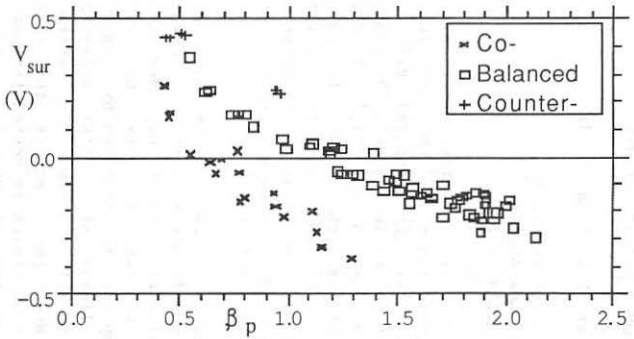

Figure 2: Variation of V_{sur} with β_p for co-, balanced-, and counter-injection.

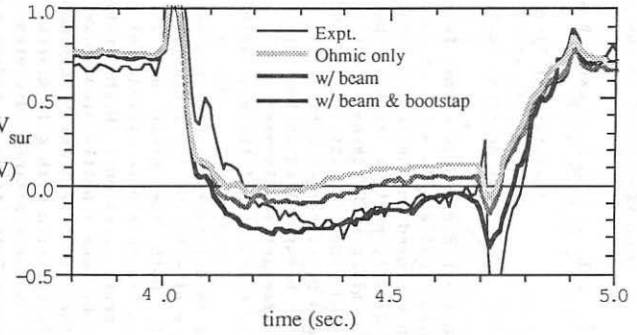

Figure 3: Measured and calculated V_{sur} time variation for various driven current models.

HIGH-RESOLUTION INTERFEROMETRY ON THE TEXT TOKAMAK

S.K. Kim, D.L. Brower, W.A. Peebles, N.C. Luhmann, Jr.

Institute of Plasma and Fusion Research
University of California, Los Angeles
Los Angeles, California 90024 U.S.A.

A multichannel, heterodyne, far-infrared laser interferometer system with high spatial ($\Delta x \simeq 1.5$ cm) and high phase ($\Delta n \leq 10^{11}$ cm^{-3}) resolution has been employed on the TEXT tokamak to study; (1) the temporal evolution of the density profile (with gas puffing and pellet injection); (2) density profile scaling with plasma parameters such as the current (I_p), toroidal field (B_T) and density ($\bar{n}_e$); and (3) propagation of density pulses introduced by either an oscillating gas puff or by MHD sawtooth activity. The latter has resulted in the first density pulse propagation investigation of interferometrically-measured, Abel-inverted sawtooth perturbations providing a measure of the associated diffusion coefficient.

The twin-frequency laser source operates at 432 μm ($\simeq$ 60 mW) with an IF frequency of $\simeq$750 kHz.[1] A schematic of the interferometry system is shown in Fig. 1. Both the probe and local oscillator beams are expanded in one dimension via parabolic cylindrical mirrors in order to view the entire plasma cross section. High spatial sampling is achieved by arranging corner-cube GaAs Schottky-diode mixers in a linear array (the array has slots for 29 mixers with minimum spacing of 1.5 cm). The system is typically operated with $\leq$ 15 mixers which are spaced across the plasma profile as the experiment dictates. TEXT is an ohmically-heated tokamak of major radius R=1m and minor radius a=0.27m operating at $100 \leq I_p \leq 400$ kA, $10 \leq B_T \leq 2.8$ T, and $10^{13} \leq \bar{n}_e \leq 10^{14}$ cm^{-3}

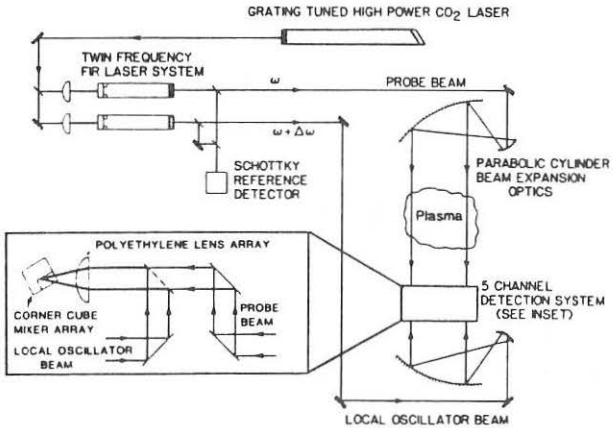

Figure 1. Schematic of the multichannel, heterodyne, far-infrared laser interferometer system.

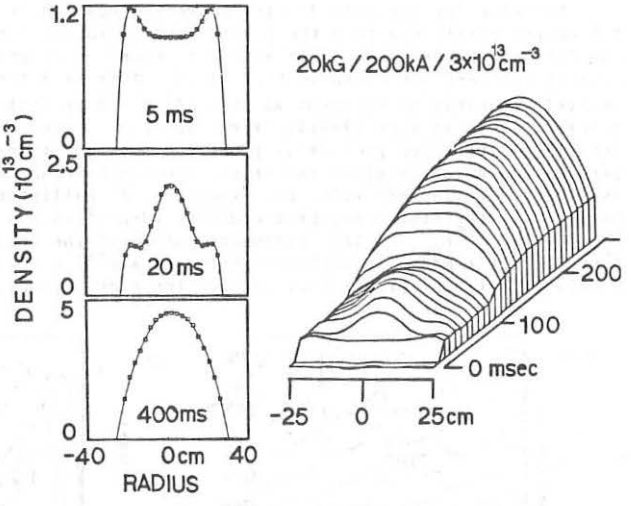

Figure 2. Typical density profile time evolution.

A typical time history of the plasma density profile is shown in Fig. 2. During the start-up phase of the discharge the profile is hollow, eventually becoming centrally peaked. The first 100 ms are usually accompanied by considerable MHD activity (Mirnov oscillations) as the discharge establishes itself. The large gas puff at ≈ 100 ms is used to bring the plasma to the desired density. At this time the profile becomes somewhat flatter due to edge fueling but soon reaches the normal parabola-like peaked profile. By fixing the central chord averaged density and varying I_p and B_T, the profile scaling with q_a is studied. Achieving higher q_a by changing I_p or B_T results in a more narrowly peaked density profile as shown in Fig. 3. At low q_a, the density profile becomes very flat at the center. In addition, for a fixed q_a, increasing the plasma density serves to broaden $n_e(r)$ (see Fig. 3). The associated changes in density scale lengths at high n_e are thought to be responsible for the appearance of an ion feature, possibly related to ion-temperature-gradient-driven instabilities, observed in the density fluctuation spectra.[2]

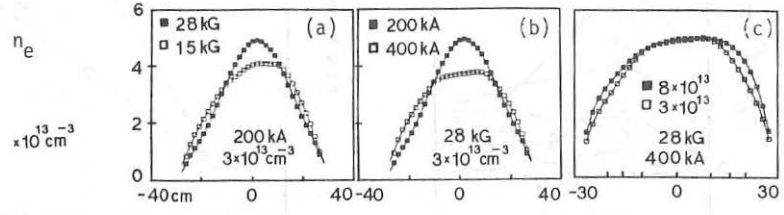

Figure 3. Scaling of $n_e(r)$ with (a) B_T, (b) I_p, and (c) $\bar{n}_e$, where the amplitudes are normalized.

Evidence for sawtooth density pulse propagation is shown in Fig. 4(a), for chords positioned from the plasma edge to inside the mixing radius. The (amplitude) normalized, time-averaged (over ≃ 30 periods), Abel-inverted density sawteeth are shown in Fig. 4(b). Away from the plasma edge, the sawteeth exhibit an exponential fall-off which is indicative of a diffusive process. This is more clearly seen in Fig. 4(c), where the sawtooth density perturbation profile is plotted at various times during the sawtooth period. Immediately after the crash, a broad peak appears at r≃19cm which eventually collapses with no evidence of ballistic propagation. The position of the stationary peak could be identified as the mixing radius; $r_{mix} \simeq (2)^{0.5} r_{q=1}$. The diffusive nature of the density sawteeth is also supported by a measured amplitude fall-off $\propto r^{-4}$, outside the mixing radius. Source effects complicate analysis for the edge region.

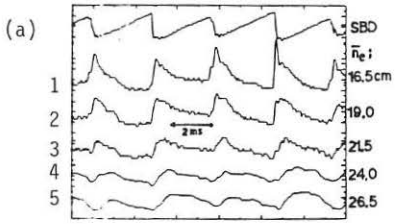

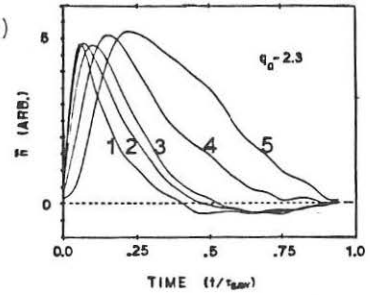

Figure 4. I_p = 300 kA, B_T = 2 T, $\bar{n}_e = 4 \times 10^{13}$ $p_{cm^{-3}}$;
(a) line-averaged density traces;
(b) amplitude-normalized, Abel-inverted sawtooth time history;
(c) profile evolution of sawtooth density perturbation;
(d) peak arrival time of inverted sawtooth versus position.

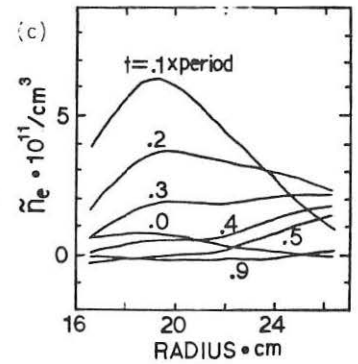

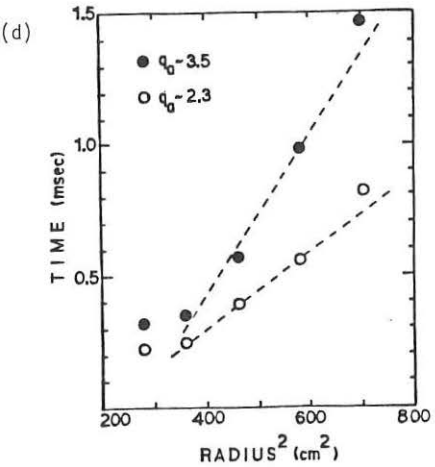

By neglecting the convective term in the continuity equation, which can be justified for a sawtooth density pulse, and staying away from the edge (or source) region, one can arrive at the simple diffusion equation; $\partial n/\partial t = \nabla\cdot[D_e \nabla n_e]$. Then density pulse propagation analysis, analagous to heat pulse propagation analysis, can be performed (without any assumptions about T_e).[3] Standard t_p versus r^2 plots are shown in Fig. 4(d) for two values of q_a. The slope indicates a diffusion coefficient, $D_e \simeq [(8\times\text{slope})^{-1}] \simeq 8$ (4) m^2/s for $q_a = 2.3$ (3.5), which is anomalously large compared to oscillating gas puff measurements. The diffusion coefficient measured from density pulse propagation is approximately equal to the electron thermal diffusivity arrived at from heat pulse analysis; i.e. $D_e = \chi_e$. This observation, together with the strong phase correlation between density and temperature sawteeth, strongly suggest that the heat transport induced by sawteeth is directly coupled with particle transport and is not a purely conductive process as is frequently assumed.

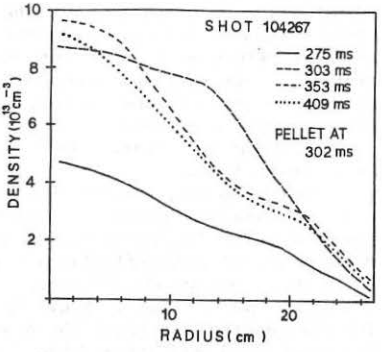

Figure 5. Density profile evolution during pellet injection; $I_p = 250$ kA, $B_T = 2.8$ T.

Recent experiments on TEXT have included pellet injections which introduce dramatic changes to the density profile. Preliminary results showing the time history of the $n_e(r)$-profile with pellets are shown in Fig. 5. Abruptly after injection, a significant increase in the density and profile broadening is observed. Pellet deposition appears to be roughly 10 cm off axis. Eventual relaxation yields a narrow, centrally-peaked profile. For this injection, $\Delta n/n_e \simeq 1$ and sawtooth activity is suppressed suggesting increased confinement. Correlation between the observed changes in $n_e(r)$ and density fluctuations will be the focus of future experiments.

This work is supported by the U.S. Department of Energy under contract No. DE-AC05-78ET53043 through subcontract No. UT-1-24120-52019.

[1]W.A. Peebles, R.L. Savage, Jr., D.L. Brower, S.K. Kim, T. Lehecka, J. Howard, E.J. Doyle, N.C. Luhmann, Jr., to be publ. in Int. J. of Infrared and Millimeter Waves.

[2]D.L. Brower, W.A. Peebles, S.K. Kim, N.C. Luhmann, Jr., W.M. Tang, P.E. Phillips, UCLA Institute of Plasma and Fusion Research, rep. no. PPG-1056, April, 1987. Also see D.L. Brower et al., this meeting.

[3]M. Soler, J.D. Callen, Nucl. Fusion 19,703(1979).

COMPRESSION OF DETACHED PLASMAS IN TFTR

J.D. Strachan, C.E. Bush, H.P. Furth, B. Grek, D.W. Johnson
D. Mansfield, S.S. Medley, D. Mueller, H. Park,
J. Schivell, G. Tait, G. Taylor, K.L. Wong, S. Yoshikawa
Plasma Physics Laboratory, Princeton University
Princeton, NJ 08544 USA

Both free-expansion and detached plasmas separate the plasma boundary from the limiter. The free-expansion plasma [1] occurs when a controlled rapid increase in the vertical magnetic field inwardly translates a plasma in contact with the outer limiter. The increase in vertical field is stopped when the plasma is well-separated from the limiter. The subsequent expansion of the plasma can be used to diagnose convective transport. The detached plasma [2,3] occurs when all the input power is radiated from the plasma periphery. In this case, the minor radius is determined by the energy balance (edge emissivity) [3,4] and the radiating boundary of the plasma can be well-removed from the limiter. The radiated power is a time-resolved measure of the energy accountability and, in particular, it is possible in these plasmas to diagnose the time delay between transients in the input power and the output radiative power. Such time delays are essentially the energy confinement time.

In this paper, results are reported from similar TFTR discharges in which a detached plasma underwent a major radial compression of the free-expansion type. A 2.57 m major radius, 0.50 m minor radius, 4.5 Tesla, 0.60 MA detached plasma was compressed in major radius by 0.25 m in a time of about 20 msec. For these discharges, the bolometer radiation pattern [5], Fig. 1, indicated that the plasma remained detached during and after the compression. The 25% in-out asymmetry in the peak edge radiation (Fig. 1) was not evident in the total power radiated (in versus out) indicating a variation in the width of the radiating layer that was evident both before and after the compression.

During the major radial compression (Fig. 2a) from 2.57 m to 2.32 m ($C = 1.108$), the plasma current was programmed to rise from 0.60 MA to 0.66 MA (Fig. 2b) which is the increase expected from compression theory [1]. The total radiated power (Fig. 2c) nearly doubled as a result of the compression and decayed back to the precompression values in about 150 msec. The peak radiative emissivity (Fig. 2d) also doubled indicating a doubling of the product of the electron density with the impurity density in the radiating layer in contrast to the factor of 1.51 increase expected if both densities were controlled entirely by the compression. The minor radius (as measured by the bolometer array) reduced from 0.50 m to 0.44 m (Fig. 2b) instead of to 0.475 m as expected from compression theory.

In the 150 msec following the compression, the energy radiated is 47 kJ more than the ohmic input (Fig. 2b) while theoretically the energy added to the plasma by the compression was 19 kJ. The principal result of the compression was for the plasma to eventually lose nearly 28 kJ (or 20%) of its precompression energy. The radiative decay duration (an exponential time constant of about 60 msec for a duration of 150 msec)

is an indication of the energy confinement time which by kinetic analysis was 210 msec for the precompression plasma and 140 msec for the steady-state post-compression plasma. Since the current is programmed in TFTR, it is possible that skin currents occur which account for some of the radiation.

During the free-expansion phase, the detached plasma did not expand during the first 150 msec (Fig. 2c) and then expanded slowly at 0.5 m/sec for another 150 msec. In Ref. [1], the free-expansion plasmas expanded at 7 m/sec and the plasma boundary encountered the limiter 50 msec after compression. Overall, the expansion measurements reported here are in sharp contrast to those of Ref. [1], even though the confinement degradation is similar. This result points out the importance of measuring local radiation losses for the interpretation of free-expansion experiments.

The horizontal line-integrated density (Fig. 2a) increased from $n_e\ell = 4.07 \times 10^{15}cm^{-2}$ to $4.75 \times 10^{15}cm^{-2}$ as expected by compression theory [1]. Subsequently, $n_e\ell$ decreased about 5% in the first 150 msec and somewhat faster thereafter. Since the plasma inside the radiating layer did not lose many particles, there was not significant particle

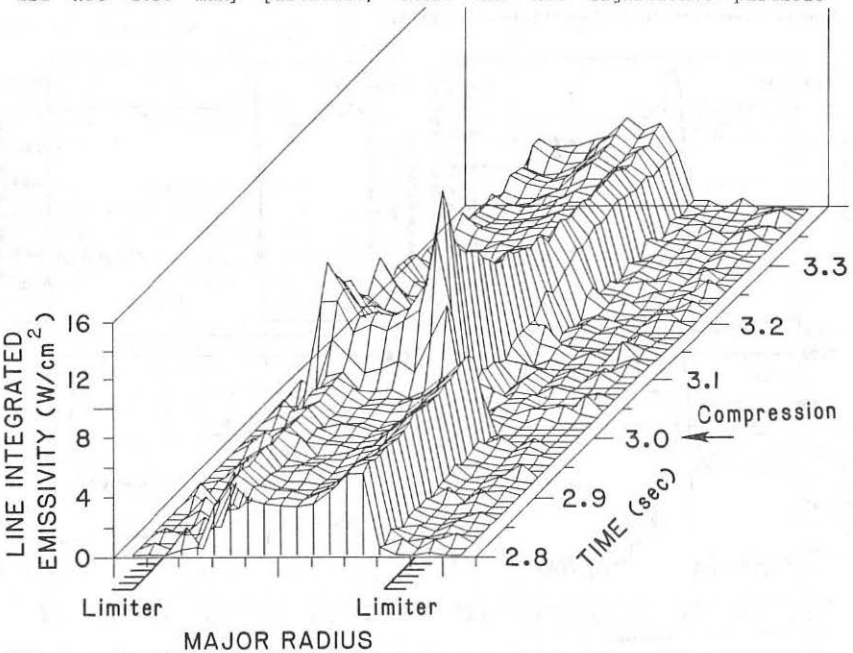

FIG. 1. Isometric display of the bolometer array data. The compression occurred at 3.0 sec. The vertical axis is the chordal radiated power. The hollow radiation pattern is characteristic of the detached plasma and indicates that nearly all the radiation arises from a surface layer.

transport across the cold plasma region. The vertically viewing interferometer channels [6] can resolve the density in the region outside the plasma edge both before and after the compression (Figs. 3a,d). The density of the cold plasma in this region increases by a factor of three. The density just outside the radiating layer (Fig. 3a) evolved in time like the edge emissivity (Fig. 2d). The plasma density inside the radiating layer was large ($> 5 \times 10^{13} cm^{-3}$), poloidally symmetric, and time independent (Figs. 3b,c).

One aim of this experiment was to diagnose the energy confinement time of the compression heating from the time delay of the associated radiative loss. This result was not achieved because the total radiated energy associated with the compression was 2.5 times larger than the compression energy deposited in the plasma. We speculate that the extra energy was extracted from the plasma as is consistent with a reduced kinetic energy content from 131 kJ to 98 kJ following the compression. The zero-order interpretation of the 60 msec time constant of the radiative losses (Fig. 2c) is that transiently there was a 60 msec energy confinement time just following compression.

ACKNOWLEDGMENTS. This work was supported by the U.S. Department of Energy Contract No. DE-AC02-76-CHO-3073.

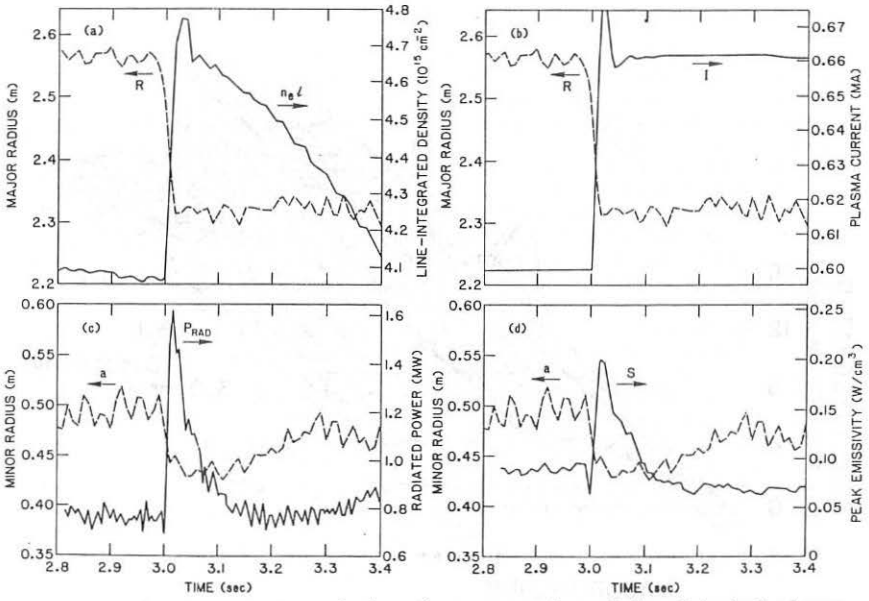

FIG. 2. Plasma parameters during the compression of the detached plasma (a) major radius and horizontal line integrated density, (b) plasma current, (c) total radiated power and minor radius, (d) peak emissivity from the plasma periphery.

REFERENCES

[1] G. Tait et al., Plasma Phys. and Contr. Nucl. Fus. Res., 1984, Vol I, 141 (IAEA, Vienna).

[2] J.D. Strachan et al., Contr. Fus. and Pl. Phys., Proc. 12th EPS Conf., Budapest, Vol. I, (1985) p. 339.

[3] J.D. Strachan et al., J. Nucl. Mat. 145-147, 186 (1987).

[4] S. Yoshikawa and M. Chance, PPPL-2362 (1986).

[5] J. Schivell and C. Bush, Rev. Sci. Instr. 57, 2081 (1986).

[6] D. Mansfield et al., Rev. Sci. Instr. 57, 1999 (1986).

[7] B. Lipschultz, J. Nucl. Mat. 145-147, 15 (1987).

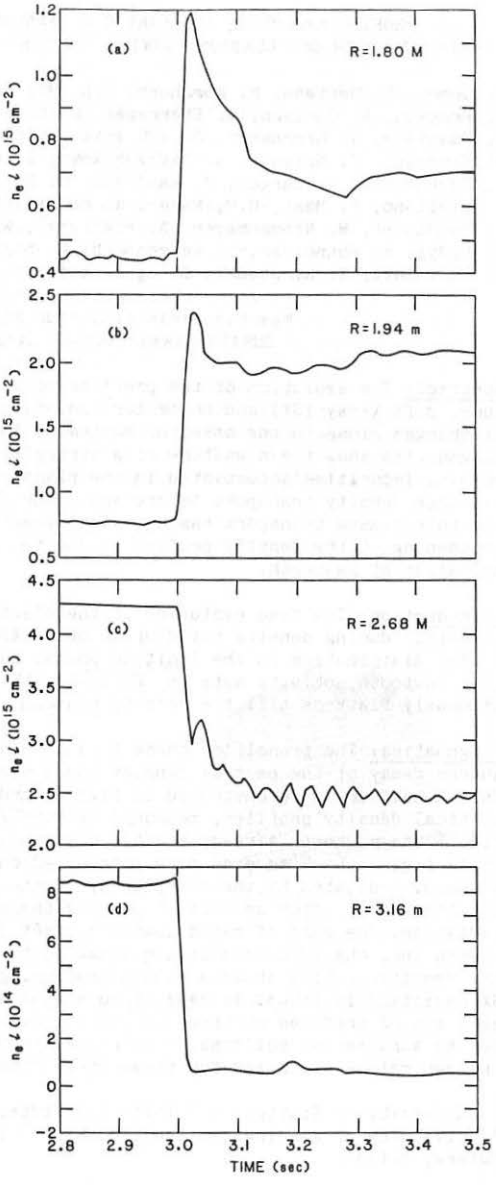

FIG. 3. Vertical line-integrated density. (a) at R = 1.80 m or between the inner wall and plasma radiating boundary both before and after compression, (b) at R = 1.94 m (a = 38 cm) or within the radiating layer of the post-compression plasma, (c) at R = 2.68 m (a = 36 cm) or within the radiating layer of the post-compression plasma, (d) at R = 3.16 m or between the outer limiter and the plasma radiating boundary both before and after compression.

PROFILE EVOLUTION AND PARTICLE TRANSPORT CLOSE TO THE ONSET OF SAWTOOTH OSCILLATIONS DURING THE DENSITY RAMP-UP PHASE IN ASDEX

O. Gehre, V. Mertens, M. Kornherr, E.R. Müller, and G. Becker, H.S. Bosch, H. Brocken, A. Carlson, A. Eberhagen, G. Dodel[1], H.-U. Fahrbach, G. Fussmann, J. Gernhardt, G. v.Gierke, E. Glock, O. Gruber, G. Haas, W. Herrmann, J. Hofmann, A. Izvozchikov[2], E. Holzhauer[1], K. Hübner[3], G. Janeschitz, F. Karger, M. Kaufmann, O. Klüber, K. Lackner, M. Lenoci, G. Lisitano, F. Mast, H.M. Mayer, K. McCormick, D. Meisel, H. Murmann, J. Neuhauser, H. Niedermeyer, A. Pietrzyk[4], W. Poschenrieder, H. Rapp, A. Rudyj, F. Schneider, C. Setzensack, G. Siller, E. Speth, F. Söldner, K. Steinmetz, K.-H. Steuer, S. Ugniewski[5], O. Vollmer, F. Wagner, D. Zasche

Max-Planck-Institut für Plasmaphysik
EURATOM Association, Garching, FRG

Abstract: The evolution of the profiles of electron density and temperature, soft X-ray (SX) and bolometer radiation is investigated in ASDEX discharges close to the onset of sawteeth. For the transition phase these diagnostics show the signature of a strong sawtooth-like collapse, which removes impurities accumulated in the plasma center. A comparison of electron density transport before and after the transition indicates that the bulk plasma transport has not significantly changed and the observed broadening of the density profile is due to the additional relaxation mechanism of sawteeth.

Introduction: The time evolution of the electron density profile is studied in detail during density build-up in ohmic ASDEX divertor discharges. After a flat distribution in the ignition phase, the profile continues to peak till sawtooth activity sets in. Following this event, the profile continuously flattens till the density plateau is reached.

Diagnostics: The transition phase to a sawteething discharge often shows a sudden decay of the central density and a strong broadening of the profile. This behaviour is demonstrated in figs. 1 and 2, which show 3-D-plots of vertical density profiles, measured by HCN-laser interferometry /1/. In fig. 1 the sawteeth already start during the rising phase of the density, while fig. 2 shows an even more pronounced onset at the beginning of the plateau, indicated by the sharp decay of the center of the distribution. A similar decay, after an initial peaking phase, is also observed in the SX radiation. The case of rapid sawtooth onset is confronted with a less common one, characterized by a gradual sawtooth development during which the density profile shows a smooth braodening and no central peaking of the SX radiation is found. In case of no sawtooth development at all, the density and SX profiles continue to peak, generally terminated by a disruption due to a radiation collapse. A comparison of the temporal development of the central SX radiation for these three cases is shown in fig. 3.

[1] University of Stuttgart; [2] Ioffe Institute; [3] University of Heidelberg; [4] University of Washington, Seattle, USA; [5] Inst. for Nuclear Research, Swierk, Poland

The density profiles reached shortly before a distinct transition to the sawtooth phase are characterized by a nearly constant shape, independent of plasma current I_p, toroidal field B_t, dI_p/dt and safety factor q(a). For deuterium plasmas more peaked profiles are found as compared to hydrogen, similar to an investigation made for the density plateau phase of sawteething ASDEX discharges /2/. A faster density rise normally leads to a more pronounced transition at broader profiles.

A 3-D-plot of radial SX profiles measured during the time window of the transition is shown in fig. 4. The strong decay is only seen on channels corresponding to the plasma core within the radius of the q=1 surface. This radius is identified from the inversion point of SX and ECE, when sawteeth have started, and stays constant within measurement resolution. The picture also shows that the transition does not always occur in a single decay but may include a cascade of steps. An Abel inversion of SX channels immediately before the decay gives central emission values, which are at least one order of magnitude higher than bremsstrahlung. Shortly before the transition bolometer profiles show the build-up of a central peak (fig. 5), which vanishes with the onset of sawteeth. The electron temperature profile measured by quasi-stationary YAG scattering before and after the transition is presented in fig. 6. It indicates a pronounced flattening of the central region during the event.

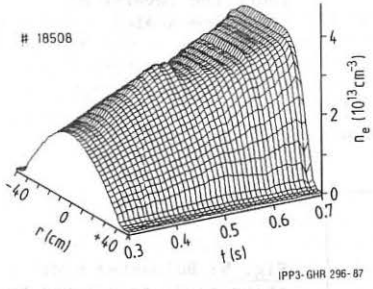

Fig. 1: Time evolution of the electron density profile close to the onset of sawtooth oscillations, transition to the sawtooth regime during the density build-up phase.

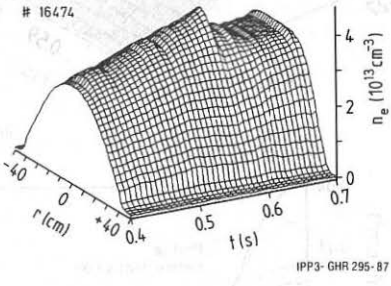

Fig. 2: As in fig. 1, but with more pronounced transition at the beginning of the density plateau.

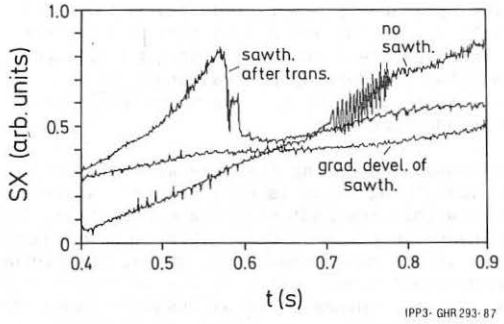

Fig. 3: Temporal development of the central SX radiation for a rapid sawtooth onset as compared to the cases of gradual sawtooth development and no sawteeth.

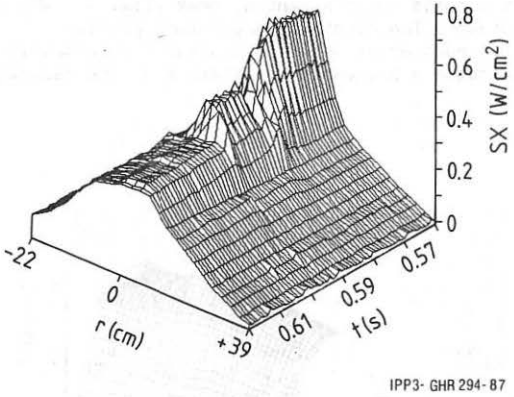

Fig. 4: SX radiation profiles during the transition to the sawtooth regime, showing a strong decay in the plasma core region.
(note the reverse of the time scale)

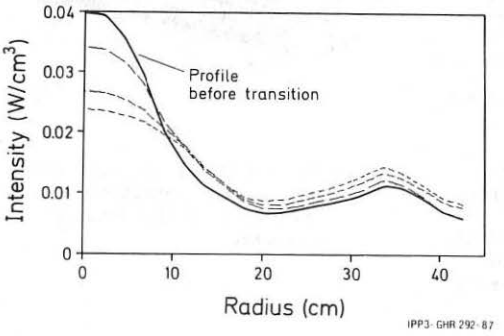

Fig. 5: Bolometer radiation profiles showing the build-up of a central peak before the transition. The solid curve gives the profile reached immediately before the onset of sawteeth.

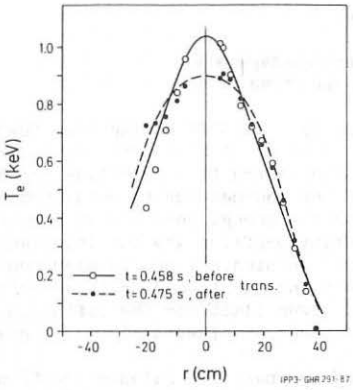

Fig. 6: Electron temperature profiles measured shortly before and after the transition to a sawteething discharge, indicating a pronounced flattening of the central region.

In summary, the transition to the sawtooth regime shows the signature of a strong sawtooth-like collapse, removing metal impurities from the center of the discharge, which have accumulated there during density build-up. No m=1 precursors are found, however, and the strong MHD activity seen during this phase, which was not studied in detail, does not allow to exclude a more complicated instability with higher mode numbers. The connection to impurities is supported by experiments, where krypton pulses were injected into the plasma. With increasing krypton content, indicated by higher initial levels of central SX radiation, the onset of sawteeth is shifted to later times and MHD activity during the transition increases. At too high impurity content no sawteeth develop and the discharge disrupts.

Transport: Electron density transport has been investigated shortly before and after the collapse. Using the continuity equation in cylindrical geometry, fluxes have been calculated neglecting sources. These fluxes in the plasma core region can be interpreted in terms of a model of electron transport consisting of diffusive and convective driving terms:

$$\Gamma(r) = -D(r)\cdot n'(r) - n(r)\cdot v(r).$$

The fluxes analyzed in the phase without sawteeth and, after the transition, averaging between sawtooth crashes, could be described by the same set of values for D and v. This indicates that the bulk plasma transport has not significantly changed after sawtooth onset. The observed broadening of the density profile is attributed to the started sawtooth activity, balancing the counteracting inward fluxes.

References:

/1/ Gehre, O., Course and Workshop on "Basic and Advanced Fusion Plasma Diagnostic Techniques", Varenna 1986, to be published.

/2/ Gehre, O., Becker, G., Eberhagen, A., and ASDEX team, Proc. 13th Europ. Conf. on Controlled Fusion and Plasma Heating, Schliersee 1986, EPS Europ. Conf. Abstr. 10 C, part I, p. 220-223.

PARTICLE BALANCE IN NEUTRAL-BEAM-HEATED TOKAMAK PLASMAS

G. Becker

Max-Planck-Institut für Plasmaphysik,
EURATOM Association, Garching, FRG

ABSTRACT: The particle balance in H discharges in ASDEX during the steady-state ohmic and H phases is investigated by means of transport simulations. Profiles of particle sources and outward and inward flux densities are computed. The magnitude and radial extent of the sources due to cold atoms and beam fuelling and the corresponding convective energy loss are determined. It is further shown that the measured density profiles are not invariant to changes in particle source and confinement. Constraints on the electron heat diffusivity, the diffusion coefficient and the inward drift velocity are derived. An expression representing a lower limit for the diffusion coefficient in the presence of particle sources and inward fluxes is given.

Introduction: From the steady-state energy and particle balance equations with neutral injection it is possible to derive constraints on the electron heat diffusivity χ_e, the diffusion coefficient D and the inward drift velocity v_{in} /1/. Such relations are used to develop scaling laws and are applied in transport simulations. One prerequisite for such studies is to know the radial extent of the particle and energy sources due to neutral injection and the corresponding convective energy losses. The paper deals with the particle sources, particle confinement and resulting constraints for transport coefficients in injection-heated plasmas. The topical question of density profile invariance with changing particle sources is studied. Results from transport simulations with modified versions of the BALDUR code /2, 3/ are used. The neutral-gas transport is calculated by a Monte Carlo code. The particle source due to neutral injection is treated by following the fast neutrals by means of a Monte Carlo code.

Steady-state particle balance: Several discharges exhibiting long plateaus of current, density and beta were analysed. The example shown in Fig. 1 is an H discharge with I_p = 380 kA, $\bar{n}_e = 3.5\times10^{13}$ cm^{-3}, B_t = 2.15 T and P_{NI} = 3.45 MW ($H^0 \rightarrow D^+$, E_0 = 40 keV). The computations are compared with measured density and electron temperature profiles and with $\beta_{p_\perp}$ from the diamagnetic loop. Good agreement is obtained by applying the coefficients /4, 5/

$$\chi_e^{OH}(r) = 1.6\times10^{16} A_i^{-1/2} B_t n_e(r)^{-1} T_e(r)^{-1} q(r)^{-1} \text{ cm}^2 \text{ s}^{-1} \quad (1)$$

$$D^{OH}(r) = 0.4 \ \chi_e^{OH}(r) \quad (2)$$

in the ohmic phase and

$$\chi_e^{H}(r) = 2.6\times10^{6} \ r_n(r)^{-1} q_a B_t(R_o)^{-1} \text{ cm}^2 \text{ s}^{-1} \quad (3)$$

$$D^{H}(r) = 0.4 \ \chi_e^{H}(r) \quad (4)$$

in the H phase. The inward drift velocity is given by $v_{in}(r) = 0.5\ D(r)\ r_{Te}(r)^{-1}$ cm s^{-1}, and the ion heat diffusivity used is three times the neoclassical values according to Chang and Hinton. The ion mass number is

denoted by A_i. The toroidal magnetic field B_t is in kG, n_e is in cm^{-3}, T_e is in keV, q_a is the cylindrical q at the plasma radius a=40 cm and R_o = 167 cm is the major radius of the plasma. The quantities $r_n = -n_e/(\partial n_e/\partial r)$ and $r_{Te} = -T_e/(\partial T_e/\partial r)$ are in cm.
Under steady-state conditions the particle balance with anomalous outward diffusion and anomalous inward drift reads

$$-D \frac{dn_e}{dr} - v_{in} n_e = \Gamma_i + \Gamma_b \qquad (5)$$

where Γ_i and Γ_b are the flux densities due to the ionisation of cold atoms and due to the beam fuelling, respectively. The particle balance in the ohmic phase is shown in Fig. 2. Since the plasma is impermeable to cold neutrals ($\lambda_o \ll a$ with mean free path λ_o), the interior of the plasma is almost source-free. This gives rise to nearly equal outward and inward fluxes, the typical difference being only 10 % of each of these fluxes. Obviously, the main contribution due to Γ_i occurs outside r≈0.8 a. The detailed Γ_i profile is given in Fig. 3.
Results from transport analysis of the H phase are presented in Fig. 4. It should be mentioned that almost identical results are obtained in L discharges. In contrast to the ohmic phase, the outward flux clearly exceeds the inward flux. For $r \lesssim 0.7$ a the dominant source is due to beam fuelling, while Γ_i still prevails in the edge region. As can be seen, at r= a/2 one obtains $v_{in}\, n_e \approx \Gamma_b \approx -0.5\, D\, dn_e/dr$. Figure 5 represents a detailed plot of $\Gamma_b(r)$. Comparison with the energy flux density $P_b(r)$ shows that the average energy per absorbed particle $\bar{E} = P_b(r)/\Gamma_b(r)$ = 23.8 keV only varies by ±0.6 keV over the whole cross-section, so that to very good approximation P_b can be set proportional to Γ_b everywhere.
In ohmic plasmas the convective power loss is only significant in the edge region, where Γ_i is large. With neutral injection, however, high convective losses $P_c \approx 2.5\,(T_e+T_i)\,\Gamma_b$ also occur in the plasma bulk owing to the large particle source and high temperatures. The ratio $P_c/P_b \approx 2.5\,(T_e+T_i)/\bar{E}$ amounts to about 30 % at r=2a/3. With increasing heating power the fraction of P_b lost by convection grows with the temperature sum to unacceptably high values, unless E_o and $\bar{E}$ are correspondingly raised.
The response of the density profile shape to changes in the particle source distribution is demonstrated in Fig. 6. During the ohmic phase the measured density profile is parabolic, while it is more triangle-shaped in the H phase. Evidently, the density profile shape is not invariant to changes in particle source and confinement.

Constraints on transport coefficients with injection heating: General expressions for transport coefficients are derived from approximate particle and energy balance equations. Using $\Gamma_i \ll \Gamma_b$ for $r \lesssim 0.7$ a in Eq. (5) yields

$$\frac{v_{in}}{D} \approx r_n^{-1} - \frac{\Gamma_b}{n_e D} \qquad (6)$$

Unlike in the source-free case ($v_{in}/D = r_n^{-1}$), the ratio v_{in}/D is here determined by the beam-fuelling profile as well, which has to be taken from code calculations. To avoid this disadvantage, we eliminate Γ_b with the help of the energy balance.

For $r \lesssim 0.7$ a the losses due to charge exchange and radiation are negligibly small. At injection powers much higher than the ohmic input and negligible ion heat conduction one obtains

$$q_e(r) \approx P_b(r) - P_c(r) \qquad (7)$$

where q_e is the flux density due to electron heat conduction. With $P_b(r) = \bar{E}\Gamma_b(r)$ and $P_c \approx 2.5\,(T_e+T_i)\,\Gamma_b$ it follows that

$$\Gamma_b \approx -[\bar{E} - 2.5(T_e+T_i)]^{-1}\, n_e \chi_e \frac{dT_e}{dr} \qquad (8)$$

Replacing the particle source in Eq. (6) yields

$$\frac{v_{in}}{D} \approx r_n^{-1} + [\bar{E}-2.5(T_e + T_i)]^{-1} \frac{\chi_e}{D} \frac{dT_e}{dr} \qquad (9)$$

This relation holds under stationary conditions for $P_{OH} \ll P_{NI}$ and $\Gamma_i \ll \Gamma_b$. An even simpler formula is obtained by setting χ_e/D equal to a constant. It was shown above that $\bar{E}$ is a constant which is usually large compared with the temperature sum. The ratio v_{in}/D can be determined from measured density and temperature profiles without knowing the beam-fuelling source. Using, for instance, the approximations $n_e(r) = n_e(0)\,(1-r/a_1)$ and $T_e(r) = T_e(0)\,(1-r/a_2)$ yields $v_{in}/D \approx (a_1-r)^{-1}$ - const, i.e. the increase of v_{in} with radius is much stronger than that of D.

The weak radial dependence of $P_b = \bar{E}\Gamma_b$ in the range $0.25 \leq r/a \leq 1$ (see Fig. 5) results in $q_e = -n_e \chi_e dT_e/dr \approx$ const (see Eq. (7)). With the above T_e profile one thus obtains $\kappa_e = n_e\chi_e \approx$ const and $D(r) \sim \chi_e(r) \sim n_e(r)^{-1}$. According to Eq. (5) the diffusion coefficient reads $D = -(\Gamma_i+\Gamma_b+v_{in}n_e)/(dn_e/dr)$. In the case $v_{in}=0$ one obtains the expression

$$D(r) = -\frac{\Gamma_i(r) + \Gamma_b(r)}{\frac{dn_e}{dr}(r)} \qquad (10)$$

which represents a lower limit, since for given particle sources and density profile a finite inward flux always corresponds to a higher diffusion coefficient. The minimum D can also be given when the anomalous inward flux is unknown. Equation (10) is especially useful for predictive code simulations, because it yields the minimum D values which are able to produce the measured density gradients.

References

/1/ Becker, G., in Controlled Fusion and Plasma Heating (Proc. 13th Europ. Conf. Schliersee, 1986), Part I (1986) 224.

/2/ Post, D.E., Singer, C.E., McKenney, A.M, BALDUR: A One-dimensional Plasma Transport Code, PPPL Transport Group, TFTR Physics Group, Rep. 33 (1981).

/3/ Becker, G., ASDEX Team, Neutral Injection Team, Analysis of Local Transport in Neutral-beam-heated L and H Plasmas of ASDEX, Max-Planck-Institut für Plasmaphysik, Garching, Rep. IPP III/98 (1984).

/4/ Becker, G., Nucl. Fusion 27 (1987) 11.

/5/ Becker, G., Nucl. Fusion 24 (1984) 1364.

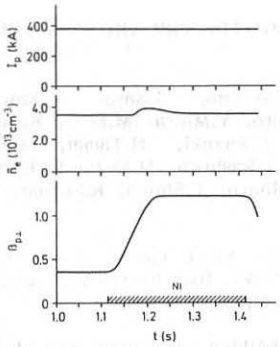

Fig. 1: Time evolution of plasma current, line-averaged density and poloidal beta in an H discharge.

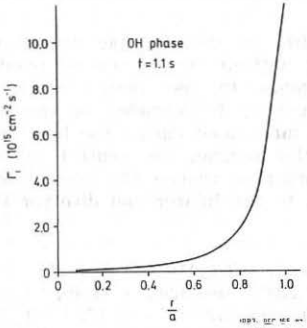

Fig. 3: Γ_i profile in the ohmic phase.

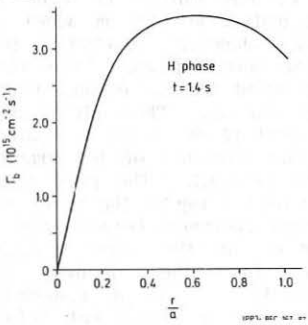

Fig. 5: Γ_b profile in the H phase.

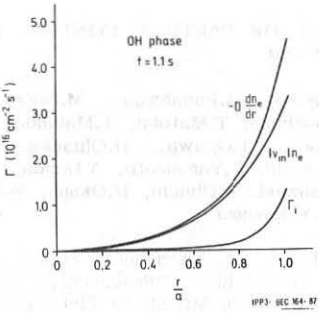

Fig. 2: Particle balance in the steady-state ohmic phase.

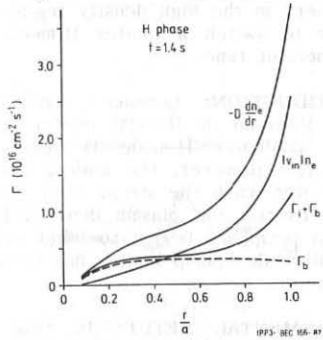

Fig. 4: Particle balance in the steady-state H phase.

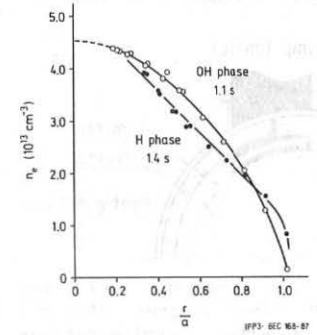

Fig. 6: Density profiles with ohmic heating and neutral-beam injection.

EFFECT OF PARTICLE CONTROL BY A PUMP LIMITER ON CONFINEMENT IN JFT-2M

S.Sengoku, A.Funahashi, M.Hasegawa,* K.Hoshino, S.Kasai, T.Kawakami, H.Kawashima, T.Matoba, T.Matsuda, H.Matsumoto, Y.Miura, M.Mori, K.Odajima, H.Ogawa, T.Ogawa, H.Ohtsuka, T.Shoji, N.Suzuki, H.Tamai, Y.Uesugi, T.Yamauchi, T.Yamamoto, A.Honda, I.Ishibori, Y.Kashiwa, M.Kazawa, K.Kikuchi, Y.Matsuzaki, K.Ohuchi, H.Okano, W.Sato, T.Shibuya, T.Shiina, K.Suzuki, T.Tani and K.Yokoyama

Department of Thermonuclear Fusion Research, Naka Fusion Research Est., Japan Atomic Energy Research Institute,Tokai, Naka, Ibaraki 319-11, Japan
*On leave from Mitsubishi Electric Co., Tokyo, Japan

A pump limiter is shown to reduce the buildup of neutral gas at plasma periphery in the high density regime resulting to minimize the threshold heating power to switch a limiter H-mode and to reduce the degradation of energy confinement time.

INTRODUCTION: Enhanced confinement with an H-mode like transition has been observed in JFT-2M limiter discharges without strong neutral buildup./1/ Such a limiter H-mode is very advantageous to the design of a fusion reactor. However, the energy confinement time is degraded or the H-mode terminates when the strong cold gas fuel is introduced during the beam heating phase to rise the plasma density./1/ In this regime, the neutral gas at the plasma periphery begins to build up. In order to reduce the neutral buildup, a small-scale pump limiter has been applied to the limiter and divertor H-mode discharges.

EXPERIMENTAL SETUP: In this experiment, Ti-gettered JFT-2M tokamak is operated with D-shaped limiter (R=1.28m, a=0.32m, κ=1.46, I_p=320kA, B_t=1.24T) or single-null divertor (R=1.29m, a=0.27m, κ=1.47, I_p=230kA, B_t=1.26T) configurations (Fig.1). Working gas is deuterium. Used pump limiter PL has throats in both electron and ion drift side (3.5 cm wide) and an expansion chamber (V =78 ℓ) followed by Zr/Al getter pump. The effective pumping speed at the expansion chamber is about 800 ℓ/s. The molybdenum pump limiter head (2 cm thick) is coated with TiC. The direction of ion grad**B** drift is upside in Fig.1. The pump limiter is installed on the top of the torous because the enough clearance between the plasma and limiter at the outer midplane is required for the limiter H-mode transition./1/ As a standard case gas-puff valve is closed just before the hydrogen neutral-beam-injection (NBI). /2/

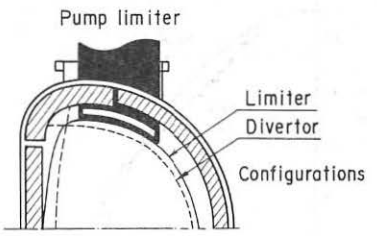

FIG.1 Cross-section of the JFT-2M. The limiter (Δ=0 mm) and divertor configurations at t=0.8 s are shown. Hatched areas are for graphite guard limiter and divertor plate.

EFFECT OF THE PUMP LIMITER ON CONFINEMENT: Figure 2 shows the time evolutions of typical parameters for the limiter discharges of medium density (line averaged electron density of the target plasma $\bar{n}_e$=3.5x10^{13} cm^{-3} at t=0.7 s) heated by balanced NBI (injected power P_{NBI} of 1.2 MW) with and without the pump limiter (solid and dashed lines, respectively). The distance between the magnetic surface intersecting the inner limiter and the pump limiter head Δ is 3 mm. The stored energy W_s increases substantially at the H-mode transition and then decreases in time corresponding to the beginning of the increase in radaiton loss power in both the cases (Fig.2 a). The evident charges with the pump limiter in the H-mode phase are the lower recycling light near the inner wall, the faster density rise and the slower density profile relaxation following quick broadening (Fig.2 b). The recycling light near the neutralizer plates of pump limiter is also reduced in this phase (Fig.2 c). The edge electron temperature inferred from the electron cyclotron emissivity (Fig.2 d) is slightly higher with the pump limiter.

In the Ohmic heating (OH) phase of the limiter discharges, the global energy confinement time τ_E* is improved by the pump limiter at around the critical density above which the gas pressure begins to build up/2/ ($\bar{n}_e$=(3-4)x10^{13} cm^{-3} in Fig.3 a). In the H-mode phase with pump limiter, where the particle intake to the pump limiter is drastically decreased (Fig.2 c), τ_E* is comparable to the value without pump limiter. However, the pump limiter allows continuous gas feed during NBI phase and exhibits the highest $n\tau$ value (a data set of open squares over closed squares in Fig.3 a). Without the pump limiter, the attainable $n\tau$ with the continuous gas feed is lower than that of the standard gas-puff case.

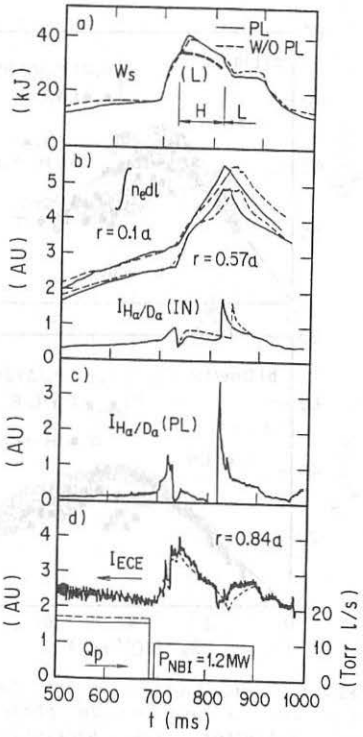

FIG.2 Typical time evolutions of a)plasma stored energy W_s obtained by poloidal field analysis, b)vertical line-integrated electron density and recycling light near the inner wall $I_{H\alpha/D\alpha}$ (IN), c)$I_{H\alpha/D\alpha}$ near the neutralizer plates of the pump limiter (PL) and d)electron cyclotron emissivity I_{ECE} proportional to the edge electron temperature for the limiter discharges with (——) and without (----) pump limiter. [(L) for W_s of an L-mode discharge, H and L for the H- and L-mode phases, Q_p for the gas-puff program, Δ=3 mm]

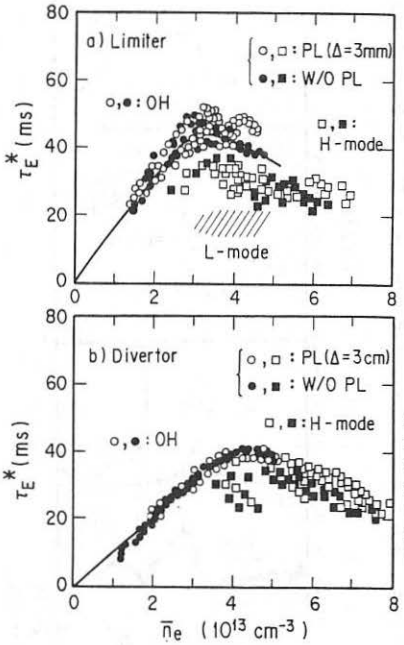

FIG.3 Comparison of τ_E^* for the OH, L- and H-mode phases of a)limiter and b)divertor discharges with and without pump limiter. (-0.1 MW<dW_s/dt<0.2 MW)

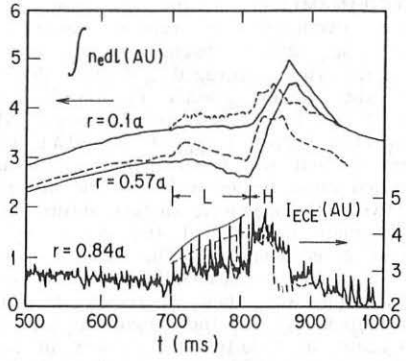

FIG.4 Time evolutions of the line integrated electron densities and the edge I_{ECE} of the limiter discharges with (——) and without (----) pump limiter with P_{NBI} of 0.59 MW and 0.68 MW, repectively ($\bar{n}_e$= 3.9x10^{13} cm^{-3} at t=0.7 s).

In the divertor H-mode discharges, we also observe the similar effect of the pump limiter with 0.8 MW co-injection while Δ is about 3 cm from the separatrix surface (mechanical limit) as shown in Fig.3 b.

EFFECT OF THE PUMP LIMITER ON NEUTRAL BUILDUP AND THRESHOLD POWER: Figure 4 shows the line integrated electron densities and the edge I_{ECE} comparing the cases with and without pump limiter with P_{NBI} close to the threshold heating power to switch the H-mode P_{th} for the limiter discharges (the target plasma density $\bar{n}_e$=3.9x10^{13}cm^{-3} where the neutral gas builds up without pump limiter and does not with pump limiter). The pump limiter suppresses the increase of the density during the L-mode phase as shown in Fig.4 and, therefore, allows higher edge temperature at the pre-transition sawtooth peak, which triggers the H-mode, with decreased heating power by about 100kW. This can be related to the reduction of neutral buildup by the pump limiter.

The neutral buildup at the OH phase increases P_{th} as clearly shown in the without pump limiter case (Fig.5 a and d). By applying the pump limiter, the non-buildup region is extended as shown by the ratio of the pressure with to without pump limiter (hatched region in Fig.5 b). In this

extended region, the electron temperature at the pre-transition sawtooth peak is higher with pump limiter even though with lower P_{NBI} (Fig.5 c). The P_{th} with pump limiter is well decreased down to the value of non-buildup phase without pump limiter (Fig.5 d). Further access of the pump limiter to the plasma gives further extension of the non-buildup region (dashed line in Fig.5 b). The H-mode still appears with Δ = -12 mm and P_{NBI}= 1 MW.

CONCLUSIONS: The effects of the small-scale pump limiter on τ_E* or $n\tau$ are not so drastic. It is, however, clearly shown that the particle control by a pump limiter reduces the neutral gas buildup resulting to the reduction of the required heating power for the limiter H-mode transition as well as to the increase of $n\tau$ values of the limiter and divertor H-mode discharges. This can expand the operational regime of the H-mode. We observe the limiter H-mode transition even if Δ is sufficiently negative. This means that the pump limiter is compatible to the H-mode discharges. The results obtained here give a guide line to the future large-scale pump limiter experiments.

ACKNOWLEDGEMENTS: The authors are grateful to Drs. M. Tanaka, K. Tomabechi and S. Mori for their continuous encouragements.

/1/ S. Sengoku et al., "Regime of improved confinement in neutral-beam-heated limiter discharges of a tokamak", submitted to Phys. Rev. Letters.
/2/ S. Sengoku and the JFT-2M team, J. Nucl. Mater., **145-147** (1987) 556.

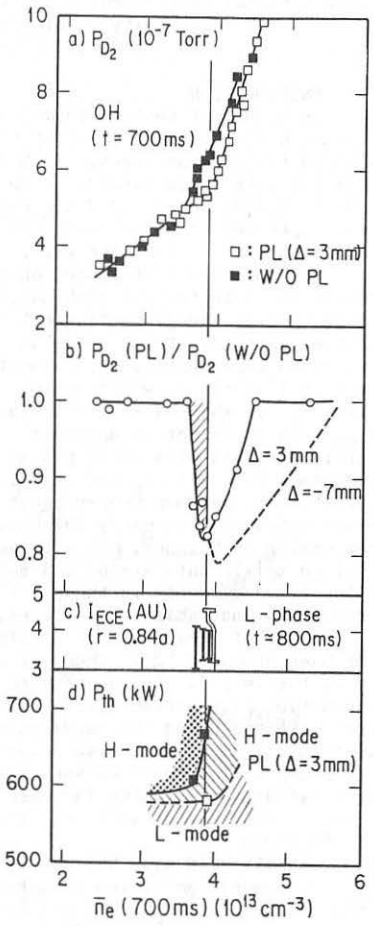

FIG.5 a)Peripheral deuterium neutral-pressure P_{D_2} just before NBI (t=0.7 s) measured by a magnetically shielded quadrupole mass spectrum analyzer,/2/ b)the ratio of P_{D_2} with to without pump limiter, c)I_{ECE} at the plasma edge (a bar corresponds to the top and bottom of the sawtooth oscilation at the pre-transition with the same power as in Fig.4) and d)threshold power P_{th} plotted against $\bar{n}_e$ of the taget plasma for the limiter discharges. Open and closed symbols correspond to the cases with and without pump limiter.

CONFINEMENT ANALYSIS OF AUXILIARY HEATED JET DISCHARGES

K Thomsen+, V Bhatnagar++, J D Callen*, J P Christiansen, J G Cordey, M Evrard++, D Gambier**, N Gottardi, T Hellsten, D G Muir, P J Lomas, P Smeulders, P R Thomas

JET Joint Undertaking, Abingdon, Oxfordshire, OX14 3EA, UK
+Risø National Laboratory, Denmark, ++LPP-ERM/KMS, 1040 Brussels, Belgium,
*University of Wisconsin, Madison, WI 53706, USA,
**CEA, Fontenay-aux-Roses, France

1. INTRODUCTION

Up to 9MW of neutral beam heating (NBI) and up to 7MW of ion cyclotron resonance heating (ICRH) and up to 16MW of combined heating have been applied to JET discharges. In NBI experiments, both H and D beams have been injected into D discharges. ICRH heating scenarios with H or ^{3}He minority ions in D discharges and H minority ions in ^{3}He discharges have been tried. This paper reports experiments in which the plasma was limited by an outboard limiter or the inner wall.

The dependence of stored energy W on total input power P is approximately the same for all combinations of heating methods (ie, the degradation of the global energy confinement time τ_ε is approximately independent of heating method). Power scans at constant plasma current I_p show that the best data representation is a scaling with W increasing linearly with P (offset linear), in which the slope $\Delta W/\Delta P$ is the incremental confinement time, τ_{inc}. Whereas W clearly increases with I_p for fixed P, the scaling of τ_{inc} with I_p is not as apparent. This is mainly due to the lack of sufficient data with fixed plasma parameters. The plasma density n increases both with I_p and additional heating power, which makes it difficult to perform proper power scans at fixed density. A scaling law for W was obtained from early NBI results at I_p = 1, 2 and 3MA using standard regression techniques. This showed $\tau_{inc}[s] = 0.047\ I_p\ [MA]$ [1], which when applied to all data exhibits a substantial scatter. The scatter in W versus P for fixed currents is thought to be due to differences in the power deposition and radiation profiles, and in density.

A way of including these effects in analyses of confinement properties has been proposed [2]. There is strong evidence that the energy transport is diffusive [3]. By assuming that the heat flux is given generally by heat conduction plus convection in the form $\underline{q} = -n\chi\nabla T + \underline{q}_{conv}$, the heating effectiveness η and the ideal incremental confinement time τ_χ have been derived. Thus an effective power input, $P_{eff} = \eta P$, can be calculated from power deposition profiles and radiation profiles for a certain form of the heat diffusivity χ. The incremental confinement time can be written as $\tau_{inc} = \eta\tau_\chi$. Results from analyses utilising this method will be discussed.

2. DENSITY SCAN WITH NBI

A closer examination of data scatter from NBI heating experiments (D° into D^+) at fixed I_p = 3MA and B_T = 3.4T reveals that τ_{inc} is decreasing with increasing density. At low density ($n < 1.7 \times 10^{19} m^{-3}$) τ_{inc} = 0.28s, while at high density ($n > 1.7 \times 10^{19} m^{-3}$) τ_{inc} = 0.14s as shown in Fig 1. We have analysed these data in two steps with a constant n and χ model.

profile effects using a constant χ model and are shown in Fig 4. A regression analysis yields τ_χ[s] = (0.12 ± 0.03) I_p [MA]. Even though the change from total input power P to P_{eff} increases the slopes of the lines substantially, there is still a non-zero offset, (ie, $W = \tau_\chi P_{eff} + W(0)$ with $W(0) > 0$).

6. CONCLUSION

Analysis has shown that the observed dependences of incremental confinement time $\tau_{inc} = \eta\tau_\chi$ with density and resonance position are mainly due to power deposition profile effects on the heating effectiveness η. The data scatter is greatly reduced when corrected for radiation losses. After correction for both radiation and heating profile effects ICRH results show an improvement in τ_χ with plasma current. However, this is still not as strong as the NBI and combined heating data which show τ_{inc}, $\tau_\chi \propto I_p$. Future higher power and current experiments should clarify this dichotomy.

7. REFERENCES

[1] Cordey J G et al, IAEA-CN-47/A-II-3, Plasma Physics and Controlled Fusion, Kyoto, Japan, 1986.

[2] Callen J D, Christiansen J P, Cordey J G, Thomas P R, Thomsen K, JET Preprint P(87)10, submitted to Nuclear Fusion.

[3] Tubbing B J D, Lopez-Cardozo N J, JET Report R(87)01.

[4] Jacquinot J J et al, IAEA-CN-47/F-I-1, Plasma Physics and Controlled Fusion, Kyoto, Japan, 1986.

[5] Bhatnagar V P et al, this Conference.

Fig 1: W (magnetic) vs P from NBI experiments (3MA, 3.4T) with corrections due to heating profile effects (B) and radiation losses (A) indicated.

Fig 2: τ_{inc} (diamagnetic) vs normalised plasma radius from On/Off axis ICRH experiments ($(H)^3He$, 2MA) with $\eta = \tau_\chi(1-\rho^2)^2$ shown by the solid line.

Fig 3: W (kinetic) vs P with and without corrections from ICRH current scans ($(^3He)D$, 5MA, 3.4T and $(H)^3He$, 1MA, 2.2T).

Fig 4: a) W (magnetic) vs P from current scans with combined heating. The symbols are defined in b) where W (magnetic) vs P corrected for heating profile effects are shown for the same data set.

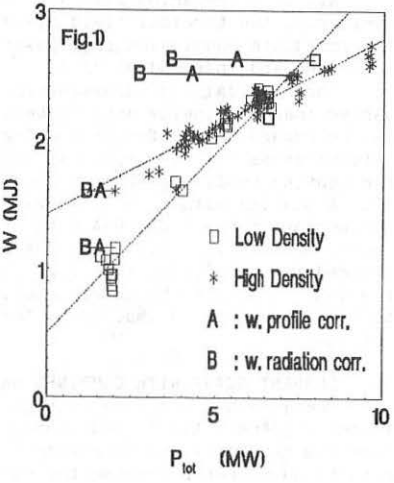

The penetration depth of the neutral beams decreases with increasing density, which means that the power deposition profiles are less peaked than the ohmic heating profile at low densities while they are quite flat at high densities. The correction due to different heating effectiveness η of the differing deposition profiles are indicated by the letter B in Fig 1. The remaining difference in slopes disappears when the effective power lost by radiation is also taken into account (letter A in Fig 1). The offset W(o) is different for low and high density (0.5MJ and 0.9MJ) while τ_χ is independent of density (0.57s).

3. ON/OFF-AXIS HEATING WITH ICRH

Narrow power deposition profiles ($\Delta r \leq a/5$) have been observed in experiments with ICRH heating of minority ions [4]. By modelling the heating profile with a δ-function located at the minority ion cyclotron resonance position, information about the heating effectiveness η can be obtained from experiments in which the resonance position was varied. The variation of τ_{inc} with the heating resonance position r_h is shown in Fig 2, for ^{3}He-plasmas with H minority ions at I_p = 2MA (using different frequencies 28.4 -37.2MHz and toroidal fields 1.7 - 2.35T).

An attractive feature of these experiments was the low level of radiation experienced in ^{3}He-discharges, in which corrections for radiation losses could be ignored. The ICRH heating effectiveness depends on r_h. To explain the variation of τ_{inc} shown in Fig 2, it is necessary to introduce a χ that increases with radius. With $\chi = \chi_o/(1 - r_h^2/a^2)$, the model gives $\eta(r_h) = (1 - r_h^2/a^2)^2$, which is shown by the dashed line in Fig 2. The mean value of τ_{inc} for on-axis heating has been used for τ_χ (= 0.2s).

4. CURRENT SCANS WITH ICRH

All ICRH scenarios give similar confinement scaling properties. Similarly, the toroidal field plays a minor role in the scaling of τ_{inc}. The immediate conclusion from power scans at different currents is that $\tau_{inc} \approx 0.2$ sec and independent of I_p.

The poloidal and paramagnetic corrections to the vacuum field are much larger than originally anticipated. Thus, especially the 5MA experiments can be regarded as off-axis heating experiments. Using the heating effectiveness $\eta = (1 - r_h^2/a^2)^2$ in Sec 3, the power input has been corrected for heating profile effects and have greatly improved the 5MA data (see Fig 3). A scaling with $\tau_\chi \propto I_p^{0.5}$ was obtained, after correction [5]. Finally correction of the 1 and 5MA data for radiation losses provide a further improvement of τ_χ (~0.37s) at 5MA and the 1MA results were only slightly changed to $\tau_\chi \sim 0.19$s, (see Fig 3). The radiation correction to the other the data remains to be carried out. However, the 1MA data still seems better than would be implied by the $\tau_\chi \propto I_p$ scaling derived from the NBI data.

5. CURRENT SCANS WITH COMBINED HEATING

Combined NBI and ICRH heating up to 16MW has been successful in increasing the total stored plasma energy. Power scans at different currents have shown an improvement in τ_{inc} with increasing current. These results have been corrected for radiation losses and power deposition

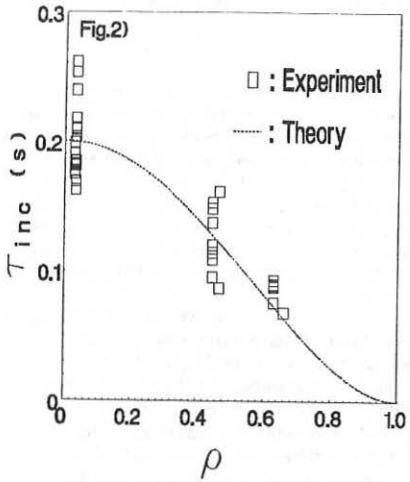
Fig.2)
□ : Experiment
----- : Theory
τ_{inc} (s)
0.3
0.2
0.1
0
0
0.2
0.4
0.6
0.8
1.0
ρ

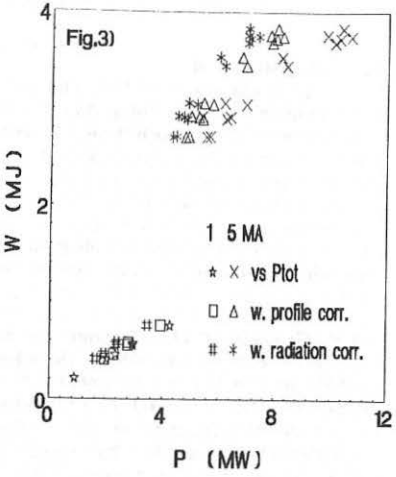
Fig.3)
1 5 MA
* X vs Ptot
□ Δ w. profile corr.
* w. radiation corr.
W (MJ)
4
2
0
0
4
8
12
P (MW)

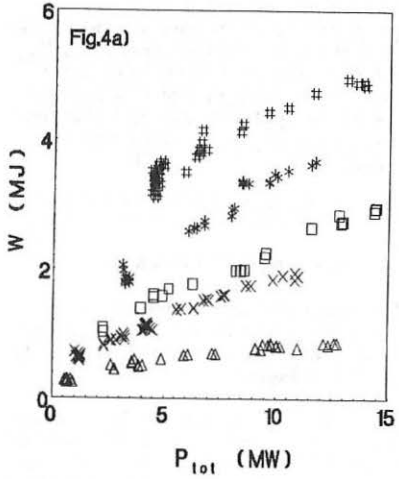
Fig.4a)
W (MJ)
6
4
2
0
0
5
10
15
P_{tot} (MW)

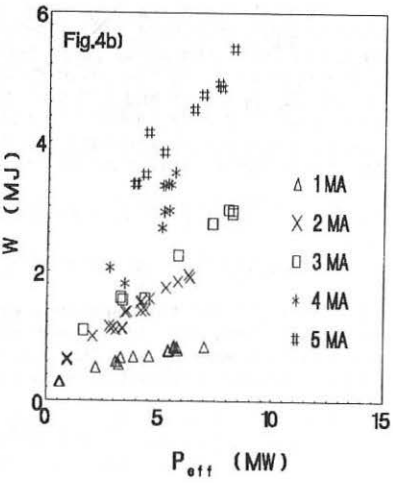
Fig.4b)
Δ 1 MA
X 2 MA
□ 3 MA
* 4 MA
# 5 MA
W (MJ)
6
4
2
0
0
5
10
15
P_{eff} (MW)

ELECTRON HEAT TRANSPORT IN TOKAMAKS

P H Rebut, M L Watkins and P P Lallia
JET Joint Undertaking, Abingdon, Oxfordshire, OX14 3EA, UK

1. INTRODUCTION

Earlier work [1-4] on the role of the magnetic field topology in determining tokamak behaviour, such as anomalous electron heat conduction and degradation of confinement with additional heating, relies on an equilibrium being established between laminar surfaces, magnetic islands and ergodic domains in a plasma. This concept leads to a change in the plasma behaviour when the interaction of sets of magnetic islands produces a surrounding ergodised region. An analysis, based on the non-dimensional structural parameters which describe the dominant physical processes and the non-dimensional shape parameters which generally describe the geometry of the plasma or its composition, is summarised in Section 2. This analysis can be interpreted in terms of a critical temperature gradient, a specific form of which (together with the heat flux which results when this gradient is exceeded) is consistent with a plausible physical mechanism for the sustainment of the magnetic islands. This mechanism relies on the directed kinetic energy of electrons compensating the resistive dissipation of the induced currents needed to maintain the topology (Section 3). The resulting model is found to agree with JET experimental data in terms of the global scaling of the stored electron energy (Section 4) and the detailed profile analysis using transport code simulations of JET discharges (Sections 5 and 6).

2. DIMENSIONAL ARGUMENTS

Heuristic scaling laws have been derived on the basis of non-dimensional parameters [3]. The dominant physical processes are described by normalised structural parameters representing the plasma pressure, β, the resistivity, Δ, the power flow, ϕ and the diamagnetic thermal drift speed, Ω. Granular and relativistic effects are ignored for the present discussion. Taking account of the number of independent variables which can be constrained externally, a single relationship must exist between the parameters. This must be of the general form:

$$\phi = \phi(\beta, \Delta, \Omega) \quad \text{where} \quad \phi = \frac{F}{nkTv_s}$$

and

$$\beta = 2\mu_o nkT/B_t^2 \quad ; \quad \Delta = \eta J/B_p v_s \quad ; \quad \Omega = (2m_e/kT)(k\nabla T/eB_t)^2 \qquad (1)$$

applicable to all tokamaks and, given the geometric and magnetic configurations, the input power and the plasma density, serves to define the plasma temperature. The ohmic heating power can be written as $\phi = \Delta/\beta$ and in ohmically heated plasmas equation (1) becomes :

$$g(\beta, \Delta, \Omega) = 0 \qquad (2)$$

JET experimental results strongly suggest a large resilience to changes in the electron temperature profile in the conduction zone. It is therefore reasonable to interpret equation (2) mainly as defining a critical temperature gradient. We propose that:

$$\Omega = \Omega_c(\Delta,\beta) \quad \text{and} \quad \Omega_c(\Delta,\beta) \propto \Delta/\beta \tag{3}$$

We suggest that this form for the critical temperature gradient applies for all forms of input power. Of course, with strong heating, further departures from the critical temperature profile are to be expected. We propose as a form for equation (1):

$$\phi = -\Omega^{\alpha}[\Omega^{1/2} - \Omega_c^{1/2}]H[\Omega^{1/2} - \Omega_c^{1/2}] + \phi_{neo} \quad , \quad \alpha = 0, \tfrac{1}{2}\ldots \tag{4}$$

where ϕ_{neo} represents all the normal heat losses through the electron channel and H is a function which is zero (or unity) for Ω <(or >) Ω_c.

3. PHYSICAL MODEL

Consistent with the concept of a chaotic magnetic topology involving small magnetic islands being responsible for the transport properties, we present a plausible argument to define the temperature gradient and the electron heat flow. The power balance between the directed kinetic energy of electrons and the resistive dissipation of the induced currents, $\mathcal{J}$, needed to maintain the magnetic topology of the islands may be expressed:

$$\tfrac{1}{2} m_e n \left(\frac{\nabla T}{2eB_t}\right)^2 v_{the}\, \sigma_{erg} \propto E\, \mathcal{J}\, \sigma_{erg}\, L \tag{5}$$

or

$$\tfrac{1}{2} m_e n\, v_{the} \left(\frac{\nabla T}{2eB_t}\right)^2 \propto E\, B_t\, \gamma^2 \tag{6}$$

where σ_{erg} is the cross-section of the ergodic magnetic flux and L is the length needed to cross one chain of islands. Thus the temperature gradient is related to the overlapping parameter γ. For low collisionality, γ exceeds a certain critical value, $\gamma_c \sim 0.9$, in which case equation (6) reduces to equation (3). The heat flux is then:

$$F = -\nu \frac{\delta^2}{R} v_{the}\, n_e k \nabla T_e\, (\gamma - \gamma_c) + F_{neo} \quad \text{with} \quad \gamma = \gamma_c\, \nabla T_e/\nabla_c T \tag{7}$$

δ is related to the interspace between the chain of islands and ν is a numerical factor. Equation (7) could be written in the form:

$$F = -\chi\, n_e k(\nabla T_e - \nabla_c T) H(|\nabla T_e| - |\nabla_c T|) + F_{neo} \text{ with } \chi = \nu\gamma \frac{\delta^2}{R} v_{the} \tag{8}$$

Specifically, $\alpha = 0$ gives the following expressions for $\nabla_c T$ and χ:

$$\nabla_c T = \nu_c \left[\frac{EB_t^{\,3}}{n_e \sqrt{T_e}}\right]^{1/2} \frac{1}{q} \qquad \chi = \nu_H \frac{\nabla T_e}{B_t} \frac{q^2}{q'} \tag{9}$$

where $\nu_c = 3.5$ and $\nu_H = 4.0$ with E in Vm^{-1}, B_t in T, n_e in $10^{19} m^{-3}$ and T_e in keV. These expressions are used in Section 4-6. However, a more suitable form for equation (8) may be with $\gamma\delta \propto (\nabla T_e/2eB_t) q^2/q'/v_{thi}$ (corresponding to $\alpha = \tfrac{1}{2}$).

4. GLOBAL SCALING

Expressed in terms of the input variables of electron density, n_e, toroidal magnetic field, B_t, plasma current, I (MA), the average size of the plasma, ℓ, and the input power, P (MW) (independent of the heating method, namely, ohmic, NBI or ICRF), the global electron energy content, W_e (MJ), can be deduced from equations (3) and (4) and written as:

$$W_e = \alpha_1 Z^{1/4} n_e^{3/4} B^{1/2} I^{1/2} \ell^{11/4} \left[1 + \alpha_2 \frac{M^{1/2} P}{n_e^{1/2} Z^{1/2} B \ell^{3/2}}\right]^{1/2} \qquad (10)$$

M is the atomic number and Z is the effective charge. From a regressional fit to about 1200 data points from JET limiter discharges, the coefficients α_1 and α_2 are found to be respectively 2.3×10^{-2} and 3. The comparison between the fitted and calculated values is shown in Figure 1, where the range of the experimental conditions is also shown. A more refined treatment requires the direct simulation of the plasma profiles.

5. SIMULATION OF ELECTRON ENERGY TRANSPORT

A simplified 1-D electron energy transport code which uses equations (8) and (9), ohmic and additional input power and experimental density profiles (but ignores ion transport and radiated power) has been used to compare computed and experimental data. For two values of the plasma current the comparison in terms of the global energy content is shown in Figure 2. Simulations also show the possibility of a pedestal in the electron temperature when a high shear is introduced at the edge, thereby simulating an H-mode.

6. FULL TRANSPORT CODE SIMULATIONS

A range of JET discharges has also been simulated using the above model for electron transport (equations (8) and (9)) in the 1-1/2D predictive transport code, ICARUS. Other features of the model are basically those used previously [5].

Computed electron temperature profiles are compared with the experimental ones after the collapse of the sawtooth in various ohmic discharges with different electron densities and currents (Figure 3). Other characteristics of the discharge, for example, ohmic power, radiated power, confinement times, are also well represented.

With neutral beam injection the observed degradation in confinement is obtained without changing the transport model. The electron temperature profiles at the end of the ohmic phase and the L-mode are well simulated, as also is the temporal behaviour for the central electron temperature during the transient between the OH and L-mode (Figure 4).

7. CONCLUSIONS

A model for electron heat transport in tokamak plasmas which in a single formulation accounts for both the anomalous behaviour in ohmic plasmas and the degradation of confinement with additional heating has been proposed. Some shape parameters (such as, T_e/T_i, r/R, $T\nabla n/n\nabla T$) are possibly hidden in the evaluation of ν_c and ν_H. While this model does not yet have an established theoretical basis, it is nontheless consistent with the theory of ergodic magnetic fields and JET experimental results.

ACKNOWLEDGEMENTS

We are pleased to acknowledge the assistance of Dr K Thomsen in preparing the JET data used in Figures 1 and 2.

REFERENCES

[1] Rebut, P H and Lallia, P P, Proceedings of the 7th International Conference on Plasma Physics (Kiev, USSR, April 1987).

[2] Rebut, P H et al, in Plasma Physics and Controlled Nulcear Fusion Research (Proc 11th Int Conf, Kyoto 1986) paper IAEA-CN-47/E-III-4.

[3] Rebut, P H and Brusati, M, Plasma Physics and Controlled Fusion, 28 (1986)113.

[4] Rebut, P H and Hugon, M, in Plasma Physics and Controlled Fusion Research (Proc 10th Int Conf, London, 1984), 2(1984)197.

[5] Watkins, M L et al, Proc 13th Eur Conf on Cont Fusion and Plasma Physics, Schliersee, 1986,10C(I), EPS(1986)156.

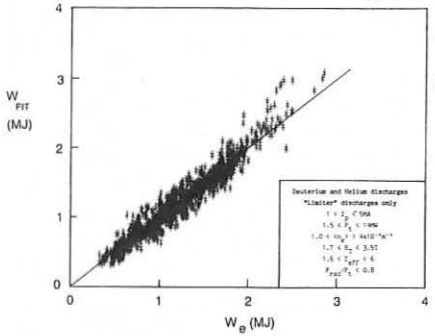

Fig 1: Total stored electron energy versus the fit proposed in Eq(10).

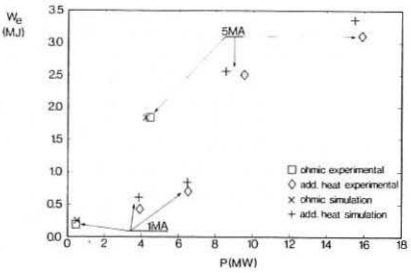

Fig 2: Total stored electron energy versus total input power for 1&5MA.

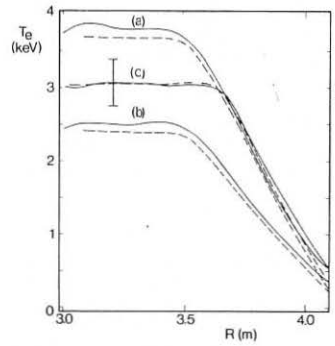

Fig 3: Experimental (—) and computed (---) electron temperature profiles for a)3MA,1.6x10^{19}m^{-3}; b)3MA,3.2x10^{19}m^{-3};c)5MA,3.2x10^{19}m^{-3}

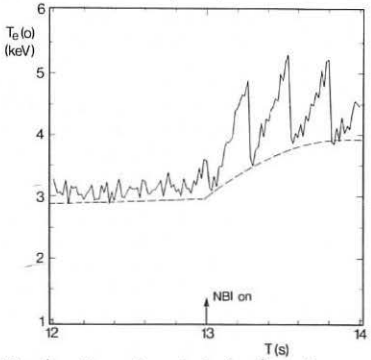

Fig 4: Experimental (—) and computed (---) central electron temperature for a 2MA X-point discharge in OH and L- mode with NBI.

ION ENERGY TRANSPORT IN JET DISCHARGES

G. Bracco+, M. Brusati, S. Corti, F. Rimini, F. Romanelli+
C. Sack, A. Taroni, F. Tibone, V. Zanza+

JET Joint Undertaking, Abingdon, Oxon., OX14 3EA, UK
+Associazione ENEA-Euratom sulla Fusione, Frascati, Italy

Introduction

Simulation of JET experimental results with predictive transport codes have always shown a tendency to require rather large (3-8) "anomaly factors" for the neoclassical ion thermal conductivity χ_{ineo} in order to reproduce the measured central value of the ion temperature T_{io} [1]. However, no firm conclusion on the radial (not to mention the functional) dependence of χ_i was possible in the absence of reliable measurements of T_i-profiles.

Interpretation of passive charge exchange (NPA) data has led to the determination of JET ion temperature profiles [2] in both ohmic and auxiliary heated discharges at low and moderate density [$\bar{n} \leq 2\times10^{19}m^{-3}$]. These discharges have been analysed with an interpretative transport code (JICS) and simulated with a predictive transport code (JETTO) in order to assess both magnitude and radial dependence of χ_i. The anomalous character of χ_i has been confirmed and results are similar to those reported for Doublet III [3]. A revised expression of χ_i based on η_i-modes has also been derived and its range of validity assessed.

Interpretative Code Analysis

In this analysis, χ_i is derived from the ion energy balance equation where the experimental profiles of ion and electron temperatures and Z_{eff} are supplied as input. A fundamental assumption, adopted also in the case of predictive code simulations, is that the electron-ion energy coupling be classical, with impurity corrections taken into account via Z_{eff}. Only ohmic and RF heated discharges have been considered so far, since in these cases a reliable T_i profile is provided by the NPA diagnostic under the assumption that the departure of the ion distribution function from thermal is negligible [2]. RF power deposition profiles are also given as input data to JICS when required and have been computed by means of a ray tracing code [4].

The ion heat diffusivity χ_{iexp} derived from JICS at r = 0.6 a for a few representative cases is shown in Fig.1. The values are in the range (1-3)m^2/sec, also typical for χ_e in the same cases. Both the numerical value of χ_{iexp} and its radial dependence are different from χ_{ineo} [5]. This is illustrated by Fig.2, where the ratio χ_{iexp}/χ_{ineo} is shown as a function of radius for one representative case. The value χ_{iexp}/χ_{ineo} in the so-called confinement zone ($0.3 \leq \frac{r}{a} \leq 0.7$) varies from 5 to more than 10.

The scatter in the data reflects the uncertainty associated with the experimental values and the numerical determination of ∇T_i, and not surprisingly it becomes very large in the external region.

Predictive Code Simulation and Theory

In the predictive approach to the problem of determining χ_i, various models for χ_i are introduced in the code and the resulting ion temperature profiles are compared with the experimental ones. In the examples considered here all the relevant quantities are either simulated by the code well within the experimental error bars (e.g. T_e, see [6]) or taken from JET data banks to which the JETTO code is linked (e.g. radiation profiles). This ensures that uncertainties in the modelling of other phenomena do not affect the determination of χ_i more than experimental uncertainties.

Results from the predictive code confirm the findings of the interpretative code. In particular, it is clear that at least at low density ($\bar{n} \approx 10^{19} m^{-3}$) the usual approach with $\chi_i = \alpha \chi_{ineo}$, $\alpha \approx 5$ does not allow a good simulation of JET T_i profiles, either in ohmic or in RF heated discharges. A typical example of results is shown in Figs.3,4. The same figures show that better simulations can be obtained with $\chi_i \approx \chi_e$, χ_e being an electron thermal conductivity that allows reproduction of T_e-profiles [6]. Such a choice for χ_i has been found to determine in transport codes a central value of T_i and an ion energy content consistent with experimental observations also in cases at higher density where no T_i profile is yet available and the usual approach $\chi_i = \alpha \chi_{ineo}$ cannot be excluded.

Comparison of these results on χ_i in JET discharges, characterised by rather flat density profiles, as well as those reported in other devices (e.g. [3]) with theoretical models suggests that a major role in determining χ_i could be played by the so-called η_i-mode ($\eta_i = d\ln T_i / d\ln n_i$). Previous tests on an expression of χ_{in_i} failed in reproducing ion thermal fluxes available at the time in JET [7]. The derivation of χ_{in_i} has been recently reviewed [8] leading to a reduction of the coefficient χ_{in_i} used in [7]. In addition, a theoretical expression of the threshold η_{ic} for the instability derived in [8] has been introduced in place of the assumption $\eta_{ic} = \text{const} \approx (1\text{-}1.5)$.

The new expressions in the code are:

$$\chi_i = \chi_{ineo} + \alpha\, \chi_{in_i}, \quad \chi_{in_i} = \omega_{*i}\, \rho_i^2\, \Omega_i / b_i = 2.6\times10^{19}\, \frac{T_i^{3/2}}{B_t^2}\, n_i^{1/2} f\left(1 - \frac{\eta_{ic}}{\eta_i}\right) \varepsilon_n^{1/2}.$$

Here standard notations are used [8], $b_i = 0.1$ and $\Omega_i = 0.8\, \varepsilon^{1/2} \eta_i^{1/2} f(1 - \eta_{ic}/\eta_i)$. $f = (1-\eta_{ic}/\eta_i)^{1/2}$ is derived in [8] for $\eta_i \geq \eta_{ic} = 1 + 2.5(\varepsilon_n - 0.2)$ if $\varepsilon_n > 0.2$, $\eta_{ic} = 1$ elsewhere ($f=0$ for $\eta_i < \eta_{ic}$); $\varepsilon_n = (\nabla \ell n n)^{-1}/R$ and α is a numerical coefficient to be determined from simulations and hopefully close to 1.

Results from the code show that reasonable ion thermal fluxes and χ_i values are obtained in all tested cases inside the so-called transport region if $\alpha \approx 0.5\text{-}1.0$. However, central values of T_{iexp} require that χ_{in_i} should not be switched off when η_i falls below η_{ic}. This happens mainly in the central region where η_{ic} becomes rather large ($\gtrsim 4$). An empirical working prescription seems to be to replace the threshold function $f(1 - \eta_{ic}/\eta_i)$ with a function $(\eta_i/\eta_{ic})^{\beta}$, $\beta \approx 1\text{-}1.5$.

In the external region the available experimental information, albeit less reliable than elsewhere, does seem to require a χ_i increasing with radius. This is not consistent with the T_i dependence of χ_{in_i} and would require some further modification to χ_{in_i} or an additional mechanism at work. Results of simulations with χ_{in_i} are also shown in Figs.3 and 4.

Conclusions

Results of interpretative and predictive transport codes show that both the magnitude and the functional dependence of χ_{ineo} are not consistent with the available experimental profiles of T_i (and T_e) at least at low density.

A better term of comparison than χ_{ineo} for χ_i seems to be the electron thermal conductivity; $\chi_i \simeq \chi_e$ is generally a better prescription for JET simulation than $\chi_i \simeq 5\ \chi_{ineo}$, especially at low density.

Reasonable results for T_i in the central and intermediate plasma region are provided if $\chi_i = \chi_{ineo} + \chi_{in_i}$ is used in a transport code; χ_{in_i} needs, however, some modifications from the theoretical expression derived in [8].

References

[1] Taroni, A. et al, 12th European Conference on Controlled Fusion and Plasma Physics, Budapest, 2-6 September 1985, Vol.I, p.22.

[2] Corti, S. et al, 13th European Conference on Controlled Fusion and Ploasma Heating, Schliersee, 14-18 April 1986, Vol.I, p.109.

[3] Groebner, R.J., et al, Nucl. Fus. 26, 543 (1986).

[4] Bhatnagar, V. et al, Nucl. Fus. 24, 955 (198).

[5] Chang, C.S., Hinton, F.L. Phys. Fluids, 25, 1515 (1986).

[6] Taroni, A., Tibone, F. paper presented at this conference.

[7] Düchs, D.F. et al, Eleventh International Conference on Plasma Physics and Controlled Nuclear Fusion Research, Kyoto, 13-20 Nov. 1986.

[8] Romanelli, F., JET report in press.

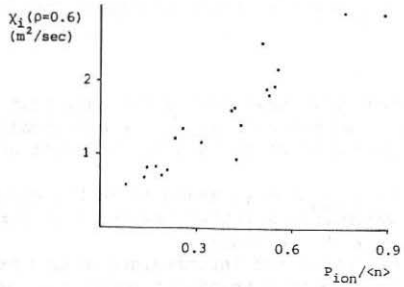

Fig. 1 : χ_{iexp} in the confinement zone as a function of input power per particle (in MW $/10^{19}$ ions m^{-3}).

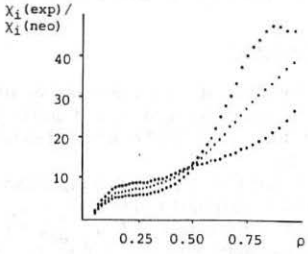

Fig. 2 : The ratio χ_{iexp}/χ_{ineo} as a function of radius at three times during the flat-top of a "monster" sawtooth (#11133, B_t= 2.2T, I_p=2.0MA, $<n_e>$=1.5 $10^{19}m^{-3}$, P_{RF}=4.5MW).

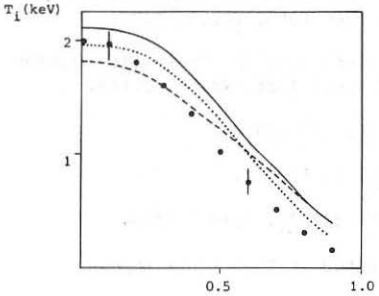

Fig. 3: Comparison of experimental (full circles) and computed T_i-profiles in an ohmic case. The models used are χ_i= 5 χ_{ineo} (solid line), $\chi_i=\chi_{ineo}$ + χ_e (dotted line) and χ_i= χ_{ineo} + χ_{ini} (dashed line). In χ_{ini} we have used $f=n_i/n_{ic}$ (#8961, B_t= 2.5T, I_p=2.5MA, $<n_e>$=1.7 $10^{19}m^{-3}$).

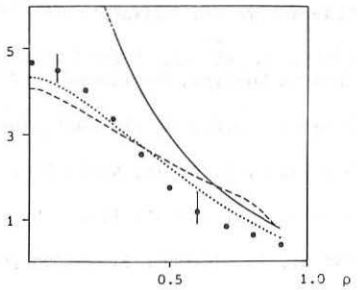

Fig. 4: Comparison of experimental and computed T_i-profiles at the end of the flat-top of a "monster" sawtooth. Symbols and models are as in Fig. 3. The RF-heated plasma is that of Fig. 1.

HEAT TRANSPORT IN JET

M. Brusati, A. Galway, H. Hamnén, F. Rimini, T. Stringer

JET Joint Undertaking, Abingdon, Oxon., OX14 3EA

Introduction

A number of JET pulses, representative of the different regimes of operation, have been analysed using the 1½-D time dependent JET transport analysis code, JICS. This evaluates the components of the electron and ion energy equations in flux surface coordinates, using as input the experimental profiles of electron density and temperature, from far-infra-red interferometry (FIR) and electron cyclotron emission (ECE) respectively, the effective Z from Bremsstrahlung, and the ion cyclotron (ICRH) and neutral beam injection (NBI) power deposition profiles computed from ray tracing and pencil beam codes respectively.

When the bulk ion velocity distribution is thermal, its temperature profile is obtained from the neutral particle analyser (NPA) diagnostic, and the local ion diffusivity χ_i is then calculated directly from energy balance. When the majority ions have a high energy tail due to neutral beam slowing down, the central value of the ion temperature is provided by X-ray crystal and/or charge-exchange recombination spectroscopy. The profile is then evaluated assuming $\chi_i \sim \alpha/n_e$, and adjusting its absolute magnitude iteratively to produce satisfactory agreement between the resulting total stored plasma energy and the stored energy measured by the diagnostic locp.

Of the OH and ICRH pulses only those for which the NPA ion temperature profile is available have been analysed. The philosophy was to concentrate on a limited number of pulses which are fully diagnosed, rather than including a large number of incompletely diagnosed ones. Because of the limited number of pulses, the behaviour illustrated may not be representative of the full range of operation of JET. The conclusions reached are therefore preliminary.

Results

The temperature profiles show a fair degree of "profile consistency". In Fig.1 $T_e^{-1}\, dT_e/dr$, measured at 60% of the plasma radius, is plotted against the input power to the electron, divided by the electron density, for a number of additionally heated plasmas. The temperature gradient was extracted from the ECE data without smoothing, and so is sensitive to small random variations in T_e. Despite the considerable variation in the energy deposition profile, between on- and off-axis ICRH, NBI, and combined ICRH and NBI, and a variation in q from 3.5 to 9, the variation in the relative temperature gradient is surprisingly small. Similarly, there is no clear dependence of $T_i^{-1}\, dT_i/dr$ on the input power to the ions, though the scatter is now greater. Thus the ions may also show profile consistency.

Quite generally, the electron and ion thermal diffusivities derived from JICS are comparable in magnitude. The ion diffusivity shows no correlation with neoclassical theory, as found also by Bracco et al [1]. It is almost an order of magnitude larger and its radial variation and parameter scaling appear to be different.

The electron thermal diffusivity is shown as a function of radius in Fig.2, for typical ohmic and ICRF heated steady state plasmas. Most of the

RF-power goes into the electrons, either due to direct damping of the wave on the electrons, or as a consequence of collisional power transfer from the high-energy minority ion tails. Examples of on-axis and off-axis ICRF heating are shown. In the on-axis case, the thermal diffusivity exceeds that for the ohmic case over the entire plasma cross section. In the off-axis case however, the diffusivity is lower inside the RF deposition layer and higher outside, thus maintaining virtually the same temperature profile shape. (The reason for the overall lower levels of the diffusivity in the off-axis case as compared to the on-axis, is the higher radiation in the former). A surprising feature about the off-axis case is the rapidity with which the diffusivity and the temperature react in the central region of the plasma. These changes occur on a timescale much faster (<20ms) than would be expected from the energy confinement timescale (~0.3s). Similar effects have been observed in JET pellet injection experiments, where the "cold front" induced by the pellet propagates extremely rapidly inside the q=1 surface [2].

Recent experiments in JET have studied ohmic and auxiliary heated plasmas in the X-point configuration (single and double null), [3]. For NB-heated single null plasmas, a clear L→H transition has been observed, with the global energy confinement time more than doubling. These plasmas are generally quenched by a radiative collapse due to impurity accumulation. Local energy transport analysis shows an overall decrease in the thermal diffusivity in the L→H transition, see Fig.3.

Comparison with Theory

Within the mixing radius, typically 0.5m to 0.6m in low q JET pulses, energy transport is generally dominated by sawtooth relaxations, which periodically flatten the temperature and density profiles. In the edge plasma, typically r > 1.2m, radiation may dominate the energy transport. To explain the anomalous transport between these radii, several different instabilities have been proposed. The most commonly invoked are the dissipative trapped electron mode (DTEM), the ion temperature gradient mode, and the η_e mode [4].

In Fig.4 the theoretically predicted electron thermal diffusivity for the DTEM [5] is plotted against the experimental local diffusivity derived by JICS, for the representative selection of additionally heated plasmas in JET. The prediction is for the collisional or the collisionless forms of the DTEM, whichever is appropriate for the experimental parameters. The predicted values tend to be higher than those measured, by about an order of magnitude. The predicted diffusivity should include an undetermined numerical factor, arising from uncertainty in the saturated fluctuation amplitude. This factor, which is set to unity in Fig.4, could possibly explain the discrepancy in magnitude. However, the lack of any correlation between the predicted and experimental diffusivities is more difficult to explain and supports the earlier conclusion [6] that the DTEM is not the dominant source of anomalous transport in JET pulses. A similar comparison, using the predicted thermal diffusivity for the η_e mode [4], again showed no correlation.

The ion temperature gradient mode is frequently referred to as the η_i mode, because it becomes unstable only when $\eta_i = d\,\ell n\, T_i / d\,\ell n\, n_i$ exceeds a critical value. The anomalous transport predicted for this mode is large, larger even than for the DTEM. This has led to the expectation that this high anomalous transport will prevent η_i from exceeding its critical value

by much. Because of its complex dependence on plasma parameters, in prediction codes the critical value is commonly taken to be 1.5, a mean value. Romanelli [7] recently evaluated the threshold, and found it to increase linearly with $\varepsilon_n = n/(R\ dn/dr)$ when $\varepsilon_n > 0.3$. Figure 5 shows the ratio of the measured η_i to Romanelli's predicted threshold, as a function of radius. While the correlation is far from convincing, it is not inconsistent with a rapid increase in diffusivity when η_i exceeds the threshold, bearing in mind the error bars on the measured η_i.

Another clue to the local transport process is given by the JET "monster sawteeth", [8]. During the sawtooth rise phase, the central temperature rises almost adiabatically, with small transport losses. The sawtooth rise is then abruptly terminated by a rather sharp "knee". The corresponding temperature profiles are shown in Fig.6. This is consistent with a strong loss process which is switched on when the local temperature gradient exceeds a threshold value.

It should be pointed out that the JET pulses used for comparison with theory are mostly additionally heated. Publications which found experimental evidence for DTEM transport [5,9] also concluded that the η_i mode provides the dominant loss mechanism when η_i exceeds its threshold. It appears from Fig.5 that additionally heated plasmas in JET generally do exceed this threshold, which may be why no evidence for the DTEM is seen.

Conclusions

A number of representative JET pulses have been studied from the point of view of local transport properties. Based on this preliminary study, it appears that:

i) The electron and ion loss channels are of comparable importance.

ii) The ion thermal diffusivity does not appear to be neoclassical, either in magnitude, radial scaling or parameter dependence.

iii) The temperature profile shapes are rather independent of heating method and location. Changing the heating profile alters the thermal diffusivity profile so as to maintain the same temperature profiles. The change in the diffusivity profile occurs on a timescale much faster than would be expected from the energy confinement timescale.

iv) The thermal diffusivities show no obvious correlation with prediction for either the dissipative trapped electron mode, or the η_e-mode. A correlation may possibly exist between the measured η_i and the predicted critical value for the η_i mode.

References

[1] G. Bracco, et al, this conference (1987).

[2] A.D. Cheetham et al, this conference.

[3] M. Keilhacker, this conference.

[4] P.N. Guydar, et al, Phys. Rev. Lett. 57 (1986) 2818.

[5] R.E. Waltz et al, 11th IAEA Conf. Kyoto, paper A-VI-1-3 (1986).

[6] D.F. Düchs et al, ibid, paper A-VI-1-1 (1986).

[7] F. Romanelli, to be published.

[8] D.J. Campbell, et al, this conference.

[9] F. Romanelli, W.M. Tang and R.B. White, Nucl. Fusion 26 (1986) 1515.

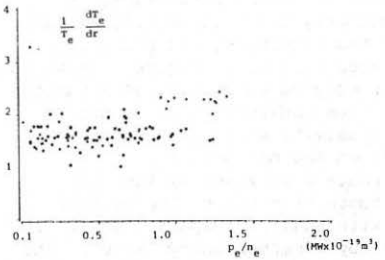

Fig 1: T_e^{-1} dT_e/dr at r=0.6a versus input power per electron

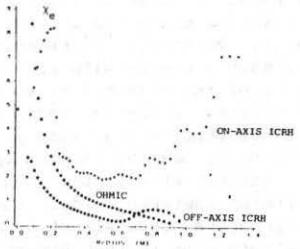

Fig 2: χ_e vs radius for ohmic heated, on-axis ICRH, and off-axis ICRH pulses

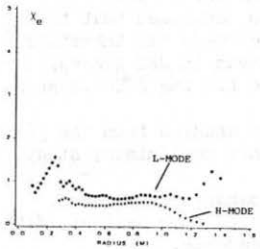

Fig 3: χ_e vs radius during the L-mode and H-mode phases of a beam heated pulse

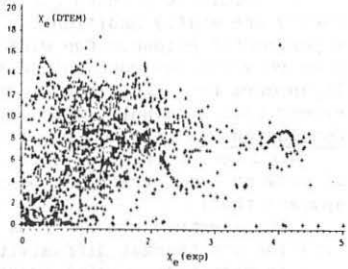

Fig 4: Comparison of the experimental electron thermal diffusivity with that predicted for the DTEM

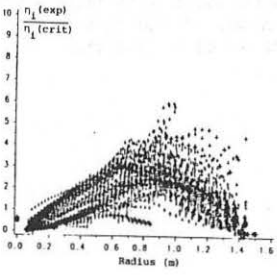

Fig 5: Ratio of the measured n_i to the critical value as a function of radius for several additionally heated pulses

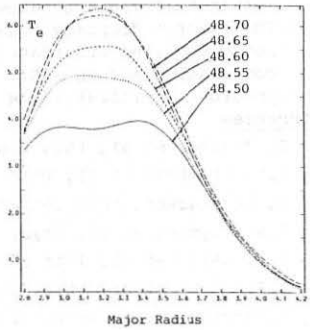

Fig 6: Electron temperature profiles at 50msec intervals during the ramp of a monster sawtooth

INFERENCE OF χ_e FROM PHASE SHIFT ANALYSIS OF X-RAY SIGNALS IN FT

L. Panaccione, A.A. Tuccillo

Associazione EURATOM-ENEA Sulla Fusione, Centro Ricerche Energia Frascati, C.P. 65 - 00044 Frascati, Rome (Italy)

INTRODUCTION

The measurement of electron thermal conductivity, χ_e, is of great interest in today's tokamak.

Apart from the power balance analysis, a possible way to obtain χ_e is to analyse the diffusion process of a small heat perturbation. The sawtooth activity is a useful phenomenon for this purpose because of its occurrence in a wide range of discharges in tokamaks. The inference of χ_e from sawtooth heat pulse propagation is usually done by measuring the increment with radius of the delay time of the sawtooth peak, according to

$$\Delta t_p \cong \Delta r^2/9\chi_e \tag{1}$$

valid within the diffusion region [1].

In FT discharges, this method has been applied to soft X-ray emission signals and $2\omega_{ce}$ emission signals [2].

Another method to obtain the χ_e is to consider the dependence on radius of the phase shift of the Fourier components of small periodic heat perturbation propagating signals [3,4].

A program has been developed in order to analyse FT discharges using this method. A brief description of the program is presented below, as well as some first results.

BRIEF DESCRIPTION OF THE METHOD

The analysis of the electron heat balance equation for small periodic heat perturbations leads to the following relationship between the phase, ϕ_k, of the Fourier components of the electron temperature and the radius, r

$$\phi_k(r) = \left(\frac{3k\omega}{4\chi_e}\right)^{\frac{1}{2}} r \tag{2}$$

where k is the harmonic order and ω is the fundamental angular frequency [3,4]. Equation (2) is a good approximation as long as the following holds

$$r > \left(\frac{\chi_e}{3k\omega}\right)^{\frac{1}{2}}$$

This condition is satisfied in the experimental cases considered here, in the diffusion region.

From Eq. (2), the phase shift between two radii, r_1 and r_2, can be written as

$$\Delta\phi_k = \left(\frac{3k\omega}{4\chi_e}\right)^{\frac{1}{2}} \Delta r \qquad (3)$$

with

$$\Delta\phi_k = \phi_k(r_2) - \phi_k(r_1)$$

$$\Delta r = r_2 - r_1$$

From Eq. (3), χ_e can be written as

$$\chi_e = \frac{3k\omega}{4} \left(\frac{\Delta r}{\Delta\phi_k}\right)^2 \qquad (4)$$

If Δr is small enough, Eq. (4) can give a local value of χ_e, along the radius.

Equation (4) is valid in a diffusion region.

APPLICATION OF THE METHOD TO FT DISCHARGES

In FT discharges, this method has been applied to soft X-ray emission signals corresponding to line integrals along parallel viewing chords in a poloidal plane. For this purpose, a program has been implemented to automatically elaborate experimental data. This program has been tested on artificial data generated by a full transport and sawtooth simulation code [5]. The agreement is quite good, within the approximations of such a calculation. Signals coming from each possible pair of contiguous chords are analysed and a value of χ_e is carried out; hence, the behaviour of χ_e along the radius is obtained.

The position in the Hugill plot of the shots considered is shown in Fig. 1. Figure 2a,b,c,d,e shows the χ_e obtained using the method described for some typical discharges in the explored ranges of density and q_L.

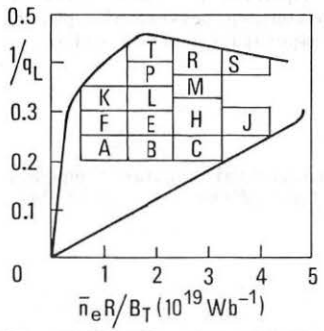

Fig. 1: Hugill plot of discharge parameters considered.

This method gives good results as long as the sawtooth signal is sharp and incisive. Referring to Fig. 1, good values of χ_e are obtained when the discharge is in the central part of the explored region. As a general result, in the diffusion region where the method works properly, the values of χ_e obtained are in agreement with the values obtained from the power balance and from the increment with radius of the delay time of the sawtooth peak, within a factor 2.

The radius range of validity is de-

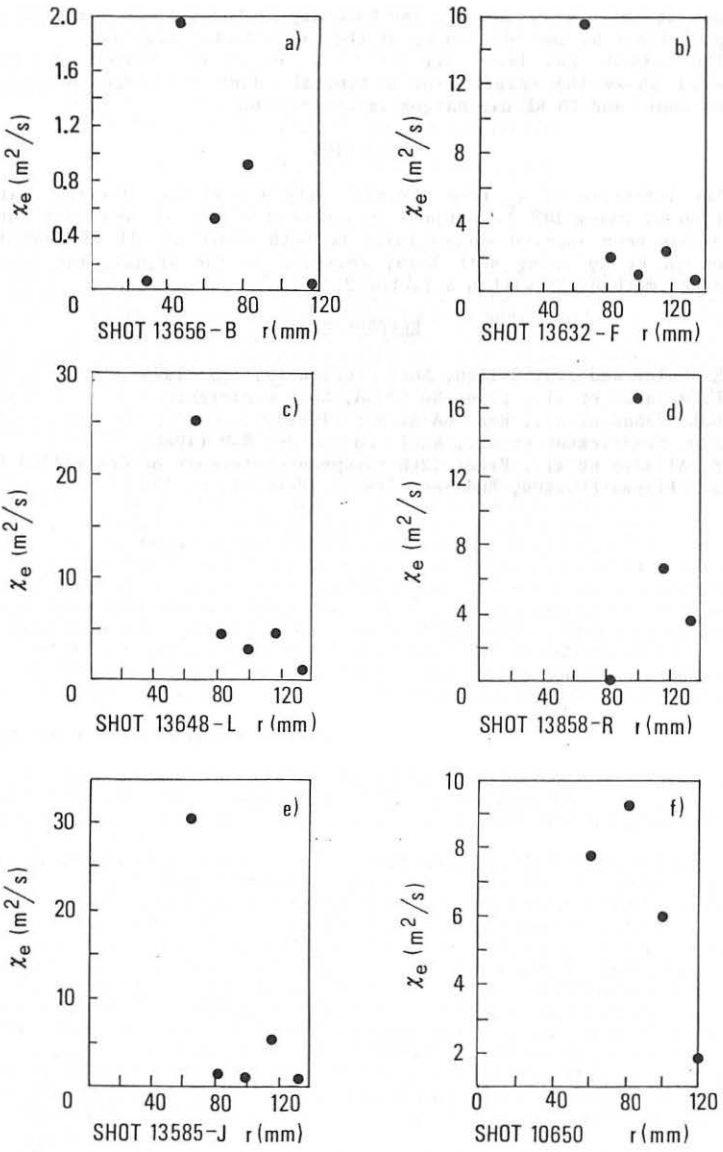

Fig. 2: Electron thermal conductivity χ_e along the radius in FT discharges.

termined at the lower limit by the boundary of the diffusion region and at the upper limit by the flattening of the experimental signal.

The method has been applied to a few LH RF heated discharges. Figure 2f shows the results for a typical LH RF discharge. A comparison between ohmic and LH RF discharges is under study.

CONCLUSION

The inference of χ_e from a signal with a periodic electron heat perturbation by using DFT techniques is a method which can be easily automated. It has been applied successfully to both ohmic and LH RF heated discharges in FT by using soft X-ray emission as the signal. The agreement with other methods is within a factor 2.

REFERENCES

[1] M. Soler and J.D. Callen, Nucl. Fusion 19, 703 (1979).
[2] F. Alladio et al., paper No 0396A, this Conference.
[3] G.L. Jahns et al., Rep. GA-A17858 (1985).
[4] E.D. Fredrickson et al., Nucl. Fusion 26, 849 (1986).
[5] F. Alladio et al., Proc. 12th European Conference on Controlled Fusion and Plasma Physics, Budapest (1985), Part. I, p. 138.

MHD ACTIVITY AND ENERGY LOSS DURING BETA SATURATION AND COLLAPSE AT HIGH BETA POLOIDAL IN PBX

H.W. Kugel, S. Sesnic, K. Bol, M. Chance, H. Fishman, R. Fonck
G. Gammel, R. Kaita, S. Kaye, B. LeBlanc, J. Manickam, W. Morris,[a]
M. Okabayashi, S.F. Paul, M. Reusch, and H. Takahashi

Plasma Physics Laboratory, Princeton University
Princeton, New Jersey 08544, USA

1. Introduction.

One of the central issues in high-β experiments, in medium to high-q tokamak plasmas, is whether the observed temporal β saturation and collapse are caused by ballooning, ideal kink, or tearing modes. Several explanations have been proposed for the β-limits found for different tokamaks and experimental conditions. In ISX-B, for example, a deterioration in confinement at high-β (ie., a soft β-limit) was observed, but this deterioration did not exhibit a correlation with the observed m=1/n=1 mode [1], and hence, ballooning modes were proposed as a possible cause for this β-limit [2]. In PBX, in low-q ($q \leq 3.5$), high current-ramp discharges [3], and in D-III [4], for certain limiter discharges, a disruptive β-limit attributed to the n=1 external kink mode was observed. ASDEX [5] and PBX [6] studied very similar types of neutral beam heated discharges which typically underwent transitions into the H-mode. After this transition, β rose initially, but then saturated and eventually "collapsed" at constant plasma current and heating power. In ASDEX, since the ERP's (ELM's) alone could not explain the additional energy losses during the saturation and collapse phases, and since no other observed MHD activity could be held responsible for the saturation and collapse, ballooning modes were invoked to explain this β-limit. In PBX, however, it was possible to correlate these additional energy losses with various observed MHD phenomena (ie., sawteeth, fishbones, continuous mode, and ERP's), and there was no need to postulate the existence of ballooning modes. The PBX investigations reported previously [6] were performed at medium q-edge (4 to 5) and β-poloidal (1 to 1.2) values. In this paper we report the extension of β saturation and collapse studies to high q-edge (>6), high β-poloidal (>2) discharges. We will conclude that globally the high β-poloidal discharges generally behave similarly to those at lower β-poloidal reported previously [6], but that the detailed behavior of the MHD depends on β-poloidal.

2. Experimental Conditions and Results.

The plasma parameters in these high q-edge, high β-poloidal, H-mode discharges were as follows: I_p = 250 kA, B_t = 1.7 T, q-edge = 7, P_{inj} = 5 MW, plasma elongation = 1.3, a_{mid} = 37 cm, R = 152 cm, indentation = 5%, $<\beta_t>$ = 1 to 1.5 %, and the Troyon-Gruber scaling parameter β_c ($\mu_o I_p / a_{mid} B_t$) = 0.6 to 0.8.

In PBX, we were able to examine directly the relation between MHD activity and energy loss using a unique diamagnetic loop which had a very short response time and high amplitude resolution and was placed inside the vacuum chamber. There was a very good correlation between the energy losses observed with the diamagnetic loop and the MHD events as observed in the x-ray diodes, Mirnov signals, neutron losses, charge exchange fast particle effluxes, and Hα emission. A typical discharge is shown in Fig. 1; shown are the displaced toroidal flux as measured by the diamagnetic loop, and the Hα emission from the divertor. The first neutral beam was injected at 350 ms, with another following at 400ms, and finally with the last two beams injecting at 450 ms. All four beams were injecting until 660 ms. Since the plasma current and shape were held constant during neutral beam injection, the displaced toroidal flux signal generally reflects the evolution of β-poloidal. The L-mode lasted until 485 ms, at which time the transition to the H-mode occurs.These discharges did not exhibit sawteeth, and the transition to the H-mode often appeared to be triggered by relatively strong fishbones. After the H-mode transition, the discharge can be subdivided into three phases: β increase, saturation, and collapse.

a. β-Increase Phase. After the transition to the H-mode, over a period of 20 ms, the internal energy increased at a rate of 0.9 MW, and the confinement improved steadily except for the

strong fishbone at 495 ms. There was little or no MHD activity during the period of increasing β except for this fishbone. During the last part of the β-increase phase, fishbones became more severe resulting in nonnegligible loss of fast particles. This was the cause of the start of the β-saturation phase at 520 ms.

b. β-Saturation Phase. As shown in Figs. 1 and 2, the saturation period lasts for about 50 ms, ending at 570 ms. This period was characterized by three kinds of MHD activity, each with varying energy loss: fishbones, ERP`s (Edge Relaxation Phenomena), and a continuous mode. There are two types of fishbones, their difference being the modulation strength in various signals. The weaker fishbones are characterized by a weaker modulation of the x-ray signal, charge exchange fast particle effluxes, and Mirnov fluctuations, a smaller change in the modulation frequency, a smaller drop in diamagnetic signal, and an almost imperceptible and slow drop in neutron flux. The plasma energy loss is less than 0.4 % and the neutron flux drop is less than 2 %. The duration of the burst is also short, less than 0.5 ms. The frequency of the fishbone is typically between 20 and 30 kHz, whistling down to half of this frequency during the burst.

The stronger fishbones have higher energy losses of up to 1.5 %, larger neutron flux drops of up to 8 %, and greater than a factor of two increase in the charge exchange efflux for the weaker fishbone. The effect that most distinguishes the stronger fishbones from the weaker ones is the effect on the x-ray radiation. The horizontal-viewing diodes indicate an out-in plasma column motion: the inner diodes show a jump-up in signal, and the outer diodes a jump-down. The vertical-viewing diodes show only a jump-up in the signal, which increases strongly toward the edge of the plasma (up and down). The inferred plasma reconfiguration during the fishbone is very different from the sawtooth-like crash at lower q-edge and β-poloidal values. Here, the plasma appears to be pushed inward and further elongated.

The ERP`s often occur 1 to 2 ms after any fishbone and always after a stronger fishbone.The ERP duration is normally few hundred μs. A possible sequence of events is that the fishbone expels energy from the center, the energy propagates outward and builds-up near the edge. After 1 to 2 ms, an ERP occurs, and energy is lost over a large region. This would imply that ERP`s may not be just an edge instability but may involve a large part of the minor radius. The ERP instability may be induced by high pressure, temperature, or current gradients that may have built-up in response to the initial central energy expulsion. The energy loss due to the ERP is of the order of 1 %.

There is another type of the MHD activity, which is characteristic of only the β-saturation phase and is never observed during the β-collapse phase. This is an n=2 or n=3 mode as determined by the radial magnetic field coils with a higher unknown m number. This mode is seen in the x-ray diodes in Fig. 2 from 566 to 569.5 ms. The mode frequency is usually between 30 kHz (n=2) to 60 kHz (n=3) and the mode amplitude is saturated. This mode contributes very little to the additional energy losses, and is therefore not a strong participant in the β-saturation process.

The repetition time of the weaker fishbones is 1 to 2 ms, while that of the strong fishbones is about 5 ms. Using these repetition rates and the energy losses involved in each event, it is possible to account fully for the energy losses during the β-saturation, and thereby to ascribe the β-saturation effect to the three types of MHD behavior: weak fishbones, strong fishbones, and accompanying ERP`s. These additional energy losses are close to a total of 1 MW and are sufficient enough to cause the β-saturation .

c. β-Collapse Phase. The β-collapse phase begins usually with the onset of a strong n=1 mode and is characterized by two types of MHD activity: a quasi-continuous n=1 mode and ERP`s. In Figs. 1 and 2 this phase starts at 570 ms and lasts until the end of the beam injection at 660 ms. Both the continuous mode and the ERP's can be seen in Fig. 3.

At the beginning of the β-collapse phase, the amplitude of the continuous n=1 mode is modulated. A larger amplitude mode results in a stronger loss of fast particles, a larger drop in neutron flux, and a bigger loss of plasma energy from the diamagnetic signal, thus establishing a correlation between the energy loss and the amplitude of the continuous mode. After the initial period, the mode amplitude saturates in the central part of the plasma column, but it continues to burst at the edge; the modulation is seen as a decrease in mode frequency and amplitude, and these decreases occur at the time of each ERP. This modulation of the external part of the mode is well correlated with the change in the fast particle eflux, and the decay in the neutron flux and plasma energy. Using the correlation of this mode with the diamagnetic loop signal, the increase in modulation of the fast particle losses, and the drop in neutron flux, we can conclude that this mode is reasponsible for both

the thermal and beam energy loss.

In Fig. 4, we compare this continuous mode at high β-poloidal and high q-edge with the mode at medium β-poloidal and medium q-edge. The relative modulation and the phase of these two modes is shown as a function of the vertical position in the bean. Although there are differences in the details of the phase structure of these modes, they both show a gradual, continuous phase shift across the central part of the plasma. They both have a phase change of approximately 180° between z=-20 and +20 cm. The large difference is in vertical distribution of the relative amplitude modulation. The medium β-poloidal and medium-q case (#255) clearly shows a strong odd mode (possibly m=1) with radial coupling to strong higher m number modes, whereas in the case of high β-poloidal and high-q (#5214), the radial coupling is stronger and there is no one dominant internal mode.

The ERP events as shown in Fig. 3 correlate well with sudden drops in the diamagnetic signal, with Hα spikes, with the drops in the external x-ray diodes, with the high frequency bursts (100 kHz and higher) in the radial field signal, and with the decrease in the fast particle loss modulation. They do not correlate at all with the drops in the neutron flux, indicating that the ERP losses represent only thermal energy losses. The ERP's contribute 0.5% energy loss per event with a repetition time of 1.4 ms.

If we assume that the underlying plasma confinement properties during the β-collapse phase are the same as those at 500 msec when little or no MHD was present, we can determine what additional losses are ascribable to the MHD activity during the β-collapse. With this assumption, the dW/dt term at 580 ms should have a value of +1.1 MW. The total additional loss required to explain the β-collapse is 1.4 MW. An increase in radiated power, as measured by bolometry, accounts for 450 kW of this loss. The ERP's contribute 400 kW to the loss, leaving 550 kW attributable to the n=1 continuous mode, thus making this mode contribute a comparable amount to the β-collapse.

3. Conclusions.

We have shown that the observed β–saturation and collapse in PBX can be explained in terms of long wavelength MHD and ERP activity, and that there is no need to invoke ballooning modes. The β–saturation and collapse phases are different in terms of the MHD activity. The saturation phase is dominated by the fishbones, ERP`s, and n=2 or n=3 modes, but only the fishbones and ERP`s contribute substantially to the energy loss. The β–collapse is caused primarily by a strong n=1 continuous mode, and to a lesser extent ERP`s, and additional radiation losses. The n=1 continuous mode is responsible for both thermal and beam energy losses, and the ERP`s only for thermal energy losses. This continuous mode for high β-poloidal differs strongly from the one observed at medium β-poloidal by not having a m=1 component, and by exhibiting a strong radial coupling of modes and no one dominant internal mode.

[a] Permanent address: Balliol College, Oxford University, U.K.

Acknowledgements

We wish to acknowledge the contributions of P. Couture, W. Heidbrink, K. Ida, K. Jaehnig, G. Jahns, G. Navratil, N. Ohyabu, D. Ward and the PBX Engineering and Technical Staff. This work supported by the U.S. DoE Contract No. DE-AC02-76-CHO-3073.

References

1. J.L.Dunlop, *et al.*, Phys. Rev. Lett. 48, 538 (1982).
2. M. Murakami, *et al.*, in Plasma Physics and Controlled Nuclear Fusion Research (Proc. 10th Inter. Conf., London, 1984) Vol. I (IAEA, Vienna, 1985) 87.
3. K. Bol, *et al.*, Phys. Rev. Lett. 57, 1891 (1986).
4. R.D. Stambaugh, *et al.*, in Plasma Physics and Controlled Nuclear Fusion Research (Proc. 10th Inter. Conf., London, 1984) Vol. I (IAEA, Vienna, 1985) 217.
5. O. Gruber, *et al.*, Proc. of 11th Inter. Conf. on Plasma Phys. and Contr. Nucl. Fusion Res.
6. M. Okabayashi, *et al.*, Proc. of 11th Inter. Conf. on Plasma Phys. and Contr. Nucl. Fusion Res.

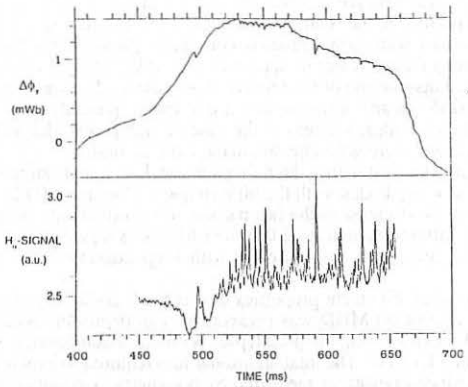

Fig. 1. Diamagnetic loop and Hα signals from the divertor region during neutral beam injection.

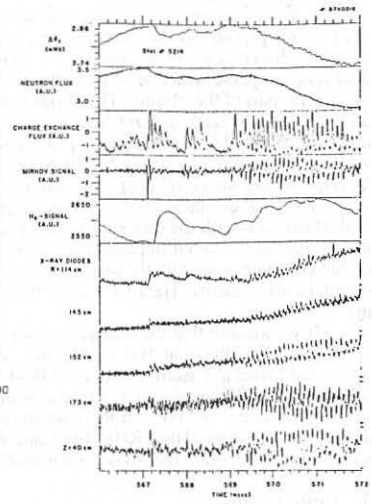

Fig. 2. Signals from various diagnostics during the last part of β-saturation.

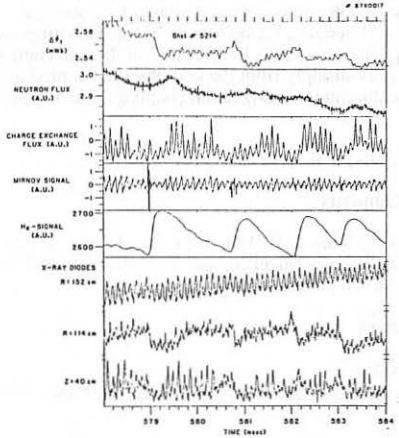

Fig. 3. Signals from different diagnostics during a part of the β-collapse phase.

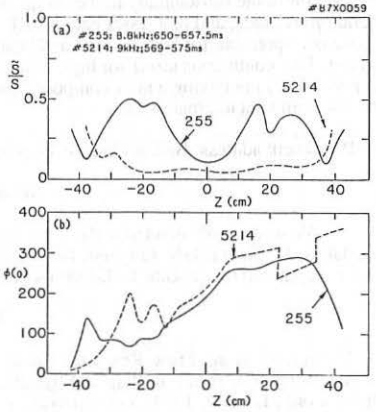

Fig. 4. Comparison of the amplitude modulation and the phase change of the n=1 continuous mode during the β-collapse phase for medium q-edge medium-β (#255), and for high q-edge high β-poloidal (#5214).

BETA LIMITS AND MHD ACTIVITY IN TFTR

A W Morris†, E D Fredrickson, K M McGuire, M G Bell, M S Chance, R J Goldston, R Kaita, J Manickam, S S Medley, N Pomphrey, S D Scott, MC Zarnstorff

Princeton University, Plasma Physics Laboratory, Princeton New Jersey

High power tangential neutral beam injection into TFTR [1] has allowed a study of a variety of MHD phenomena at lower ion collisionality ($\nu_{*i} \sim 10^{-2} - 10^{-3}$) than was possible on smaller tokamaks. The parameter regime for the beta limit studies is 0.5MA< I_p <1.3MA, 5MW< P_{inj} <20MW, 0.5-2.0s injection, $R_{geom} = 2.3 - 2.57$m (usually 2.45m), $a_p = 0.6 - 0.85$m (usually $0.8m$), $3 < q_{cyl} < 12$ with low pre-injection density in a well conditioned vessel. A beta limit exists at high q that is substantially below that expected from simple application of the Troyon limit. Some discussion of phenomena at low q ($q_\psi(a) = 3, 2.5$) will also be given.

Discharges near the β limit: The chief characteristics of the β limit as observed in TFTR are discussed in [2]. Fig 1 shows the envelope of the TFTR data along with the location of some discharges with coherent MHD activity. Although the bound at high q_{cyl} is lower than the Troyon limit [3], q_{cyl} and the profiles are different from those used in that study. Calculations with the PEST code reveal that the plasmas may be unstable to $n = 1$ ideal-MHD modes, with $n = 2$ stable. $q(0) \approx 1 - 1.5$ excludes the broader current profiles required for higher β_n at high $q(a)$. High-n ballooning modes are calculated (in a torus but without FLR corrections) to be unstable over part of the profile in some cases. In general, however, the steepest calculated pressure gradients appear in the shots with best confinement, and this indicates that such modes would affect transport only in the best discharges. Attempts to exceed the TFTR β limit have been made using lower I_p at high P_{inj}. No improvement is found and in fact there is a dependence on I_p: the attainable β_n falls for $I_p < 0.7$MA ($q_{cyl} \sim 7$). It is also found that there is an optimum P_{inj} for a given I_p, above which the achievable β fails to increase or drops. This optimum is about 11MW for 800kA but has not appeared at 19MW for 1MA.

The β limit is manifest in one of two ways: i) the plasma disrupts either with loss of plasma current, or with loss of typically 50% of the kinetic energy content or ii) the energy content reaches a maximum, then falls with time at constant P_{inj}. For ii), with $I_p \leq 1$MA, $n_e(r)$ broadens and $T_e, T_i(0)$ and the neutron emission (I_n) fall, almost always accompanied by coherent MHD activity. As I_p is raised, however, a similar collapse of the energy content is sometimes seen, but far from the β limit. This is not always associated with MHD activity, and the discharge may be reverting to TFTR high I_p, n_e confinement scaling, and is at present thought to be a different phenomenon. The presence of MHD activity does not depend just on macroscopic parameters such as $\beta_p, q(a)$ (Fig 1), and the value of $q(0)$ is expected to be important. The target plasma generally has sawteeth ($r_{inv} \sim 5 - 10$cm) which disappear at the start of injection. Experiments with I_p ramped down (typically 1.2MA to 0.9MA in 0.25s, ending just before injection) have produced some high q_{cyl} shots with sawteeth and bursting $m = 1$ modes during NBI with no other MHD activity for 2s injection, consistent with a high current density being frozen into the core. Changes in the injection angle and $P_{co}/P_{counter}$ (and hence in the beam driven currents) have had no reproducible effect on the MHD activity. Possible changes in Z_{eff} and impurities have yet to be investigated.

As reported in [2] perhaps the most remarkable feature of the MHD behaviour of these high-q plasmas is the occurrence of $m = 3, n = 2$ modes in the absence of $n = 1$ activity. Fig 1 shows that (3,2) modes are common and that they appear over a wide range of parameter space (particularly for behaviour (ii) above). (2,1) modes cover a similar range, but $m = 1$ modes and sawteeth are rare at high q (except with current ramp down). $f_{mode} < 20$kHz,50kHz for the (2,1), (3,2) modes respectively. A few good confinement discharges show a centrally localised higher m mode (from SXR array), but this is apparently benign. The (3,2) modes are identified using Mirnov coils at the vessel wall ($R = 2.65$m,$a = 1.10$m, $\Delta\theta = 22.5°$) and are only observed (for high q_{cyl}) with high power auxiliary heating, when pressure and neoclassical effects on MHD theory are expected to be significant. The low value of m at the wall is unambiguous despite the high values of $q(a), \beta_p$. The absence of (3,2) modes in current ramp-down discharges suggests that high $q(0)$ may destabilise this mode (Δ' calculations indicate $q(0) > 1.3$ is unstable) and that $q(0)$ (or $r_{q=1}$ before injection) is indeed an important parameter. The soft x-ray (SXR) signals are consistent with a (3,2) island: there is one more phase change than expected for an ideal-MHD (3,2) distortion. The data indicates a displacement of $\sim 10cm$ at $r = 25cm$ is typical, consistent with estimates of the island size from $\tilde{B}_\theta(wall)$. (2,1) modes of similar size are observed interchangeably with (3,2) modes, and are also apparently resistive - the internal structure is more complex than for the $m = 2$ second harmonic of $m = 1$ sawtooth precursors.

Calculations of I_n give some indication of a loss/redistribution of fast particles during MHD activity. Transport codes (SNAP and TRANSP codes), without beam loss processes, are used. At low I_p(600kA) and $\overline{n_e}$, I_n is over-estimated (typically by a factor 2) for cases with strong MHD activity and I_n falling by 30 – 50% during injection: n_{beam} is too high in the code, suggesting loss of beam ions is required. Time dependent calculations are less sensitive to systematic errors and show the discrepancy appears when I_n begins to fall. At higher I_p, $I_{n,calc}/I_{n,measured}$ does not change as much, but the contribution to $I_{n,calc}$ from beam ions rises and that from thermal ions falls. Estimates of the influence of the low-m, n ripple ($\delta r/R \sim 3\%$ near the island for observed modes) on the trapped thermal and beam ions [4] suggests that their transport could indeed be significantly affected, depending on the velocity profile. A loss/redistribution mechanism for passing ions may also be required to explain the data.

At lower q, or with current ramp down (see above) sawteeth or bursts of $n = 1$ activity appear (Fig 2). The bursts and oscillations are visible in the charge exchange signal only near the injection energy and are most pronounced for near perpendicular views (for $R_{tan} = 0.91$m, 1.47m but not 2.13m). f_{mode} falls through the burst as with fishbones and the mode reported in [5] and its value (5kHz for near balanced injection) is of the same order as the trapped particle precession rate, but some data suggest f_{mode} changes with the net co-injected power. There is no obvious high frequency burst as reported in [5] and E_{dia}, I_n do not drop, indicating the modes are not harmful at present levels. These modes appear as $m = 1$ on the SXR diodes, but as higher m (~ 5, but not a simple structure) on the Mirnov coils. This is the expected behaviour for an ideal-MHD mode and modelling of the SXR emission for PEST $n = 1$ eigenmodes agrees with experiment in the central region of the plasma.

Disruptions: Fig 3 shows a disruption at the β limit. It is seen that I_{SXR}, I_n fall on a $100\mu s$ timescale (after a gamma burst). E_{dia} falls on a timescale of a few ms: the measurement is limited by the vessel time constant (several ms). The limiter temperature rises in $\sim 20\mu s$ [2].

Note the two-stage drop in I_n. There is a rapidly growing oscillatory precursor ($\tau_g \sim 100\mu s$) which has an $m = 1$ structure in the plasma core. The mode structure on the Mirnov coils is not simple - just as with the $m = 1$ bursts above. The timescale of the growth suggests a pressure driven mode, probably with inadequate time for formation of a large island. The PEST code shows that the growth rate of the $n = 1$ internal kink increases rapidly from zero as $q(0)$ drops below unity for these high β_p discharges and the appearance of a $q = 1$ surface is an attractive model for these disruptions. In general disruptions do not follow a period of degraded confinement with (3,2) or (2,1) modes. It is notable that disruptions can occur far from the β limit [2], early during injection when the beam pressure dominates. Disruptions of the ohmic target plasma at these q values do not occur.

Low-q_ψ operation: Experiments with co-injection and q_ψ close to the rational values 3.0, 2.5 reveal increases of $\sim$ 15% in E_{dia} and $\sim$ 50% in particle density after a clear transition, reminiscent of limiter discharges on JFT-2M [6]. There is a drop in toroidal rotation velocity (and hence a temporary energy source from rotational energy and a consequent improvement in heating efficiency [7]) and a sharp fall in the measured H_α emission from the inboard side. There is evidence from SXR and Mirnov signals of a slowly rotating mode (3,1 for $q_\psi = 3$, 5,2 for $q_\psi = 2.5$) at the plasma edge during the transition, correlated with a rotating structure in the H_α emission, which peaks at the x-point of the locking/unlocking mode. This structure is also apparent on the electron temperature (ECE) and suggests that a form of helical divertor may be present. The central plasma continues to rotate, albeit at a reduced speed, as shown by Doppler shift measurements and the simultaneous presence of $n = 1$ modes in the centre of the plasma with a higher frequency than the edge mode.

Conclusions: The β limit as seen on TFTR is close to the limit due to $n = 1$ ideal-MHD modes even in this high q regime. This limit is substantially below the extrapolated Troyon limit. The modes correlated with the degraded confinement appear to be resistive in origin, and appear (experimentally) to be sensitive to $q(0)$ and $q(r)$ near the axis. There is initial evidence that these instabilities play a significant role in the fast ion dynamics. Although the profiles may be close to the high-n ideal-MHD ballooning threshold, no direct evidence of ballooning modes has been found. Experiments in limiter discharges with q_ψ near to 3, 2.5 show a transition to a state of apparently improved particle confinement with indications of a stationary helical perturbation.

The authors are grateful for discussions with J Strachan and H Mynick. This work was supported by US DOE contract No DE-AC02-76-CHO-3073.

† Balliol College, University of Oxford, UK.

References:

[1] Strachan, J D *et al* Phys Rev Lett **58**, 1004 (1987)
[2] McGuire, K M *et al*, Proc 11th IAEA Conf, Kyoto, paper A-VII-4 (1986)
[3] Troyon, F, Gruber, R *et al* Plasma Phys and Nucl Fus **26**, 209 (1984)
[4] Mynick, H, Nuclear Fusion **26**, 491 (1986)
[5] Heidbrink, W W *et al* Phys Rev Lett, **57**, 835 (1986)
[6] Odajima, K *et al* Proc 11th IAEA Conf, Kyoto, paper A-III-2 (1986)
[7] Goldston, R J *et al* Proc 11th IAEA Conf, Kyoto, paper A-II-1 (1986)

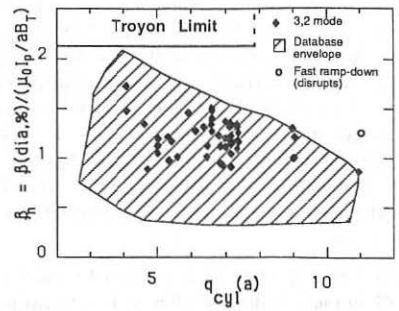

Figure 1: Location of $m = 3, n = 2$ modes and the β limit on TFTR. $q_{cyl} \equiv \frac{5a_p^2 B_\phi}{R_{geom} I_p(MA)}$. The full data set is hatched.

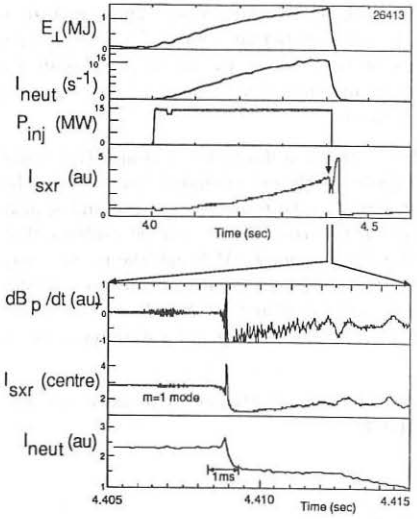

Figure 3: Waveforms for a disruption at the β limit. $I_p = 950kA, P_{inj} = 14.6MW$, $P_{cntr} = 5.6MW, \beta_p = 2.0, \overline{n_e} = 2.9 \times 10^{19} m^{-3}$, $q_{cyl} = 7.2$. Note I_n falls by $\sim 30\%$ in $100\mu s$. The plasma position changes at 4.409s and I_p decays 4.42-4.44s ($4.5 \times 10^7 A/s$).

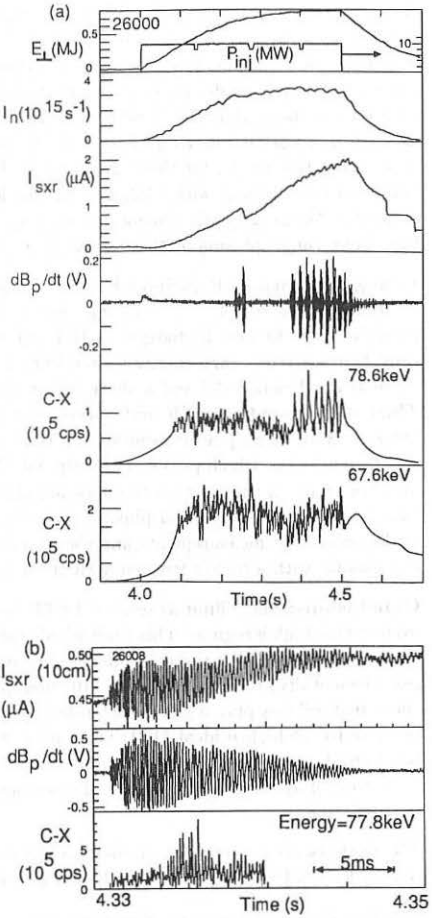

Figure 2: Example of $n = 1$ bursting mode (with a sawtooth at $t = 4.25s$). $P_{co} = P_{counter}$, $I_p = 0.9$MA, $q_{cyl} = 4.1$, $\beta_p = 1.2$. Note absence of effect of the mode on I_n, E_{dia}. In (a) the C-X sampling rate changes at 4.08 and 4.5s. In (b) (not the same shot) the timing of the C-X data is uncertain to a few ms and is from 4.33-4.34s only.

TEMPERATURE SCALING OF OHMICALLY HEATED DEUTERIUM PLASMAS IN TEXTOR

H. Kever, G. Waidmann

Institut für Plasmaphysik der Kernforschungsanlage Jülich GmbH,
Association EURATOM-KFA, 5170 Jülich 1, FRG

Introduction.
Measurements of the electron temperature and the energy content by two independent methods, i.e. ECE - measurement of T_e and measurement of the plasma diamagnetism to obtain β_{pol}, have been performed on TEXTOR to include larger plasma currents and higher toroidal magnetic field strengths. The results of both measurements confirm scaling laws derived from the assumption of anomalous electron heat conduction in an Ohmically heated plasma with Spitzer resistivity. Dependences of the electron temperature on the plasma density n are attributed to systematic changes in Z_{eff} which enters through the resistance. The possibility to achieve thermonuclear burn in larger devices by increasing the plasma currents is discussed.

Electron temperatures from ECE-measurements.
The diagnostic technique has been described elsewhere /1/. Ir the plasma core, the temperature is determined by the input of Ohmic heating power and the losses due to thermal conduction; radiation losses for not too high degrees of plasma contamination are small. Therefore, in the steady state (and for the temporal averages if oscillatory contributions enter the quantities in question) the power balance per unit length for a plasma with cross-section of radius r reads

$$\pi r^2 \eta j^2 - 2\pi r Q_r = 0 \quad , \qquad (1)$$

where near the axis $\eta j^2 = \eta_0 j_0^2 = \text{const}$ (index 0 denotes the axis), and Q_r is the radial energy flux density. If for the latter

$$Q_r = -K_e \frac{\partial T}{\partial r}$$

i.e. neglecting convective contributions, then upon integration of equ. (1) up to a radius $r_1 \ll a$ with $K_e \simeq \text{const}$, we obtain

$$r_1^2 \eta j^2 = 2 K_e [T(r=0) - T(r_1)].$$

For temperatures distributed (in the temporal average) according to $T = T_0[1-(r/a)^2]^\lambda$, the difference between the temperatures at the center of the plasma and at $r = r_1$ becomes

$$T_0 - T(r_1) \simeq \lambda r_1^2 T_0/a^2.$$

Writing the expression for the Spitzer resistivity $\eta = \gamma(Z_{eff})\, Z_{eff}\, \eta_1 / T_0^{3/2}$, where η_1 is the value of the plasma resistivity for $Z_{eff}=1$ and $T_0 = 1$ keV, and $\gamma(Z_{eff})$ is the correction factor of the resistivity for $Z_{eff} \neq 1$ (compared to the Lorentz gas approximation), then the power balance becomes

$$\gamma(Z_{eff})\ Z_{eff} I_p^2 = (2\lambda a^2/\eta_1 K_e)\ T_o^{5/2}, \qquad (2)$$

where another form factor occuring upon replacement of the current density by the total plasma current I_p has been absorbed in the value of λ.

Since the dependence of γ on Z_{eff}, within realistic ranges of Z_{eff}, is rather weak, for constant profile shapes the central electron temperature is expected to scale as

$$T(o) = \text{const.}\ (Z_{eff}^{1/2}\ I_p)^{4/5}. \qquad (3)$$

For the series of discharges from which the experimental results presented here have been extracted, Z_{eff} was found to behave as nZ_{eff} = const. Therefore, if one neglects the difference of the exponent 0.8 in equ. (3) from 1, a linear relationship between T(0) and $I_p/n^{1/2}$ holds. The experimental results are shown in fig.1. Due to a different normalization, the results are represented as T(0) vs.$1/qn^{1/2}$ where q is the safety factor at the limiter. Replacing in equ. (3) the plasma current by the safety factor, the temperature scaling in the linear approximation reads

$$T(0) = \text{const}\ \frac{a^2}{R} B_T/qn^{1/2}. \qquad (4)$$

In effect, representing the I_p-dependence by a q-dependence, the scaling should show also an almost linear dependence on the toroidal field strength B_T. This is seen in the upper part of the diagramme, where the measured values of the temperature are displayed for a toroidal field of B_T=2.3 Tesla, whereas the other points on the main line are obtained for B_T = 2 Tesla. For the same values of $(qn^{1/2})^{-1}$, the measured values of T(0) at higher B_T are in the ratio of the toroidal field strenghts larger than the ones on the main line.

Concerning the dependence of Z_{eff} on n, the existence of simple algebraic relations seems to be rather the rule than an exception; cf. references /2,3/ for the results from JET and TFTR, respectively. In fig.2, the degree of approximation to the experimental results of TEXTOR is shown by displaying nZ_{eff} vs. n. As can be seen from the diagramme, nZ_{eff} is approximately constant. If more generally one observes $n^{\alpha}Z_{eff}$ = const, and Z_{eff}, as is assumed here, merely acts through the resistance on T_e, the dependence of the electron temperature on the plasma density should be weaker than $n^{-\alpha/2}$, i.e. for α = 0.5 (as is observed under other discharge conditions also in TEXTOR), this dependence is very weak and hardly observable. No explanation has been found for the $Z_{eff}(n)$-dependence which probably is a consequence of global plasma-wall interactions (i.e. ones which not only affect the peripheral plasma).

Determination of β_{pol}.
Unlike the ECE-measurements which give local values of T_e, the magnetic loop measurements of the plasma diamagnetism primarily give volume averaged plasma quantities resp. relationships between them. Under the assumption that the spatial distributions of the quantities in question in the steady state persist, the relations

$$T_e(0) = \text{const}\ \bar{T}_e,\ T_i(0) = \text{const}\ \bar{T}_i$$

hold and allow immediate inferences to connect the results of either measurement. By definition, β_{pol} is related to the plasma pressure and the current strength through

$$N_e \bar{T}_e + \bar{T}_i \Sigma N_i \sim \beta_{pol} I_p^2, \qquad (5)$$

where the bars denote volume averages and the N's are the particle numbers per unit length, and all ion species are assumed to have the same ion temperature T_i. Supposing a scaling law for $T_e(0)$ of the form as expressed in equ. (4), one expects for β_{pol} a dependence

$$\beta_{pol} \sim \left(1 + \frac{T_i}{T_e} \frac{\Sigma N_i}{N_e}\right) \frac{n^{1/2}}{I_p}. \qquad (6)$$

Uncertainties derive from the expression in the bracket. However, in Ohmically heated discharges T_i is less than T_e, e.g. $T_i = 0.7\ T_e$, and also $\Sigma N_i/\Sigma Z N_i$ is smaller than one, especially when Z_{eff} is large. Therefore, the scaling law of β_{pol} in lowest order should be,

$$\beta_{pol} = \text{const}\ \frac{n^{1/2}}{I_p} \qquad (7)$$

The results of the measurements are shown in fig.3. There is obviously much more scatter in these measurements than in the ECE results, but the linear relationship between β_{pol} and the quantity $n^{1/2}/I_p$ is evident and supports the scaling law found for T_e from the ECE-measurements.

Conclusions

On the basis of the measurements and the scaling laws obtained, achievement of plasma temperatures in the range of burn conditions by Ohmic heating alone seems to be possible. The favourable dependence of the temperature on the plasma density can be ruled out, since this dependence according to our interpretation is a consequence of the change of Z_{eff} with n; but Z_{eff} cannot be changed by orders of magnitude. Therefore, only the current is the relevant quantity. With an estimated ion temperature of $T_i = 1$ keV for $T_e = 1{,}5$ keV, the linear dependence of T on I_p would require currents above 8 MA to reach $T_i = 10$ keV. Since the power with which the current strength really enters the scaling law is 0.8, the plasma current actually required is about 15 MA. The requirement to keep the safety factor in the operational range of stable tokamak plasmas implies toroidal fields above 8 Tesla and/or an increase in the size of the machines. Scaling of the heat losses may not change, since the values of the electric current density and other gradients of relevant plasma parameters remain the same as in the present operational regimes. An assessment of the possibilty to achieve thermonuclear burn by Ohmic heating alone clearly requires to take additional radiation losses into account.

References

/1/ G. Hrehuss, G. Waidmann, Proc.12. Europ. Conf. Contr. Fusion & Plasma Physics, Budapest 1985, Part I, p. 118
/2/ J.G. Cordey et al., ibid., Part I, p. 26
/3/ M.G. Bell et al., Plasma Phys. & Contr.Fusion Vol.28,No.9A, (1986) 1329

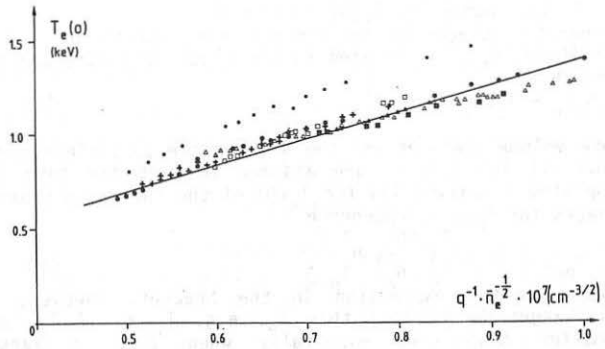

Fig. 1

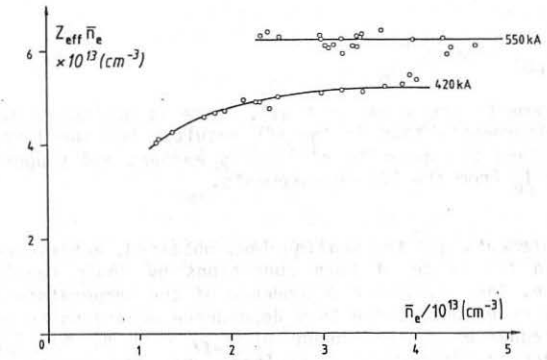

Fig. 2

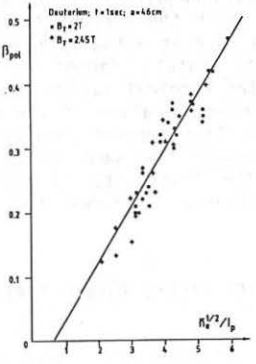

Fig.1 Electron temperature on axis $T_e(o)$ versus $1/q\bar{n}_e^{1/2}$

Fig.2 Dependence of $Z_{eff}\,\bar{n}_e$ on average electron density $\bar{n}_e$.

Fig.3 Variation of β_{pol} with $\bar{n}_e^{1/2}/I_p$.

CONFINEMENT SCALING OF TEXTOR FROM OHMIC TO ICRH DOMINATED DISCHARGES

R.R. WEYNANTS*, M. JADOUL, A.M. MESSIAEN*, P.E. VANDENPLAS, G.VAN WASSENHOVE, T. DELVIGNE, D.I.C. PEARSON, G. VAN OOST

Laboratoire de Physique des Plasmas - Laboratorium voor Plasmafysica
Association "Euratom-Etat belge" - Associatie "Euratom-Belgische Staat"
Ecole Royale Militaire - B 1040 Brussels - Koninklijke Militaire School

Recently, a number of confinement scaling laws [1-3] have been proposed covering the transition from pure OH discharges to conditions with strong additional heating. The predictions of these three laws are compared here with the TEXTOR data set obtained from power, density and current scans.

Confinement models.

The TEXTOR scaling model [1] assumes that ohmic and auxiliary heating are characterized by different confinement times τ_{OH} and τ_{aux} respectively. The global energy E is the sum of two contributions $E_{OH}' = \tau_{OH} P_{OH}'$ and $E_{aux} = \tau_{aux} P_{aux}$, where $P_{OH}' = V'I_p$ is the modified OH power and P_{aux} the applied auxiliary power. In this model the global confinement time τ_E then reads

$$\tau_{E,T} = \frac{\tau_{OH} V'I_p + \tau_{aux}(P - V'I_p)}{P} , \qquad (1)$$

with $P = P_{OH}' + P_{aux}$.

The JET model [3] assumes that there is no discontinuity in τ_E(or χ_e) at the transition from the OH to the auxiliary heated phase and that both regimes can be described by $E = E(o) + \tau_{inc} P$; i.o. above a very low power threshold the transport coefficient χ_e increases abruptly. The major fraction of the ohmic power and the totality of the auxiliary power thus contribute to the energy content with a common confinement time τ_{inc}. One then obtains $E = E_{OH} + \tau_{inc} P_{inc}$, where $E_{OH} = E(o) + \tau_{inc} P_{OH} = \tau_{OH} P_{OH}$ and $P_{inc} = P_{aux} + P_{OH}' - P_{OH}$. Finally,

$$\tau_{E,J} = \frac{\tau_{OH} V I_p + \tau_{inc}(P - V I_p)}{P} \qquad (2)$$

Noting that in some machines the OH confinement at high density loses the density dependence of the Neo-Alcator scaling and recognizing that this density dependence also fails in auxiliary heated discharges, Goldston [3] conjectured in 1983 that the transport regime governing the high density OH phase is the same as that in the auxiliary heated phase and proposed a scaling

$$\tau_{E,G} = (\tau_{OH}^{-2} + \tau_{aux,G}^{-2})^{-1/2} , \qquad (3)$$

where τ_{OH} is the well-known Neo-Alcator scaling $\tau_{OH} = a\, \bar{n}_e\, a^{1.04} R^{2.04} q^{0.5}$, $\tau_{aux,G} = F_A I_p P^{-0.6}$, and a and F_A are numerical constants.

---

* Senior research associate at the NFSR, Belgium

The OH phase of TEXTOR.

Recently we reported [4] that the OH phase of TEXTOR can exhibit at high density a saturated confinement which was shown to be due to detachment of the discharge from the limiter. The detachment can be influenced by operational procedures and we found that, by proper machine conditioning, unsaturated OH confinement and attached operation are possible up to the highest densities ; an example is shown in Fig. 1. For the machine conditions prevailing at the time the data was collected, detachment sets in at $\bar{n}_e \simeq 4.2 \times 10^{13} cm^{-3}$ at I_p = 478 kA and can be recognized by the slowing down of the energy increase, and the increase of loop voltage (curves labelled D : detached conditions). When applying ICR heating(P_{aux}=1.15 MW) to a detached plasma ($\bar{n}_e > 4.2$) one notes that larger relative energy increases are obtained than at lower densities. Our interpretation [4] is that the RF performed a catalytic role in restoring the unsaturated OH confinement. Note that both the energy increments and voltage decrements with RF are density independent when referred to curves A which are for OH under attached conditions.

Fitting procedure.

Previous analyses have established the parametric dependences of the confinement times τ_{OH}, τ_{aux}, τ_{inc} and $\tau_{aux,G}$ appearing in Eqs. (1-3).Hence we assume

$$\tau_{OH} = F_{OH}\, \bar{n}_e\, q^{\alpha} \qquad (4) \qquad \tau_{inc} = F_{inc}\, I_p \qquad (6)$$

$$\tau_{aux} = F_{aux}\, I_p \qquad (5) \qquad \tau_{aux,G} = F_A\, I_p\, P^{-0.6} \qquad (7)$$

For each scaling model we then have two fitting parameters (F_{OH}, F_{aux}), (F_{OH}, F_{inc}) and (F_{OH}, F_A) respectively. F_{OH} is obtained by fitting Eq.(4) to the unsaturated OH data only. A discussion in the preceding paragraph has shown that this is the appropriate OH regime during RF heating. Furthermore, V in Eq. (2) will always be the attached loop voltage (see Fig.1). We should stress that we did not include a systematic B_T scan in our data set (B_T = 1.9 - 2T) : our use of q in Eq. (4) therefore only ascertains the I_p dependence implicit in q. The best value of α is 0.8 for $350 \lesssim I_p < 500$ kA and 0.5 for $200 < I_p \lesssim 300$ kA. A different choice of α leads to different F_{OH} values.

Results :

Figures 2-5 show the comparison of Eqs (1)-(3) with sets of TEXTOR confinement data, gathered, as much as possible, in successive discharge sequences. The experimental τ_E values are found from energies which are the average of diamagnetic and kinetic data. The RF power P_{aux} is the total power leaving the antennae. From the time rate of change of the energy an effective absorption coefficient (see also [5]) $\beta = 0.9 \pm 0.1$ could be derived. No attempt has been made to correct the data for this factor.

The best overall fit is obtained with the following fitting parameters:

$$F_{OH} = 12.7 \pm 2 \text{ at } \alpha = 0.8 \qquad F_{inc} = 35 \pm 7$$

$$F_{aux} = 54 \pm 10 \qquad F_A = 132 \pm 40$$

when the units used are ms(τ), MA(I), MW(P) , $10^{13} cm^{-3}$($\bar{n}_e$) and V(V). It is interesting to note that the TEXTOR OH data is thus on average 30 % higher than the published Neo-Alcator scaling [3]. The errorbars on F_{aux}, F_{inc} and F_A can reflect to some extend a deviation from the linear $I_p$dependence in

the respective pertaining confinement times as well as the usual scatter in experimental data.

The TEXTOR and JET models are practically undistinguishable : obviously, the experimental loop voltage decreases are not high enough to clearly separate them. The Goldston model suffers from the fact that our TEXTOR OH data does not show (except for occasional detached plasmas) the strong saturation at high density. The scatter in the RF data obtained with this model is clearly higher than with the two others. It is interesting to note that in the domain of applicability of the Kaye-Goldston scaling [6] ($P_{tot}/P_{OH} > 3$) the present data set has confinement times 1 to 1.25 times larger than Kaye-Goldston, the main discrepancy being due to an experimental density dependence somewhat stronger than $n_e^{0.26}$ as precricted by this scaling. Even operation at $P_{tot}/P_{OH} = 5$ is not enough to resolve the fundamental question as to the asymptotic, high power limit of τ_E.

References.

1. A.M. MESSIAEN et al., Plasma Phys. and Controlled Fusion 28, 71(1986).
2. J.G. CORDEY et al., Proc.11th Int.Conf.Plasma Physics and Controll.Nucl. Fusion Research,Kyoto 1986, paper IAEA-CN-47/F-I-4.
3. R.J. GOLDSTON, Plasma Phys. and Controlled Fusion 26, 87 (1984).
4. R.R. WEYNANTS et al., LPP-ERM/KMS Report 85,Brussels 1987, submitted to PRL.
5. F. WAGNER et al., Plasma Phys. and Controlled Fusion 28, 1225 (1986).
6. S.M. KAYE and R.J. GOLDSTON, Nucl. Fusion 25, 65 (1985).

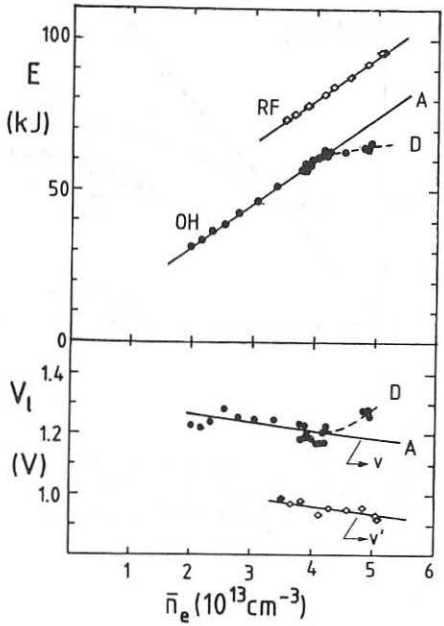

Fig. 1.

Energy E and loop voltage V_ℓ as a function of $\bar{n}_e$. In OH the plasma is detached above $n_{e,d} = 4.2 \times 10^{13} cm^{-3}$. With RF, $1.6 < P\ (MW) < 1.7$ ($I_p = 478$ kA, $B_T = 1.9$ T).

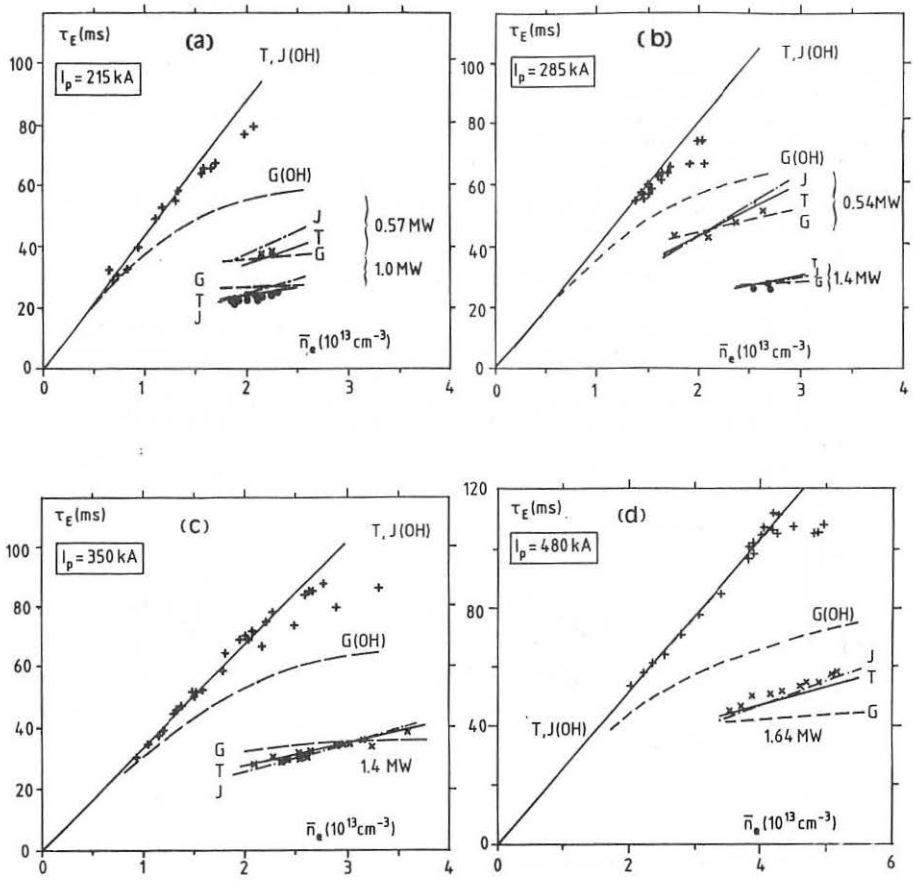

Fig. 2.

Comparison of experimental confinement time τ_E with predictions of confinement models : T ≡ Eq.(1), J ≡ Eq.(2), G ≡ Eq.(3). B_T = 2 T for (a) - (c) and 1.9 T for (d). In (a) α = 0.5 was used and F_{OH} = 18.

A MODEL FOR PELLET ABLATION IN JET

M L Watkins, W A Houlberg*, A D Cheetham, A Gondhalekar,
R Granetz, F Hendriks, J O'Rourke, P M Stubberfield

JET Joint Undertaking, Abingdon, Oxon OX14 3EA, UK
*Oak Ridge National Laboratory, Oak Ridge, TN 37831, USA

1. INTRODUCTION

Solid deuterium pellets have been injected into JET discharges for a wide variety of plasma conditions (including limiter, inner wall and X-point discharges) with ohmic heating alone, and in combination with ICRF (up to 6MW) and NBI (up to 8MW of 75kV deuterium injection). The pellets are injected in the mid-plane along a major axis of the plasma. The penetration of these pellets is compared with that determined by the neutral gas shielding (NS) model [1] and the neutral gas and plasma shielding (NGPS) model [2]. A suitable model is proposed for the effective ionisation radius in the NGPS model which determines the ionised shield parameters. For present JET experiments penetration is found to be consistent with electron ablation alone. The lack of fast ion effects is interpreted in terms of expected energy and power thresholds.

2. EXPERIMENTAL DETERMINATION OF PENETRATION

An array of soft X-ray diodes viewing horizontally behind the pellet yields a qualitative view of the time-dependent pellet ablation rate and an accurate measurement of the time at which the ablation process ends (Figure 1). The structure is similar to that exhibited by the D_α light viewed along the pellet path. Pellet penetration depth is determined from this data together with data from an array of soft X-ray diodes viewing the pellet trajectory vertically (Figure 2). These signals also provide the pellet speed in the plasma (0.75-1.2km/s) which may be compared with the speed deduced from time-of-flight measurements in the pellet launcher. Pellets, nominally 3.6mm and 4.6mm cylinders of equal diameter and length, penetrate a distance 0.5-1.2m, the distance between the limiter and the magnetic axis being about 1.1m.

3. NEUTRAL GAS AND PLASMA SHIELDING MODELS

In the NS model monoenergetic electrons are shielded from the pellet by a layer of dense molecular hydrogenic gas. A fit to the numerical solution of the hydrodynamic equations of mass, momentum and energy in the neutral shield, assuming uniform volumetric heating, leads to a relationship between the energy flux and the thickness of the neutral shield. An energy balance at the pellet surface provides a second relation between the energy flux and the ablation rate. The NGPS model extends the solution of the neutral shield by treating the electrons as having a Maxwellian distribution and adding contributions from fast ions with both of these effects increasing ablation. A cold plasma shield extending along the magnetic field is also present, increasing the shielding of incident electrons and thus decreasing ablation. The effective ionisation radius is considered as the only free parameter in our applications of the NGPS model.

The plasma response during pellet ablation is represented by adiabatic mixing of the ablatant plasma with the plasma electrons in the NS model (collisional plasma), whereas the incident electron distribution function is depleted in the NGPS model (collisionless plasma) which is more appropriate for JET plasmas.

4. COMPARISON BETWEEN EXPERIMENT AND THEORY

JET geometry and plasma parameters (electron density profiles from 7 vertical chords of an FIR interferometer and temperature profiles from 2nd harmonic ECE data) are used to assess variations in the ablation model. The data set used for the comparison between the experimentally determined penetration distance and that obtained by modelling is considerably extended beyond that of Ref [3] and now contains about 100 discharges. Integration of the FIR chordal data indicates that the smaller pellets contain about 85% of the mass of a 3.6mm cylinder while the larger pellets contain about 70% of the mass of a 4.6mm cylinder. This mass discrepancy appears to be systematic and likely arises during pellet formation and acceleration rather than during the ablation process. We use 85% of the mass for all of the 3.6mm diameter pellets (spherical radius of 1.95mm assumed) and 70% of the mass for the 4.6mm diameter pellets (spherical radius of 2.34mm assumed).

The pellet velocities determined from time-of-flight and vertical soft X-ray data agree to within about 10% - this yields no significant difference in calculated penetration depths. Variation of the pellet size from 60-95% leads to less than ±5cm in the calculated penetration depths around the reported values. Uncertainties in the electron density and temperature data is greatest in the outer edge of the plasma; sensitivity to the density variation is weak while variation of the electron temperature in the expected range leads to an error of ±5cm in the calculated values. Measured penetration depths are accurate to within half the separation between vertical soft X-ray chords or ±3cm.

4.1 Ohmic Heating Alone

The NS model does not reproduce very well the penetration in ohmic discharges, especially for deeper penetration (Figure 3a). This is because the neutral shield solution for monoenergetic incident electrons does not adequately represent the penetration of electrons from the tail of the distribution when the electron temperature exceeds about 1keV [2]. The agreement between theory and experiment is improved but consistently low with the NGPS model and an ionisation radius fixed at r_o = 3.5mm independent of pellet radius, r_p (Figure 3b), the model used in earlier predictive calculations for JET[4]. This agreement can be further improved by fixing the thickness of the ionised shield at 1mm, that is, an ionisation radius of $r_o = r_p + 1$mm (Figure 3c).

4.2 Additional NBI and ICRF Heating

With additional heating the NS model again shows discrepancies between calculated and experimental depths comparable to those for ohmic discharges. The NGPS model with a 1mm thick ionised shield and ignoring any fast ion contributions to the ablation process gives an adequate fit to the data (Figure 3d) with a spread comparable to that found in ohmic

discharges. From this we conclude that fast ion effects are not important at the present power levels. During high power NBI shots, the electron temperature in the outer plasma rises above 450eV where the shield thickness to stop electrons becomes greater than that to stop 80kV deuterium ions [2]. Furthermore, even with 8MW of NBI injection the fast ion energy flux in JET is an order of magnitude lower than the electron energy flux at all radii.

5. CONCLUSIONS

It is found that the NGPS model, which includes both a dense neutral gas shield and a cold plasma shield extended along the magnetic field lines, reproduces the JET experimental data for pellet penetration when the effective thickness of the neutral gas layer is set at 1mm. Good agreement is found on the basis of electron ablation alone indicating that fast ion effects during NBI and ICRF heating are not important for the present levels and densities of fast ions. Detailed theoretical models of the spatial and energy distribution of fast ions during ICRF heating have not yet been developed for evaluating their effect on pellet ablation.

REFERENCES

[1] Milora S L, Foster C A, IEEE Trans on Plasma Sci PS-5 (1978) 12.

[2] Houlberg W A, Milora S L, Attenberger S E, "Neutral and Plasma Shielding Model for Pellet Ablation", submitted to Nuclear Fusion.

[3] Gondhalekar A, et al, in Plasma Physics and Controlled Nuclear Fusion Research (Proc 11th Int Conf, Kyoto, 1986) IAEA, Vienna, to be published.

[4] Watkins M L, Houlberg W A, Kupschus P, Stubberfield P M, Taroni A, Proc 13th Eur Conf on Cont Fusion and Plasma Heating, Schliersee, 1986, 10c(I), EPS (1986) 156.

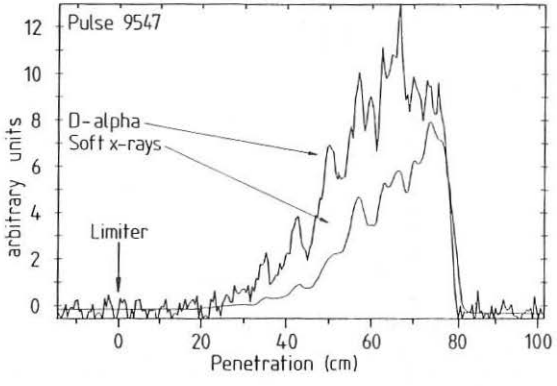

Fig 1: Typical D_α and soft X-ray signals as a function of the distance of the pellet from the outer limiter

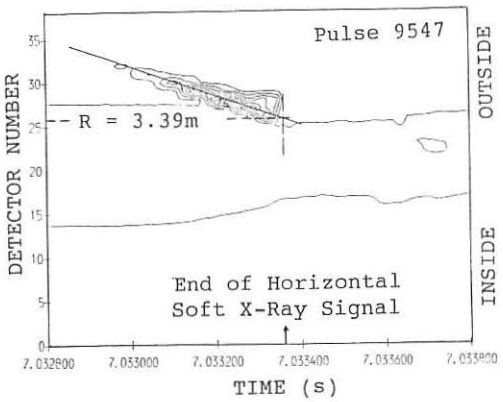

Fig 2: Intensity contours of vertical soft X-ray data during pellet injection. The slope of the curve passing through the peaks determines velocity and the end point is the maximum penetration depth.

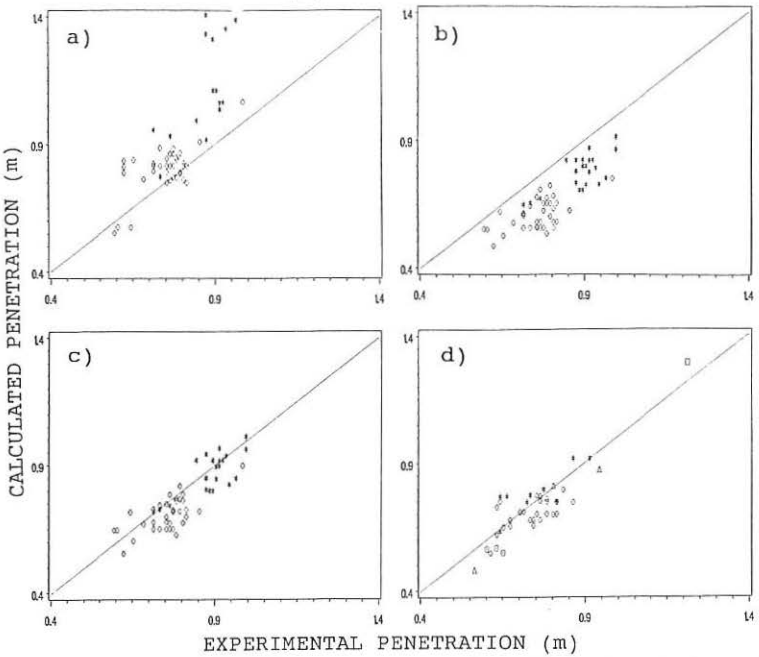

Fig 3: Calculated penetration depth vs experimental penetration depth for: a) NS model in OH; b) NGPS model in OH with r_o = 3.5mm; c) NGPS model in OH with $r_o = r_p$ + 1mm; and d) NGPS model in NBI and ICRF with $r_o = r_p$ + 1mm. Distances are measured from the limiter.

PROFILE EFFECTS ASSOCIATED WITH PELLET FUELING OF JET

A D Cheetham, D J Campbell, A Gondhalekar, N Gottardi,
R Granetz, P D Morgan and J O'Rourke

JET Joint Undertaking, Abingdon, OX14 3EA, UK

ABSTRACT

Pellet fueling experiments have been performed on JET using a single-shot pneumatic injector giving 4.6 mm (4.5×10^{21} atoms) or 3.6 mm (2.2×10^{21} atoms) diameter cylindrical deuterium pellets with velocities between 0.8 and 1.2 $km\cdot s^{-1}$[1]. In this paper the effects of pellet fueling on the density and temperature profiles of OH discharges are described. In particular the consequences of pellet penetration into the $q<1$ region are examined. It is shown that for significant modification of the density profile in JET, the pellet must penetrate the $q=1$ surface and major deposition must occur within the $q<1$ region. During pellet injection, the peak electron temperature drops by a large factor. But no evidence is found in JET for a low temperature front travelling faster than the pellet, in the plasma outside the sawtooth inversion region. However, when the pellet reaches this region very rapid (<50 μs) equalization of T_e occurs throughout the sawtooth inversion domain.

ELECTRON DENSITY PROFILE, $n_e(r)$

During pellet fueling there are three timescales to consider: (a) pellet ablation and penetration (<1ms), (b) inward transport of the ablated pellet material and peaking of the density profile (<500ms), (c) relaxation back to pre-pellet conditions (≥1s). Pellet ablation and penetration in JET have been modelled successfully using a modified neutral gas shielding model [1,2]. Immediately after ablation the density profile is hollow, fig.1a, the degree of hollowness depending on the penetration of the pellet, which in turn depends on the target plasma parameters. The density profile recovers to a peaked shape in ~200ms, with a central density 1.5 - 2 times larger than the pre-pellet value. Evolution to a peaked profile is discontinuous when sawteeth occur. Analysis of the density profile and its evolution for pellet fueled discharges has been made using a model of electron flux $\Gamma_e = -D\nabla n_e + Vn_e$. The diffusion coefficient $D(r)$ and the convection velocity $V(r)$ thus deduced are similar in magnitude to those for gas fueled discharges which showed a large scatter but no systematic dependence on $\bar{n}_e$, I_ϕ, B_ϕ or heating mode [3,4].

Analyses of individual pellet cases show that in the outer limiter configuration, V/D changes from $-0.2\ m^{-1}$ before pellet injection to $-0.4\ m^{-1}$ immediately after, reverting to $-0.2\ m^{-1}$ about 1s later, as evidenced by the more peaked density profile after pellet injection, which subsequently returns to its original form. In JET, significant peaking of the density profile does not take place unless pellet deposition within the $q<1$ region occurs. The peakedness of the density profile can be quantified by an effective minor radius, $r_e(t)$, of a torus of major radius R equal to that of the plasma column, and uniform density equal to the peak density $n_e(0,t)$, and containing the same total number of

electrons as in the plasma, $N_e(t)$, where

$$r_e(t) = \left[N_e(t)/n_e(0,t)\ 2\pi^2R\right]^{1/2}.$$

Fig.2a shows how $r_e(t)$ (normalized to the pre-pellet value, $r_e(0)$) evolves after pellet injection, for three pellets penetrating to different distances r_p from plasma center. We see that the profiles take ~0.5s to reach maximum peakedness, minimum $r_e(t)/r_e(o)$, then return to the pre-pellet shape after another 0.5s. The minimum value of $r_e/r_e(o)$ (corresponding to maximum peakedness) is plotted against pellet penetration (deduced from X-ray camera observations) in fig.2b. The graph shows clearly that deeper the penetration, greater is the peakedness of the density profile. Also, significant peaking occurs only if the pellet penetrates beyond the sawtooth inversion radius r_c. For the discharges examined here $40 \leq r_c(cm) \leq 50$. The most peaked profiles obtained in JET, with $n_e(o)/\bar{n}_e \sim 2$ and $n_e(o) \sim 1.2 \times 10^{20}\ m^{-3}$, have been observed in the magnetic separatrix configuration formed during single-null X-point operation. The target plasma conditions were such that the pellet penetrated to the center of the plasma, fig.1b.

ELECTRON TEMPERATURE PROFILE, $T_e(r)$

In Alcator-C [5] and TFR [6], the presence of a low temperature front propagating faster than the pellet, cooling the plasma ahead of the pellet, is inferred from high speed measurements of electron temperature at different plasma radii during pellet injection. The velocity of the cool front is deduced to be typically about twice that of the pellet. The observations have been interpreted as evidence of enhanced electron termal diffusivity, χ_e, and an increase of a factor ≥ 100 above the normal value has been deduced for OH plasmas. Further speculations about dependence of χ_e on the electron temperature profile have also been made [6]. Measurements of temperature front propagation in JET have been made using the 38 chord soft X-ray array that views the plasma diameter from above at the same toroidal location as the pellet flight path, and a 12 channel ECE array located 135° toroidally away from the pellet. Fig.3a is a plot of position (X-ray chord number) against time. The path of the pellet and the penetration depth are shown for three pulses, and the time at which the chord integrated X-ray signal starts to decrease, indicating cooling (corresponding to t_1 in [6]) is plotted. We see that at radii $r > r_c$ the signal starts to decay 10-50 μs before the pellet arrives, but there is no evidence of a cold front travelling much faster than the pellet (V~1 Km/s). When the pellet reaches the sawtooth inversion radius r_c, as determined from tomographic reconstruction of the X-ray data, immediately (<50 μs) the electron temperature over the whole central region decreases. Fig.3b shows a similar plot for a series of pulses with a higher value of q(a) such that the $q<1$ region is smaller. The same behaviour is seen again. The observations of figs.3a and 3b, which are based on chord integrated soft X-ray measurements, are confirmed by ECE measurements of local T_e. The extremely fast timescale of the profile collapse is comparable to that seen during the sawtooth collapse phase in JET, and implies a χ_e far in excess of the value determined by heat pulse propagation, $\chi_e \sim 2.5\ m^2 . s^{-1}$ [7], for OH JET discharges. Thus there is evidence for enhanced χ_e inside the sawtooth inversion region, but not in the region $r > r_c$ as claimed elsewhere [6].

The duration of pellet ablation (<1 ms) is much shorter than the sawtooth period in JET (~100 ms). The pellets are injected randomly at different stages of the sawtooth cycle, from shot to shot. The anomalously high value of χ_e, however, is independent of the phase of the sawtooth with respect to pellet injection. The similarity between the enhanced central transport which is observed during pellet injection, and that seen at a sawtooth collapse suggests a common origin for the rapid thermal loss in the two processes. Furthermore, it underlines previous observations in JET that during sawtooth collapses, thermal transport can take place on a timescale much faster than that predicted if macroscopic magnetic reconnection were to occur and cause it [8].

REFERENCES

[1] A Gondhalekar et al., 11th IAEA Conference on Plasma Physics and Controlled Nuclear Research, Kyoto, Japan, 1986. Paper IAEA-CN-47/I-I-6.

[2] M L Watkins et al., "A Model for Pellet Ablation in JET". This conference.

[3] A Gondhalekar et al., Bull. Am. Phys. Soc., 30 (1985) 1525.

[4] A Cheetham et al., 13th European Conf. on Contr. Fusion and Plasma Physics, Schliersee 1986, Europhysics Conference Abstracts, 10c I (1986) 240.

[5] C Gomez et al., Bull. Am. Phys. Soc., 29(1984)1320.

[6] L Laurent et al., Plasma Physics and Controlled Fusion, 28, 1A (1986) 85.

[7] B J D Tubbing et al., "Heat pulse propagation in relation to the energy confinement in JET". This conference.

[8] D J Campbell et al., Nuclear Fusion, 26(1986)1085.

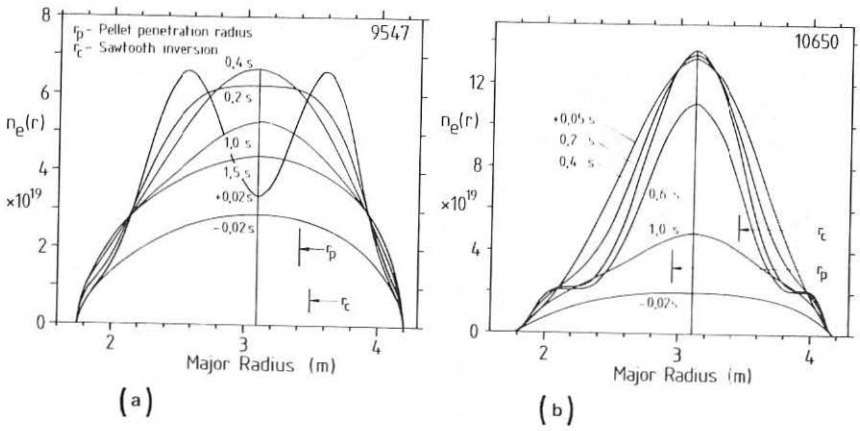

FIG 1: Temporal evolution of the density profile for 1.5s after pellet injection in (a) Limiter discharge, I_ϕ=3 MA, B_ϕ=3.1 T, q(cyl)=3.5; (b) X-point discharge, I_ϕ=2 MA, B_ϕ=2.2 T, q(cyl)=3.3

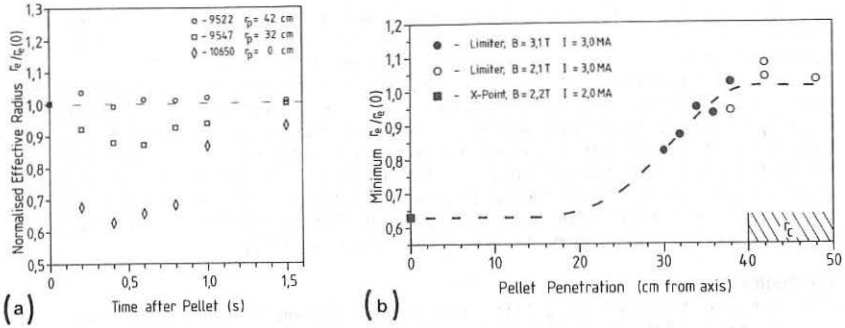

FIG 2: (a) $r_e(t)/r_e(0)$ for three different pulses.
(b) Minimum $r_e(t)/r_e(0)$ taken from (a), as a function of pellet penetration.

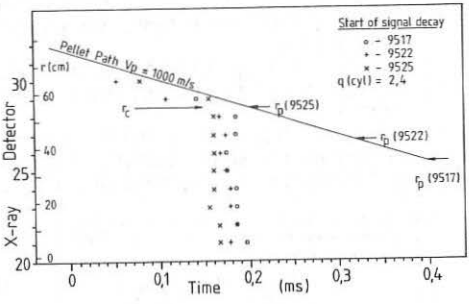

FIG 3:

X-ray detector (radial position) Vs. time, showing the pellet path and the start of the decay of the chord integrated X-ray flux for that detector.

(a) I_ϕ=3 MA, B_ϕ=2.1 T, q(cyl)=2.4
(b) I_ϕ=3 MA, B_ϕ=3.1 T, q(cyl)=3.5

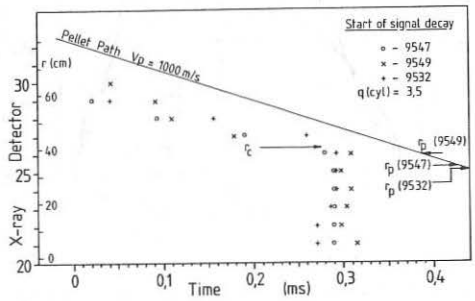

MEASUREMENT OF PLASMA PARAMETERS IN THE LUMINOUS REGIONS OF PELLETS INJECTED INTO TOKAMAKS

D.H. McNeill, G.J. Greene, J.D. Newburger, D.K. Owens, G.L. Schmidt, and D.D. Schuresko*

Plasma Physics Laboratory, Princeton University, Princeton, New Jersey 08544, U.S.A.

The properties of ablating pellets injected into large tokamaks are an active subject of research today because of the extensive use of pellet fuelling.[1] Measurement of the lineshapes of atomic hydrogen lines emitted by pellets provides information on the electron density and temperature in the luminous region of the pellet cloud. Knowledge of these parameters may help in determining the mechanism and rate of pellet ablation. This paper supplements previously published data[2] on the electron density and temperature at the moment of peak luminosity in the emitting region of solid deuterium pellets injected into the PLT tokamak plasma with time resolved polychromator data which yields the time dependence of the electron density and temperature for single pellets. In unfragmented pellets the electron density rises (from minimum measured values of 2-3x10^{15} cm^{-3} up to 1-5x10^{17} cm^{-3}) along with the H alpha intensity (which rises as high as 15 kW or more) throughout the pellet lifetime, while the electron temperature falls from about 4 eV to 2 eV or less. At the end of the pellet flash the wide Stark-broadened H alpha profile is often combined with a narrow peak at the line center from intense emission in lower density regions. The polychromator used for this experiment is being modified and installed on the TFTR tokamak for more detailed studies of pellet behavior.

The earlier PLT data were obtained using a single channel monochromator that was tuned in wavelength from one shot to the next together with a fixed broadband H alpha monitor. In that experiment the sampling rate was 10 kHz and the detector amplifier decay time, ≈100 μs; hence, the measurement was weighted to the most intense portion of the pellet flash. The shot-to-shot variability of the data precluded time resolution. Here the earlier data are extended in two ways: numerous samples (50 μs apart with an amplifier fall time of ≤20 μs) were taken during each pellet flash with a polychromator which permitted evaluation of the pellet plasma parameters at each sample time.

Light from the pellets was collected by a 400-μ-diam quartz fiber that viewed the pellets a distance of ≈80 cm from the pellet path roughly normal to their trajectory at its midpoint. The output of the fiber was collected by a lens and focussed onto the entrance slit of the polychromator. The polychromator has ten channels with photomultiplier detectors. In the experiments we recorded data from a monitor (a single 15.5 nm fwhm interference filter centered near the D alpha line, 656.1 nm, with a photomultiplier detector) and from 7 of the polychromator channels. The 7 channels had passbands centered at wavelengths from 636 to 657 nm with base widths of up to 4.0 nm. Because the spectral intensity of the line varies rapidly over the wide bandwidths of the individual channnels, the observed polychromator and monitor signals must be compared with computed profiles

which have been obtained by taking the convolution of the measured instrument function of each of the channels with theoretical Stark broadening profiles[3,4] for various densities and temperatures. Profiles were calculated using a continuum background corresponding to various temperatures under the assumption that the emitting region for the continuum is the same as that for H alpha; that is, the temperature was evaluated using the line-to-continuum intensity ratio. Figure 1 shows the expected signals in the monitor (plotted on the ordinate) and eight polychromator channels (The channel labelled 9 was not used.) for an electron density of $1 \times 10^{17} cm^{-3}$ and temperatures of 10, 20, and 40 kK. The temperature variation of the profile is evident

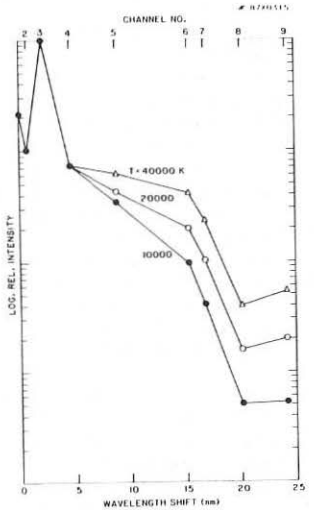

Figure 1

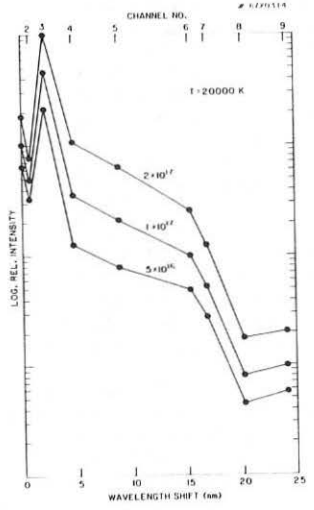

Figure 2

at these and lower densities. At densities an order of magnitude higher, on the other hand, the temperature dependence of the profile is weak. Figure 2 shows the relative variation with density in the calculated signals from the monitor and eight polychromator channels for densities of 0.5, 1, and 2×10^{17} cm^{-3} with a temperature of 20 kK. The fits with the experimental data were excellent except at the end of the pellet lifetime, when the signal in the monitor and channel 2 were higher than the computed profiles that fit the remainder of the channels. This appears to be the result of additional emission near the line center from lower density regions outside the pellet core.

The parameters of the tokamak plasmas into which the pellets were injected were typical of PLT: line average electron densities of $\approx 2 \times 10^{13}$ cm^{-3} and peak electron temperatures of 1-1.3 keV. Pellet electron

densities as low as $2x10^{15}$ cm^{-3} were measured in the first 100 μs of the flash from many of the pellets. At earlier times signals could be detected in the first polychromator channel and monitor, but that was not sufficient to derive a density. As the signals extended into the third channel, it was clear that the line was broadening, and when the signal levels were adequate it was possible to obtain a density value. At the earliest times for which a density could be obtained, the temperature was usually 30-40 kK. At later times, the density was greater, the signal extended to more channels (usually all eight) and the temperature fell to 20 kK or slightly less at the end of the pulse. Peak densities of $1-10x10^{17}$ cm^{-3} were observed at the end of pellets which entered the discharge in single unfragmented form. For these pellets the overall duration of the flash as seen by the H alpha monitors was ⩽300 μs. Figure 3 shows the time variation in the density (cm^{-3}) derived from the Stark broadening measurements for nine pellets. The time scale has been set arbitrarily so that a time of 250 μs corresponds to the peak intensity seen by the polychromator. (Because of a limited viewing aperture, the peak in the polychromator monitor signal occurs earlier than that in the external H alpha monitors, which occurs at the end of the pellet lifetime.) The lowest and second from the top of these traces are from pellets which appear to have been in fragments that entered the discharge over an extended period, so that the overall duration of the flash from them was longer. For most pellets the electron density in the luminous region is increasing continuously until the end of the flash, with a doubling time on the order of 50 μs. One striking feature of the

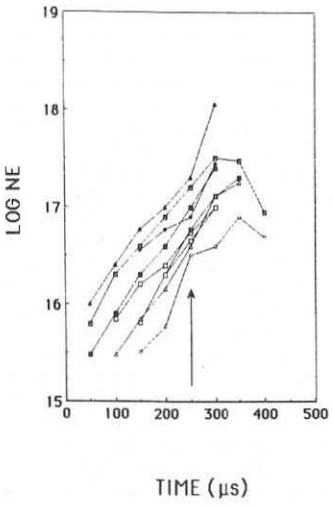

Figure 3

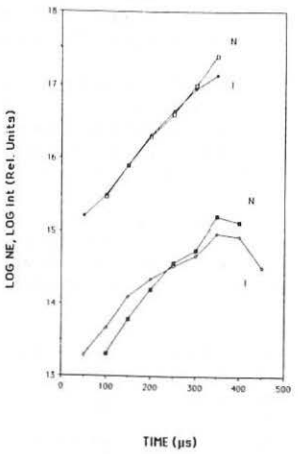

Figure 4

pellets is that the total intensity of the H alpha emission from them is approximately proportional to the electron density measured by Stark broadening over much of their lifetime. This is illustrated in Figure 4 which shows the relative electron density and H alpha intensity (seen by the external monitors) for two of the pellets shown in Figure 3. The upper pair of curves are for a single, intact pellet.

These observations require further analysis and comparison with other data to be obtained in future experiments. For example, ion cyclotron resonance heating powers of ≤200 kW were applied to some of the target plasmas in this experiment, but the power was too low to produce the changes in ablation behavior observed at high RF powers. Some general indications of the pellet ablation behavior may be obtained from the present experiment as follows: if the emitting region is assumed to be in local thermodynamic equilibrium and the pressure of the plasma in the pellet cloud exceeds that of the surrounding plasma (Both of these statements appear to be true in the last 100-150 μs of the pellet flash), then the top comparison of Figure 4 indicates that the volume of the emitting region was inversely proportional to the electron density, provided self-absorption over most of the linewidth can be neglected. For a fixed surface area of the emitting region, the particle efflux from the pellet is then proportional to the luminous intensity. The broadband H alpha line monitor in the polychromator was calibrated absolutely. Thus, for example, in one shot the H alpha power was 3.1 kW when the electron density was 8×10^{16} cm^{-3} and the temperature 2 eV. If the radius of the emitting region is taken to be 1 cm, then the efflux of particles from the emitting shell is approximately 4×10^{23} particles/s, and the ratio of H alpha photons to escaping particles is roughly 0.03. Photographic evidence of the emission region dimensions and other time resolved data are needed to develop a more precise understanding of the pellet behavior, including the ablation rate and the large fluctuations observed in the total H alpha signal.

The present apparatus is now being installed on the TFTR tokamak. Several changes are being made improve the system: (1) a diffuser will be used on the collecting fiber to avoid angular variations in the system's collecting efficiency; (2) higher sampling rates and faster amplifiers (500 kHz) will be used; (3) both H alpha and H beta monitors will be used (to obtain T_e by the line ratio method); and, (4) the most sensitive channels near the line center will be attenuated to enhance the relative signal levels in the outer channels.

This work has been supported by the U.S. Department of Energy under contract No. DE-AC02-76-CH03073.

REFERENCES

*Permanent address: Oak Ridge National Laboratory, Oak Ridge, TN 37830.

[1]M. Kaufmann, Plasma Physics and Controlled Fusion 28, 1341 (1986).

[2]D.H. McNeill, G.J. Greene, and D.D. Schuresko, Phys. Rev. Lett. 55, 1398 (1985).

[3]H.R. Griem, Plasma Spectroscopy, McGraw-Hill, New York (1964).

[4]H.R. Griem, Spectral Line Broadening by Plasmas, Academic Press, New York (1974).

HYDROGEN AND DEUTERIUM PELLET INJECTION INTO OHMICALLY AND ADDITIONALLY ECR-HEATED TFR PLASMAS

TFR Group (presented by H.W. DRAWIN)
Association EURATOM-CEA
Département de Recherches sur la Fusion Contrôlée
Centre d'Etudes Nucléaires, Cadarache
13108 St PAUL LEZ DURANCE/FRANCE

ABSTRACT :

The ablation clouds of hydrogen and deuterium pellets injected into ohmically and electron cyclotron resonance heated (ECRH) plasmas of the Fontenay-aux-Roses tokamak TFR have been photographed, their emission has been measured photoelectrically. Without ECRH the pellets penetrate deeply into the plasma, the clouds are striated. Injection during ECRH leads to ablation in the outer plasma region. The position of the ECR layer has no influence on the penetration depth which is only a few centimeters. The ablation clouds show no particular structure when ECRH is applied.

EXPERIMENTAL SET-UP

Single solid hydrogen and deuterium pellets were injected into TFR plasmas (major radius R_o = 0.98 m, plasma radius a $\simeq$ 0.18 m) using a pneumatic pellet injector constructed by the SBT, CEA Grenoble. The pellet velocities were $v_p \simeq$ 700 m/s. $1.3.10^{19}$ atoms per pellet were on the average deposited in the plasma. The pellets were injected in radial direction, the pellet trajectory was observed under an oblique angle $\beta(r)$ with respect to the injection plane, see figure 1. The $H_\beta(D_\beta)$ emission was measured simultaneously by means of a photomultiplier connected to a fast acquisition device.

The electron cyclotron waves of frequency ν = 60 GHz were launched by wave guide antennas placed in the equatorial plane at torus ports opposite to the pellet injection port.

The experiments were carried out under the following conditions : plasma current $I_p \simeq$ 110 kA, toroidal magnetic field induction B_Φ = 2.1 to 2.4 T corresponding to r = -1 to +11.6 cm for the position of the resonance layer relative to the center ($r = \rho$) of the torus chamber. The mean electron density was $\langle n_e \rangle \simeq 1.2.10^{19}$ m^{-3}, the ohmic power $\simeq$ 150 kW without ECRH. Additional ECRH was provided by three gyratrons, with 150 kW/gyratron absorbed power in the plasma. During ECRH the ohmic power decreased to a level of appr. 80 to 90 kW. All measurements were carried out during the current plateau of the discharge. The plasma column showed generally strong horizontal displacements five to ten milliseconds after injection of a first pellet. It was therefore not possible to make reproducible multi-pellet injection experiments for these particular plasma parameters.

RESULTS

1. Injection into ohmically heated plasmas

The time-integrated photographic pictures of the ablation clouds show bright and dark zones (striations) when a pellet is injected into only ohmically heated plasmas (figure 2a and Ref. [1]). The variation of emission along a pellet trajectory is also seen on the photomultiplier H_β signals (so-called ablation profile). Figure 3 shows an ablation profile $I(H_\beta)$ placed at the correct radial position. Also shown is the Abel-inverted radial electron density profile $n_e(r)$ immediately after pellet injection. In the present series of experiments an average penetration depth of $L_p \simeq 12$ cm was measured. The pellets did not reach the q = 1 surface situated at appr. r=4.5cm. The positions of the striations were note reproducible.

2. Injection into ECR heated plasmas

The ablation changes drastically when the pellet is injected during ECRH. Ablation takes place in the very outer region of the plasma column. Time-integrated photographies show no striations, see figure 2b. The visible emission extends in toroidal direction over the whole region covered by the optical device (appr. 25 cm). (In contrast to this, undoped pellets have for injection into only ohmically heated plasmas a toroidal extension of only a few centimeters [1,2]). The photomultiplier signals exhibit no special structure either. Figures 4 and 5 show for two different positions of the ECR layer the H_β ablation profile and the n_e profile. Figure 6 gives the position of the ablation maximum as a function of the position of the ECR layer. The latter has practically no influence on the pellet penetration depth which has on the average a value of $L_p \simeq 4$ to 5 cm. Also the number of applied gyrotrons does practically not affect L_p.

The reduced penetration of the pellet into the plasma during ECRH is possibly due to the presence of suprathermal electrons entering deeply into the pellet thus causing precocious evaporation. A similar effect has been seen during lower-hybrid wave heating [3].

The large toroidal extension of the ablation clouds is probably due to the long ionization time in the outer plasma region compared to the diffusion time of the neutral gaz.

On the basis of these experiments one cannot exclude difficulties in pellet fueling during LH current drive assisted by ECR waves and during powerful ECR heating.

ACKNOWLEDGEMENT

We thank the ECRH team of the FOM-Instituut voor Plasmafysica "Rijnhuizen", The Netherlands, for having ensured the ECR-heating during our pellet injection experiments.

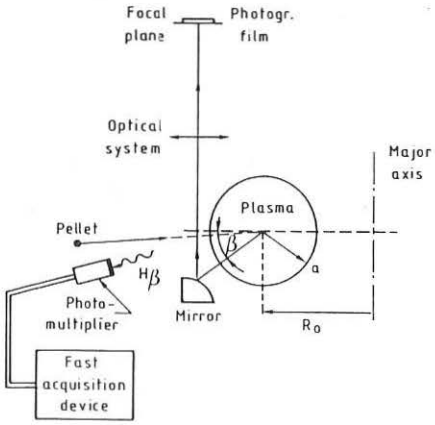

Fig. 1 - Optical measuring system

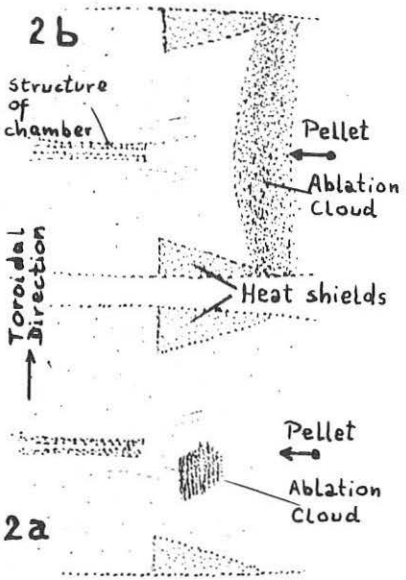

Fig. 2 - Schematic presentation of photographies showing undoped pellet ablation clouds in the TFR chamber.
a. Injection into ohmically heated plasmas
b. Injection into ECR-heated plasmas

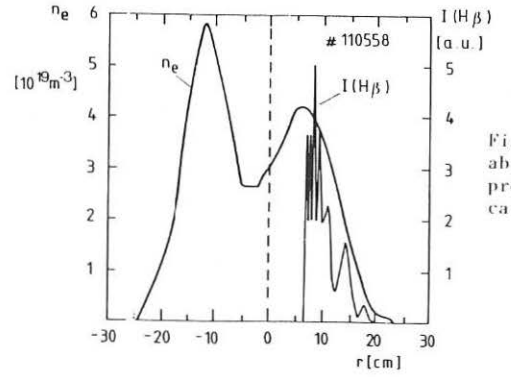

Fig. 3 - Intensity $I(H_\beta)$ of H_β ablation profile and radial n_e profile for injection into ohmically heated plasma.

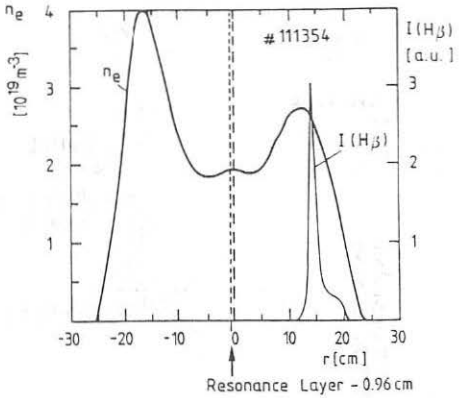

Fig. 4 - As figure 3 but for injection into ECRH plasma. Resonance layer at -0.96 cm.

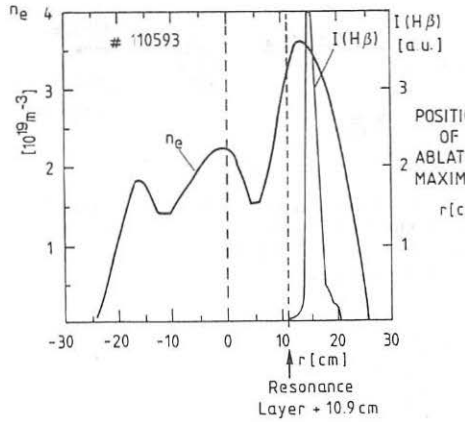

Fig. 5 - As figure 3 but for injection into ECRH plasma. Resonance layer at +10.9 cm.

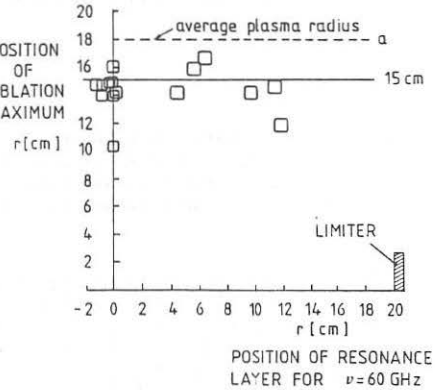

Fig. 6 - Position of the ablation maximum as a function of the position of the resonance layer.

REFERENCES

[1] TFR Group, Europhys. Lett. 2 (1986) 267

[2] TFR Group, "Pellet Injection Experiments on the TFR Tokamak", Report EUR-CEA-FC-1321, Cadarache, February 1987

[3] Kaufmann, M., Plasma Phys. Contr. Fusion 28 (1986) 1341

CHARACTERISTICS OF THE H-MODE IN DIVERTOR CONFIGURATION ON JFT-2M TOKAMAK

N.Suzuki, Y.Miura, M.Hasegawa*, K.Hoshino, S.Kasai, T.Kawakami, H.Kawashima, T.Matoba, T.Matsuda, H.Matsumoto, M.Mori, K.Odajima, H.Ogawa, T.Ogawa, H.Ohtsuka, S.Sengoku, T.Shoji, H.Tamai, Y.Uesugi, T.Yamamoto, T.Yamauchi, K.Hasegawa, A.Honda, I.Ishibori, Y.Kashiwa, M.Kazawa, K.Kikuchi, Y.Matsuzaki, K.Ohuchi, H.Okano, E.Sato, T.Shibata, T.Shibuya, T.Shiina, T.Tani and K.Yokoyama

Japan Atomic Energy Research Institute
Tokai-mura, Naka-gun, Ibaraki-ken, 319-11, Japan
* On leave from Mitsubishi Electric Co.

ABSTRACT Parameter dependences of the H-mode in a single-null divertor configuration were surveyed on JFT-2M. Threshold power for the H-transition increases with surface safety factor and depends on gas species. Gross energy confinement time increases with plasma current and does not depend on gas species.

1. INTRODUCTION and EXPERIMENTAL CONDITIONS

Several tokamaks with a divertor have shown a possibility of the high confinement mode (H-mode). JFT-2M[1] has capability of elongated limiter discharges and open divertor discharges, and in both configurations the H-mode has been observed[2,3]. In this paper we concentrate on the H-mode in the single-null divertor configuration, where distance between the null point and divertor plates is around 7 cm and clearance between plasma surface and poloidal limiters is larger than 8 cm (Fig.1). Poloidal limiters and divertor plates are made of graphite, stand apart from inner wall surface by 65 mm and 80 mm respectively. Co- and counter injection of hydrogen neutral beam with each maximum power of 0.8 MW were used . net input power is estimated as 90 % of torus input for co-injection and 70 % for counter-injection. In this experiment, Ti-gettering was used to obtain a clean plasma, dominant metal impurities are iron and titanium. Good monitors for the H-transition are Hα/Dα signals from 3 directions, edge temperature Tedge by ECE, edge density Nedge by FIR interferometer and plasma stored energy Ws by magnetics (diamagnetics and magnetic fitting method).

2. THRESHOLD POWER and DENSITY for the H-TRANSITION

As well known, there exist the threshold input power Pth and electron density Nth for the H-transition and they depend on various parameters such as magnetic configuration, safety factor, gas species, cleanliness, direction of grad B drift and so on. On JFT-2M, Nth has no clear dependence on safety factor and is nearly the same for H, D and He divertor discharges. Its range is 1.5 - 2.0 x 10 E13 / cc and which lies on the low density region expressed by the neo-Alcator scaling, where ohmic confinement time depends on safety factor. But observed Nth has no such dependences, so it seems to indicate a

significant effect of absolute density itself for the H-transition.

The threshold input power Pth was investigated with Ip-scan and Bt-scan. Pth increases with Bt and decreases with Ip. So its parameter dependence can be summarized as dependence on the safety factor. The safety factor q is defined usually in two manners, that is a cylindrical one q-cyl and a surface one q-s defined on a little inside magnetic surface. Within the same single-null configuration, it is difficult to say which is a better choice. But we can observe the H-transition also in double-null divertor and D-shaped limiter discharges[4], so to compare various configurations, q-s seems to be reasonable choice rather than q-cyl as the safety factor determining the H-transition. In the H-mode two types of $H\alpha/D\alpha$ signal (burst and burst-free) are recognized. For the burst case, increases of electron density and radiation power are pulled down at every burst. On the other hand, for the burst-free case density and radiation power increase up to some limit where H to L-transition occurs, then during the L-phase reduction of radiation power seems to prepare again necessary conditions for the H-transition. These features of H-mode depend especially on input power level. For H plasma, power range of the burst type is comparatively wide up to about double of Pth. For D plasma, the burst-free type is dominant and the burst type is limited around Pth. The Pth dependences on the safety factor and gas species are shown in Fig.2. The Pth increases nearly with q-s in high q region (>3) and roughly constant in low q region (<3). In the low q region, reason for the scattering of Pth is not clear, but it may comes from severe conditions for MHD activities. It must be noted that Pth is well expressed only with q-s for different plasma current.

Gas species also affect Pth. At same q-s of 3, Pth for H plasma is about 0.5 MW and larger than Pth of 0.2 MW for D plasma. Pth for He plasma was checked at one case and just below that for H plasma. This effect is also not clear to be attributed to intrinsic effect of gas species or to other accompanying effects such as profiles. Other factors observed experimentally are Ti-gettering and direction of ion grad B drift, they affect Pth by a factor of 2. Finally, outer clearance between plasma surface and limiters is a severe factor, as we can suppress the H-transition by insertion of a outer movable limiter nearly to plasma surface. Necessary outer clearance for the H-mode is 3 - 4 cm at power level of 0.8 MW. Bottom clearance is not so severe as outer one, and inner one can be guess from the H-transition in inside-touched limiter discharges. These clearance conditions suggest a key importance of scrape-off layer for the H-mode.

3. CONFINEMENT CHARACTERISTICS

Confinement improvement in the H-mode is clearly seen as additional increase of stored energy Ws by magnetics. This increase of Ws seems to come from formation of the so-called 'pedestal' in electron temperature and density profiles at the begining of the H-mode, then density increase contributes Ws rise rather than increase of temperatures. Throughout the H-phase is there some process to maintain the pedestal at plasma edge. The edge electron temperature

Tedge by ECE jumps up at the H-transition and keeps almost constant during the H-phase for H plasma. but decreases gradually down to the L-phase value for D plasma. And for high q case without sawtooth oscillations, Tedge rises slowly. So it is difficult to find out one threshold value for Tedge. Different time behaviour of Tedge between H and D plasma seems to come from impurity accumulation level measured as radiation loss power. On the other hand, electron density keeps to rise up till the H to L-transition occurs. Though precise pressure profiles have not been obtained, formation of pressure pedestal may be a key feature and grad P at the edge may be limited by some pressure-driven instabilities and/or MHD instabilities.

Improved confinement can be expressed with the gross energy confinement time τg and the incremental confinement time determined from power-scan experiments. But the latter involves large ambiguity within limited power-scan range. because of power dependent features of H-mode types especially in H plasma. So the τg of H-mode at same power level is compared for H, D and He plasma together with that of ohmic phase τoh . The τg for the H-mode is defined around peak Ws, because there is no steady state for the burst-free case. The τoh is a peak value in the density-scan data. So the density region for each confinement times is spread widely. Dependence of confinement times on Ip is shown in Fig.3. The τoh is nearly constant against Ip and depends on gas species, however, the τg is linearly proportional to Ip up to the lowest q limit of 2 and no dependence on gas species can be seen. This feature of H-mode confinement is very simple and interesting. Especially for H plasma, the τg exceeds the τoh enough at the lowest q. Figure 4 shows dependence of confinement times on Bt. The τoh is linearly proportional to Bt and there exists also dependence on gas species. But the τg has no dependence on Bt and gas species. The reason for these features of the H-mode remains as an open question, but it is clearly shown that the gross energy confinement time of the H-mode can exceed the ohmic one in H plasma.

ACKNOWLEDGEMENT

The authors are grateful to Drs. A.Funahashi, K.Suzuki, Y.Tanaka, M.Tanaka, K.Tomabechi and S.Mori for their continuous encouragement. We also thanks theory group for useful discussions.

REFERENCES

[1] T.Shoji, et al. in Proc. of 11th Europ. Conf., (Achen 1983) Vol.1, p.55

[2] S.Sengoku, et al., "Confinement and Fueling Studies during Additional Heating Phase in JFT-2M Tokamak" in 7th Conf. on Plasma Surface Interaction, (Princeton 1986), J. Nucl. Mater. 145/147 (1987) 556.

[3] K.Odajima, et al., "Confinement Studies of Additional Heated Plasma in JFT-2M Tokamak" in Proc. of 11th Int. Conf. on Plasma Phys. and Cont. Nucl. Fusion Research, (Kyoto 1986), IAEA-CN-47/A-III-2

[4] H.Matsumoto, et al., "Studies of H-mode in the Limiter Discharges on JFT-2M Tokamak" to be presented in this conference.

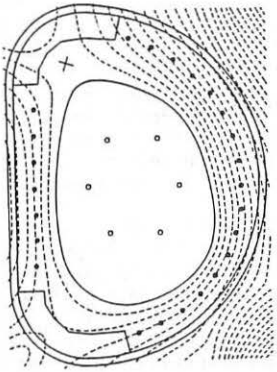

Fig.1 Single-null divertor configuration. o: filament current position for 'Magnetic Fitting' code, o: limiter position, x: null point.

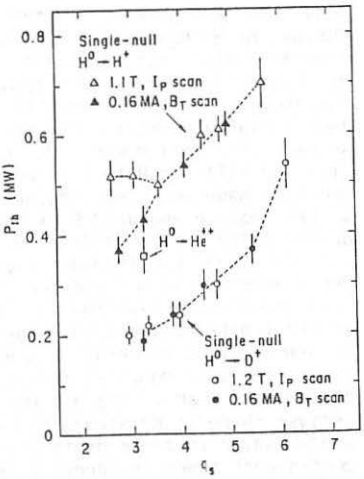

Fig.2 Threshold power Pth for the H-transition. Ip-scan (0.11-0.28 MA), Bt-scan(0.65-1.4 T). q-s: surface safety factor.

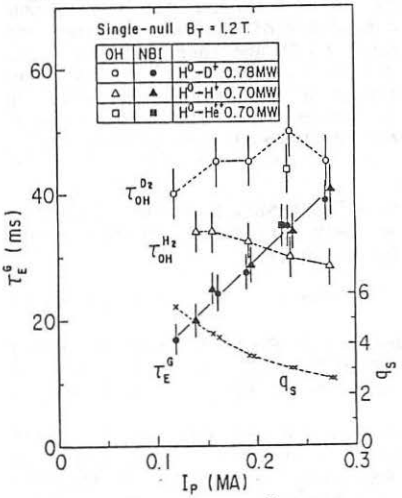

Fig.3 Dependence of gross energy confinement times on Ip for H, D and He plasma.

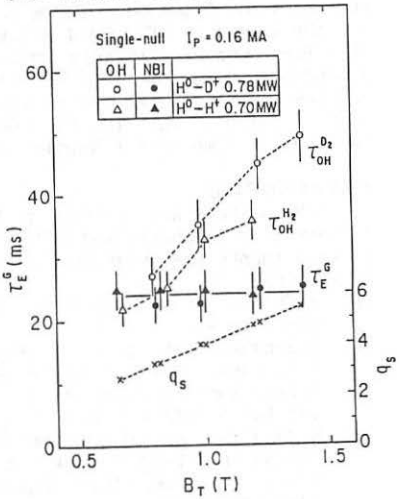

Fig.4 Dependence of gross energy confinement times on Bt for H and D plasma.

MODIFICATION OF SAWTOOTH BEHAVIOR USING RHF ON HT-6B TOKAMAK

Xie Jikang, Huo Yuping, Chen Jiayu, Li Guoxiang, Guo Decuan
Qin Pinjian, Fan Hengyu, Deng Chuanbao

Institute of Plasma Physics, Academia Sinica,
P.O.Box 26 Hefei, Anhui, P.R.China.

1. INTRODUCTION

While tokamak parameters approach the ignition condition, sawtooth becomes more and more important. Sawteeth set the limit of the central plasma temperature on a tokamak no matter how high the input power is. [1] [2]

As sawteeth has been widely observed and investigated on many tokamaks, some important phenomena can not be properly explained by kadomtsev model. New alternative theoretical model were presented. [3][4][5] But because of the restriction of diagnostics and experiment there still exist a gap between theory and experiment.

On HT-6B tokamak experiment of suppressing MHD perturbations has been carried out. The result shows that a weak resonant helical field (RHF) with a helical mode can suppress the resonant mode of MHD perturbation as well as other modes with different m numbers[6]. Further investigation found accompanying the outer mode suppression sawtooth behavior was modified obviously in its magnitudes, repetition periods and precursor oscillations and sometimes it might turn into a total different perturbation mode which did not appear during normal operation conditions. The experiment result is reported and the mechanism of the sawtooth modification is discussed in this paper.

2. MODIFICATION OF SAWTOOTH BEHAVIOR UNDER INFLUENCE OF RHF

On HT-6B tokamak there are two helical windings (l=2, n=1 and l=3, n=1) which can be used in DC or pulsed regime. Sawteeth and Mirnov oscillations and measured by an array of Au-Si surface barriar diodes, magnetic probes and cos mθ magnetic loops.

Three types of discharges are identified with respect to the defferent internal mode features, (A) sawtooth free (B) typical sawtooth and (C) 20-30 KHz oscillation on plasma centre. By applying a proper RHF, A type or C type might transfer to B type [Fig1] and in B type discharges the repetition period of sawteeth enlarged (from about 200 μs up to larger than 300 μs) and sawtooth magnetude increased by a factor of 3-5 [Fig.2].These phenomena are discussed detailly in the follows.

3. RELATIONSHIP BETWEEN SAWTEETH AND m=1 PRECURSOR

As discussed in [6], for plasma RHF is a local disturbance near q=1

surfaces but it can not only suppress the resonant outer MHD mode, but also coincidently effects all the modes concentrated near different q surface. In Fig.1, the S.X. ray signals through the central chords, which are idntified to be 1/1 mode, decreases whereas the sawteeth are triggered on with large magnitude. In Fig.3, after turning off RHF, sawteeth cease but about 20 KHz oscillations enhance again on S.X. signals inside q=1 surface ($r_s \cong 4$cm). This indicates that the internal disruptions characterized by sawteeth are not solely caused by growth of m=1 tearing mode.

4. MODIFICATION OF SAWTOOTH BEHAVIOR ACCOMPANIED WITH CHANGE OF ENERGY CONFINEMENT AND PARAMETER PROFILES

A careful comparison shows that in a B type discharge the ramp up slope of the sawteeth increases with RHF. That means the increase of the sawteeth magnitude is not simply because of the extension of repetition period which can be explained as the suppression of m=1 mode, moreover the central temperature increases more rapidly. This must result from the improvement of energy confinement at the plasma centre region.

The time delay between RHF turning on/off and response on sawteeth does not match the MHD characteristic time but varies according to the effectiveness of RHF. In Fig.3] the sawteeth continue about two cycles, that is to say in the order of millisecond which is comparable to the energy confinement time ($\cong 700$ μs).

When sawtooth magnitude becomes rather large with RHF, the inverse radius r_s increases and intensity of ECE increases which indicates the temperature rise near the plasma center.

All properties mentioned above verifies that the modification of sawtooth behavior is always accompanied with the change of energy confinement and profiles of plasma parameters.

How can a weak external RHF obviously influence the internal plasma energy processes?

5. GLOBAL CORRELATION OF INTERNAL AND EXTERNAL MODES

RHF experiments showed a strong correlation between the MHD modes with different m numbers. A weak RHF could only superpose less than 1% disturbance on the poloidal field of the discharge. It might resonantly influence the corresponding 3/1 or 2/1 mode and subsequentially affect all modes existed. Whenever the modes decreased, sawteeth appeared or increased in magnitude and period.

In a extreme case (normally with higher n_e) a C type discharge dominated by 20 KHz oscillations were taken place by giant sawtooth discharge which is characterized by inversed sawtooth on 8 cm and 10 cm (near to the edge of plasma) S.X. signal and even giant sawtooth-like oscillation on magnetic probes indicating significant change of plasma inner inductance resulting from rapid loss of plasma energy content. Such a distinct change was triggered by a weak RHF. [Fig.4]

In another extreme case (with lower n_e) RHF triggered different discharge mode with no typical sawtooth but a series of minor disruptions with the same repetition period like sawteeth symbolized as periodic spikes on both magnetic loop and S.X. signals. This kind of instability has been mentioned on our report on last European Conference but the difference is at this time only one RHF was applied with a mediat value. [Fig.5]

6. SUMMARY

The MHD instability in HT-6B plasma shows a global mode. A weak RHF may resonantly affect a local component, and result in a overall transition of the mode structure. Subsequently the property of plasma confinement and profile are modified and sawtooth behavior changed. Investigation of m=1 precursor shows that growth of magnetic island might not be the sole reason of the sawtooth collapse.

The experiment result gives an oppertunity that one can use RHF or other similar methodes to improve internal stability property and get rid of the occurrence of internal disruptions by a local moderate disturbance on a tokamak plasma.

7. REFERENCES

[1] Compbell,D.J., et al., Nuclear Fusion 26 (1986) 1085
[2] Furth, H.P., International Conf. on Plasma Phys. Lansanne 1984
[3] Wesson,J.A., Plasma Physics and Controlled Fusion 28 (1986) 243
[4] Wesson,J.A., et al., IAEA-CN-47/E-I-1-1
[5] Boyd, D.A., et al., IAEA-CN-47/A-VI-4
[6] Xie, J.K., et al., IAEA-CN-47/A-V-6

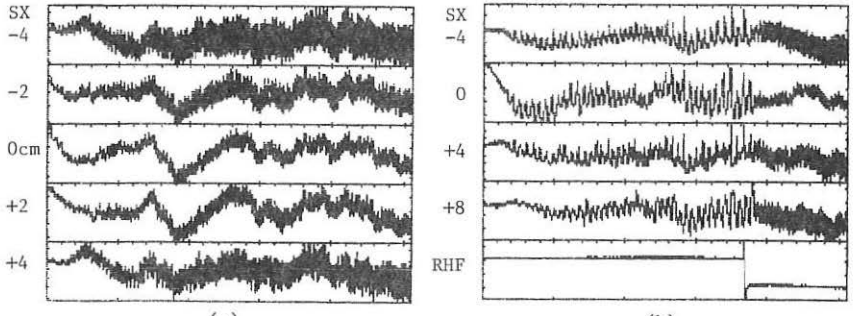

Fig.1 (a) S.X. signals on -4, -2, 0, +2, +4cm chord with 20 KHz signals
(b) S.X. signals showing sawteeth with RHF and transferring to 20 KHz oscillation when RHF turns off

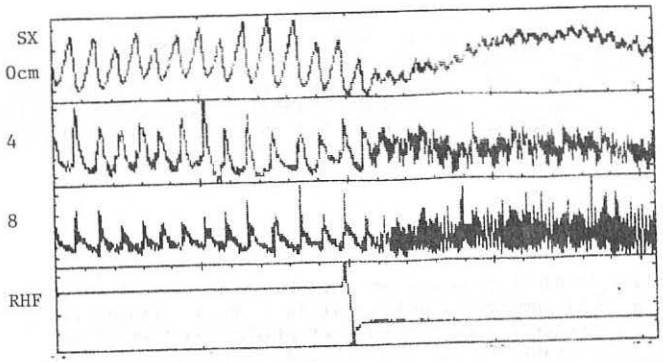

Fig.2 The large sawtooth magnitude decreases when RHF turns off.

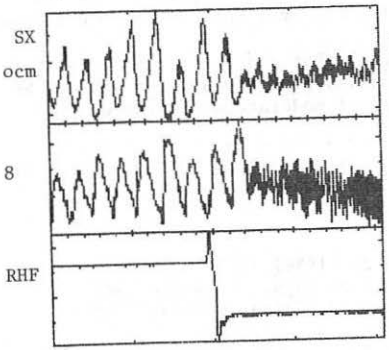

Fig.3 large sawteeth continuing about two cycles when RHF turning off to be campared with Fig.2

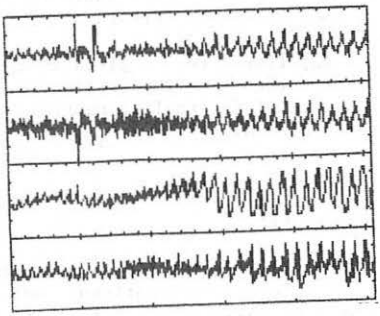

Fig.4 RHF triggerring large sawteeth observed on Mirnov Probes

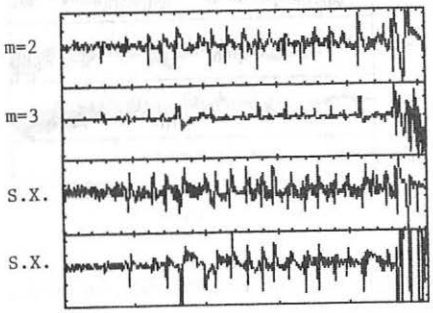

Fig.5 a mediat RHF causing a new discharge mode, symbolized by spikes with sawtooth period on magnetic loops and S.X. signals

THE STUDY OF RUNAWAY ELECTRON CONFINEMENT TO PROBE THE ELECTROMAGNETIC TURBULENCE IN OH, L-AND H-DISCHARGES OF ASDEX

F. Wagner, G. Fussmann, G. Becker, H.S. Bosch, H. Brocken, A. Carlson, A. Eberhagen, G. Dodel[1], H.-U. Fahrbach, O. Gehre, J. Gernhardt, G. v.Gierke, E. Glock, O. Gruber, G. Haas, W. Herrmann, J. Hofmann, A. Izvozchikov[2], E. Holzhauer[1], K. Hübner[3], G. Janeschitz, F. Karger, M. Kaufmann, O. Klüber, M. Kornherr, K. Lackner, M. Lenoci, G. Lisitano, F. Mast, H.M. Mayer, K. McCormick, D. Meisel, V. Mertens, E.R. Müller, H. Murmann, J. Neuhauser, H. Niedermeyer, A. Pietrzyk[4], W. Poschenrieder, H. Rapp, A. Rudy, F. Schneider, C. Setzensack, G. Siller, E. Speth, F. Söldner, K. Steinmetz, K.-H. Steuer, N. Tsois[5], S. Ugniewski[6], O. Vollmer, D. Zasche

Max-Planck-Institut für Plasmaphysik,
EURATOM Association, Garching, FRG

and

O.J. Kwon and P.H. Diamond, The University of Texas, Austin, USA

ABSTRACT Confinement studies of runaway electrons have been performed in order to elucidate the nature of electromagnetic turbulence and its role in ohmically and beam heated L- and H-plasmas. Under ohmic conditions, the confinement time τ_R of runaway electrons depends strongly on the choice of q_a; in the L-mode, τ_R degrades with beam power; in the H-phase, runaway electrons are again well confined. With plausible assumptions, a correlation length of the underlying microturbulence of 0.1 cm is found which requires a magnetic perturbation $B_r/B_0 \sim 10^{-4}$ to be consistent with L-mode confinement.

The confinement of runaway electrons (R.E.) has been studied in ASDEX in ohmically and beam heated L- and H-mode plasmas. R.E. are produced within the first hundred ms when the loop voltage reaches values up to 10V. Thereafter, the R.E. production rate decreases sharply; at 0.3s $n_e^{-1} dn_R/dt \sim 4 \times 10^{-4}$ s^{-1} and is still decreasing. In the birth phase of R.E., the plasma T_e- and n_e-profiles are still very broad probably resulting in a largely homogeneous R.E. density. During the current ramp-up phase (typically 600-800 ms), R.E. are continuously accelerated. After about 1 s (with the plasma current being in the plateau phase) the R.E. distribution reaches steady state at a mean energy of about 1 MeV and with maximal energy around 10 MeV.

R.E. are measured via the thick target hard X-ray bremsstrahlung emitted when their orbit intersects a molybdenum target placed at the plasma mid-plane a few cm outside the separatrix on the low field side. During the current ramp-up phase the hard X-ray radiation increases because the electrons become increasingly energetic though their number does not further increase. The transition of rational q-surfaces across the plasma surface destabilizes the magnetic field topology resulting in transiently

[1] University of Stuttgart; [2] Ioffe Institute; [3] University of Heidelberg; [4] University of Washington, Seattle, USA; [5] N.R.C.N.S. "Democritos", Athens, Greece; [6] Inst. for Nuclear Research, Swierk, Poland;

enhanced R.E. losses. Fig. 1a shows the initial discharge phase when current and density are ramped up and Fig. 1b displays the hard X-ray radiation indicating the sequence of rational q-surfaces moving from the interior across the separatrix. It is interesting to note that despite the anomaly of the magnetic field topology at the plasma surface of the magnetic limiter configuration (with q equal to infinity at the separatrix and a narrowly spaced sequence of rational q-surfaces at the plasma edge), the transit of a rational q_a-surface (q_a corresponding to the cyclindrical one ignoring the anomaly) still affects the quality of the magnetic field topology. During the subsequent plateau phase, R.E. are continuously lost; from the exponential decrease of the hard X-ray radiation a characteristic time is inferred which is interpreted as the confinement time of R.E. since the population and energy distribution of the R.E. is invariant during this period. Figure 2 plots the R.E. confinement time τ_R versus q_a in an ohmic B_O-scan. τ_R is generally a few 100 ms; for comparison, the global energy confinement time is between 80 and 90 ms. τ_R is clearly correlated with q_a and has a sharp minimum at $q_a = 3$ (the actual MHD q-value is only slightly larger because of the low β_p-values of the ohmic plasma). The confinement of R.E. is sensitively correlated with the quality of the magnetic field configuration. Away from $q_a=3$, τ_R has improved by at least a factor of 2. At the unfavourable case of $q_a = 3$, the hard X-ray radiation is strongly modulated by the sawteeth occurring in the plasma center /1/. Away from $q_a=3$, no distinct modulation is observed both at lower and higher q_a-values. This observation indicates the possibility that the resonant condition $q_a = 3$ at the edge destabilizes the plasma further in (probably at rational q-surfaces with smaller q-values) leading to enhanced transport of R.E. from the center through the edge.

The traces of Fig. 2 clearly demonstrate that the magnetic field configuration is disturbed throughout the plasma by a rational edge q_a-value. Although the R.E. respond to this degradation sensitively, the bulk plasma properties are not affected at all as shown in Figure 2 for the global energy confinement time τ_E. There is no other known global quantity of the main or the divertor plasma (which are known to sensitively respond to confinement changes of the main plasma, such as shown in Fig. 5) which is affected by the degraded field topology.
Figure 3 shows the variation of the hard X-ray radiation during a neutral injection pulse into the ohmic plateau phase. τ_R is sharply reduced and R.E. are quickly lost. (A second beam pulse later in the discharge does hardly show any increased radiation confirming the expectation that no R.E. are produced in the plateau phase). With NI, there is a simultaneous degradation of the confinement of R.E. along with the one for energy and particles (see Fig. 4). The sensitivity of the R.E. confinement on the quality of the magnetic field topology clearly indicates a substantial degradation already at low beam power causing a sharp drop in τ_R. Furthermore, sawteeth strongly modulate the hard X-ray radiation in the beam phase for all q_a-values (see Fig. 3) in a way it was only observed for rational q_a-surfaces at the edge in the OH-phase.

It is interesting to note that τ_R in the degraded L-regime of a NI-heated plasma does not depend on q_a like in the OH-phase. With NI, τ_R is sharply reduced but increases monotonously with B_O without a notch at $q_a=3$. Evidently, NI degrades the quality of the magnetic field structure to such

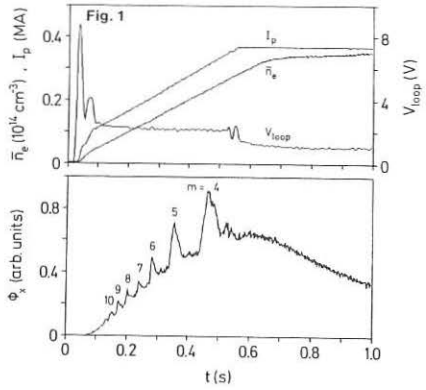

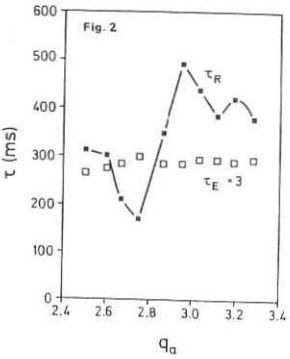

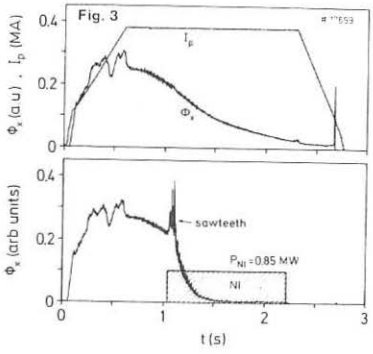

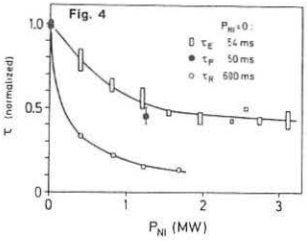

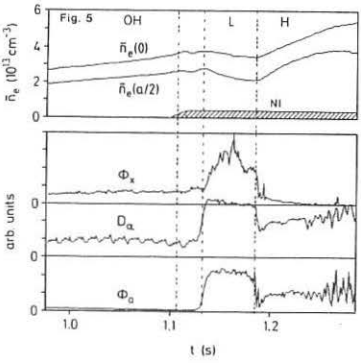

Fig.1: Current, density $\bar{n}_e$, loop voltage and hard X-ray radiation ϕ_X during current ramp-up.

Fig.2: Global energy (τ_E) and runaway electron (τ_R) confinement time in an ohmic B_T-scan.

Fig.3: Comparison of ϕ_X in an OH- and NI-discharge; the sawtooth modulation of ϕ_X is indicated.

Fig.4: τ_E, τ_R and particle confinement time τ_p versus NI-power normalized to the OH-values (as given).

Fig.5: Time dependence of 2 $\bar{n}_e$-traces, ϕ_X, H_α-radiation and particle flux ϕ_a in the divertor chamber for OH→L and L→H transition.

an extent that the additional geometrical disturbance is negligible. The uncorrelated q_a-dependence of τ_R and τ_E in the OH-phase raises doubts whether the OH confinement of the bulk plasma is indeed caused by the magnetic turbulence which is evidently responsible for the confinement of R.E. The question remains whether under beam heating conditions magnetic turbulence primarily determines transport or whether it accompanies dominant drift-like fluctuations simply because of rising β_p. In this context it is important to note that the confinement of R.E. sharply improves at the H-transition though β_p further increases due to improved global confinement. Both in the L- and H-phases we observe a clear correlation in the confinement properties of the bulk plasma and R.E.

Fig. 5 plots the time dependence of the hard X-ray flux together with the H_α-radiation in the divertor chamber (a measure of the energy flux into the divertor) and the flux ϕ_D of particles backscattered from the target plates (a measure of the particle flux). The simultaneous OH→L and L→H-transition is shown in the three signals all governed by different confinement properties. The sharp onset of the L-phase a few ms after beam initiation also indicates that the magnetic turbulence is obviously not due to rising β_p.

With the hypothesis that unlike the ohmic confinement, the degradation in the L-phase is predominantly due to magnetic turbulence, we can characterize the structure of the underlying mode from the ratio τ_E/τ_R. It is known that the ratio of τ_E/τ_R is not given by the inverse ratio of the electron velocities since the coupling of the R.E. to the mode is reduced by the shift of the $\vec{k}\cdot\vec{B}$ resonance due to magnetic drift effects /2/. These effects can be considered by a radial structure function S such that

$\tau_E/\tau_R = v^R/v^{th} \cdot S$ (v^R, v_R^{th} are the R.E. and thermal velocities, respectively). S depends on $L_s V_D/\delta X v^R$ (L_s= shear length, V_D^R = R.E. drift velocity, δX = radial correlation length) and can be approximated by $\exp-(L_s V_D^R/\delta X\, v^R)^2$ /3/. With the ratio of τ_E and τ_R at high beam power (see Fig. 4), $\delta X \simeq 0.1$ cm is calculated. This value is used to estimate the relative amplitude of the fluctuation

$\tilde{B}_r/B_o = (\chi_e^{th} \tilde{k}_\theta \delta X/\pi\, v^{th} L_s)^{1/2}$ (χ_e^{th} = thermal heat diffusivity, $\tilde{k}_\theta$ = average poloidal wave number) necessary to fully explain the level of thermal heat transport. Assuming poloidal mode number m=8 (Ref. /4/), the result $\tilde{B}_r/B_o \sim 10^{-4}$ is in agreement with the level of magnetic field fluctuations at the plasma edge deduced from measurements outside the separatrix (Ref. /4/). Scaling studies indicate that $\delta X \propto n^{0.2} B_o^{1.3} p^{0.1}$ and $\tilde{B}_r/B_o \propto n^{-0.1} B_o^{0.1} p^{0.6}$. Thus c/ω_{pe}-turbulence /5/ is an unlikely candidate while a model along the line of resistive pressure driven modes offers more promise.

References

/1/ G. Fußmann et al., in Plasma Phys. and Contr. Nucl. Fusion Research, 1978, Vol. 1, IAEA, Vienna (1979) 401.
C.W. Brown and J.D. Strachau, Nucl. Fus. 22 (1982) 1090.
/2/ H.E. Mynick and J.D. Strachan, Phys. Fluids 24 (1981) 695.
/3/ O.T. Kwon and P.H. Diamond, to be published.
/4/ G. Dodel, F. Holzhauer et al., this conference.
/5/ B.B. Kadomtsev, O.P. Pogutse in Plasma Phys. and Contr. Nucl. Fusion Research, 1984, Vol. 2, IAEA, Vienna 81985) 69.

STABILITY ANALYSIS OF ASDEX-H-MODE DISCHARGES

K. Grassie, O. Gruber, O. Klüber, M. Kornherr, H.P. Zehrfeld

Max-Planck-Institut für Plasmaphysik
Association Euratom-IPP, D-8046 Garching

1. Introduction : Due to the accessability of the H-regime, β_p values close to the Troyon limit can be achieved in ASDEX discharges with neutral particle injection at a moderate power level. In the last couple of years detailed β_p-optimization studies have been performed in a large range of values for the toroidal field ($1.2 < B_t < 2.7$ T) and plasma current ($0.2 < I_P < 0.48$ MA) with beam powers up to 4.5 MW.
In many cases a 'hard-β saturation' is observed, when β approaches β_c, i.e. after reaching its maximum value β decreases to a lower stationary level with $\beta/\beta_c \sim 0.7$. This stationary phase lasts of the order of 100 ms and is a peculiar property of ASDEX-high-β discharges — in contrast to Doublet-III, where generally a disruption occurs a couple of ms after β has reached its maximum.
Clearly it is of considerable interest to investigate the MHD activity of these discharges and compare them with theoretical calculations in order to get more insight in the physical mechanisms that govern the high-β_p phase. Our tool for this investigation is the GA-3D-CART code, which is based on the large aspect ratio expanded MHD equations at finite β. This set of equations is solved for realistic ASDEX equilibria, which have been determined by the Garching free boundary flow equilibrium code NIVA. The necessary profile information has been obtained from a detailed analysis of measured profiles by means of the PPPL code TRANSP [1,2].
For a detailed investigation of the MHD-characteristics of ASDEX-H-mode discharges we refer to O. Klüber et al. [3]; a description of the CART-code is given in Ref.[4].

2. Linear results : Typical results for the perturbed, linearized $n = 1$ magnetic flux ψ(x,y) for discharges with medium β_p ($\beta_p \sim 1$) and large β_p ($\beta_p \sim 2$) are presented in Ref.[5] for constant vacuum resistivity $\eta_V = 10^{-2}$ (in rationalized emu).
We generally find that the global MHD-activity is mainly caused by tearing or pressure driven modes. External kink contributions are weak for our cases ($\Delta\tilde{\gamma} < 10\%$), as can be shown by moving the conducting wall to the plasma surface. A change in the driving mechanism for the instability with increasing pressure is indicated by the η-scaling of the growth rates. It turns out that low-β_p -discharges scale like $\eta^{3/5}$, as expected for tearing modes, whereas an interchange mode scaling $\tilde{\gamma} \sim \eta^{1/3}$ is found for high-β_p -discharges. Contour-plots of the magnetic flux show that the predicted mode activity is concentrated at the outer side of the torus and that the poloidal wavelength there is in general smaller than that at the inner side [5,6]. This behaviour is not only in contradiction with experiment, but also with the expectation based on the assumption that the main part of the perturbed current flows parallel to the equilibrium magnetic field. Then, since the field line slope is smaller at the inner side of the torus, one expects a shorter poloidal wavelength there. This discrepancy is considered a consequence of the particular treatment of toroidal effects by the reduced equations.
Another problem consists of the observation of large poloidal mode numbers, which clearly exceed the q_a value of the discharge under consideration [3]. An example is the high-β_p discharge #18041 ($\beta_p \simeq 1.92$) with $q_a = 3.4$ and a measured value of $m \simeq$

$4, n = 1$. It turns out that a simulation of these results with constant vacuum resistivity is impossible. This problem can be resolved by noting that small vacuum resistivities increase the effect of the perturbed current density on the evolution of the corresponding magnetic flux, if we assume the ratio of convection and resistivity term to depend only weakly on η_V. Since

$$J = -\nabla_\perp^2 \psi \sim (m^2 + n^2)\psi_{m,n}, \tag{1}$$

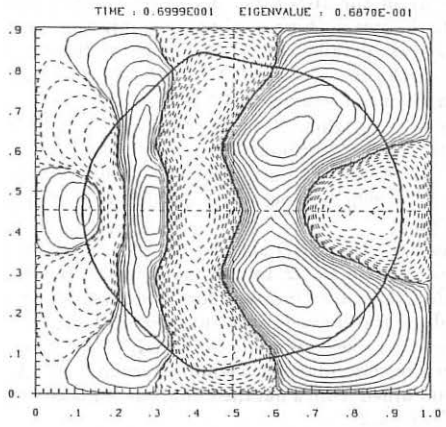

Fig.1

we expect a stronger attenuation of the high-m contributions at the plasma surface compared to the case with large η_V. On the other hand, experimental data suggest a strong insulation between the conducting wall and the plasma surface, since high m-numbers persist close to the vacuum vessel. We therefore increase η_V exponentially from its value at the plasma boundary to a large resistivity near the wall. Furthermore this treatment naturally leads to stronger effects at the inner side of the torus, where the equilibrium magnetic flux is smaller than at the outer side. As can be seen in Fig.1 for the discharge #17005 ($\beta_p \simeq 2.1$), this procedure leads to the required large m-values as well as to the correct mode asymmetry.

3. Non-linear results : For a detailed comparison with experiment we have to perform non-linear calculations, which require the superposition of all Fourier components of the expansion in toroidal direction. In practice it turns out that three Fourier components are sufficient. The non-linear evolution is started with the corresponding linear $n = 1$ eigenfunction. Higher n's will pick up their values by convolution with the $n = 1$ contribution. The amplitudes for the initial eigenfunctions have to be chosen such that the evolution remains in the linear phase for a couple of Alfven times. Usually, since the Strauss equations in high-β ordering do not lead to a true saturation in the non- linear phase, the evolution is stopped as soon as the calculated perturbed magnetic field at the outboard side of the torus reaches the measured amplitude.

This procedure, however, suffers from the serious drawback that in most of the cases the experimental level is reached when the discharge is still in the linear phase. If, on the other hand, non-linear effects turn out to be strong, they are most likely due to numerical errors caused by a continously steepened gradient of the perturbed pressure at the outer side of the torus. Thus, for a reasonable comparison with experiment, these calculations are of limited use only.

Since instability, as well as saturation in the non-linear phase are intimately related to the pressure evolution, we introduce a diffusive damping term for the perturbed pressure with a factor linearly dependent on $p_{max} = max(p(x,y))$, which we consider to be a re-introduction of a numerically not properly treated effective pressure diffusion :

$$\frac{\partial p}{\partial t} = -\vec{v}_\perp \cdot \vec{\nabla}_\perp p + C p_{max} \nabla_\perp^2 p. \tag{2}$$

The constant C is chosen such that the corresponding saturated value for $\tilde{B}$ matches the experimental level. Typically we find $\tilde{B} \sim C^{-1}$.
We note in passing that we have tried alternatively to reduce the pressure steepening by the inclusion of some specific terms of order ϵ^3, which ensure the correct treatment of the sound wave, i.e. with finite velocity, and lead to an equilibration of the perturbed pressure along lines of constant flux. However, these effects are significant only if the ratio of growth rate $\gamma = \tilde{\gamma} v_A$ and sound velocity v_s satisfies

$$\frac{\gamma}{v_s} = \tilde{\gamma}\frac{v_A}{v_s} = \tilde{\gamma}\frac{B}{\sqrt{\mu_0 \gamma_H p}} << 1, \tag{3}$$

where $\tilde{\gamma}$ is the normalized growth rate as calculated by the code and v_A the Alfven velocity. For the parameter values of the discharges under consideration this inequality is not satisfied. The corresponding results predict equilibria to be more unstable by ~30% if the additional terms are taken into account. Therefore these terms do not achieve the non-linear saturation for the presently discussed discharges.

4. Comparison with experiment : Comparisons of numerical results (solid lines) with measurements (circles) are shown in Fig.2a,b for a medium and a large β_p discharge, respectively.

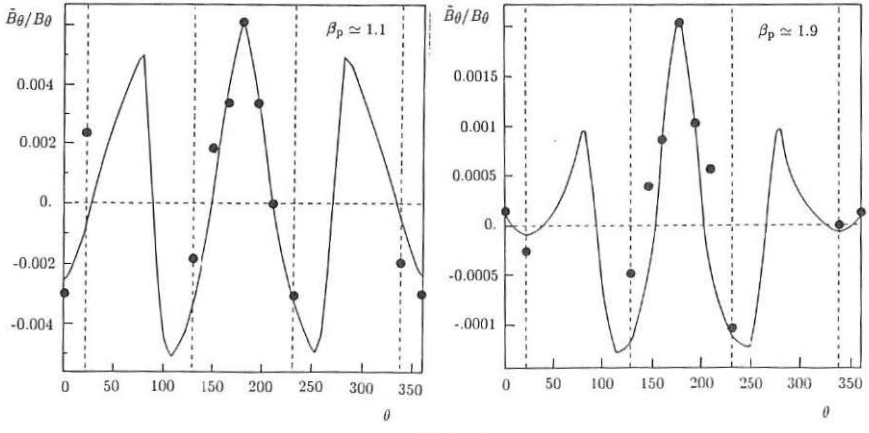

Fig.2a,b

Plotted is the quantity $\tilde{B}_\theta$ versus poloidal angle at a fixed toroidal position after saturation in the non-linear phase. Due to the large outside-inside amplitude ratio, nonlinear effects turn out to be stronger at the inner side of the torus.
Note that the vertical dashed lines indicate the limited poloidal range covered by Mirnov probes. This experimental restriction clearly makes a unique determination of the poloidal mode number difficult. However, as can be seen in Fig.2 the comparison with data in the experimentally testable poloidal region shows a reasonable agreement with respect to phases as well as to amplitudes.

The deviation of the observed soft X-ray wave forms from pure $\sim sin(n\phi)$ can be regarded as a measure of non-linear effects. This offers the possibility to compare our saturation mechanism and thus the corresponding $n > 1$ contributions with data.

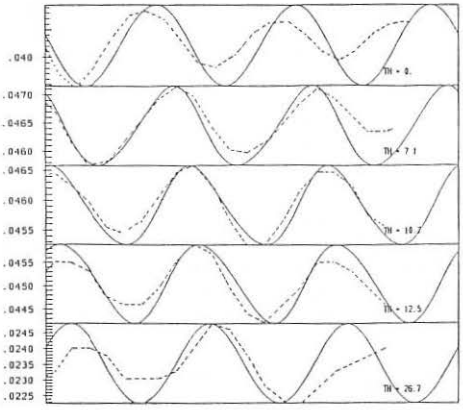

In Fig.3 we confront measured soft X-ray traces (dashed lines) versus time for the discharge #18041 with calculations of the line integrated squared perturbed pressure (solid lines) [7]. The missing doubled frequency in the central channel indicates, in agreement with experiment, the weak $m = 1$ contribution. Our results show that the phase differences of the various traces are reproduced to good accuracy. For this special case it turns out that the ratio of $n = 2$ to $n = 1$ contributions is less then 10%.

Fig.3

In summary, global MHD-stability calculations have been carried out for H-mode, high-β_p -ASDEX discharges. It has been shown that at high β_p the discharges are subject to a pressure driven tearing instability, whereas at low β_p the instability is principally of tearing type. When the vacuum resistivity is exponentially increased from its value η_p at the plasma surface to a large value (we have used $\eta_V(max) = 10^{-1}$) near the conducting wall, we find large poloidal mode numbers for the analyzed high-$\beta_p$discharges - in agreement with experimental observations.

Non-linear calculations with forced saturation by an effective pressure diffusion term predict amplitudes of non-linear contributions to the $n = 1$ eigenfunctions of the order of 10%. These effects turn out to be stronger at the inner side of the torus, mainly because of the large outside-inside amplitude ratio. Calculations for $\tilde{B}_\theta$ versus poloidal angle as well as the line integrated perturbed pressure, which we compare with SXR-data, are in reasonable agreement with experiment.

REFERENCES

1. R. Hawryluk, Physics of Plasmas Close to Thermonuclear Conditions, Vol I, Varenna (1979), (EUR-FU-BRU/XII/476/80).
2. O. Gruber, et al., 13th European Conf. on Controlled Fusion and Plasma Heating ,Schliersee 1986, p. 248.
3. O. Küber, et al., 13th European Conf. on Controlled Fusion and Plasma Heating , Schliersee 1986, p. 136.
4. Lee J.K., Phys. of Fluids **29** (1986), p. 1629; Nucl. Fusion **26** (1986), p. 955.
5. K. Grassie, et al., Inter. Workshop on Turbulence and Anomalous Transport in Magnetized Plasmas, Cargese 1986, p. 279.
6. O. Gruber, et al., 11th Inter. Conf. on Plasma Physics and Controlled Nuclear Fusion Research, Kyoto 1986.
7. J.L. Dunlap et al., Phys. Rev. Lett. **48** (1982), p. 538.

EPS Abstract, Madrid 1987

RESONANT MAGNETIC PERTURBATION STUDIES IN CLEO

T N Todd, S Iyengar* and P S Haynes

Culham Laboratory, Abingdon, Oxon, OX14 3DB
(UKAEA/Euratom Fusion Association)

*Attached under an EMR agreement with Oxford University

Tokamak discharges frequently exhibit disruptive behaviour attributed to tearing and/or kink modes of low m,n, causing internal relaxations or sudden global energy losses. Such low m modes should be sensitive to variations in the current density profile, leading to the possibility of modifying their behaviour by perturbing the local flux surfaces with resonant magnetic perturbations (rmp) as previously investigated on Pulsator, TORIUT 4, HT6B TOSCA etc. CLEO is a large aspect ratio (90cm/13cm) device, with rmp windings consisting of four flat rectangular coils mounted above and below the torus, at toroidally opposite locations. With appropriate interconnections the coils can be made to create a variety of magnetic perturbations, with principal mode numbers of 1,1; 2,1; 1,0(3,2) or 2,0(2,2). The coils were driven by a current-feedback transistor amplifier, producing DC pulses of preprogrammed rise and fall time and amplitude. Each of the plasma equilibrium control circuits was modified to null the pick-up from the saddle coil field and its time derivative. The island structures generated by each possible coil configuration have been calculated using field line tracing (with the vacuum perturbation superimposed on a model equilibrium, ie neglecting the plasma response) and by Fourier analysis over representative toroidal surfaces. Significantly different results are produced, due to the detailed trajectories followed by the field lines with respect to the perturbing fields not being explored by the transform analysis. For the principal resonances both techniques yield the same radial field amplitudes, of ≈ 10 Gauss maximum, or ≈ 6% of the typical poloidal field strength.

The experimental investigations carried out include the effect of the m=1, n=1 and 2,2 modes on sawteeth during $2\omega_{ce}$ ECRH at 28 GHz, and of the 2,1 and 3,2 modes on the OH disruptive density limit. Of interest to construction engineers, the effect of each of the four modes on plasma start-up and soft X-ray profile evolution (including OH sawteeth initiation) has been evaluated, with the possibility of inhibiting the rise of central current density at rational central q values.

Preliminary analysis suggests that at this level of perturbation there is remarkably little effect on any of the gross plasma parameters (eg V_{loop}, gas demand, SXR flux profile). Penetration of the pseudo-helical field through the thick metallic structure of CLEO was verified using internal coil probes, and by operating at surface q ≈ 2.8, where disruptions could be initiated at any density with a 2,1 perturbation at q=2 of $\tilde{B}_r/B_\theta \approx 4\%$. At q ≈ 3.2 the density limit was unusually low (3 x 10^{12}/cc at 9 kA) but improved to ≈ 5 x 10^{12}/cc as the 1,0 (ie 3,2) perturbation was raised to the maximum level available. This density range should be compared to that found for 9 kA at higher toroidal field values in these Ti-gettered discharges, ≈ 9→11 x 10^{12}/cc independent of perturbation type or amplitude.

Analyses will be presented of the effects of the varous rmp configurations and amplitudes on sawtooth behaviour, density limits, plasma initiation and global confinement, with emphasis on the fast-digitised Mirnov coil and SXR flux data.

MHD STABILITY IN JET WITH PEAKED PRESSURE

T C Hender*, P S Haynes*, D C Robinson* and A Sykes*

JET Joint Undertaking, Abingdon, Oxon, OX14 3EA, UK

*Culham Laboratory, Abingdon, Oxon, OX14 3DB, UK.
(UKAEA/Euratom Fusion Association)

Introduction

A possible scenario to optimise the fusion product, for D-T operation in JET, is to have very peaked temperature ($T_o \sim 16$keV) and density ($n_o \sim 2 \times 10^{20}m^{-3}$) profiles, within a central ($q \sim 1$) low shear region [1]. This scenario is compatible with degraded confinement associated with powerful heating. To optimise the L-mode confinement time for this case a high current I = 7MA (at $B_T = 3.5T$) is proposed. At this current it is necessary to reduce the structural stresses by operating at an elongation $b/a \sim 1.7$, to closely align the flux surfaces with respect to the T F coils. The envisaged parameters for this case have a high central β to maximise the fusion product $\beta_o \sim 20\%$. The corresponding $\langle\beta\rangle \sim 3\%$ is well below the Troyon limit of 4.5% [2]. The Troyon limit however is based on optimising with respect to relatively broad pressure profiles. In this paper we investigate the effect on ideal and resistive MHD stability of constraining the pressure profile to be peaked.

Intermediate and low n internal modes

In low shear regions a class of intermediate-n pressure gradient driven instabilities can exist [3]; these are sometimes called infernal modes. These modes, unlike the ballooning modes, have only one resonance within the radial extent of the mode and are thus sensitive to the radial location of the resonance. Figure 1 shows the growth rate (in poloidal Alfven units) as function of central q_o for the n=3,4 and 5 infernal modes when $q = q_o (1 + (r/0.71)^{12})^{1/6}$, $\beta_o = 12\%$ and $P \propto \psi^4$

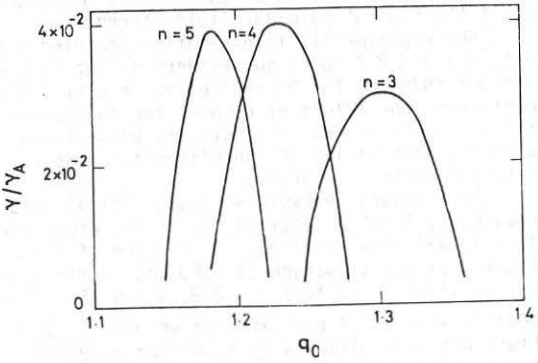

Fig 1 Growth rate of infernal modes (γ) v q_o

(ψ being the equilibrium poloidal flux). These parameters give a very flat central q and a peaked pressure profile. The equilibria have JET aspect ratio but a circular boundary has been used (because of computer memory limitations). Preliminary studies show that the results do not change significantly with ellipticity for b/a < 1.4. As expected the infernal mode stability is sensitive to the radial location of the resonance (ie q_0) and for example the n=4 (predominantly m=5) mode growth rate peaks near q_0 = 1.25. The results shown in Fig 1 are from a fixed boundary code but since these are radially localised internal modes their stability is insensitive to the wall location. For the n=4 mode we find a critical $\beta_0 \simeq$ 8%. For the case shown in Fig 1 the entire region between q_0 = 1.15 and 1.35 is unstable to the n=3, 4 or 5 mode. By considering higher n (> 6) this domain of instability can be extended closer to q_0 = 1. Also near q_0 = 1 the n=1 low shear internal kink modes (which have been proposed as an explanation for JET sawteeth [4]) are unstable. For the parameters envisaged in the D-T operation scenario [1] the requirement for stability to these modes is $q_0 \gtrsim 1.1$. Thus there is no reasonable value of q_0 for which stability to the n=1 and infernal modes occur when a low shear core and peaked pressure profile ($\beta_0 \gtrsim 10\%$) are considered.

Ballooning, Mercier and External Kink Modes

The conditions which are most detrimental for the infernal modes (ie low shear in the core and high pressure gradient) are optimal for the ballooning modes [5]; under these conditions relatively easy access to the second ballooning mode stable regime occurs. If however we increase the shear in the core (to improve the infernal mode stability) then access to the second stable region becomes much more difficult.

Figure 2 shows the effect on JET β-limits of constraining the pressure profile to be relatively peaked ($P \propto \psi^4$). The parameters for this study are I = 7MA, B_T = 3.5T and b/a = 1.68 and the equilibria are specified by $P' = a\psi^3$ and $FF' = \psi - a\psi^3 + b\psi^4$ (where $F = RB_T$). Comparing with a study by Sauremann [2] for identical parameters but broader pressure profiles ($P\alpha\ \psi^2 + a\psi^3$) shows the peaking has caused $\langle\beta\rangle$ to decrease from 4.7 to 2.7%. We have tried several other FF'

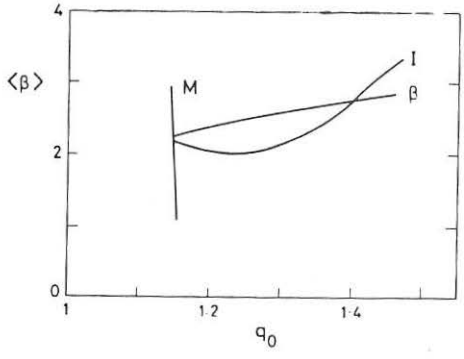

Fig 2 Mercier (M), Ballooning (B) and Kink mode (I) stability boundaries for $P\alpha\ \psi^4$

parameterisations in an attempt to improve the β-limits of the peaked pressure profile cases; for profiles which have moderate shear in the core region we have not been able to significantly improve the β-limit.

To make a systematic study of the effect of peaking the pressure profile on the β-limit, we have used a code which optimises the ballooning mode stability on each flux surface. Normally the optimisation criterion is to make the ballooning modes marginally unstable on every flux surface. However, by making the ballooning modes increasingly stable on the outer flux surfaces the pressure profile is correspondingly peaked. Figure 3 shows how $\langle\beta\rangle$ and β_0 vary as the peaking of the pressure profile ($P_0/\langle P\rangle$) is varied using this technique for a moderately sheared q-profile with $1.2 \leq q \leq 3.6$. The fully optimised case, ie ballooning modes marginally stable on every flux surface, corresponds to a peaking $P_0/\langle P\rangle = 3.2$. Thus in this case by increasing the peaking beyond 3.2 the critical $\langle\beta\rangle$ must decrease; but what is not so obvious is that β_0 should also decrease. This is a rather disappointing result since we are attempting to optimise the fusion product by maximising P_0.

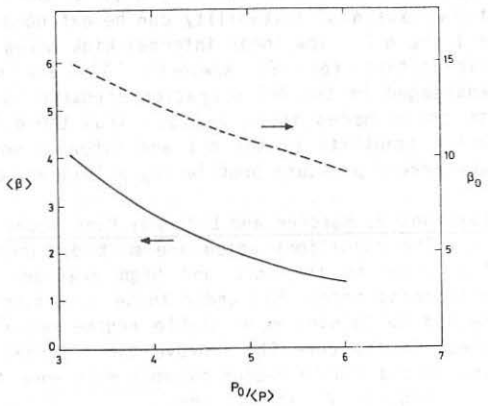

Fig 3 Decrease in critical $\langle\beta\rangle$ and $\langle\beta_o\rangle$ as pressure peaking is raised

Thus with I = 7 MA and B_T = 3.5 T it does not appear possible to achieve the required β_0 (~20%) in the first ballooning mode stability regime. We have, however, been able to increase the β_0 limit by reducing B_T. For B_T = 2.5T the first stability ballooning β-limit improves (α $1/B_T$) and for $q_0 \gtrsim 1.6$ direct access to second stability appears possible (even for peaked pressure profiles). However since $P_\alpha \sim \beta^2 B^4$ we have not been able to achieve a sufficient increase in β, by reducing B_T, to raise the alpha power. We have had more success in improving the ballooning β-limits, for moderately sheared cases, by going to rather broad pressure profiles. For example for I = 7MA, B_T = 3.5T and b/a = 1.68 we have been able to achieve second stability with $\beta_0 \gtrsim 30\%$ by using the broad profiles $P \propto \psi^{1.4} + a\,\psi^{2.5}$.

Resistive Stability

Here we are mainly interested in the n = 1 and 2 resistive tearing modes which are associated with the major disruption. These are generally stabilised by average curvature effects in JET [6] but for the peaked pressure profiles this effect is weaker since the local pressure gradient at q = 2 (and $^3/_2$) is smaller. However for the relatively rounded q-profile, peaked pressure cases ($P \alpha \psi^4$) of Fig.2 we still find complete tearing stability for $S \gtrsim 10^7$. (Here S is the magnetic Reynolds number $\sim 10^8$ for JET). However as the q-profile is flattened (and the current profile is broadened) so the tearing modes are increasingly destabilised.

Conclusions and Discussions

For I = 7MA and b/a = 1.7 we find that the main ideal instabilities (ballooning, n = 1 kink and infernal modes) impose a limiting central $\beta \lesssim 10\%$ when the pressure is relatively peaked ($P \sim \psi^4$); this leads to a factor of 4 reduction in the α power compared with that envisaged in ref [1]. However if we broaden the pressure profile then access to second stability regime is relatively easy and $\beta_0 > 30\%$ is possible. Such profiles have Q > 1 and require $\tau_E \lesssim 1s$.

Acknowledgement

This work was performed under a task agreement between Culham Laboratory and the JET Joint Undertaking.

References

[1] P H Rebut et al, paper A-I-2 IAEA Kyoto (1986)
[2] H Saurenmann et al, Lausanne report LRP 263/85
[3] R J Hastie et al, Nucl Fusion 21 (81) 187
[4] J A Wesson, Plasma Phys 28 (86) 243
[5] S Seki et al, Nucl Fusion 27 (87) 331
[6] T C Hender et al, paper A-V-3 IAEA Kyoto (1986)

PLASMA BEHAVIOUR IN HL 1 TOKAMAK

QIN Yun-wen XU Guang-bi RAN Li-bo
YANG Jin-wei XU De-ming YANG Qing-wei
XU Wen-bing HU Gao QAIN Shang-jie

Southwestern Institute of Physics
P.O.Box 15, Leshan, Sichuan
People's Republic of China

The HL-1 device is a medium-sized tokamak with copper shell of thickness d=5cm [1]. The experimental results obtained in the first phase of operation, 1985 - 1986, are summarized in Refs.[2-4]. The parameters of operation are: B_T =0.3-2.8T, I_p =50-150kA. In this paper the plasma behaviour revealed by the experimental results is discussed.

HL-1 discharge sustains over hundreds milli-seconds. The flat-top time is about 150-200ms, but the current decays very slowly and lasts more than 300ms, sometimes, up to 800ms. Fig. 1 shows oscillograms of loop voltage and current for typical discharges with different filling pressure. As mentioned in Refs.[2-4], by the end of flat-top, the iron-core of transformer starts becoming saturated. In the case of the low filling pressure, it exhausts its Volt-seconds very quickly and begins working as an air-core with low efficiency. In fact, the discharge is almost discoupled with the primary winding after saturation of the iron-core($U \simeq 0$). The intensive hard X-ray and enhanced emission at frequency $\omega < \omega_{ce}$has been observed for such type of discharge at the current decay phase. This enhanced emission seems to be associated with runaway instabilities (i.e. generation of oscillations by the anomalous Doppler resonance, $\omega = \omega_{ce} - k_z V_z$)and the discharge at the decay phase supposes to be dominated by a strong component of runaway electrons[5].

In the case of the high filling pressure, the loop voltage at the decay phase is apparently differentiated from zero($U \gtrsim 1V$). The hard X-ray level is low and the enhanced emission at frequency near ω_{ce} has not been observed. Therefore, there is a low density plasma not excluding a possible weak component of runaway electrons.

Runaway electrons are more easily formed in the low density plasma. Their interaction with the limiter and vessel increases the impurity content, resulting in the increase of loop voltage. Consequently, the iron-core becomes saturated quickly. It can be explained that the iron-core saturation is connected with the property of discharge at decay phase. Moreover, the higher filling pressure makes the cold boundary layer thicker. The cold

boundary layer weakens the plasma interaction with limiter and vessel, resulting in the reduction of impurity content and also in the decrease of loop voltage. Therefore, the iron-core saturation is connected with the filling pressure.

On HL-1 tokamak, weak instabilities usually develop close to the end of or after the plasma current flat-top and are observed to be associated with m=2,3 modes. Both modes have the same frequency, 4-7kHz and the same order of value $\tilde{B}_\theta/B_\theta$, but $\tilde{B}_\theta^{m=2}/B_\theta > \tilde{B}_\theta^{m=3}/B_\theta$. Besides m=2, 3 modes, there is also m=4 mode with small amplitude. The m=2 oscillation is 180° out of phase compared with the m=3,4 oscillations. They seem to be coupled.

In the condition of present operation parameters, the major disruption with current broken-down seldom occurs. It was caused by the new movable limiter at the beginning. The thick copper shell plays probably an important role in stabilizing the major disruption.

The stable-operation regime has been given in Ref.[3]. The further analysis has distinguished two MHD activity areas(Fig. 2). The disruption occurs, when the discharge trajectory on Hugill plot crosses the area I at the current decay phase(trajectory a). The area II is located on the right from the area I at the top. When the discharge current reaches the area II, the disruption takes place and the current starts decay(trajectioy b). Between these two areas there seems a narrow window ($5.8<\bar{n}_e R/B_T<6.6\times10^{14}\,cm^{-2}T^{-1}$) which allows the discharge to break through $q_L=3$ activity. The similar feature of the stable-operation regime has been found on FT tokamak[6]. At the present time, the HL-1 plasma density is determined by the filling pressure and the time evolution of density is not sufficiently controlled. This situation and the others (as discussed below) can not allow us to analyze the stable-operation regime experimentally in detail.

On HL-1 tokamak the power supply for ohmic heating consists of a capacitor system and a DC flywheel generator. The capacitor system produces the initial plasma current with a restricted current rise time less than 24 ms. Under the present condition of the density time behaviour, the current rise rate is too high to overcome the MHD activity at $q_L=3$. The higher DC generator voltage has been used to obtain the slow current ramp up after fast rise of plasma current provided by capacitor bank to overcome the MHD instability at $q_L=3$. In this case the iron-core of transformer exhausts its Volt-seconds very quickly and the kind of discharge oscillogram showed in Fig. 3 has been obtained. This type of discharges usually crosses $q_L=3$ through the window between areas I and II (see trajectory c in Fig. 2). Sometimes, they can also cross the area I without disruption at the rise phase. After meeting the

area II, they go down along the window at the decay phase (see trajectory d).

From a series of experimental facts, it is indicated that the HL-1 plasma current channel is narrower than the area determined by the limiter. For example, discharges with $q_L \approx 3$ for limiter radius of 16 cm are stable, while discharges with $q_L < 3.8$ for limiter radius of 20 cm are unstable when the other parameters are kept. The value $\int n_e dl$ from the microwave interference measurement appears almost the same for discharges using the limiter radius of 20 cm and 16 cm. These facts propose the cold plasma layer of 3 cm in the discharge with limiter radius of 20 cm. It is consistent with the numerical calculation results (Fig. 4). The calculation is based on the ohmic law for discharge and equations for displacement and density measurements. The narrow current channel seems to be connected with the boundary cooling caused by impurity emission and leads to some specific properties for HL-1 discharge including the property of MHD activities mentioned above. The impurity content remains to be decreased.

Acknowledgements

The authors are grateful for invaluable support from all HL-1 group members.

References

[1] LI Zheng-wu, 9th European Conference on Controlled Fusion and Plasma Physics, Invited Papers(Oxford, 1979)485.

[2] QIN Yun-wen, Asia-Pacific Physics News 1(1986) 24.

[3] HL-1 TOKAMAK GROUP, in Plasma Physics and Controlled Nuclear Fusion Research (Proc. 11th Inter. Conf. Kyoto, 1986), IAEA-CN-47/A-VII-1.

[4] QIN Yun-wen, et al., Nuclear Fusion and Plasma Physics(Chinese) 6(1986)206.

[5] LI You-yi et al., ibid. 7(1987)20

[6] F. Alladio, et al., Nuclear Fusion 26(1986)11.

Figure Captions

Fig.1 Oscillograms of loop voltage and current for typical discharges (B_T=2T, I_P=100 kA; 1. No.1282, $P_{H_2}=5\times10^{-4}$ torr, 2. No.1287, $P_{H_2}=1\times10^{-3}$ torr).

Fig.2 HL-1 stable-operation regime.

Fig.3 Oscillogram of loop voltage and current for discharge using rising DC generator voltage (No. 1883, B_T=2.1T, $P_{H_2}=9\times10^{-4}$ torr).

Fig.4 Numerical calculation results for plasma radius a and equilibrium displacement Δ (No. 2847, B_T=2.3 T, $P_{H_2}=1.2\times10^{-3}$ torr, I_P=100 kA).

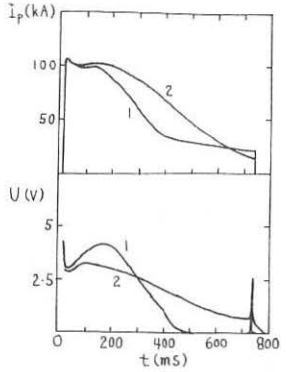

Fig. 1

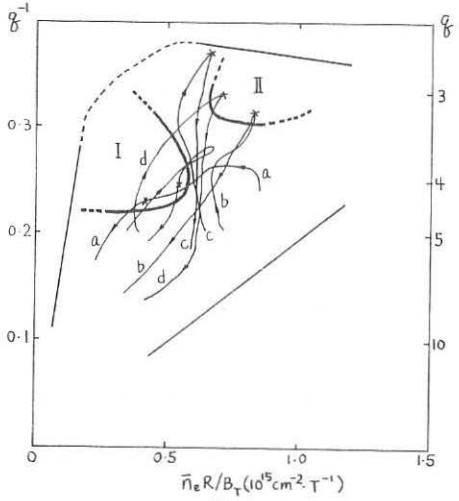

Fig. 2

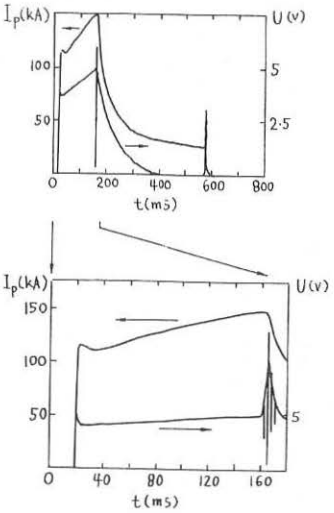

Fig. 3

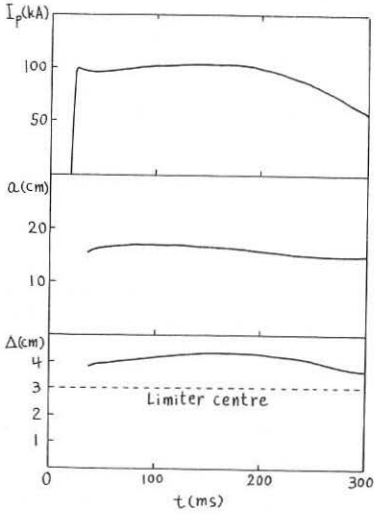

Fig. 4

RUNAWAY FLUCTUATIONS IN THE TJ-I TOKAMAK

L.Rodriguez R. and A.P.Navarro

Asociación EURATOM/CIEMAT
28040 Madrid, SPAIN.

INTRODUCTION

Hard-X-ray flux has been studied under different operational conditions ($\bar{n}_e$ = .1 - 1. x 10^{19} m^{-3}, B_T = .7 - 1.5 T) in the TJ-I tokamak (R_o =.3 m, a =.1 m, b = .12 m, B_T < 1.9 T, I_p < 70 kA) in order to correlate the presence of hard-X-ray flux fluctuations and the runaway electron confinement time τ_r.

Hard-X-ray spectra were obtained using a typical pulse height amplitude analysis system based on a collimated 3" NaI(Tl) detector. Electronics was modified in such a way that pulses could be temporally resolved and up to four different spectra were accumulated during built-up, plateau (two spectra) and run-down of the plasma current. The system was calibrated with a Cs^{137} source. Runaway confinement times were deduced from these spectra using our 1-D model (1). Simultaneously, a second collimated NaI(Tl) detector, working in the current mode, was used to monitor fluctuations in the total HXR flux. A camac controlled digitizing system, with sampling frequency up to 500 kHz was used to store HXR signal, together with $\tilde{B}_\theta$, V_L and I_p signals. Frequency spectra for those signals are deduced using Fast Fourier analysis.

EXPERIMENTAL RESULTS

1.- Fluctuations.

Discharges with HXR fluctuations have been only obtained in TJ-I for low toroidal magnetic fields (B_T = .8 T) in H_2 plasmas. Fluctuation amplitude decreases when electron density increases ($\bar{n}_e$ =.1 - 1.x10^{19} m^{-3}). Plasma current in those discharges was around 35 kA.

For all these discharges, fluctuations appear at the center of the discharge accompanied by spikes in the loop voltage and preceded by MHD activity that grows and vanishes during the time the fluctuations are present. These fluctuations do not seem to affect the plasma current intensity. These magnitude traces for a typical discharge with fluctuations are shown at Fig.1.

To correlate the fluctuation effect on the different magnitudes, a frequency analysis was made using FFT. Frequency spectra obtained for HXR fluctuations present a dominant frequency around 5 kHz with a relative amplitude of two orders of magnitude over the background (fig 2.). Correlation of these fluctuations with MHD activity could not be clearly determinated although in some cases $\tilde{B}_\theta$ frequency spectra presented some structure at the same frequency that HXR signals. The loop voltage spectrum

does not give any clear dominant frequency but V_L signal shows a negative spike in coincidence with the rising part of the HXR signal (fig. 3). The amplitude of those spikes decreases along the discharge. I_p Fourier analysis doesn't present any correlation with others magnitudes.

In an attempt to obtain other operational regimes with HXR fluctuations, a B_T scan (at 1. T, 1.3 T, 1.5 T) was made and for each B_T value a $\bar{n}_e$ scan was also achieved. No fluctuations have been obtained for those conditions.

2.-Effect on runaway confinement.

Pulse height amplitude spectra have been measured with fluctuations (B_T =0.8 T, $\bar{n}_e$ = 10^{19} m^{-3}) and without fluctuations (B_T = 1. T, $\bar{n}_e$ =10^{19} m^{-3}), (fig. 4). Moreover spectra were taken during the built-up, plateau and rundown of the the discharge, in order to evaluate HXR confinement time along the discharge, before, during and after fluctuations. Qualitatively, the following differences appear :

a) For discharges with HXR fluctuations, there are HXR all along the discharge. In the case of non fluctuations, HXR only appear after the built-up.

b) Discharges with fluctuation present, around the plateau, clearly rounded spectra for the lower energy part.

From the HXR spectrum analysis, confinement time of the runaway electrons has been obtained using the above mentioned model (1). Results are sumarized in the table I.

DISCUSSION

The observed regime for HXR fluctuations in TJ-I : Non-disruptive discharges with low toroidal magnetic field, q-value around 3 and E/E_D in order of .1, a clear relationship between HXR fluctuations with V_L spikes and relatively large MHD oscillations is more similar to the corresponding to "disruptive instabilities" described by Mirnov and Semenov (2) than to the Parail and Pogutse (3) model, that would requiered higher B_T . Besides, in our measurements a $\bar{n}_e$ electrons density increase seems to affect only fluctuation amplitude that only disappear when increasing B_T . Taking into account that our model (1) gives a slide-away electron distribution function for the TJ-I tokamak, the obtained HXR spectra show a loss of low energy runaway electrons in the rounded part of spectra, if we consider that high energy electrons are contributing at the low part of the spectrum in the same way that low energy ones.

A first interpretation of this phenomenon could be a deceleration of the electrons with energy 30 kev$\langle E_{e//} \langle$ 500 kev. The longitudinal energy of these electrons would be transfered to the thermal part of the electron distribution. A decrease of the runaway confinement time in the central part of the discharge in coincidence with the fluctuations show a faster loss of energy that could be due to the transformation of longitudinal energy to transverse during this pertubation. The growing flux at the end of the discharge, without any fluctuations in the signal gives a longer confinement, that seems to indicate that there is no energy transfer in

this part of the discharge, so that the primary electron distribution has been restored.

SUMMARY AND PLANS

An operational HXR fluctuation regime for low B_T , no clear dependence on $\bar{n}_e$ has been found in the TJ-I tokomak. During these fluctuations, confinement time of runaway electrons decreases and HXR spectra present a loss of low energy photons, probably due to a loss of longitudinal energy for runaway electrons in the range 30 kev $< E_{e//} <$ 500 kev.

These measurements have been made with a value of Z_{eff} around 3. Future experiments are planed when lower values of Z_{eff} are present in order to decrease E/E_D . Electrostatic probes will be used trying to detect plasma waves in the presence of HXR fluctuations in an attempt to correlate them.

REFERENCES

(1)-L. Rodriguez R. and A.P. Navarro.13 th E.P.S. Conf., Vol 10CI,272 (1986).
(2)-S.V. Mirnov and I.B. Semenov. Sov. Phys. JETP 33,1134 (1971).
(3)-V.V. Parail and O.P. Pogutse, Nucl. Fus. 18, 303 (1978).

	B_T (T)	$\bar{n}_e$ (m^{-3})	Time intervales (ms)				
			2-6	6-10	10-14	14-16	
W/ FLUCT.	0.8	1.x10	.9	.6	.6	.9	τ_r (ms)
W/O FLUCT.	1.	1.x10	-	.7	.6	.4	τ_r (ms)
			$\Delta\tau_r = .2 \times \tau_r$				

TABLE I : Confinement times for runaway electrons in four intervals of discharges with and without fluctuations.

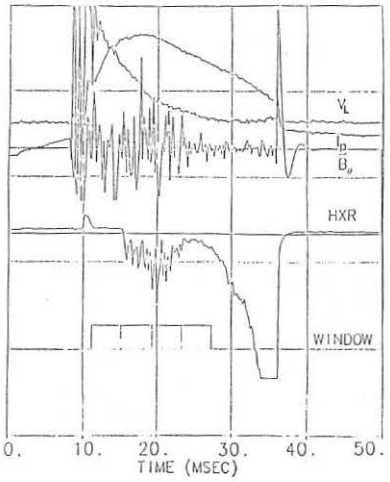

Figure 1.-Plasma discharge with fluctuations (B_T =.8 T, $\bar{n}_e$ =10^{19} m^{-3}) and time window for HXR spectra.

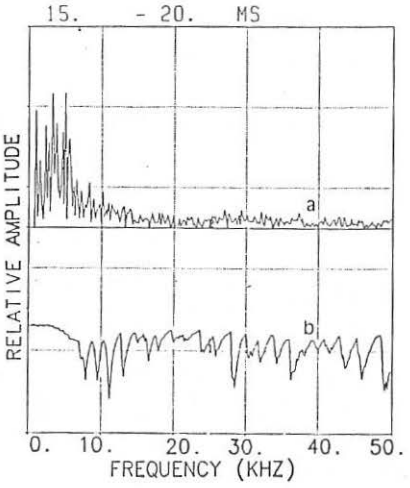

Figure 2.-a) HXR frequency spectra b)HXR flux signal in the time domain.

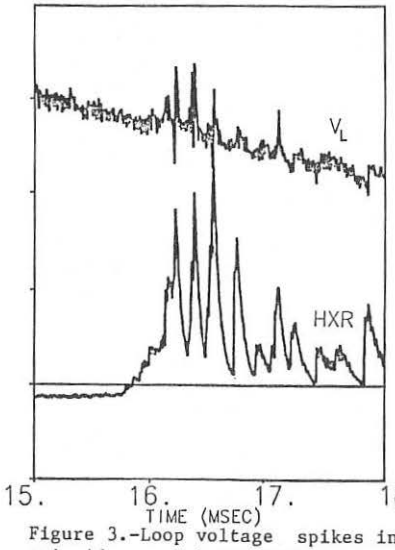

Figure 3.-Loop voltage spikes in coincidence with HXR fluctuations.

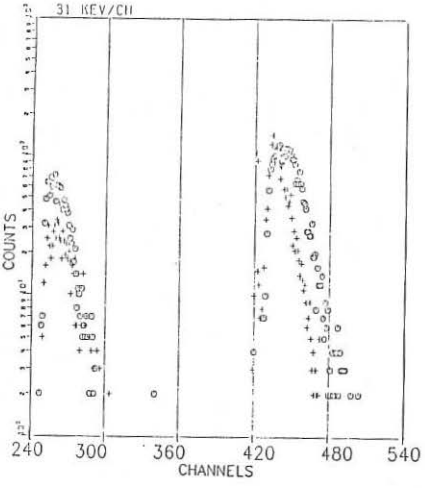

Figure 4.-HXR spectra in the plateau of the discharge (+ : with fluctuations, o : without fluctuations).

HELICAL COILS FOR INSTABILITY AND DISRUPTION STUDIES ON "TOKOLOSHE" TOKAMAK

D P Coster, J A M de Villiers, J D Fletcher, G Nothnagel, J R O'Mahony, D E Roberts and D Sherwell

Fusion Studies Division
Atomic Energy Corporation of South Africa
P O Box 4587, Pretoria, 0001

Introduction Resonant, ℓ =1, 2 and 3 helical windings are being fitted to the Tokoloshe tokamak. They are almost complete, and helical, as opposed, for example, to the partial ℓ =1 winding of Pulsator[1] or the saddle coils of Tosca[2]. With such windings we expect clean island structure (large primary, small satellites) for small coil currents. The low aspect ratio of Tokoloshe (R/a=2,17, a=24 cm) however exaggerates the satellite islands and a design to minimize these is discussed. So far, the ℓ =1 winding has been installed, and preliminary field measurements for the true coil path compared with theory.

Design of Helical Coils The primary aim has been to obtain, individually, pure m/n = 1/1, 2/1, 3/1 modes. A field line in a high aspect ratio tokamak has the winding law $\phi \simeq q(\theta - \epsilon \sin\theta)$ and a resonant helical winding would be chosen to obey this law. Such a winding creates a large primary island with small satellites due to discreteness and toroidicity. On Tokoloshe the field line approximately follows the above law (as shown by field line tracing on model Tokoloshe equilibria, B_T=0,6T, I_p=100kA), but such a winding now gives enhanced satellites owing to strong toroidal effects. A winding law of the form $\phi = m/n(\theta - \delta_{mn}\sin\theta)$ was chosen and δ_{mn} varied to investigate the nature of the primary island resonance peak and satellite island size.

The results are shown for the ℓ =1 and ℓ =2 windings in Figs 1a&b, where full island size, normalized to minor radius, Δ_{mn}, is plotted against δ_{mn} at constant coil current, I_ℓ = 680A. The 1/1, 2/1, 3/1 modes are found to be dominant (see Fig 4b). The primary island is found to be approximately constant over a wide range of δ_{mn}. An interesting additional feature however is the vanishing of some satellites for certain δ_{mn}, and we use these effects to choose the winding law. These phenomena are not sensitive to the q profile but are found to change with Shafranov shift d_o of the eqilibrium flux surfaces. Figs 1a&b thus show two sets of data for the cases $d_o = 0$ and d_o =4 cms (the maximum observed on Tokoloshe). We have chosen to minimize the 3/1 island for both ℓ =1 and ℓ =2 windings to facilitate disruption studies (as has been found advantageous on Tosca[2]) and hence have chosen δ_{1l}=40°, δ_{2l}=48° to give the smallest 3/1 island for the range of d_o studied. The remaining island in each case, and any residual 3/1 island, can be cancelled by means of their respective resonant windings.

An explanation for the vanishing of higher order satellites is as follows. We have found on Tokoloshe that a pure helical field $B_{\mu} = \sin(m\theta - n\phi)$ induces a primary m/n island, and higher order satellites. Fourier analysis of the designed $\ell=1$ field shows that the $\sin(2\theta - \phi)$ component changes sign as δ_{II} is increased (Cosine terms are always zero because of symmetry). Regarded as a pure 2/1 field, it induces 2/1 and 3/1 islands out of phase with these satellites of the pure 1/1 field, and of sufficient amplitude to cancel them. A physical explanation is clear from Fig 2 where for increasing δ_{II}, the $\ell=1$ winding is seen to lie increasingly along the $\ell=2$ path, $\phi = 2\theta$, of opposite sense. A strong, out of phase, 2/1 field component is then expected. Similar arguments apply to the $\ell=2$ results of Fig 1b.

A law of the form $\phi = \theta - \delta_{II} \sin\phi$ has been tried, a simple form of that explored for Tore-Supra[3], and we have found that it gives only mild satellite suppression.

Field Measurements Imposed windings. In Fig 3 we show a plan of the vacuum chamber with It will be seen that, for $\ell=1$ and $\ell=2$, they avoid the large ports but do have to cross vertical observation ports and the main vacuum flanges. We have installed the $\ell=1$ winding and in Fig 4a show the measured 2-D Fourier spectrum of its field, and in Fig 4b the results of a Biot-Savart calculation for the theoretical law. The analysis was done at 3 toroidal and 50 poloidal points for 6 radial positions. The agreement is satisfactory considering the small number of toroidal positions (further measurements are being performed to determine high-n modes).

Discussion In Fig 5 we show pure 1/1 island structure with no observable satellites, for values of δ_{mn} as chosen above, I_1 = 680A and I_2 = -125A. This, and the field measurements, indicates the possibility of obtaining uniquely pure islands in the experiment. In addition combinations of 1/1, 2/1, and, we expect, 3/1 islands can be created by appropriate choice of I_{ℓ}. These capabilities should allow accurate study of mode stabilization effects and disruption mechanisms such as island overlap and connection of islands to the wall.

REFERENCES

1) Fussman, G. et al. in Plasma Physics and Controlled Nuclear Fusion Research, IAEA, 1, 401 (1979)
2) Morris, A. W., Ellis, J. J. and Robinson, D.C., Proceedings of the International Workshop on Magnetic Reconnection and Turbulence, Cargese, 323 (1985).
3) Fuchs, G. et al, Berichte der Kernforschungsanlage, Jülich, Nr 1993 (1985).

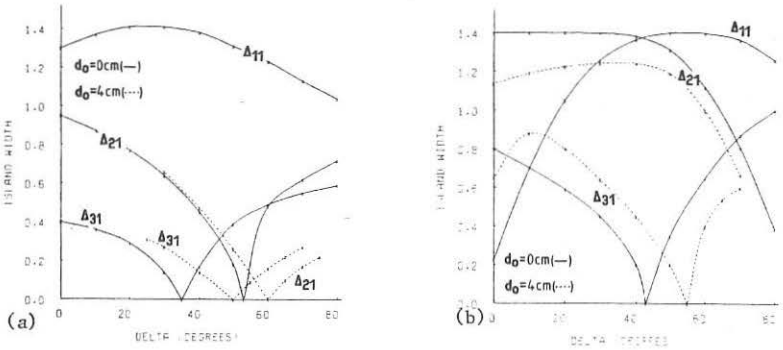

Fig 1 Island size versus winding law parameter for (a) ℓ =1 and (b) ℓ =2 windings.

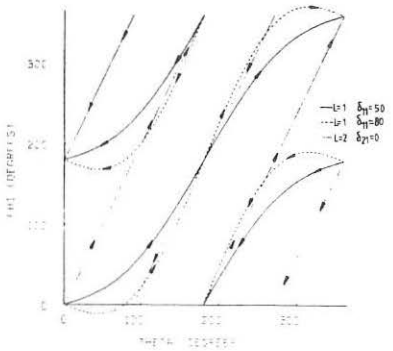

Fig 2 Approach of the ℓ =1 winding to a partial ℓ =2 path of opposite sense, as δ_{11} increases.

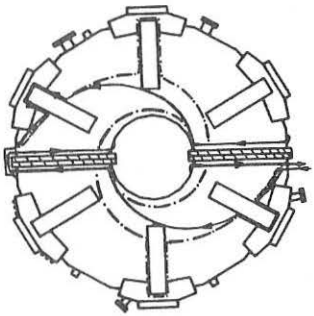

Fig 3 Designed ℓ =1 (——) and ℓ =2 (—·—) windings.

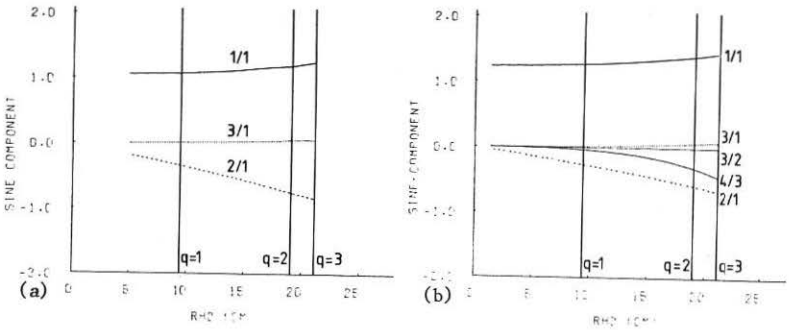

Fig 4 Fourier spectra of (a) experimental and (b) theoretical, ℓ =1 fields. Note small 3/2 and 4/3 amplitudes at rational surfaces.

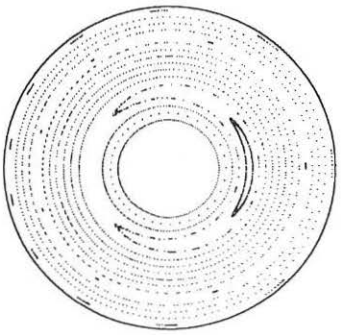

Fig 5 Primary 1/1 island with 2/1 and 3/1 satellite suppression.

14th European Conference on Controlled Fusion and Plasma Physics

SPECIFIC TURBULENCE ASSOCIATED WITH SAWTOOTH RELAXATIONS

TFR Group, A. TRUC* and D. GRESILLON*

Presented by J. OLIVAIN

Association EURATOM-CEA
Département de Recherches sur la Fusion Contrôlée
Centre d'Etudes Nucléaires de Cadarache
13108 Saint Paul Lez Durance CEDEX, France

A new type of turbulence, associated with sawtooth relaxations, is detected by scattering experiments.

The experiment is performed on TFR, during ohmic regime of auxiliary heating phases, all conditions where sawteeth are detected. The turbulence observations are made with a CO_2 laser scattering experiment. The scattering volume corresponds to a vertical chord which can be radially scanned. The detected light, corresponding ot two simultaneous K wave numbers, is frequency analyzed and is recorded on digitizers. On the other hand, soft X-ray emissions, associated to several vertical chords, are addressed to the same digitizers.

Attention is focused during the crash period of the sawtooth. Whereas the integrated over all frequency signal shows continuity, filtered signals, at fairly high frequencies, exhibit a large spike. The duration of this enhanced turbulence is about 30 μs and coincides with the major period of crash [1].

Detail analysis of this specific new turbulence, including frequency, wave number and spatial localisation, will be given.

[1] TFR Group and A. Truc
C.R. Acad. Sci. Paris, Note 600 (1986)

* Permanent address : Laboratoire de Physique des Milieux Ionisés, Ecole Polytechnique, 91128 Palaiseau (France)

MICROTURBULENT FLUCTUATIONS IN THE TORTUR TOKAMAK

TORTUR TEAM: A.J.H. Donné, C.J. Barth, B. de Groot, H.A. van der Laan, H.J. van der Meiden, G.J.J. Remkes, W. van Toledo, W.A. de Zeeuw and H. de Kluiver.

Association Euratom-FOM, FOM-Instituut voor Plasmafysica, Rijnhuizen, P.O. Box 1207, 3430 BE Nieuwegein, The Netherlands

In the TORTUR tokamak (R = 0.46 m; a = 0.085 m; B_{max} = 3.0 T) hydrogen plasmas are produced by plasma currents up to 60 kA during about 40 ms. By the application of elevated loop voltages, a stationary weakly turbulent state is brought about with an enhanced dissipation, possibly due to low-frequency electromagnetic turbulence [1]. The reduction in apparent conductivity as compared to Spitzer values lies between 2-4. As a result, relatively high values of the electron temperature ($\lesssim$ 1 keV) are obtained at high plasma densities (~ 10^{20} m^{-3}). In the higher current range (> 35 kA), the plasma beta follows the Troyon scaling ($\beta \approx 7\times10^{-3}$ at I_p = 50 kA). Despite the weakly turbulent medium, the energy confinement times ($\lesssim$ 2.5 ms) follow closely the currently used scaling-law values. Above 55 kA, internal ($q<1$) disruptions are starting with occasionally major disruptions preventing any significant increase in temperatures and beta values. Turbulent heating effects due to fast (10 μs) toroidal current pulses from a high-voltage bank superimposed on the plateau current have been described earlier [2] . A typical TORTUR shot is shown in Fig. 1.

Microturbulent plasma fluctuations have been studied by means of collective scattering of 4-mm waves at 90° [3] in the frequency range from 500 Hz up to 100 MHz. Regions of plasma fluctuations near 1 MHz and between 5 and 55 MHz have been observed during the plateau phase, apart from the commonly observed spectral region (20-700 kHz) which is attributed to low-frequency electrostatic and magnetic drift waves of various types [4,5]. The intensities registered as a function of frequency and time are shown in Figs. 2a-c and 3a-c, respectively, for the three spectral regions. The slow-time periodicities which modulate the signals are familiar for tokamak discharges at relatively high q-values. Synchronous modulation of T_e and I_p are shown in Figs. 3d and e.

Region A: 20-700 kHz. With a high time resolution the low-frequency region exhibits a definite structure of a fundamental regime and higher harmonics instead of the usually presented massive broadened region. This sequence of peaks is the fourier analysis of rapidly relaxating bursts with typical growth times $\tau \sim 1/f_{fundamental}$. In view of the reduced collisionality factor $\nu^*_{eff} \equiv \nu_{ei}/\omega_f \approx 2$ near the position of the scattering volume (r = 65 mm), the low-frequency drift waves can be interpreted in terms of growth and quenching of unstable universal-type drift waves together with dissipative trapped electron instabilities from a 5% group of mirror-trapped electrons [5]. However, the presence of a spectral contribution due to oscillations of magnetic origin should also be considered [6]. From the measured growth rate of the spectrum and the mixing-length relation we made an estimate for the fluctuation level at r = 65 mm, yielding $\tilde{n}/n \approx 8\times10^{-3}$.

Region B: 0.7-3 MHz. This region is not yet extensively reported in literature. It is much weaker than the A-region. However, again $\Delta f \approx f$ indicating the turbulent character of the fluctuations.

Thomson scattering spectra (90°, λ = 694.3 nm at r = 5 and 60 mm) invariantly reveal at least two symmetrical satellites on the smooth, almost

gaussian, scattering spectrum (see Fig. 4). The satellites correspond with electron groups with the local Alfvén speed. Their intensities correspond with a partial population of about 5% (≈ $3\text{-}5\times10^{17}$ m^{-3}) at r = 5 mm. Partial densities at the edge are $1\text{-}3\times10^{17}$ m^{-3}.

In view of the above observations and of the high β_{pol}-values, the B-region is interpreted as revealing the presence of temperature-gradient driven turbulence of high-mode microtearing instabilities. The magnetic field fluctuation level can be estimated with the relation [7]: $\tilde{B}_\perp/B \sim \frac{1}{2}\beta q \cdot |\tilde{n}/n|$. Insertion of the acceptable value $\tilde{n}/n = 8\times10^{-3}$ yields for I_p = 30 kA, $\tilde{B}_\perp/B \approx 1.5\times10^{-5}$ at r = 60 mm.

The identification of the satellites in the Thomson spectra with perpendicularly deflected electron streams giving local magnetosonic shocks is strengthened by checking the approximate equality of the kinetic energy of this electron group to the perturbed magnetic field energy, yielding for the number density of streaming electrons in the scattering volume 1×10^{17} m^{-3}.

It may be remarked that the electron-temperature gradient-driven microtearing modes have a real oscillatory part and a growing imaginary part. The relation between the diamagnetic electron drift frequency, ω_{*e}, and the real part of the tearing modes is approximated by [8]: $\omega_p/\omega_{*e} = 1 + (0.6)[1 + \ell n(\nu_{ei}/\omega_{*e})]\eta_e$. For the TORTUR parameters we find ($\eta_e \approx 4\text{-}5$, $\nu_{ei}/\omega_{*e} \geq 3$) that $\omega_p/\omega_{*e} = 6\text{-}7$, being satisfactorily close to the experimental ratio of frequencies at the maximum of S_k in the regions B and A: $\omega_B/\omega_A = 7\pm3$.

Region C: 5-55 MHz. For the TORTUR discharge parameters, the runaway current in the plateau stage is estimated to be $I_{RA} \leq 70$ A, which is about 0.18% of the total current. It is supposed to be strongly concentrated near the axis. For this population, the threshold runaway energy, E_{RA}, amounts to some 6 keV. The interaction of the runaway electrons via the anomalous Doppler effect with various bulk plasma modes and with the gradient-driven modes results in limitation of the runaway energies via pitch-angle scattering of the electron distribution. This happens for energies $E_b > 3(\omega_{ce}/\omega_{pe})^2 E_{RA} \approx 80$ keV for TORTUR, which is not in contradiction with experimental data from soft X-ray and ECE spectroscopy [9].

The slow periodic modulation of the spectral intensity in region C (see Fig. 3c) with typical relaxation rise times of 0.5 ms gives another support for the presence of the tail population. Free acceleration of electrons during 0.5 ms followed by quenching (scattering) in a fluctuating toroidal electric field of 2 V/m indeed gives electron energies near 100 keV.

Fluctuations after the application of a turbulent heating pulse

Finally, the strong time-dependent variations in the three spectral regions after application of a high-voltage turbulent heating pulse (see Fig. 1) offers support for the proposed identification of the physical nature of the various regions. This can be inferred from Figs. 5a-c. After the pulse, a rather flat temperature profile results, whereas the density gradient is increased [10]. Indeed, a remarkable increase on a fast timescale (~ 100 μs) can be observed for the low-frequency electrostatic drift waves of region A (Fig. 5a). In contrast, the regions B and C have completely disappeared. Evidently, $\eta_e \equiv \partial \ell n\, T_e/\partial \ell n\, n_e$ is decreased by the flattening of $T_e(r)$ and the peaking of n(r), together with a temporary increase of $\nu_{ei}(r)$, such that unstable microtearing modes are suppressed [10].

However, after thermalization of the poloidal magnetic energy of the peaked-up current profile at t = 2 ms, ΔT_e increases dramatically and so does n_e. Indeed, the B-region increases towards the previous level in less than 1 ms. Similar remarks apply to region C, albeit that the increase is delayed somewhat, probably because the tail electrons require some 0.5 ms to be sufficiently accelerated for instability action.

Acknowledgement. This work was performed under the Euratom-FOM association agreement with financial support from ZWO and Euratom.

References

[1] F.A. Haas et al., Plasma Phys. Contr. Fusion 29 (1987) 145.
[2] N.J. Lopes Cardozo et al., Europhys. Conf. Abstr., 10C (1986) 276.
[3] F. Huussen et al., Plasma Phys. Contr. Fusion 27 (1985) 447.
[4] P.C. Liewer, Nucl. Fusion 25 (1985) 543.
[5] M. Venema et al., Rijnhuizen Report 84-152 (1984).
[6] Equipe TFR, Plasma Phys. Contr. Fusion 25 (1983) 641.
[7] R.E. Waltz, Phys. Fluids 26 (1985) 577.
[8] N.T. Gladd et al., Phys. Fluids 23 (1980) 1182.
[9] N.J. Lopes Cardozo, Rijnhuizen Report 85-160 (1985).
[10] H. de Kluiver et al., Subm. to Plasma Phys. Contr. Fusion.

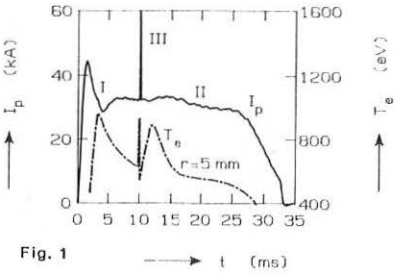

Fig. 1

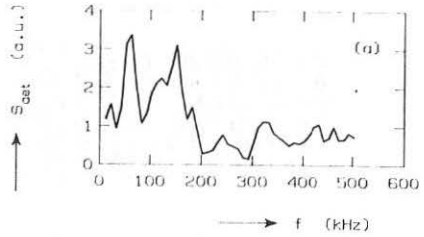

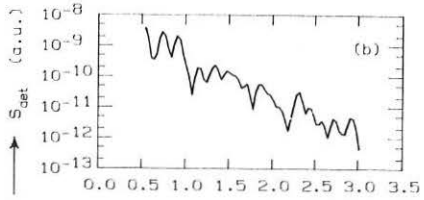

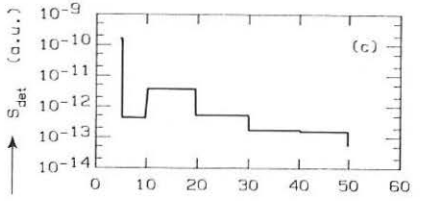

Fig. 2

Fig. 1. Time development of I_p and T_e (r = 5 mm).

Fig. 2. Power spectra of the density fluctuations in the three regions.

Fig. 3. Low-frequency modulations on the density fluctuations (a-c), T_e(d) and I_p(e).

Fig. 4. Thomson-scattered spectrum (a) and deviations from fitted gaussian (b).

Fig. 5. Behaviour of the density fluctuations after the turbulent heating pulse.

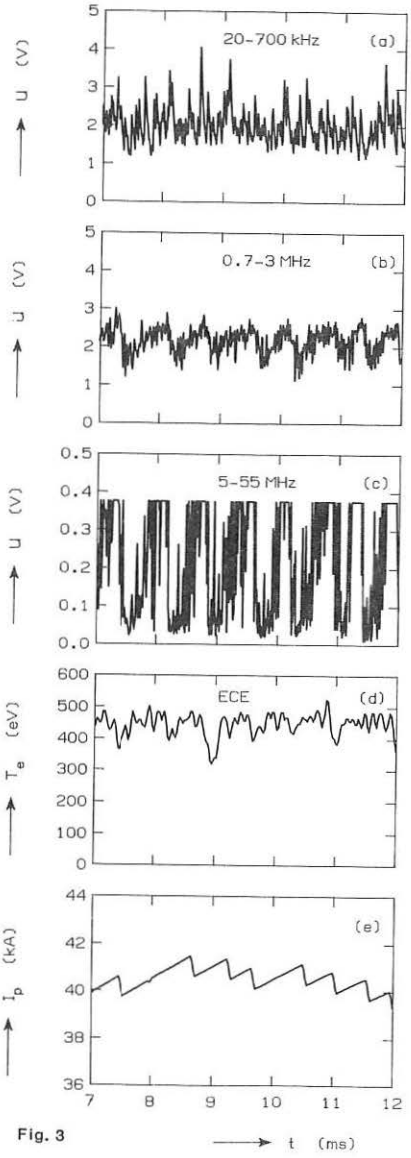

Fig. 3

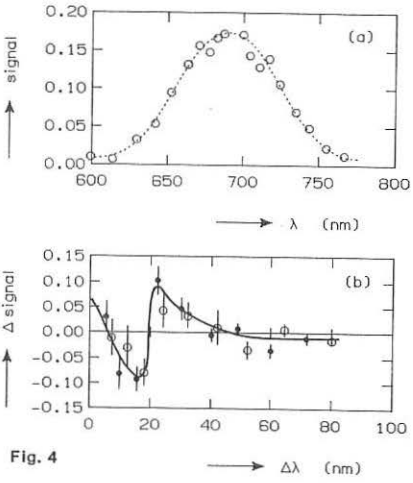

Fig. 4

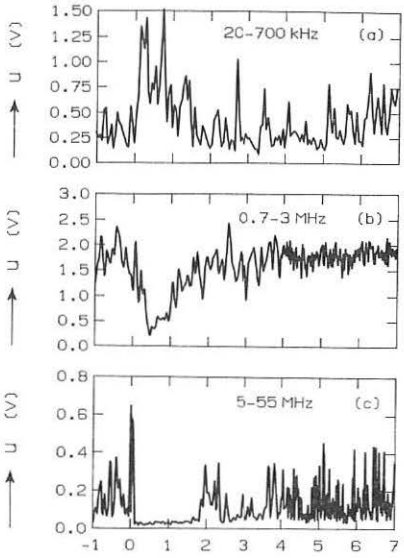

Fig. 5

MEASUREMENT OF DENSITY TURBULENCE AND BROADBAND MAGNETIC FLUCTUATIONS ON ASDEX

G. Dodel, E. Holzhauer, and J. Massig
Institut für Plasmaforschung, Universität Stuttgart, Fed. Rep. of Germany

J. Gernhardt, ASDEX-, ICRH-, LH-, NI-, and Pellet-Teams,
Max-Planck-Institut für Plasmaphysik, EURATOM-Association, Garching, FRG

Broadband fluctuations of the electron density and the magnetic field were observed under various operational conditions of ASDEX using a laser scattering experiment and Mirnov coils, respectively. The aim of such measurements is to reveal the physical nature of the fluctuations and their possible correlation to anomalous particle and energy transport properties.

1. Density fluctuations.

The scattering system using a 119 μm CH_3OH laser and homodyne detection is described in more detail elsewhere [1]. It is able to detect density fluctuations propagating in nearly vertical direction. Movable optics allow a stepwise $k_\perp$-scan within one tokamak discharge and a shot to shot spatial scan of a large part of the poloidal plane. The spatial resolution is ± 1 cm in the vertical direction and depends on $k_\perp$ in the horizontal direction. For $k_\perp \leq 10\ cm^{-1}$, where the dominant part of the fluctuation spectrum is found, the measurements are chord-averaged. The $k_\perp$ resolution is ± 3.2 cm^{-1}.

The temporal development of the fluctuation spectra could be monitored with fixed frequency channels. Plateau phases of the tokamak discharge allowed frequency spectra to be scanned continuously with a spectrum analyzer.

a) Ohmic heating
In the range $5\ cm^{-1} \leq k_\perp \leq 20\ cm^{-1}$ the frequency integrated scattered power $P_s(k_\perp)$ decreases as $k_\perp^{-\alpha}$, where $\alpha \approx 4$. The frequency power spectra $P_s(f)$ for fixed $k_\perp$ are broadband. A frequency roll-off on the order of 6 dB/100 kHz is observed above 100 kHz. The root of the frequency integrated power $P_s^{1/2}$ scales linearly with the mean electron density $\bar{n}_e$ in the range $5 \times 10^{12}\ cm^{-3} \leq \bar{n}_e \leq 5 \times 10^{13}\ cm^{-3}$ (Fig. 1). This corresponds to a nearly constant relative fluctuation level $\tilde{n}_e/n_e$.

b) Neutral beam injection (NI) heating.
L-discharges: With neutral injection the frequency spectra $P_s(f)$ become broader with increasing heating power. In the majority of L-discharges the frequency integrated scattered power increased above the ohmic level during neutral injection as illustrated in Fig.2. A maximum enhancement by a factor of ~9 was observed with co-injection. In a series of counter-injection shots at constant n_e the increase of P_s with P_{NI} was approximately linear for P_{NI} up to 3.5 MW.

H-discharges: The temporal development of the fluctuation spectra at the transition from the L-phase into a burstfree H-phase is shown in Fig. 3. A comparison of the low- and high frequency channels shows a broadening of

the spectrum and a decrease in the frequency integrated scattered power although the line density $\bar{n}_e$ increases. A similar observation was reported in [3]. There is evidence for a shift in the $k_\perp$ spectrum towards longer fluctuation wavelengths. In contrast to the sharp L-H transition indicated by the D_α-monitor in the divertor chamber the frequency integrated scattered power changes on a much longer time scale, which corresponds to the global change in the density and temperature profiles.

In normal H-discharges with edge-localized modes the behaviour of the scattering signals is irregular.

c) Ion cyclotron resonance heating.
The scattering signals increase above the ohmic level for $k_\perp \leq 5\ cm^{-1}$ as reported also by [4]. Density fluctuations with $k_\perp \leq 7.5\ cm^{-1}$ are observed at the heating frequency (33.5 and 67 MHz).

d) Lower hybrid heating and current drive.
No significant changes in the low-frequency density fluctuations with respect to the ohmic phase are found.

e) Sawtooth activity.
Precursors to the sawtooth crash in the soft X-ray signals are observed in the frequency range > 500 kHz. There is experimental evidence that they are localized only inside the q=1 surface. Increased fluctuations below 500 kHz are also found outside the q=1 surface, but only after the sawtooth crash [1].

f) Pellet injection.
An increase of the scattered signal is observed which starts with the ablation of the pellet. For single pellets the scattered signal decreases with the relaxation of the radial density profile [1].

In order to obtain a conclusive picture of the nature of the density turbulence and possible correlations to anomalous transport properties the measurements will be extended to wavenumbers below $5\ cm^{-1}$.

2. Magnetic fluctuations.

Mirnov coils in the limiter shadow of ASDEX were used to demonstrate the existence of broadband magnetic fluctuations with radial and poloidal components. Above about 70 kHz the temporal evolution of these spectra is distinctly different from the coherent Mirnov oscillations and their harmonics at lower frequencies.

If we assume that the field due to current disturbances decays like a vacuum field outside the plasma boundary in a cylindrical geometry, we can estimate the dominant poloidal mode number. For L-mode discharges with NI the plasma position, and thus the distance to the Mirnov coil, were varied. From the observed radial decay length a value of $m \geq 10$ is deduced. Typical fluctuation levels at the probe position were $\tilde{B}_r/B_t \approx 10^{-5}$. From 70 kHz to 200 kHz the spectral power density drops by a factor of 10. No qualitative

difference was seen in the temporal development of the radial and poloidal field components.

a) Ohmic heating.
The power spectra of the magnetic fluctuations are not correlated with those of the density fluctuations. During a linear density ramp the signal power of the magnetic fluctuations decreased slightly in contrast to the density fluctuations (Fig. 1).

b) Additional heating (L-phase).
The signal power increases for all types of heating used and the frequency spectrum broadens. An example recorded during an L-discharge with NI is given in Fig. 2.

c) Additional heating (H-phase).
After the transition into a burstfree H-phase the signal power begins to increase again as shown in Fig.4. When edge localized modes, indicated by spikes in the D_α signal, appear, the magnetic fluctuation signal is strongly modulated.

d) Sawtooth activity.
In the presence of sawteeth (during additional heating) the fluctuations suddenly increase at the time of the sawtooth crash, similarly to the D_α-signal observed in the divertor chamber [2].

e) Influence of boundary layer.
The magnetic probe signals seem to depend on conditions in the plasma boundary layer, as can be seen in the case of gas puffing or the modulation by edge localized modes.

3. Summary.

Significant but distinct changes in the fluctuation spectra have been observed in the various operating regimes of ASDEX. When comparing the behaviour of the density and magnetic field fluctuations it should be kept in mind that the two diagnostics have different spatial weighting functions, defined by the scattering volume in the former case and by the distance from the probe and the mode number m in the latter case. Further experiments will be needed before a comparison with proposed theoretical models for the fluctuations and their propagation mechanism inside the plasma can be made.

References

[1] Dodel, G., Holzhauer, E., Massig, J., Vogel, T., Ignacz, P., ASDEX-, ICRH-, LH-, NI-, and Pellet-Teams, in "Basic and Advanced Diagnostic Techniques for Fusion Plasmas", Varenna (Italy), Sept. 1986,Vol.II,p.589 DOC. CEC EUR-10797 EN.
[2] IPP Garching, Annual Report 1986, p. 15
[3] Crowley, T., and Mazzucato, E., Nucl. Fusion 25, (1985), 507
[4] TFR Group, and Truc, A., Plasma Phys., 27, (1985), 1057

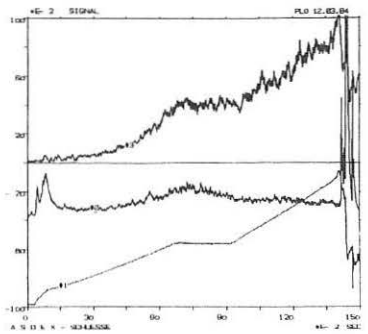

Fig.1 Density- and magnetic fluctuation signals in a shot with density ramping.
From top to bottom:
rms-scattering signal $P_s^{1/2}$;
f = 100 ± 15 kHz; $k_\perp$ = 7.5 cm^{-1}.
Magnetic signal power;
f = 100 ± 15 kHz.
Line electron density $\bar{n}_e$.
(Full time interval of abscissa: 1.5 s)

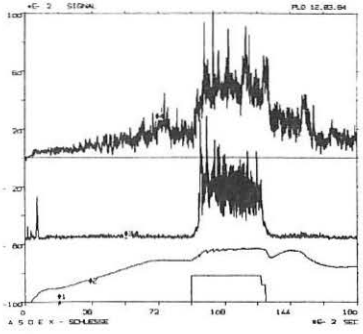

Fig.2 Density- and magnetic fluctuation signals in a L-discharge with NI.
From top to bottom:
Scattering signal P_s; f = 60 kHz - 1600 kHz; $k_\perp$ = 7.5 cm^{-1}.
Magnetic signal power;
f = 100 ± 15 kHz.
Line electron density $\bar{n}_e$.
NI beam monitor; P_{NI} = 2.64 MW.
(Full time interval of abscissa:1.8 s)

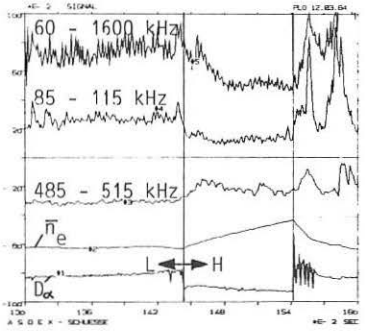

Fig.3 Density fluctuation signals in different frequency channels at the transition from an L-phase into a burstfree H-phase. $k_\perp$ = 5 cm^{-1}. Lower traces: line electron density $\bar{n}_e$ and D_α-monitor. (Full time interval of abscissa: 300 ms).

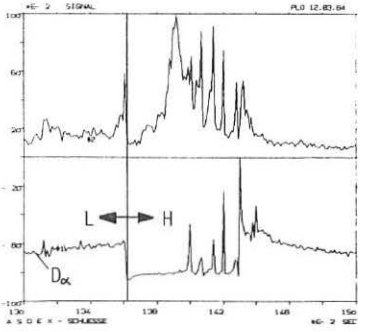

Fig.4 Magnetic fluctuation signal power at the transition from an L-phase into a burstfree H-phase followed by edge localized modes; f = 100 ± 15 kHz. Lower trace: D_α-monitor. (Full time interval of abscissa: 200 ms).

MAGNETIC FIELD PERTURBATIONS AS A TOOL TO INFLUENCE GLOBAL DISCHARGE CONDITIONS

G. Fuchs, K.H. Dippel, A. Nicolai, G.H. Wolf and the TEXTOR Team
Institut für Plasmaphysik der Kernforschungsanlage Jülich GmbH
ASS. EURATOM - KFA

Introduction

Ergodization of magnetic field lines has been proposed as a possible mechanism to explain the anomalous transport observed in plasma confinement devices [1]. A magnetic perturbation consisting of several helical modes will create magnetic islands at the resonant surfaces. Above a certain amplitude, overlapping of the different islands will occur, which leads to a structure involving multiply connected regions, where field lines get mixed. This deteriorates the containment of the plasma.

In the boundary region of fusion machines, the loss of confinement might, however, be beneficial because due to the enhancement of particle recycling the plasma temperature and thus wall erosion could be reduced [2], albeit on the expense of the hot confinement volume.

In this paper we report measurements which have been made on TEXTOR to investigate the influence of small external perturbations of the confining field on both, the core confinement and the plasma parameters in the boundary.

Experimental Arrangement

The coil system to perturb the confining field consists of 4 coils (16 turns each) which are switched as a magnetic octupole (cf. fig.1). The Fourier components of the perturbation field are of the order of 0.1% of the main field. Although the perturbation amplitude decreases with the distance from the coils, it is not negligible in the plasma core. The perturbation coil current can be programmed in a wide range, only limited by an inductive time constant of about 20 ms, and the pulse width of 4 s at the maximum current of 8 kA per turn. The TEXTOR machine parameters may be found in [3]. Experiments have been performed for plasma densities $n = 1...4\times10^{13}$ cm^{-3} (line averaged), plasma currents $I_p = 200...480$ kA and with a main field of 2 T.

Plasma Boundary

Instantaneously with the rise of the perturbation field we observe structures appearing in the boundary region. These structures exhibit the shape of magnetic islands (see [4;5]), which persist even in those cases where, according to calculations of the Liapunov coefficients, the perturbation was large enough to cause stochasticity. A possible explanation for this discrepancy may be given by the fact that the mixing of field lines leads to fine graining only after many ($10^3...10^4$) revolutions around the torus, whereby a particular field line, except for jumps between different islands, takes similar pathways to surround an island. This effect is enhanced because two overlapping islands usually contain cores, which are disconnected from the rim. The particles diffusing from the hot plasma core into this structure stream predominantly in the region of the island rims to the limiters where they recombine. The interaction of this flow with the recycling particles produces the observed pattern. We can reproduce the experimentally observed structures in Poincaré plots, if a set of magnetic field lines is being started just inside the "stochastic region" and traced about 8 turns around the torus.

Structures in the boundary are also indicated by the localized H_α luminescence measured at different toroidal positions, by the radial density profile in the boundary, measured with a lithium probing beam [6], and by the dependence of the pressure in the pump limiter chamber (135° away from the perturbation coils in toroidal direction) on the plasma current (cf. fig. 2). Although the geometry of the perturbation field was not optimized to create such islands which give a maximum enhancement of pumping on the TEXTOR ALT I pump limiter [4], pressure increases in the pump limiter chamber by up to a factor 2 could be obtained. The electron temperature measured with Langmuir probes, located in the limiter shadow 2 cm off the tangent surface, is almost unaffected by the perturbation field. However, deeper inside the boundary the desired cooling of the electrons seems indeed to exist, since the C II luminiscence has been observed to increase with the application of the perturbing field, whereas the C IV luminescence decreases at the same location.

Global Effects

No effects of the perturbation fields on the q - and density - limit have been found. The average particle lifetime $\tau_p^* = \tau_p/(1-R)$ (R is the recycling coefficient), however, has been affected. Although no systematic tendency has been obtained, this phenomenon is attributed to localized modifications of the plasma wall contact.

The Mirnov coil signals from MHD-modes (m = 2;n = 1) which were occasionally present, disappear already at low amplitudes of the perturbation field, most probably as a result of the blocking of the rotation of these modes.

Transition of Confinement

Whereas the above phenomena occured about synchronously with the application of the relevant amplitude of the perturbation field, influences on the confinement are delayed by about 100 ms with respect to the rise of the perturbation field. Above a well (±1%) defined threshold value of the perturbation field, and after the above delay, a full disruption or a transition to a new discharge state occurs. The threshold value needed for the response depends on q (see also [7]) and is given in fig.3. In case of the transition (fig. 4), the density profile flattens, whereby the total number of plasma particles is reduced by a factor of about 2, although the density in the boundary even rises.

The average core electron temperature is, after a short decrease followed by a recovery, unchanged within a few percent. This is consistent with the experimental fact that - for given plasma current - the loop voltage remains unchanged. However, the frequency and the amplitude of the sawteeth is reduced (cf. fig.4). It is worthwile to note, that this transition to a deteriorated confinement regime cannot be reversed by switching off the perturbation field, instead MHD-modes appear which eventually lead to a disruption. Both, the density profile and the Mirnov coil signals indicate, that together with the transition the axi-symmetry of the plasma is lost.

Model Considerations

Possible reasons for disruptions at a definite level of the perturbation field have been previously discussed (e.g. [7]). Here it is assumed, that the transition is caused by a significant enhancement of the "radial" transport processes specifically in those regimes where islands have been created or are already overlapping: the enhanced losses thus are assumed to stem from parallel heat conductivity $\chi_\parallel$ contributing via the radial components B_r of the perturbation field. The enhanced transport is compared to the one without perturbation field using an enhancement factor $k = \chi_\parallel \Delta r/\chi_\perp L$.

To obtain an estimate of the enhancement factor, $\chi_\perp$ is taken from [8] and the island width Δr and the length L to bridge Δr along a field line are calculated in cylindrical geometry, in which case the formulae [9]

$$\Delta r = \sqrt{\frac{2 B_r R}{m B_\varphi} \frac{\partial \iota}{\partial r}}$$

$$L = 2\pi R N \qquad N = \sqrt{\frac{B_\varphi}{B_r R} \frac{\partial \iota}{\partial r}} \quad K(\sin^2 m\vartheta/2)$$

can be used, where K is the complete elliptic integral. For the current density needed to derive ι we make the ansatz

$$j = \frac{B_\varphi}{R} \iota(0) \left[1 - \frac{r^2}{a^2}\right]^p$$

which gives values close to those measured with polarimetry, for p = q(a). The temperature profile needed for $\chi_\parallel$, is assumed to be proportional to $j^{2/3}$. The radial dependence of the transport enhancement factor k, calculated under these assumptions is, for a special case, shown in fig. 5.

With increasing perturbation field, the island widths grow, the number of toroidal turns N, needed to bridge a given radial distance within the island structure decreases, and more islands with increasing m numbers give significant contributions to the enhancement, all of these leading to an increase of the transport enhancement. When islands located around different rational surfaces overlap above a certain field perturbation, the island rims, where N is large, are eliminated, which

again accelerates the increase of k. At about the experimental value of the perturbation field, where the deterioration of the confinement is observed, the enhancement factor exceeds 1 for plasma radii outside the q = 1 surface.

Conclusions

The experiments show, that helical perturbation fields create island structures in the boundary, which can be used to enhance pumping and appear to cool the boundary. The observation of islands in the boundary layer even for cases of field stochasticity is attributed to boundary conditions on the plasma pressure which lead to a structured flow pattern.

The most pronounced effect on the plasma confinement in the core is a transition to reduced confinement, triggered by the perturbation, but delayed by about a characteristic skin time. Model considerations on the enhancement of parallel heat transport around islands, although giving the correct order of magnitude, cannot yet explain the sharp onset of the transition which, however, is also believed to be due to island effects.

[1] A.B. Rechester and M.N. Rosenbluth; Phys. Rev. Let. **40** 38 (1978)
[2] W. Feneberg and G.H. Wolf; Nucl. Fusion **21**. 669 (1981)
[3] H. Soltwisch et al.; Plasma Phys. and Contr. Nucl. Fus. **26A** 23 (1984)
[4] K.H. Dippel et al.; J. Nucl. Mat. **145-147** 3 (1987)
[5] N. Ohyabu et al.; Nucl. Fusion **25** 1684 (1985)
[6] A.Pospieszczyk and G.G. Ross; submitted to Rev. Sci. Inst.
[7] F. Karger et al. Plasma Phys. and Contr. Nuc. Fus. Res., **1**, 207 (IAEA Vienna 1975)
[8] Y. Cao and G. Waidmann; this issue
[9] G. Fuchs, A. Nicolai, B. Steffen and G.H. Wolf; Jül. Report 1820 (1982)

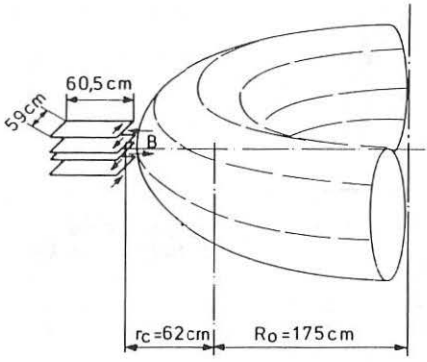

Fig. 1 Schematic of the perturbation coils. They can be tilted by $\pm 15^{\circ}$

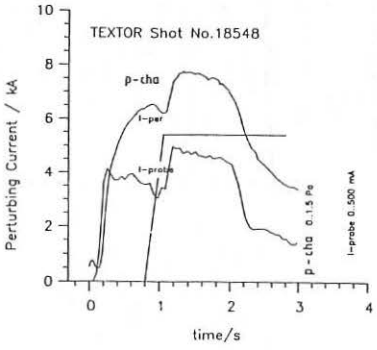

Fig. 2 The perturbation field current I-per, the pressure in the pump limiter chamber p-cha and the ion current to a Langmuir probe near the pump limiter for a discharge without changeover.

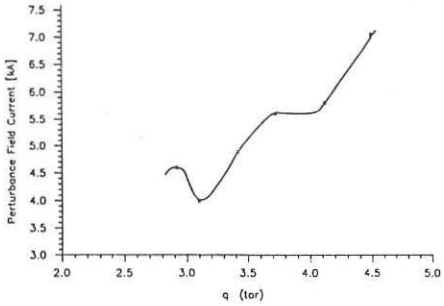

Fig. 3 The minimum perturbation field current needed to cause a changeover or a disruption versus the (toroidal) q. The points are reproducible within $\pm 1\%$ for fixed discharge conditions. The minima near rational q values can be obtained by both, a variation of Ip or a.

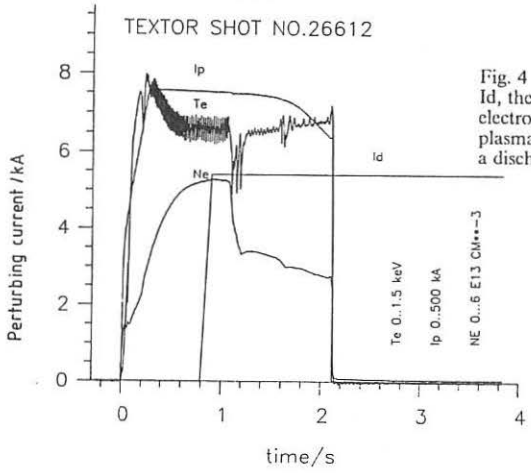

Fig. 4 The perturbation field current Id, the plasma current Ip, the electron temperature Te (ECE) and the plasma density Ne (HCN interferometry) for a discharge with changeover.

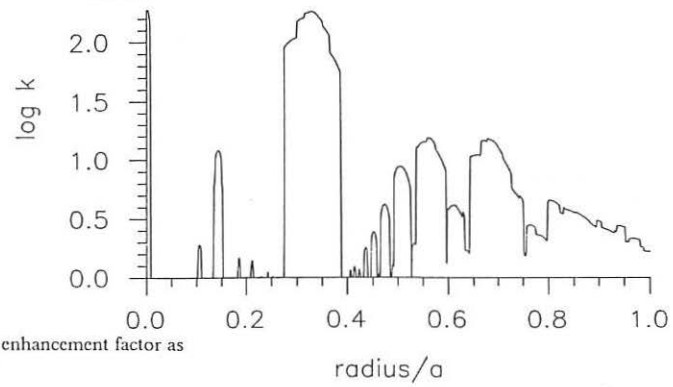

Fig. 5 The transport enhancement factor as explained in the text.

EVALUATION OF ELECTRON HEAT CONDUCTIVITY FROM SAWTOOTH PROPAGATION STUDIES IN TEXTOR

Y. Cao and G. Waidmann

Institut für Plasmaphysik, KFA Jülich, Association EURATOM-KFA
5170 Jülich, Federal Republic Germany

Abstract: The propagation of inverted sawteeth was studied in quasi-stationary plasmas in TEXTOR. The electron heat conductivity χ_e was deduced from time of flight measurements of heat pulses emitted into the outer plasma region.

1. Introduction

Sawtooth phenomena were studied in TEXTOR by means of ECE-diagnostics in the current plateau phase of quasistationary OH-discharges. The propagation times and amplitudes of heat pulses emitted from the central plasma were systematically measured in the radial regime between the q = 1 - surface and the boundary plasma. Highly reproducible discharges were produced after fresh conditioning of the inner surface of the plasma vessel. Scanning radiometric measurements were performed on the high and low field side of the plasma cross section. A numerical model first suggested by Callen and Jahns /1/ was modified and used to simulate transient heat propagation from a pulsed heat source into the boundary plasma. The good agreement between numerical model and experimental data allows the evaluation of the average electron heat conductivity $\bar{\chi}_e(r)$ in the outer confinement region of the tokamak plasma.

2. Heat Pulse Propagation Studies

Local measurements of electron temperature perturbation were carried out by ECE diagnostic technique /2/. A fixed frequency radiometer was used to observe the central part of the plasma inside the q = 1 - surface. It delivers time reference marks by registration of normal sawteeth. Two variable frequency radiometers were installed to observe heat pulses outside of q = 1 on the high and low field side of the plasma column. Time of flight measurements were performed by simultaneous registration of normal and inverted sawteeth. A frequency scan on a shot to shot basis provided the radial profile information. The sawtooth inversion radius r_s was found by inspection of sawtooth details in a transition regime. It agrees reasonably with the q = 1 - surface as found by polarimetric measurements /3/. Sufficiently far outside of the inversion radius clear inverted sawteeth are recorded which represent transient heat pulses. Fig. 1 shows time of flight data for heat pulses observed during the stationary phase of OH-discharges. The propagation time t_p increases nonlinearly with radial distance. The q = 1 - surface is marked by 2 straight bars. Fig. 2 presents for the low field side of TEXTOR the time t_p versus $(r - r_2)^2$ and demonstrates a quadratic dependence with radius for distances $r > 1.4\ r_s$.

A deviation is observed in the vicinity of the plasma boundary. This result suggests a diffusive type of electronic heat transport from the q = 1 region towards the plasma edge.

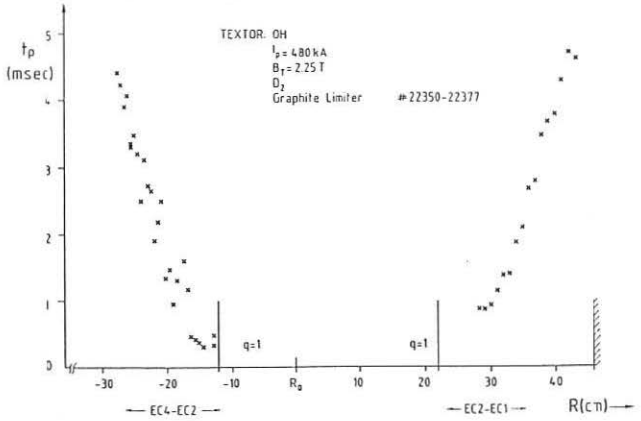

Fig. 1 Propagation time t_p versus radial distance

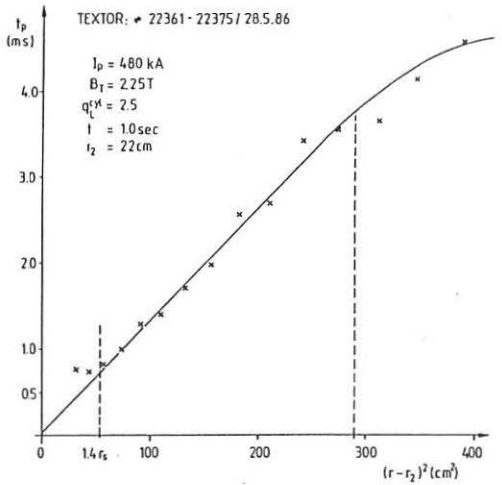

Fig. 2 Propagation time t_p versus r^2 on the low field side of the TEXTOR machine

3. Numerical Model and Experimental Results

For the interpretation of the propagation pattern of local temperature perturbations (s. Fig. 2) a cylindrical model /1/ was modified and used to simulate transient heat pulses on their way along the density gradient into the boundary plasma. In Ohmic discharges the temperature perturbations outside of the inversion radius were small, less than 10 % of the stationary electron temperature. The density perturbation was even smaller. The energy balance equation for the electrons was reduced by neglecting the source and sink terms ηI_p^2, radiation and equilibration. The linearized cylindrical heat conduction equation was numerically solved with the ansatz for the heat conductivity coefficient:

$$\chi_e(r) = \chi_0/n_e(r)$$

and density profiles as found experimentally in TEXTOR. Initial conditions for the mixing regime, where the emitting heat source is located in our numerical model, were specially chosen. A general discussion of simple models and errors introduced by assumptions made is given in /4/. Good agreement between measured heat pulses and simualted temperature perturbations was found for the different radial positions studied. Fig. 3 shows in a comparison the decay of the measured amplitude of the temperature perturbation (X) versus radius. Included in Fig. 3 are the values obtained by model calculation (●). The simulated values are fitted at the point FP. The amplitude decays as $(r-r_2)^{\alpha}$, the exponent being $\alpha = -1{,}56$. This decay exponent can approximately be deduced by an analytic treatment of the heat conduction problem. From the calculated time of the maximum of the heat pulses and the measured time of flight an average value of $\bar{\chi}_e$ is evaluated. Fig. 4 shows these $\bar{\chi}_e$ - values for two very different discharge types versus the radial coordinate r_2. For a peaked electron density profile (X I_p = 372 kA; $n_e = 2{,}8 \times 10^{13}$ cm^{-3}) a strong increase of $\bar{\chi}_e$ with radius was found. A broad density profile (▲ I_p =480 kA; $n_e = 4.6 \times 10^{13}$cm^{-3}) however gave a lower $\bar{\chi}_e$ - value and exhibited a slower $\bar{\chi}_e$ - increase with radius. The values found in this way are in qualitative agreement with data obtained form energy balance transport code calculations for Ohmic heating in TEXTOR /5/ or in ASDEX /6/. They show however lower values than the experimental χ_e-data published from TFTR /7/.

4. References

/1/ J.D. Callen, G.L. Jahns: Phys. Rev. Lett. 38 (1977) 491

/2/ G. Hrehuss, G. Waidmann: 12th Europ. Conf. on Controlled Fusion and Plasma Heating, Budapest (1985), Part I, 118

/3/ H. Soltwisch et. al.: 11th Int. Conf. on Plasma Physics and Controlled Nucl. Fus. Res., Kyoto (1986)

/4/ W.J. Goedheer: Nucl. Fusion 26, No. 8 (1986), 1043

/5/ A. Nicolai: this conference: paper 0212 A

/6/ M. Keilhacker et.al.: Plasma Physics and Contr.Fusion 28,1A (1986),29

/7/ E.D. Fredricksen et. al. Nucl. Fusion 26, No. 7 (1986), 849

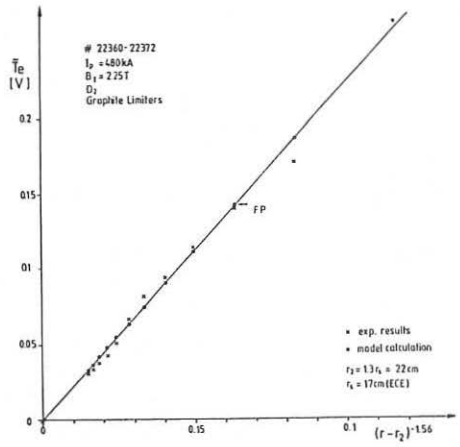

Fig. 3 Sawtooth amplitude $\tilde{T}$ versus $(r-r_2)^{-1.56}$

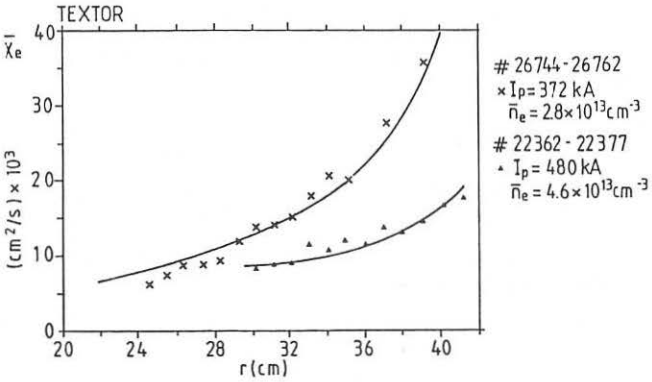

Fig. 4 $\bar{\chi}_e$ versus radius for two different electron density profiles

MODELLING OF TEMPERATURE PROFILE RESPONSES TO HEATING PROFILES IN JET

J.D. Callen*, J.P. Christiansen, J.G. Cordey

JET Joint Undertaking, Abingdon, Oxon. OX14 3EA, UK
*University of Wisconsin, Madison, WI 53706, USA

1. Introduction

Temperature profiles in tokamak plasmas have been characterised as exhibiting a high degree of "profile consistency" [1]. However, some variation in the temperature profiles have been observed with changes in the heating profile [2]. In this work [3] we seek to explain the temperature profile variations and global transport scaling due to changes in the heating profile using local heat transport models that are consistent with other, local measurements of heat transport in JET.

Global indications of changes in the temperature and current profiles in JET are shown in Figs.1,2. Figure 1 shows that the equilibrium ratio of the average temperature to the peak temperature increases as the heating profile broadens with decreasing safety factor q. Figure 2 shows that neutral beam broadens the electron temperature profile after injection. The current profile broadens on a longer time scale which is of the order of the magnetic diffusion time scale, as expected. Ref.[3] provides full details of the work presented here.

2. Local Heat Transport Models

Two recent developments [4,5] have helped to clarify the form of local models appropriate for describing heat transport in JET. First [4], the heat diffusion coefficient derived from heat pulse propagation measurements (χ_{HP}) has been shown to be independent of auxiliary heating power and to be approximately equal to that deduced from the incremental energy confinement time τ_{inc} [6]. Second, the total (electron plus ion) heat flux through the confinement zone of the plasma has been shown to be fit best [5] by

$$\underline{q} = -n\chi\underline{\nabla}T + \underline{q}_{flow} = -n\chi\underline{\nabla}T - \underline{q}_{pinch}. \qquad (1)$$

The nondiffusive flow term q_{flow} is found [3-6] to be negative, which indicates a heat pinch [7] or critical temperature gradient onset phenomenon [8]. Possible interpretations of it are discussed in [3].

Two specific local heat transport models [7] based upon Eq.(1) are used below to predict the temperature profiles for given heating profiles:
1) Constant heat pinch model: $\chi(r)$ and $q_{pinch}(r)$ are assumed to have given spatial profiles, but to be independent of parameters like T, input power.
2) Nonlinear χ model: $q_{flow} = 0$ and $\chi \sim (\underline{\nabla}T)^{\beta}$.

3. Temperature Profiles Induced by Various Auxiliary Heating Profiles

Temperature profiles for given heating profiles $Q(\underline{x})$ are calculated from the flux-surface-average equilibrium heat balance equation $\langle\underline{\nabla}\cdot\underline{q}\rangle = \langle Q\rangle$. Using Eq.(1), the heat balance equation can be integrated once to yield an equation for the radial temperature gradient. To solve for the temperature profile we must choose a particular local heat transport model.

In what follows we use for simplicity n(r) = constant and a cylindrical geometry approximation.

Constant heat pinch model. The predicted temperature profiles are given by a double radial integral of the heating profile Q(r) and hence relatively insensitive to small changes in Q. Such profiles induced by a variety of heating profiles Q(r) ranging from peaked on axis (dotted line) through flat (solid dark line) to peaked at the plasma edge (dashed line) are indicated in Fig.3. The temperature profiles are plotted on a logarithmic scale normalised at the half radius [9]. Fig.3 shows that only very modest temperature profile variations are expected for physically relevant changes in the heating profile. The ratio $\langle T\rangle/T(0)$ for these profiles are in agreement with the ranges indicated in Fig.1.

Nonlinear χ model. The predicted temperature profiles depend on a double radial integral of the $1/(\beta+1)$ fractional power of the heating profile Q(r); they are even less sensitive to variations in Q than those shown in Fig.3.

JET data for centrally peaked heating. The experimental temperature profiles that result from a variety of JET auxiliary heating profiles are shown in Fig.4. Comparing Fig.4 with Fig.3 we see that the weak temperature profile variations caused by changes in the heating profile are in reasonable agreement with the theoretical predictions. The best agreement occurs for $\beta<<1$ and for χ increasing radially.

Localised off-axis heating. In JET experiments the ICRH heating profile is highly peaked ($\Delta r \lesssim a/5$) near the radial location of the cyclotron resonance r_h. Both the heat pinch and nonlinear χ models predict the $\Delta T(r)$ due to ICRH to be constant inside the heating radius. However, the magnitude of $\Delta T(0) = \Delta T(r_h)$ and the radial fall off of ΔT with r outside of r_h depends on the model chosen. Comparisons of the ΔT obtained experimentally with the theoretical predictions in hydrogen minority ^{3}He majority plasmas are shown in Fig.5. Again, we find that there is best agreement between the experimental data and the local transport model predictions for $\beta<<1$ with χ increasing radially.

3. Global Transport Scaling

The stored energy $W=(3/2)\int d^3x\, n(T_e+T_i)$ derived from the constant heat pinch model is expressed as

$$W = \tau_\chi(1+\xi)\,\{[P_{in}]_{eff} + P_{pinch}\} = \tau_{inc}\,P_{in}(a) + W(0), \qquad (2)$$

where

$$\tau_{inc} = \eta\tau_\chi(1+\xi)/2,\ \tau_\chi = 3ab/4\bar{\chi},\ \xi=\langle n_iT_i\rangle/\langle n_eT_e\rangle,\ [P_{in}]_{eff} = \eta P_{in}(a). \qquad (3)$$

The heating effectiveness parameter η defined in [3] is unity for delta function heating on axis and zero for edge localised heating.

The global transport scaling law given in Eq.(2) has the offset-linear form that has been found [6] to characterise JET data quite well. The energy confinement time $\tau_E=W/P_{in}$ exceeds τ_{inc} for low power levels (e.g. ohmic heating), but approaches it for high input power levels. The

incremental confinement time τ_{inc} approaches the ideal incremental energy confinement time τ_χ when $\eta \to 1$ (central heating) and $\xi \to 1$.

4. Discussion and Conclusion

The temperature profiles predicted by local heat transport models have been shown to be in good accord with JET experimental results. The weak temperature profile responses to changes in the heating profiles explain "profile consistency", at least to the extent it is observed in JET. The local transport model which best characterises JET data is based on a heat pinch (or excess ∇T) model with a heat diffusion coefficient $\chi(r)$ that increases with radius. The global transport scaling law derived from this model exhibits a linear-offset form and provides definitions for the incremental energy confinement time τ_{inc} and the heating effectiveness η. These latter definitions provide a basis for taking account of heating profile effects in determinations of the energy confinement scaling in auxililary heated tokamaks.

References

[1] B. Coppi, Comments on Plasma Phys. and Cont. Fusion 5, 261 (1980).

[2] D.V. Bartlett et al., EPS Schliersee conference, Vol.10C, part I, p.236; J. Jacquinot et al., Phil. Trans. R. Soc. Lond. (to be published 1987); J. Jacquinot et al., 1986 Kyoto IAEA meeting paper F-I-1.

[3] J.D. Callen et al., JET-P(87)10, March 1987 (submitted to Nuclear Fusion).

[4] B.J.D. Tubbing, N.J. Lopes Cardozo, JET-R(87)01 (abridged version submitted to Nuclear Fusion; see also N.J. Lopes Cardozo et al at this conference).

[5] J.D. Callen, J.P. Christiansen, J.G. Cordey, D. Muir (at this conference).

[6] J.G. Cordey et al., 1986 Kyoto IAEA meeting paper A-II-3.

[7] E.D. Fredrickson et al., Nuclear Fusion 26, 849 (1986).

[8] P.H. Rebut et al., 1986 Kyoto IAEA meeting paper E-III-4.

[9] R.J. Goldston et al., 1986 Kyoto IAEA meeting paper A-II-1.

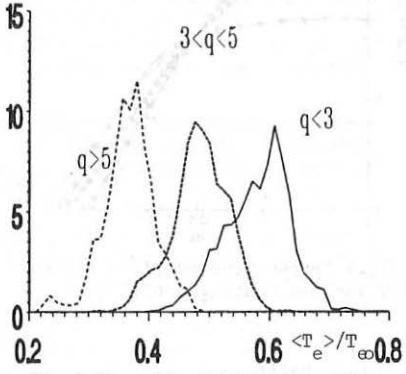

Fig.1 Normalised histogram of occurrences of average to peak temperature ratios for various safety factor ranges.

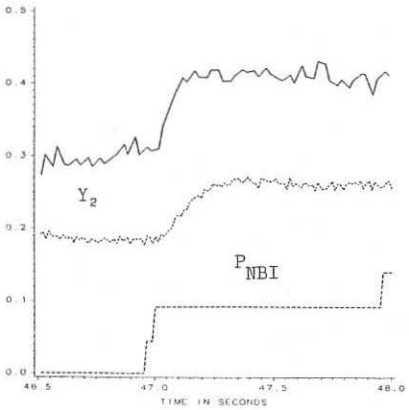

Fig.2 Temporal change of average to peak temperature ratio and a measure of current profile width Y_2 as neutral beam heating is applied.

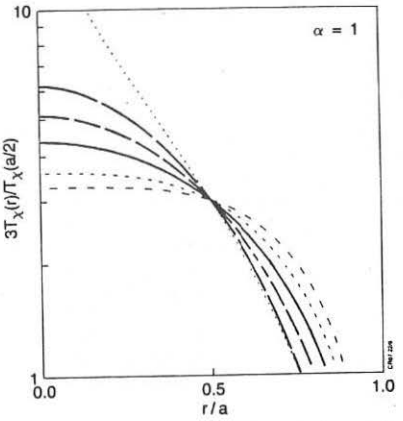

Fig.3 Temperature profiles induced by by various heating profiles for heat pinch model.

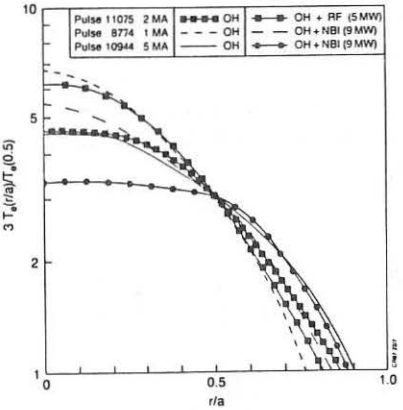

Fig.4 Temperature profiles induced by various heating profiles.

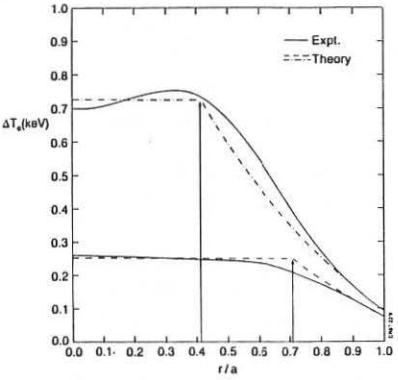

Fig.5 Comparison of the temperature change due to localised ICRH in JET with local transport model predictions

STUDY OF THE BROADBAND MAGNETIC TURBULENCE IN THE TCA TOKAMAK

F. Ryter, A. Pochelon and F. Hofmann

Centre de Recherches en Physique des Plasmas
Association Euratom - Confédération Suisse
Ecole Polytechnique Fédérale de Lausanne
21, Av. des Bains, CH-1007 Lausanne / Switzerland

ABSTRACT Poloidal structures of magnetic turbulence are studied and their persistence along the magnetic lines is analysed. This can give an estimate of the minor radii of the observed turbulence.

INTRODUCTION The study of broadband magnetic turbulence features is important to determine its nature and its possible effects on the transport. This paper presents measurements of the magnetic turbulence on the TCA tokamak (B_T=1.5 T, R=61.5 cm, a=18 cm), newly equipped with 96 magnetic coils placed in the scrape-off layer. The spatial properties of the turbulence and its relation to confinement have been presented earlier[1] and this work concentrates on the study of the poloidal structure of the turbulence and its transformation along field lines. Figure 1 gives the layout of this system where the subsystems of coils A,B,E and T will be referred to as arrays. T is a vertical radial array ranging from r=20.7 cm to 27.7 cm and E is identical but in the equatorial plane. A and B are identical arrays placed symmetrically with respect to the equatorial plane and composed of 18 B_θ coils at z=±22 cm and 14 B_r coils at z=± 21.3 cm. The coils are therefore not at constant radius (20.5 cm≤r≤24.5 cm) but each coil is oriented to measure only either the B_r or the B_θ field component. All the B_θ coils have dimensions 10×10×5 mm^3 and all the B_r coils 10×5×5 mm^3. The small size of the coils and their close spacing allow very large poloidal mode numbers up to m ≈80 to be detected. In this study, the broadband magnetic turbulence is measured between 40 kHz and 800 kHz, well above the 10 kHz Mirnov frequency. Although the coherence is bounded between 0 and 1, due to the finite number of samples used, the coherence between two completely uncorrelated signals is 0.17.

I. RADIAL COHERENCE AND POLOIDAL MODE NUMBER The coherence between the coils of array T and E shows that the B_θ and B_r fluctuating fields are highly coherent in the radial direction between the plasma and the vacuum vessel as illustrated in Fig. 2. Thus the vacuum field model is appropriate to estimate the poloidal mode number $m(B_\theta)$ from the radial decrease of the B_θ field component. Figure 3 shows the comparison of the experimental points with this model, which yields $m(B_\theta)\approx 6$ at 200 kHz and $m(B_\theta)\approx 8$ at 800 kHz. This method cannot be applied to the B_r component because of the influence of the wall. We should stress that this result is obtained for a single shot in the same radial direction. Moreover, we have successfully applied this method to determine the Mirnov oscillation mode numbers m=2 and m=3, already identified independently by the standard method.

II. COHERENCE IN THE POLOIDAL PLANE The coherence between the coils in arrays A and B has been studied in detail for I_p=130 kA, q_a=3.1. No

up-down asymmetry was found and we shall not distinguish between A and B. Figures 4 and 5 show the coherence and the phase between the central B_θ or B_r coil (R=61.5 cm) and the neighbouring B_θ and B_r coils. For frequencies above 400 kHz, phase jumps of π are seen. In the B_r-B_r case of Fig. 4, they correspond to a minimum in the coherence followed by a secondary maximum as ΔR is increased. This is characteristic of a stationary wave with the statistical wavelength $\lambda_\theta(B_r)$ defined as twice the distance between two phase jumps. For frequencies below 400 kHz the phase plot is typical of a travelling wave and around 400 kHz the phase is representative of both features.

These results are also seen, although less clearly, in the B_θ-B_θ case of Fig. 5. The secondary maxima are lost, probably because the poloidal coherence length is shorter than $\lambda_\theta(B_\theta)$. We see, however, that $\lambda_\theta(B_\theta) \simeq 1.5\lambda_\theta(B_r)$. The poloidal number m can be estimated for the two cases and we find $7<m(B_\theta)<9$ for 400 kHz$\leq f \leq$800 kHz, in good agreement with the results of Fig. 3, and $9<m(B_r)<12$ for 400 kHz$\leq f \leq$800 kHz.

We also calculated the coherence between one B_r reference coil and the B_θ coils (Fig. 6). The coherence between B_r and B_θ is very low at the same position, but increases to a maximum as the separation from the reference coil is increased. The phase plot indicates that the poloidal wavelength of this structure is $\lambda_\theta(B_r)$. This figure reveals that, statistically, the turbulence in one poloidal plane is symmetrical with respect to the radial direction. The asymmetry of the curves is probably due to a small misalignment between the array and the plasma.

III. LONG DISTANCE COHERENCE The coherence in the toroidal direction has been studied between arrays T and A. Taking one B_r or B_θ coil of array T as the reference coil, the coherence with the coils of array A is measured. The resulting coherence curves are comparable with the corresponding ones given in Figs. 4, 5 and 6. The central point of the structures is displaced away from the position R=61.5 cm in such a way that the coherent structures would appear to persist along magnetic field lines. Figure 7a, for q_a=3.6, shows a good example of the results obtained for a q_a-scan. The position of the maxima depends on the frequency and the curves become broader at higher frequencies, which is opposite to the trends within one A or B array, as seen in Fig. 5. This reveals a poloidal diffusion of the coherent structures, as they propagate in the toroidal direction, stronger at higher frequencies. Moreover, as q_a is varied, the peak value of the coherence plots diminishes whereas its width increases.

From these results, we attempted to determine the radius of the magnetic surfaces on which the turbulence "propagates". For this purpose, we assume, firstly, that the poloidal structure of the turbulence is transmitted from its origin towards the arrays in the radial direction, and secondly, that the maxima of coherence in array A are the images of the reference T coil through the magnetic rotational transform. This method is shown in Fig. 7b which shows, in the poloidal plane of array A, the transformation of the radial line supporting the array T by the rotational transform of the field lines, including toroidal effects. If the coherence of the turbulence, for a given frequency, followed one field line, the position of the maximum would define the poloidal rotation of this line on its way toroidally from the position of array T to that of A

($\Delta\phi$ = 113°). We can, therefore, find the magnetic lines supporting the turbulence for each frequency, as indicated by the arrows in Fig. 7b. The higher frequencies are located at the plasma surface whereas lower frequencies are in the scrape-off layer. This method gives similar results when applied to other values of q_a between 3.1 and 8.9. Significant toroidal coherence is not restricted to that found between arrays T and A, and other measurements, not described here, show correlation over large toroidal distances (up to at least $2\pi R$).

IV. DISCUSSION We have shown, with two different methods, that modes of low poloidal numbers are involved in the magnetic turbulence and that the poloidal dispersion relation cannot be the linear extrapolation of ω/k=const., valid at low frequency (Mirnov oscillations). This would have implied m≈30 at 200 kHz and also that m increased by a factor of 4 between 200 kHz and 800 kHz. The correlation between B_r and B_θ shown in Fig. 6 implies that the B_r and B_θ fields have a common source. It is then difficult to understand how the poloidal wavelengths $\lambda_\theta(B_r)$ and $\lambda_\theta(B_\theta)$ are different by a factor of 1.5. At the present time, it is not possible to attribute this factor to experimental errors in the estimated $\lambda_\theta(B_r)$ and $\lambda_\theta(B_\theta)$, or to the physics of the turbulence. The results of paragraphs 2, 3 and 4 point to a change in the nature of the turbulence above 400 kHz. In fact, travelling waves seem to dominate the low frequency part, whereas the higher frequency part shows characteristics of stationary waves.

ACKNOWLEDGEMENTS We acknowledge the collaboration of Ch. Hollenstein, M.L. Sawley, W. Simm, discussions with P.A. Duperrex and H. Weisen and the support of the TCA Team. This work was partly supported by the Fonds National Suisse de la Recherche Scientifique.

REFERENCE [1] P.A. Duperrex et al., Phys. Lett. 106A, 133 (1984), Ch. Hollenstein et al., Cargèse Workshop 1986, Proc. edited by D. Grésillon, M.A. Dubois, or Lausanne report LRP 306/86, Sept. 1986.

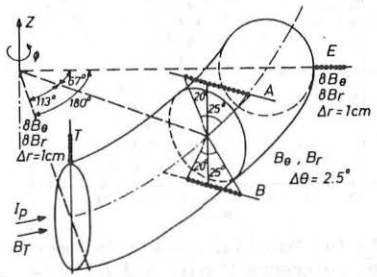

Fig. 1: Layout of magnetic probes

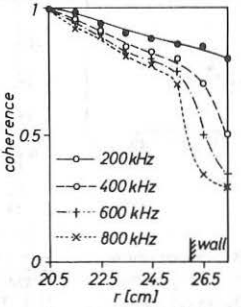

Fig. 2: Radial B_θ-B_θ coherence: coherence and phase between the coil at r=20.5cm and the others.

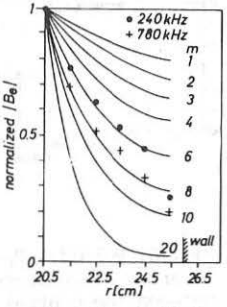

Fig. 3: Radial decrease of the fluctuating B_θ amplitude; solid lines: calculated points: measured

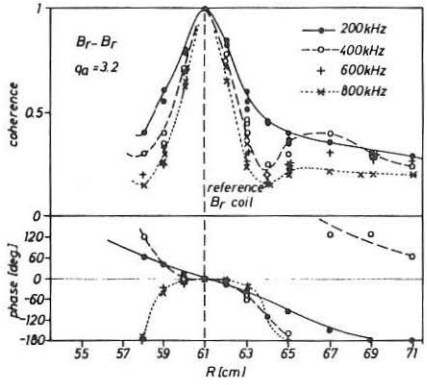

Fig. 4: Poloidal B_r-B_r coherence in array A: coherence and phase between the central coil at R = 61 cm and the others

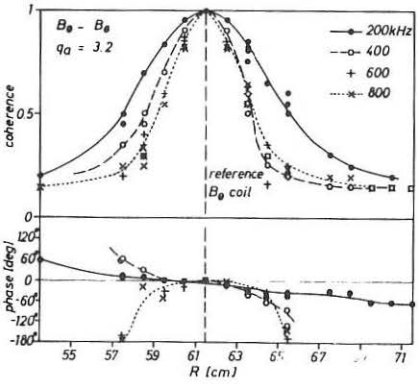

Fig. 5: Poloidal B_θ-B_θ coherence in array A: coherence and phase between the central coil at R=61.5cm and the others

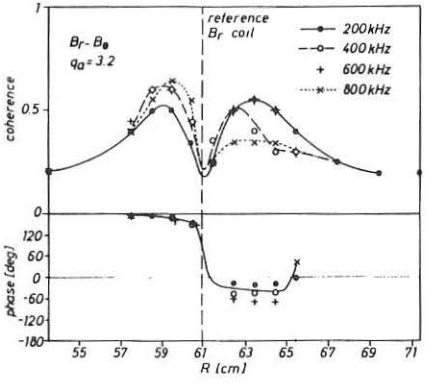

Fig. 6: Poloidal B_r-B_θ coherence in array A: coherence and phase between the central B_r coil and the B_θ coils

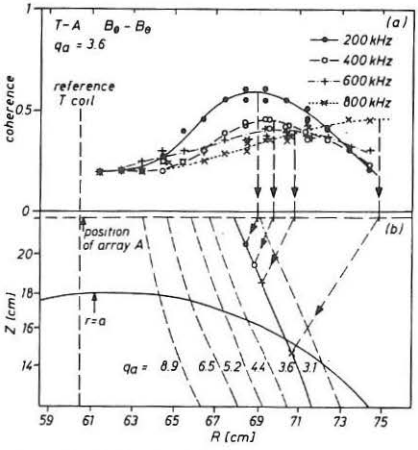

Fig. 7: (a) Poloidal B_θ-B_θ coherence between reference T coil and A coils (b) Image, in the poloidal plane of array A, of the radius supporting array T, through the rotational transform for different q_a values. The arrows, along the radial directions indicate how the position of the coherence maxima is related to the magnetic lines.

COMPARISON OF TRANSPORT MODELS WITH CONFINEMENT PROPERTIES OF TEXTOR IN PRESENCE OF ICRH

A.M. MESSIAEN*, R.R. WEYNANTS*, R. KOCH, G. VAN WASSENHOVE

Laboratoire de Physique des Plasmas - Laboratorium voor Plasmafysica
Association "Euratom-Etat belge"- Associatie "Euratom-Belgische Staat"
Ecole Royale Militaire - B 1040 Brussels - Koninklijke Militaire School
and

A. ROGISTER, G. HASSELBERG

Institut für Plasmaphysik, Kernforschungsanlage Jülich GmbH, Association Euratom-KFA Jülich

1. Introduction.

We compare the predictions of various models of electron thermal transport with the experimental data set of TEXTOR. The electron heat transport equation is solved using the anomalous transport coefficients derived on the one hand from the saturation of the dissipative trapped electron mode instability [1] and on the other hand from a short wavelength collisionless instability driven by electron temperature gradient (η_e modes)[2]. For comparison a simple neo-Alcator heat transport coefficient [3] is also used for the ohmic heated (OH) cases.

The TEXTOR data set provides the energy content E(from diamagnetism), the central electron and ion temperature T_{eo} (from ECE) and T_{io} (from neutron yield), electron density (n) and current density (j) profile parameters (from HCN interferometer and polarimeter) as a function of ICRH power [4]. RF pulses of 0.5 s or more are considered, such that stationary current profiles are achieved : the experimental temperature profile can thus be derived from j(r) assuming neoclassical conductivity σ_{NC} [5]. The value of Z_{eff} is computed from T_{eo} and the loop voltage V_ℓ assuming a central q value of 0.8.

2. Model.

We use the global heat conduction equation where radiation and convection losses are neglected (as justified from a predictive transport analysis of TEXTOR [6]) as well as the ion heat flux and the charge exchange contribution :

$$n\chi_e \partial Te/\partial r = - \{ \frac{xq_a}{q} \frac{I_p V_\ell}{(2\pi)^2 aR} + \frac{a}{x} \int x \, j_{RF} dx \} \qquad (1)$$

where we have : x = r/a (a : small radius), I_p : plasma current, $q_a = q(r=a)$, R : large radius, T_e : electron temperature. The first term on the RHS of Eq.(1) gives the ohmic power contribution whereas the second term corresponds to the rf power delivered to the plasma. We choose an rf power density $j_{RF} \propto x^p(1 - x^\lambda)$ normalized by the condition $\int j_{RF} dv = P_{RF}$ (P_{RF} : total RF power). p and λ parametrize the rf power deposition profiles. For the diffusivity χ_e we use the three following expressions (computed for a = 0.46m, R = 1.75m, B_t = 2T, MKSA units are used except T_e in keV and n in $10^{13}cm^{-3}$, D_2) (i) $\chi_{eR} = 0.325\ T_e^{1.5}\ \hat{s}\ b_p(\nu^*)(1 + 0.6\ d_p(\nu^*))(\nu^* q)^{-1}\ g(E)(C_{fit}\ c - 2)^{4.63}$ where we have ν^* : collisionality ,

$\hat{s} = \frac{r}{q}\frac{dq}{dr}$, $c = 0.11 \frac{q^2}{\hat{s}\nu^*} b_n(\nu^*) L_N^{-1} L_T^{-1}$, and $L_N^{-1} = \frac{1}{N}\frac{dN}{dr}$, $L_T^{-1} = \frac{1}{T_e}\frac{dT_e}{dr}$,

$E = (qR\,\hat{s}\,L_N^{-1})^{-1}$. The functions b_n, b_p, d_p, g are defined in [1]. C_{fit} is a fitting paramater. (ii) $\chi_{e,G} = 3.747\, C_{fit} \frac{\sqrt{T_e}\,\eta_e(1+\eta_e)\hat{s}}{n\,q\,R}$ with $\eta_e = L_T^{-1}/L_N^{-1}$ [2]. (iii) $\chi_{e,A} = 2\, C_{fit}(n\, T_e\, q)^{-1}$ [3].

3. Integration procedure.

The first order differential Eq. (1) for T_e is solved taking I_p, V_ℓ, $n(x)$ and Z_{eff} (assumed independent of x) as input from experiment. The integration is started near the plasma edge, at $x = x_i$, with the initial values of T_e, dT_e/dx, q, dq/dx derived from the experimental data using the neoclassical σ_{NC}. We choose x_i such that $T_e(x_i) \sim 100$ eV to ensure the validity of the $\chi_{e,R}$ model. At each step $x = x_n$ of the integration the current density $j = \sigma_{NC} V_\ell/(2\pi R)$ and $q = q_a x^2 I_p/I_x$ ($I_x = I_p - 2\pi \int_a^r jrdr$) are computed. The electron energy content $E_e = \int n\, T_e dV$ and the plasma current $I_c = \int_a^o 2\pi rjdr$ that would be obtained/consumed if the temperature remained constant in the region $x_n > x \geq o$ are also computed. The integration is stopped at $x = x_e$ for which either the total current is consumed ($I_c = I_p$) or $q = 0.7$ is reached whichever occurs first.

4. Results and discussion.

In order to compare the computed and experimental post-sawtooth crash T_e profiles, a number of quality criteria (to some extend arbitrary) can be formulated : (i) $q(x_e) \tilde{=} 1$, (ii) $x_e = x_{q=1} \tilde{=} 0.25(2\pi/q_a)^{1/2}$, i.e. the experimental position of the q = 1 radius in TEXTOR [8], (iii) $\Delta I_p = I_p - I_c \tilde{=} 0$, (iv) $T_e(x_e) \tilde{=} T_{eo}$, (v) an estimation of the plasma energy content $E = E_c(1 + T_{io}/T_{eo})$ close to the experimental value. C_{fit} is adjusted once for all for each χ_e model for a reference discharge condition ($I_p = 0.35$ MA, $n = 3 \times 10^{13}$cm^{-3}, $P_{RF} = 0$). It is remarkable that we could succeed in satisfying approximately all these rather demanding conditions. This is shown on Fig. 1 where the T_e profiles obtained for the three transport models are compared with the experimental profile (computed from T_{eo} and $j(r)$ using σ_{NC}). The positions of x_i and of the experimental as well as the computed $x_{q=1}$ are indicated together with the locations where $I_p = I_c$ on each T_e profile. The different evolution of $\chi_e(x)$ for the three models in spite of similar $T_e(x)$ profiles is striking.

The values of C_{fit} are not changed for the other computed cases. Fig. 2 shows the T_e curves for a typical ICRF heated case. As expected, the $\chi_{e,A}$ model is unable to describe the heated case and is very sensitive to the deposition profile. The $T_e(x)$ curve obtained from $\chi_{e,R}$ is practically insensitive to the latter whereas a T_e increase of $\sim$ 20 % (going from centered to excentered $\mathcal{P}_{RF}$ profile) is observed for the $\chi_{e,G}$ model. Henceforth we choose $p = 1, \lambda = 3$ which fit best the excentered profiles predicted for TEXTOR by ray-tracing [7]. It is shown also that for these two models the criteria of quality are not as well fulfilled as for the reference case. On Fig. 3a, b and c the solid lines give the experimental energy versus the central chord density $\bar{n}$ for three values of I_p with and without ICRH (only non detached plasmas are considered [9]). The corresponding values, calculated for the 3 models in OH(R,G,A) and for the 2 relevant models with ICRH (R,G) are given. The global agreement is quite

satisfactory particularly at low I_p. At high I_p the three models give a value of E ∿ 15 % higher than the experimental one but the general behaviour is good. It should be cautioned that the good energy fit is partly due to the imposed integral condition on the temperature profile, e.g. $I_c = I_p$. Fig. 3 however does not reflect to what extends the criteria of quality are fulfilled. One can find in table I the mean quadratic values $\bar{\varepsilon}_i$, for the OH and ICRH cases, of the relative errors $\varepsilon_1=(I_p-I_c)/I_p$, $\varepsilon_2=(q(x_e)-1)$, $\varepsilon_3=(x_e-x_{q=1})/x_{q=1}$, $\varepsilon_4=(T_e-T_{eo})/T_{eo}$. It appears that in OH, the results of the $\chi_{e,R}$ model are as satisfactory as the neo-Alcator model ($\chi_{e,A}$) and better than the $\chi_{e,G}$ one. The $\chi_{e,R}$ model does not degrade for ICRH discharges and exhibits much lower r.m.s. errors on $q(x_e)$ and $x_{q=1}$, and therefore on the T_e profiles, than the $\chi_{e,G}$ model.

References.

[1] HASSELBERG G., ROGISTER A., Nucl. Fus. 26, 797 (1986).
[2] GUZDAR P. et al., Phys. Rev. Letters 57, 2818 (1986).
[3] BECKER G., Nucl; Fus. 24,1364(1984) ; GRUBER O.,ibid. 22,1349(1982).
[4] MESSIAEN A. et al.,Plasma Phys.& Contr.Fus. 28, 71 (1986) ; WOLF G. et al., ibid., 28, 1413 (1986).
[5] SOLTWISCH H. et al.,Proc.invited papers,I.C.P.P.Lausanne 1984,Vol 1,499.
[6] NICOLAI A. et al., this conference (1987).
[7] WEYNANTS R.R.et al.,Europhysics Conf.Abstracts(Schliersee 1986) Vol. 10C, Part II, 33.
[8] SOLTWISCH H. et al., Proc. 11th Int. Conf. Plasma Phys.Contr. Fus. Kyoto 1986, IAEA-CN-47/A-V-1-31.
[9] WEYNANTS R.R. et al. LPP/ERM/KMS Report 85, Brussels 1987 ; submitted for publication.

* Senior research associate at the NFSR, Belgium.

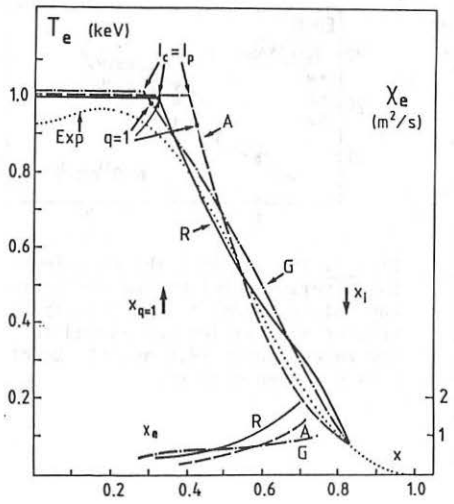

Fig. 1. Profiles of T_e computed for the three models (R,G and A) compared to the experimental one (Exp) derived from the measured T_{eo} and j(r) . ($\bar{n} = 3 \times 10^{13} cm^{-3}$, $I_p = 350$ kA, OH, $C_{fit,R} = 1.25$, $C_{fit,G}=0.278$, $C_{fit,A} = 0.5875$) The χ_e profiles are also shown .

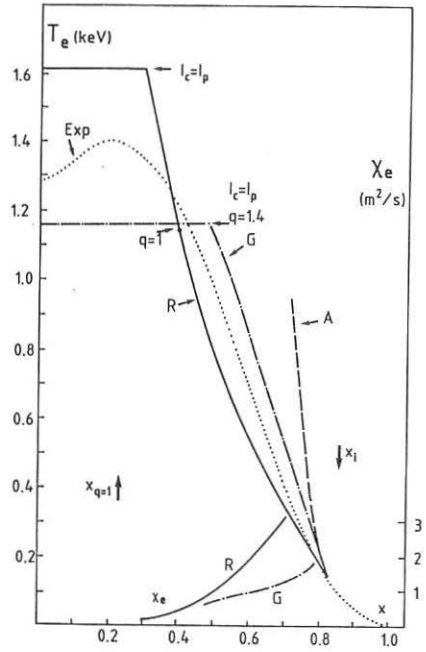

Fig. 2. Same curves as in Fig. 1 but for P_{RF} = 1.1 MW (same values of $\bar{n}$, I_p and C_{fit} as for Fig. 1 ; excentered $\mathcal{P}_{RF}$ profile : p = 1, λ = 3).

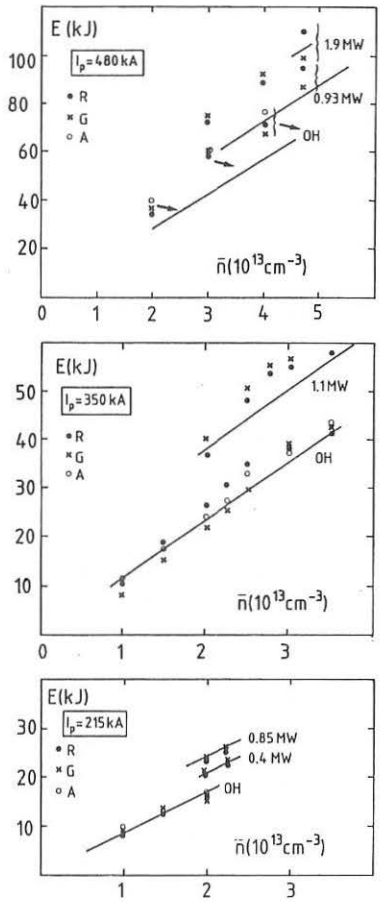

Fig. 3. The locus of the experimental E versus $\bar{n}$ for OH and for various values of P_{RF} (solid lines); crosses and circles correspond to the three models (R,G and A). Model A is not used with RF.

	$\chi_{e,R}$ OH	$\chi_{e,G}$ OH	$\chi_{e,A}$ OH	$\chi_{e,R}$ ICRH	$\chi_{e,G}$ ICRH
$\bar{\varepsilon}_1$	5.3%	7.8%	5.9%	2.0%	1.7%
$\bar{\varepsilon}_2$	6.8%	13.2%	7.9%	4.9%	23.0%
$\bar{\varepsilon}_3$	4.4%	10.4%	6.4%	5.0%	21.0%
$\bar{\varepsilon}_4$	5.2%	7.1%	5.9%	5.8%	5.2%

Table 1.

HEAT FLUX ANALYSIS OF AUXILIARY HEATING DATA FROM JET

J P Christiansen, J G Cordey, J D Callen* and D G Muir

JET Joint Undertaking, Abingdon, Oxon, OX14 3EA, UK
*University of Wisconsin, Madison, WI53706, USA

ABSTRACT

A new method for analysing local heat transport has been applied to data from neutral beam heated discharges in JET. Estimates of heat diffusivity obtained by this method are found to agree with results from heat pulse propagation studies and results deduced from empirical scaling laws for global confinement.

1. INTRODUCTION

A new method has been proposed [1] for interpreting measurements of the spatially resolved electron temperature profile by examination of the parametric dependence of the heat flux through a given flux surface. In this paper we describe the results obtained by applying this method to data from neutral beam heating power scan experiments on JET. The power scans have been performed over a range of plasma currents (1 to 5MA) and the beam power has been increased in steps of approximately 1MW up to 9MW. In the analysis the total heat flux q is compared with local plasma parameters, eg, density, temperature, current and their gradients. The analysis suggests the following relationship:

$$\underline{q} = -\chi\, en\nabla T + \underline{q}_{pinch} \quad , \qquad (1)$$

where χ is a heat diffusion coefficient and q_{pinch} represents a heat pinch. SI units are used with temperatures in eV and currents in units of MA.

2. CALCULATION OF HEAT FLOW

In a steady state plasma configuration the power balance equation for electrons and ions is:

$$\langle \nabla \cdot \underline{q} \rangle = \langle Q_\Omega + Q_{NB}^e + Q_{NB}^i \rangle = \langle Q \rangle \quad , \qquad (2)$$

where $\langle\ \rangle$ denotes a flux surface average. Q is the total heating rate and includes ohmic heating and power deposition from the neutral beam to electrons and ions. The radiation loss rate is not included in (2). A preliminary analysis of selected JET pulses shows Q_{RAD} to be highly peaked in the outer region $0.9 < x < 1$. The flux surface label x used in the analysis varies from 0 to 1 and we integrate equation (2) from x = 0 up to 3 representative radii x = $^1/_2$, $^2/_3$, $^3/_4$. This integration yields for the heat flux:

$$q(x) = \frac{a}{\frac{dV}{dx}} \int_0^x Q(x') \frac{dV}{dx'} dx' \quad , \qquad (3)$$

where a is minor radius and V is the volume enclosed by a surface x. The ohmic contribution to Q is $E_\phi^2/\eta_\parallel$, $E_\phi = V_o/2\pi R$ where V_o is the loop voltage calculated from magnetic measurements. The neoclassical resistivity is determined from the electron temperature profile. The neutral beam power deposition is computed from Fokker-Planck equations using electron density and temperature data; the computation assumes the slowing down of injected ions to be complete. The q(x) heat flux data thus obtained is now analysed together with density and temperature data from approximately 350 observations. Each observation involves a time average over 0.4 sec of the data and typically 2-4 observations per plasma pulse are used. Figure 1 shows radial profiles of the heat flow q(x) before (full curves) and during neutral beam heating (dashed curves) for 3 pulses with 1, 3 and 5MA. It can be seen that a substantial change (by a factor 20) occurs for the 1MA pulse.

3. DEPENDENCE OF HEAT FLOW ON LOCAL PARAMETERS

Standard linear regression analysis has been applied to the heat flux data by fitting it to an empirical expression like:

$$q_{fit} = - C\, e\, n^{\alpha}\, \nabla n^{a}\, T^{b}\, \nabla T^{\beta}\, I^{\gamma}\, J^{c} - q_{pinch}. \qquad (4)$$

The heat pinch term labelled q_{pinch} may depend on n, ∇n etc in a way different from the first term of (4). The data at 1MA eliminates any ∇n dependence and the data as a whole eliminates any current density J dependence. Since T and ∇T are strongly related either but not both, may be used. In the 1MA data alone the ∇T dependence is stronger than the T dependence. The best fit to all the data is thus:

$$q_{fit} = - C\, e\, n^{\alpha}\, \nabla T^{\beta}\, I^{\gamma} + q_{pinch}. \qquad (5)$$

In (4) and (5) I denotes the current flow inside a surface x. The values of the exponents ± their standard deviations are:

$$\alpha = 0.75 \pm 0.11, \quad \beta = 0.74 \pm 0.12, \quad \gamma = -0.78 \pm 0.11.$$

Also $$C = 11.34 \pm 2.31, \qquad q_{pinch} = 9.1 \pm 3.5\ .$$

The large uncertainty in q_{pinch} is due to the scatter in the data as shown in Figure 2. By constraining two of the 3 exponents to be equal to 1 in 3 separate regression analyses the standard deviations drop and

$$\alpha = 1.01 \pm 0.02, \quad \beta = 1.02 \pm 0.04, \quad \gamma = -0.99 \pm 0.02\ .$$

This result strongly suggests that

$$q = -C_o/I\ en\ \nabla T_e - q_{pinch}, \quad C_o = 8.0 \pm 0.2, \quad q_{pinch} = 4.3 \pm 0.6\ , \qquad (6)$$

represents the best fit to the data on q. Figure 3 shows a plot of values of q against q_{fit} all evaluated at x = ¾. The different symbols refer to the plasma current (as in Figure 1): open circles (1MA), full circles (2MA), triangles (3MA), squares (4MA), asterisks (5MA). Additional attempts to allow for density and temperature dependence of q_{flow} either fail or

increase the standard deviations of the fitting parameters beyond the confidence level.

4. HEAT DIFFUSIVITY

The heat diffusion coefficient inferred from (6) is:

$$\chi = 8.0/I(x)m^2/sec \qquad (7)$$

This estimate shows that χ would decrease as x and $I_\phi(x)$ increase. When the analysis of 3 is carried out at $x = {}^1/_2$ and $x = {}^2/_3$ we find that the best estimate of C_o decreases to about 4.0 at $x = {}^1/_2$. The value of χ obtained from (7) for $I_\phi(x={}^3/_4) \approx 2.75$MA is $2.9m^2/sec$ and this agrees well with the result $\chi_{HP} = 2.4 \pm 0.7 m^2/sec$ obtained from heat pulse propagation measurements [2]. Figure 4 shows values of q (full triangles) and q_e (open triangles) against $n\bar{V}T$ for a range of 3MA pulses; q_e is that part of q delivered directly to the electrons. The shaded area in Figure 4 represents the relationship between q and $n\bar{V}T$ which follows from the heat pulse propagation measurements.

From (7) we can derive an incremental confinement time [1] using an average χ.

$$\tau_{inc} = \eta \tau_\chi = \eta \frac{3ab}{8\bar{\chi}} (1 + \xi) \qquad (8)$$

where a and b are the semi-axes of the elliptic plasma cross-section; η is the heating efficiency [1] of neutral beam heating and varies for JET from 0.3 to 0.6; ξ is the ratio ion to electron energy content and is typically 0.4-0.5. From (8) we find $\tau_{inc} \approx (0.04 - 0.08)\, I(sec)$, which compares favourably with the scaling law $\tau_{inc} = 0.047\, I(sec)$ obtained from JET data on global confinement [3].

5. SUMMARY

Several approximations have been made in this study of heat flux in JET: omission of radiation loss, ion-electron energy exchange, radial variation of safety factor, departures from equilibrium etc. Such approximations mitigate against a further analysis of the detailed dependence of χ upon local parameters, but do leave scope for future work. The difference between the fitted expressions (5) and (6) is such that it is difficult to extract more than the dependence (7) of χ from the data. This dependence of χ upon $I_\phi(x)$, or the average poloidal field, is very pronounced in the JET data. It indicates the highest incremental confinement to occur at high plasma currents.

6. REFERENCES

[1] CALLEN J D, CHRISTIANSEN J P, CORDEY J G, THOMAS P R, THOMSEN K, JET Preprint P(87)10, submitted to Nuclear Fusion.
[2] TUBBING B J D, LOPEZ-CARDOZO N J, JET Report R(87)01.
[3] CORDEY J G et al, Paper IAEA-CN-47/A-II-3, Plasma Physics and Controlled Fusion, Kyoto, Japan, 1986.

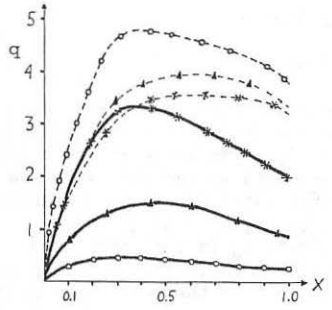

Fig 1: Radial profiles of heat flow for 3 pulses of 1MA(o), 3MA(Δ), 5MA(*). Units of q are $10^4 Wm^{-2}$ in all Figures.

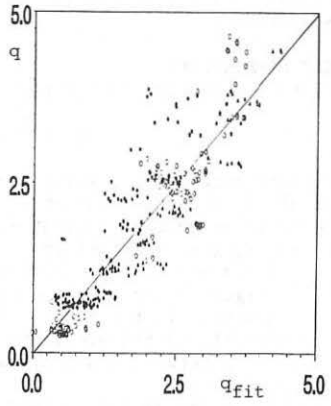

Fig 2: Values of q plotted against values of q_{fit} given by (5). The symbols are explained in the text.

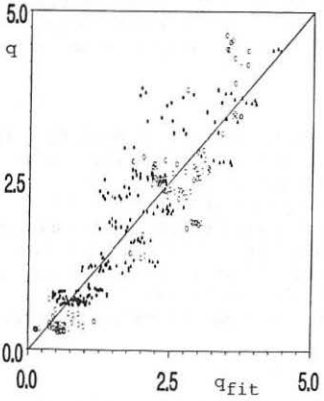

Fig 3: Values of q plotted against q_{fit} given by (6).

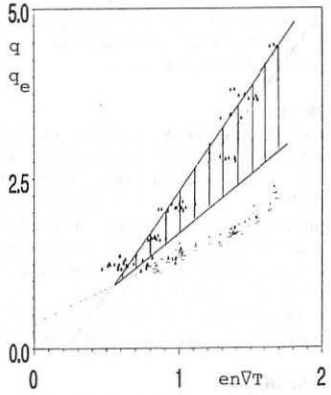

Fig 4: q(▲) and q_e(Δ) vs enVT. The shaded area is the range given by heat pulse propagation measurements. Units of enVT are 10^4 Jm^{-4}.

ASDEX HEAT PULSE PROPAGATION AS A FORCED BOUNDARY PROBLEM

K.S. Riedel, A. Eberhagen, G. Becker, O. Gruber, K. Lackner, O. Gehre V. Mertens, J. Neuhauser
H.B. Bosch, H. Brocken, A. Carlson, G. Dodel[1],
H.U. Fahrbach,G. Fußmann, J. Gernhardt, G. v.Gierke, E. Glock,
G. Haas, W. Hermann, J. Hofmann, A. Izvozchikov[2], E. Holzhauer[1], K. Hübner[3],
G. Janeschitz, F. Karger, O. Klüber, M. Kornherr, M. Lenoci, G. Lisitano,
F. Mast, H.M. Meyer, K. McCormick, D. Meisel, E.R. Müller, H. Murmann,
H. Niedermeyer, A. Pietrzyk[4], W. Poschenrieder, H. Rapp, A. Rudyj,
F. Schneider, C. Setzensack, G. Siller, E. Speth, F. Söldner, K. Steinmetz,
S. Ugniewski[5], O. Vollmer, F. Wagner

Max-Planck Institute für Plasmaphysik,
EURATOM Association, D-8046 Garching, Fed. Rep. of Germany

[1]University of Stuttgart, [2]Ioffe Institute, [3]University of Heidelberg,
[4]University of Washington, Seattle, USA, [5]Inst. for Nuclear Research, Swierk, Poland

Traditionally, two types of methods are used to determine the eletron heat conductivity, χ: initial value and Fourier. Initial value analyses compare the observed temporal evolution during the rise phase of the heat pulse with Kadomtsev's model for sawtooth reconnection. The crucial disadvantage is that one must make assumptions about the plasma inside the mixing radius, namely one assumes that χ is known and unchanged inside the $q = 1$ surface and therefore the natural thermal equilibrium is the temperature before the crash. Fourier methods average over the sawtooth period and thus the results are heavily weighted in favor of the slow decay phase of the heat pulse. During this latter phase the initially sharp spatial gradients of the pulse have relaxed and Ohmic heating and electron ion energy transfer as well as boundary conditions become important.

To analyze the ASDEX heat pulse, we solve the heat equation numerically as a forced boundary value problem. The measured time evolution of the first electron cyclotron emission channel outside the mixing radius is used as input for the the time dependent boundary condition. The electron heat conductivity is then given a functionally parametrized form such as $c/n(r)$, where the parameter is determined by a best fit to the channels located outside the input channel.

This approach has several important advantages over the standard method of fitting the arrival time of the peak of the pulse to a theoretically initialized perturbation. The region inside the mixing surface, where the conductivity may be anomalously large, is excluded from consideration. No assumptions on the position of the $q = 1$ surface or the radial redistribution of energy are necessary. The conversion of magnetic energy into heat is automatically taken into account. Finally, the ECE measurements give a time history of the heat pulse at a few spatial locations and the method makes effective use of this information.

We use a standard Crank-Nicholson scheme with $T(r = r_o, t)$ evolving in time. Convective, dissipative and reheat terms may be included. The time interval may be the

rise phase, the entire sawtooth period, or the entire sequence of sawteeth to simulate the effect of pulse pile up.

To model the boundary layer outside the separatrix we assume that the temperature decays exponentially with a decay length λ. We integrate the heat equation over the last half grid point and define $\alpha\chi(1) = \lambda\chi_{bl}$ where χ_{bl} is the effective conductivity outside the separatrix. Thus the last half mesh volume evolves as

$$\frac{\Delta r}{2}\frac{\partial T}{\partial t} = \chi[-\alpha T - \frac{\partial T}{\partial r}]$$

where the minus denotes the inside derivative. Since the boundary layer is believed to be a highly nonlinear function we treat α as a free parameter. Results which depend sensitively on α are of little value.

The method is tested on a standard Ohmic discharge with the following parameters, $q(a) = 3.3, T(0) = 1075ev, n = 2.4 * 10 * *13, Z_{eff} = 1.3$. The input channel is at 18.1cm and the fit channel at 25.6 cm. Ten sawteeth are averaged over the sawtooth period.The period is 13ms,the crash time is 1ms,the amplitude is 90ev,and the peak of the pulse arives at r=18.1cm in 1.65ms and at 25.6cm in 2.65ms. Figure 1 compares the smoothed experimental data with numerical calculations for $\chi = c * n(.47)/n(r)$ during the first 5ms of the pulse. The top curve is $c = 8.8m^2/sec$, the middle curve is $7.7m/sec$ and the bottom curve is 6.5. The best fit to least squares integral is 7.35, to the relative least squares, (time averaged temperature at 25.6cm normallized to 1.0) is 6.8 and the best fit to time integral of $T_{measured} - T_{num}$ is 7.7. The boundary heat flux parameter α is 2.0. Thus the choice of norms varies the result by 5%. The power balance χ is between 1.2 and $2.0m^2/sec$. In practice, the pulse has four characteristic parameters,the amplitude of the peak, slope of the temperature rise ,the time of arrival of the peak and the slope of the decay. We are able to fit the first two parameters with a chi of approximately $7m^2/sec$. When the radial dependence is varied from constant to inversely proportional to density the value of chi at the input channel varies only a few percent during the rise and early decay phase. The discrepency between the observed and computed time of arrival of the peak is larger. Since in fitting the peak we are essentially specifying the second derivative of $T(t)$, the poorer fit is to be expected. It may also be partially related to the presence of convection.

The temporal decay depends on both the assumed radial profile of χ and on the heat transfer parameter α. As α decreases, the rate of increase of χ with radius must increase. Figures 3a,b,c give the computed values of the temperature at $r = 25.6$ for $\alpha = 0.1, 2.0$ and 40.0 respectively. In each case, the top curve is $\chi = 7.3m^2/sec$, the middle curve is $7.3n(.475)/n(r)$ and the bottom curve has a inverse square dependence on density. Clearly the boundary condition determines the radial variation of χ.

We now analyze the same case with the initial value approach and determine χ by fitting the differential time of arrival of the peak at 18.1 and 25.6. We assume a parabolic current profile and initialize the code with the perturbation given by conservation of energy and flux. The experimental temperature and density profiles are used. For a differential time of arrival of 1ms we find $\chi = 4.1m^2/sec$. The temporal evolution at

18.1 and 25.6 cm are displayed in Fig 3a,b. The amplitude of the temperature pertubation just outside the mixing radius is in good agreement with theory. The actual crash time of one msec is comparable with the time of arrival. The difference in arrival times occurs because the initial value approach assumes that the crash is instananeous. The forced boundary value approach automatically took this into account. For neutral beam cases, the crash time is .1ms and the agreement will be better.

The most disturbing discrepency is the surprisingly large magnitude of the heat pulse away from the mixing radius. The theoretical prediction is based on a dipole character of the initialization. By assuming thermal equilibrium after the crash is the temperature before the crash, there is a net lack of thermal energy inside the $q = 1$ surface. This absence of heat mixes with the excess outside the inversion radius and causes a rapid decay. If the conductivity inside the $q = 1$ surface were greatly enhanced after the crash, the natural profile would be the flat final profile. Thus the heat pulse would propagate like a monopole localized between the inversion and mixing radii.

The experimental observations in ASDEX and TFTR seem to suggest that the temperature at the $q = 1$ surface is held constant throughout the sawtooth period. This is an intermediate case between a dipole and a monopole.

In conclusion, the forced boundary value method allows quantitative analysis of the time evolution of the measured signals. The major source of error are the spatial resolution of the ECE spectrometer and the lack of knowledge of the correct boundary condition. By averaging over several shots it should be possible to determine both the physical boundary condition and the radial profile of χ. For the sample ohmic case analyzed here we find that the heat pulse conductivity is a factor of four to five higher than the power balance conductivity and that the initial valve approach significantly underestimates the heat pulse χ.

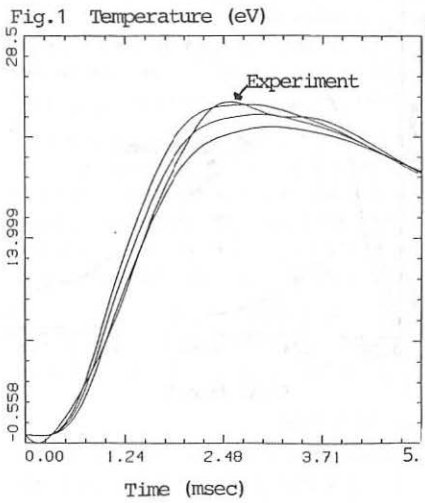

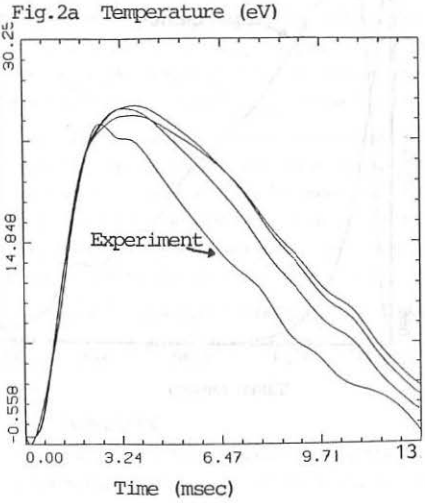

Fig.2b Temperature (eV)

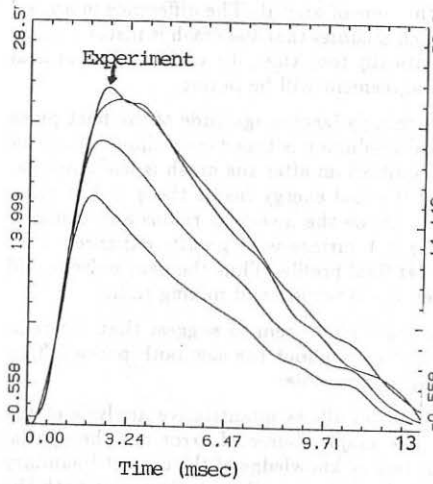

Fig.2c Temperature (eV)

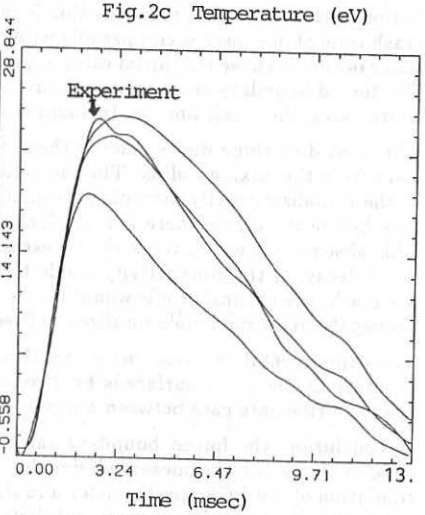

Fig.3a Temperature (eV9

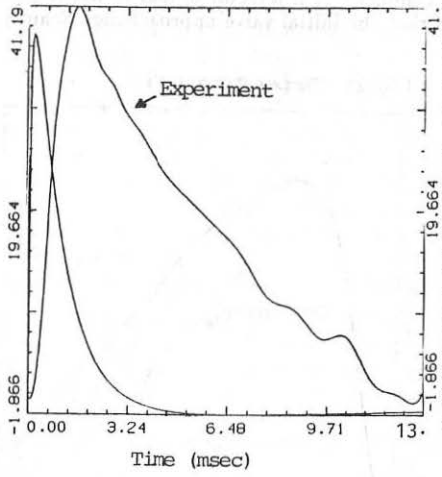

Fig.3b Temperature (eV)

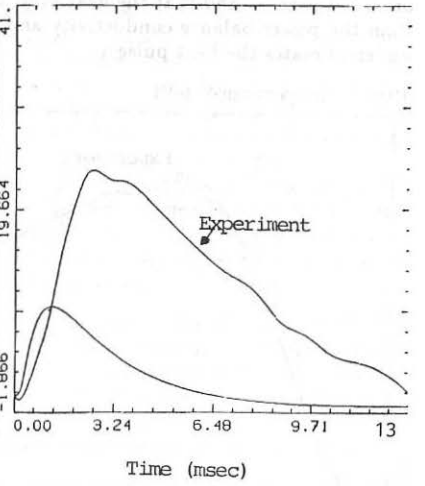

HEAT PULSE PROPAGATION IN RELATION TO THE ENERGY CONFINEMENT IN JET

N.J. Lopes Cardozo+, B.J.D. Tubbing+, D.J. Campbell, A. Cheetham, A. Gondhalekar.

JET JOINT UNDERTAKING, ABINGDON, OXON, OX14 3EA, UK.

+ On attachment from: FOM Instituut voor Plasmafysica, Nieuwegein, The Netherlands.

INTRODUCTION

Heat Pulse Propagation (HPP) studies [1-3] have in general resulted in values for the heat diffusivity χ_e of the electron channel that exceed the estimates based on the evaluation from the power balance. No satisfactory explanation for these discrepancies has been given yet. In this paper (see also [4]), which summarises the main results of heat pulse studies in JET, we set out to resolve these discrepancies. We examine the relation between the static (power balance) and dynamic (HPP) methods of assessing χ_e.

THE INCREMENTAL HEAT DIFFUSIVITY

Fig.1a is a plot of total stored energy W versus total input power P (n_e=2.5 10^{19} m^{-3}, B_T=3T, I_p=3MA). The plot shows that $\tau_E \equiv W/P$ decreases with increasing input power. In JET, as in many other machines, these W(P) plots can be described by an offset straight line, the slope of which is called the incremental energy confinement time $\tau_{E,inc} \equiv dW/dP$.

From the energy confinement time we derive a value $\chi_{e,pb}$ for the heat diffusivity at a radius r = 2/3 a, using the well-known relation $\chi_{e,pb} = ab/4\tau_E$ (Eq1), where a,b are the horizontal and vertical minor radii. This expression is derived assuming that the heat flow per unit area in the electron channel, q_e, can be expressed as $q_e = - n_e \chi_e \nabla_r T_e$ (Eq2). Since χ_e may depend on $\nabla_r T_e$, a change of q_e induced by a variation of $\nabla_r T_e$ is governed by the incremental heat diffusivity $\chi_{e,inc}$, defined by $\chi_{e,inc} \equiv (1/n_e) dq_e/d\nabla_r T_e$. It can be shown that $\chi_{e,inc}$ is related to $\tau_{E,inc}$ by the analog of Eq1, $\chi_{e,inc} = ab/4\tau_{E,inc}$. From Fig.1a we derive $\tau_{E,inc}$ = 210 ms, and $\chi_{e,inc}$ = 2.5 $m^2 s^{-1}$, for the discharge conditions concerned.

The concept $\chi_{e,inc}$ can be further illustrated by evaluating a local power balance at r=2/3 a. This is the radius at which the HPP measurements are done. Fig.1b shows the local temperature gradient ∇T_e versus the power P_e transported by the electrons through the flux surface (of area S), with P_e normalised on local density. The plot has again the character of an offset straight line, the slope of which yields the incremental heat diffusivity. The fitted line in the plot corresponds to $\chi_{e,inc}$ = 2.5 $m^2 s^{-1}$, consistent with the value derived from $\tau_{E,inc}$. It is important to observe that the χ_e relevant to a perturbation of the temperature gradient is $\chi_{e,inc}$ and not $\chi_{e,pb}$.

ANALYSIS OF HEAT PULSE PROPAGATION

The fast collapse of the sawtooth instability flattens the electron temperature profile from the centre up to the mixing radius r_{mix} on a timescale of ≈100 μs. After the collapse, the

profile relaxes to the unperturbed profile of just before the next collapse. At radii outside r_{mix}, we observe the heat pulse signals. Fig.2 shows two typical examples of the electron temperature signal vs. time for six radial positions. From the measured heat pulse traces a value for χ_e can be derived, which we denote by $\chi_{e,hp}$.

The heat pulse perturbs, in first order, only the temperature and the temperature gradient. The perturbed heat flow is then $\tilde{q}_e = n_e \chi_e \tilde{\nabla T_e} + n_e \tilde{\chi}_e \nabla T_e$ (Eq3), where χ_e is not a constant, but a function of the perturbed quantities, T_e or ∇T_e. As we have shown in [5], a T_e dependence would hardly affect the evaluation of $\chi_{e,hp}$. Hence we consider here only a functional dependence on ∇T_e. Then, the heat diffusivity relevant to the perturbation is by definition

$$\chi_{e,hp} = \frac{1}{n_e} \frac{\partial}{\partial \nabla T_e} q_e = \chi_e + \left(\frac{\partial}{\partial \nabla T_e} \chi_e\right) \nabla T_e \qquad \text{(Eq4)}$$

in which χ_e represents the equilibrium value. Depending on the form of $\chi_e(\nabla T_e)$, $\chi_{e,hp}$ will be larger than $\chi_{e,pb}$. Under the condition that the offset linear behaviour of $q_e(\nabla_r T_e)$ shown in Fig.2 is valid on a time scale faster than the heat pulse, $\chi_{e,hp}$ should be equal to $\chi_{e,inc}$.

INSTRUMENTATION AND DATA PROCESSING

The HPP signals are measured with a twelve channel ECE grating polychromator [2], with a radial line of sight in the median plane and a radial resolution of ± 3 cm. The heat pulse signals are characterised by a delay time t_p and an amplitude A (see Fig.2). From the t_p and A values, we derive a heat pulse velocity $v_{hp} = dr/dt_p$ and a radial damping rate $\alpha = ad(\log A)/dr$, as the characteristic parameters. As is shown in [6], $\chi_{e,hp}$ can be derived from v_{hp} and α ; $\chi_{e,hp} = 4.2\ v_{hp}/\alpha$.

RESULTS FOR ADDITIONALLY HEATED DISCHARGES

We limit the discussion here to a set of auxiliary heated limiter discharges with $I_p = 3$ MA, $2.9 < B_T < 3.5$ T, with total power varied from 2.1 to 13.5 MW. Fig.3 shows the $\chi_{e,hp}$ values and the $\chi_{e,pb}$ values (from Eq1) as a function of total input power. While the increase of $\chi_{e,pb}$ with power represents the deterioration of confinement, $\chi_{e,hp}$ is a constant within the experimental error. Its value is $\chi_{e,hp} = 2.5 \pm 0.5\ m^2 s^{-1}$. A further illustration of the constancy of $\chi_{e,hp}$ under increasing power is given in Fig.2, where signal traces of two different discharges with 2.5 and 10.4MW resp. are shown to be almost identical.

DISCUSSION

On the basis of the constancy of $\chi_{e,hp}$ with respect to the input power and on the basis of the numerical agreement between $\chi_{e,hp}$ ($2.5 \pm 0.5\ m^2 s^{-1}$) and the estimates for $\chi_{e,inc}$ ($2.5 \pm 0.5\ m^2 s^{-1}$) we conclude that indeed the identification $\chi_{e,hp} = \chi_{e,inc}$ is correct. It then follows that the heat diffusivity χ_e is a function of ∇T_e on a timescale much faster than the heat pulse (ie. a few ms). We propose a specific dependence of the type given in Fig.4. This 'critical gradient' model is consistent with both the observations of $\chi_{e,pb}$ and $\chi_{e,hp}$. The model can be interpreted to represent a micro instability that starts to grow above a

threshold value of ∇T_e. At high ∇T_e, the instability saturates, and $\chi_{e,pb}$ goes to its asymptotic value $\chi_{e,hp}$. The ratio $\chi_{e,hp}/\chi_{e,pb}$ is largest just above the critical gradient, which is the normal operating range for ohmic discharges. We speculate that below the critical gradient χ_e has a low, eg. Alcator-Intor, value.

A different interpretation of the offset linear behaviour [3,7] is that the total heat flow is the net result of the outward diffusive flow, governed by a heat diffusivity of value $\chi_{e,inc}$ and an inward heat pinch, the mechanism of which is unexplained.

If χ_e increases with ∇T_e, this will naturally give rise to a certain rigidity of the electron temperature profile. Our model is thus capable of explaining a certain degree of profile consistency', without invoking non-local transport (see also [7]).

FIRST RESULTS DURING PELLET INJECTION

HPP measurements were performed on two discharges (B_t=3.4T, I_p=3MA), in which the sawtoothing continued normally after injection of a deuterium pellet. Table 1 shows the results. $\chi_{e,hp}$ is given before injection, in an interval between 0.1 and 0.5 s after injection, and in an interval 2 s after injection of the pellet.

Table 1

time	48.4-50	50.1-50.5	52-53 s
11014	2.2±0.5	1.7±0.4	2.2±0.4
11016	1.6±0.5	0.9±0.3	2.2±0.5
pulse		$\chi_{e,hp}$ (m^2/s)	

The trend is a substantial drop of $\chi_{e,hp}$ after injection of the pellet. The low value persists for about 0.5 s. Thereafter $\chi_{e,hp}$ returns to its pre-pellet value. It is interesting to note that the reduction of $\chi_{e,hp}$ goes together with a decrease ∇T_e after the pellet injection. ∇T_e (at r = 2/3 a) is reduced from 4 keV/m to 2.6 keV/m in the interval between 0.1 and 0.5 s after the pellet. The latter value is lower than the lowest obtained in ohmic heating steady state conditions, ie. $\geq$ 3 keV/m. This observation is consistent with the critical gradient model. However, because the plasma is far from the steady state, these results should be treated with care.

REFERENCES

1 Callen J D, Jahns G L, Phys. Rev. Letters 38 (1977) 971

2 Tubbing B J D ea., Proc. 12th. Europ. Conf. Budapest, 9F1 (1985) 138

3 Frederickson E D, ea., Nucl. Fusion 26 (1986) 849

4 Tubbing B J D, Lopes Cardozo N J, JET report JET-R(87)01

5 Tubbing B J D, Lopes Cardozo N J, Wiel M J van der, subm. to Nucl. Fusion.

6 Lopes Cardozo N J, ea., to be published.

7 Callen J D, ea., JET report JET-P(87)10, subm. to Nucl. Fusion

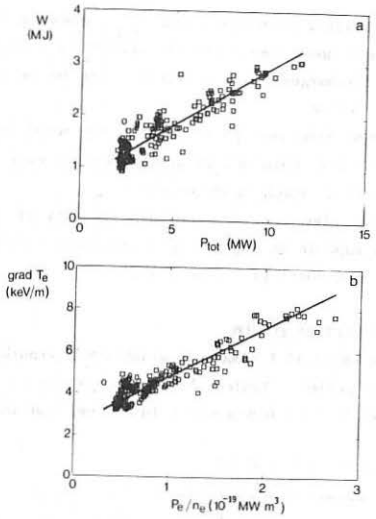

Fig.1 Global and local power balance.
a) The total kinetic energy content W as a function of the total input power P, for a selection of JET data: I_p = 3MA, B_T = 3.4 T, n_e=2.5 10^{19} m^{-3}.
b) $\nabla_r T_e$ vs P_e/n_e (P_e is the power transported by the electrons), evaluated at r = 2/3 a for the same selection of data.
The full lines correspond to $\chi_{e,inc}$=2.5 m^2/s.

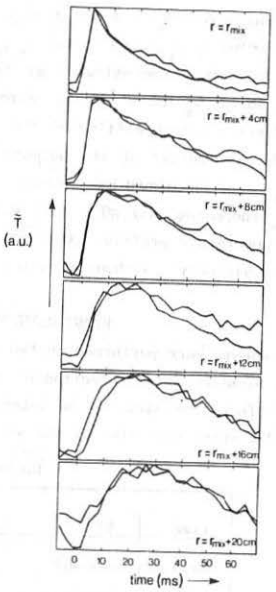

Fig.2 Heat pulse signals in two discharges, with P=2.7 and 10.4 MW resp. Note that while the input power is quadribled the pulse shapes have not changed.

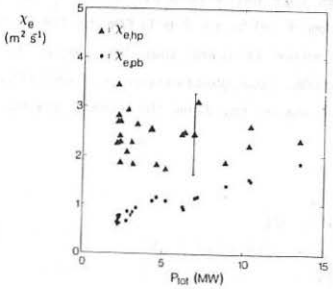

Fig.3 The measured values of $\chi_{e,hp}$ and the corresponding values of $\chi_{e,pb}$ as a function of input power. While $\chi_{e,hp}$ is constant, $\chi_{e,pb}$ increases with increasing power, thus showing the deterioration of the global confinement.

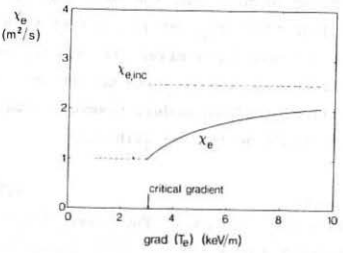

Fig.4 Sketch of the critical gradient model. This dependence of χ_e on $\nabla_r T_e$ allows a unified description of the heat pulse results and the power balance analysis.

RADIATION BEHAVIOUR OF GAS AND PELLET REFUELLED HIGH DENSITY DISCHARGES IN ASDEX

K.F. Mast, E.R. Müller, H.U. Fahrbach, H. Krause, R.S. Lang, P. McCarthy, W. Sandmann, D. Zasche, G. Becker H.B. Bosch, H. Brocken, A. Carlson, A. Eberhagen, G. Dodel[1] G. Fußmann, O. Gehre, J. Gernhardt, G. v.Gierke, E. Glock, O. Gruber, G. Haas, W. Herrmann, J. Hofmann, A. Izvozchikov[2], E. Holzhauer[1], K. Hübner[3], G. Janeschitz, F. Karger, M. Kaufmann, O. Klüber, M. Kornherr, K. Lackner, M. Lenoci, G. Lisitano, H.M. Mayer, K. McCormick, D. Meisel, V. Mertens, H. Murmann, J. Neuhauser, H. Niedermeyer, A. Pietrzyk[4], W. Poschenrieder, H. Rapp, A. Rudyj, F. Schneider, C. Setzensack, G. Siller, E. Speth, F. Söldner, K. Steinmetz, K.-H. Steuer, S. Ugniewski[5], O. Vollmer, F. Wagner

Max-Planck Institut für Plasmaphysik, Garching bei München, W. Germany
[1]University of Stuttgart, [2]Ioffe Institute, [3]University of Heidelberg,
[4]University of Washington, Seattle, USA, [5]Inst. for Nuclear Research, Swierk, Poland

Abstract. Pellet and gas refuelled high density divertor discharges in ASDEX are investigated with regard to their radiation behaviour and energy balance. Exclusively ohmically heated deuterium plasmas in a non-carbonized (NC), carbonized (C) and titanium gettered (DP) vacuum vessel are considered. In gas refuelled plasmas the radiation power profiles are hollow with a central emissivity $\epsilon(0) \leq 10\mathrm{mW/cm^3}$ in C and $\epsilon(0) \leq 40\mathrm{mW/cm^3}$ in NC and DP discharges. In C discharges P_{RAD}/P_Ω rises from 0.2 at $\bar{n}_e = 3.2 \cdot 10^{19} m^{-3}$ to 0.3 at the density limit. In NC and DP plasmas higher values from 0.3 to 0.45 are observed. Radiation from the X-points can amount to 14 % of P_Ω. In pellet refuelled discharges a central peaking of the emissivity ϵ is observed. A sudden transition from negligible or slow impurity accumulation to a fast rise could be detected in many discharges. In NC and DP pellet discharges a self-triggering of impurity accumulation was found. Measured inward drift velocities range from 60 cm/s to 130 cm/s at r=15 cm.

1. Global radiation behaviour and energy balance. This paper mainly deals with parametric studies of the total plasma radiation with a particular emphasis on X-point radiation from gas and pellet refuelled high density discharges in ASDEX. Three radiation zones are discernible with the bolometric diagnostics. The main plasma including the scrape-off layer, the regions around the two X-points and the divertor plasma [1].

Total X-point and main plasma radiation can be separated from two independent measurements of the total radiation in the main plasma chamber. Firstly with the wide-angle bolometers and secondly with the bolometer array both taking into account the X-point radiation with various weighting factors. Radial profiles of emissivity are derived by standard Abel-inversion technique.

Ohmically heated pellet and gas refuelled high density divertor discharges in deuterium are investigated with regard to their radiation behaviour and energy balance during current flattop. Carbonized (C), non-carbonized (NC) and titanium gettered (DP) discharges with safety factors q_a between 2.7 and 2.9 and plasma currents between 300 KA and 380 KA are considered here.

In gas refuelled discharges dW_p/dt the time derivative of stored plasma energy Wp is negligible small whereas during pellet injection dW_p/dt amounts up to 20 % of P_Ω and has to be taken into account in the power balance. The normalized total radiation of the main plasma $P_{RN} = P_{RAD}/(P_\Omega - \frac{dWp}{dt})$ as a function of the line averaged electron density $\bar{n}_e$ during various gas refuelled discharges is shown in Fig. 1a.

In carbonized plasmas P_{RN} amounts to 0.2 at $\bar{n}_e = 3.5 \cdot 10^{19} m^{-3}$. NC and DP plasmas radiate about 0.35 at $\bar{n}_e = 3.5 \cdot 10^{19} m^{-3}$ owing to a higher content of metals, mainly of iron. At higher densities near the density limit gas refuelled discharges with $q_a > 2.7$ (no sharp limit was detected) show a nonlinear increase of P_{RN} with rising $\bar{n}_e$. This behaviour can be attributed mainly to a decrease of the electron temperature near the separatrix due to enhanced recycling losses and line radiation of low-Z impurities (C_{III}-lines). A correlation between edge peaking of radiation power profiles (carbonized and gettered plasmas) and nonlinear behaviour of P_{RN} with $\bar{n}_e$ can be deduced from Figs. 1a and 3.

The formation of a zone of enhanced radiation near the separatrix is observed just 10–20 ms before a density limit disruption occurs. Owing to an electronic integration time constant $\tau = 10ms$ the time resolution of the bolometric diagnostics is too poor to reveal details of the radiation profile evolution. This type of poloidal symmetric thermal instability which differs from the usual Marfe evolves on a

longer time scale in JET due to its larger dimensions [2]. The normalized X-point radiation $P_{XN} = P_X/(P_\Omega - dW_p/dt)$ (Fig. 1b) enhances with increasing $\bar{n}_e$ similar as P_{RN} does. Maximum values of P_{XN}=0.14 are obtained and have to be considered in the energy balance. A titanium gettered discharge (#19514) serves as an example for a low $q_a = 2.1$ high density plasma. P_{RN} remains nearly constant until the density limit is reached and P_{XN} increases linearly with $\bar{n}_e$. The formation of a zone of enhanced edge radiation could not be detected.

In ASDEX a considerable increase of the line average density $\bar{n}_e$ and of the Murakami parameter $\bar{n}_e R/B_T$ was achieved by injecting series of deuterium pellets with a centrifuge [3,7]. We consider here only discharges with high central peaking of the density profiles during pellet injection.

A nonlinear enhancement of P_{RN} with rising $\bar{n}_e$ is observed in pellet refuelled (C, NC and DP) discharges qualitatively similar to gas refuelled plasmas. Starting from values characteristic to gas refuelled plasmas P_{RN} continuously rises until about 0.45 at the density limit (Fig. 2a). The relative increase of P_{RN} is highest in C discharges in contrast to gas refuelled discharges. Central peaking of the electron density and radiation power profile in pellet discharges is responsible for this behaviour. P_{XN} decreases with increasing $\bar{n}_e$ (Fig. 2b) owing to the high central radiation which reduces the power outflux in the scrape-off layer.

A correction of P_{RN} with the total radiation inside the inner half minor radius $P_{RAD}(a/2)$ yields nearly no variation of the corrected P_{XN} with $\bar{n}_e$. Near the density limit P_{XN} is usually smaller in pellet discharges than in gas refuelled discharges.

In pellet and gas refuelled discharges the normalized divertor radiation $P_{DN} = P_{DIV}/(P_\Omega - dW_p/dt)$ rises with $\bar{n}_e$ up to $\bar{n}_e \approx 5.5 \cdot 10^{19} m^{-3}$. Above $\bar{n}_e = 5.5 \cdot 10^{19} m^{-3}$ P_{DN} saturates which indicates the achievement of a high recycling regime in the divertor [1]. Near the density limit P_{DN} continuously decreases with $\bar{n}_e$ owing to the steady increase of the radiation in the main plasma P_{RN} and, thus, decreasing heat flux into the divertor.

The energy confinement time $\tau_E = W_p/(P_\Omega - dW_p/dt)$ shows a similar behaviour as P_{DN} near the density limit. The plasma energy W_p is derived from the diamagnetic signal, from kinetic data (twice the energy content of electrons) and from the equilibrium beta. Li is derived from the electron temerature profiles assuming neoclassical resistivity and neglecting diffusion of the poloidal magnetic field. All three energies agree better than within 10% and indicate the same trend with $\bar{n}_e$. The power on the divertor plates P_{cond} is measured with the thermographic diagnostics. Only a small fraction of the heating power is deposited on the divertor plates. The normalized power on the divertor plates $P_{CN} = P_{cond}/(P_\Omega - dW_p/dt)$ is smaller than 0.1 and reduces further near the density limit (Fig. 4). We conclude: a nonlinear rise of P_{RN} with $\bar{n}_e$ is observed in both gas and pellet refuelled C, NC and DP discharges with maximum values of $P_{RN} \approx 0.45$ at the density limit. X-point radiation plays an important role in the energy balance ($P_{XN} \leq 0.14$). Gas and pellet discharges show a different behaviour of P_{XN} with $\bar{n}_e$.

2. Profiles and impurity transport. The signal rise of the central channels of the bolometer camera originates either from a Marfe which is a low tempertaure thermal instability located at the plasma boundary [4] or from enhanced radiation from the plasma centre. A Marfe is accompanied by a strong increase of the line intensities from low ionization stages of low Z impurities, e.g. CIII lines ($T_e \approx 10eV$). In contrast radiation peaking at the plasma centre is indicated by a simultaneous rise of intensity of central soft X-ray channels and of Fe XVI lines. Considering spectroscopic, soft X-ray and bolometer signals we can separate Marfes from radiation peaking at the plasma centre.

Normalization of the radiation emitted from the outer half of the minor plasma radius to the total radiation P_{RAD} yields a quantitative parameter indicating the profile shape (Fig. 3). All gas refuelled discharges (with sawtooth activity during current flattop) show edge peaked radiation profiles. The central radiation power density in C discharges is less than $10mW/cm^3$ and in NC and DP discharges it is somewhat higher $\leq 40mW/cm^3$ but still negligible related to the central ohmic heating power $P_\Omega(0) \approx 200mW/cm^3$.

In low $q(q_a \leq 3)$ pellet discharges the central peaking of the density and the radiation power profile is correlated. During a typical discharge there is first a phase of negligible or slow impurity accumulation, which may suddenly turn into a fast accumulation at the plasma core. Three different scenarios for this transition are experimentally observed: a) one pellet is missing during a series of pellets (Fig. 5), b) after pellet injection if no density limit disruption occurs, c) in NC and DP discharges the q on axis may considerably rise above 1.0 owing to a pronounced flattening of the T_e-profile with rising central

radiation power density (Fig. 6). A self-triggering of accumulation occurs then if $P_{RAD}(0)/P_\Omega(0) \geq 1$ (see also [6]).

Case a) is demonstrated in Fig. 5 for a discharge with density feed back. From t=1.5s until t=2.1s the T_e- and n_e-profiles remain nearly unchanged with a small rise of $n_e(0)(\leq 20\%)$. Strong sawtooth activity is observed during pellet injection which obviously prevents an accumulation of impurities averaged over a pellet cycle. After a last sawtooth possibly triggered by the pellet at t=1.89s a fast accumulation starts inside a minor radius r=10cm (Fig. 7). One finds from the chord-intensity profile in Fig. 7 a transport of impurities from the outer plasma regions $r > 10cm$ to the plasma core. It seems that the impurity accumulation is immediately stopped by the next pellet (Figs. 5,5a). A neoclassical theory [5] predicts from $\frac{dp_i}{dr}$ an inward drift velocity $v_D = 100cm/s$ at r=15 cm. At this position the maximum gradient of the pressure profile of plasma ions is observed. An inward drift velocity of $v_D = 65cm/s$ at r=15 cm is derived for case a) [5] which is in good agreement with theory. One can speculate that pellets change the outward transport of impurities by triggering sawteeth resulting in a higher cycle averaged diffusion coefficient. More details are given in [5].

References

/1/ Müller, E.R., Behringer, K., Niedermeyer, H., Nucl. Fus. 22 (1982) 1651.

/2/ Mast, K.F., Krause, H., Behringer, K., Rev. Sci. Instr., Vol. 56, No.5, 1985.

/3/ Niedermeyer, H., Büchl, K., Kaufmann, M., et al., Proc. of the 13th European Conf. on Controlled Fusion and Plasma Heating, Schliersee (1986), Part I, 168.

/4/ Neuhauser, J., Schneider, W., Wunderlich, R., Nucl. Fus. 26, (1986), 1679.

/5/ Feneberg, W., Mast, K.F., Neoclassical Impurity Transport in Ohmically Heated Pellet Discharges, this conference.

/6/ Fussmann, G., Janeschitz, G., et al., Study of Impurity Accumulation in the ASDEX Tokamak, this conference.

/7/ Kaufmann, M., et al., Pellet Injection with Improved Confinement in ASDEX, to be published.

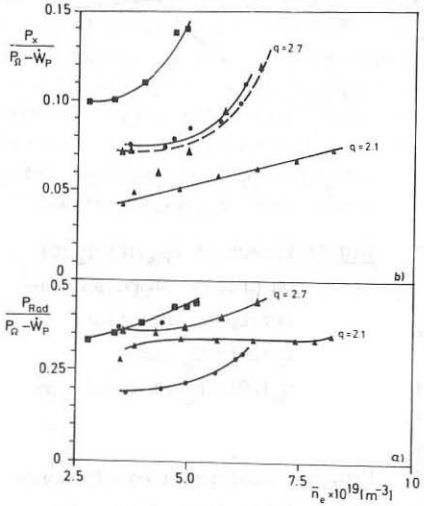

Fig.1a,1b: Gas-refuelled

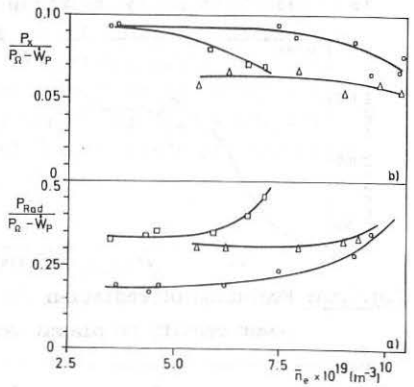

Fig.2a,2b: Pellet-refuelled

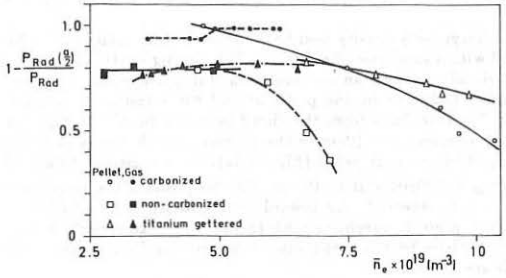

Fig.3: $P_{Rad} - P_{Rad}(\frac{a}{2})$ related to P_{Rad}. $P_{Rad}(\frac{a}{2})$ = radiation from outer plasma column $\frac{a}{2} \leqslant r \leqslant a$

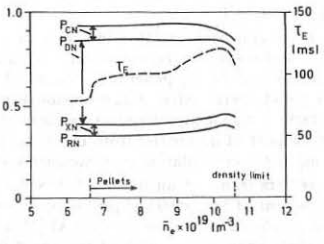

Fig.4: Energy balance for a pellet refuelled DP-plasma.

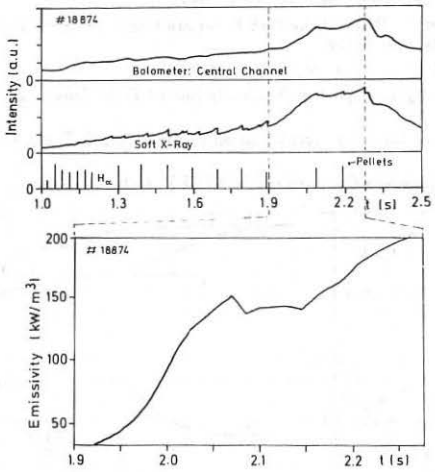

Fig.5,5a: Evolution of radiation power density on plasma axis.

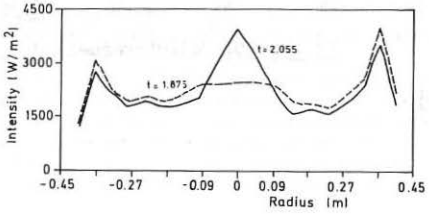

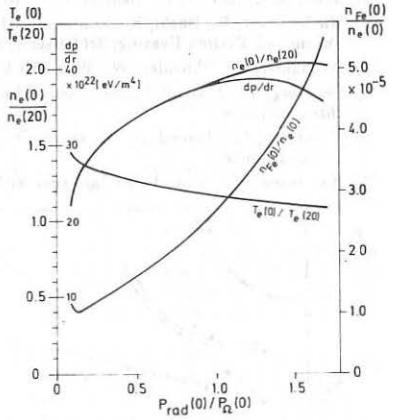

Fig.6: Effect of $P_{Rad}(0)/P_\Omega(0)$ on profile shape and impurity accumulation
$T_e(20) = T_e$ and
$n_e(20) = n_e$ at r = 20 cm

Fig.7: Radial profiles of chord-intensity before and during accumulation

PLASMA STUDY IN T-10 TOKAMAK BY REFLECTED MICROWAVE SIGNAL.

Buzankin V.V., Vershkov V.A., Dreval V.V., Zhuravlev V.A.

ABSTRACT.

Description and the testing results of two plasma investigation techniques by a reflected microwave signal in T-10 tokamak are given in paper. The first technique is a radar modification. The scheme measures a time delay for a microwave signal reflected from plasma. The time delay measurement is performed independently of microwave signal frequency. This method allows to study not only the plasma density profiles at the probe signal frequency scanning but also density oscillations at a constant frequency of the microwave signal, in difference from the technique developed on TFR [1].

The second technique is intended for the plasma turbulence study by the reflected signal phase oscillation. The phase oscillations are measured by the heterodyne scheme. This scheme allows to measure the phase oscillations independently of amplitude fluctuations. This technique, in comparison with a traditional method of studying the plasma turbulence based on the laser scattering radiation, has a better space resolution and allows to study a long wave turbulence.

Three types of turbulence have been registered by this technique in T-10 plasma. The first type has a range 50-200 kHz and studied at many tokamaks by the laser scattering radiation [2]. The second one has a frequency range 15-20 kHz and probably it is the tearing mode instability. The third type has a frequency higher than 1 MHz, its physical nature has not been determined yet. The study of turbulence amplitude distribution along the radius, dependent on the regime of tokamak operation, has been done.

[1]. Simonet F. Rev. Sci. Instrum. 56(1985)№5, p.664.

[2]. Liewer P. Nuclear fusion 25(1985)№5, p.543.

OPTIMAL STABILIZATION OF THE PLASMA COLUMN HORIZONTAL POSITION IN TOKAMAK BY THE ADAPTIVE CONTROL SYSTEM

Gribov Yu.V., Kuznetsov E.A., Mitrishkin Yu.V., Chuyanov V.A., Shakhovets K.G.

The paper solves the problem of the plasma column optimal horizontal stabilization in tokamak. The relay autooscillations system is applied in the solution. The system forms a closed circuit of the following sections: a) control object (plasma in tokamak), b) executive device (the control coil and the thyristor commutator as the relay element, c) control device for the feedback signal.

The plasma column may be presented as a linear stable object with the input affected by the total of uncontrolled disturbance and by the control coil current. The linear object is stable, so we can minimize the amplitude of the input signal oscillations that provides for the minimum amplitude of the output signal that is the plasma column displacement. In synthesiring the control device algorithm, the input signal minimization rules out dynamics of the object. All this simplifies essentially the algorithm, presented as follows.

The optimal threshold for the commutator switching is developed from the continuous disturbance values and the disturbance derivative with the preset time lags of the executive device into account. The sign of the threshold value is determined by the voltage sign at the control coil. The input signal of the object fluctuates about the positive ahd negative threshold values providing for the minimum amplitude when autooscillations are at the maximum frequency. The minimum amplitude at every quasi-period is determined by the minimum time lags of the relay element and by the disturbance value and its derivative.

The control device makes use of the object's adaptive model evaluating continuously uncontrolled disturbance and the object amplification coefficient.

The system was applied in tokamak "TUMAN-3" that reduced plasma limiter interaction with decreasing plasma loop voltage.

MHD PERTURBATION IN HL-1 TOKAMAK

Q D Gao, G C GUO, Z H Wang, Q W Yang, S K Yang
B L Jiao, S J Qian
Southwestern Institute of Physics
P O Box 15, Leshan, Sichuan, China

INTRODUCTION

Although a significant amount of experimental and theoretical work has been devoted to studying the MHD behavior in a tokamak plasma, some of the problems remain poorly understood. HL-1 is a medium sized (R=1.02m, a=0.2m), ohmically heated tokamak with a thick copper shell [1] on which a variety of MHD phenomena has been observed. It is quite interesting to investigate the characteristic of the MHD perturbation in HL-1 and compare it with the results from other tokamaks.

MHD PERTURBATION DURING CURRENT RISE

The fluctuations of the poloidal magnetic field were measured by the arrays of magnetic pick-up coils which are located at a radius 30.5cm between the liner and the copper shell. The poloidal mode numbers m=2,3,4 has been identified by Fourier analysis of the signals from the pick-up coils. As the liner is a very thin (0.5mm) GH39 steel bellows, the frequency response could be quite flat in the range 3 - 15KHz.

By changing the capacity of the capacitor banks and the connection of the primary ohmic heating windings HL-1 can be operated with different current rising rates in the start up phase. Different mode instabilities are developed simultaneously since the current rising rates are rather high ($\dot{I}p \sim 10KA/ms$ - 20KA/ms). But for the discharges with longer current rising time the m=4,3,2 modes have different growth rates. Usually the m=4 mode grows to the maximum first, after a few mili-seconds the m=3 reaches the maximum and the m=2 grows even more slowly (Fig. 1a). This difference of growth rates may be caused by the strong current skin effect which keeps the current profile at the plasma boundary steeper. For the more rapid current rising case the m=4 and 3 modes grow to the maximum at the same time, but no obvious m=2 fluctuation is observed (Fig. 1b). Snice the skin effect is much stronger in this case, the q=4 and 3 surfaces are very close to each other in the unstable region but the q=2 surface is possibly located at the area with flattened current profile.

The MHD perturbation in current rise phase is complex and it can usually be divided into two stages. In the first stage when the plasma current is relatively low, a sequence of positive spikes corresponding to burst of the mode activity appear on the loop voltage signals. These perturbations disturb vertical rather than horizontal plasma displacement and sometimes can be avoided. Following the first stage, there appear m=4 and 3 "soft" disruptions which produce large negative spikes and sharp decrease in the current rising rate.

MHD INSTABILITIES

During the plateau phase the instabilities of m=2,3,4 are developed simultaneously. The measured fluctuation amplitudes for different modes are decreased successively in the order of m=2,3 and 4 when "soft" disruption happens. But this order is reversed for the unstable discharges without disruption. For the m=2 fluctuation the amplitude varies with the safty factor at the limiter q_L as shown in Fig. 2. According to the measurements made in the peripheral plasma region with a Langmuir probe, the plasma has a cold blanket the thickness of which varies with the plasma radius and it probably correlated with the recycling from the cold wall. Considering the influence of the safty factor q_L on the current distribution [2], a current density profile

$$j(x) = j(0)[(1-\gamma^2x^2)^{\mu}-(1-\gamma^2)^{\mu}], \qquad \gamma^2=q_L/5$$

is assumed. Solving the MHD equation for the perturbed radial magnetic field $\tilde{B}_r$ with $\mu=3$, the relation between the magnitude of the perturbed poloidal field and the safty factor q_L seems to fit the experimental results rather nicely. This indicates that the current profile in HL-1 is peaked and becomes more peaked as the safty factor q_L is increased, which is consistent with other measurements.

The observed fluctuation frequency is independent of the poloidal mode numbers. Refering to the m=2 mode, we observed mode growing, mode saturation with small amplitude and well defined mode structure during disruption phase. Collecting all these experimental results together, a relation between the fluctuation frequency and the normalized amplitude can be drawn as shown in Fig. 3. When the amplitude is small the frequency decreases linearly with the amplitude increasing, but this trend is saturated as the

amplitude grows to causing disruption. Except for disruption phase, a simple model based on the assumption that slowing-down of the fluctuation is due to an increased flattening of Te(r) and $n_e(r)$ caused by wider magnetc island seems to explain the frequency variation. Disruption changes the magnetic topology dramatically, so there is no obvious effect of the magnetic island on changing the profile for a disruptive plasma. During fast current ramping in the start up phase, due to the influence of strong skin effect on the current profile the mode frequency and amplitude rise and fall almost in phase with each other.

SAWTEETH

Sawtooth oscillations are seen on the soft X-ray signals for discharges with plasma current larger than 100KA. They usually occur on the later part of the plateau phase. The radius of the q=1 surface determined from the sawteeth inversion scales as $r_s \propto a/q_L$ when the plasma radius varies. The repetition time of the sawtooth oscillation varies in a quite wide range, but its precise dependence on the plasma parameters is difficult to determine. Comparing the sawtooth periods measured from different shots and from one shot at different time, a rough scalig $\tau_s \propto \bar{n}^2/Ip$ was obtained for Te$\sim$1Kev (Fig. 4). Taking the inversion radius scaling and constant toroidal magnetic field in one shot into consideration, the sawtooth period is roughly in proportion to $1/r_s$. In some discharges the sawtooth period becomes longer when the inversion radius decreased obviously with time. These are different from the previous empirical scaling for sawtooth period [3].

ACKNOWLEDGEMENT

The authors wish to thank the engineering support team for their invaluable contribution to this work.

REFERENCES

[1] HL-1 Group, Proc. 11th Int. Conf. on Plasma Physics and Controlled Nuclear Fusion Research, Kyoto (1986), Paper IAEA-CN-47/A-VII-1
[2] Yu. B. Esiptchuk, K. A. Razumova, Proc. 13th Euro. Conf. on Controlled Fusion and Plasma Heating, Schliersee (1986), Invited paper
[3] EQUIPE TFR, Proc. 6th Int. Conf. on Plasma Physics and Controlled Nuclear Fusion Research, Berchtesgaden (1976) Vol.1, 279

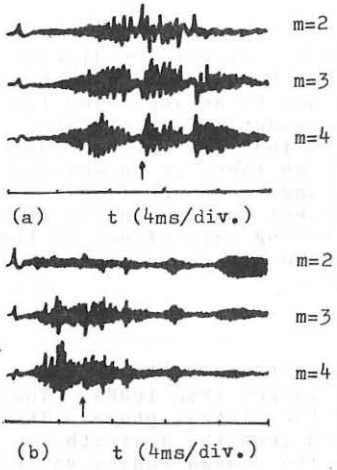

Fig.1 Waveforms of Mirnov oscillation during current rise phase. (The arrows indicate the time when Ip reaches the maximum) (a)$\dot{I}p \sim 10KA/ms$, (b)$\dot{I}p \sim 20KA/ms$

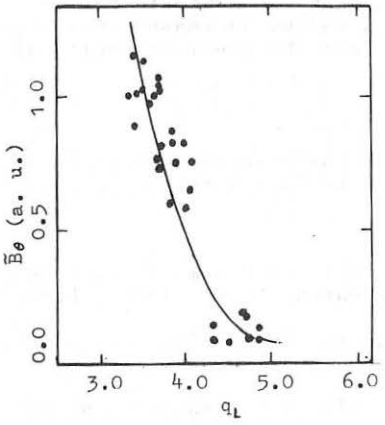

Fig.2 m=2 fluctuation amplitude as a function of the safty factor q_L

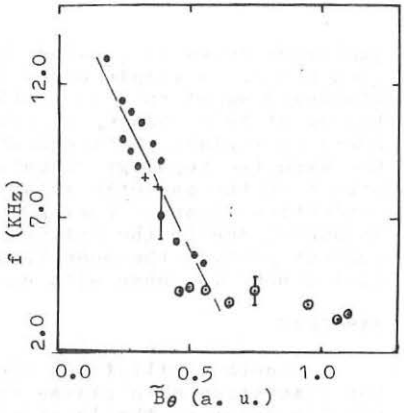

Fig.3 Fluctuation frequency versus normalized amplitude
• during mode growing
⊙ during disruption
+ during mode saturation

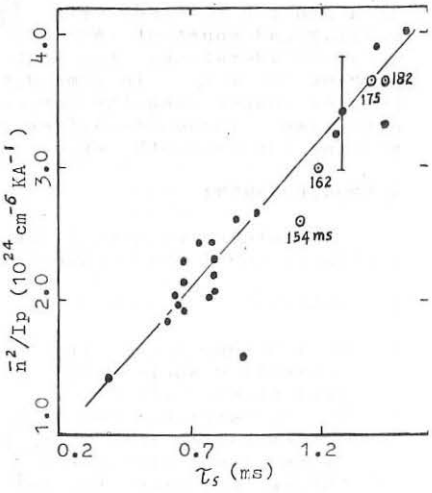

Fig.4 The sawtooth period versus $\bar{n}^2/Ip$
⊙ data from shot 2504

DISRUPTIVE FEATURE IN OHMICALLY HEATED HL-1 PLASMA

GUO Gancheng, GAO Qingdi, WANG Zhanhe
YANG Qingwei, CHEN Jiefu, QING Yunwen
XU Guangbi

Southwestern Institute of Physics
P.O.Box 15, Leshan, Sichuan
People's Republic of China

ABSTRACT: The disruptive feature in ohmically heated HL-1 plasma has been studied by means of measuring the perturbation of poloidal magnetic field and soft X-ray emission. At the plasma current rise phase, the m=4 and m=3 are major MHD activities, and during the current plateau, the m=2 mode plays a principal role in the growing process of instabilities. Double sawteeth have been also observed on HL-1 device. The growth of MHD activities leads to q=2 sawtooth oscillations, during the q=2 relaxations. The q=2 sawteeth are followed by soft major disruption.

DISRUPTIVE MHD ACTIVITY DURING PLASMA CURRENT RISE PHASE

The disruptive MHD activities take place frequently during current rise phase. The fluctuations of poloidal magnetic field have been detected with eight pick-up coils arranged around a poloidal cross-section. The Fourier analysis of coil signals shows that the voltage spike as disruption occurrence is a multi-mode helical perturbation, they are m=4, 3 and 2. When the MHD m=4 and 3 mode amplitudes reach maximum, the boundary q-value approximately equals to 4.2 and 3.6 respectively and there is maximal propability of disruption at the both q_L values (showed Fig. 1). The early disruptions ($q_L > 4.8$) showed a clear positive voltage spike, and the later disruptions ($3.4 < q_L < 4.8$) showed a negative voltage spike preceding the positive one. The early disruptions (positive spike) due to runaway would be suppressed by the increasing the hydrogen filling pressure up to $P_H > 0.133P_a$ at $dI_p/dt=7—25kA/ms$ but later disruptions are seen due to MHD activities.

q=1 SAWTOOTH ACTIVITIES Generally, the soft X-ray line integral signals from surface barrier diodes exhibited the sawtooth oscillations without gas puffing. The normal sawteeth inside q=1 surface are shown in Fig. 2. It has been shown experimentally that the soft X-ray sawtooth relaxation is mainly due to electron temperature relaxation. We have obtained the electron temperature from the soft X-ray emissions using the absorber method and deduced directly that

the variation of T_{e0} is about 10% before and after the sawtooth crash. The reverse radius of q=1 sawteeth is about 3.5—4.8 cm and it is away from axis as the density is raised with time.

The double sawtooth have been observed and studied in detail on the large and medium-size tokamak devices JET[1], TEXT[2], etc. We have frequently observed the double sawtooth oscillations as well on HL-1. It occurs usually in ohmically heated HL-1 plasma with plasma current I_p =95—150kA and plasma electron density $\bar{n} \simeq 1.3 \times 10$ cm . The characteristic of double sawtoothing is apparently shown in Fig. 3. The subordinate oscillation does not affect the hot plasma core, while a full reconnection of enclose magnetic axis causes the main oscillation. It implies that there is a hollow current profile, i.e. there are two or three q=1 surface immediately after the main disruption. The m/n=1/1 successor oscillations have not been apparently observed and the amplitude of the m/n=1/1 precursor oscillations is small; according to the preliminary experimental results, the collapse time of sawteeth is not shorter than the expected and consistent with Kadomtsev theory. We plan to accurately study the characteristics for normal sawteeth and double sawteeth in HL-1 plasma.

q=2 SAWTOOTH AND EVOLUTION OF INTERNAL AND EXTERNAL DISRUPTIONS The another important feature of disruptive instabilities in ohmically heated HL-1 plasma is that the growth of MHD activities leads to q=2 sawtooth oscillations. Fig. 4 shows the time evolution of soft X-ray fluctuation signals. In general, the growing of m=2 mode lead to the disappearance of q=1 sawteeth. After the sawtooth activities disappear, simultaneously with the growing of m=2 mode, the spatial profile of soft X-ray intensities is apparently flatten rather than peaked like other devices, for example, JIPP T-II[3]. It is deduced that the current profile is modified from peaking shape during internal disruption into flatting shape with steep gradient near q=2 resonant surface (q(0)>1). Such profile leads to m=2 mode growing rapidly and occurrence of the q=2 sawtooth oscillations due to the full magnetic reconnection inside the q=2 surface. In our case, there seems to be a thick cold boundary plasma due to impurity cooling. The low current density at q=2 surface and a large central region where $q \geq 1$ are formed as the current density is flat after the sawtooth activities disappear, so that the discharge exhibits periodic q=2 minor disruptions or sawteeth similar to those associated with the q=1 surface. During the minor disruptions, the m=2 signal is strongly modulated by sawteeth, while the sawteeth themselves are strongly modulated at the same frequency as m=2. Fig. 5 shows that the q=2 sawteeth are inverse at r=-11.5cm and its inversion radius is $r_{s2} \sim$11cm. The repetition time of q=2

sawteeth is $\tau_{s2} \sim 2$ms and the variation of electron temperature associated with the q=2 sawtooth oscillations is about 20%. Usually, the repetitive minor disruption is followed by the soft major disruption. It is accompanied with that the central electron temperature profile returns into the peaked shape due to ohmic heating. The soft major disruption does not lead to the current broken down. After the soft major disruption, there are two cases as usual, either the stable dicharge with the sawtooth activities is maintained until the current ended or the minor disruption takes place again followed by the stable discharge or the circulation of repetition minor disruptions. The measurement results show that the growing phase of m=2 mode between the q=1 sawtooth disappearance and the q=2 sawtooth occurrence extends over 6—12ms for different discharge conditions.

Mostly, on HL-1 device, there are three phases of the disruptive instabilities: disappearance of q=1 sawtooth activity, growth of m=2 magnetic island, and external disruption. The last one is triggered by contact of the large m=2 island with the limiter or "gaseous" limiter resultting eventually in lost energy. The MoXIV line intensity increases by a factor of 5 in the hard major disruption shows that the plasma impacts on the limiter seriously.

ACKNOWLEDGEMENTS

The authors wish to thank engineers for their invaluable support to this work

REFERENCES

1. D.J.CAMPBELL, et al. Nucl. Fusion Vol. 16 No. 8 (1986) 1085
2. S.B.KIN, Nucl. Fusion Vol. 26 No. 9 (1986) 1251
3. S.TSUJI, et al. Nucl. Fusion Vol. 25 No. 3 (1985) 305

FIGURE CAPTIONS

FIG. 1. MHD activities of plasma current rise phase (No.2142, B_T=2.1T, I_p=120kA, hydrogen filling pressure = 0.107P_a)

FIG. 2. Normal sawtooth (No. 1809, B_T=1.69T, I_p=90kA, hydrogen filling pressure = 0.040P_a)

FIG. 3. Double sawteeth (No. 1790, B_T=2.16T, I_p=95kA, hydrogen filling pressure = 0.040P_a; No. 1902, B_T=2.5T, I_p=152kA, hydrogen filling pressure=0.113P_a)

FIG. 4. q=2 sawteeth (No. 1763, B_T=2.32, I_p=130kA, hydrogen filling pressure =0.067P_a)

FIG. 5. Time evolution of soft X-ray fluctuation signals (No.2433, B_T=2.25T, I_p=120kA, hydrogen filling pressure =0.133P_a; No.2299, B_T=2.2T, I_p=110kA, hydrogen filling pressure =0.107P_a)

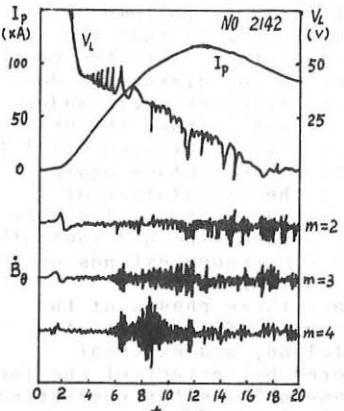

Fig. 1

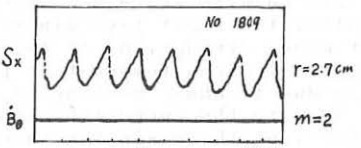

Fig. 2

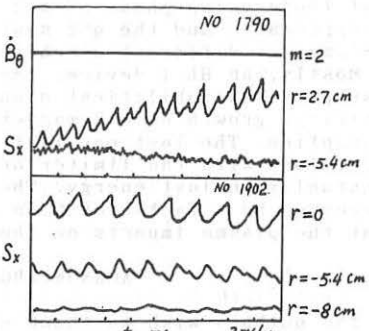

Fig. 3

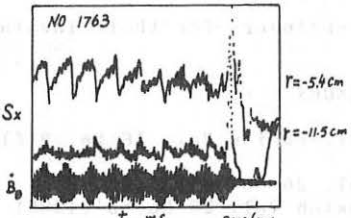

Fig. 5

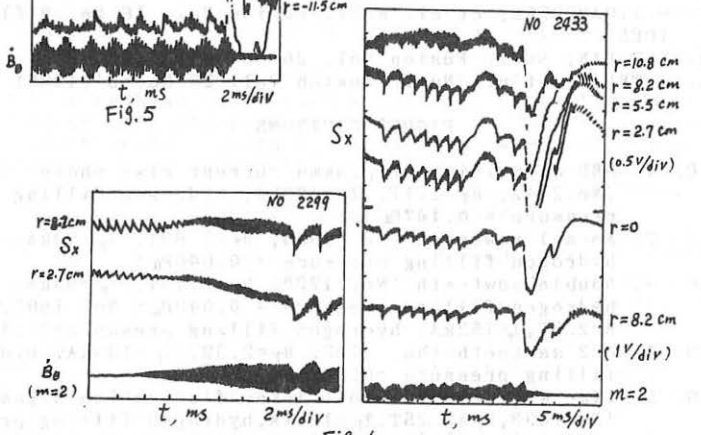

Fig. 4

RESPONSE OF PLASMA PROFILES TO NEUTRAL BEAM POWER DEPOSITION IN ASDEX

E. Speth, O. Gruber, K. Lackner, H. Riedler[6], A. Stäbler, O. Vollmer, G. Becker, H.S. Bosch, H. Brocken, A. Carlson, A. Eberhagen, G. Dodel[1], H.-U. Fahrbach, G. Fußmann, O. Gehre, J. Gernhardt, G.v.Gierke, E. Glock, G. Haas, W. Herrmann, J. Hofman, A. Izvozchikov[2], E. Holzhauser, K. Hübner[3], G. Janeschitz, F. Karger, M. Kaufmann, O.Klüber, M. Kornherr, M. Lenoci, G. Lisitano, F. Mast, H.M. Mayer, K.McCormick, D. Meisel, V. Mertens, E.R. Müller, H. Murmann, J.Neuhauser, H. Niedermeyer, A. Pietrzyk[4], W. Poschenrieder, H. Rapp, A. Rudyj, F. Schneider, C. Setzensack, G. Siller, F. Söldner, K.Steinmetz, K.-H. Steuer, S. Ugniewski[5], F. Wagner, D. Zasche

Max-Planck-Institut für Plasmaphysik
EURATOM Association, D-8046 Garching

[1] University of Stuttgart, [2] Ioffe Institute, [3] University of Heidelberg, [4] University of Washington, Seattle, USA, [5] Inst.for Nuclear Research, Swierk, Poland, [6] Schiedel-Stiftung, Austria

1. INTRODUCTION

Profile consistency has been the subject of an ongoing discussion. From the prevailing results of different experiments /1,2,3,4,5/ did not emerge a consistent pattern yet. Among the open questions we address two topics in this paper: namely (1) how the plasma profiles in the H-regime respond the variations of the deposition profile and (2) more generally, to what extent the observed resilience of the plasma profiles would be consistent with a local but nonlinear relation between temperature - or pressure gradients and the local heat flow.

2. H-MODE EXPERIMENTS

Heating profile experiments in the L-regime have previously been reported from ASDEX /1,2,3/, where the most extreme cases of hollow deposition could be realised by working at elevated densities ($\bar{n}_e$ = $1.1 \cdot 10^{14}$ cm^{-3}) /3/. Due to the upper density limit of $(7 \div 8) \cdot 10^{13}$ cm^{-3} observed for the H-regime on ASDEX in non-pellet-fuelled discharges, the deposition profile in the present H-mode experiments could be varied only over a more restricted range. In particular we have injected 40 keV H^0 and 45 keV D^0 respectively into D^+-plasmas with otherwise identical parameters (I_{pl} = 420 kA, $\bar{n}_e = 6.2 \cdot 10^{13}$ cm^{-3}, P_N = 1.7 MW). Figure 1 shows the deposition profiles of the total power to ions and electrons as computed with the FREYA-code including the ohmic power. The subsequent response of the pressure profiles is shown in Fig. 2: there is no significant difference. The beam-induced change on plasma composition and the known isotope effect on confinement should be small, since the profiles analysed are taken 150 msec after the beams are turned on.

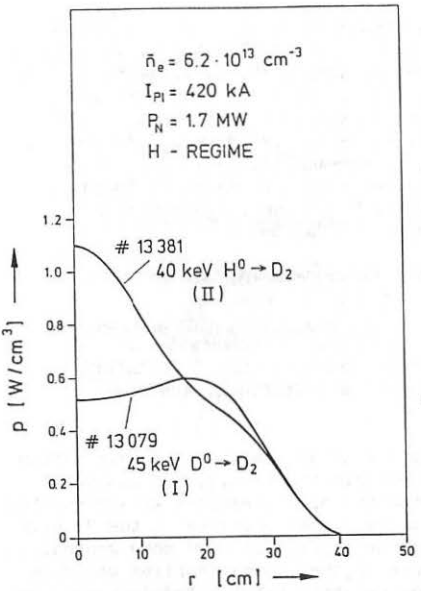

Fig. 1:
Deposition profiles of the total power to ions and electrons including ohmic power.

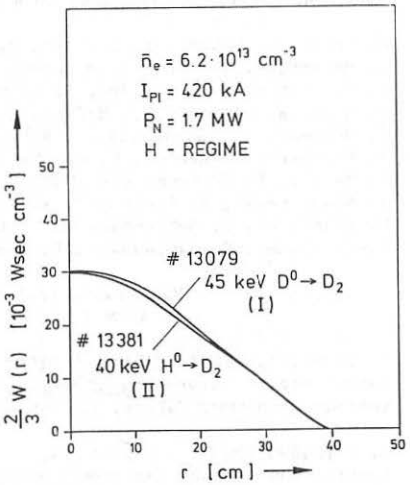

Fig. 2:
Resulting experimental pressure profiles for the power deposition cases of Fig. 1
$2/3\ W(r) = \int n_e(r)(T_e(r)+T_i(r))dV$
The T_i-profiles not being known precisely, electron pressure and ion pressure form factors were assumed to be identical and the integrated energy content was normalised to the diamagnetic signal (fast ions neglected).

Typical parameters of the two cases are compared in Table 1. Although the Te-profiles (not shown here) establish the well-known differences to those in the L-regime, (pedestal at the edge) their shape agrees within the error bars, and also the previous findings in the L-regime concerning deposition profile changes /1/ are valid: $\tau_{Ee}(0)$ shows a 60 % enhancement, τ_E (a) is about 15 % higher, $T_e(0)$ is marginally higher for hollow deposition. Thus the conclusions drawn previously /1,2/ for profile invariances in the L-regime appear to be applicable to the H-regime too at least within the range of presently accessible deposition profiles.

Table 1

	# 13 079 (45 keV $D^0 \rightarrow D_2$)	# 13 381 (40 keV $H^0 \rightarrow D_2$)
$T_e(0)$	(1.33 ± 0.15) keV	(1.25 ± 0.17) keV
τ_E (a)	58 msec	51 msec
$\tau_{Ee}(0)$	158 msec	96 msec

(Concerning the rather lowish global confinement times (for the H-mode) one should note that the burst frquency of the ELM's dramatically increases when approaching the upper density limit in the H-mode; consequently the confinement time is considerably reduced in comparison to the medium density cases or the quiescent H*-mode.)

3. NONLOCAL HEAT TRANSFER

Theoretical examinations by other groups have shown the incompatibility of predictions of standard first principle drift wave theories with the experimentally observed T_e-profiles. This resilience has led to the proposition /6/ that a globally acting principle has to be invoked to explain their very weak variation with any change of power deposition. As an alternative explanation, we compare the response predicted by empirical heat transport laws containing a nonlinear relation between temperature- or pressure-gradients and the local heat flow.
For the stated purpose of a rather qualitative illustration we make a number of simplifying assumption which otherwise would have to be viewed critically. So we do not distinguish between electron and ion transport (assuming $T_e = T_i$). We use in the following calculations two heat transport models, a linear one

$$q_{heat} = - f_1(r) \cdot \nabla p \qquad (1)$$

and a quadratic one

$$q_{heat} = f_2(r) \cdot (\nabla p)^2 \qquad (2)$$

with f_1 and f_2 chosen as $f_1(r) = f_2(r) = (1 + (r/a)^2)^3$. Only relative variations will be considered, so that no absolute coefficient values need to be specified (q_{heat} ... radial heat flux density).

As a realistic example we consider the two extreme deposition profiles reported in /2/, which are more or less identical to the ones in Fig. 1. The corresponding unnormalised profiles are shown in Figs. 3a and 3b. They show, in spite of the large apparent difference in the power deposition, a remarkable small difference already for the linear transport model case, which is further diminished when changing over to the quadratic transport law.
The above examples show that on the basis of presently available data it seems difficult to rule out a local, nonlinear transport law as an explanation of the observed profile resilience in tokamaks. A nonlinear transport law of the form (2) would automatically link profile resilience to confinement degradation with power as globally observed in

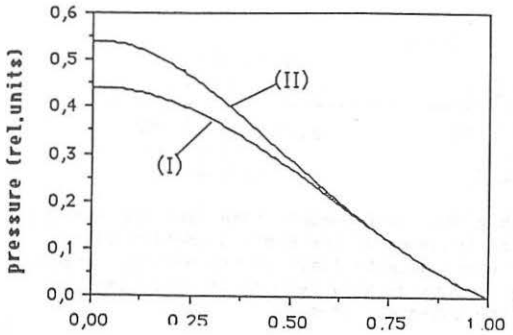

Fig. 3a:

unnormalized pressure profiles predicted by the linear transport law for the power deposition cases of Fig. 1.

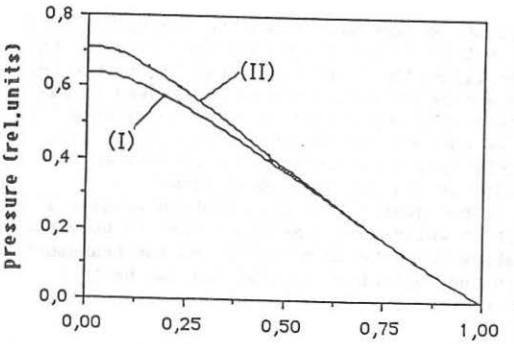

Fig. 3b:

unnormalized pressure profiles predicted by the quadratic transport law for the power deposition cases of Fig. 1.

L-discharges. Power independence of confinement times as observed in ASDEX H-mode discharges could however be made compatible with strong profile resilience e.g. by an ansatz $q_{heat} \sim (\nabla p/p) \cdot \nabla p$. The considerations can of course not rigorously disprove the explanation that plasma profile shapes are determined by some non-local principle. One so far unanswered argument in favour of such a more global explanation is the sharp transition between L- and H-mode behaviour, and the obvious non-existence of mixed situations where part of the plasma volume is in the L- and the other in the H-regime.

REFERENCES

/1/ E. Speth et al., Proc. 12th EPS Conference, Budapest (1985), Vol. II, 284
/2/ F. Wagner et al., Phys. Rev. Lett. 56 (1986) 2187
/3/ E. Speth et al., Proc. 13th EPS Conference, Schliersee (1986), Vol. II, p. 281
/4/ R.J. Goldston et al., ibid. P. 41
/5/ J.G. Cordey et al., Proc. 11 Int. IAEA Conf., Kyoto (1986) paper A-II-3.
/6/ H.P. Furth, Plasma Physics and Contr. Fus. 28, 9A (1986) 1305

FUSION IGNITION EXPERIMENT WITH NO AUXILIARY HEATING

R. Carrera, E. Montalvo and M. N. Rosenbluth

University of Texas at Austin*

The crucial step to prove that fusion energy is accessible in a controlled manner is the realization of an experiment in which stable ignited plasmas are produced. An experiment (IGNITEX) to produce and control thermonuclear ignited plasmas is considered here. The original concept was proposed by M. N. Rosenbluth, W. F. Weldon and H. H. Woodson[1]. Some of B. Coppi's ideas[2] for a compact thermonuclear experiment are used in conjunction with recent advances in the technology of high current systems to envision a novel ignition tokamak system with 20 Tesla toroidal field on axis and plasma currents in excess of 12 Megamperes.

The IGNITEX device is a single-turn coil high-field compact tokamak capable of reaching and controlling fusion ignition with ohmic heating alone[3]. A copper-alloy single-turn coil operating at low voltages permits very high filling factors and then, a high-strength toroidal field magnet system. The mechanical stresses are reduced to tolerable levels by preloading the coil structure and by using a central compression bar. The electromagnetic pulse is lengthened by cryogenic precooling of the magnet system to liquid nitrogen temperature. Because of the low impedance of the nonconventional magnet system a special power supply is required that can provide a very large pulse of current at very low voltage. A set of twelve homopolar generators, each one rated to 12.5 MA, 10 volts and 1.GJ are used in parallel to feed the single-turn coil. An internal poloidal field magnet system formed by ten toroidal single-turn coils can induce the plasma currents required for fusion ignition and provide for plasma equilibrium and shaping. This system permits bucking of the single-turn coil, then increasing the strength of the toroidal field magnet, and provides a high coupling to the plasma, then minimizing the requirements for the poloidal field system power supply. Because of the thick single-turn coil surrounding the plasma, the magnetic flux requirements are lower than in a conventional tokamak. A set of five homopolar generators that swing the current in the coils from 22 MA to -15.7 MA along the discharge serve as the power supply for the internal poloidal field system.

In a deuterium-tritium plasma ignition is a state in which the fusion reaction rate is high enough for the plasma heating due to alpha particles to be greater than the plasma power losses due to conduction, convection and radiation. A self-sustained thermonuclear fusion reaction is then produced. The energy confinement in ignited plasmas is not yet known. In the calculations presented here the heating due to the alpha particles is assumed to degrade the plasma energy confinement as auxiliary heating does in present tokamak experiments. Bremsstrahlung and cyclotron radiation losses also contribute to the cooling of the plasma.

The plasma column has a major radius of 150 cm and the minor radius is 47cm. An elongation of the plasma cross section 1.6 with no triangularity has been considered. Theoretical calculations of the plasma power balance at the flat-top of the plasma discharge (using conventional energy confinement scalings) indicate that the IGNITEX experiment has an ample margin for ignition without auxiliary heating. The device is designed to approach ignition ohmically at very low plasma beta ($< 1\%$) which makes the experiment simple and reliable.

In addition the IGNITEX experiment can prolong the ignited phase of the plasma for a time interval of several plasma energy confinement times by controlling the thermal instability associated to plasma ignition. The basic mechanism that damps the thermal excursion and prevents the plasma from reaching the disruptive limits is the plasma cyclotron radiation. The plasma dynamics simulations presented here (Figs. 1 to 6) assume that the energy confinement follows the Kaye-Goldston scaling. This implies that the path to ignition is basically described by the NeoAlcator scaling. At density levels close to and during the ignited phase of the plasma discharge the energy confinement is deteriorated by the non-ohmic plasma heating. Also, the current and field are considered to be ramped up in the first 3 seconds of the discharge, maintained in a flat-top of 5 seconds and shut down in two seconds. It is shown that ignition can be attained after 4 seconds of plasma initiation. The alpha heating power starts rising before the ohmic heating power in the plasma decreases significantly. Neoclassical ohmic heating is sufficient to start the self-sustained fusion reaction. The neutron wall load at ignition is 3 Mw/m^2 and during the ignited phase reaches a maximum value of 8 Mw/m^2, when uniform deposition is assumed.

The results of preliminary estimates[4] indicate that the nonconventional technology and the simplicity of the IGNITEX design make the cost of the experiment relatively low (~ $100M).

In conclusion, the IGNITEX experiment appears to provide a very direct and cost-effective way of producing ignited plasmas for scientific study.

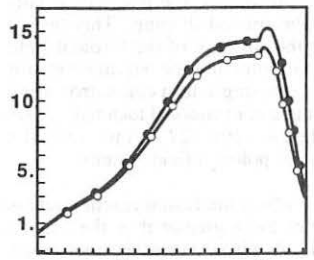

Ion and electron temperatures

Fig. 1

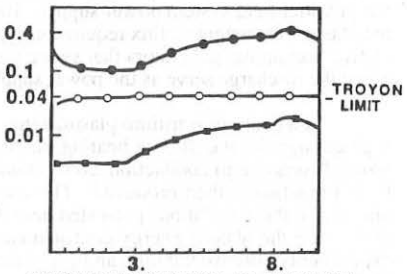

Volume-averaged toroidal and poloidal betas. Troyon beta limit.

Fig. 2

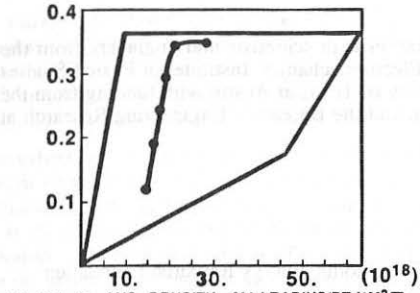

1/Q PSI -vs- AVG. DENSITY • MAJ RADIUS•BT (1M²/T)
● = (1/Q PSI) -vs- (DEN • R•BT) PLASMA EVOLUTION
Hugill diagram

Fig. 3

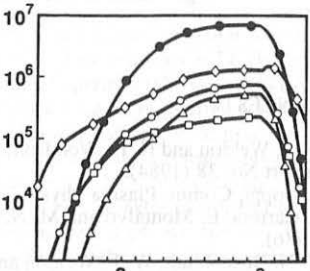

POWER PER UNIT WALL AREA (W/M²) -vs- TIME (SEC)
□= BREMSSTRAHLUNG △= CYCLOTRON
O = TOTAL POWER DUE TO RADIATION
●= NEUTRON POWER ◊ = PLASMA LOSS
Power losses to the first wall

Fig. 4

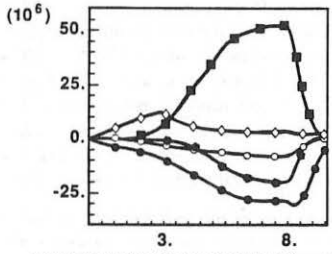

AVERAGE ELECTRON POWERS (WATTS) -vs- TIME (SEC)
■= FUSION ●= ELECTRON ENERGY CONFINEMENT
O = BREMSSTRAHLUNG ● = CYCLOTRON
◊ = OHMIC HEATING
Electron power balance contributing terms

Fig. 5

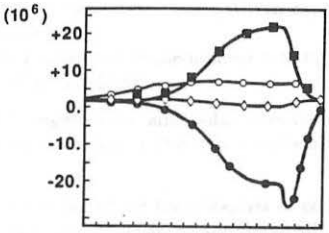

AVERAGE ION POWERS (WATTS) -vs- TIME (SEC)
■= FUSION ●= ION ENERGY CONFINEMENT
O = ION-ELECTRON EQUILIBRATION
◊ = LOSS DUE TO FUSION REACTIONS
Ion power balance contributing terms

Fig. 6

*This project is being pursued in collaboration with scientists and engineers from the Center for Fusion Engineering, Center for Electromechanics, Institute for Fusion Studies and Fusion Research Center at The University of Texas at Austin with funding from the Texas Atomic Energy Research Foundation and the Bureau of Engineering Research at U.T.

REFERENCES

1. W. F. Weldon and H. H. Woodson, Texas Atomic Energy Research Foundation Report No. 38 (1984).
2. B. Coppi, Comm. Plasma Phys. Cont. Fusion **3**, 47 (1977).
3. R. Carrera, E. Montalvo and M. N. Rosenbluth, Bull. Am. Phys. Soc. **31**, 1565 (1986).
4. M. N. Rosenbluth, W. F. Weldon and H. H. Weldon, Basic Design Report for the Fusion Ignition Experiment (IGNITEX). Preliminary proposal to the U.S. Department of Energy (March, 1987).

PHYSICS CONSIDERATIONS FOR THE COMPACT IGNITION TOKAMAK

R. Parker,[1] D. Post,[2] G. Bateman,[2] M. Bell,[2] P. Colestock,[2] J. Helton,[3] W. Houlberg,[4] M. Hughes,[5] D. Ignat,[2] S. Jardin,[2] J. Johnson,[2] S. Kaye,[2] C. Kieras-Phillips,[2] L-P. Ku,[2], G. Kuo-Petravic,[2] B. Lipschultz,[1] J. Manickam,[2] M. Peng,[6] M. Petravic,[2] M. Phillips,[5] M. Porkolab,[1] N. Pomphrey,[2] J. Ramos,[1] J. Schmidt,[2] D. Sigmar,[1] R. Stambaugh,[3] D. Stotler,[2] D. Strickler,[6] A. Todd,[5] N. Uckan,[4] J. Wesley,[3] K. Young[2]

Introduction. As presently conceived, the world's fusion program will enter during the next decade into the burning plasma phase, beginning with $Q \lesssim 1$ experiments in TFTR and JET and culminating with operation of an International Tokamak Experimental Reactor (ITER) devoted to study of the engineering problems associated with a long-pulse, ignited (or near-ignited) tokamak. The Compact Ignition Tokamak (CIT), scheduled for operation near the middle of the decade, is viewed as a bridge between these initiatives and has a research program focused on resolution of alpha particle physics issues which occur on the timescale $\tau_{pulse} \sim 10\tau_E$. The early experience with ignited plasmas gained in CIT should be extremely useful to an ITER. In addition to providing early confirmation of the design assumptions, the CIT will provide a basis for detailed design decisions which can be made after the main parameters are set, for example detailed design of the divertor and the auxiliary heating and fueling subsystems. Equally important, the CIT experience should be valuable in developing ITER operating scenarios during the phases of startup, burn-initiation and control, and shutdown.

Aside from the programmatic role just described, CIT will permit study of a number of important and intriguing physics issues associated with collective phenomena which can occur in the presence of a sufficiently intense and energetic α-component. Some of the more important of these include:

- Effect of $P_\alpha >> P_{aux}$ on the plasma profiles and resultant global energy confinement, including sustainability of the H-mode and effect on χ_i through excitation of the η_i-mode;
- Effect of the α-power on the sawtooth including effect on τ_E and also on MHD stability through modification of $p(\psi)$ and $q(\psi)$ profiles /1,2/;
- Effect of the α-precession resonance on destabilization of n=1 internal kinks (fishbones) or high n ballooning modes /3,4,5/;
- Effect of super Alfvénic ($v_\alpha > v_A$) alpha particles on global or kinetic Alfvén eigenmodes and the possibility of anomalous spatial α-diffusion /6,7/;
- Effect of fast-α losses (due to ripple, sawteeth, fishbones, low mode-number tearing modes, etc.) on central impurity accumulation and ensuing fuel dilution.

The last point includes the effect of self-consistent changes in the ambipolar electric field due to all α-losses thereby classifying it as a collective phenomenon even if α-driven instabilities are not directly involved.

Machine Description. The CIT design concept is motivated by the potential of combining the good confinement properties of compact, high-field tokamaks with the additional advantages

[1] Massachusetts Institute of Technology, Cambridge, MA
[2] Princeton Plasma Physics Laboratory, Princeton, NJ
[3] GA Technologies Inc., San Diego, CA
[4] Oak Ridge National Laboratory, Oak Ridge, TN
[5] Grumman Aerospace Corporation, Princeton, NJ
[6] Fusion Engineering Design Center, Oak Ridge, TN

which accrue from shaping, *e.g.*, improvement in confinement (H-mode) in the auxiliary heating regime. A divertor has been chosen as the baseline configuration not only as a means of confinement improvement but also as being more prototypical of future devices. This, together with the desire for longer pulse length and more conservatism in the engineering approach have caused a general growth in size relative to the 1 m major radius typical of early Ignitor designs.

The design parameters given in Table I reflect compromises which have been made between the conflicting requirements of fixed project cost and the objective of reaching ignition with substantial margin relative to both confinement and stability limits. The field of 10 T is the maximum which can be produced using power and energy from sources available at the PPPL site; an upgrade to 12 T is feasible by installing additional power and also adding an external structure which limits the vertical separating stress in the inner leg of the toroidal field (TF) magnet.

The tradeoffs involved in locating the main PF coils inside vs outside of the TF have been carefully examined. Locating the PF coils internal to the TF brings them closer to the plasma and permits a broader class of equilibria to be obtained. This configuration is also efficient in total consumption of PF energy, however the required increase in TF energy tends to offset this gain. Although somewhat enhanced TF performance is possible with internal PF coils, the engineering risks increase considerably with this choice as the PF coils are then trapped and machine assembly becomes more complex. For these reasons, an external PF system has been chosen, supplemented by several internal coils, each capable of carrying up to about 0.5 MA. These coils will be used for fine-tuning the plasma shape, control of the divertor heat loads and stabilization of the axisymmetric instability.

TABLE I. CIT Machine Parameters (5/87)

R	1.75 m	P_α	$\leq$ 60 MW
a	0.55 m	$q_\psi(a)$	3 (3.6)
κ	$\leq$ 2.0	$\beta_T = 3I/aB$	5% (4%)
δ	0.4	TF Flat Top	5s
B	10 T (12 T)	Φ	41 v-sec
I	9 MA		

Confinement. Within the context of present-day understanding of confinement and operational limits, CIT is being designed with a substantial ignition margin thus permitting a wide variation in operating parameters in order to comprehensively study those collective phenomena which arise due to the presence of the energetic α-component. Using a "neo-Alcator" scaling of $\tau_e = .07naR^2q_{cyl}$ and a Murakami-Hugill scaling for the density limit of $< n > = 1.5\ B/Rq_{cyl}$, (where $< >$ implies a volume average), the ignition margin, P_α/P_{loss}, is proportional to B^2a at fixed T and q. Many other confinement scalings, including Kaye-Goldston "L-mode" scaling /8,9/, improve with increasing B^2a, and CIT has been designed to maximize this figure of merit. The plasma current was also maximized consistent with the engineering design constraints for the poloidal field system and MHD stability considerations for the safety factor, q, at the plasma edge. A large current is necessary to allow a high beta at high field ($\beta \sim I/aB$), and to maximize energy confinement, since $\tau_e \sim I$ for most auxiliary-heated confinement scalings. The confinement properties of the CIT design have been analyzed using a number of confinement scalings. One way of characterizing the confinement properties is to plot power balance contours in density and temperature space (POPCON graphs) /10/. In this type of analysis, a power balance is computed for a range of densities and temperatures with given profiles, and contours

of constant required auxiliary heating power are drawn. Ignition is identified as the region above the zero power contour. The accessible operating space is confined to densities below a density limit (taken to be $< n > = 1.5B/Rq_{cyl}$ and to betas below the beta limit (taken to be 3I/aB). The confinement model has the form $\tau_E^{-2} = \tau_{OH}^{-2} + \tau_{AUX}^{-2}$ where $\tau_{OH}(\tau_{AUX})$ is the ohmic (auxiliary-heated) confinement time. Generally, the neoAlcator value is used for τ_{OH} and the regression fit given by Kaye and Goldston /8/ is inserted for τ_{AUX}, where, since $\tau_{KG} \sim P^{-0.6}$, the total power $P = P_{OH} + P_{AUX} + P_\alpha$ is used. With this analysis and with relatively flat density profiles ($n(r) \sim (1\text{-}(r/a)^2)^{0.5}$), CIT does not ignite. However, ignition is easily achieved (Fig.1) with an enhanced "L-mode" scaling ($\tau_{AUX} = 2\tau_{KG}$) used as a model characterization of the "H-mode" which retains degradation with increased power. In fact, detailed analyses show that an enhancement of ~ 1.3 over Kaye-Goldston allows ignition, albeit with a small operating window. For more optimistic scalings such as the ASDEX-H /11/, ignition is easily achieved. CIT has been designed with a poloidal divertor and is expected to be capable of H-mode operation.

Ignition can be obtained with "L-mode" scalings if the density profile is allowed to be more peaked than $(1\text{-}(r/a)^2)^y$, with $y \geq 1.5$ /12,13/. Such peaked profiles would be obtained by a combination of pellet fueling, off-axis ICRF heating, and careful tailoring of the current profile during ramp-up to postpone the onset of strong sawtooth oscillations. Time dependent analyses of these scenarios have been carried out by 1 1/2 D transport code simulations using BALDUR and WHIST.

In summary, CIT ignites with a modest enhancement of a factor of 1.3 times "L-mode", and is able to ignite with "L-mode" scaling if the density profile can be sufficiently peaked by pellet injection. It thus has margin for parametrically investigating the energy confinement questions associated with intense alpha particle heating which are crucial to the present ETR designs, all of which have less confinement margin than CIT.

MHD Stability. The ideal MHD stability and β-limit depend strongly on the pressure and current profiles. Optimized profiles yield stable operating regimes with β well above that required for ignition. More realistic profiles such as those which would result from sawtoothing activity have broad, nearly shearless regions in which high-n ballooning and low-n infernal modes limit the pressure gradient and reduce the β-limit. Profiles which are optimized for $P(\psi)$ but which also obey an ohmic constraint yield β-values close to the Troyon limit ($\sim 3I/aB$) except for isolated, nearly rational values of q_a corresponding to $\beta = 0$, current-driven kinks /14,15/.

Impurity Control. Impurity control and power handling capacity are key issues for high power, ignited experiments. The principal impurity control system for CIT is a double null poloidal divertor which also has the additional advantage of enhancing the energy confinement with H-mode operation. The high density, compact approach to ignition leads to very high average heat loads on the wall, on the order of 1.5–2 MW/m^2 for CIT. In addition, the first wall hardware must be able to withstand the damage of disruptions which will cause very high peak loads, on the order of 100's to 1000's of MW/m^2. Because graphite can withstand very high peak loads without melting, it will be used to protect the vacuum vessel, and as the material for the divertor plates. The present divertor plates are inclined with respect to the flux surfaces to reduce the peak heat fluxes of ~ 100 MW/m^2 normal to the flux surface to the ~ 5 MW/m^2 required to keep the surface temperature of the graphite below the sublimation point. The divertor configuration is somewhat open, but is also designed to isolate the recycling neutrals away from the main plasma as much as possible. The highly shaped divertor plates that are required to reduce the peak heat fluxes impose severe requirements on the control of the X-point and plasma configuration, reduce the flexibility of plasma operation, and are sensitive to the

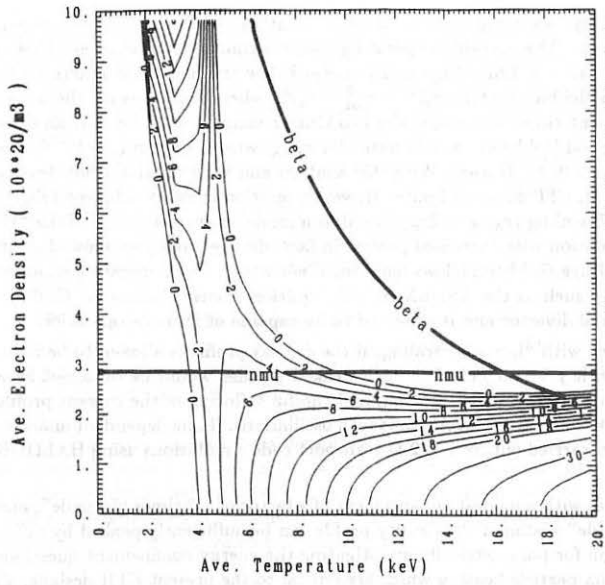

FIG.1 Equilibrium power balance contours in an n-T plane for a CIT device with the parameters of Table I. Each contour corresponds to a fixed auxiliary-heating power and ignition is given by the contour $P_{AUX} = 0$. The Hugill-Murakami density and Troyon-β limits discussed in the text are also shown.

profile of the plasma edge parameters. Studies of alternative designs with increased flexibility are presently underway.

References

/1/ "Effect of Sawtooth Oscillations and Ballooning Modes on Ignition in CIT," G. Bateman, *et al.*, Bull. Am. Phys. Soc. **31**, (Nov. 1986, Baltimore), 7Q7.

/2/ "CIT MHD Stability," M. Hughes *et al.*, ibid, 7Q11.

/3/ "Alpha Particle Loss Due to Ripple and MHD Modes," S. Zweben, *et al.*, Sherwood Theory Conf. (April, 1987, San Diego) 3A25.

/4/ "Stability of Shaped Tokamaks with Energetic Alpha Populations", D. Spong, *et al.*, ibid, 2C23.

/5/ D. Spong, *et al.*, Phys. Fluids **28** (1985) 2494.

/6/ K. Tsang, *et al.*, Phys. Fluids **24** (1981) 1508.

/7/ Y. M. Li, *et al.*, Phys. Fluids **30** (1987), in press.

/8/ S. M. Kaye and R. J. Goldston, Nucl. Fusion **25** (1985) 65.

/9/ S. M. Kaye, Phys. Fluids **28** (1985) 2327.

/10/ W. A. Houlberg, S. E. Attenberger, L. M. Hively, Nucl. Fusion **22** (1982) 935.

/11/ O. Gruber, Int. Conf. Plasma Physics (Lausanne, 1984) vol.1, 67-96.

/12/ "Delaying Sawtooth Oscillations in the Compact Ignition Tokamak," G. Bateman, PPPL-2373 (1986).

/13/ "Simulation of a Compact Ignition Tokamak Discharge (CIT-2L)," D. F. Stotler and G. Bateman, PPPL-2415 (Feb. 1987).

/14/ "MHD Stability Analysis of the Compact Ignition Tokamak (CIT)," M. W. Phillips, *et al.*, Sherwood Theory Conf. (April, 1987, San Diego) 1D10.

/15/ "MHD Equilibrium and Stability Considerations for CIT," J. Manickam, *et al.*, ibid, 3A15.

EFFECT OF CURRENT RISE ON ICRF HEATED PLASMAS IN THE JIPP T-IIU TOKAMAK

K. TOI, T. WATARI, R. AKIYAMA, R. ANDO, Y. HAMADA,
S. HIROKURA, K. IDA, E. KAKO, K. KAWAHATA, Y. KAWASUMI,
S. KITAGAWA, K. MASAI, K. MATSUOKA, A. MOHRI, S. MORITA,
N. NODA, I. OGAWA, Y. OGAWA, K. OHKUBO, M. SAKAMOTO,
M. SASAO, K. SATO, K.N. SATO, S. TANAHASHI,
Y. TANIGUCHI, K. YAMAZAKI

Institute of Plasma Physics, Nagoya University,
Nagoya 464, JAPAN

Abstract

In limiter tokamak JIPP T-IIU, improvement of edge plasma transport is observed during high power ICRF heating, at the same time current density (j_ϕ) profile is *actively* controlled by an additional current rise(CR). D_α emission is reduced by ~ 40 %, compared with no CR discharge. Fall-off length of electron density in the scrape-off layer is remarkably reduced. Edge electron temperature derived from the intensity ratio of OVI lines is by about 2 times higher. Soft X-ray emission along the peripheral chord ($r/a_L \sim 0.7$) is enhanced by a factor of 2. Plasma stored energy is higher by $\sim 30\%$.

1. Introduction

The confinement of tokamak plasmas is usually degraded by high power additional heating(L-regime). In the regime shapes of electron temperature(T_e) profile are approximately same for various deposition profiles of heating power, that is, T_e profile follows the so-called profile consistency. The reason seems to be due to the *consistency* in a current density(j_ϕ) profile, which may be tailored by the plasma itself through island formation due to low m (≥ 2) tearing modes. On stable ohmic heating plasma, local MHD pressure balance will be well-established by strong coupling of ohmic heating power and current density through Ohm's law. However, intense additional heating disturbs the pressure balance considerably, because in all of present heating experiments only the gradient of plasma kinetic pressure is changed without controlling j_ϕ-profile actively. In other words, j_ϕ-profile is modified indirectly through tokamak plasma transport or magnetic island formation. The violation in MHD pressure balance may enhance the plasma transport so that pressure difference should be reduced. For H-mode observed in divertor configuration [1] large pressure change is supported by high global shear region near plasma boundary untill j_ϕ-profile is favourably tailored by transport process. It is predicted from the above consideration that the transport enhancement during high power additional heating may be avoided by controlling j_ϕ-profile actively at the same time of the heating. One of the most promissing j_ϕ-profile is that with a

pedestal near the plasma boundary, which is favourable for tearing mode stability and may be realized in H-mode discharge.

In JIPP T-IIU, ICRF heated plasma exhibits typical L-mode scaling [2]. This paper reports on ICRF heating property with active current density profile control. The current density profile is controlled by an additional current rise [3]. This control method is a transient technique and may be unappropriate for application to a large tokamak. The primary interest of this experiment is to clarify whether or not confinement degradation during high power additional heating is avoided by active control of the current density profile.

2. Experimental Setup

RF power up to 1.1 MW is injected to a deuterium plasma with hydrogen minority (typically, $n_H/n_e \simeq 10$ %). The ion cyclotron and hybrid layers are located near the plasma center ($r \leq 5$ cm), where rf frequency is 40 MHz and toroidal field 2.7 T. At the same time of rf pulse, the plasma current is purposely raised from 180 kA to 250 kA by applying inductive electric field in the quasi-steady state. The electron density is also raised by gas puffing during the current rise and rf heating, so that edge electron heating becomes moderate. Otherwise, Mirnov oscillations are enhanced by CR or rf.

3. Experimental Results

We compare two types of discharges shown in Fig. 1 : case I without CR ,and case II with CR, where electron density and injected rf power are adjusted almost same in both cases. The rf power is more than three times of ohmic heating power. The peak of total radiation loss (bolometer) P_r is same, but the temporal evolution is different. The plasma stored energy in case II is appreciably higher(~ 30 %) than case I. We have investigated plasma behaviours near the plasma boundary by spectroscopic method and electrostatic probes. In this experiment two main limiters of graphite are installed. VUV spectrometer is located 90° away from the limiters and the probes are located 45° away from the closer limiter. Note that edge plasma parameters are monitored at the region away from the special region such as a limiter. As seen from Fig.2, D_α emission is reduced by ~ 40 % in case II(i.e., with CR). It is enhanced during rf pulse in any discharge without CR. The light impurity lines such as CIII and OVI behave in the same way as D_α. The temporal evolution of these lines correlates well with that of electron density measured by electrostatic probes near the limiter radius ($r - a_L \equiv \Delta r \sim 1$ cm; a_L : limiter radius), while the density at $\Delta r \sim 2$ cm is remarkably depressed (Fig.3). The fall-off length of n_e profile near the the plasma edge becomes very short. The above data indicate the improvement of plasma particle confinement near the plasma boundary, which is due to the reduction of particle recycling. Figure 3 also shows the temporal evolution of electron temperature near the plasma boundary estimated from the intensity ratio of OVI lines(1032 Å and 150 Å), which are predicted to be localized near the plasma boundary ($r/a_L \sim 0.8 - 0.9$) because of high $\bar{n}_e \geq (5 \times 10^{13}\ \mathrm{cm}^{-3})$.

The electron temperature in case II is about double of that in case I. Moreover, in case II, soft X-ray emission of E $\geq$ 1 keV along the peripheral chord ($r/a_L \sim 0.7$) starts to rise more rapidly from the middle of CR-phase (t $\sim$ 135 ms). This is interpretted by considerable increase in T_e and also n_e in the peripheral region. In case II, electron temperature obtained from electron cyclotron emission at $r/a_L \sim 0.7$ is about 600 eV. Central electron and ion temperatures in case II surpass those of case I from the middle of CR-phase. Impurity accumulation takes place more remarkably in case II, as seen from time behaviours of OVIII, FeXX (Fig.2) and soft X-ray emission from the plasma center (Fig.4). This may be due to improvement of impurity comfinement rather than enhancement of inward convection velocity. It is predicted that the improvement of edge plasma transport is due to the realization of j_ϕ profile with a pedestal by active control method [3] instead of self organization process by island formation. The solution of magnetic diffusion equation on the basis of experimental data shows the pedestal in j_ϕ profile. Indeed, Mirnov signal in case II is reduced by 30 - 40 % compared with case I. These favourable phenomena in case II cause the appreciable increase in plasma stored energy (Fig. 1). The discharge in case II has some similarities to H-mode observed in divertor configuration [1], although the degree of the improvement of global confiment is not remarkable. Clear improvement may be realized if j_ϕ profile is more finely tailored by various active control techniques.

4. Conclusion

This experiment suggests that additionally heated tokamak plasmas may not suffer the serious confinement degradation even in limiter configuration if current density profile is controlled by active method such as additional current rise or noninductive current drive, instead of self organization process through magnetic island formation.

References

[1] F. Wagner et al., Phys. Rev. Lett. **49** (1982) 1408, and **53** (1984) 1453.
[2] T. Watari et al., Proc. 11th Intern. Conf. on Plasma Phys. and Controlled Nucl. Fusion Res., Kyoto (1986), IAEA-CN-47/F-I-5.
[3] K. Toi et al., Nucl. Fusion **19** (1979) 1643, and **22** (1982) 465.

Figure Captions

Fig. 1 Comparison of ICRF heated discharges without and with additional current rise.
Fig. 2 Time evolution of D_α, CIII, OVI, OVIII and FeXX lines.
Fig. 3 Time evolution of electron densities near the limiter, and edge electron temperature derived from OVI-line intensity ratio.
Fig. 4 Time evolution of soft X-ray emissions along the center and peripheral chords.

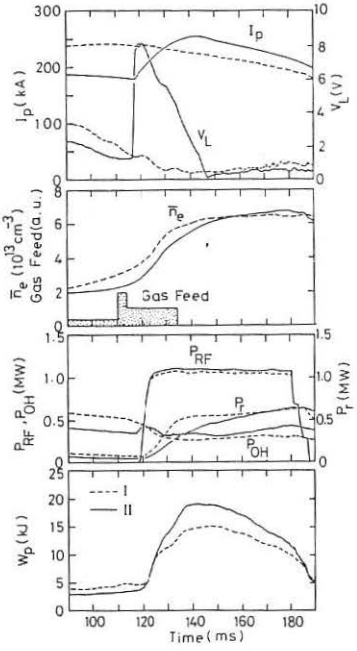

Fig. 1

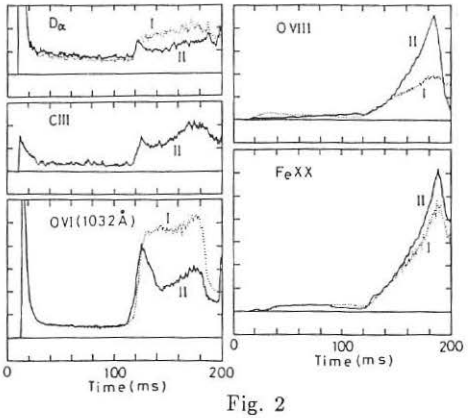

Fig. 2

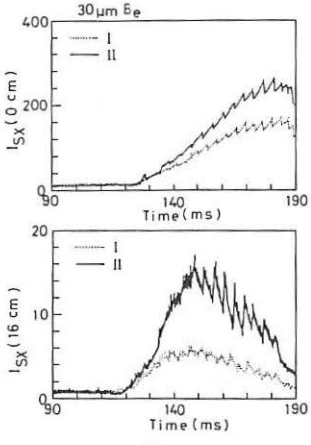

Fig. 4

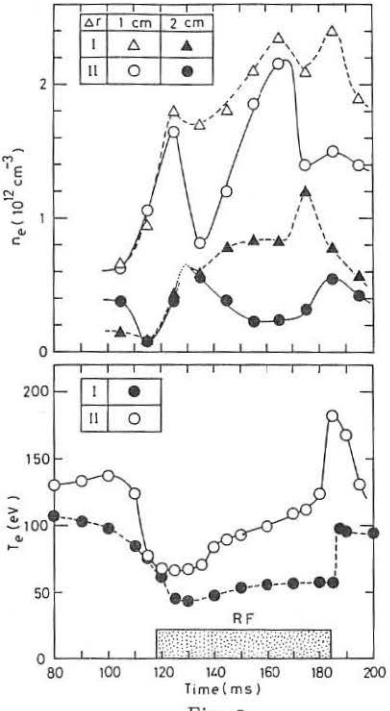

Fig. 3

MOMENTUM TRANSPORT AND SCALING EFFECTS OBSERVED IN NEUTRAL BEAM HEATED ROTATING PLASMAS IN JET

D Stork, A Boileau, F Bombarda(1), D J Campbell, C Challis, W G Core, B Denne, P Duperrex(2), R Giannella(1), L Horten, T T C Jones, E Källne, A Pochelon(2), J Ramette(3), B Saoutic(3), D Schram(4), J Snipes, G Tallents, E Thompson, G Tonetti(2), M von Hellerman and J Wesson.

JET Joint Undertaking, Abingdon, UK.
(1) EURATOM-ENEA Association, Frascati, Italy.
(2) EURATOM-CRPP Association, Lausanne, Switzerland.
(3) EURATOM-CEA Association, CEN Cadarache, France.
(4) Eindhoven University of Technology, Eindhoven, The Netherlands.

1. INTRODUCTION

Rotational phenomena have been studied in JET discharges with plasma currents from 1-3 MA and high power (≤10 MW) neutral Beam Injection (NBI). Deuterium beams at energies up to 80 keV and hydrogen beams at energies up to 65 keV have been applied. The simultaneous effects of NBI and high power (≤7.5 MW) ICRF on rotation, the dependence of central rotational velocity on NBI power, and temporal and profile effects in rotational velocity have been studied.

2. DIAGNOSTICS

Toroidal rotation on JET has been measured using several diagnostics.

a) Central (major radius R=3.1m) angular velocities $[\omega_\phi(0)]$ were determined from the Doppler shift of the He-like NiXXVII resonance line observed by an x-ray crystal spectrometer [1]. This measured ω_ϕ averaged over a region centred on zero minor radius (r) with half-width ≈0.4 m.

b) MHD diagnostics used were pickup coils to measure $\tilde{B}$ and a Fabry-Perot interferometer detecting electron cyclotron emission (ECE). The rotation of the activity was inferred from frequency measurements. The coils [2] detected the m=2,3 components of n=1 MHD activity at the plasma edge. The ECE diagnostic [3] measured m=1, n=1 activity at normalised minor radius r/a ≈ 0.3.
These diagnostics were of use when MHD activity was significant ($\tilde{B}_\theta/B_\theta(a) \sim 1\text{-}3 \times 10^{-5}$).

c) For some shots additional spectroscopic measurements were made. An XUV spectrometer [4] measured Doppler shifted lines of ionised states of Nickel and Carbon and angular velocity profiles were obtained.
A Charge Exchange Recombination Spectroscopy (CXRS) diagnostic was also used on Doppler shifted light from excited C^{+5} and O^{+5} ions. This measured rotation at R=2.3 m (inboard) and at r/a ~ 0.6. [5].

3. SCALING PROPERTIES OF CENTRAL ROTATIONAL VELOCITIES

On application of NBI to the plasma, a strong toroidal rotation was observed on all diagnostics. The rotation took between 0.5-1.0 second to reach quasi-steady values.
The quasi-steady state values of $v_\phi(0)$ derived from the Ni XXVII Doppler shift are plotted in figure 1 against the beam power per particle $P_b/\langle n_e \rangle$.

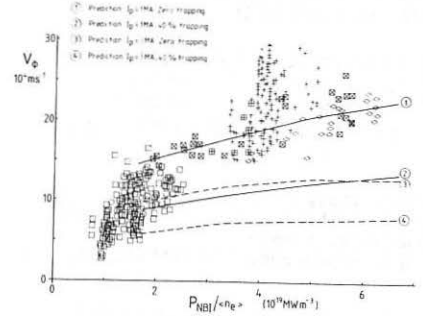

FIGURE 1: CENTRAL ROTATIONAL VELOCITY COMPARISON WITH GYROVISCOUS SCALING.

□	5MA	OUTER LIMITER	D* - D CO AND COUNTER INJECTION
○	5MA	OUTER LIMITER	H* - D CO INJECTION
⊗	5MA	INNER WALL LIMITER	D* - D CO INJECTION
⊕	2MA	X POINT	D* - D CO INJECTION
⊠	2MA	X POINT	D* - D COUNTER INJECTION
◇	1MA	INNER WALL LIMITER	D* - D CO INJECTION

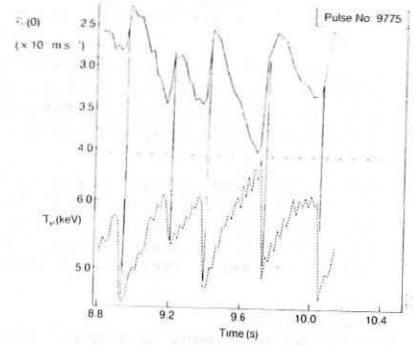

FIGURE 2: SAWTEETH EFFECTS ON ROTATIONAL VELOCITY AS MEASURED BY NIXXVII DOPPLER SHIFT

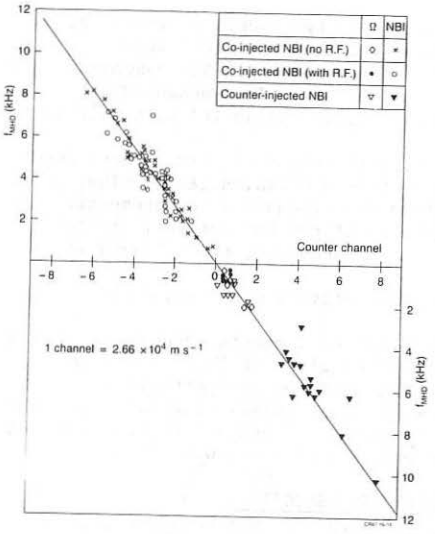

FIGURE 3: CORRELATION BETWEEN EDGE MHD MEASUREMENT OF ROTATION AND CENTRAL ION DOPPLER SHIFT MEASUREMENT (IN TERMS OF SPECTROMETER CHANNEL SHIFT). LINE IS

$2\ \pi f_{MHD}\ (R+a) \times R.V\phi_{MN}(R)$.

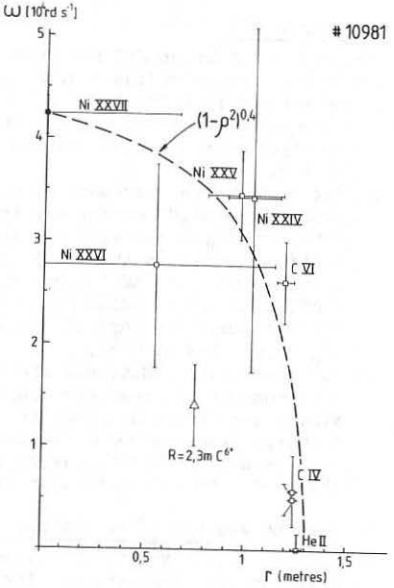

FIGURE 4: ROTATIONAL PROFILE MEASUREMENT (5MA PLASMA)

■ CRYSTAL SPECTROMETER
△ CXRS DIAGNOSTIC
□ XUV SPECTROMETER

$v_\phi(0)$ tends to saturate with increasing $P_b/\langle n_e\rangle$ and to increase slightly with increasing plasma current. The highest values of $v_\phi(0)$ were slightly below half the fluid sound speed (C_s). H° and D° injection induced similar rotations. Counter injection data are similar to co-injection data once the Ohmic plasma rotation (measured by the MHD diagnostics) is taken into account. This rotation was ~ 2-2.5 10^4 ms^{-1} counter to I_p and has been corrected for in figure 1.
The data have been compared with the scaling predictions for $v_\phi(0)$ based on the gyroviscous theory of Stacey et al [6].
Gyroviscous theory predicts $v_\phi(0)$ scales as:

$$v_\phi(0) \simeq \frac{f_p(o)}{V_p} \cdot \frac{\langle n_e\rangle}{n_d(o)} \cdot \frac{\overline{2m_b}}{E_b} \cdot \frac{2\ R_o \cdot eZ_{eff} B_T(o)}{} \cdot \frac{(1-f_T)P_b/\langle n_e\rangle}{T_{i,OH}(0)+C(P_b/\langle n_e\rangle)} \quad (1)$$

where $f_p(o)$ is the peaking factor for the NBI momentum deposition on axis; V_p is the plasma volume; $\langle n_e\rangle$ is the volume averaged density; $n_d(o)$ is the axial deuteron density; $T_{i,OH}(0)$ is the central Ohmic ion temperature; C is the ion heating efficiency $[\Delta T_i(0)/P_b/\langle n_e\rangle)]$; f_T is the fraction of injected particles injected in trapped orbits contributing no net momentum to the plasma.
Using the JET ion heating data [7], gyroviscosity predictions as in fig. 1 are obtained for two values of trapped particle fractions. These discharges have closer to 40% trapped beam but the data are well above the '40% trapped' prediction from gyroviscosity. The gyroviscous prediction is within a factor of ~ 2-5 of the data but the scaling with I_p is in the opposite direction to any which might be inferred from JET data.
Gyroviscosity is also not affected by plasma collisionality and this conflicts with the observation of strong rotational velocity sawteeth on JET. These are shown in figure 2 with the crystal spectrometer at temporal resolution ~20 ms. The sawteeth correlate well with variations in electron temperature suggesting that the decreasing collisicnality of the plasma between sawteeth affects the central momentum transport.

4. MHD AND PROFILE EFFECTS IN MOMENTUM TRANSPORT

The sudden decrease of $v_\phi(0)$ at a sawtooth collapse is suggestive of the importance of MHD effects in momentum transport.
In extreme cases such as locked modes, MHD activity appears to play a strong role. At the appearance of a locked mode in the plasma, the rotation of the ions is seen to stop on a ~ 100 ms timescale in spite of the continued presence of the driving beams [8].
Where 'high' ($\delta B_\theta/B_\theta \geq 10^{-4}$) MHD activity was present, the rotational angular velocity determined from edge MHD activity was equal to the central toroidal angular velocity determined from the crystal spectrometer. This is shown in figure 3 and could be taken as evidence of a momentarily flat ω_ϕ profile during periods of high MHD activity. It is also possible that it merely indicates toroidal mode coupling driving the edge mode from a mode resonant on a rational q_ψ surface nearer the plasma centre and rotating with the central velocity [2]. The second possibility would lead to an MHD rotational 'profile' which was sheared relative to that of the bulk plasma.
On some shots in which XUV rotational profiles were taken the profiles of

the impurity ions appeared fairly flat. In figure 4 a parabolic function with γ_ϕ value $\simeq$ 0.4 can be drawn through data from the XUV spectroscopy and the crystal spectrometer. These diagnostics assume ω_ϕ is uniform on a flux surface when fitting, which is backed up by recent measurements on Doublet III [9]. Gyroviscosity predicts breaking of this uniformity to $O(\varepsilon)$ and some evidence that $\omega_\phi(\rho)$ is not uniform comes from the CXRS diagnostic. This is shown in figure 4 where a γ_ϕ value of ~ 2 would seem more appropriate for the inboard variation of ω_ϕ. The CXRS diagnostic generally gives $1 \leq \gamma_\phi \leq 2$.

5. EFFECTS OF RF ON NBI-INDUCED PLASMA ROTATION

ICRF was applied to JET discharges with rotation driven by NBI. ICRF tuned to ^3H_e minority in the plasma was largely ineffectual in altering rotation but when tuned to H minority in the plasma the RF caused a sharp drop of up to a factor 2 of rotational velocity. The central rotational velocity clamped (no sawteeth), often for long periods in the case of the so-called 'monster sawtooth' [10] shots where sawteething on the other plasma parameters (eg: $T_e(0)$) was also absent. The change in rotational velocity occurred over a period of 0.5-1.0 secs.
A possible explanation is that ICRF coupled to H minority is able to couple to the beam ions at $2\omega_{CD}$ for deuterium beams. The effects of this have been calculated and observed in other JET discharges [11]. Coupling imparts perpendicular momentum to the beams and preferentially scatters beam particles into trapped orbits where they impart negligible momentum to the plasma. With this reduction in the momentum driving term the rotational velocity drops. The RF also causes a density rise which decreases the penetration of the beam neutrals and deposits more fast ions in trapped orbits in the outer plasma. The cumulative effects of these two sources have been calculated using value measured post-RF increase in neutron yield from the plasma. Within an accuracy ~ 10-20% it is found that the change in rotational velocity can be accounted for by a change in the driving term (from the parallel momentum) from the effect of ICRF beam coupling in this manner.

REFERENCES

[1] Gianella R, et al, Bull. Am. Phys. Soc. 31(9),1590 (1986)
[2] Snipes JA, et al, 13th EPS Conf. on Contr. Fus. & Plasma Htg.(1986), (Europhysics Conference Abstracts) Pp 152-155
[3] Campbell DJ, et al, JET-P(86)05 (1986)
[4] Behringer K, Ramette J, et al, these proceedings.
[5] Horton LD, et al, Bull. Am. Phys. Soc. 31(9),1590 (1986)
[6] Stacey WM Jr, et al, Nucl. Fus. 26(3),293-302, (1986)
[7] Thompson E, et al, these proceedings
[8] Snipes JA, et al, these proceedings
[9] Burrell KH, et al, submitted for publication to Nuclear Fusion (1987)
[10] Campbell DJ, et al, 11th IAEA Conf. on Plasma Phys. & Contr. Nuc. Fus. Research (Kyoto, 1986) IAEA-CN-47/A-VII-5
[11] Anderson D, et al, 13th EPS Conf. on Contr. Fus. & Plasma Htg. (1986), (Europhysics Conference Abstracts), Pp.97-99.

PHENOMENOLOGICAL AND PREDICTIVE STUDIES OF CONFINEMENT AND GLOBAL HEATING IN JET NEUTRAL BEAM HEATED LIMITER PLASMAS

E Thompson, D Bartlett, F Bombarda(1), G Bracco(1), D J Campbell, C Challis, J P Christiansen, J G Cordey, S Corti, A Costley, G Duesing, R Giannella(1), A P H Goede, L Horton, T T C Jones, E Kallne, O Kaneko(2), P J Lomas, D Muir, J Snipes, A Staebler(3), D Stork, P M Stubberfield, G Tallents, P R Thomas, K Thomsen, M von Hellerman and M L Watkins.

JET Joint Undertaking, Abingdon, U.K., (1) EURATOM-ENEA Association, Frascati, Italy, (2) Institute of Plasma Physics, Nagoya, Japan, (3) IPP Garching, FRG.

INTRODUCTION

NBI experiments have been performed using a wide range of target plasmas to establish the scaling of the global energy confinement with plasma current (I_p), toroidal magnetic field (B_T) plasma density (n_e) and input power (P_{TOT}) for both H°(≤65 keV) & D°(≲80 keV) injection into D plasmas. This paper describes results obtained with the plasma boundary defined by either the 8 outboard graphite limiters, or by the graphite inner wall protection tiles. The results of NBI experiments in X-point plasmas are presented elsewhere [1].

The JET vacuum vessel and graphite surfaces are conditioned by baking and glow discharge cleaning. They were maintained at 290°C during these experiments. The plasma density behaviour during NBI varied according to limiter configuration and is described in [2]. In summary the onset of NBI led to a transient density increase under all conditions. For outboard limiters the density rises linearly during NBI. On the inner wall tiles, a much lower density increase was obtained. This pumping was further improved during the 'hot-ion' campaign by conditioning the inner wall surfaces using Helium Ohmic discharges prior to NBI discharges.

GLOBAL ENERGY CONFINEMENT

The total plasma energy content from diamagnetic loop measurements (W^{DIA}) of all NBI plasmas is well described by a linear function of P_{TOT} when all other controllable parameters are constant [3]. Energy contents determined from poloidal field measurements and kinetic pressure profiles show similar behaviour and the three stored energy measurements are in reasonable agreement. The energy contents are roughly proportional to plasma current. These dependences have been built into an offset linear scaling law [3] of the form (figure 1)

$$W^{DIA} = 0.225\ n_e^{0.6}\ I_p^{0.5}\ B_T^{0.4} + 0.047\ I_p\ P_{TOT} \qquad (1).$$

The scaling of the energy content of Ohmic discharges is reproduced by the scaling of the intercept in (1). The dependence of W on the relevant parameters is described equally well by a power law fit, which is shown in figure 2

$$W^{DIA} = 0.27\ P_{TOT}^{0.37}\ I_p^{0.67}\ \langle n_e \rangle^{0.41}\ B_T^{0.24} \qquad (2)$$

The data is also well described by L-mode scaling [5].

From local transport analysis [4] which includes the NBI power deposition profile it can be concluded that the plasma thermal conductivity apparently depends upon the poloidal field only.
The 3 MA data obtained after He conditioning were not used in the above fitting procedure and they exhibit higher values of τ_{inc} ($= \delta W/\delta P_{TOT}$) than high density pulses. The measured density profiles of these discharges also show a tendency towards being slightly more peaked than other types of NI discharges.

Heating Efficiency with NBI

NBI electron heating efficiency on JET has been constrained by the relatively low values of injection energy (30-60 keV/AMU). The electron heating efficiency (figure 3) tends to saturate at electron temperature values 5-6 keV where the total power input to the electrons (NBI + Ohmic + Equipartition) has fallen to a low level.
In contrast, ion heating efficiency increases with the power per particle (figure 4). The spectroscopic N_i^{26+} temperature measurements shown in figure 4 are calculated to be at most 1-2 keV higher than the deuterium temperature at the highest values. The discharges following helium conditioning show the best ion heating, partly because lower densities are accessible than in limiter discharges. This results in the decoupling of the ions from the electrons as the equipartition time (τ_{ei}) becomes larger than the energy confinement time.
These 'High T_i' discharges gave the highest neutron rate obtained on JET ($2.8\ 10^{15}\ s^{-1}$) of which approximately half can be attributed to beam-plasma reactions.

Enhanced Confinement in Inner Wall Discharges

The energy content of the inner wall (3 MA, 3.4 T) plasmas falls into 2 groups ('A' and 'B' in figure 5). The type A plasmas were those immediately following helium conditioning. They showed reduced recycling evidenced by a steady-state density and the lowest values of deuterium-α light during NBI.
The measured electron energy contents (W_e) in the two groups were identical within errors so the difference in W^{DIA} must reside in the ions. The calculation of stored energy using the measured central ion temperature and dilution factor from the measured Z_{eff} indicates that the ion temperature profile was more peaked than that of the electrons in these shots. This is confirmed by preliminary results obtained by a neutral particle analyser array.

Power Balance in Hot Ion Plasmas

The data for 3.0 MA/3.4 T plasmas with $5.0 < P_{TOT} < 7.0$ MW has been compared with results from a simple 0-D model. The model uses characteristic times based on L-mode scaling for loss rates in both channels and classical equipartition between them. The predictions of this model reproduce the data tolerably well (figure 6). This indicates the energy confinement is no different in character between hot ion and high density regimes.
Local transport analysis is limited by the preliminary nature of ion temperature profiles, nevertheless the available data does show that, in

contrast to high density plasmas, the ion loss channel dominates within the central half minor radius in hot ion plasmas. Ion convection and conduction have comparable magnitudes in the centre and equipartition returns a large power fraction to the electrons in the outer plasma. In these respects JET hot ion plasmas are similar to TFTR supershots [6].

REFERENCES

[1] Keilhacker M, et al, these proceedings.
[2] Jones TTC, et al, these proceedings.
[3] Cordey JG, et al, 11th Int. Conf. on Plasma Phys. & Contr. Nucl. Fus. Research (Kyoto 1986), IAEA-CN-47/QA-II-3.
[4] Callen J, et al, 'Modelling of temperature profile responses to Heating Profiles in JET', these proceedings.
[5] Goldston RJ, Plasma Phys. & Contr. Fus. 26,1A,87-103 (1984).
[6] Hawryluk RJ, et al, 11th Int. Conf. on Plasma Phys. & Contr. Nucl. Fus. Research (Kyoto 1986), IAEA-CN-47/A-I-3.

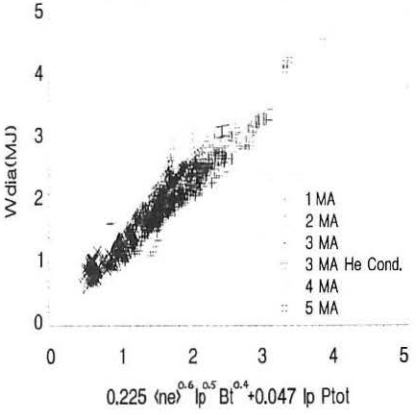

Figure 1 : Offset linear scaling law plotted against JET NBI stored energy measured by diamagnetic loop (W^{DIA}).

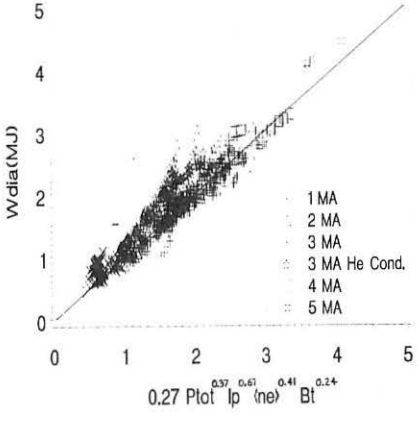

Figure 2 : Power law fit to NBI W^{DIA} measurements.

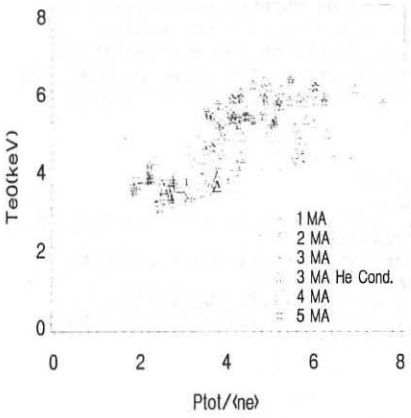

Figure 3 : Central electron temperature from ECE measurements for NBI discharges as a function of total power (P_{tot}) normalised by volume averaged density ($\langle n_e \rangle$).

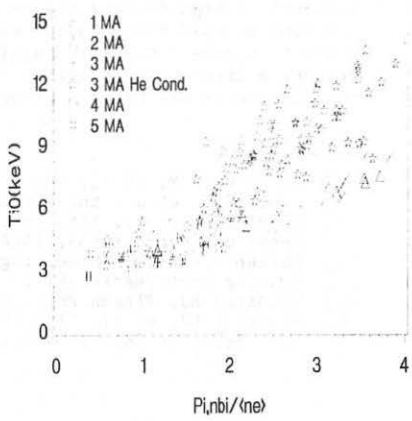

Figure 4 : Central ion temperature ($T_i(o)$) for Ni^{26+} ions in NBI discharges measured by Doppler shift of the NiXXVII line as a function of calculated power to the ions (P_{bi}) normalised by volume averaged density ($\langle n_e \rangle$).

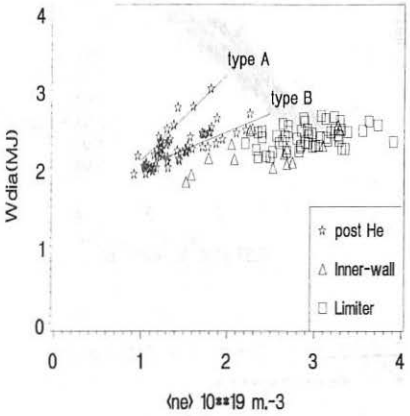

Figure 5 : Diamagnetic stored energy measured as a function of volume averaged density for 3 MA/3.4 T NBI discharges.

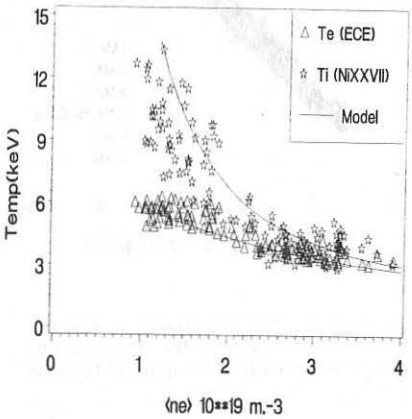

Figure 6 : Measured $T_i(o)$ and $T_e(o)$ for NBI discharges compared to predictions from the simple O-D code (see text).

PARTICLE CONFINEMENT STUDIES ON OHMICALLY-HEATED PLASMAS IN TFTR USING GAS MODULATION TECHNIQUES

D.K. Mansfield, P.C. Efthimion, R.A. Hulse, S.S. Medley, H.F. Dylla, E. Fredrickson, R.J. Goldston, R.J. Knize, P.H. LaMarche, H.K. Park, and V. Vershkov*

Princeton University Plasma Physics Laboratory, Princeton, NJ 08544 USA

ABSTRACT

Experiments utilizing single gas puffs have been performed in the Tokamak Fusion Test Reactor (TFTR) in an effort to understand particle transport. The resulting density perturbations were measured using a ten channel far-infrared laser interferometer.

The data was analyzed to yield transport coefficients by regression analysis of the particle balance equation and modelling using a modified MIST transport code. For the case of a low density ohmically heated plasma commonly used as target plasmas for neutral beam injection, the two analysis techniques gave transport profiles with minimum values in the core region ($D \tilde{=} 0.4\ M^2/S$, $V \tilde{=} 0.1\ M/S$) that increase rapidly in the outer half of the plasma ($D \tilde{=} 1.0\ M^2/S$, $V \tilde{=} 4\ M/S$ at $r/a = 0.75$).

In all cases, the density perturbations were kept in the 5 percent range to minimize any changes in plasma equilibrium. However, even at this low level of perturbation, the central ion temperature was observed to drop 15 percent during the 0.05 sec gas puff. This is considered indicative of a degradation of the ion confinement.

1. INTRODUCTION

TFTR is a machine well-suited for the study of particle transport in tokamaks because it is large and because it has a sensitive ten channel far-infrared interferometer for detailed measurements of the temporal and spatial evaluation of the density profile. To that end, experiments have been carried out which involve observing the response of the electron density profile to a 50 ms single gas puff [1]. In all cases the gas puff was kept as small as possible ($\Delta n/n \sim 5\%$) to avoid perturbing the plasma equilibrium conditions. The equilibrium conditions used in this study ($n_e = 1.2 \times 10^{19} m^{-3}$, $I_p = 1.4$ MA and $B_t = 4.8$ T) were similar to those of target plasmas for the so-called TFTR supershots in the hope that this type of particle transport study might shed some light on that extremely promising regime.

The graphite tile inner wall of TFTR (i.e., the bumper limiter) was employed as the limiting surface for all discharges studied. In all cases the graphite was pre-conditioned by running against it a series of approximately ten low density discharges in He^+. This procedure reduces residual levels of D_2 and H_2 in the graphite thereby lowering the effective particle recycling coefficient and permitting a density pump-out in subsequent D^+ discharges. This conditioning and the comcomitant pump-out have been seen to be necessary for entrance into the TFTR supershot regime.

The electron density profile data were analyzed to yield particle

*Permanent address: Kurchatov Institute, Moscow, USSR

transport coefficients by two separate procedures. The details and results of those procedures are outlined below.

2. SIMULATION OF THE INCREMENTAL DENSITY PROFILE USING THE MIST CODE

During the gas puffing experiment, the temporal and spatial response of the electron density profile was measured using a ten channel far-infrared laser interferometer. By averaging the results from a series of eight identical discharges, very low-noise data could be taken with this diagnostic. The averaged data was then inverted and the inverted profile was subtracted from an extrapolation of the profiles taken just before and well after a single gas puff. The result of this subtraction represents only the contribution to the density which was caused by the gas puff. This contribution as shown in fig. 1 clearly takes the form of a density pulse (albeit asymmetric) which propagates from the plasma edge toward the core. The subsequent (symmetric) decay of this incremental profile when the gas puff is terminated has also been clearly seen using this technique. Also, seen in fig. 1 is the persistence of a hollow density profile as the crest leaves the plasma periphery and approaches the core.

The first of these procedures involved a simulation of the incremental density profile using MIST, a code which solves the particle balance equation (given below) using transport coefficients specificed as inputs [2].

$$\frac{\partial N}{\partial t} = \frac{-1}{r}\frac{\partial}{\partial r}\left(r\Gamma[r,t]\right) + S(r,t) \qquad (1)$$

Where N is the density, Γ is the particle flux, and S is the source.

By assuming that the ratio of the pinch velocity to the diffusion coefficient is constant in time and consistent with the equilibrium density profile measured just before the gas puff one can then modify both the shape and magnitude of the diffusion coefficient (and with it the pinch velocity) in an effort to reproduce the salient features of the experimentally observed incremental density wave. The results of that analysis are shown in fig. 2.

The persistence of a hollow incremental density profile (fig. 1) is also evident in the incremental density simulation, (fig. 2) and is indicative of particle transport coefficients that are large at the plasma edge and fall to a minimum at the plasma center.

3. REGRESSION ANALYSIS OF THE ELECTRON DENSITY DATA

The **full** profile (as contrasted to the **incremental** profile) was used as an input to the TRANSP program, which, using an empirical model for the source function then integrated Eq. (1) in order to solve for the particle flux [3]. After dividing that flux into diffusive and convective parts as given in Eq. (2) below, a regression analysis was then carried out at a series of radial points to determine the values of both the diffusion coefficient D and the pinch velocity V.

$$\Gamma(r,t) = -DVn(r,t) + Vn(r,t). \qquad (2)$$

The ratio of the velocity to diffusion coefficients obtained by this regression analysis is consistent with the equilibrium shape as is to be

expected from a fit to the full profile with a small perturbation. The derived V profile was seen to be much larger than the neoclassical Ware velocity as also calculated by TRANSP. In addition, the particle diffusivity thus obtained was similar to that used in the previously described MIST analysis and comparable to the equilibrium thermal diffusivity calculated by TRANSP.

4. THE EFFECT OF GAS PUFFING ON ENERGY TRANSPORT

During the course of the single gas puff experiments, the electron and ion temperatures were measured as functions of time by an ECE radiometer and an x-ray crystal spectrometer respectively. Shown in fig. 3 are the ion and electron temperature traces taken during the course of a single gas puff. As seen, the central electron temperature initially rises in response to the puff while the edge electron temperature falls. In addition, the central ion temperature falls as a result of the puff; this is interpreted as a degradation of ion energy confinement. Also shown in this figure is the ion temperature trace calculated by TRANSP using the electron temperature as an input and employing neoclassical ion transport [4]. Clearly neoclassical ion transport fails to predict correctly even the sign of the observed change in the ion temperature in response to the gas puff. However, an η_i ion transport model recently applied to TRANSP has simulated the decrease in ion temperature seen during gas puffing.

5. CONCLUSIONS

By observing the propagation of a small wave of density in a TFTR ohmic discharge, we have been able to arrive at a radial profile for the particle diffusion coefficient. This has been done by two separate techniques and the results have been demonstrated to be reasonably consistent with transport coefficients having minimum values ($D = 0.4\ M^2/S$, $V = 0.1\ M/S$) in the core which increase rapidly in the outer half of the plasma ($D = 1.0\ M^2/S$, $V = 4\ M/S$ at $r/a = 0.75$).

In addition, the electron temperature profile as well as the ion energy transport have both been seen to be affected in an unexpected manner by as small a density perturbation as was employed in this work.

This work was supported by U.S. DoE Contract No. DE-AC02-CH0-3073.

REFERENCES

1. N.L. Vasin, V.A. Vershkov, and V.A. Zhuravlev, Sov. J. Plasma Physics, 10, 525 (1984).
2. R.A. Hulse, Nuclear Technology/Fusion 3, 259 (1983).
3. R.J. Hawryluk, in Proceedings of the Course in Physics Close to Thermonuclear Condtions, Varenna, Italy, (Commission of European Communities, Directorate General XII, Fusion Program, Brussels, 1980).
4. C.S. Chang and F.L. Hinton, Phys. Fluids 20, 1493 (1982).

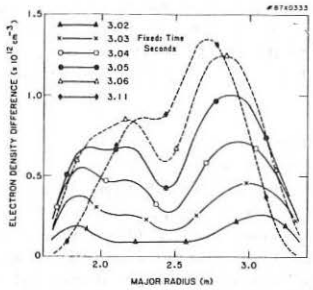

Figure 1
The measured incremental density wave. The gas puff was turned on at t = 3.0 sec and off at 3.05 sec. One should note that the form of the wave changes very little from t = 3.06 sec to 3.11 sec.

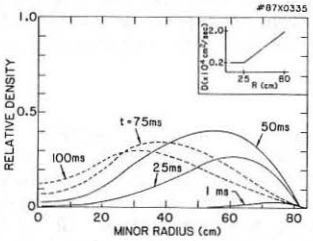

Figure 2
A simulation of the incremental density wave as generated by the MIST code. One can see the persistence of a hollow profile as the crest approaches r/a = 0. This is indicative of reduced transport in the plasmas core as compared to the edge (see insert).

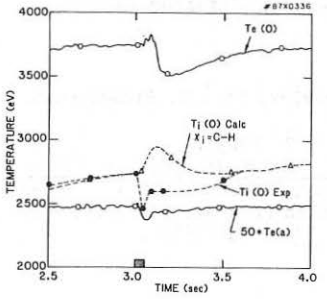

Figure 3
The ion and electron temperature as measured during the puff. Also shown is the ion temperature calculated neoclassically.

PARTICLE TRANSPORT IN TFTR OHMIC PELLET INJECTION EXPERIMENTS

R.A. Hulse, P. Efthimion, B. Grek, K. Hill, D. Johnson,
D. Mansfield, W. Morris, D.K. Owens, H. Park, A. Ramsey,
J. Schivell, G.L. Schmidt, F. Stauffer, B. Stratton, J. Timberlake

Plasma Physics Laboratory, Princeton University
Princeton, NJ 08544 USA

INTRODUCTION - The large perturbation and changing gradients found in pellet injection experiments provide a unique opportunity for the study of particle transport in tokamaks. On the TFTR tokamak, such studies[1,2] have the advantage of a large, circular plasma, well-diagnosed using a 10-channel far-infrared interferometer and 76-point Thomson scattering for detailed measurements of the time-evolving density profiles. Preliminary particle transport results for four selected plasmas of differing character will be presented, concentrating on simple, primarily diffusive models which were found to reproduce most of the observed density evolution in these cases.

ANALYSIS - TRIUMPH is a new, 1-D radial particle transport code which simultaneously solves up to 32 models with individually specified particle transport and source parameters. These models were initialized to the experimental profile immediately after the pellet deposition, which will be denoted as t=0 in the following discussions. Diffusion coefficient profiles of the form $D(r) = D(0) + [D(a) - D(0)](r/a)$ and $D = D(0) + [D(a) - D(0)](r/a)^2$ were surveyed for $D(a) \geq D(0)$ over the range $0.003\ m^2/s \leq D(0) \leq 0.3\ m^2/s$, $0.01\ m^2/s \leq D(a) \leq 1.0\ m^2/s$, along with $D \propto n^{-1}$ and $D \propto n^{-1/2}$ forms. For the convective term, models with $v = 0$, $v \approx v_{ware} \approx -0.05$ m/s, and $v/D = \partial \ln(n_0)/\partial r$ were tested. This latter choice of a v/D corresponding to the initial t = 0 profile scale lengths was motivated by cases where the profile shapes remained relatively constant during the decay. In addition, for the special case of shot 24863 (see below), other models for v(r) were also examined. The radial profile shape for an edge particle source was obtained from a neutral deposition calculation, while different feedback models acting on the model versus experimental data difference were used to determine the total source rate versus time for each model. Zero source models were also tested for all cases.

Overall, the basic TRIUMPH survey for each shot examined over 400 possible models. For D(r), the density-dependent forms were not particularly successful when considered over all the shots examined, while the algebraic forms, particularly $D(r) = D(0) + [D(a) - D(0)](r/a)^2$, generally yielded satisfactory results. Best fit models of this form will be presented here. Except for early stages of shot 24863, low velocity models proved reasonable. Given this result, $v = 0$ solutions are presented here as a particularly interesting special case. Taking a ware-like $v(r) \approx -0.05$ m/s typically resulted in models with higher D(0) relative to these $v = 0$ solutions. Models with non-zero sources were generally necessary. The results presented here used

a source rate for each model which attempted to track the experimental total number of particles as a function of time, given the constraint of non-negative values for the source amplitude.

The basic success of the specific model parameters reported here relative to the majority of the other possibilities surveyed was clear. However, it must be emphasized that these results do not represent exclusive fits to the data. In the interest of unifying our preliminary results, some selection of trial model forms and subjective distillation of the results has necessarily been employed. Also, the range of acceptable solutions depends sensitively on the level of detail which can be substantiated in the measured density profiles. This is particularly true for details of the behavior near r = 0, such as the timescale for the flattening of initially hollow profiles.

In addition to TRIUMPH modeling, for some cases particle fluxes were calculated using the TRANSP analysis code to integrate the continuity equation directly using the experimentally determined time-dependent density profile. Regression fits were then obtained to a diffusive/convective form for the flux, thereby obtaining a result for D(r) and v(r).

RESULTS - Pellet fueling to achieve very peaked, slowly decaying, high density plasmas is of great interest. Figure 1 shows a shot (18681) of this type, which decayed with a nearly constant profile shape. The model shown has $D = 0.01 + 0.09\ (r/a)^2\ m^2/s$, $v = 0$. Using the regression analysis for this case yielded a D(r) profile with an RMS deviation of ≈ 20% from this model inside of r ≈ 0.6 m, where the source function is small.

Decay of peaked pellet-fueled plasmas to a peaked profile on a broad pedestal is frequently seen; for example, shot 25697, shown in Fig. 2. The model shown has $D = 0.005 + 0.195\ (r/a)^2\ m^2/s$, $v = 0$. Also shown is the t = 2 s profile using the same transport model, but with a zero source. Comparison demonstrates the action of the edge particle source in producing the observed broad density pedestal. It is interesting to note that the lower central density of this plasma compared with the case in Fig. 1 makes such a pedestal more prominent. In an attempt to compare density and impurity transport, scandium was injected into this plasma 0.5 s after pellet injection. MIST code[3] modeling of the observed VUV time behavior of ScXVII and ScXIX line brightnesses showed agreement with models similar to that given for the electron density evolution, but at somewhat higher $D(a) \approx 0.4\ m^2/s$. However, this modeling also showed these charge states to peak near r ≈ 0.4 m, and therefore the impurity transport interior to this radius was not well determined by this data.

The presence of a strong, inward, convective (pinch) velocity in the transport flux could be most directly inferred by observation of a rising central density in a plasma for which a monotonically decreasing radial profile would provide only outward-directed diffusive flows. Figure 3 shows a shot (24863) which seemingly demonstrates such behavior. However, an unusual feature is apparent on the TFTR horizontally viewing SXR diode array for this shot, which can be interpreted as a growing, locked MHD mode in the central plasma

region. D(r) surveys with an extended range of v(r) forms were unsuccessful in modeling both the central density rise and subsequent decay with any given choice of time-independent transport coefficients. In Fig. 3, a model initialized at t = 0.3 s with D = 0.1 + 0.2 $(r/a)^2 m^2/s$, v = 0, is shown as approximating the decay phase.

Perhaps the most interesting cases for transport analysis are those where the initial deposition leaves a hollow density profile. In this case, the internal density gradients change sign through zero as the profile flattens, providing an especially interesting test of the transport. Such a case is shown in Fig. 4, for shot 28970. The central density flattens at t ≈ 0.2 s, and then relaxes to a peaked profile on a broad pedestal by t ≈ 0.6 s, reminiscent of shot 25697. Just after t ≈ 0.6 s, a large sawtooth crash is seen to dramatically redistribute the central density and flatten the profile. The model shown has D = 0.003 + 0.497 $(r/a)^2 m^2/s$, v = 0, which reproduces the range of behavior until the sawtooth crash quite well.

CONCLUSIONS - With the exception of the initial phase of shot 24863, all these results can be reasonably well-modeled throughout the entire 1 to 2 seconds of post-pellet density evolution using time-independent D(r) profiles of simple radially increasing form, with low D(0) and a zero or Ware-like convective velocity. Sawteeth, when they occur, clearly play a dramatic role in core particle transport for these peaked profiles. The development of centrally-peaked profiles on broad density pedestals can be seen to be the result of good central confinement of an initially peaked deposition profile, together with poorer edge confinement and particle replacement by edge sources.

ACKNOWLEDGMENT - This work was supported by the U.S. Department of Energy Contract No. DE-AC02-76-CHO-3073.

REFERENCES

(1) G.L. Schmidt, et al., IAEA-CN-47/A-III-4 (1986).
(2) M.H. Redi, et al., Princeton University Plasma Physics Laboratory Report, PPPL-2368 (1987).
(3) R.A. Hulse, Nucl. Technol./Fus. 3, 259 (1983).

FIGURE CAPTIONS

FIG. 1. Experimental (solid) and model (dotted) density profiles for 18681 at t = 0.0, 0.5, 1.0, and 1.8 s after the pellet.

FIG. 2. Experimental (solid) and model (dotted) density profiles for 25697 at 0.0, 0.5, 1.0, and 2.0 s after the pellet. A zero source model profile at 2.0 s (open diamonds) is also shown.

FIG. 3. Experimental (solid) density profiles for 24863 are shown at 0.0, 0.2, 0.3, 0.6, and 1.0 s. Model profiles (dotted), are initialized at 0.3 s, after the initial central density rise phase, and are shown at 0.6 and 1.0 s.

FIG. 4. Experimental (solid) and model (dotted) density profiles for shot 28970, showing the initially hollow profiles at t = 0, with profiles at 0.2, 0.6, and 0.625 s later. A large sawtooth occurred between the 0.6 and 0.625 s profiles.

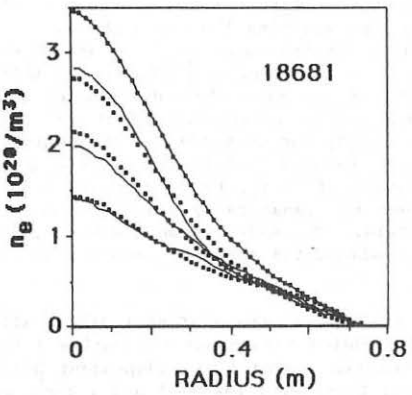

Fig. 1

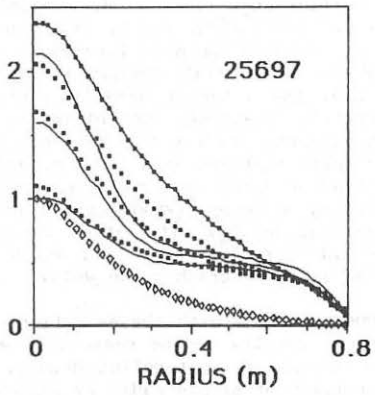

Fig. 2

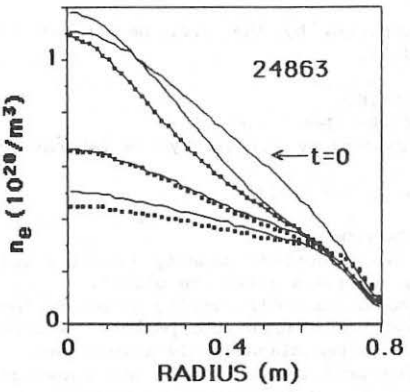

Fig. 3

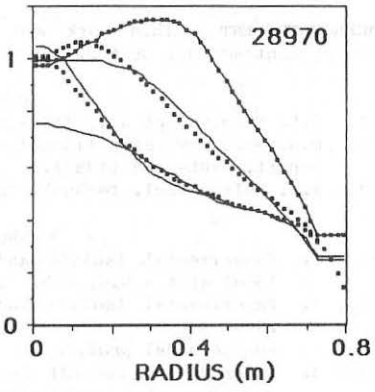

Fig. 4

MULTI-PELLET INJECTION IN TFR

TFR Group (presented by A. GERAUD)
Association EURATOM-CEA
Département de Recherches sur la Fusion Contrôlée
Centre d'Etudes Nucléaires de Cadarache
13108 St Paul Lez Durance Cedex, France

ABSTRACT : Four successive hydrogen pellets have been injected into deuterium plasma of the TFR Tokamak (major radius R = 0.98 m, minor radius a = 0.2 m). Each pellet corresponds to 50 % of the initial average density and penetrates at about half radius. After filling up, the density profile generally hollow just after injection, evolves slowly towards a slightly more peaked shape. Transport analysis of the long time scale density relaxation shows generally no change in particle transport coefficients, except in a particular case where the time interval between two pellets has been reduced from ~ 40 ms to ~ 20 ms.

PELLET INJECTION SYSTEM : A multi-pellet injector developped at "Service des Basses Températures de Grenoble", based on the so called "in situ condensation" [1] has been installed on TFR. The injector is composed of six identical cells in a single cryostat : gas is admitted inside a tube initially under vacuum ; then a small length of the tube, the freezing cell, is cooled down below the solidification temperature and hydrogen solidifies inside it ; when pellet formation is over, the residual gas is evacuated and the pellet is propeled by applying high pressure pulse by opening a fast valve. The pellet parameters are : length = 1 mm, diameter = 0.85 mm, velocity = 700 m/s and average number of H atoms per pellet entering the plasma $\sim 1.3\ 10^{19}$

A time integrated photography of the ablation clouds shows [2] zones of strong a weak light emission. After densitometric scan of these striations, pellet identification is obtained by comparison of the structures on the densitograms and on Hβ emission measured with a photomultiplier connected to a fast acquisition device.

TIME EVOLUTION OF THE CENTRAL ELECTRON DENSITY AND TEMPERATURE

The evolution of a typical plasma with a four pellet injection is shown in figure 1a : just after the fourth pellet, the central line density and the average density are more than twice the preinjection value. After the two first pellets, the central electron temperature has dropped from 1.6 keV to about 0.8 keV, the third and the fourth pellet not producing further decrease. This behaviour may be explained both by a reduction of the relative incremental density ($\Delta \bar{n}_e / \bar{n}_e$ = 50 % for the first pellet and 25 % for the last one), and by an increase of the energy confinement time ($\tau_e \propto n_e$) [3].

DENSITY PROFILES : The $n_e(r,t)$ profile is deduced by means of an Abel inversion from the data of infrared interferometry along eight chords, obtained with a time resolution of 400 μs. Photographies of the ablation zone show a penetration to about half radius, which can not be measured with an accuracy better than -2 and +2.5 cm, owing to the dispersion of the pellet trajectory and the oblique angle of

sight used [2]. Because of this outer deposition of matter the profile is hollow (profile B fig. 1b) or nearly flat, depending on $\Delta n_e / n_e$, just after injection. It fills up within 5 to 10 ms when it is hollow, and generally, after this filling up phase, it remains nearly homothetic to the preinjection profile or evolves slowly (15-20 ms) towards a slightly more peaked shape ; nevertheless it happens that the peaking occurs faster (< 10 ms) and be more pronounced. This is the case for the shot presented on figure 1 : the peaking already appears as early as 8 ms after the second pellet, increasing during the density relaxation and after each following injection. This particular behaviour could be linked to a deeper penetration of the second pellet, bigger than the average with $1.8\ 10^{19}$ atoms [4], at a radius where the local particle confinement time τ_p ($\tau_p(r) = \int_o^r n_e\ \rho\ d\rho / r\ \Gamma(r)$) is higher : calculations with MAKOKOT code show an increase of τ_p by a factor 2.5 between r = 10.5 and r = 8 cm.

PARTICLE TRANSPORT : The density profile relaxation after pellet ablation has been simulated with the transport code MAKOKOT. The density profile measured just before the pellet sublimation has been used as initial condition. Two cases have been studied : the first one is a "standard" case, (S), without significant peaking of the density profile and with a large time interval of ~ 40 ms between pellet 2 and 3. In the second case, (P), which is presented on figure 2, the third pellet arrives ~ 20 ms after the second one. In all cases q(a) = 4.6 and the sawtooth activity is very low before injection. In the (S) case, the long time interval between pellet 2 and 3 allows the plasma to recover more completely its quasi equilibrium temperature and density profile, and the sawtooth oscillations become more visible on soft X ray signal (fig. 2a), owing to the increased density and to the higher temperature. The Te profile was not measured and the following profile has been used in the simulation :

$$Te(r,t) = Te(o,t)\ (1 - 0.8\ \frac{r^2}{a^2})^{3.6}$$

with q(o) = 0.95 and q = 1 at r = 4 cm, Te(o,t) given by ECE measurements. The particle flux Γ is modelled by : $\Gamma = -D\ \nabla n_e - \frac{r}{a}\ v n_e$, where v is the inward velocity

and D the diffusion coefficient given by $D = \frac{D_A\ D_B}{D_A + D_B} + D_{neo}$ with

$$D_{A\ [cm^2 s^{-1}]} = \frac{ko}{n_e q T_e^{3/4}}\ [cm^{-3}, ev],\quad D_B = A \times 6.25\ \frac{Te}{B}\ [ev, G] \text{ with } A = 5.$$

The results of the simulation are summarized on table 1. A comparison with experiment is presented on figure 3, where the central density time evolution is plotted after the 3rd pellet injection for (S) and (P) cases. In the two cases the radial density profile is given at the end of the relaxation.

No significant modifications of k_o and v are observed, at least for the (S) shot. We note that taking account of the average influence of the sawteeth leads to a better agreement with experiment (D was multiplied by 3 inside the q = 1 surface). For the shot (P), the previous coefficients allow to recover the experimental density profile after the first and the second pellet injection. However after the 3 rd and the 4th pellet it is necessary to increase v and k_o. As a consequence the central peaking parameter $\frac{av}{D(o)}$ increases slightly and Γ remains inward in the plasma core during a long time scale (~ 20 ms) but the global confinement time calculated at 16 cm is unmodified. On the contrary in the simulation of the (S) case $\frac{av}{D(o)}$ decreases due to the outward flux induced by the sawtooth oscillations.

CONCLUSION : Transport analysis of electron density profile show that generally the same transport coefficients as those required to simulate a gas fuelled discharge can be used to model the density relaxation between pellet injections. The peaking of the density profile seems to be linked essentially to the pellet penetration. However for a particular case when the time interval between two successive pellet injections is reduced transport coefficients D and V must be modified : principally the inward velocity V must be increased in order to fit the density profile in the plasma center.

REFERENCES :

[1] Lafferanderie J. et al., Proc. 14 th Symp. on Fusion Technology, Avignon 1986, p 1367
[2] TFR Group, paper 0326 A, this conference
[3] TFR Group, "Pellet injection experiments on the TFR Tokamak", Report EUR-CEA-FC 1321, Cadarache, February 1987
[4] Park P.B., Turnbull R.J., Foster C.A., Nucl. Fusion 17 (1977), 539

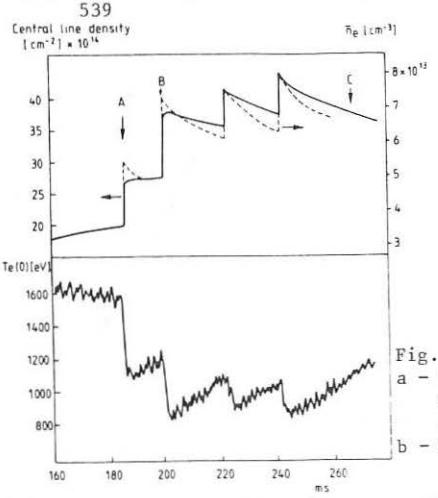

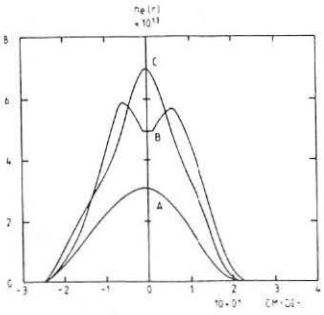

Fig. 1 - Injection of 4 pellets
a - Time evolution of the central line density, average density and central electron temperature.
b - Density profiles at three times.

	ko 10^{19}	v cm/s	D(o) cm^2/s	D (10cm) cm^2/s	$\frac{av}{D(o)}$	Zp (16 cm) ms
Before injection	1	90	680	930	2.6	45
(S) n° 1	1	90	570	960	3.1	55
#110810 n° 2	1	70	450	760	3.1	50
n° 3	1*	70	1350	800	1.	45
(P) n° 1	1	90	570	950	3.1	50
#110811 n° 2	1	70	440	730	3.2	55
n° 3	1.5	120	590	970	4.	50
n° 4	1.3	120	480	840	5.	50

* D x 3 inside q = 1

Tab. 1 - Results of the simulation

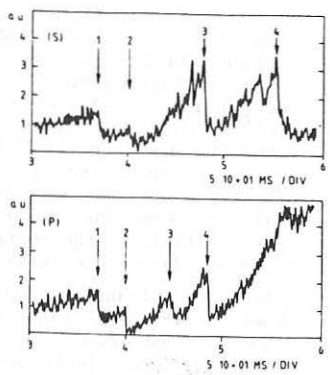

Fig. 2 - Central soft X emission for the two cases (S) and (P)

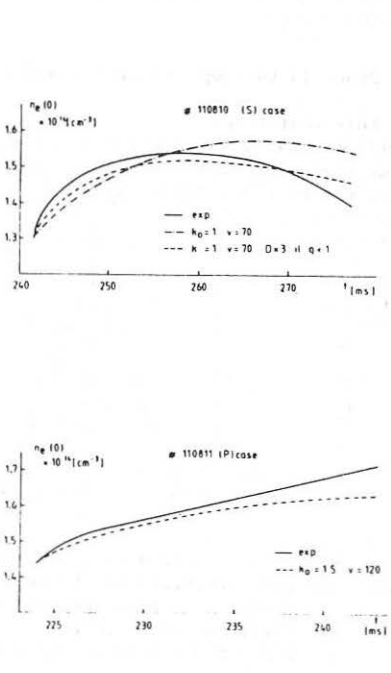

Fig. 3 - Comparison simulation-experience for the density relaxation after the 3rd pellet injection

MHD-ACTIVITIES DURING PELLET INJECTION INTO OHMICALLY AND BEAM HEATED PLASMAS ON ASDEX

M. Kornherr, O. Gehre, K. Grassie, O. Klüber, V. Mertens and G. Becker, H.S. Bosch, H. Brocken, K. Büchl, A. Carlson, A. Eberhagen, G. Dodel[1], H.-U. Fahrbach, G. Fussmann, J. Gernhardt, G. v.Gierke, E. Glock, O. Gruber, G. Haas, W. Herrmann, J. Hofmann, A. Izvozchikov[2], E. Holzhauer[1], K. Hübner[3], G. Janeschitz, F. Karger, M. Kaufmann, K. Lackner, R. Lang, M. Lenoci, G. Lisitano, F. Mast, H.M. Mayer, K. McCormick, D. Meisel, E.R. Müller, H. Murmann, J. Neuhauser, H. Niedermeyer, A. Pietrzyk[4], W. Poschenrieder, H. Rapp, H. Riedler, A. Rudyj, W. Sandmann, F. Schneider, C. Setzensack, G. Siller, E. Speth, F. Söldner, A.Stäbler, K. Steinmetz, K.-H. Steuer, N. Tsois[5], S. Ugniewski[6], O. Vollmer, F. Wagner, D. Zasche

Max-Planck-Institut für Plasmaphysik
EURATOM Association, Garching, FRG

Introduction

The combination of gas-puff and pellet refuelling provides ohmic discharges with nearly twice the confinement time and 1.5 times the Murakami limit /1/. Despite these improvements, the density built-up by a string of pellets (up to 80 pellets with maximally 700 m/s and up to 50 pellets per s) is not yet optimized. There are phases where the pellet refuelling leads to a step-like increase in density followed by those where the added mass is quickly lost between pellets. The gradual loss of density is often accompanied by a step-like decrease such that no effective density increase remains. It is interesting to note, that during these ineffective phases β does not continue to increase but may even decrease.

In this paper we describe in detail the MHD-activities during pellet injection, studied essentially with two soft-X-ray ("SX") cameras. Fig. 1 exhibits the toroidal positions of the viewed poloidal cross sections of these cameras and of the HCN-laser-interferometry in relation to the pellet injector, furthermore, the directions of the toroidal and poloidal magnetic field lines and both neutral beam injectors.

Plasma dynamics caused by pellets.

The injection of a pellet leads to a strong localized density disturbence, which is not immediately distributed over the magnetic flux surfaces, but causes a characteristic dynamic response of the plasma, which can be well studied by observing the rapidly changing SX profiles. Fig. 2 gives an example of the spatial and temporal variations of both radiation profiles in horizontal and vertical direction after an injection of a pellet into an ohmic discharge ($\bar{n} = 4 \times 10^{13}$ cm^{-3}, $I_p = 380$ kA, $q_a = 2.9$).

Within a few hundred µs a poloidally strong asymmetric distribution of SX radiation develops. The measured signals of the chords crossing the outer

[1] University of Stuttgart; [2] Ioffe Institute; [3] University of Heidelberg; [4] University of Washington, Seattle, USA; [5] N.R.C.N.S. "Democritos", Athens, Greece; [6] Inst. for Nuclear Research, Swierk, Poland

and lower halfs of the plasma cross section decrease, while the signals of the inner and upper chords increase. This m=1 like structure rotates within the viewed cross section in direction of the poloidal magnetic field lines with a typical frequency of about 1 kHz and is damped after 2 - 10 cycles. Only the edge-localized channels (omitted in Fig. 2) show a different behaviour, namely a single positive spike due to the injected pellet.

After injection of a pellet into an ohmic discharge with reversed toroidal field and plasma current the maxima and minima of the SX signals become exchanged (cf. Fig. 3); also the direction of rotation alters and corresponds again to the direction of the poloidal field lines.

In this context the following observation from HCN-interferometry is of interest: Immediately after pellet injection the lower laser beam is deflected for both magnetic field directions. This diffraction indicates strong density gradients but in both cases within the lower plasma region, passing the HCN laser beam.

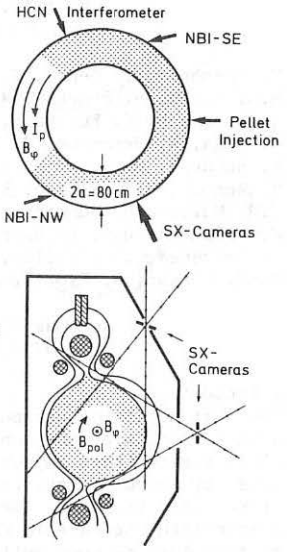

Fig.1: Schematic design of the ASDEX device.

Sawtooth activity and accumulation.

The oscillatory mode described before finally leads to a new static SX profile. The integral radiation increases from pellet to pellet and the profile becomes more and more peaked. Already after a few pellets the sawtooth activity may increase and on the time scale of typically 20 msec after pellet injection one or more strong sawteeth occur. In the example of Fig. 4 strong sawteeth are observed after the third pellet, accompanied by distinct steps on the density trace. Despite the broadening by sawteeth the density profiles remain strongly peaked in the case of pellet refuelling, which originates from an increased inward drift /2/. This enhanced drift causes also accumulation of impurities in the plasma center /3/.

In Fig. 5 two discharges are compared which only differ in plasma current. Smaller currents correspond to more peaked density profiles /4/. In both discharges a string of five pellets is injected and the temporal behaviour of the discharge is very similar. After the last pellet a strong sawtooth occurs. In case A strong sawteeth stop the further development of the accumulation phase and restore the original plasma parameters, in case B with smaller plasma current the sawteeth become suppressed and the enhanced inward drift leads to strong accumulation of electron density and heavy impurities in the plasma center. Accumulation and sawtooth activity are competing processes and the temporal development of pellet refuelled ohmic discharges depends ultimately on the strenght of the two counteracting processes.

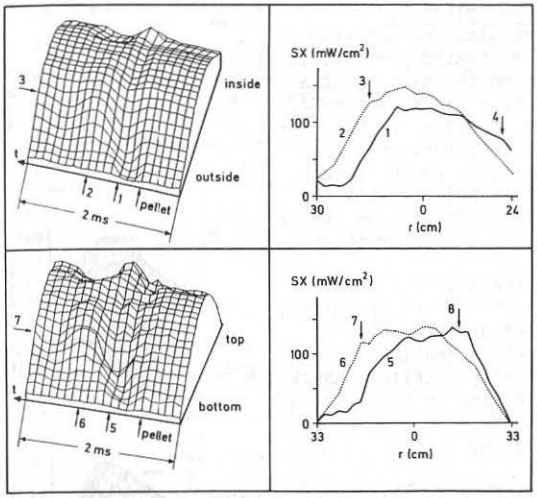

Fig.2 (above): The spatial and temporal development of SX radiation after pellet injection into an ohmic discharge. Identic numbers correspond to identic SX signals.

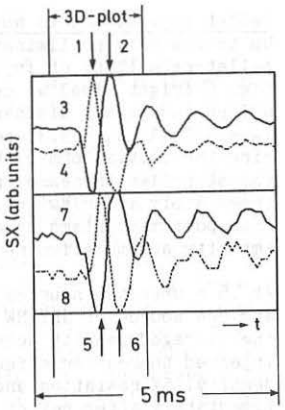

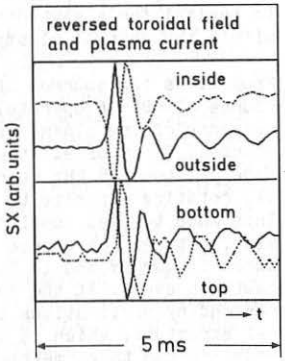

Fig.3 (right side): The temporal development of the same SX chords as shown in Fig. 2, but at reversed magnetic fields.

Fig.4 (below left side): Development of strong sawtooth activity after pellet injection.

Fig.5 (below right side): Comparison of two pellet refuelled ohmic discharges w/o and with accumulation, respectively.

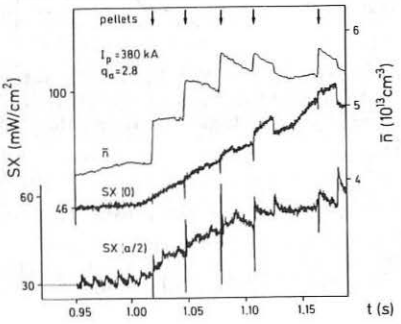

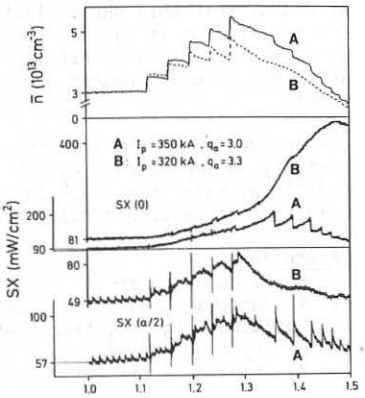

Pellet injection into NB-heated plasmas.
Up to now only preliminary results are achieved in pellet-refuelling of injection heated plasmas. In Fig. 6 (right side) we describe the history of a NBI heated plasma discharge ($\bar{n}$ = 1.4 x 10^{13} cm^{-3}, I_p = 320 kA, q_a = 3.3, power of NBI = 1.3 MW). During the initial ohmic phase we observe the typical step-like increase in density, which repeats immediately after switching off NBI; finally the transport mechanisms described before cause strong impurity accumulation resulting in a disruption.

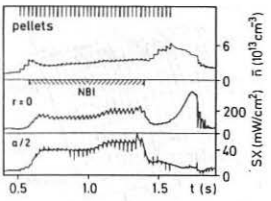

At .6 s when two sources of the NBI-SE injector and one source of NBI-NW injector start operation, the averaged density decreases and the pellets injected thereafter effect only a small rise in density. SX radiation and density profiles change immediately after pellet injection in a way which is typical for a sawtooth event, both become flat within the central plasma region.

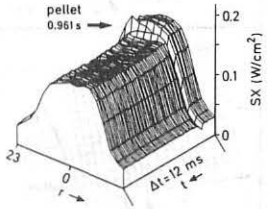

From 1.0 s two sources of NBI-NW and only one source of NBI-SE operate; at the same time the response of the plasma upon an injected pellet changes. First of all the pellet excites an m=1 mode of about 15 kHz near the inversion radius of SX, rotating opposite to the ion drift direction. This mode becomes completely damped after about 10 msec, but reappears once more with slightly reduced frequency and is finally terminated by a sawtooth event. At the same time we observe corresponding oscillations on Mirnov loops with m=4, n=1 structure, which is well explained by mode coupling due to geometrical effects /5/. There is no doubt, that this MHD-activity is triggered by the pellet, but it can also occur in NBI heated plasmas without pellet refuelling. SX radiation and density remain peaked up to the sawtooth event.

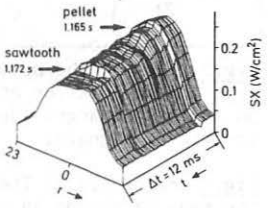

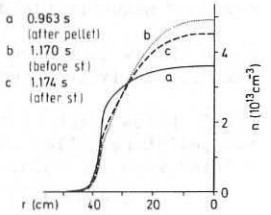

The broadening of the density profiles caused by the two kinds of sawtooth activity as described does not lead to an essential loss of particles. The additional mass of pellets is lost rather in a gradual way accompanied by simultaneous peaking density profiles.

References

/1/ H. Niedermeyer et al., Proc. 13th EPS, Schliersee 1986, part 1, p.168
/2/ V. Mertens et al., this conference
/3/ G. Fußmann et al., this conference
/4/ O. Gehre et al., Proc. 13th EPS, Schliersee 1986, part 1, p. 220
/5/ K. Grassie, to be published

PELLET INJECTOR RESEARCH AT ORNL

D. D. Schuresko, S. L. Milora, S. K. Combs, C. A. Foster, P. W. Fisher, B. E. Argo, G. C. Barber, C. R. Foust, F. E. Gethers, M. J. Gouge, H H. Haselton, J. E. Moeller, N. S. Ponte, D. W. Simmons, and J. H. Whitson

Oak Ridge National Laboratory,* Oak Ridge, Tennnessee, 37831, U.S. A.

Several advanced plasma fueling systems are under development at the Oak Ridge National Laboratory (ORNL) for present and future magnetic confinement devices. These include multishot and repeating pneumatic pellet injectors, centrifuge accelerators, electrothermal guns, a Tritium Proof-of-Principle experiment, and an ultrahigh velocity mass ablation driven accelerator. A new eight-shot pneumatic injector capable of delivering 3.0 mm, 3.5 mm, and 4.0 mm diameter pellets at speeds up to 1500 m/s into a single discharge has been commissioned recently on the Tokamak Fusion Test Reactor. The so-called Deuterium Pellet Injector (DPI) is a prototype of a Tritium Pellet Injector (TPI) scheduled for use on TFTR in 1990. Construction of the TPI will be preceded by a test of tritium pellet fabrication and acceleration using a 4 mm bore "pipe gun" apparatus. A new repeating pneumatic pellet injector capable of 2.7 mm, 4 mm, and 6 mm operation is being installed on the Joint European Torus to be used in ORNL/JET collaborative pellet injection studies. A 1.5 m centrifuge injector is being developed for application on the Tore Supra experiment in 1988. The new device, which is a 50% upgrade of the prototype centrifuge used on D-III, features a pellet feed mechanism capable of producing variable-size pellets (1.5-3.0 mm diameter) optimally shaped to survive acceleration stresses. Accelerating pellets to velocities in excess of 2 km/s is being pursued through two new development undertakings. A hydrogen plasma electrothermal gun is operational at 2 km/s with 10 mg hydrogen pellets; this facility has recently been equipped with a pulsed power supply capable of delivering 1.7 kJ millisecond pulses to low impedance arc loads. A unique ultrahigh velocity concept that utilizes an intense electron beam to generate thrust by partially ablating a solid hydrogen pellet is also under development. An 0.5 m long prototype launcher operating at 30 kV, 30 amperes is scheduled for testing in August 1988.

1. Introduction

Pellet injection has produced dramatic improvements in tokamak plasma performance in several recent and ongoing experiments[1], including peration at higher densities, improved energy confinement, reduced impurity levels, and profile tailoring for auxiliary heating. Pellet injector development to support the needs of present day large tokamaks and future devices is being actively pursued at ORNL. The upcoming fusion experiments will require 2-6 mm pellets (hydrogen, deuterium, and tritium), produced at 5-10 per second repetition rates for periods ranging from several seconds to steady-state, at maximum attainable speeds, perhaps in excess of 5-10 km/s.

*Research sponsored by the Office of Fusion Energy, U. S. Department of Energy, under Contract No. DE-AC05-840R21400 with Martin Marietta Energy Systems, Inc.

2. Repetitive Pellet Injector Technology at 1-2 km/s Speeds

Both single-barrel repeating pneumatic[2] and multiple-barrel discrete[3] shot pellet injectors which can deliver 2-6 mm hydrogen and deuterium pellets at 1-1.6 km/s speeds have been used in pellet injection experiments on the Tokamak Fusion Test Reactor. A versatile pellet injection system, consisting of three single-barrel repeating pneumatic pellet injectors mounted in one common vacuum enclosure, is presently being installed on the Joint European Torus. Individual extruders provide solid hydrogen to each gun assembly; reciprocating solenoid-driven breech tubes repetitively cut and chamber pellets. The injectors deliver 2.7 mm, 4.0 mm, and 6.0 mm size pellets at 5 Hz, 2.5 Hz, and 1 Hz repetition rates, respectively, for periods of several seconds duration; velocities up to 1.5 km/s are attainble for deuterium pellets at 100 bar propellant supply pressures (hydrogen).

A mechanical accelerator which will feature 1.5-3.0 mm pellets at 1-1.5 km/s speeds is being developed for use on Tore Supra in 1988. This injector will utilize a novel pellet forming technique capable of generating sequences of pellets for periods of 10-30 seconds. The pellet generator functions by punching pellets from a rim of deuterium frozen onto a continuously turning cryogenically cooled wheel. The pellet punch can be translated radially inward or outward with respect to the edge of the deuterium rim, thus generating pellets of the desired size. The pellets are shaped into rounded tetrahedrons or "tacos" by the punching mechanism, which is the proper shape to minimize acceleration stresses.

3. High Velocity Pellet Injector Development

The development of a high velocity pneumatic pellet accelerator, which operates with hydrogen plasma propellant, is aimed at the goal of extending the performance of present day pneumatic pellet injectors into the 2-5 km/s range[4]. The prototype accelerator consists of a vortex-stabilized arc discharge plasma generator coupled to the breech tube of a "pipe gun" pneumatic pellet injector[5]. The arc chamber is designed for arc initiation at 1-4 bar pressures, and is constructed from high temperature materials (tungsten or tantalum cathodes, graphite anode, Macor insulators). Electrical power is supplied to the arc from a 5-stage LC-line/pulse transformer supply which can produce 1 ms pulses at 5 kA currents into 0.1 ohm loads. The arc is triggered as hydrogen gas is admitted into the arc chamber; the ohmic dissipation increases the rate of rise of the gun breech pressure from 30 bar/ms to greater than 100 bar/ms. Muzzle velocities increase from 1.0 km/s to 1.3 km/s for 25 mg deuterium pellets, and from 1.3 km /s to 2.0 km/s for 10 mg hydrogen pellets; these increases represent 5-10% conversion of electrically dissipated energy to projectile kinetic energy. Muzzle velocity data for four pairs of shots with and without arc initiation are plotted vs the constant base pressure velocity calculated from the gun and pellet parameters and the maximum breech pressure in Fig. 1. Also shown are data for the repeating pneumatic injector adapted from Figs. 3 and 7 of ref. 1, and idealized gun theory performance curves for hydrogen gas at 293 K and 2000 K. It is apparant from the comparison between these data that the arc heating results in increased

propellant sound velocities, and therefore in higher sustained pellet base pressures over the acceleration interval.

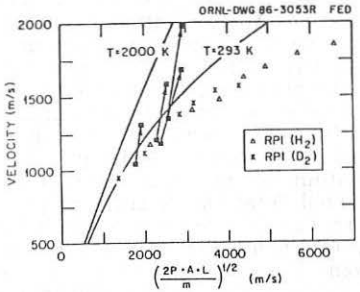

Fig 1. Electrothermal gun performance.

An ablation-driven pellet launcher, powered by an intense electron beam, as is conceptually shown in Fig. 2, is the effort being pursued at ORNL with the aim of attaining pellet velocities in excess of 5-10 km/s. Composite sticks of hydrogen propellant with deuterium pellet loads are continuously loaded into a guide rail configuration. The rear surface of these pellets is ablated by a 30 A beam of 30 kV electrons generated in an e-beam source designed for high quality electron optics. External magnets provide a solenoidal magnetic field to compress and confine the e-beam. First order modelling of the accleration, using the neutral shielding model to calculate the e-beam attenuation in the ablatant, coupled to the rocket equation and to power and mass balances at the pellet/ablatant interface, indicates that ablating 1.6 cm long propellant sticks should propel 4 mm deuterium payloads to 14 km/s. A test of prototype accelerator is scheduled for August 1988.

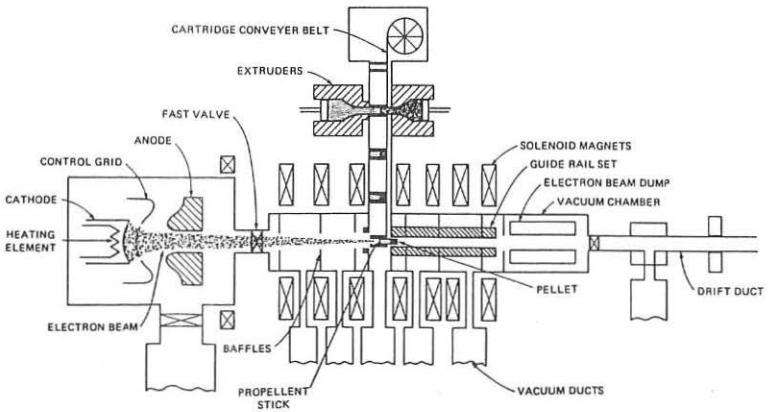

Fig 2. e-beam accelerator concept.

4. The Tritium Proof-of-Principle (TPOP) Experiment

The Tritium Proof-of-Principle (TPOP) experiment is being assembled at ORNL for testing with tritium at Los Alamos National Laboratory's Tritium Systems Test Assembly later this year. TPOP is a single-shot "pipe gun" injector, similar to the unit presently in use in the high velocity development work. With the exception of the high pressure propellant valve stem tip, which is Vespel, the gun is all metal construction, thus insuring tritium compatibility. The gun and pellet injection line are to be located in a glove box, which also house all necessary tritium handling equipment. The system is designed to accommodate enough tritium for one day of operation at TSTA. Helium-3 will be cryogenically removed from the tritium to prevent blocking of the cryopumping action in the gun by non-condensible gas during pellet formation[6]. During operation, a pellet size aliquot of tritium will be metered into the barrel and frozen. The gun and glove box system has been designed to accommodate several types of fast valves and velocity booster concepts. Tritiated gas mixtures produced in the system will be removed and processed by an external vacuum system which is part of the TSTA facility.

5. References

1. Collected papers from the International Pellet Fueling Workshop, LaJolla, California, Oct. 30-Nov. 3, 1985. ORNL Conf-8510266.
2. S. K. Combs et al., *Rev. Sci. Instrum.*, **56**(6), 1173 (1985).
3. S. K. Combs et al., *Rev. Sci. Instrum.*, to be published (1987).
4. D. D. Schuresko et al., *J. Vac. Sci. Tech.*, to be published (1987).
5. S. K. Combs et al., *Rev. Sci. Instrum.*, **57**, 2636 (1986)
6. P. C. Souers, Cryogenic Hydrogen Data Pertinent to Magnetic Fusion Energy, UCRL-52628 (1979).

RADIATED POWER DURING NEUTRAL BEAM INJECTION ON TFTR

C.E. Bush*, J. Schivell, S.S. Medley, A.T. Ramsey, B.C. Stratton, H.F. Dylla, B. Grek, R.J. Goldston, H.W. Hendel, D.W. Johnson, P.H. LaMarche, D.K. Mansfield, D.C. McCune, H. Park, G. Taylor, M. Ulrickson, and R.M. Wieland

Princeton University Plasma Physics Laboratory, Princeton, NJ 08544 USA

INTRODUCTION

A variety of confinement and operating regimes are realized on the Tokamak Fusion Test Reactor (TFTR). This is due to the availability of nigh beam power with both co- and counter-injection, pellet injection, and two diffferent graphite limiter configurations: an inner bumper or belt limiter and an outer movable limiter. Both ohmic and neutral beam injection, NBI, heated plasmas may be run on the inner and/or outer limiter, and, in the case of the detached plasma regime [1], without limiter or wall contact. Different confinement regimes are obtained depending on whether or not the limiters are pre-conditioned using high power helium discharges. Power loss studies determine the impurity radiation and energy transport characteristics of each regime. Uncollimated bolometers provide the total of radiative loss P_{rad}, plus thermal charge exchange (CX), P_{thcx}, and its toroidal distribution, and collimated bolometer arrays give radially resolved volume emission data, $Q_{rad + thcx}$. Infrared diagnostics are used to determine the power flow to the limiter, and a pair of tangentially viewing bolometers are used to estimate power lost via CX of fast ions. Combined bolometric and spectroscopic measurements provide a detailed picture of impurity behavior and power accounting in TFTR. Results are presented here to show some power loss characteristics of several regimes.

POWER ACCOUNTABILITY: OUTER LIMITER OPERATION

A detailed accounting of input power for OH and NBI heating has been done for plasmas run on the outer limiter. The outer limiter is narrow, less than one of the 20 TFTR toroidal sectors wide, and is subjected to high heat loading; this results in surface temperatures high enough to be measured accurately using an infrared camera. The results of the power balance for outer limiter operation are plotted in Fig. 1. Losses, $P_{rad} + P_{thcx}$, are measured using bolometry while P_{lim} is determined from infrared camera measurements. Data shown are for ohmic, L-Mode NBI, and energetic ion regime [2] plasmas. Also included are data for which neon was intentionally added to obtain 100% radiative loss in NBI discharges while IR measurements confirmed that P_{lim} was negligible. For the majority of discharges of Fig. 1, the total power radiated was < 50%, and with the contribution from the uniform bulk plasma often in the range of 25-35%. Using a toroidal array of six bolometers collimated narrowly in the toroidal direction only, the toroidal distribution [3] of radiated power was found to be significantly peaked at the limiter sector during NBI with outer limiter operation. A toroidal asymmetry correction factor of ~ 1.15 is included in the data of Fig. 1.

*Permanent address: Oak Ridge National Laboratory, Oak Ridge, TN 37830

CO-ONLY VS. SUPERSHOTS: INNER LIMITER OPERATION

A new enhanced confinement or "supershot" regime [4] is being studied on TFTR using mainly inner bumper limiter operation. This regime is characterized by energy confinement times up to 3 times higher than in L-Mode and is obtained with high power nearly balanced NBI and extensive conditioning and degassing of the inner limiter. Other signatures are high ion temperature and neutron source strength, S. For comparison, Fig. 2 shows P_{rad} and S during the beam pulse of a supershot and a co-NBI only plasma, both with P_{NB} ~ 12 MW. P_{rad} for the two plasmas is nearly the same while S differs by a factor of 3. However, spectroscopy data analyzed with MIST code impurity modeling indicate that impurity behavior in the two cases is somewhat different. The results of the analysis are given in Table I. The pre-beam plasma has very low density and the carbon concentration of 16% $\bar{n}_e$ is responsible for the high Z_{eff} of 6.6. By the end of the beam pulse, $\bar{n}_e$ is significantly higher and Z_{eff} is reduced by beam fueling to ~ 4 for both co-only and balanced beam heating. These discharges were from near the end of the 1986 run. For earlier supershots Z_{eff} was in the range of 2.5-3.5. Concentration of Fe and Ni are higher by an order of magnitude for the supershots tnan for co-only; however, the contributions of these metals to Z_{eff} and the total radiated power are small. The radiated power fraction decreases with beam power for both co-only and co + ctr injection, and results showing this trend for the latter are plotted in Fig. 3. The fraction decreases from ~ 70% for the ohmic phase to 25-35% for P_{NB} > 10 MW.

Further impurity radiation and power balance comparisons between the co-only plasmas and supershots are complicated by two effects of inner limiter operation. First, the inner limiter surface area is large and results in surface temperatures which are too low for use in determining P_{lim}, and second, plasma interaction with the inner limiter leads to a highly radiating layer of plasma on the inner half periphery of the minor cross section. This layer causes a high degree of in-out asymmetry in the chord integrated vertical array bolometer data [5] for ohmic and NBI heating. A 3-D plot of the chord integrated data from the vertical array for the co-NBI case of Fig. 2 is given in Fig. 4, and the effect of the inner limiter layer is clearly evident. Only the outer half of the distribution is representative of the bulk plasma impurity radiation profile. Figure 5 shows the results of Abel inversion of the outer half profile data for four beam power levels for discharges used in Fig. 3. The peaks of the volume emission profiles are shifted to larger minor radii as P_{NB} is increased up to ~ 10 or 11 MW. Information at radii less than ~ 15 cm is lost due to the distorting effects of the bright layer near the inner limiter.

FAST ION LOSSES

At low density, a fraction (~ 10-20%) of the fast ions is calculated to be lost as fast CX neutrals while they are slowing down from initial beam energies of ~ 90-100 keV to the final elevated thermal plasma temperature. This fraction decreases during the beam pulse as $\bar{n}_e$ increases. The fast CX neutrals have toroidal velocity components large enough that they impinge on the walls at angles which do not fall within the acceptance angles of the radially directed TFTR bolometers. The arrays are collimated both radially and toroidally, and the wide-angle

bolometers, though uncollimated radially, are even more narrowly collimated in the toroidal direction. Therefore, a pair of tangentially viewing bolometers has been installed to study the fast CX-neutral losses; their viewing arrangement is illustrated schematically in Fig. 6. The bolometers view in opposite directions with very nearly the same toroidal tangency radius. For simplicity only one co-beamline is shown. TFTR currently has three co- and one counter-beamlines. Time resolved data for the two bolometers are shown in Fig. 7 for an energetic-ion regime plasma heated by 8 MW of co-only NBI power. In general, both bolometers would have equal impurity radiation and equal thermal CX (except for rotation) contributions to their net signals. However, for co-only injection, such as for Fig. 7, fast ion CX losses are detected only by the co-CX bolometer; thus, this signal is the larger of the two. In contrast, the burst of power at ~ 5.3 sec, due to laser blowoff injection of Fe impurity, is bulk plasma radiation and thus is about the same size for both bolometers. The data of Fig. 7, when correlated with plasma simulation studies, lead to the conclusion that the fast ion CX loss at ~ 5.4 sec. was ~ 13% of the total input power. Simulations indicate that these losses can be > 30% of the input power for the lowest density energetic ion plasmas.

This work was supported by U.S. DoE Contract No. DE-AC02-CHO-3073.

[1] Strachan, J.D., et al., J. Nucl. Mater. 145-147, (1987) 186.
[2] Murakami, M., et al., Plasma Phys. Contr. Fusion 28, (1986) 17.
[3] Bush, C.E., et al., Rev. Sci. Instrum. 57, (1986) 2078.
[4] Strachan, J.D., et al., Phys. Rev. Lett. 58 (1987) 1004.
[5] Schivell, J., and Bush, C.E., Rev. Sci. Instrum. 57, (1986)

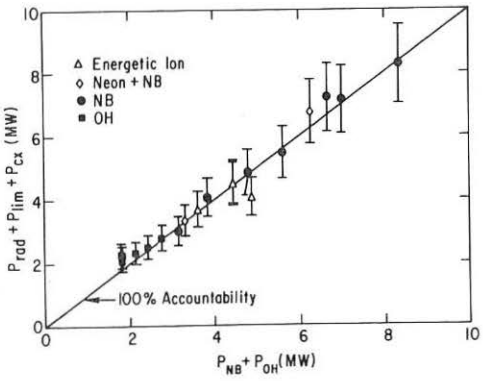

Fig. 1 Power accountability was very good with outer limiter operation.

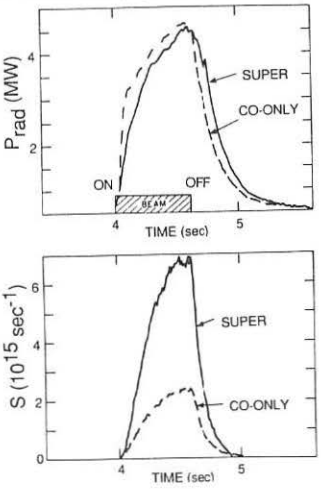

Fig. 2 Comparison of typical super and co-only shots.

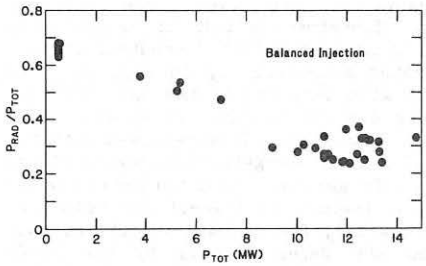

Fig. 3 Bulk plasma fraction radiated vs. input power.

Shot:	Ohmic	Super	co- only
P_{beam},MW	0.0	12.0	13.1
$\bar{n}_e$, 10^{19} m^{-3}	0.59	2.6	2.0
Z_{eff}	6.6	4.0	4.1
n_D/n_e	.006	.61	.43
n_C/n_e	.16	.049	.079
n_O/n_e	<.01	.007	.011
n_{Fe}/n_e	.00055	.00073	.00007
n_{Ni}/n_e	.00060	.00094	.00006

Table I. Impurity fraction and Z_{eff} from Spectroscopy & MIST.

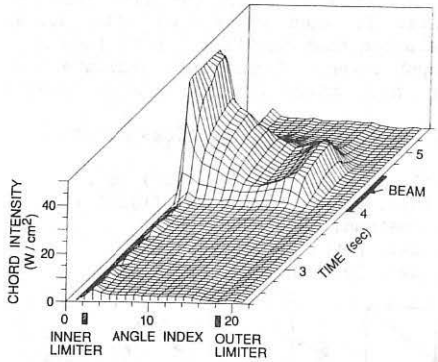

Fig. 4. In-Out asymmetry in vertical array data for inner limiter operation.

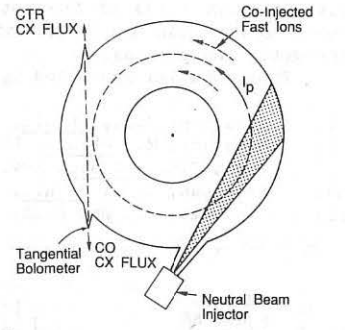

Fig. 6 Oppositely viewing tangential bolometer pair.

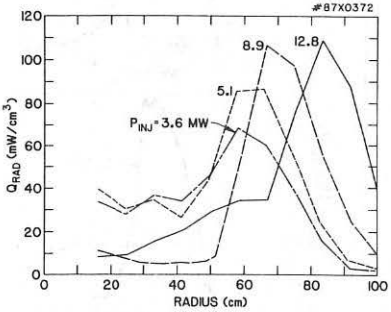

Fig. 5. Volume emission profile from Abel inversion of vertical array data.

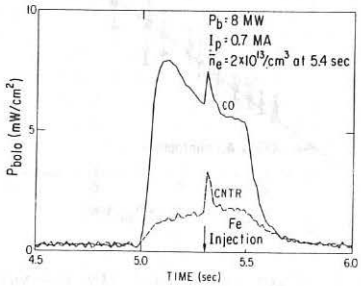

Fig. 7 Tangential bolometer signals for low $\bar{n}_e$ and co-NBI.

BOLOMETRY STUDIES IN THE TJ-I TOKAMAK

M.A.Ochando, A.P.Navarro, J.Guasp and TJ-I Group.

Asociación EURATOM/CIEMAT
28040 Madrid, SPAIN.

INTRODUCTION

Global energy losses are a matter of great interest in plasma confinement studies, where appreciable discrepancies between theoretical estimations and experimental data arise (1). Several devices (pyroelectric detectors, thermopiles, thin-foil bolometers, etc.) have been tried in order to optimize the determination of these losses, including time and spatial resolution.

In the present work, a single movable detector (a thin-film Ge bolometer) has been used in the TJ-I tokamak (R_o =.3 m, a_p =.1 m) with a twofold objective: first, to check the capability of a single movable detector to determine radial emission profiles and, second, to measure global power losses in the TJ-I tokamak when operating under different conditions.

The former goal arises from the future task of determining energy losses in the flexible heliac TJ-II to be built at CIEMAT (2). Owing to the non-circular plasma shape, a number of detector arrays have to be used to determine local power emissivity. Longer and more stable discharges may enable a shot to shot study with single detectors instead of detector arrays.

The later one is derived from the need of knowing the plasma radiation profile in the TJ-I tokamak and its dependence on plasma parameters, e.g., toroidal field, plasma current and electron density. Furthermore, an interesting test on the collimator shape could be made in this small tokamak due to the low aspec ratio (R/a = 3) in order to choose the most suitable geometrical arrangement. This test will be also useful to design the collimators of the TJ-II bolometers (R/a = 7).

The low aspect ratio of this tokamak forced us to design a toroidal limited view collimator. The aperture at the end of the collimator tube consists of two welded stainless steel discs, the outer of which being 1 mm thick with a 2 mm diameter hole at the center and the inner one being 3.5 mm thick with a vertical slit 0.1 mm wide. This geometry allows to observe the whole poloidal section and limits the toroidal view at the plasma center section to about 1-2 cm when plasma radii are longer than 5 cm. Fig.1 shows the collimator aperture and the plasma views (V1, V2) from the two extreme positions of the detector (D). Detector displacements through the collimator tube enables to observe poloidal plasma sections with resolutions at the center ranging from about 3 cm to full plasma minor radius.

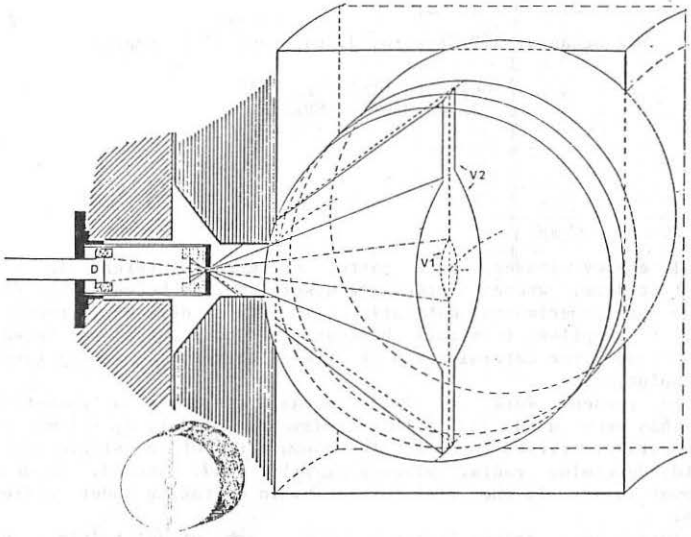

FIG.1 TOROIDAL LIMITED VIEW COLLIMATOR

RADIAL SCAN

A qualitative radiation emission profile has been determined from several repetitive discharges in the TJ-I tokamak. Due to the low bolometer signal levels when operating in the typical TJ-I conditions, shown in fig.2, global measurements rather than time-resolved should be performed.

Using the experimental set up illustrated in fig.1, the distance of the bolometer foil to the plasma center was varied, shot to shot, from 1.2 cm to 4.4 cm at steps of 1 mm. This leads to a set of integrated signals at the bolometer output plotted in fig.3a.

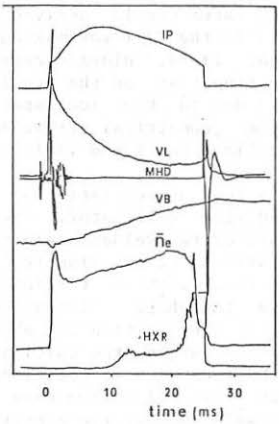

FIG.2 TJ-I DISCHARGE TRACES

By subtracting the signals for two successive detector positions and taking into account the volume shapes viewed by the detector (fig.1), we can obtain the line integrated power emission curve marked as b in fig.3. Assuming radial symmetry for TJ-I plasma losses we can deduce its radial profile by the usual Abel inversion method. Results are presented at fig.4.

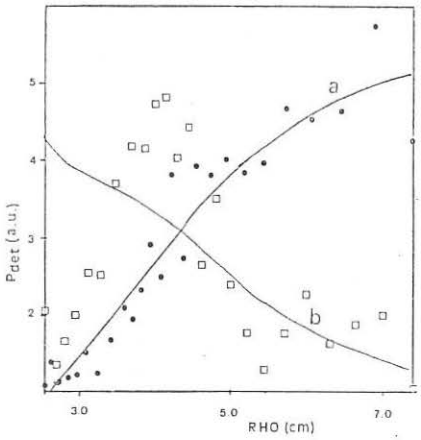

FIG.3 RADIAL SCAN
a) Integrated measurements
b) deduced line integrals

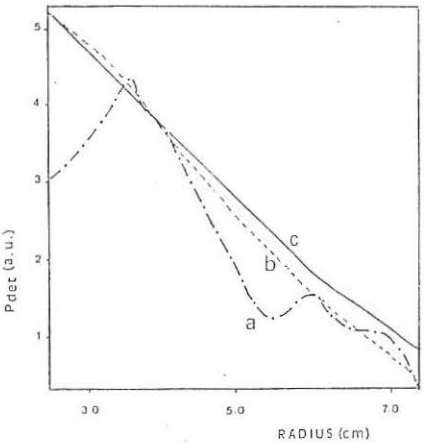

FIG.4 RADIAL PROFILES
a) From raw data
b) From smoothed data
c) Theor. estimation

A slightly hollow profile is deduced when raw data are used. Nevertheless, data fitting smoothes, due to the large uncertainties introduced by the low signal levels, the line integral curve and generates a flatter profile more in agreement with the theoretical predictions for TJ-I (3). A triangular shape profile for T_e and a parabolic one for n_e, (T_{eo}=350 eV, $n_{eo}=3.10^{19}$ m^{-3}), were used in these simulations.

GLOBAL B_T , I_P AND $\bar{n}_e$ SCANS.

The dependence of the plasma energy losses in TJ-I has been determined when toroidal field, plasma current or electron density are modified. Results for global power losses referred to ohmic power are summarized in fig.5.

Fig 5a clearly shows a linear dependence of the plasma power losses on the toroidal field. B_T ranges from 0.8 to 1.5 T with constant I_P and $\bar{n}_e$.

I_P was varied in the range 25 to 42 kA, while B_T and n_e were maintained constant. Unfortunately, the TJ-I tokamak does not have any current feedback stabilization system, so that we had to use the I_P value at the flat top of the discharge (see fig.2). Fig.5b shows the behaviour of power losses as a function of the plasma current, from which an IP^{λ} ($\lambda \sim .5 - .7$)

dependence can be observed.

Finally, n_e was changed from .5 10^{19} m^{-3} to 2.2 10^{19} m^{-3}, and power losses measured for each case, at B_T and I_P constants. A linear dependence, as it is shown in fig. 5c, was obtained.

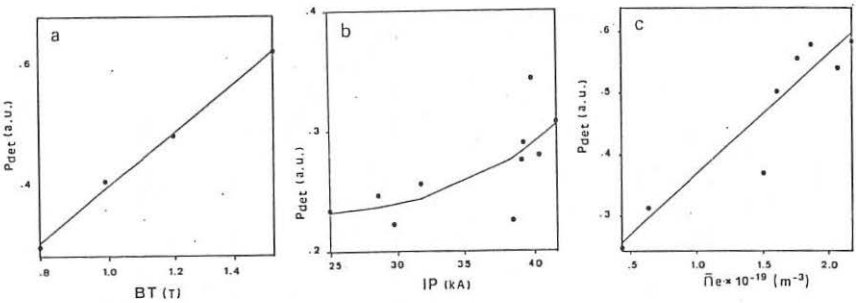

FIG.5 TJ-I POWER LOSSES
a) B_T scan b) I_P scan c) n_e scan

SUMMARY

Measurements in TJ-I tokamak, using a movable Ge bolometer and an adequate collimator design, have demonstrated the capability to deduce power losses radial profiles using only one detector in a shot to shot basis. For TJ-I typical discharges, a slightly hollow profile is obtained, but higher sensitivity is required to confirm this feature. Global power losses scans for the TJ-I operational space give a dependence $P_r \propto I_P^{7}\ \bar{n}_e\ B_T$.

ACKNOWLEGMENT

This work was possible thanks to the loan from the W-VII A, (Max Planck IPP, Garching), of a Ge bolometer and its associated electronics.

REFERENCES

(1) P.H.Edmonds and A.C.England, Nucl. Fusion 18, 23 (1978)

(2) TJ-II GROUP and ATF DESIGN TEAM, 12th EPS Conf. Vol.9F, I, 441 (1985)

(3) J.Guasp, "Plasmator. Código Numérico de Simulación de Transporte de Plasma en Tokamaks", Report JEN-459, (1979)

Neoclassical Impurity Transport in Ohmically Heated Pellet Discharges

W. Feneberg, K.F. Mast, and G. Becker, H.S. Bosch, H. Brocken, A. Carlson, A. Eberhagen, G. Dodel[1], H.-U. Fahrbach, G. Fussmann, O. Gehre, J. Gernhardt, G. v.Gierke, E. Glock, O. Gruber, G. Haas, W. Herrmann, J. Hofmann, A. Izvozchikov[2], E. Holzhauer[1], K. Hübner[3], G. Janeschitz, F. Karger, M. Kaufmann, O. Klüber, M. Kornherr, K. Lackner, M. Lenoci, G. Lisitano, F. Mast, H.M. Mayer, K. McCormick, D. Meisel, V. Mertens, E.R. Müller, H. Murmann, J. Neuhauser, H. Niedermeyer, A. Pietrzyk[4], W. Poschenrieder, H. Rapp, A. Rudyj, F. Schneider, C. Setzensack, G. Siller, E. Speth, F. Söldner, K. Steinmetz, K.-H. Steuer, N. Tsois[5], S. Ugniewski[6], O. Vollmer, F. Wagner, D. Zasche,

Max-Planck-Institut für Plasmaphysik
EURATOM Association, Garching, FRG

Abstract
Pellet refuelled high density divertor discharges in ASDEX which are ohmically heated often show a sudden transition from a status of negligible or slow impurity accumulation to a fast accumulation at the plasma core. From bolometric measurements we estimate the inward drift velocity of medium z impurities and compare the results with theoretical predictions based on the neoclassical momentum equations for a two ion fluid which contain inertia and parallel viscosity.

I. Theory The theoretical calculations performed to explain the experimental observations are based on the neoclassical momentum equations for a two ion fluid (i= back ground ions, z= impurities) using a friction term derived from a shifted Maxwellian distribution only. Compared with earlier calculations /3, 4, 5/, poloidal and toroidal rotation of the background plasma is taken as two free parameters and in the impurity momentum balance parallel viscosity in the collisional and plateau regime as given in Ref. /6/ is taken into account. Parallel electric field effects are neglected corresponding to an ordering in $z \cdot m_i/m_z < 1$ (i.e., z,m_z impurity charge and mass, m_i the bulk ion mass). In addition to our previous work /7/, the complete inertial term is taken into account and it is shown to give an important contribution even in the case of zero toroidal rotation, where we obtain the following expression for the impurity transport velocity perpendicular to one magnetic surface in a geometry of circular surfaces with minor radius ρ: $\langle V_{z,\rho} \rangle = \tilde{n}_s T \varepsilon^2/(ZeB\rho)$
($T=T_e=T_i=T_z$ being the temperature, B the toroidal field z·e the ionic charge, $\varepsilon=\rho/R$, R the major radius). The radial flux depends only on the quantitiy $\tilde{n}_s$ which describes the up and down asymmetry in a Fourier expansion $n_z=n_z^{(o)}(1+\varepsilon\tilde{n}_c\cos\theta + \varepsilon\tilde{n}_s\sin\theta)$.
The quantity $\tilde{n}_s$ itself depends very sensitively on the radial electric field, i.e. in the case of zero toroidal rotation considered here from the poloidal rotation of the background plasma.

[1] University of Stuttgart; [2] Ioffe Institute; [3] University of Heidelberg; [4] University of Washington, Seattle, USA; [5] N.R.C.N.S. "Democritos", Athens, Greece; [6] Inst. for Nuclear Research, Swierk, Poland;

Fig. 1 shows results for neoclassical inward drifts calculated with the parameters of two typical pellet discharges in ASDEX under the assumption of zero order impurity pressure gradient $p_2^{(0)\prime}$ to be far away from accumulation equilibrium.

$$(p_i'/n_i >> P_2^{(0)\prime}/z \cdot n_2^{(0)}.$$

In opposite to the work of Rutherford /3/ which has neglected the effect of inertia and therefore has to be modified completely, the impurity transport depends beside the parameter Ω of collisionality defined as in our previous JET report /8/ also on the parameter $A^2 = V_{z,\Theta}^{2\ (0)} / \left(\frac{\varepsilon}{q} C_{z,s}\right)^2$,

where $V_{z,\Theta}^{(0)}$ is the zero order impurity rotation velocity, $C_{z,s}$ the impurity sound velocity and q the safety factor.
We have always from radial momentum balance

$$V_{z,\theta}^{(0)} = V_{i,\theta}^{(0)} - 1/eB\ (P_i'/n_i - P_2^{(0)\prime}/z n_2^{(0)}),$$

where $V_{i,\theta}^{(0)}$ is the bulk plasma poloidal rotation velocity. The inward drift has a maximum for $V_{z,\theta}^{(0)}=0$, when the radial electric field E_ρ vanishes and is much smaller when the background plasma is at rest ($V_{i,\theta}^{(0)}=0$), the case which fits best to experiment. In this case theory even predicts a flow reversal for heavy impurities when $A^2 \geq 2$ an effect caused by the coefficient of parallel viscosity and leading to an interesting possibility to prove the neoclassical theory.

II. Experimental observations A transition to a phase of fast accumulation is observed a) if one or more pellets are missing during the injection of a pellet series, b) after pellet injection if no density limit disruption occurs and c) in discharges with the central radiation power density $P_{rad}(0)$ conparable to the local ohmic heating power $p_\Omega(0)$. This is observed in carbonized discharges but mainly in non-carbonized plasmas with an intrinsic higher content of iron /1/. A kind of self-triggering of accumulation occurs if the q on axis rises to values considerably above one due to high central radiation power density.
After the transition into the fast accumulating state the radiation power profiles always strongly peak in a narrow zone $r \leq r_o$ around the magnetic axis ($r_o \leq 15$cm). Little change in density and temperature profiles is observed during the transition period. No substantial variation of the radial inward drift velocity of impurities is thus expected from the neoclassical theory (see above). The postulation of a rapid decrease of the effective diffusion coefficient of impurities inside $r \leq r_o$ and no change of their inward drift velocity can explain the transition from a slow into a fast accumulation.
Sawtooth inversion radii r_{inv} similar to r_o were found in soft X-ray measurements. The onset of fast accumulation in cases a) and b) inside a zone of minor radius $r_o \approx r_{inv}$ only occurs if no pellets and no sawteeth are present. In case c) the transition occurs during repetitive pellet injection in a phase with continuous flattening of the T_e-profile, thus rising q on the plasma axis q(0). One can speculate that pellets still trigger sawteeth with q(0) just above one in case a) and b) by locally disturbing the n_e- and T_e-profile. A further rise of q(0) owing to increasing

$p_{rad}(0)/p_{\Omega}(0)$ suppresses the sawtooth activity during pellet injection. A simple analytical model is derived in order to estimate the accumulation of impurities on the plasma axis. The linearised transport equation for impurities with charge Z in cylindrical approximation is

$$-D_z(r)\cdot r\cdot\frac{\partial^2 n_z}{\partial r^2} - (D_z(r)+r\frac{dD_z}{dr})\frac{\partial n_z}{\partial r} + V_{DZ}(r)\cdot r\frac{\partial n_z}{\partial r} + (V_{DZ}(r)+\frac{dV_{DZ}}{dr}\cdot r)\, n_z = -r\frac{\partial n_z}{\partial t} \qquad (1)$$

with $n_z(r,t)$=density, $v_z(r)$= inward drift velocity (neoclassical) and $D_z(r)$=effective diffusion coefficient of impurities Z.
We define $D_z(r)$ as

$t<0$ $D_z(r)=D_i$ $\leftarrow (r\leq r_o)$ $\quad D_z(r)=D_o (r_o<r<a)$ (r_o=15 cm, a=plasma minor radius = 40 cm)
$t\geq 0$ $D_z(r)=D_a$ $\swarrow$

Expansion of $v_z(r)$ near the axis yields $v_z=V_{D1}\cdot r$ ($v_{D1}<0$). Fast impurity accumulation starts at t=0 and no saturation of $n_z(0,t)$ is experimentally observed until a density limit disruption occurs. For a time interval $0\leq t\leq t_A$ (t_A is estimated below) we define the velocity for outward diffusion at $r=r_o$

$$V_{DIF} = \frac{dn_z(r,0)}{dr}\cdot D_z(r)/n_z(r,0)_{/r=r_o} \qquad (2)$$

A time t_A is defined at which the increase of V_{DIF} at $r=r_o$ is
$\Delta V_{DIF} = V_{DIF}(r_o,t_A)-V_{DIF}(r_o,0) = 0.3\cdot V_z(r_o)$
and an experimentally detectable decrease of the time constant τ is expected. Equation 1 is simplified to

$$V_z^*(r)\cdot r\frac{dn_z}{dr} + (V_z^*+\frac{dV_z^*}{dr}\cdot r)n_z(r,t) = -r\frac{\partial n_z}{\partial t} \qquad (3)$$

$v_z^*(r) = V_z(r)+V_{DIF}(r) = V_{D_1}(1-D_a/D_i)\cdot r = V_D^*\cdot r$.
Starting from a quasi-stationary impurity distribution $n_z(r,0)= n_o\cdot\exp((v_{D1}/2D_i)r^2)$ ($r\leq r_o$) at t=0, the distribution of impurities z evolves as

$$n_z(r,t) = n_o\cdot\sum_{\zeta=0}^{\infty}\frac{(-1)^{\zeta}}{\zeta!}(\frac{r}{\lambda\cdot a})^{2\zeta}\cdot\exp(2|V_D^*|(\zeta+1)t) \qquad (4)$$

$1/\lambda\cdot a = (|V_{D1}|/(2D_i))^{0.5}$
and the central density of impurities is $n_z(0,t)=n_o\cdot e^{2/v_D^*\cdot t}$

Figure 2 represents t_A/τ_0 ($\tau_o<\tau, \tau_o=1/(2|V_{D_1}|)$ $\tau=1/2|V_D^*|$) as an upper limit of t_a/τ. Experimentally we always find $t_A/\tau>1$ (Fig. 3) and thus $t_A/\tau_0>1$. We deduce from Fig. 2 the ratio D_a/D_i to be always less than 0.3. The inward drift velocity at $r=r_o$ is derived from the experimental τ as $V_z(r_o)=r_o/2\cdot\tau$ and should always be smaller than the theoretical value.

The concentration of iron (the dominating metal in ASDEX /2/) on the plasma axis is derived from $p_{rad}(0)$ and $n_e(0)$ assuming coronal equilibrium. We always find a constant τ during accumulation and no saturation (Fig. 3).

References

/1/ Mast, K.F., Müller, E.R., et al., Radiation Behaviour of Gas and Pellet refuelled High density discharges in ASDEX, this conference.
/2/ Fußmann, G., Journal of Nuclear Materials 145-147 (1987) 96-104.

/3/ Rutherford, P.H., Phys. of Fluids, 17, 9 (1984).
/4/ Burrel, K.H., Ohkawa, T., Wong, S.K., Phys. Rev. Lett., 47, 7 (1981).
/5/ Stacey, W.M.Jr., Sigmar, D.J., et al., Nucl. Fus. 25, 4 (1985).
/6/ Callen, J.D., et al., IAEA-CN-47, Kyoto, Nov. 1986.
/7/ Feneberg, W., Kornherr, M., Smeulders, P., et al., Budapest, Sept. 1985.
/8/ Feneberg, W., Mast, F.K., Gottardi, N., Martin P., JET-R(86)07.

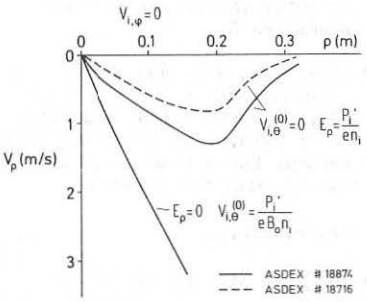

Fig.1: Neoclassical impurity inward drifts calculated for iron in a typically ASDEX pellet discharge for two different rotation velocities. Z(ρ) from corona equilibrium.

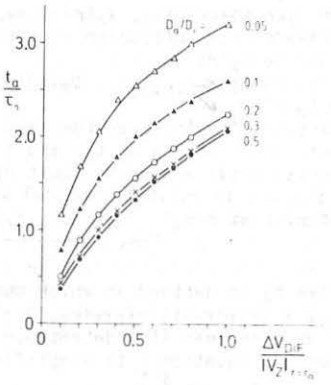

Fig.2: The increase ΔV_{DIF} of the difference outward velocity V_{DIF} related to the inward drift velocity $V_Z(r_o)$ during accumulation.

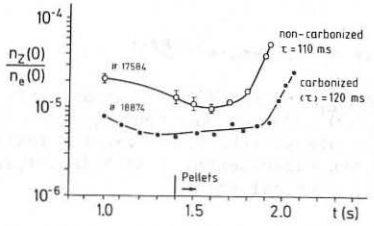

Fig.3:
#17584: non carbonized pellet discharge in D_2. The dominating metal is iron $n_z(0) \approx n_{Fe}(0)$.
18874: carbonized pellet discharge. The T_e-profile is constant for 1.5 s≤t≤2.1 s ($T_e(0)$=780 eV = 30 eV). The time constant τ represents an average value for iron and titanium.

Conclusion The theoretically predicted inward drift velocity at r = 15 cm, V_z = 75 cm/s for #18716 and V_z = 110 cm/s for #18874 agree well with the bolometrically detected V_z = 43 cm/s for #18716 and V_z = 63 cm/s for #18874. The experimental values of V_z are always smaller than the theoretical V_z.

TOROIDAL ROTATION AND MOMENTUM CONFINEMENT IN DITE

N C Hawkes and N J Peacock

Culham Laboratory, Abingdon, Oxfordshire, OX14 3DB
(Euratom/UKAEA Association)

I INTRODUCTION

This paper extends previous work [1] on damping of the toroidal momentum, induced by tangential injection of H° beams into the DITE tokamak. Particular attention is paid in this paper to the quantitative relation between the size of the magnetic field perturbation due to the bundle divertor and the degree of rotation damping. Results are reported for Co- and Counter- injection of the H° beams. An attempt is also made to construct a spatial profile of the rotation. A residual rotation is measured in purely ohmic discharges. As in [1] the toroidal plasma velocity is measured by the spectral shifts of line radiation from central ions such as Fe XIX recorded using a spectrometer with electronic read-out [2]. The toroidal momentum is then taken to be the product of the spectral shifts and the average electron density, n_e, with an appropriate proportionality constant.

II RESULTS

Applying the divertor fields part way through an ohmic discharge 'brakes' any residual rotation and discloses a slight Doppler shift in the Fe XIX emission otherwise undetectable with our fixed tangential line of sight. This shift which has to be taken into account in the beam injection analysis (below), corresponds to a rotation speed of 2.6×10^4 ms^{-1}, directed against the positive ion plasma current. Reversal of the plasma current reverses the direction of rotation, in accordance with results from other tokamaks [3]. From the force balance equation,

$$-E_r = \frac{1}{en_e}\frac{\partial P_i}{\partial r} - V_\phi . B_\theta + B_\phi . V_\theta \qquad (1)$$

a radial electric field of $-3000 V.m^{-1}$ is derived from the residual rotation with the discharge centre negative, although it is recognised [3], that the density and temperature gradient terms can not be ignored.

With the application of neutral beam injection, rotation speeds up to $1.5 \times 10^5 m.s^{-1}$ are observed, in the direction of beam injection. Rotation speeds are seen to depend upon plasma density in such a way that at a given beam power the product of speed and density, ie, momentum, is constant. It is further found that momentum scales linearly with injected beam power, FIG 1, ie, is proportional to the driving force. The slope of the momentum-force line gives a value of 10ms for the momentum confinement time in steady state whereas measurements of the rise and fall times of momentum, taking into account the varying plasma density, yield values of 35 and 20ms respectively. Uncertainty in the conversion from central rotation speed to global momentum due to a lack of detailed knowledge of the velocity profiles has led us to investigate details of $V_\phi(r)$. Measurements of the spectral shifts of a number of ions besides Fe XIX

allow us to estimate the shape of the velocity profile, FIG 2. With a single tangential viewing chord, no deconvolution analysis has been made to allow for the variation of the toroidal velocity along the major radius (constant angular rotation). The shape of the profile is also critically dependent on the radial position of Si XII which has been estimated using a diffusive transport model. Nevertheless, within a factor of two, the density $n_e(r)$ and $V_\phi(r)$ profiles are similar and our method for calculating the global plasma momentum, $\alpha\ n_e V_\phi(o)$, seems justified.

Because we lack data on the momentum profiles on a routine basis we place most confidence on the measurements of momentum decay times. These, however, show a significant amount of shot to shot variation, although exhibiting the same trends as the steady state momentum confinement time. Thus in the analysis of this work we use the steady state momentum confinement times multiplied by a factor of two to agree with the momentum decay times. The rise times of momentum show a still larger shot to shot variation and are therefore not used in the analysis.

The momentum confinement time, τ, at 20ms is much shorter than neoclassical [4] which predicts values around 40s for DITE parameters. In constrast and in agreement with our results, the gyroviscosity theory of [5] gives 22ms for the same parameters, and with $Z = Z_{eff} = 2.5$.

III RIPPLE DAMPING

Data sets of discharges were made for divertor currents of 0, 5, 10 and 18kA which is the full divertor operating current. A number of discharges are run at each divertor current with various neutral beam powers. A plot of τ versus input force, FIG 3, shows a reduction in τ with increasing divertor current, decreasing to ~ 20% of maximum at full divertor current.

The divertor is believed to damp toroidal rotation through its perturbing effect on the main tokamak field. According to the theory of [6], although not strictly applicable to the case of a large, localised perturbation such as the bundle divertor, this damping effect should scale nearly as the square of the perturbation, ie, as the square of the divertor current in this instance. Equation (52) in [6] expresses momentum decay time as:

$$\tau^{-1} = 1.02 \left(\frac{\theta . V_T}{\nu_{ii} r}\right)^2 \left(\frac{r}{R}\right)^2 \frac{(n\delta)^2}{(n\delta)^2+\theta^2} \nu_{ii} \qquad (2)$$

where $\delta = \frac{\Delta B_\phi}{B_\phi}$, $\theta = \frac{B_\theta}{B_\phi}$, $n_e \sim 2.5 \times 10^{19} m^{-3}$ and $n = 1$. The divertor field perturbation at 18kA varies from 100% at the outer major radius of the plasma, at the null point to ~ 5% on axis, and lower on the inner major radius of the plasma. Since the toroidal extent of this perturbation extends only over ~ 0.1 of the minor axis in DITE, the applicable value of δ is expected to be small; of order 1%. The denominator in equation (2) is dominated by θ^2 with $\theta \sim 6\%$, thus τ depends nearly on δ^2 as stated.

Before making the comparison with theory we must allow for the other damping mechanisms present with the divertor off. Assuming there is an anomalous momentum diffusity causing a maximum momentum confinement time τ_{anom} with zero divertor current, we plot $\tau^{-1} - \tau^{-1}_{anom}$ against divertor current squared in FIG 4, where the points are measurements and lines are

the evaluations of equation (2) assuming effective values of δ at full divertor current ranging from 0.4 to 0.8%. Reasonable agreement is found with $\delta(18kA) = 0.6\%$.

IV CONCLUSIONS

In the analysis of toroidal momentum damping in DITE it appears that the local δB_ϕ perturbation due to divertor can be modelled successfully using ripple camping theory [6] appropriate to the collision dominated regime. In undiverted discharges the magnitude of the damping is of the same order as that predicted by gyroviscisity provided Z_{eff} is used exclusively in the expressions for the damping constants [5].

V REFERENCES

[1] Hawkes N C and Peacock N J., Nuclear Fusion, 25, 8, (1985) 971.
[2] Hawkes N C and Peacock N J., Review of Scientific Instruments 57, 8, (1986) Part 2, 2035.
[3] Suckewer S et al. Nuclear Fusion 21, 10, (1981) 1301.
[4] Cowley S C and Bishop C M. Culham Laboratory Report CLM-M109.
[5] Stacey W M Jnr., et al. Nuclear Fusion 26, 3, (1986), 293.
[6] Tsang K T and Frieman E A., Physics of Fluids 19, 5, (1976) 747.

VI ACKNOWLEDGEMENT

The author would like to thank the DITE Group for their support and advice during this series of experiments.

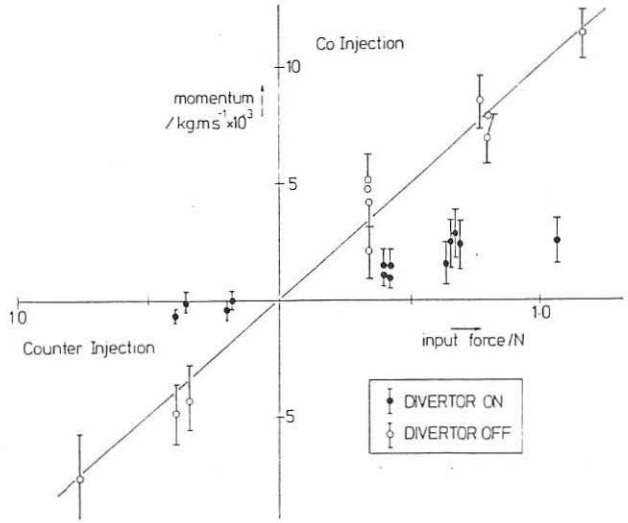

FIGURE 1: Variation of plasma momentum with input force arising from neutral injection. Negative input force refers to counter-injection discharges with the plasma current reversed. Plasma is Helium, results for Deuterium are similar.

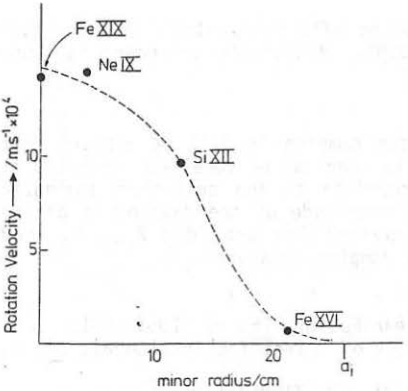

FIGURE 2: Estimated velocity profile from observations of different impurity lines. Fe XIX and XVI have been localised by previous spatial measurements, Ne IX and Si XII are localised through the use of a diffusive transport model.

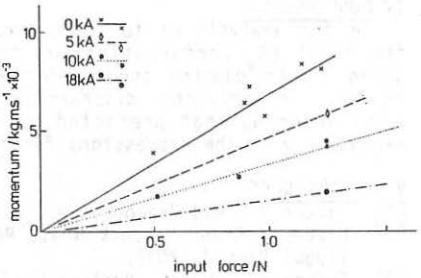

FIGURE 3: Showing the effect on momentum damping of increasing the divertor current from 0 to 18kA. Deuterium plasma.

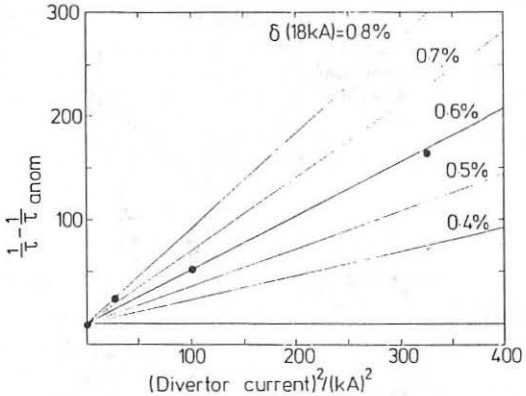

FIGURE 4: Variation of inverse momentum confinement time, τ^{-1}, less the unperturbed inverse momentum confinement time, with divertor current squared. Points are experimental values of figure 3 and lines are evaluations of equation (2).

EQUILIBRIUM AND STABILITY OF TOKAMAK PLASMA WITH LIMITER CURRENTS

V.I. Belashov, N.N. Brevnov, Yu.V. Gribov, S.V. Putvinskii
I.V. Kurchatov Institute of Atomic Energy, Moscow, USSR

It is known that electric current passing between the top and bottom limiters influences plasma equilibrium in tokamak. In particular, this effect can be important for a fast compression along the major radius. Besides, it is interesting to use these limiter currents for the control over the discharge equilibrium in tokamak.

Theoretical and experimental investigations of the plasma equilibrium and stability with limiter currents are described. It is shown that in the case with toroidal axisymmetric limiters an additional force $f = -\frac{1}{c} I_l B_s 2d$ appears. Hence, the limiter currents influence both the plasma equilibrium and the plasma cross-section.

With the rail limiters new effects arise depending on the voltage polarity between the top and bottom limiters. For a certain voltage polarity and sufficient value of the limiter current the discharge loses its stability in the vertical direction. This instability appears in the T-13 tokamak as short pulses of the limiter currents ($J \leq 3 \kappa A$), without any effect on plasma parameters. In case of the opposite voltage polarity, the discharge is stabilized in the vertical direction, but the limiter currents $J \geq 60 A$ result in disruption. Possible explanations of the observed phenomena are discussed.

ENERGY CONFINEMENT IN T-13 TOKAMAK

A.V.Abramov, V.I.Belashov, A.V.Bortnikov,
N.N.Brevnov, S.N.Gerasimov

I.V.Kurchatov Institute of Atomic Energy, Moscow, USSR

At the tokamak T-13 has been studied the energy confinement of the electron component for Ohmic heating regime. Discharge parameters: plasma current J_p = 6... 30 kA, $\langle n_e \rangle = 3.10^{12} \ldots 2.10^{13} cm^{-3}$, $\langle T_e \rangle$ = 75... 110 eV, q_a=2.9...7.6, a = 7...7,5 cm, R = 40...76 cm, B_T = 0.45 ... 1T. All results of experiments correspond to linear dependence of τ_E from $\langle n_e \rangle$. Three type of regimes with different character of the energy confinement were found out. The discharge current value is the parameter that defines the type of regime. The dependence of $\hat{\tau}_E = \tau_E / \langle n \rangle = f(J_p)$, when magnitudes of q, a and R are fixed, has maximum at J_p = 8... 12 kA. If $J_p \simeq$ 6 kA and $J_p \gtrsim$ 17 kA value of $\hat{\tau}_E$ 2 - 3 time less than $\hat{\tau}_{E\,max}$. The dependence of τ_E from plasma discharge parameters coincides with alcator scailing ($\tau_E = 5\ 10^{-19}\ na^2 q^{1/2}$) if $J_p \simeq$ 6 kA and INTOR scailing equation supplementary multyplied at "q" ($\tau_E = 1{,}5\ 10^{19} \langle n \rangle a^2 q$) for $J_p \gtrsim$ 17 kA.

In these both cases $\hat{\tau}_E$ is independent from R.

For current discharge range J_p = 8... 12 kA, we observe maximum value which changes with major radius as R^2. Low level MGD activity is typical for this regime and experimental results may be described by T-13 scailing: $\tau_E = 10^{19} \langle n \rangle R^2 q^{1,3} B_T^{-0,33}$ [c, cm^{-3}, cm, G] , which if is satisfied dimensional analysis $\tau_E = \frac{3}{2} \frac{q R}{v_{Te}} \Pi_\varepsilon \frac{R}{a}$. $\Pi_\varepsilon = \pi a^2 e^2 \langle n \rangle / m_e c^2$ - dimensionless line density, v_{Te} - electron thermal velocity.

B

STELLARATORS

CONFINEMENT STUDIES OF NEUTRAL-BEAM-HEATED CURRENTLESS PLASMAS IN HELIOTRON E

Y.Takeiri, F.Sano, O.Motojima, M.Sato, S.Sudo, T.Mutoh, K.Akaishi, M.Nakasuga, K.Kondo, K.Hanatani, H.Zushi, H.Kaneko, T.Mizuuchi, H.Okada, N.Noda, R.Takahashi, M.Murakami*, H.C.Howe*, A.Iiyoshi, and K.Uo

Plasma Physics Laboratory, Kyoto University, Uji, Japan
*Oak Ridge National Laboratory, Oak Ridge, Tennessee, U.S.A.

ABSTRACT

The effects of the wall carbonization on plasma confinement are described for NBI currentless plasmas in Heliotron E. The wall carbonization (in-situ carbon coating) has been applied to suppress the radiative loss of high Z impurities. As a result, the intensity of iron emissions was reduced by more than an order of magnitude. After carbonization, quasi-steady plasmas with the volume-averaged beta value of about 2 % were maintained, and the gross energy confinement time became longer than that before carbonization. The improvement of the confinement time with carbonization is discussed.

I. Introduction

Heliotron E is a helical system characterized by a large rotational transform, a deep helical field ripple and a strong magnetic shear [1]. In the recent experiments of high-power plasma heating, the central-chord ion temperature (from neutral particle analysis) of more than 1.2 keV was achieved with NBI (at $\bar{n}_e \sim 2.5\times10^{13}\,cm^{-3}$) and 1.6 keV with ICRF (at $\bar{n}_e \sim 0.6\times10^{13}\,cm^{-3}$), and the central electron temperature (from Thomson scattering) of 1.4 keV with ECH (at $\bar{n}_e \sim 0.5\times10^{13}\,cm^{-3}$) was also obtained [2]. The NBI system consists of three nearly perpendicular (28°, 11° and 0°) beam lines with the total injection power of $\lesssim 4$ MW at the energy of 23-30 keV. The hydrogen neutral beams are injected into the target plasma initiated by ECH (53.2 GHz). Last year the wall carbonization was found to be effective in reducing an iron impurity, and, as a result, a high density and high β plasma was maintained in quasi-steady state. In this paper, the effects of the wall carbonization on MHD feature of high β plasmas and gross energy confinement time are discussed.

II. Carbonization and High β Experiment

The wall carbonization technique was applied in Heliotron E in order to suppress a radiation loss due to high Z impurities such as iron. The torus wall was carbonized with DC glow discharge with methane/hydrogen gas mixture at room temperature. The carbon coating rate was around 200 Å/hour and the film thickness was 300-500 Å. Titanium gettering was also performed after carbonization. Figure 1 shows typical time behaviour of $\bar{n}_e$(line-averaged electron density), P_{bol}(bolometer power) and intensity of FeXVI and FeIX in NBI heated plasmas at B_h=0.94T before and after carbonization. The electron temperature and density profiles before and after carbonization are also shown in the figure. After carbonization, the intensity of iron emissions was reduced by more than an order of magnitude in comparison with that before carbonization. The electron temperature and density profiles became broader than those before carbonization. Before

carbonization, in high β plasmas the bolometer power and the intensity of iron emission were gradually increased with time and, then, in many cases the plasma was not sustained for a long time. On the other hand, after carbonization, the gradual increase of the bolometer power and the intensity of iron emission were not observed and, as a result, a long-pulse operation of a high-density plasma became possible and the plasma internal energy was increased. The strong recycling on the carbonized wall due to the hydrogen atoms contained in the carbon film also contributed to sustainment of the high-density plasma, and the achievable density was increased up to $\bar{n}_e=1.8\times10^{14}$ cm^{-3} at $B_h=1.9$ T in operation with combination of gas and pellet fuelling. The recycling coefficient, which was estimated from the time-variation of the density, changed from more than 1.5 to nearly 1 in one shot. The total number of the plasma particles was estimated to be almost the same as the number of hydrogen particles absorbed in the top surface layer of the carbon film. Thus, at present, low density plasmas cannot be obtained due to the desorption of the absorbed hydrogen particles in the top surface layer.

Since the wall carbonization suppressed the radiative loss of high Z impurities that was the dominant loss channel for high β plasmas before carbonization [3], quasi-steady plasmas with the volume-averaged beta value $\langle\beta\rangle$ of about 2 % were maintained at $B_h=0.94$ T. Figure 2 shows the correlation of the cosine coil signals with the density-profile

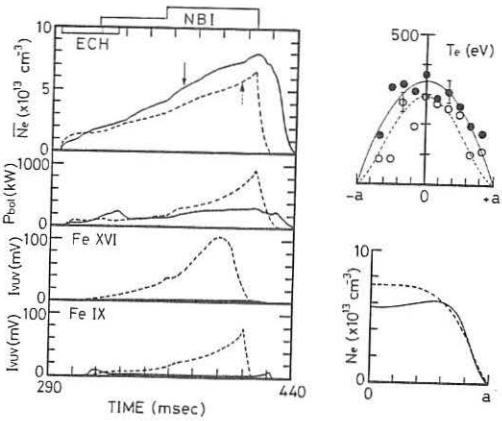

Fig.1 Typical time behaviour and the electron temperature and density profiles before (dotted lines or open circles) and after(solid lines or closed circles) carbonization. $B_h=0.94$T. The arrows indicate the timings when the profiles were measured.

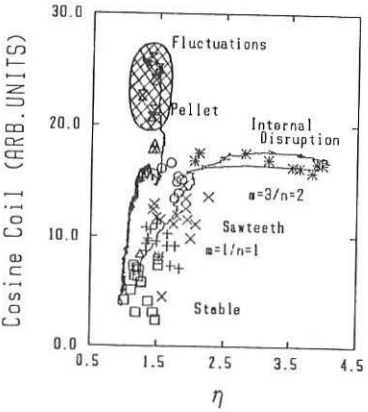

Fig.2 Correlation of the cosine coil signals with the density-profile peaking parameter η ($=\bar{n}_e$(center cord)/$\bar{n}_e$(peripheral cord)).

peaking parameter η (=$\overline{n_e}$(center cord)/$\overline{n_e}$(peripheral cord)) [4]. The cosine coil signal is observed to be proportional to $<\beta>$, and $n_e(r)$ becomes more peaked as η increases. The plasmas after carbonization are indicated by the hatched region in the figure. After carbonization, broad density profiles were easily achieved because of the strong recycling on the carbonized wall. Therefore, through the "stable pass" (Q pass) [5] without causing the pressure driven instability (m=1/n=1), $<\beta>$ was increased. However, fluctuations which appeared in the region of r/a > 0.8, were observed in the enhanced $<\beta>$ plasmas.

III. Confinement Scaling Study

The data analyses are performed with the ORNL-developed transport-analysis code, PROCTR [6] together with the PPPL-developed LOCUS database system [7] for scaling studies. Figure 3 shows the scaling of the gross energy confinement time τ_E^G derived from the profile analysis at B_h=1.9 T. τ_E^G is defined as $\tau_E^G = W_p$(plasma internal energy)/P_{heat}(plasma heating power). In this figure, the vertical axis indicates the experimental τ_E^G and the horizontal axis indicates the predicted τ_E^G with adjustment of the coefficient of the τ_E^G scaling ($\tau_E^G \propto P_{heat}^{-0.64}\,\overline{n}_e^{0.54}$) in ref. [2]. The τ_E^G after carbonization was improved by factor of about 1.3 compared with that before carbonization.

Next we address the question which is responsible for the improvement of confinement with carbonization, the electron or ion confinement. Generally the electron confinement time (defined as the ratio of the plasma-electron internal energy to the total electron-loss power including the radiation-loss power) tends to decrease compared with the ion confinement time (defined as the ratio of the plasma-ion internal energy to the total ion-loss power) as the heating power of NBI, P_{heat}, is increased. The carbonization is found to suppress this decrease of the electron confinement time. Figure 4 shows the electron-loss anomaly factor, defined as the ratio of the total electron loss (including the radiation loss) to the neo-classical electron loss (including helical ripple contribution) at r=2a/3, as a function of the line averaged density, $\overline{n}_e$. The bolometer power (used as the radiation power in the profile analysis),

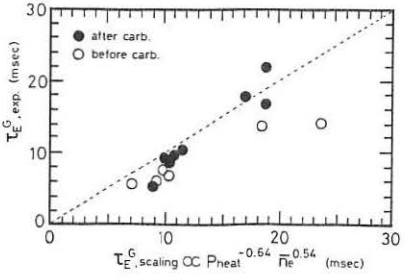

Fig.3 Scaling of the gross energy confinement time τ_E^G derived from the profile analysis at B_h=1.9 T.

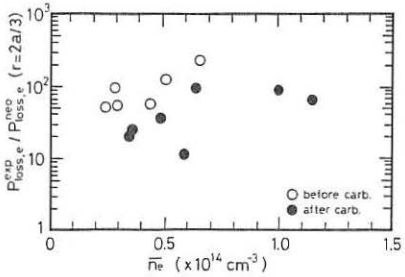

Fig.4 Electron-loss anomaly factor (including the radiation loss) at r=2a/3, as a function of $\overline{n}_e$.

which seems to increase with an increase in the injection power, was observed to decrease after carbonization. As shown in Fig.4, the electron-loss anomaly factor before carbonization was higher than that after carbonization. On the contrary, at r=a/3 the electron-loss anomaly factor was almost unchanged between before and after carbonization. This result is considered to correspond to the broader profile of the electron temperature after carbonization, as shown in Fig.1. Therefore, the electron internal energy at the plasma periphery (r=2a/3) was increased with carbonization. As a result, the electron confinement time was improved and the gross energy confinement time τ_E^{Δ} became longer after carbonization than that before carbonization. At the low field (B_h=0.94T), the similar analyses show the reduction of the electron-loss anomaly factor at the plasma periphery (r=2a/3), although the operational space was rather narrower. The reduction of the radiation loss with carbonization is considered to be responsible for the decrease of the electron-loss anomaly factor (including the radiation loss) at the plasma periphery (r=2a/3) after carbonization.

VI. Summary

We have described the effect of the wall carbonization on plasma confinement in neutral-beam heated currentless plasmas. The wall carbonization in Heliotron E was effective for improving the gross energy confinement time and obtaining high pressure plasmas. As a result, the quasi-steady plasmas with the volume-averaged beta value of about 2 % were sustained. However, low density plasmas were not realized at present due to the strong recycling. The profile analysis showed that the improvement of the gross energy confinement time with carbonization was ascribed mainly to the reduction of the radiation loss.

Acknowledgements

The wall carbonization was performed as a collaborational work with the following groups ; the research group of Prof. Yamashina, Hokkaido Univ., the group of Dr. Sakamoto, the Institute of Physical and Chemical Research, and Profs. Amemiya and Sugai, Nagoya Univ.. This collaboration was supported by a Grant-in-Aid for Science Research from the Ministry of Education, Science and Culture in Japan.

References

[1] K.Uo, A.Iiyoshi, T.Obiki, et al., in Plasma Physics and Controlled Nuclear Fusion Research 1980 (Proc. 8th Int. Conf. Brussels, 1980), Vol.1, IAEA, Vienna (1981) 217.
[2] K.Uo, A.Iiyoshi, T.Obiki, et al., in Plasma Physics and Controlled Nuclear Fusion Research 1986 (Proc. 11th Int. Conf. Kyoto, 1986), IAEA-CN-47/C-I-1.
[3] F.Sano, T.Obiki, O.Motojima, et al., Nucl. Fusion **26** (1986) 473.
[4] H.Zushi, O.Motojima, M.Wakatani, et al., Nucl. Fusion, to be published.
[5] O.Motojima, F.Sano, M.Sato, et al., Nucl. Fusion **25** (1985) 1783.
[6] H.C.Howe, "Physics Models in the Toroidal Transport Code PROCTR", ORNL/TM-Draft (1987).
[7] J.A.Murphy, "The LOCUS Data base System ISAM Version 4.0", PPPL-TM-364-R (1986).

LOW-ASPECT-RATIO TORSATRON REACTOR AND ATF-II STUDIES*

J. F. Lyon, B. A. Carreras, S. L. Painter and J. S. Tolliver, Oak Ridge National Laboratory; and I. N. Sviatoslavsky, University of Wisconsin, Madison

ORNL studies of stellarator reactors and of a large next-generation stellarator experiment (ATF-II) are focused on low-aspect-ratio $\ell = 2$ torsatrons. The most developed reactor concepts studied elsewhere have R = 20-25 m with plasma aspect ratio $A = R/\bar{a} \geq 12$ and coil aspect ratio R/r_{coil} = 4.4-6.6. We have studied stellarator reactors one-half to one-third this size in order to extend the options available for an attractive reactor. The reactor cases found have R = 8-11 m with $R/\bar{a}$ = 3.9-7.8 and R/r_{coil} = 2.5-4.5. The potential advantages of a more compact reactor are: smaller size, weight and cost; smaller size of components; better access for fabrication, assembly and maintenance; and higher power density. The main physics concerns are electron transport at low collisionality and equilibrium beta limits, which can only be resolved by experiment.

The magnetic configurations were chosen to be similar to that of ATF with a magnetic well and $\iota(0) \simeq 0.35$, $\iota(\bar{a}) \simeq 0.95$ because this allows high $\langle\beta\rangle$ and operation in the second stability region. The three coil configurations studied are shown in Fig. 1. The increasing distance between the coils for plasma and maintenance access as R/r_{coil} is decreased is evident in the figure. Cases 1, 2 and 3 have m (number of field periods) = 12, 9 and 6; R/r_{coil} = 4.49, 3.24 and 2.50; $R/\bar{a}$ = 7.78, 4.66 and 3.87; and $\delta = R/\Delta$ = 9.50, 8.64 and 6.62, respectively, where Δ is the plasma edge to coil center distance.

Configuration Studies. At low aspect ratio, beta limits are expected to be set by equilibrium limits and fragility of flux surfaces rather than by stability limits. The conventional wisdom indicates a critical beta value $\beta_c \propto A$ since $\beta_c \propto \iota^2/A$ and $\iota \propto A$. However, our calculations using the stellarator expansion and constant helical pitch show that β_c only varies from 0.15 to 0.21 as ι^2/A varies from 0.11 to 0.5.

The most important issue relating to the equilibrium beta limit at low A is the fragility of the magnetic surfaces. The method of Cary and Hanson has been used to determine the winding law for the HF coil which gives the largest plasma radius for the $m = 6$ and $m = 9$ cases. The resulting winding laws, $\phi = (\ell/m)(\theta - \alpha \sin\theta) + \sum \beta_n \sin(n\theta)$ where the modulation α is the dominant term ($\alpha \sim 1/2$), have approximately constant pitch in a toroidal coordinate system. Combining an outward shift of the magnetic axis with the HF coil optimization for the $m = 6$ case leads to configurations ranging from $A = 3.4$ for $\iota_a = 0.88$ and $\alpha = 0.795$ to $A = 3.7$ for $\iota_a = 0.94$ and $\alpha = 0.446$. A similar optimization has been performed by distributing currents in a poloidal field coil set. The effect of shaping the cross section of the torus on which the HF coils are wound has also been studied and is found to be similar to that caused by changing the HF coil winding law.

Equilibrium beta limit calculations have been performed using the stellarator expansion method and the more accurate 3-D VMEC and NEAR codes for the $m = 6$ configuration. The stellarator expansion calculations assuming flux conservation give

equilibrium beta limits $\langle\beta\rangle \simeq 5$–$7\%$, depending on the pressure profile. The 3-D calculations with approximate flux conservation indicate a higher equilibrium beta limit, $\langle\beta\rangle \simeq 10\%$, based on the increase of the toroidal shift with beta.

Transport Studies. A major concern for low A torsatrons is the scaling of electron transport losses in the $1/\nu$ regime where $\chi_e \propto \epsilon_h^{3/2}\epsilon_T^2 \propto 1/A^2$. WHIST 1-D transport code calculations have been performed for the $m = 6$, 9, and 12 cases for a variety of assumptions to study these losses and their sensitivity to various parameters. The transport calculations assume the electric-field-dependent neoclassical model for ripple-induced losses formulated by Shaing for ions and electrons, the Hinton-Hazeltine value for axisymmetric neoclassical transport multiplied by two for ions and twenty for electrons, and twice the neo-Alcator anomalous transport value for electrons. Fixed radial profiles for the plasma density and electric field are assumed because of the large uncertainties in particle transport and in the self-consistent radial electric field.

Figure 2 shows the results for an $m = 9$ case where contours of constant auxiliary power input, fusion power produced, and volume-averaged beta are plotted in a $\langle n\rangle - \langle T\rangle$ plane. Here $\langle n\rangle$ is the volume-averaged electron density and $\langle T\rangle$ is the density-averaged mean plasma temperature. This reference case assumes: D-T plasma, $R = 10.25$ m, $\bar{a} = 2.2$ m, $B = 5$ T, Gaussian external power deposition profile $e^{-(r/b)^2}$ with $b = \bar{a}/2$ and a fraction $f_i = 0.7$ to the ions, a potential profile $\phi = \phi_0[1 - (r/a)^p]$ with $p = 2$ and $\phi_0 = 2\,T_i(0)$, and density profiles $n \propto [1 - f(r/a)^2]^q$ with $f = 0.9$ and $q = 2$. The light lines indicate auxiliary heating powers ranging from 200 MW to 0 (the heavy ignition line), the dark lines indicate the thermal runaway contour (to the right of which $\partial P/\partial T < 0$) and the 4000 MW fusion power (1200 MW electric power) contour, and the dashed lines indicate contours of constant $\langle\beta\rangle$. A path to a 4 GW operating point at $\langle n_e\rangle = 2 \times 10^{14}\ cm^{-3}$ requiring $\simeq$ 30 MW auxiliary heating is indicated by the dotted curve. At the operating point shown, $T_i(0) = 10.4$ keV, $T_e(0) = 11.1$ keV, $\langle T\rangle = 9.4$ keV, $\langle\beta\rangle = 6.3\%$, and $n\tau = 3 \times 10^{14}\ cm^{-3}$ s. Compared to the reference $R = 10.25$-m $m = 9$ case, the $R = 8.01$-m $m = 6$ case requires about the same power for ignition but achieves it at a higher value of temperature and beta, whereas the $R = 11.02$-m $m = 12$ case requires about half the power to reach ignition but again at a higher value of temperature and beta.

Sensitivities to the parameters R, $\bar{a}$, B, b, f_i, $\phi_0/T_i(0)$, p, f and q have been studied in detail for the $m = 9$ case. For the base case ignition occurs at $\langle T\rangle = 10.1$ keV for $\langle n\rangle = 10^{14}$ cm^{-3} and $\langle T\rangle = 7.1$ keV for $\langle n\rangle = 2 \times 10^{14}$ cm^{-3}. Ignition does not occur, or only at higher densities with large auxiliary heating powers, if the potential if zero or the density profile is broad ($q \lesssim 3/2$). Less margin for ignition occurs if the field is reduced ($B = 3.5$ T), the edge density is increased ($f = 0.8$), ϕ is linear in r ($p = 1$), or all the auxiliary power goes to the electrons ($f_i = 0$). The ignition margin is increased if the density profile is more peaked, the field is increased ($B = 7$ T), the potential is increased ($\phi_o/T_i(0) = 5$) or is broader ($p = 4$), the edge density is reduced ($f = 0.95$), or the reactor is larger (by 25%). There is little effect if the auxiliary heating profile shape changes ($b = \bar{a}$ or $\bar{a}/4$) or all the power goes to the ions ($f_i = 1$).

Engineering Feasibility Studies. The minimum size for $m = 6$, 9, and 12 reactors is determined by constraints on plasma-wall separation, coil shielding requirement and material, dewar and coil case thickness, and current density and elongation for thehelical field coils. The largest reduction in reactor size results from two measures under the inboard (small R) portion of the helical field coils: the use of tungsten rather than stainless steel for coil shielding and the elimination of the tritium breeding blanket at these locations. The minimum size is given by $R = 0.25\delta^2[\epsilon + (\epsilon^2 + 4x/\delta)^{1/2}]^2$ where $\epsilon = [\pi B_o/2\mu_o mj(w_{coil}/d_{coil})]^{1/2}$ and x is the constant plasma edge to coil edge distance, most of which is due to coil shielding. Assuming $B_o = 5$ T, $w_{coil}/d_{coil} = 2$, $j = 5$ kA/cm^2 and $x = 0.92$ m (2% cooling power for coils, 3×10^{10} rads/30 years, and 8 year coil anneal) gives $R = 11.02$ m, 10.25 m and 8.01 m, with $\bar{a} = 1.42$ m, 2.20 m and 2.07 m, for the three cases. Increasing the coil shielding by a factor of 10 only adds 0.98 m to R for the $m = 9$ case. Decreasing j to 3.5 kA/cm^2 only adds 0.52 m to R for this case.

An engineering analysis gives the following parameters: neutron wall loading of 3.40 MW/m^2, 2.42 MW/m^2 and 2.85 MW/m^2; reactor core mass of 8,444 tonnes, 10,683 tonnes and 9,160 tonnes; net electrical output (assuming 36% electrical efficiency and 1.58 blanket energy multiplication factor) of 5.90 GW, 5.85 GW and 5.86 GW; and a mass utilization factor (kW$_{elect.}$/tonne) of 251, 197 and 230, respectively, for the $m = 12$, 9 and 6 cases for 4 GW fusion power. This study indicates that all three cases look attractive as reactors and that there is margin to relax some of the constraints.

Figure 3 shows a sketch of a reactor cross section for the intermediate ($m = 9$) case with $R = 10.25$ m. As presently envisaged the reactor would be contained in an evacuated toroidal enclosure which has fixed vertical walls and rotatable lids with hatches. The HF coils, shield, blanket, etc. are supported on the massive fixed cylindrical vertical sides. The coils are supported at the outer midplane perimeters by cold/warm struts which are flexible enough to make allowance for expansion and contraction. Service lines all penetrate the vacuum chamber through the side walls and are recessed out of the way for vertical extraction of blanket modules. During maintenance periods, the lids are unsealed and rotated about the reactor axis such that the access hatch indexes over the area to be maintained. To remove a blanket segment, vertical motion has to be accompanied by rotation in order to extract the segment from between the coils.

ATF-II Studies. There are many more options available for an ATF-II (H vs D vs D-T operation, copper vs superconducting coils, pulsed vs steady-state operation, physics goals, etc.) than for a reactor. D-T versions of an ATF-II have been studied using the WHIST transport code and show similar results to that for the larger (reactor) cases. For example, a copper-coil $m = 9$ D-T burner with $R = 4$ m and $B = 5$ T requires $\simeq$ 10 MW of auxiliary heating power to reach ignition at $\langle T \rangle \simeq 20$ keV where $\simeq$ 100 MW of fusion power is produced at $\langle n \rangle = 5 \times 10^{13}$ cm^{-3}.

*Research sponsored by the Office of Fusion Energy, U.S. Department of Energy, under Contract No. DE-AC05-84OR21400 with Martin Marietta Energy Systems, Inc.

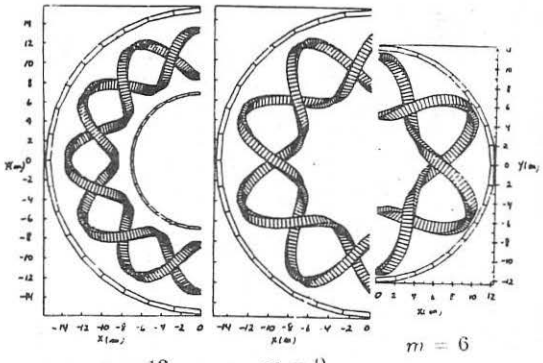

Fig. 1. $m = 12$, 9 and 6 torsatron coils sets.

Fig. 2. Contours of input power, fusion power and $\langle\beta$ for $m = 9$ R =10.25-m reactor.

Fig. 3. Cross section of $m = 9$ R =10.25-m reactor.

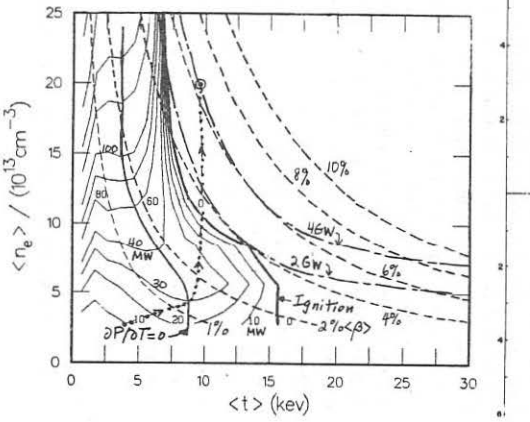

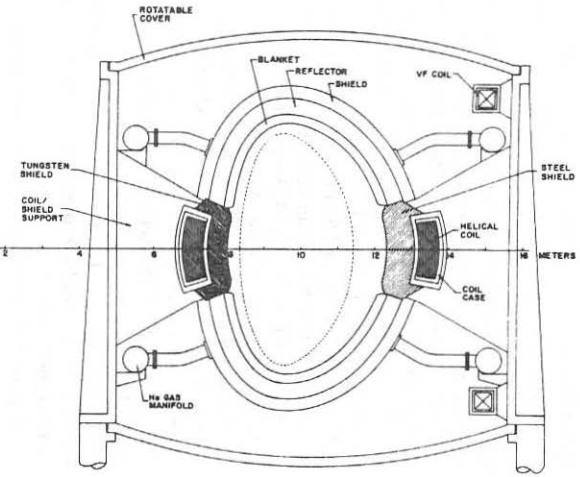

STATUS OF THE ATF TORSATRON PROGRAM

J. F. Lyon, B. A. Carreras, T. C. Jernigan, R. L. Johnson, M. Murakami and G. H. Neilson representing the ATF design, construction, and operating groups.

Oak Ridge National Laboratory

The ATF torsatron (1) will be the world's largest stellarator when it starts operation in the Fall of 1987 and the first large device of this type in the U.S. since the Model C Stellarator shut down in 1969. A sketch of ATF is shown in Fig. 1. The ATF device and plasma parameters are: R = 2.1 m, r_{coil} = 0.46 m, $\bar{a}$ = 0.3 m ($R/\bar{a}$ = 7), V_{pl} = 3.7 m^3, and B_o = 2 T for a 5-s pulse and 1 T steady state. ATF has 10 m^2 of port area, including twelve 0.6 × 0.9 m ports, for heating and diagnostic access. The standard magnetic configuration characteristics are: ℓ = 2, m = 12, $\iota(0)$ = 0.35, $\iota(\bar{a})$ = 0.95, and 0.7% vacuum magnetic well depth. The helical field coil set was optimized to permit direct access to the second stability region and has the potential for stable volume-average $\langle\beta\rangle \gtrsim 8\%$. The two helical field (HF) windings and the three poloidal field (PF) coil sets allow study of a large variety of stellarator configurations including those with helical and bifurcated magnetic axes. Magnetic configuration parameters can be varied over a wide range: $\iota(0)$ from 0 to 0.5, $\iota(\bar{a})$ from 0.8 to 1.2, $\Delta\iota/\bar{\iota}$ from 0.65 to 2, $\Delta V'/V'$ from 5.2% well to ~ 20% hill, and $r_{\text{helical}}/\bar{a}$ from 0 to 0.75.

The ATF program studies include: scaling of beta limits and plasma behavior in the second stability regime; transport scaling at low collisionality and the role of the ambipolar electric field; control of plasma density and impurities with pump limiters/divertors and pellet fueling; plasma heating with NBI, ECH and ICH, magnetic configuration optimization; and long-pulse to steady-state operation. High power heating is being provided to meet these objectives: 3-4.5 MW, 0.3-s, 40-kV H° NBI; 0.4-MW cw ECH at 53.2 GHz; and 2 MW cw ICH at 5-30 MHz.

ATF performance can be estimated from scaling laws derived from Heliotron-E data by the LHS design team. The LHS scaling laws (2) used are $\tau_{1E}(s) = 0.21\bar{n}_e(10^{14}\ \text{cm}^{-3})^{0.66}B_o(T)^{0.53}P(\text{MW})^{-0.53}a(m)^2R(m)$ and $\tau_{2E}(s) = 0.17(\bar{n}_e)^{0.69}B_o^{0.89}P^{-0.58}a^2R^{0.75}$. The estimates for B_o = 1.9 T, P = 4 MW and high density ($\bar{n}_e = 2 \times 10^{14}$ cm^{-3}) are τ_E = 34-42 ms, $n\tau_E$ = 1-1.3 × 10^{13} cm^{-3} s, and T_o = 1.7-2.1 keV for parabolic profiles. Higher temperatures are obtained at low density ($\bar{n}_e = 2 \times 10^{13}$ cm^{-3}): T_o = 3.5-4.7 keV. High $\langle\beta\rangle$ is obtained at high

$\bar{n}_e(2 \times 10^{14}\ \mathrm{cm}^{-3})$ and low B_o: $\langle\beta\rangle$ – 3.7-5.8% for $B_o = 1$ T and 7.5-14.9% for $B_o = 0.5$ T.

The physical mechanisms behind the LHS scaling laws need to be clarified. There are uncertainties in the power deposition for near-perpendicular neutral beam injection for fast ion orbit losses and in the size scaling, and the confinement could be affected by resistive ∇p-driven turbulence, magnetic braiding due to error fields, low-m, n MHD activity, impurities, and electric fields. These mechanisms may be different in ATF: ATF has tangential NBI and larger $\bar{a}$ with larger plasma-wall separation; theory predicts that the beta self-stabilization mechanism in ATF should stabilize low-m, n MHD activity and reduce resistive ∇p-driven turbulence so that confinement may improve with increasing β; and control of impurities and electric fields may differ in ATF. WHIST 1-D transport code calculations have also been done using the Shaing neoclassical electric-field-dependent ripple transport model for ions and electrons, Hinton-Hazeltine axisymmetric neoclassical transport (with multipliers of 2 and 20 for the ions and electrons, respectively), and a Neo-Alcator anomalous χ_e. The 1-D transport code results depend sensitively on how the density profile and the electric field are determined. The WHIST predictions are generally higher (up to a factor of 2-3) than the LHS scaling would indicate for both fixed density and potential profiles or profiles determined by the ambipolarity condition.

The two helical field coils shown in Fig. 1 each consist of 12 identical segments (180° in poloidal extent) connected by bolted joints and supported independently of the vacuum vessel. This allows parallel fabrication and testing of the ATF components: the HF segments, the PF coils, the structural shell segments, all of which were successfully manufactured to the required high accuracy ($\sim 0.1\%$), and the less critical, helically contoured, thin (6 mm) vacuum vessel, which had some problems. Anomalous shrinkage in the $\sim$ 1 km length of welds connecting the $\simeq$ 1200 shaped pieces composing the vacuum vessel led to too small a major radius and a long repair process, now successfully completed. Completion of the ATF construction is expected in July 1987 and first plasma operation at 1 T with 0.2 MW ECH in September 1987.

A tentative program plan for the first two years is shown in Fig. 2. The Phase I operating periods (I-A and I-B) are aimed at commissioning the facility and establishing the basic capabilities needed for the main program. The first experimental plasma will be produced with ECH at the second harmonic ($B_0 = 0.95$ T). A brief target plasma phase (I-A) has been planned to permit a preliminary characterization

of the ECH plasmas. Between Phases I-A and I-B, many of the basic confinement diagnostics will be installed, and magnetic surface mapping studies will be carried out in order to verify the accuracy of the ATF magnetic configuration. Neutral beam heating will be initiated in Phase I-B. Two tangential beam systems, one co- and one counter-, will be commissioned in this period. Physics objectives include initial assessments of global confinement properties with high-power heating and of currents and momenta resulting from balanced and unbalanced tangential injection. With the machine, heating, diagnostic, and analysis capabilities in place, more detailed studies will begin in Phase II, starting in early 1988.

*Research sponsored by the Office of Fusion Energy, U.S. Department of Energy, under Contract No. DE-AC05-84OR21400 with Martin Marietta Energy Systems, Inc.

REFERENCES

1. J. F. Lyon, B. A. Carreras, K. K. Chipley, M. J. Cole, et al., Fusion Technol., 10, 179(1986).
2. LHS design team, private communication (1987).

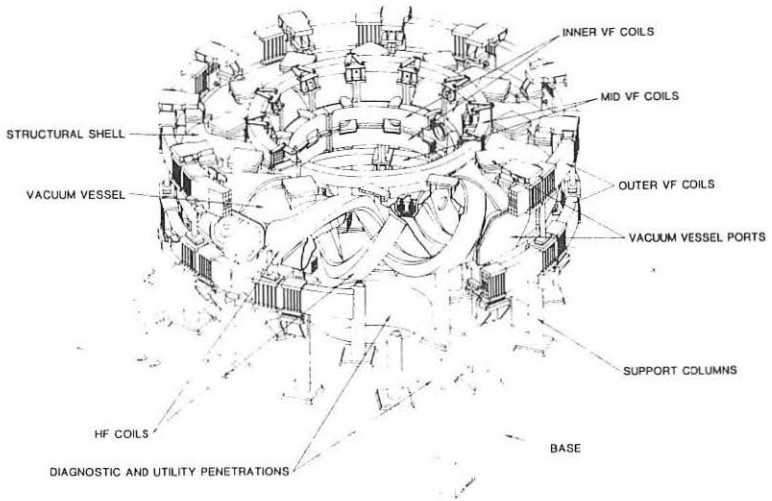

Fig. 1. Sketch of the ATF torsatron

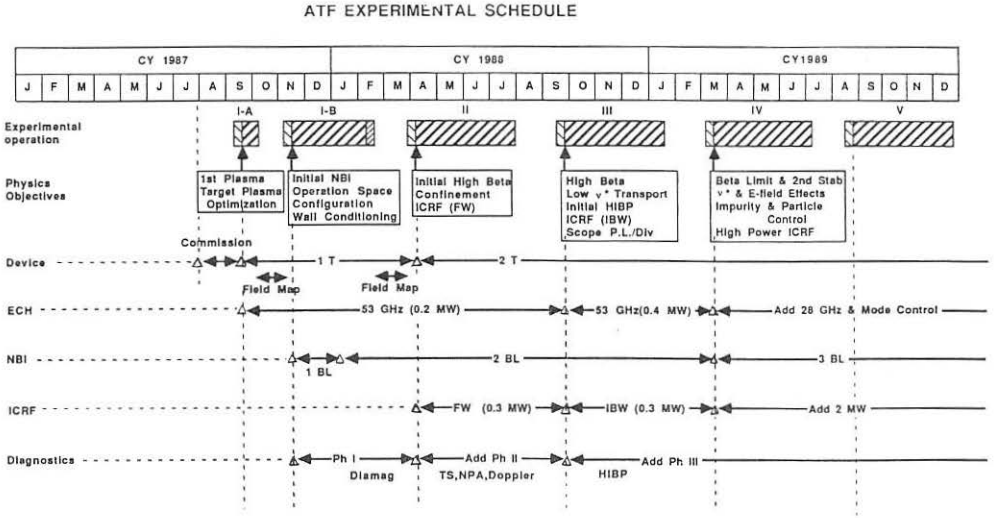
ATF EXPERIMENTAL SCHEDULE
CY 1987
CY 1988
CY1989
J F M A M J J A S O N D J F M A M J J A S O N D J F M A M J J A S O N D
I-A
I-B
II
III
IV
V
Experimental operation
Physics Objectives
1st Plasma Target Plasma Optimization
Initial NBI Operation Space Configuration Wall Conditioning
Initial High Beta Confinement ICRF (FW)
High Beta Low ν* Transport Initial HIBP ICRF (IBW) Scope P.L./Div
Beta Limit & 2nd Stab ν* & E-field Effects Impurity & Particle Control High Power ICRF
Commission
Device
1 T
2 T
Field Map
Field Map
ECH
53 GHz (0.2 MW)
53 GHz(0.4 MW)
Add 28 GHz & Mode Control
NBI
2 BL
3 BL
1 BL
ICRF
FW (0.3 MW)
IBW (0.3 MW)
Add 2 MW
Diagnostics
Ph I
Add Ph II
Add Ph III
Diamag
TS,NPA,Doppler
HIBP

Fig. 2.

A UNIFIED THEORY OF RIPPLE TRANSPORT IN STELLARATORS, AND A SELF-CONSISTENT CALCULATION OF STELLARATOR TRANSPORT.

W. N. G. Hitchon, C. D. Beidler, W. D. D'Haeseleer and J. L. Shohet

Torsatron/Stellarator Laboratory
University of Wisconsin-Madison
Madison, Wisconsin 53706 U.S.A.

I. Ripple Transport

An expression for the transport due to particles trapping and detrapping in the stellarator field

$$B = B_o\,(1 + \varepsilon_t(r)\,\cos\theta - \varepsilon_h(r)\,\cos(\ell\theta + p\phi))$$

which is valid for all low collision frequencies (not just in some asymptotic limit) has been obtained by power series solution of the bounce-averaged kinetic equation

$$-\Omega_E \frac{\partial f}{\partial \theta} + v_d \sin\theta \frac{\partial F_M}{\partial r} = \frac{\nu}{2\varepsilon_h} \frac{1}{A'(k^2)} \frac{\partial}{\partial k^2} A(k^2) \frac{\partial f}{\partial k^2} \qquad (1)$$

for f, the perturbed portion of the distribution function. In the above equations, $\varepsilon_t(\varepsilon_h)$ is the magnitude of the toroidal (helical) magnetic field ripple, Ω_E is the poloidal precessional frequency due to the $\vec{E} \times \vec{B}$ drift, v_d is the ∇B drift velocity, ν is the ninety-degree deflection frequency and k^2 is a particle's pitch-angle variable defined by

$$k^2 = \frac{\kappa/\mu B_o - 1 - \varepsilon_t \cos\theta + \varepsilon_h}{2\varepsilon_h} \qquad (2)$$

with κ the kinetic energy of the particle and μ its magnetic moment. Particles trapped in local helical ripple wells satisfy $0 < k^2 < 1$. The expressions $A(k^2)$ and $A'(k^2)$ represent functions of complete elliptic integrals which have k^2 as their argument. In particular $A(k^2) = E(k)-(1-k^2)\,K(k)$ and $A'(k^2) = dA/dk^2$, where K(E) is the complete elliptic integral of the first (second) kind.

The method of solution for the kinetic equation begins by assuming that the perturbed portion of the distribution function may be written

$$f = \left(\frac{\partial F_M}{\partial r}\right)\,(X(k^2)\,\cos\theta + Y(k^2)\,\sin\theta)\ . \qquad (3)$$

Given this assumption, the kinetic equation separates into a pair of coupled, partial differential equations. It is further assumed that X and Y may be expanded as power series in k^2, $X = \sum_{n=0}^{\infty} X_n (k^2)^n$ and $Y = \sum_{n=0}^{\infty} Y_n (k^2)^n$ and that $A(k^2)/A'(k^2) \simeq k^2$. The solution is given by

$$X(k^2) = X_o h - Y_o g - v_d/\Omega_E \qquad (4)$$

$$Y(k^2) = Y_o h + X_o g$$

where

$$h = \sum_{n=0}^{\infty} (-1)^n \left[\left(\frac{k^2}{\hat{\nu}}\right)^n \frac{1}{(2n)!}\right]^2$$

$$g = \frac{k^2}{\hat{\nu}} \sum_{n=0}^{\infty} (-1)^n \left[\left(\frac{k^2}{\hat{\nu}}\right)^n \frac{1}{(2n+1)!}\right]^2 \qquad (5)$$

with $\hat{\nu} \equiv \nu/2\epsilon_h\Omega_E$.

To complete the solution, boundary conditions at $k^2 = 1$ (the interface between locally trapped particles and those particles which are not ripple trapped) must be applied to obtain X_o and Y_o. To do so, one passes to the collisionless limit, where $\partial f/\partial k^2(k^2 = 1^+)$ may be written $(-\partial f/\partial\theta)(\partial k^2/\partial\theta)^{-1}$. This expression is then evaluated at $\theta = \pi$ since particles detrapping on the outside of the device retrap almost immediately, due to the very short length of their toroidally blocked orbits, and hence are the most collisionless. This, as well as symmetry considerations, requires that $Y(k^2 = 1) = 0$. Calculating $\partial f/\partial k^2(k^2 = 1^-, \theta = \pi)$ and requiring continuity of the derivative of f at this point yields a second boundary condition, $\partial X/\partial k^2(k^2 = 1) = -2\epsilon_h X(k^2 = 1)/\epsilon_t$, allowing one to obtain X_o and Y_o and thereby complete the solution.

To test the validity of this solution, particle diffusion coefficients were obtained by the appropriate numerical integration of f and compared with results obtained computationally from (1) a "hybrid" bounce-averaged guiding center Monte-Carlo numerical simulation, and (2) a numerical Drift Kinetic Equation Solver (DKES). These results are shown in Figure 1. Solid lines represent the ripple contribution as obtained by applying the results of the series solution outlined in this work and the purely axisymmetric portion obtained from an expression of Rosenbluth, Hazeltine and Hinton. The dashed line is the sum of the two solid lines. Open circles enclosing plusses and open, empty circles denote Monte-Carlo numerical points for $E_r > 0$ and $E_r < 0$, respectively. Solid circles denote DKES numerical points (the formulation of DKES, like the formulation of the analytic theory, does not differentiate between the signs of the radial electric field). The insert shows the magnitude of B along a field line. It is evident from the figure that the agreement is excellent between the analytic prediction and the numerical data points.

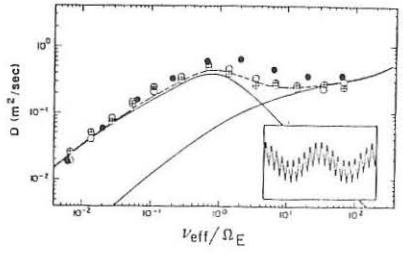

II. Self Consistent Transport

The goal of this research is the self-consistent computation of interesting "observables" such as transport fluxes, parallel flows, Pfirsch-Schluter and bootstrap currents and the ambipolar electric field, in the low collision frequency regimes in stellarators. We are solving the problem numerically and utilize ideas employed in a bounce-averaged transport study done by Mynick and Hitchon, (M/H) and concepts based on the moment formalism developed by Hirshman. The moment approach points out the importance of the "parallel viscous force density" $\langle \underline{B} \cdot \underline{\nabla} \cdot \underline{\underline{\pi}} \rangle$ in that it is the quantity that gives rise to the bootstrap current and the so-called "axisymmetric flux". In order to find $\langle \underline{B} \cdot \underline{\nabla} \cdot \underline{\underline{\pi}} \rangle$, two important requirements must be satisfied: the collision operator must be momentum conserving and the distribution function must have the correct variation along a field line. The first point necessitates adjustment of the collision operator in the M/H code, which uses a Lorentz operator. For non-helically trapped particles momentum balancing terms in C must be added. This requires non-trivial adjustments in the MH code. (The DKES code developed by Hirshman et al., computes the parallel viscosity only approximately, for the same reason. The error introduced by using only a Lorentz operator is of the order of f_T, the fraction of trapped particles. Since $f_T \sim \sqrt{2\varepsilon}$ and $\varepsilon \sim 0.1$, this might not be negligible. Both codes, M/H and DKES, find the distribution function in stellarators. Both codes should be considered as complementary because each makes certain approximations to make the computation numerically tractable.) The issue of variation along the field line of the distribution function requires interpretation. The bounce-averaged output $\bar{f}$ of the M/H treatment is averaged over the helical ripples, but not over the "tokamak-like" variation of the B-field. The equation solved for toroidally blocked and passing particles is the same as that in a tokamak. It is important to recognize however that the boundary conditions are totally different: collisional and collisionless en- and detrapping are properly included. There is a continuous flow in phase space across the trapping boundary $k^2 = 1$ (k^2 is the ripple-depth parameter). Hence this $\bar{f}$ does contain important parts of $\langle \underline{B} \cdot \underline{\nabla} \cdot \underline{\underline{\pi}} \rangle$, if not all of them (given that $C(f)$ is momentum conserving). The direct contribution to the viscosity of the ripple trapped particles (and the helical ripple induced perturbation on the "tokamak-like" blocked particles) is evidently not included. Its importance is expected to be small, but examination of this issue is called for.

To find the higher order corrections to $\langle \underline{B} \cdot \underline{\nabla} \cdot \underline{\underline{\pi}} \rangle$, we use the bounce-averaged $\bar{f}$ to calculate the non-bounce averaged $\tilde{f}$ which does include the mod-B ripple variations along a fieldline. We set $f = \bar{f} + \tilde{f}$, where $\tilde{f} \ll \bar{f}$ since $\tilde{f} \sim v_{dr} F'_M / \nu_{eff}$ or $\sim v_{dr} F'_M / \omega_\theta$ which is the width of a "superbanana", whereas $\tilde{f} \sim v_{dr} F_{M'} \tau_b$ being the width of a small helical banana. The equation for the non-bounce-averaged $\tilde{f}$ follows from subtracting the bounce-averaged equation from the total one. For ripple trapped

particles this leads to

$$v_{\|} \frac{\partial \tilde{f}}{\partial \ell} + \tilde{v}_{dr} F'_M + \tilde{\omega}_\theta \frac{\partial \bar{f}}{\partial \theta} = \tilde{\bar{C}}(f) \ . \tag{6}$$

In this equation $\bar{f}$ is known, and smaller terms like $\bar{\omega}_\theta \, \partial \tilde{f}/\partial\theta$, $\bar{C}(\tilde{f})$ and $\tilde{C}(f)_{nba}$ have been neglected as a first approximation. $C(f)$ consists of a Lorentz part $\tilde{C}_L(f)$ and two momentum balancing parts going like $v_{\|}$ and which we represent by

$$v_{\|}(V(v) + R(v)) \ . \tag{7}$$

The first order correction for the viscosity is

$$\begin{aligned} \langle \underline{B} \cdot \underline{\nabla} \cdot \underline{\underline{\pi}} \rangle_{\sim} &\equiv \langle B \int d^3v \ mv_{\|} [v_{\|} \frac{\partial \tilde{f}}{\partial \ell}] \rangle \\ &= \langle B \int d^3v \ mv_{\|}^2 (U(v) + R(v)) \rangle \end{aligned} \tag{8}$$

Yet higher corrections can be found by reiterating the part of $\tilde{f}$ that comes from the $\tilde{v}_{dr} F'_M$, $\tilde{\omega}_\theta \, \partial f/\partial\theta$ and $\tilde{C}_L(f)$ terms. To find the contribution of the passing particles a similar equation to (6) must be considered.

At present the numerical work is being implemented. First adjustments to the M/H code have been made. The present code uses poloidal flows of forward and backwards moving particles which differ somewhat from the free streaming part (as it should physically). The resulting distribution is shown in Fig. 2.

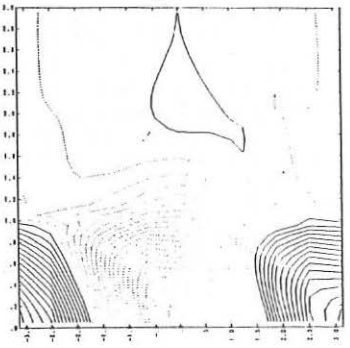

Figure 2
Constant f contours in the k^2 θ phase space.

* This work was supported by the DOE Grant Nos. DE-FG02-86ER53201 and DE-FG02-86ER53216.A000 and ORNL Grant No. 19X27434C.

VERTICAL FIELD AND DIVERTOR EXPERIMENTS IN THE IMS STELLARATOR *

D.T. ANDERSON, F.S.B. ANDERSON, R.P. DOERNER, P.H. PROBERT,
J.L. SHOHET, C.A. STORLIE, J.N. TALMADGE AND P. K. TROST

Torsatron/Stellarator Laboratory
University of Wisconsin-Madison
Madison, Wisconsin 53706 U.S.A.

Introduction

IMS is a modular, seven field period, ℓ=3 stellarator which has operated to date at a central magnetic field of 2.6 kG (B_{max} = 6 kG). A 7.27 GHz ECRF source of 3 kW is used to create and sustain the plasma for up to 10 ms duration. Plasma density profiles are characterized by hollow profiles over a wide range of plasma and operating parameters. Recent experimental and theoretical efforts have centered upon understanding variations in the plasma profiles, modular divertor structure and particle flux, and fluctuation levels, as a function of applied vertical magnetic field strength. Attainable vertical magnetic field strengths introduce a magnetic well into the central regions of the device, but are not sufficient to create a well at the q=2 surface near the separatrix of the device. Global plasma parameters ($T_e \sim 10$-12 eV, $T_i \sim 5$ eV, $n_e \sim 2 \times 10^{11}$ cm^{-3}, τ_p (particle confinement time) $\sim .6$ -1.2 ms) do not change significantly with the application of the vertical field.

Hollow Density Profiles In IMS

Density profiles of hydrogen ECR produced and heated plasmas without external applied vertical magnetic field are characterized by peaks in the edge region and centrally depressed values. The ratios of the edge to central density can vary between 3 and 10 depending upon the location of the electron cyclotron resonance layer, with lower values of the ratio attained with the resonance on the inboard side and largest values when the resonance is in a relatively flat region of field strength on the outboard side of the device. High energy tails of the electron distribution were observed with the outboard resonance by the radiometer, Thomson scattering system, and through use of probe-mounted gridded energy analyzers. Bulk electron temperature measurements showed no evidence of large temperature gradients, although the error bars on these measurements do not rule out this possibility. Maps of space potential have been obtained using an emissive probe and reveal variations in the potential on magnetic surfaces which could provide the convection necessary to maintain the hollow profiles in a steady plasma. As a first step to understanding the mechanism which produces the observed profiles, experimental investigations and modeling efforts into the transport in IMS ECRH plasmas have been undertaken.

The hollow density profiles in IMS under ECRH can be accurately modeled by including a radial convection term, V, in the particle balance equation

$$\frac{\partial n}{\partial t} = - \nabla \cdot (- D \nabla n + V n) + \gamma n \quad . \qquad (1)$$

In this equation, n is the density, D is the diffusion coefficient, V is the convection velocity and γ is the ionization rate. Because the discharge is fairly constant over the 10 msec period of ECRH, the particle balance equation may be solved in a steady state with $\frac{\partial n}{\partial t} = 0$. Due to the high neutral density and fairly flat electron temperature profile, the ionization rate $\gamma = n_o \langle \sigma v \rangle$ can be approximated as constant throughout the plasma.

The resulting equation in cylindrical coordinates, with variations only in the radial direction, is

$$0 = \frac{d^2 n}{dr^2} + \left[\frac{1}{r} - \frac{V}{D}\right] \frac{dn}{dr} + \left[\frac{\gamma}{D} - \frac{V}{D} \cdot \frac{1}{r}\right] n, \qquad (2)$$

where we have taken V and D as constants in the plasma. The equation is solved numerically and a best-fit to an experimentally measured density profile is calculated. A best-fit solution along with the experimental data points are shown in Fig. 1. Notice from Eq. 2 that this solution does not give unique values of V, D. and γ but rather V/D and γ/D.

Because the steady state analysis does not define V, D, and γ independently it is necessary to determine one of the three terms through another method. The two remaining terms may be evaluated by the relations found through the equilibrium equations. A time dependant pulse propagation experiment provides us with the additional information. A Langmuir probe is positioned at the plasma center and is pulsed to ion saturation with a square wave, modulated at 1kHz. A second probe, which can be moved radially, is maintained at ion saturation and can detect the perturbation as it propagates throughout the plasma. The input and detection signals are analysed using a Fast-Fourier transform routine to determine the phase shift as a function of harmonic number at various radial positions.

Analytically one can solve for the phase shift as a function of distance in slab geometry in a manner similar to that of Jahns et al.[1] by expanding the perturbation density in a Fourier series and substituting that expression into Eq. 1. The result is;

$$\Delta\phi = X \sin Y \, \Delta x$$

$$\text{where} \qquad X = \left[\frac{(v^2 - 4D\gamma)^2}{16D^4} + \frac{m^2\omega^2}{D^2}\right]^{1/4} \qquad (3)$$

$$Y = 1/2 \tan^{-1}\left[\frac{4Dm\omega}{v^2 - 4D\gamma}\right]$$

In the above expressions, m is the harmonic number and ω is the modulation frequency. It should be noted that since V and γ are always coupled together as $v^2 - 4D\gamma$, only D can be determined uniquely. However, by combining the steady state solution with the pulse propagation results, all three terms can be determined.

The mechanism for the radial convection is believed to be a poloidal electric field. The existance of this field can be seen from space potential measurements of the plasma, (Fig. 2). The solid curves show equipotential surfaces, the dotted ones show the magnetic surfaces. It can be observed that on a magnetic surface there exists an electric field that

produces an E x B drift in the radial direction. Calculation of the drift velocity averaged over a magnetic surface results in a net outward flow of particles.

Thus, we are able to calculate a radial convection of plasma by two methods. From the equilibrium/pulse propagation experiments we find convection velocities approximately 300-800 cm/sec. These are consistant with the values found from the E x B drifts due to poloidal electric fields where V is found to be approximately 300-500 cm/sec.

Divertor Structure and Particle Fluxes

IMS possesses a series of discrete bundle divertors as a natural consequence of the magnetic topology of the device.[2] Recent experimental efforts in the divertor area have focussed upon measuring the effects of applied vertical field by monitoring the net particle fluxes to neutralizing plates located outside the coil minor radius at the emergent flux bundle locations. Modeling of the divertor structure through a field-line tracing technique[3] predicts a significant focussing of the divertors to the inboard side of the device with application of a vertical field which shifts the surfaces inward. This effect has been confirmed experimentally with divertor fluxes to the outboard side of the device reduced several orders of magnitude from the case of no vertical field. The divertor modeling also predicts a reduction of the inboard divertors with the application of a vertical field which shifts the surfaces outward into a magnetic well configuration.

Divertor shield biasing experiments have been performed while monitoring the particle flux to a gridded energy analyzer (GEA) array located in one of the outboard divertor regions. Particle currents could be reduced by as much as 70% and increased by as much as 30% to the GEA through applicatons of bias on the order of 3 kT_e to divertor shields up to halfway around the torus from the GEA toroidal location. Measurements of the floating potential contours in one of the divertor locations showed a regions of high electric field in the center of the divertor with low-field regions surrounding the central core. The floating potential at the top and bottom of the divertor are of opposite sign, consistent with a strong curvature force acting on the particles as they enter the divertor.

Fluctuations and Vertical Field

The use of a multi-probe to examine the density fluctuation levels in IMS as a function of position and vertical magnetic field has shown a marked decrease in amplitude in edge fluctuations under magnetic well conditions. The fluctuations were found to be consistent with a minor radial efflux of plasma. Dramatic density decreases in the interior region of the profiles (50-70% density drop over a 10 microsecond period occurring at intervals of 50-200 microseconds) are associated with density increases in both the outer regions of the profiles and in the diverted particle fluxes. The reduction in fluctuation amplitude for the magnetic well case is accompanied by a sharp reduction in the hollowness of the density profiles as well.

FIGURE 1

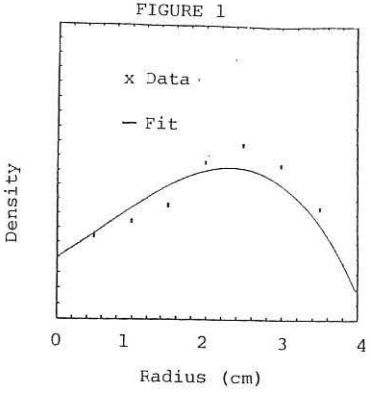

FIGURE 2

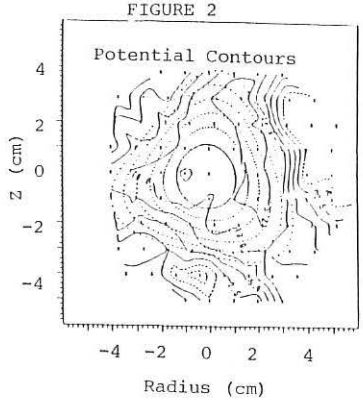

References

1. G. L. Jahns, S. K. Wong, R. Prater, S. H. Lin and S. Ejima, "Measurement of Thermal Transport by Synchronous Detection of Modulated Electron Cyclotron Heating in the Doublet III Tokamak", GA-A17858, GA Tech. Inc., San Diego, CA (February, 1985).

2. R. P. Doerner, D. T. Anderson, F. S. B. Anderson, P. H. Probert, J. L. Shohet and J. N. Talmadge, Phys. Fluids, 29, 3807(1986).

3. J. A. Derr and J. L. Shohet, IEEE Trans. Plas. Sci., PS-9, 234 (1981).

* This work was supported by the Department of Energy Grant No. DE-FG02-86ER53216.A000 and Oak Ridge National Laboratory Grant No. 19X27434C.

GENERALISED ENERGY PRINCIPLE MINIMISATION APPLIED TO MHD EQUILIBRIA WITH HELICAL SYMMETRY

M.C. Depassier*, W.A. Cooper and S.P. Hirshman+

Centre de Recherches en Physique des Plasmas
Association Euratom - Confédération Suisse
Ecole Polytechnique Fédérale de Lausanne
21, Av. des Bains, CH-1007 Lausanne / Switzerland

I. THEORY

The generalised energy principle $W = \int\int\int d^3x[B^2/2\mu_0+p_\parallel/(\Gamma-1)]$ is devised for magnetic confinement schemes that have anisotropic plasma pressure. For an adiabatic index $\Gamma > 1$, W is positive definite which guarantees that the minimum energy state corresponds to a magnetohydrodynamic (MHD) equilibrium. The parallel pressure is expressed as $p_\parallel = M(\rho)(d\Phi/d\rho)^\Gamma(1+p)/\langle 1+p\rangle^\Gamma$, where $\langle p\rangle$ represents the flux surface average of p and ρ is the coordinate that labels the flux surfaces. In systems with a coordinate of symmetry ϕ, the vanishing of the MHD force balance $\underline{F}$ component along the magnetic field lines yields the relation $\underline{F} = -(\partial p_\parallel/\partial\rho)\underline{\nabla}\rho+\underline{K}\times\underline{B}$ and demonstrates that the energetic species contribution p to the pressure has the functional form $p(\rho,B)$. The energy W is minimised with respect to an artificial time parameter t in such a manner that the mass function M, the magnetic flux functions Φ and Ψ, and the magnetic flux coordinates ρ, θ, and ϕ remain invariant. The variation of p is performed through its dependence on B. As a result, we obtain for a fixed boundary calculation that $dW/dt = -\int\int\int d\rho d\theta d\phi(F_X\partial X/\partial t + F_Y\partial Y/\partial t+F_\lambda\partial\lambda/\partial t)$, where $F_X = \sqrt{g}\underline{\nabla}Y\times\underline{\nabla}\phi\cdot\underline{F}/h$ and $F_Y = \sqrt{g}\underline{\nabla}\phi\times\underline{\nabla}X\cdot\underline{F}/h$ are the components in the covariant representation of the force balance $\underline{F}$ in the rotating Cartesian frame (X,Y,ϕ) that appropriately describes systems with helical symmetry. The Jacobian of the transformation from the (X,Y,ϕ) to the (ρ,θ,ϕ) coordinates is denoted by $\sqrt{g}$ and h is the helical pitch. The function $\lambda(\rho,\theta)$ is a periodic renormalisation parameter that determines the optimal poloidal angle θ which minimises the spectral width of the Fourier series expansion of the quantities that are required to adequately represent the equilibrium state [2]. The corresponding angle that straightens the magnetic field lines is $\theta+\lambda$. The minimisation of the binormal force component $F_\lambda = -\sqrt{g}(d\Phi/d\rho)\underline{B}\times\underline{\nabla}\rho\cdot\underline{F}/B^2$ makes the function σB_ϕ a flux surface quantity, where the anisotropy factor is $\sigma = 1/\mu_0+(p_\perp-p_\parallel)/B^2$ and B_ϕ is the axial magnetic field in the covariant representation. A prescribed effective current algorithm is included by noting that in the equilibrium state $\underline{F} = 0$, so the vector $\underline{K} \equiv \underline{\nabla}\times(\sigma\underline{B})$ satisfies the properties $\underline{K}\cdot\underline{\nabla}\rho = \underline{\nabla}\cdot\underline{K} = 0$. The effective axial current $I(\rho) = \int\int d\rho d\theta\sqrt{g}(\underline{K}\cdot\underline{\nabla}\phi)$ is thus defined and reduces to the actual current in the limit $p_\parallel = p_\perp$.[2] The absence of induced currents in stellarator configurations makes $I(\rho) = 0$ a natural choice. An accelerated steepest descent procedure is applied to iterate the Fourier amplitudes of the inverse coordinates $X(\rho,\theta)$ and $Y(\rho,\theta)$, and the function $\lambda(\rho,\theta)$ to minimise the total energy of the system till the force

amplitudes vanish within some tolerance level.[1] We are thus able to generate anisotropic pressure helically symmetric MHD equilibria, which can be diagnosed by examining the radial force balance condition $\sqrt{g}\nabla\theta\times\nabla\phi\cdot\underline{F} = 0$ that corresponds to the anisotropic helical Grad-Schlüter-Shafranov equation.[3]

II. APPLICATIONS

The scheme that we have described is applied to obtain straight scalar pressure TJ-II and anisotropic pressure ELMO Snaky torus numerical equilibria with $d\Psi/d\rho = \rho$ and $h^{-1} = 0.375$m. Five different potential TJ-II configurations that can be generated with the coil system as presently envisioned [4] are examined with $M(\rho) = M(0)(1-\rho^2)^2$ prescribed. The flux surfaces at a beta (β) value of 15% for the three most distinctive cases are shown in Fig. 1, and as can be seen, the reference case A has the largest average minor radius. The remaining two cases have similar shaped cross section as A, but with smaller minor radii. In the vacuum state, all five equilibria have a global magnetic well that ranges from 2.5% for case A to almost 8% for case E which has the largest indentation. As we increase $\beta > 20\%$, we find that the rotational transform ($\iota \equiv d\Psi/d\Phi$) is approximately conserved in case A and can vary significantly in the more indented examples.

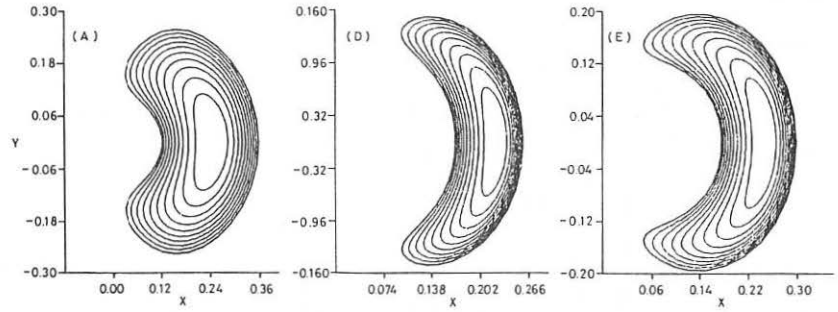

Fig. 1 The flux surfaces for three TJII configurations at $\beta = 15\%$. Note that the scales on the axes vary from case to case.

The ELMO Snaky torus equilibria are obtained with a trapped hot electron component that is modeled by $p(\rho,B) = p_h(\rho)[B_M(\rho)/B]^L$, where B_M is the minimum value of B on each surface, $p_h(\rho)$ is a Gaussian profile of halfwidth Δ centred about a chosen flux surface near the plasma edge, and the integer L is the anisotropy parameter. The conditions at zero thermal pressure with which the energetic electron layer induces a localised magnetic well on the outermost flux surfaces are investigated as a function of L and Δ. The hot electron beta (β_h) that is required is insensitive to L, but increases with Δ. However, we

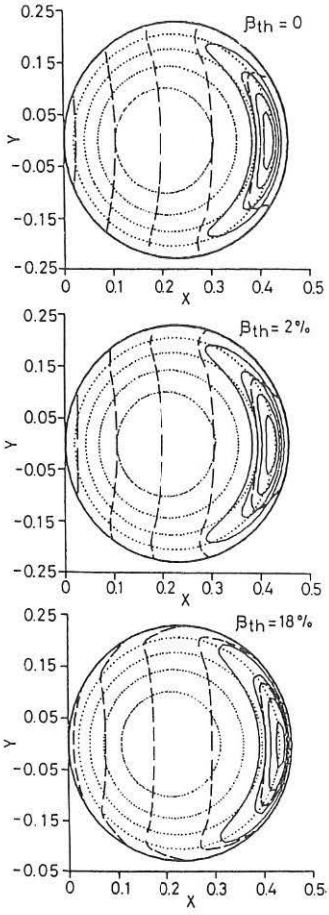

Fig. 2 The flux, mod-B, and hot pressure surfaces for an ELMO Snaky Torus that has β_h = 0.7%

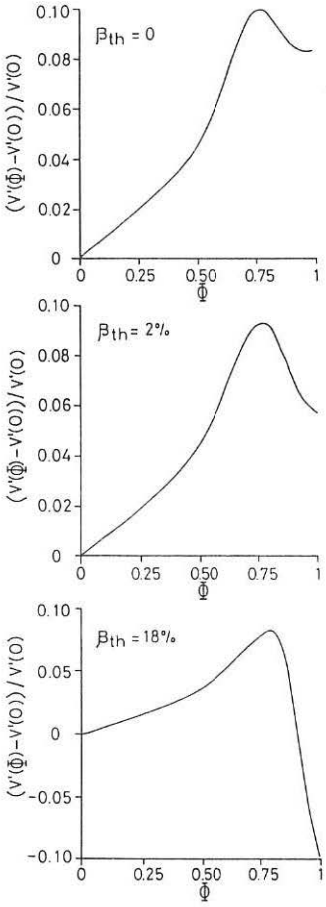

Fig. 3 The differential volume profiles that correspond to the equilibria shown in Fig. 2

find that $\beta_h < 1\%$ for $\Delta < 0.2$. To generate equilibria with finite thermal beta (β_{th}), we tailor the $M(\rho)$ profile so that the pressure gradient is concentrated in the region where the magnetic well prevails in the vacuum state and is non existent in the region of magnetic hill (which is susceptible to MHD instabilities). It can be observed in Figs. 2 and 3, respectively, that the position of the magnetic axis and the region of magnetic hill do not vary significantly with increasing β_{th} because the pressure gradients are small throughout the plasma bulk.

Present addresses:

* Universidad Católica de Chile, Casilla 114D, Santiago, Chile
\+ Oak Ridge National Laboratory, Oak Ridge, TN37831, USA

References

[1] S.P. Hirshman and J.C. Whitson, Phys. Fluids 26 (1983) 3553.
[2] R.L. Dewar, D.A. Monticello and W.N.-C. Sy, Phys. Fluids 27 (1984) 1723.
[3] R.L. Miller, Phys. Fluids 29 (1986) 1176.
[4] J. Guasp et al., in Europhysics Conference Abstracts (Proc. 12th European Conf. on Controlled Fusion and Plasma Physics, Budapest 1985), Vol. 9F, Part I, p. 441.

DISSIPATIVE MODE STABILITY IN A FINITE-PRESSURE PLASMA OF AN l=2 TORSATRON

V.V.Demchenko, P.V.Demchenko*), A.Ya.Omel'chenko

Kharkov Institute of Physics and Technology, the Ukr.SSR Academy of Sciences, 310108 Kharkov, USSR

The confinement properties of a finite-pressure plasma in stellarator-type currentless traps are determined by the stability condition of small-scale MHD modes [1]. The stabilization of small-scale ballooning modes in the ideal-conductivity plasma takes place with the plasma pressure growth. For ideal mode stabilization the plasma stability depends on the buildup of resistive MHD-modes. In the plasma pressure-linear approximation [2], the destabilizations of the gravity-dissipative mode (g-mode) are determined by the value of the vacuum magnetic hill, whose influence can be compensated by the stabilizing effect of the finite magnetic shear.

In this report we study the influence of plasma pressure cubic components on the g-mode stability in an l=2 torsatron. The stability criterion which demonstrates the destabilizing effect of the finite plasma pressure due to the magnetic hill increase has been derived.

The gravity-dissipative mode stability analysis was carried out using the general-geometry criterion $W - A_2 > 0$ [3]. The quantities W and A_2, which denote the magnetic well and the finite plasma pressure effect, respectively, can be found using the method of [4,5].

*) Kharkov State University, Kharkov, USSR

$$W=\frac{2P'}{B_0^2R}\Big\{(\mu+\varkappa_0R)^2-R^2\Big[K^2\frac{\mu+2\varkappa_0R-\mu_0^*}{\mu}-K\frac{\mu_1'\xi'+\mu_0^{*\prime}\xi'}{\mu}-K\frac{3\mu_0^{*\prime}+a\mu_0^{*\prime\prime}}{2\mu}\frac{\xi}{a}\Big]+$$

$$+\frac{RB_0^2}{2}V_{VAC.}''\Big\}+\frac{P'KR}{B_0^2\mu}\Big[\frac{P'R^2}{B_0^2\mu a^2}Ka\Big(2+\frac{3}{2}\frac{\alpha}{a}+\frac{1}{2}\alpha'-\frac{3}{4}\xi'\Big)-S\Big],$$

$$A_2=\frac{1}{4}\frac{P'^2K^2R^3}{B_0^4\mu^2a}\Big(8+12\frac{\alpha}{a}+12\alpha'-2\xi'^2\Big), \qquad (2)$$

where

$$S=\mu\Big[-\frac{5}{8}\xi'^2\xi''+\frac{15}{4}\frac{\alpha\xi'^2}{a^2}+\frac{3}{4}\frac{\alpha\xi''}{a}+\frac{5}{4}\alpha'\xi''+\frac{9}{4}\frac{\alpha'\xi'}{a}+\frac{\alpha''\xi'}{2}-\frac{15}{8}\frac{\xi'^3}{a}\Big]-$$

$$-\mu_0\Big[-\frac{1}{4}\xi'^3+\frac{15}{8}\frac{\xi}{a}\xi'^2-\frac{1}{2}\alpha'\xi'+\frac{3}{4}\frac{\xi}{a}\alpha'+\frac{3}{4}\frac{\alpha}{a}\frac{\xi}{a}+\frac{3}{2}\frac{\alpha}{a}\xi'-\frac{3}{4}\frac{\xi^2}{a^2}\xi'-\frac{3}{8}\frac{\xi^3}{a^3}\Big]-$$

$$-\mu_0''\Big[\frac{5}{8}\xi\xi'^2+\frac{3}{8}\frac{\xi^3}{a^2}+\frac{9}{4}\frac{\xi^2}{a}\xi'+\frac{1}{4}\alpha'\xi+\alpha\xi'+\frac{9}{4}\frac{\alpha}{a}\xi\Big]-$$

$$-\mu_0'''\Big[\frac{3}{4}\frac{\xi^3}{a}+\frac{1}{2}\alpha\xi+\frac{3}{4}\xi^2\xi'\Big]-\mu_0^{IV}\frac{1}{8}\xi^3,$$

K and $\varkappa_0$ are the curvature and torsion of the magnetic axis, ξ is the displacement of the magnetic surface centre relative to the torsatron geometric axis caused by plasma pressure, α is the magnetic surface ellipticity, $\mu_0^* = \mu_0 + \varkappa_0 R$, $\mu = \chi'/\varphi'$. In relations (1)-(2) μ_0 and V_{VAC}'' denote the vacuum rotational transform

$$\mu_0=2m\varepsilon_2^2\Big[\frac{R^2}{m^2a^2}\bar I_2'^2(z)-\frac{R^3}{m^3a^3}\bar I_2(z)\bar I_2'(z)+\frac{R^2}{m^2a^2}\Big(1+\frac{R^2}{m^2a^2}\Big)\bar I_2^2(z)\Big]-\varkappa_0R \qquad (3)$$

and the magnetic hill of the straight stellarator

$$V_{VAC}''=\frac{K\varepsilon_2^2}{B_0^2}\Big[-\frac{4R^2}{m^2a^4}\bar I_2(z)-\frac{4}{a^2}\bar I_2'^2(z)+\bar I_2'(z)\bar I_2(z)\Big(\frac{16m}{Ka}+\frac{16R}{ma^3}\Big)\Big], \qquad (4)$$

where ε_2 is the ratio of the helical-to-toroidal magnetic field ratio for the l=2 torsatron, m is the number of helical magnetic field periods over the torus length.

For an arbitrary plasma pressure profile the stability criterion is rather cumbersome. For this reason, we restrict ourselves to the analysis of stability for the parabolic law

of plasma pressure distribution $P = P_0(1 - a^2/a_0^2)$. In this case the MHD stability criterion of the g-mode in the l=2 torsatron is conveniently written as

$$-(\mu_J+\mu_0^*)^2+\frac{R^2K^2}{\mu_J+\mu_0^*-\varkappa_0 R}(\mu_J+\varkappa_0 R)-R^2K\frac{\mu_J'+\mu_0^{*\prime}}{\mu}\xi'-R^3K^3\frac{\mu_0^{*\prime}+a\mu_0^{*\prime\prime}}{2\mu}\frac{\xi}{a}-\frac{RB_0^2}{2}V_{VAC}''$$

$$-\frac{3}{2}\frac{R^2}{a^2}\beta_\theta^3(Ka)^4+\frac{R^2K}{2\mu}\beta_\theta^3(Ka)^3\left\{\mu_0^{*\prime}\left[\frac{1}{4}-\frac{21}{16}\left(1-\frac{a_0^2}{a^2}\right)+\frac{9}{16}\left(1-\frac{a_0^2}{a^2}\right)^2+\frac{3}{64}\left(1-\frac{a_0^2}{a^2}\right)^3\right]-\right.$$

$$\left.-a\mu_0^{*\prime\prime}\left[\frac{1}{4}+\frac{11}{16}\left(1-\frac{a_0^2}{a^2}\right)+\frac{9}{16}\left(1-\frac{a_0^2}{a^2}\right)^2+\frac{3}{16}\left(1-\frac{a_0^2}{a^2}\right)^3\right]\right\}>0, \qquad (5)$$

where $\beta_\theta=\frac{P_0R^2}{B_0^2a_0^2\mu^2}$.

In (5), the effects of finite plasma pressure are described by the terms proportional to β_θ^3; therefore, to calculate these terms, it was sufficient to determine the displacement of the magnetic surface in the pressure-linear approximation: $\frac{\xi}{a}=\frac{1}{2}\beta_\theta Ka\left(1-\frac{a_0^2}{a^2}\right)$, and the magnetic surface ellipticity α - in the pressure-squared approximation: $\frac{\alpha}{a}=\frac{1}{4}\beta_\theta^2(Ka)^2$. In the low plasma pressure limit, where the effects of finite plasma pressure can be neglected, the g-mode stability criterion transforms to the corresponding expression of [3]. If the current of helical conductors is assumed to equal zero, then the stability criterion of the gravity-dissipative mode (5) goes over to the criterion of the gravity-dissipative mode stability in finite plasma pressure of the magnetic trap with a helical magnetic axis [6].

The stability criterion analysis shows that the effect of the components cubic with respect to the plasma pressure on the g-mode stability is determined by geometric and physical parameters of the magnetic trap. The stabilizing effect of β_θ - linear components shows up in the central part of the plasma column [5], while at the plasma periphery ($a > 2/\sqrt{5}\,a_0$) the g-mode is unstable in the l=2 torsatron. In the centre of the plasma

column, as the plasma pressure grows ($\beta_\theta \sim m$), the β_θ - nonlinear components involved in the stability criterion (5) become comparable in magnitude with the linear components and produce a destabilizing effect on the plasma stability. With a further plasma pressure growth and the β_θ value becoming greater than $(m\varepsilon_2/ka)^{2/3}$, the components, cubic with respect to plasma pressure, play a predominant role in the g-mode destabilization.

Let us employ the obtained results to determine the gravity-dissipative mode stability in the designed torsatron "U-2M" with the parameters: $a/R = 0.176$; $\varepsilon_2 = 0.375$, $S_{vac} = 0.2$, $m = 2$. We obtain that for $\langle\beta\rangle \gtrsim 7\%$ the effects of finite plasma pressure destabilize the g-mode in the central part of the U-2M torsatron plasma column.

References

1. Shafranov V.D. Phys. Fluids, 1983, v.26, N2, p.357.
2. Kovrizhnykh L.M., Shchepetev S.V. Fiz. Plazmy, 1981, v.7, N9, p.419.
3. Mikhajlovskij A.B. Nucl. Fusion, 1975, v.15, N1, p.95.
4. Shafranov V.D. Nucl. Fusion, 1968, v.8, N3, p.253.
5. Mikhajlov M.I., Shafranov V.D. Plasma Phys., 1982, v.24, N3, p.233.
6. Demchenko V.V., Mikhajlovskij A.B., Omel'chenko A.Ya. Fiz. Plazmy, 1984, v.10, N3, p.509.

THE NEW FINITE-DIFFERENCE CODE POLAR-3D AND RESULTS OF ITS APPLICATION TO CALCULATING THE MHD EQUILIBRIUM AND STABILITY OF PLASMA IN 3D CLOSED CONFIGURATIONS

Degtyarev L.M., Drozdov V.V., and Poshekhonov Yu.Yu.
Keldysh Institute of Applied Mathematics
USSR Academy of Sciences, Moscow

1. The POLAR-3D code is based on the approach developed in [1,2]. According to it the ideal magnetostatics equations

$$(\nabla\times B\cdot(B\times\nabla a))\,|\nabla a|^{-2} = dP(a)/da \quad , \qquad (1)$$

$$\nabla\cdot B = 0 \quad , \quad (B\cdot\nabla a) = 0 \quad , \quad \nabla\cdot(B\times\nabla a) = 0 \quad , \qquad (2)$$

where a(r) = const are magnetic surfaces, can be reduced to a system of three equations for the scalar functions that determine the magnetic field vector B. The mixed representation of the field (in terms of the external poloidal flux $\Psi(a)$ and the current F(a)) has the form

$$B = \nabla\Psi\times\bar{B}_F + F\cdot\bar{B}_\Psi \quad . \qquad (3)$$

When substituted into (1) it leads to the 3D generalization of the Grad-Shafranov equation, and the flux representation

$$B = \nabla\Psi\times\nabla\zeta^\Psi + \nabla\Phi\times\nabla\theta^\Psi \qquad (4)$$

is traditionally used in the 3D codes [3,4]. Here the pairs $(\bar{B}_F, \bar{B}_\Psi)$ and $(\theta^\Psi, \zeta^\Psi)$ are such that each summand in (3), (4), satisfy all properties of the field (2).

2. A discrete model on an arbitrary nonregular grid is based on the finite-difference analog of the variational principle, which has the form

$$\delta\int(B^2/2 - P)\,d^3x = 0 \quad .$$

The model is constructed so that on the grids adapted to the magnetic surfaces it admits reformulations corresponding to different representations of the magnetic field, and as a result an adequate approximation of the original equilibrium problem (1), (2) can be obtained.

The POLAR-3D code yields a result in the form of the magnetic surfaces parametrization $r(a, \theta, \zeta)$; it has high performance in accuracy and speed of calculations, and operates is essentially 3D configurations with large values of β. The code usage is restricted by the condition of nested magnetic surfaces, of which the external one is supposed to be given. In symmetric systems the code operation is identical by the result to its 2D predecessor POLAR [5] which has proved be good in various applications.

3. In the results shown in Figs. 1-2 the plasma configuration is given parametrically in the cross-sections formed by the planes $\zeta = \text{const}$

$$u(a_{max},\theta,\xi) = b(\cos\theta - \delta\sin^2\theta) \ ,$$

$$v(a_{max},\theta,\xi) = \alpha b \sin\theta \ , \quad \theta \in [0, 2\pi) \ ,$$

where b , α , δ are the characteristic dimension, elongation and triangularity, respectively, while (u, v, ξ) are the local coordinates $\bar{r}(u,v,\xi) = \bar{r}_c(\xi) + u\cdot\bar{n}_c(\xi) + v\cdot\bar{b}_c(\xi)$ with the geometric axis of the system $\bar{r}_c(\xi)$ as an origin. As $\bar{r}_c(\xi)$ we choose the left "helical" line that winds k_w times on the torus of major radius R_0 and minor radius R_w and $\bar{n}_c(\xi)$ is the external normal to it, $\bar{b}_c(\xi) \sim (d\bar{r}_c/d\xi) \times \bar{n}_c$. The flux variables (a, θ, ξ) are such that $d\Psi/da = const$, and the θ = = const are the straight lines in the plane (u, v). Other notations are as follows:

$$\beta = 2\int p d^3r \,/\, \int B^2 d^3r \ , \quad \iota(\Psi) = -\left(\frac{\theta_{max}}{\xi_{max}}\cdot d\Phi(\Psi)/d\Psi\right)^{-1} ,$$

$$M(\Psi) = const\cdot\iota^{-4}\cdot(d\iota/d\Psi)^2\cdot(0.25 + \Omega\cdot dP/d\Psi)$$

is the function that determines the stability of localized modes $(M(\Psi) \geqslant 0$ is the necessary Mercier criterion). Fugures 1 and 2 show the results on the grid 12x24x32 for k_w = 1,2, the pressure profile $dP/d\Psi$ = const and the zero longitudinal current $J(\Psi) = 0$. If k_w = 2 the instability zone can be observed $\beta \leqslant 4\%$, and further on the configuration is stable by the Mercier criterion up to $\beta \approx 25\%$ due to the self-stabilization. If k_w = 1 the stability zone is continuous on the interval $0 \leqslant \beta \leqslant 20\%$.

4. Conclusions. The POLAR-3D code is an efficient tool developed to calculate the plasma MHD equilibrium in the 3D systems. Rather simply shaped magnetic traps with a spatial axis are obtained, where the Mercier criterion shows favorable values up to $\beta \approx 20$–30%.

Acknowledgement

The authors express their gratitude to V.D. Shafranov for helpful discussions and useful comments concerning a choice of geometry for the plasma configurations.

References

1. Degtyarev L.M., Drozdov V.V. Preprint, Keldysh Inst. Appl. Math., USSR Acad.Sci., N 32, 1984.
2. Degtyarev L.M., Drozdov V.V. et al. Fizika Plazmy, 11(1985), p.39-50.
3. Degtyarev L.M., Drozdov V.V., Medvedev S.Yu. Itogi nauki i tekhniki, ser. Plasma Physics, Moscow, 6(1985), p.81-134.
4. Johnson J.L., Comput. Phys. Reports, 1986, 4, p.39-69.
5. Degtyarev L.M., Drozdov V.V. Comput. Phys. Reports, 1984, 2, p.342-387.

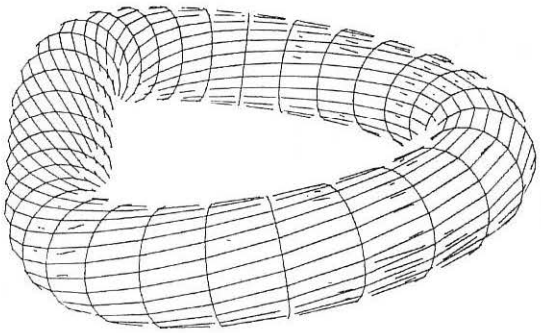

$k_w=1, R_0=4, R_w=2, B=1, \alpha=1, \delta=0.$

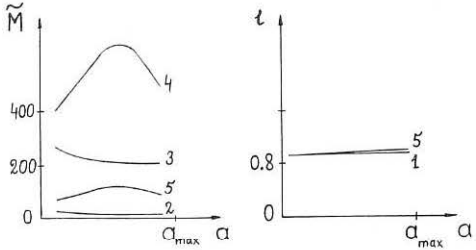

1-β=0.%, 2-β=0.7%, M̃=10·M, 3-β=2.9%, M̃=10·M,
4-β=13.1%, M̃=M, 5-β=20.%, M̃=M/10

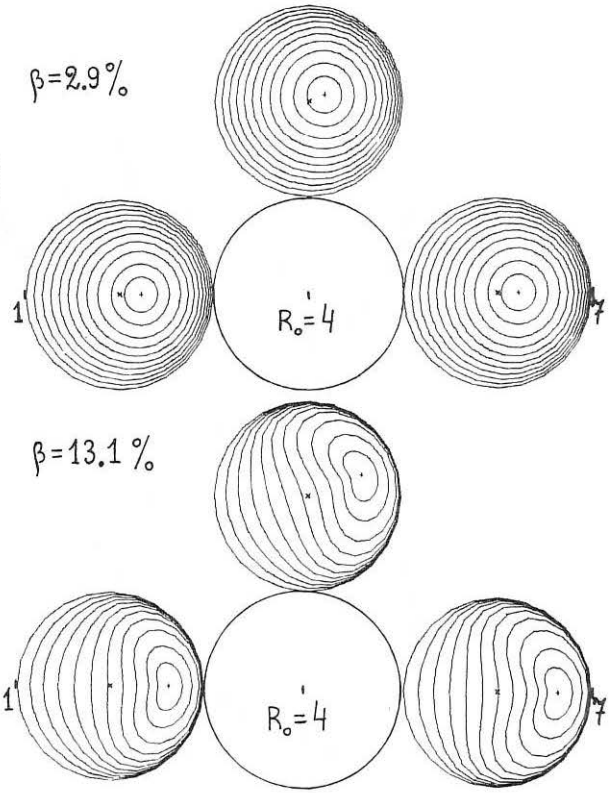

Fig.1

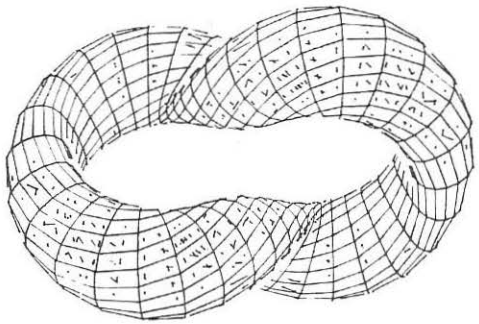

$k_w=2, R_o=4, R_w=2, \beta=1, \alpha=1.6, \delta=0.4$

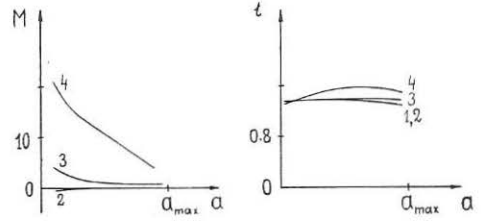

$1-\beta=0.\%, 2-\beta=3.6\%, 3-\beta=7.2\%, 4-\beta=19.7\%$

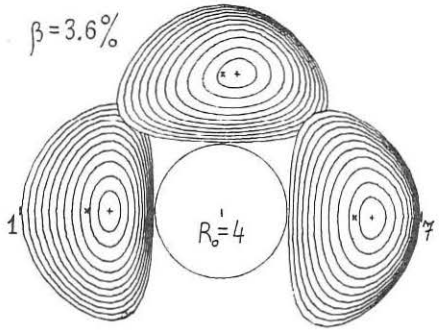

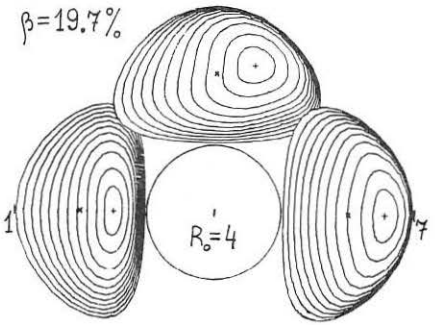

Fig. 2

MAGNETIC FLUX SURFACES DETERMINATION IN THE TJ-2 FLEXIBLE HELIAC. SIMULATION RESULTS.

A.L. Fraguas, M.A. Pedrosa and A.P. Navarro

Asociación EURATOM/CIEMAT
28040 Madrid, SPAIN.

INTRODUCTION

TJ-II is a flexible heliac device to be built at CIEMAT. This device will have the capability to change its rotational transform in a wide range, ι_o:0.8 — 3.2, and in a much less reduced range, its profile going from shearless up to moderate shear cases (1). In almost all the configurations magnetic flux surfaces have a pronounced bean shape (Fig. 1).

In the goal to scan the ι space for experimental determination of the most adequate conditions for plasma confinement, it is important to have diagnostic techniques that provide the magnetic flux structure and its variation along the discharge. Due to the expected high plasma temperatures, internal probing is not possible and it is necessary to develop techniques to infer magnetic structure from external measurements. The most general approach would be to use these data as input for an equilibrium code, adequated to the TJ-II configuration, but this is too time consuming and rules out any on-line time evolution study.

In this paper techniques are present to address this problem using approximations to reduce the computer time requirement so they can be used as monitor of the evolution of the plasma magnetic structure along the discharge. One technique is based on the simulation of the TJ-II by sets of filamentary currents (2), deduced from the mode analysis of the magnetic signals. This tecnique could provide the outermost magnetic surface in the device. Going deeper in the magnetic reconstruction is not possible with this technique due to the distortion coming from the presence of the virtual currents. So, to get a total reconstruction without using an equilibrium code, a possible approach is to develop an analytical model for the magnetic field in the TJ-II and deduce its parameters from the adjustment of the outermost magnetic surface of the previous method or directly from the magnetic array data. Figure 1 shows a typical set of magnetic coils in a poloidal sector of the TJ-II device.

SIMULATION WITH FILAMENTARY CURRENTS

In order to simulate the TJ-II magnetic structure, including the plasma contribution, a set of six circular conductors at fixed positions is assumed. Currents in these conductors are determined from the resolution of a linear equation system. The coefficients C_{mj} are the Fourier components of the magnetic field produced at the magnetic coil array by 1 kA current in each conductor, and the independent terms S_m are given by the Fourier component of the magnetic field measured at that array. Signals were simulated using the B_θ component computed for the real TJ-II conductor

structure.

$$S_m = \sum_j C_{mj} I_j$$

Figure 2 shows both the measured transverse field in the array and the reconstruction obtained with the six currents deduced with this technique. In Figure 3 the outermost transverse magnetic field contours are shown. They are relatively insensitive to the conductor locations. Table I presents the currents and locations for each conductor in this case.

Net current in the plasma can be deduced from the sum of these currents or by the S_0 mode amplitude. Reconstruction time is less than a minute for a PDP 11/44 plus the display time.

TABLE I.-Conductor locations and currents

R (m)	Z (m)	I (kA)
1.5	0.0	314. (HC)
1.72173	0.0	-1572.26
1.72173	-0.01	327.84
1.82173	-0.01	163.78
1.82173	0.0	589.03
1.82173	0.01	163.78
1.72173	0.01	327.84

SIMULATION WITH AN ANALYTICAL MODEL FOR B

The model we have assumed includes the leading fields present at the flexible heliac configuration. As a vacuum field, the B field can be derived from a magnetic potential, written as, (3):

$$\phi = \phi_T + \phi_P + \phi_{H1} + \phi_{H2}$$

where:
$\phi_T = B_o z$ is a constant toroidal field which describes the average toroidal field existing in the device.
$\phi_P = b_P \theta$ is the poloidal field produced by the hardcore currents.
$\phi_{H1} = a_1 I_1(hr)\sin(\theta - hz)$ is the l=1 field associated to the helical swing of the toroidal field coils.
$\phi_{H2} = b_1 K_1(hr)\sin(\theta - hz)$ is the l=1 field produced by the hardcore helical winding.
z is proportional to the toroidal angle and h is the helical pitch.

The model assumes helical symmetry and uses cylindrical coordinates with the circular hardcore as axis in the infinite aspect ratio limit.

B_o value is the average toroidal field in the magnetic axis of the real configuration.

The remaining parameters of the model a_1, b_1 and b_P are determined by a least squares fit to the simulated B field at points located on circular

arrays defined by the experimental setting shown at Figure 1.

Due to the 3D properties of the actual configuration the results of the fit are dependent on the toroidal position of the array. As an example fitted parameters are shown in Table II for arrays placed at toroidal angles $\varphi = 0^{\circ}$, 22.5°, 45° and 67.5° ,in all cases at 0.33 m away from the coil centers. The most suitable parameters have been determined by averaging those fitted values.

Flux surfaces obtained by field line integration of the model magnetic field computed by this model for those parameters are shown in Figure 4. The CPU time in a VAX 11/785 is about 10 sec. to fit the data and 50 sec. to trace 5 magnetic surfaces.

The model reproduces reasonably well flux surface shapes and qualitative features of the configuration. However, the axis is shifted inwards about 0.04 m and the transform value results to be $\iota_0 = 1.35$ for a reference value of 1.46.

Magnetic field reconstruction from inner input data, (array at 0.15 m from the center), notably improves the axis position and ι value. Hence, a fair configuration description is expected if field values coming from the modal method are used as input data.

TABLE II.-Model parameters

φ	0°	22.5°	45°	67.5°
a_1	$5.2\ 10^{-2}$	$7.6\ 10^{-2}$	$1.3\ 10^{-1}$	$7.6\ 10^{-2}$
b_1	$1.0\ 10^{-3}$	$1.1\ 10^{-3}$	$1.3\ 10^{-3}$	$1.1\ 10^{-3}$
b_p	$5.6\ 10^{-2}$	$5.5\ 10^{-2}$	$5.8\ 10^{-2}$	$5.5\ 10^{-2}$

SUMMARY

Magnetic structure determination for TJ-II flexible heliac, from signals in pick-up coils located around the plasma, have been addressed with some approximations in order to get time resolution in the analysis between discharges. Modal analysis, using FFT, can provide the outermost magnetic contours and the net current in the plasma. Analytical B modeling makes possible to deduce the complete magnetic flux structure when the signals at different toroidal locations are averaged.

REFERENCES

(1) J. Guasp et al., 12th EPS Conf. Vol. 9F I, 441 (1985)
(2) D.W. Swain and G.H. Neilson, Nucl. Fus. 22, 1015 (1982)
(3) A.I. Morozov and L.S.Solov'ev. "Reviews of Plasma Physics", vol.2. Ed. M.A. Leontovich. (1966)

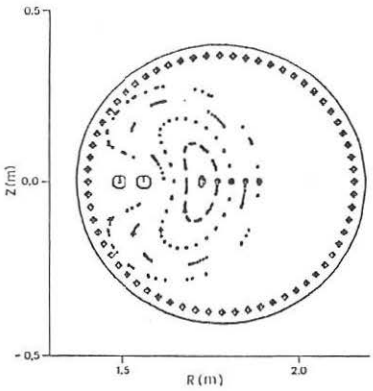

FIG.1.- TJ-II Reference configuration and magnetic coils array.

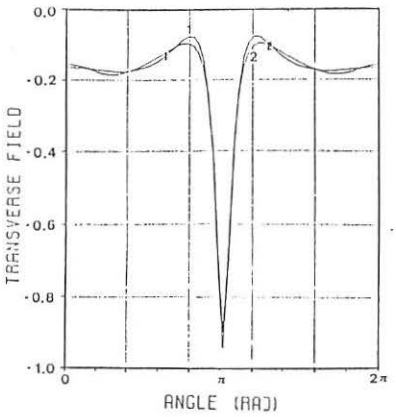

FIG.2.- (1) Measured transverse field. (2) Reconstructed transverse field.

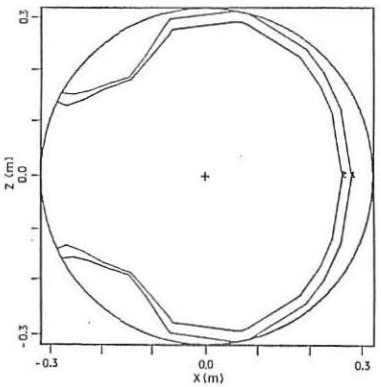

FIG.3.- Transverse field outer contours using modal analysis.

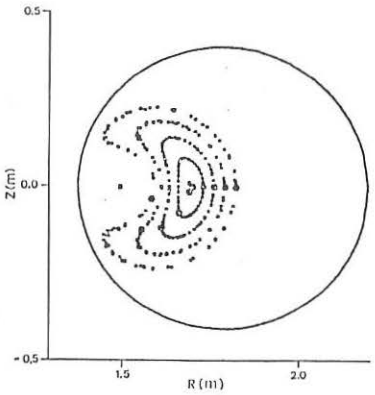

FIG.4.- Flux contours reconstruction using analytical B model.

TOMOGRAPHY TECHNIQUES FOR THE TJ-II FLEXIBLE HELIAC

J.Vega and A.P.Navarro

Asociación EURATOM/CIEMAT
28040 Madrid, SPAIN.

INTRODUCTION

The TJ-II Flexible Heliac is a stellarator to be built at CIEMAT to study the effect of helicoidal magnetic axis on plasma confinement at different ι values (1). The device incorporates the capability to change, in a wide range, its rotational transform value ,(ι/N 0.2 to 0.5) and, in a minor range, its profile (2). In any configuration, the plasma will have a bean-shaped magnetic structure that rotates poloidally when one moves in the toroidal direction (Fig.1).

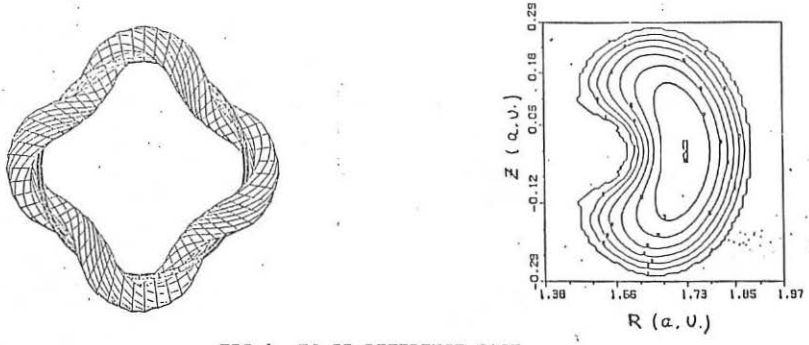

FIG.1 TJ-II REFERENCE CASE
a) Top view b) Poloidal section.

To deduce local values for those diagnostics measuring magnitudes along a chord in a plasma with this shape requires inversion techniques much more complicated than the usual Abel inversion, applied in circular plasmas (3), or the modified one for displaced circular or elliptical plasmas (4). In this paper three different techniques are considered for TJ-II: LOW ORDER MODE APPROXIMATION (LMA), GENERALIZED FOURIER TRANSFORM (GFT) and MAXIMUM ENTROPY (MEM), in order to determine its aplicability and computer requirements. Line integrals for soft-X-ray emissivity (in the 1 to 30 Kev range) were simulated for different detector arrays, assuming emissivity proportional to poloidal flux to some power (between 1 and 3). These array signals were used as input for the different algorithms to deduce local emissivity values, comparing them with the initial distributions used in the simulation process.

LOW ORDER MODE APROXIMATION

In this method (5) the local plasma emissivity is considered as:

$$E = f(r,\theta) = \sum_{m=0}^{M-1} (f_{in}(r) \cos m\theta + g_m(r) \sin m\theta) \qquad [1]$$

so, signals in the detector arrays can be expressed by:

$$S_\delta(\beta) = \sum_{m=0}^{M-1} (F_m(\beta) \cos m(\delta+\beta) + G_m(\beta) \sin m(\delta+\beta)) \qquad [2]$$

where β is the angular position of the detector in the array and δ is the angular position of the array itself (Fig.2a). Once F_m and G_m are deduced by solving the linear equation system [2], in a number of harmonics equals to the number of arrays, it is possible to obtain the $f_m(r)$ and $g_m(r)$ by modified Abel inversion and reconstruct the plasma emissivity using [1].

For the expected plasma shapes in TJ-II, harmonics up to order 3 could be enough, so in the simulation process three different arrays have been considered with 10 detectors each. Using this setup, we obtain reconstructions as that one shown at Fig.2b. Computer time requirements for these conditions in a PDP11/44 are one minute plus the display time.

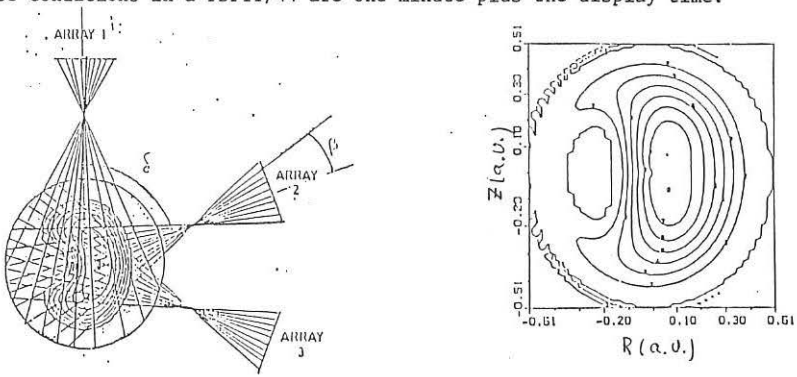

FIG.2 LOW ORDER MODE APROXIMATION
a) Detector arrays position b) X-ray emissivity reconstruction

Reconstructions fail at the plasma edge where the bean shape is more pronounced. This can be due to a need for higher order harmonics, that implies more arrays and development of inversion formula for them, or to the fact that X-ray emissivity is very low at those points, where n and T decreases drastically. We are here assuming the TJ-II reference case with T_{e0} = 700 ev and $n_{e0} = 1.3 \cdot 10^{19}$ m^{-3}, with parabolic profiles.

GENERALIZED FOURIER TRANSFORM

Based in the projection slice theorem, this technique (6) does not make assumptions on the number of harmonics to include in the reconstruction, so we can avoid, in principle, the limitations of the previous method and check if reconstructions improved at the plasma edge.

The technique uses arrays with the detectors looking through the plasma along parallel chords (Fig.3a), and computing its DFT, obtains a sample of $F(\omega_1, \omega_2)$, DFT of the two-dimensional distribution to be reconstructed (Fig.3b). With M equally spaced arrays located in a poloidal section we can deduce M slices of that distribution and, by interpolation, deduce the complete $F(\omega_1, \omega_2)$. Inverse Bidimensional Fourier Transform will provide the local emissivity distribution. Fig.3c shows the result when only 3 parallel arrays , with 11 detectors each, are used. Computer time requirement in a VAX-785 was 1 minute, plus the display time.

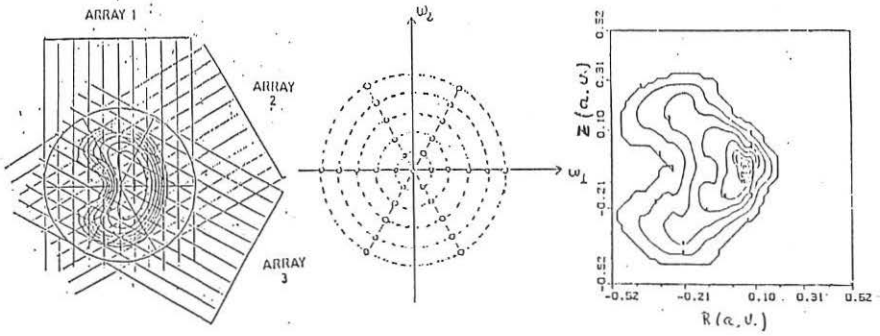

FIG 3. GENERALIZED FOURIER TRANSFORM RECONSTRUCTION
a) array set-up b) $F(\omega_1, \omega_2)$ polar raster c) Reconstruction

Results with this method shows a better reconstruction for the plasma edge. Its poor quality is due to low number of $F(\omega_1, \omega_2)$ slices for the interpolation process. Nevertheless to improve it will require a higher number of arrays , which is impossible, not only for the high cost but also for the requirement in access to the plasma due to the need for parallel arrays. Also the computer requierements make very difficult to obtain several reconstructions for a discharge.

MAXIMUM ENTROPY METHOD

Trying to determine sharp variations in the emissivity distribution without the need for a high number of detector arrays, we have considered an algebraic approach, where no mode consideration is implied. For that purpose the MEM technique has been chosen. It is based on the assumption that the emissivity distribution corresponding to a particular set of chord meassurements is that one with the maximum entropy, given by two terms: one defined by the object spatial entropy and the other from the noise. Maximizing this total entropy with the constraints of the detector array signals, enissivity and noise for each cell in the assumed grid are given by (7):

$$E_c = \exp\left[-1 - \mu - \sum_{n=1}^{N} \lambda_n S_{nc} \right]$$

$$N_n = \exp\left[-1 - \lambda_n / \rho \right]$$

where $\{\lambda_n\}$ and μ are multipliers to determine, S_{nc} the system point spread function and ρ the object to the noise entropy ratio. With the additional constraint that the noise follows a χ^2 distribution, a new set of equations is obtained (8). We are using this technique for simulation of two parallel arrays, 26 detectors each, one at the top and the other at the side of the device. Reconstructions using formulae from (7) do not approach enough the initial distribution for cpu times of several minutes in a VAX-785. So it is not possible to use this technique to obtain more than one frame image between discharges. A possible approach to speed up the technique could be to use as starting point for this method a LMA solution, but in this case the generality of the method could be lost.

SUMMARY

Three different methods have been considered for tomography reconstruction in the TJ-II Flexible Heliac. The LMA is the most restrictive in assumptions but can aproximate TJ-II case. GTF and MEM methods could improve the analysis but they require a larger amount of detector and computer time.

REFERENCES

(1) TJ-II Group and ATF Design Team, 12th EPS Conf. Vol 9F,I,441 (1985)

(2) TJ-II Group "Application for Preferential Support Phase I TJ-II Experiment" JEN, Nov. (1985)

(3) Y. Sato, Contrib. Plasma Phys. 25, 573, (1985)

(4) Y. Yasutomo el al., IEEE Trans. Plasma Sci. PS-9, 18, (1981)

(5) A.P.Navarro, V.K.Paré and J.L.Dunlap, Rev.Sci.Instr.,1634, (1981)

(6) R.M.Mersereau and A.V.Oppenheim, Proc. IEEE Vol.62, No.10, (1974)

(7) B.R.Frieden, J.Opt.Soc.Am. 62, 511, (1972)

(8) A.Holland and G.A.Navratil, Plasma Phys.Lab., Columbia Univ.(1985)

EFFECTS OF MAGNETIC AXIS SHIFT ON TJ-II HELIAC

J. GUASP, J.A. FABREGAS

JEN, Madrid. Spain

ABSTRACT:

The position of magnetic axis in TJ-II heliac [1] can be controlled by means of the vertical field coil currents. Around the usual reference case a 1 cm axis shift can be attained by changing the VF coil current 23% with inward shift corresponding to an increase in the current value, this relation mantains a remarkable constant value up to 6 cm excursions.

Under these shifts average radius decreases for either shift sign, and other magnitudes change too, mainly the magnetic well depth, each magnitude reaching an optimum for some shift value, usually different for each one. The limits of attainable shift, before substantial loss of average radius or magnetic well happens falls around 3 or 4 cm.

Another observed effect is the disymmetry on the magnetic surfaces between the outer part (zero toroidal angle) and the inner one (half a period further), two characteristics have been considered: the difference in the elongation of the magnetic axis and the difference in equatorial diameter, both magnitudes show opposite behaviour: the first one increases with outer shifting, the other one decreases. In consequence the magnetic surface cross section shape changes too. For the usual coil current settings adopted a compromise between both magnitudes is taken, so as to maximise the available plasma average radius. This leads to similar shapes for magnetic surfaces that are separated by half a period. The trajectory of this "optimal" point in the helical versus circular coil current diagram when rotational transform at axis varies is an almost straight line.

Nevertheless this "optimal" compromise does not optimises usually the magnetic well depth that instead points to another shift choice.

In addition magnitudes of paramount importance, as well for equilibrium as for stability, are the Pfirsch-Schlutter currents. The optimization of the symmetry between magnetic surfaces can be contradictory with the toroidal current minimisation given the different curvature radius of both surfaces. For this reason the effect of axis shift upon P.-S. currents has been analysed confirming that disymmetry minimisation can be contradictory with toroidal current minimisation that leads to different optimal shift choices.

As TJ-II is being designed to have the possibility for VF current coil variations it will allow experimental tests of these effects.

[1]. TJ-II and ATF Group. 12th EPS Conference. Budapest 1985, Vol. 9F-I, p. 441

RELATIVISTIC AND FINITE LARMOR RADIUS EFFECTS FOR 2nd HARMONIC OF X-MODE ON MICROWAVES ABSORPTION FOR TJ-II DEVICE

by Francisco Castejon and Jose Guasp

EURATOM/CIEMAT ASOCIATION.MADRID (SPAIN)

TJ-II device is an helical magnetic axis stellarator of Heliac type to be built at CIEMAT in Madrid, whose main charateristics are high flexibility, high potential beta and bean-shaped plasma cross-section [1].

ECRH is the intended first stage for plasma heating in TJ-II (allowing a volume average density about 1.6E13 cm-3) while later neutral beam injection will be used. In this paper we analysethe microwave injection problems in this helical configurationat about 56 GHz in order to heat the B=1 T region and using the 2nd harmonic of X-mode (O-mode absorption is negligible at 2nd harmonic as it has been verified).

As it is well known the problems of accesibility and heating lie on the situation of cut-offs and resonances in the plasma. Resonances must be reached by the waves before than cut-offs to get plasma heating. In our case, we want to reach the Electronic-Cyclotronic-Resonance (ECR) at 2nd harmonic of X-mode. To elucidate this fact, we must study the signs of Re(N^2) and Im(N^2)(N: refractive index): Wave propagation will be possible if Re(N^2)>0 and absorption will occur if Im(N^2)>0.

Regarding the results for cold plasma [2], the best situation for heating happens at toroidal angles of about 17 deg. and poloidal angle about -67.5 deg., injecting from the low field side. The highest volume average density at which it is possible to achieve heating is about 1.57E13 cm-3, and the local one is 1.94E13 cm-3; when X-mode cut-off reaches the ECR area. The upper hybrid resonance appears always inside the X-mode cut-off layer.

The model which has been used, proposed by Bornatici, Cano, De Barbieri and Engelman [4], is useful to study the absorption and propagation near harmonic frecuencies, for a weakly relativistic plasma and taking in account finite Larmor-radius effects up to 1st. order. In this work we have limited the study to cuasi-perpendicular propagation. Dispersion relation is given by:

$$-bN^4 + (2b(K_\perp - K_x) - K_\perp)N^2 + (K_\perp^2 - K_x^2) = 0$$

where:

$$b = -\frac{1}{2}\left(\frac{\omega_p}{\omega_c}\right)^2 F_{3/2}(z_2) \quad ; \quad z_2 = \frac{mc^2}{T}\left(1 - \frac{2\omega_c}{\omega}\right)$$

Kx,K⊥: Components of dielectric tensor for cold plasma.

$$K_x = -\sum_k \frac{\omega_{pk}^2}{\omega^2-\omega_{ck}^2}\left(\frac{\omega_{ck}}{\omega}\right) \quad ; \quad K_\perp = 1-\sum_k \frac{\omega_{pk}^2}{\omega^2-\omega_{ck}^2}$$

k: ions,electrons

$$\omega_p^2 = \frac{nq}{\varepsilon_0 m} \quad ; \quad \omega_c = \frac{-qB}{m}$$

n: density

From the dispersion relation we can see that there exist two branches of the X-mode. One of them resembles the branch of the cold X-mode which propagates for densities lower than upper-hybrid resonance (X-mode), and the other one (Z-mode) resembles the other branch of cold X-mode (this notation has been taking from [5]). Far from the resonances, the real part of refractive index is closely aproximated by cold plasma dispersion relation. Mode conversion is possible where the real parts of index of the two branches coincide and this happens around the upper-hybrid resonance, which can be reached only by tunnelling, since it is beyond the cut-off.

In Figure 1 we can see the magnetic and density profiles of TJ-II device along the injection line.

In Figure 2 we have plotted Re(N^2) and Im(N^2) of the two branches against incident frecuency (for electronic-T=1 Kev, B=1 T and n=1E13 cm-3). Both branches are absorbed at frecuencies near and below 56 GHz (cold 2nd harmonic ECR-frecuency for B=1 T). The Z-mode can propagate only in a narrow range of frecuencies. So, hot plasma effects make resonance appear at some lower frecuencies than 56 GHz. To study the behavior of refractive index against the frecuency is just the reverse of studying it against magnetic field. Refractive index deppends strongly upon magnetic field near the resonance.

In Figure 3 we have plotted Re(N^2) and Im(N^2) of the two branches against density (for electronic-T=1 Kev, B=1 T, and Frec=55.93 GHz). We see that X-mode is strongly absorbed.

Figure 4 is the plot of Re(N^2) and Im(N^2) for the two branches against the distance to the hardcore (central and helical conductors), in a range close to the area of B=1 T. We have taken for this the calculated profiles of magnetic field and density of TJ-II device. We have taken electronic-T=1 Kev, mean density equals 1E13 cm-3 and Frec=56 GHz.

As we inject from the low field side, only X-mode reaches the resonance,because Z-mode would start propagating in the inner part.This is only possible by mode conversion, but that does not happen at these densities and frecuencies .So, for this mean density, only X-mode is useful for heating and not Z-mode. We can see also that the absorption occurs some centimeters inner than the B=1 T layer, and that it is localized in a narrow layer of

about 2 centimeters width.

REFERENCES:

[1]: J. Guasp et al.: "Physics studies for the TJ-II device". Proceedings of the 12th European Conference on Controlled Fusion and Plasma Physics, Budapest 1985, 441.

[2]: F. Castejon, J. Guasp: "Microwave Injection Situation in Heliac device TJ-II". Submited for publication in Nuclear Fusion.

[3]: C. Alejaldre, J. Guasp: "Microwave absorption near the first and second harmonics in the flexible heliac TJ-II". Submited for publication in Nuclear Fusion.

[4]: M. Bornatici, R. Cano, O. De Barbieri, F. Engelman: "Electron Cyclotron emission and absortion in fussion plasmas". Nuclear Fusion. Vol. 23, No. 9

[5]: P. A. Robinson: "Electron cyclotron waves: dispersion and accesibility conditions in isotropic and anisotropic plasmas". J. Plasma Physics(1986), vol. 35,part 2.

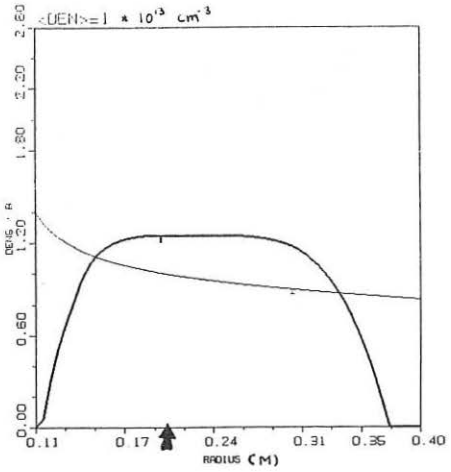

FIG. 1: Density and magnetic field profiles. The Arrow points where the magnetic field Equals 1T.

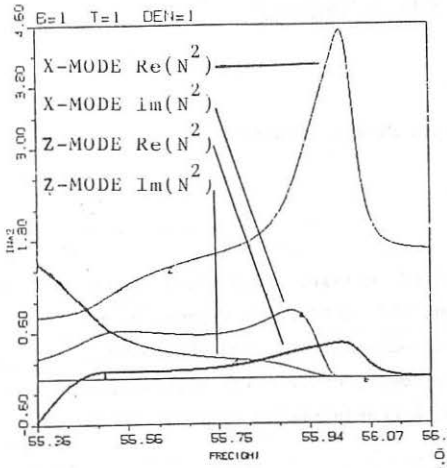

FIG. 2.- Squared refractive index against frecuency (GHz) for B=1 T, n=1 x $10^{13}cm^{-3}$ and T=1 Kev.

FIG. 3.- Squared refractive index against density (in 10^{13} cm^{-3}), for frec.=55.93 GHz, B=1 T and T=1 Kev.

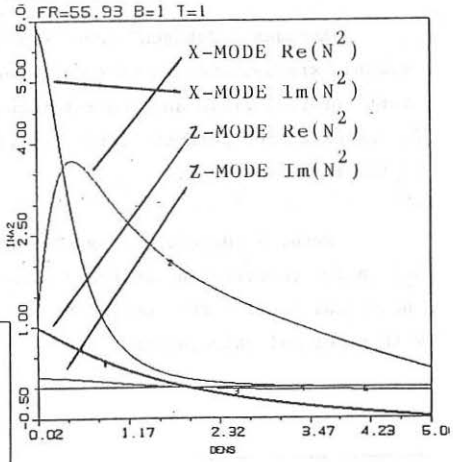

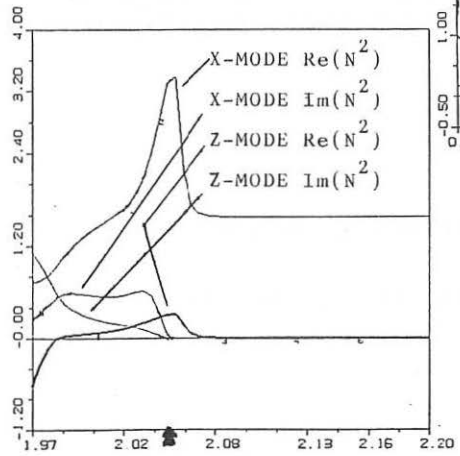

FIG. 4.- Squared refractive index against distance to the hardcore (in dm) for frec.=56 GH_ and mean density equals 1 x 10^{13} cm^{-3}. The arrow points the position of the resonance for cold plasma.

HELICAL AXIS STELLARATOR EQUILIBRIUM

L. GARCIA

Universidad Complutense. Madrid (Spain)

The three-dimensional nature of stellarator geometry makes HHD equilibrium analysis complicated. The stellarator expansion[1] reduces the equilibrium problem to a two-dimensional Grad-Shafranov equation. However, it assumes in the lowest order axial symmetry, and is, therefore, limited to systems with nearly planar axis.

Koniges & Johnson[2] have developed an asymptotic expansion for helical axis systems, in which the lowest order is given by a constant toroidal field and the rotational transform is order δ, being δ, the expansion parameter, the relative strength of the helical field to the toroidal field.

Here, we develop an expansion which takes as lowest order a helically symmetric vacuum field with finite rotational transform. An analytical model corresponding to the TJ-II flexible heliac is compared with numerical calculations.

---

[1] J.M. Greene and J.L. Johnson. Phys. Fluids 4 (1961), 875.

[2] A.E. Koniges and J.L. Johnson. Phys. Fluids 28 (1985), 3127.

MHD Mode Studies for a Topological TJ-II

A. Varias*

División de Fusión
CIEMAT
Madrid (Spain)

A modified version [1] of the spectral stability code HERA [2] is used to study the MHD stability of a straight (helically symmetric) model of TJ-II [3]. The equilibria are calculated in the flux coordinate representation of the MOMCON code [4]. The helically symmetric equilibria are constructed according to the prescription used in [5].

To investigate the influence of the basic stabilizing mechanism of Heliac equilibria on the eigenvalues ω^2 of the internal modes with poloidal mode number m, a sequence of high $< \beta >$ equilibria is generated by varying the curvature $\kappa = Rh^2/(1 + R^2h^2)$ of the magnetic axis between $\kappa = 0$ and $\kappa = 0.17$, the last value close to the actual values in TJ-II. (Here R is the distance of the magnetic axis from the symmetry axis and $h = -0.40$, where $2\pi/h$ is the helical pitch). The rotational transform per period at the axis ι_0 and at the boundary ι_E varies between $\iota_0 = 0.26$ and $\iota_0 = 0.35$, and $\iota_E = 0.16$ and $\iota_E = 0.41$, respectively. The occurrence of unstable modes will be discussed taking the topological constraint of 4 periods into account.

[1] A. Varias, *IPP internal Report* (1987)
[2] R. Gruber et el., *Comput. Phys. Comm.* **21**(1981) 323
[3] A. Perea, J.L. Alvarez Rivas et el., *12th Eur. Conf. on Contr. Fusion and Pl. Phys., Budapest 1985, ECA Vol.9F, Part I, 433*
[4] S.P. Hirshman and D.K. Lee, *Comput. Phys.Comm.* **39** (1986) 161
[5] J. Nührenberg, R. Zille and S.P. Hirshman, *this conference*

* Present adress: *Max-Planck-Institut für Plasmaphysik, IPP-EURATOM Association, D-8046 Garching bei München*

INFLUENCE OF RADIAL ELECTRIC FIELD ON THE CONFINEMENT OF FAST IONS IN A NBI HEATED HELIOTRON E PLASMA

K.Hanatani, F.Sano, Y.Takeiri, K.Kondo, H.Zushi, H.Okada, O.Motojima, R.Takahashi, M.Sato, S.Sudo, T.Mutoh, K.Akaishi, H.Kaneko, T.Mizuuchi, N.Noda, S.Nishimura, T.Aikiyo, A.Iiyoshi and K.Uo

Plasma Physics Laboratory, Kyoto University, Gokasho, Uji, Kyoto, JAPAN

1. INTRODUCTION

Fast neutral beam injection in both Wendelstein VII-A and Heliotron E showed effective heating of plasmas /1,2/ even though nearly perpendicular beams were used in these devices. Reasons for the effective heatings in the two devices, however, have been considered to be different. In WVII-A, the reason is attributed to the enhanced confinement of beam ions as well as of thermal ions due to the effects of large radial electric field, E_r. In Heliotron E, by contrast, E_r field has been considered to have only small effect on beam ion orbits. The purpose of this paper is to extend the previous work on the fast-ion confinement in Heliotron E /3,4/ and to clarify the influence of E_r field. Our recent particle orbit calculation in nonaxisymmetric plasmas has shown that resonance caused by ExB drift affects the confinement of suprathermal ions /5/. In this paper, we will first describe the orbit theory on the ExB drift resonance and its effect on the fast-ion orbit loss in Heliotron E. We will then describe an experiment which was carried out to verify the theoretical prediction about the resonant orbit loss in the perpendicular NBI experiment on Heliotron E.

2. E x B DRIFT RESONANCE

In nonaxisymmetric plasmas with E_r field, confinement of a group of particles in the velocity distribution function deteriorates when the ExB drift cancels the poloidal motion of these particles. This condition is called "resonance". Two different resonances were confirmed numerically /6/. One is toroidal resonance ($tv_{//}/R + \Omega_{ExB} = 0$) and the other is helical resonance ($\Omega_h + \Omega_{ExB} = 0$). The toroidal resonance affects helically-untrapped particles when ExB drift resonates with rotational transform t. The helical resonance affects helically trapped particles when the ExB drift cancels Ω_h due to helical field ripple e_h. Either ions or electrons are affected by the helical resonance depending on the polarity of electric potential ϕ. The numerical calculation showed that "resonant superbanana" orbits, which are much harder to be confined than transit banana orbits, appear near the condition of helical resonance.

The relevance of the two types of ExB resonances depends also on the magnetic field configuration--in particular on e_h. The confining mechanism of perpendicularly injected fast ions in WVII-A was explained by the shift

of toroidal resonance in the velocity space /6/. On the other hand, the helical resonance can have important influence on drift orbits in Heliotron E because it has a deep helical ripple; $e_h(a) = 0.3$. In the Heliotron E experiment, the effect of the helical resonance was discussed /4/ as a possible reason for up-down asymmetry observed in charge-exchange outflux of fast ions in a low energy regime ($E \lesssim 3$-4 keV).

3. VELOCITY SPACE LOSS REGION WITH E_r FIELD

The loss region of fast ions in the velocity space is an informative diagram for interpreting the performance of NBI heating. Our concern here is to see the influence of positive and negative potential on the loss region in Heliotron E. In the calculation, we assumed parabolic potential profile, $\phi = \phi_o(1 - \psi/\psi_b)$. Figure 1 (a) shows the velocity space loss region for $\phi_o = +1$kV. As was already reported /3/, the loss region in Heliotron E split into two parts, indicating the containment of deeply trapped particles. The loss region with the $\phi_o = +1$kV potential was narrower than that without potential. When we assumed an negative potential ($\phi_o = -1$kV), however, the two parts combined into a larger loss region (Fig.1(b)). Confinement of deeply trapped ($v_{\parallel} \cong 0$) particles deteriorated

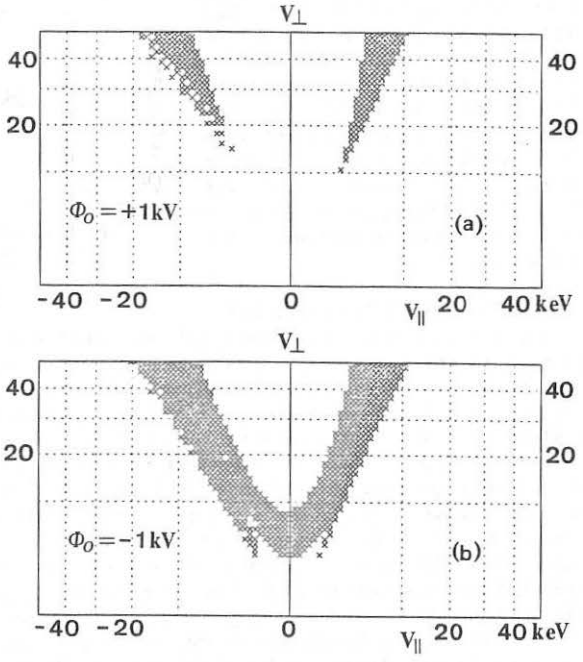

Fig.1 Potential dependence of velocity space loss region in Heliotron E.
Calculated at $\bar{r}/a = 0.5$ out side of the torus.
(a) $\phi_o = +1$ kV,
(b) $\phi_o = -1$ kV.

near the condition of the helical resonance, $E_{res} \cong -q\phi_o/e_h(a)$, owing to the resonant superbanana orbits. In contrast to the loss region in the WVII-A Stellarator /6/, the toroidal resonance found to have little effect on the loss region in Heliotron E. It must be emphasized that presence of E_r field is not always favorable to the fast ion confinement. If a large negative potential is created in the Heliotron E plasma and if the resonant energy, E_{res} is close to the injection energy, E_o(=27keV), no substantial heating by the perpendicular injection is expected.

4. POLOIDAL ROTATION MEASUREMENT

Since the possibility of the resonant superbanana loss depends on the polarity of potential, it is important to know the E_r field in the plasma. To obtain the information about E_r field, we measured poloidal rotation velocity V_p of plasmas in the experiment. Doppler shift of impurity line emission ($^{\circ}$C V; 2271A) was measured by using a Czerney-Turner type visible spectrometer. The NBI heated plasmas ($\bar{n}_e \cong 6\times10^{13}cm^{-3}$) were found to rotate in the direction of electron diamagnetic drift, indicating the presence of negative (inwardly pointing) E_r field. Figure 2 shows the measured V_p for various P_{NBI} (port through power); circle for B = 1.9T, diamond for B = 0.94T. The maximum rotation speed was about $(4\text{-}6)\times10^5$ cm/s at $\bar{r}/a \cong 0.7$. The rotation speed was much slower than that measured in the WVII-A Stellarator. In ECH plasma ($\bar{n}_e \cong 0.6\times10^{13}cm^{-3}$), the direction of poloidal rotation was opposite to that of the NBI plasmas.

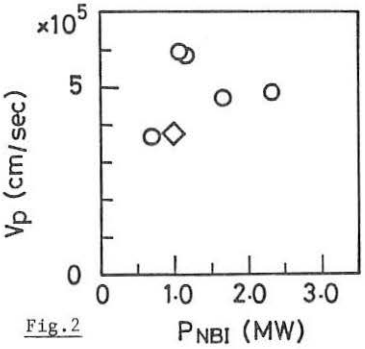

Fig.2

5. CHARGE-EXCHANGE ENERGY SPECTRUM

The poloidal rotation measurement suggested the presence of negative potential in the NBI plasma. Although negative ϕ_o corresponds to the E_r field which can cause helical resonance of ions, the magnitude of ϕ_o estimated from V_p is so small (-1 kV $< \phi_o < 0$) that the resonance does not directly affect fast ions near the injection energy E_o (=27 keV). The inferred small potential is consistent with the previous observation of confinement of perpendicularly injected beam ions in the high energy regime /5/. The estimated potential ϕ_o suggests that the helical resonance will occur in the low energy regime ($T_i < E_{res} < E_{crit}$). Here, $E_{crit} = 14.8T_e$ is the so-called critical energy. This means that fast ions suffer the resonant-orbit loss after they slow down below E_{crit}. As a result, the helical resonance can reduce the ion heating efficiency of NBI.

In order to verify the existence of the resonant superbanana loss of fast ions in the Heliotron E experiment, we have examined the charge

exchange energy spectra in the low energy regime. Figure 3 shows the energy spectrum of perpendicularly injected fast ions. The neutral particle analyzer was oriented also perpendicular to the field lines so as to detect the energy spectrum along $v_\perp$ axis in the velocity space. Around the expected resonant energy $E_{res} \cong 3$ keV, we found a depletion of fast ions in the distribution function. The relative dip in the B = 0.94T spectrum compared with the reference (B = 1.9T) spectrum is interpreted as been due to shorter toroidal drift time of resonant ions in the loss region. Note that scattering time is unchanged.

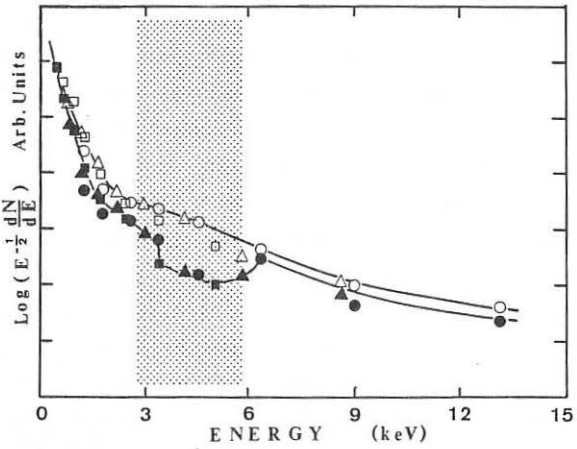

Fig.3 Charge-exchange energy spectrum of an exactly perpendicular beam. Open symbols for B = 1.9T, closed symbols for B= 0.94T. External parameters were fixed except magnetic field, B.

6. SUMMARY

In this paper, we have investigated the role of ExB drift resonance in the confinement of helically trapped fast ions in Heliotron E. Instead of the toroidal resonance, which plays major role in the beam-ion confinement in the WVII-A device, the helical resonance becomes important in the Heliotron E device. The poloidal rotation measurement of NBI plasmas suggested the presence of small negative E_r field, which can cause the helical resonance of fast ions in the low energy regime. The charge exchange energy spectrum showed a correlation with the predicted helical resonance in the Heliotron E configuration.

REFERENCES

/1/ WVII-A Team, NI Group, et al., in Contr. Fusion and Plasma Phys., (Proc. 10th Int. Conf. London 1984) Vol.2, IAEA, Vienna (1985) 371.
/2/ K.Uo, A.Iiyoshi, T.Obiki, et al., ibid. 387.
/3/ K.Hanatani, M.Wakatani and K.Uo, Nucl. Fusion 21 (1981) 1067.
/4/ K.Hanatani, Y.Nakashima, H.Zushi, et al., Nucl. Fusion 25 (1985) 259.
/5/ K.Uo and Heliotron E group IAEA-CN-47/D-I-1, (Kyoto, 1986).
/6/ K.Hanatani, F.P.Penningsfeld, H.Wobig, in Proc. Int. Stellarator/Heliotron Workshop (Kyoto, 1986).

DEVELOPMENT OF CIRCULARIZER FOR ENDLESS MIRROR DEVICE WITH l=2 HELICAL SYSTEM

S.Ikezawa, T.Yamazumi, Y.Taki, S.Takeda, S.Nagao
Department of Electronic Engineering,
Chubu University, Kasugai 487, Japan

To build the endless mirror device of racetrack type that has helical system as the curvelinear part , it is important to connect the magnetic surfaces between the helical and the mirror parts. The four circularizers (the length L) , which are mounted by space W at the mirror ends , have some times large pitch mc compared with that of the helical system (m=4). The aspect ratio R/a=4.5 keeps constant(R=45cm). In this paper we will report here the design of the circularizer of length L , current Ic , pich mc and space W.

Fig.1 shows the winding of the coil in the endless mirror. In the caliculation , the toroidal magnetic field Bt=2.5kG at the center of mirror , the helical current Ih=10kA and the vertical current Iv=0.8kA keep constant. Fig.2(a) , (b) and (c) show the magnetic surfaces in case of the circularizer currents Ic=0, 5 and 10kA , respectively. When Ic=0kA (Fig.2(a)) , the magnetic fields cannot compose the magnetic surface , because the magnetic fields are resonant and become magnetic island. When Ic=5kA (Fig.2(b)) , the resonance does not occur and they can compose the magnetic surface. However, as the Ic increases untill about 10kA (Fig.2(c)), the magnetic fields begin to be disturbed and do not compose the magnetic surfaces.

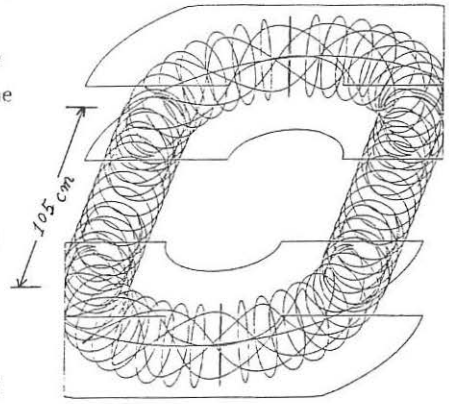

Fig.1 Winding of coil

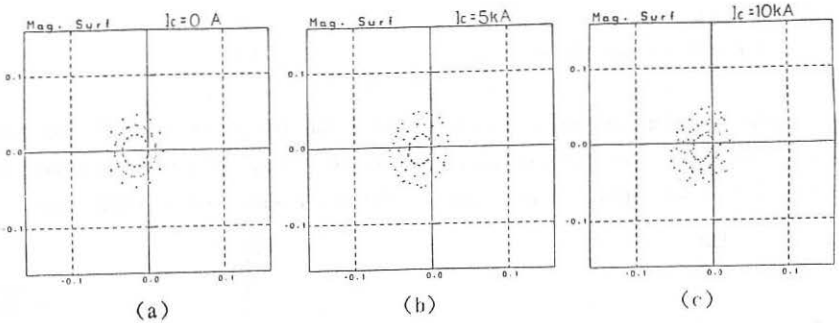

(a) (b) (c)

Fig.2 Magnetic surface at center of mirror (mc=2*m , L=30cm , W=2cm)

The plasma volume confined is depend on the cross section (S) of the most outside magnetic surface. It is hoped that the confinement cross section is controlled to be large , because the generation of fusion energy output is proportional to the volume.

With regard to Fig.2 , we have computed the effect of Ic , L , mc and W on S. Fig.3 shows the relation between Ic and S. The other parameters keep constant (L=30cm , W=2cm). In cases of mc=2*m , mc=3*m and mc=m , the cross section S of magnetic surface become maximum around Ic=3-4kA. In Fig.4 , the relation between L and S is plotted. In cases of mc=2*m and mc=3*m , there the maximum S at L=30cm. But when mc=m the relation is reversal. Because when mc=m , the magnetic surface is disturbed. Fig.5 shows the relation between mc and S. When mc=2*m , S becomes maximum in Ic=3-4kA. Fig.6 shows that S does not depend on the space W.

We summarized the parameters of the circularizer of the maximum cross section of magnetic surface in Table.2 , for the basic endless mirror device (Table.1).

Now we discuss the comparison between our results and the others [1,2]. Friman et al.[1] proposed the circularizer first in C-Stellarator device , and Gavrlov et al.[2] carried out the experiment for l=3. They presented the formulation of the best condition for the circularizer ,

as follows ;

$$L\alpha_c=\pi/l,\quad lh/\alpha=Klc/\alpha_c, \qquad \text{——— (1)}$$

Where $\alpha=2\pi/Lh$ and $\alpha_c=2\pi/Lc$ (Lh : the length of helical coil and Lc : the length of circularizer coil). They also obtained the relation K=2.2 for l=3. While in our case , L=30cm , Lh=188.9cm , Lc=122.4cm ,

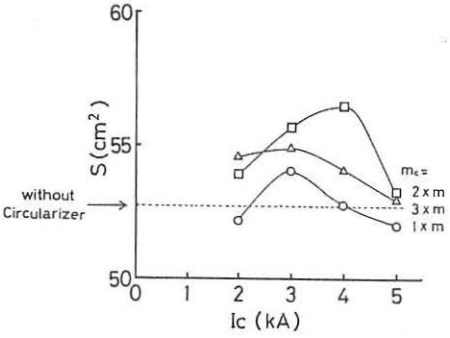

Fig.3 relation between Ic and S
(L=30cm)

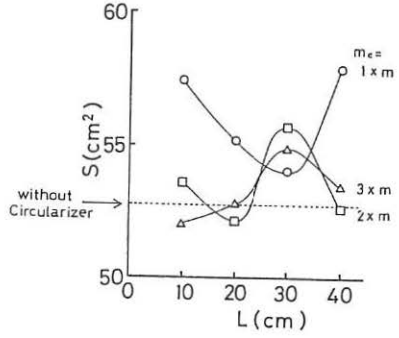

Fig.4 relation between L and S
(Ic=3kA)

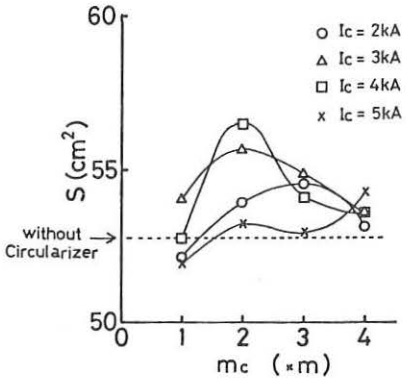

Fig.5 relation between mc and S
(L=30cm)

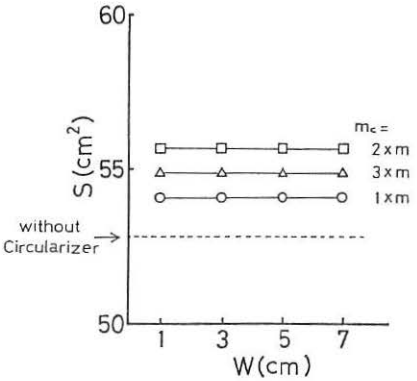

Fig.6 relation between W and S
(Ic=3kA , L=30cm)

l=2 , Ih=10KA , Ic=3KA are substituted into eq.(1) , then K=5.1 is obtained , where Lh denotes a quater length of one turn helical winding as the four circularizers are mounted in our racetrack device.

Next , the Pfrish - schlüter current in herical part may disturb the magnetic surface[3] in the rectilinear mirror part , so that the Dracon's condition that the current does not flow into the mirror part must be satisfied[4] by the circularizer.

Table.1 Basic Parameters of Endless Mirror Device

Helical Coil	
pair of coil	l = 2
pitch	m = 4
current	Ih=10kA
Vertical Coil	
current	Iv=0.8kA
Toroidal Coil	
magnetic field	Bt=2.5kG

Table.2 Parameters of Circularizer Developed

pair of coil	l = 2
pitch	mc= 8 (2*m)
length	L =30cm
space	W = 2cm
current	Ic= 3kA

References

1. E. Friman et al.,The Proposed Model C Stellarator Facility project Matterhorn. Ch. Ⅳ. NYO-7899, p.78.
2. B. I. Gavarilov, F. V. Karmanov, and G. P. Maksimov, The Operation of The Cylinderizer in The Stellarator, At. energ., 18, 273 (1965).
3. Yu. M. Loktionov and V. P. Sebko, Operation of Stellarator Circularizers in The Presence of an Axial Current, At. energ., Vol. 28, No. 3, p.263-265 (1970).
4. V.V.Arsenin , B.B.kadomtsev , V.D.Shafranov et al.;Closed Magnetic Traps with Rectilinear Sections , Plasma Phys. and Controlled Nuc. Fusion Research (1982,volⅢ) p.159.

DESIGN STUDIES ON COMPACT HELICAL SYSTEM (CHS)

M. Fujiwara, K. Matsuoka, K. Yamazaki, K. Nishimura,
T. Amano, T. Kamimura, H. Sanuki, J. Todoroki
Institute of Plasma Physics, Nagoya University, Nagoya 464, Japan

I. Introduction

In helical systems, toroidicity introduces two contradicting factors each other, that is, MHD stability beta limit $\beta_{ST} \propto A_p^{-1}$ (here A_p is aspect ratio) and particle confinement which is better in a larger A_p device. The recent development of theoretical research on helical systems presents the possibility to optimize the configuration for stable confinement of plasmas by the effect of ambipolar potential, and the localization of helical ripple to reduce transport in a low aspect ratio device (the works developed by Mynich, Boozer, Kovrizynykh and a series of ATF-1 design studies).

On the other hand, the experimental research at present is carried out in large aspect ratio devices H-E (A_p = 10-11), W7A (A_p = 15-20) and L-2 (A_p = 9-10) except JIPP T-II (A_p = 7-8). ATF-1 will be tested near future to prove the possibility of plasma confinement in a lower aspect ratio (A_p ≃ 7) helical system. In this report we present the design study of a more compact helical system (A_p ≃ 5) CHS based on the recent theoretical and experimental results.

The CHS device is now under construction and will be in operation in 1988 at the Institute of Plasma Physics, Nagoya University.

II. Configuration Studies

Selection of configuration is carried out from several key points listed as follows: (1) Plane axis helical systems are torsatron/heliotron and stellarator types. The later configuration needs helical coils and toroidal coils except modular coil systems, but the former ones compose of helical winding and poloidal coils to cancel the vertical fields induced by helical coils. From the viewpoint of simple structure to keep good accessibility, CHS employs torsatron/heliotron type configuration.

The pole number l of helical winding is determined to be l = 2 in order to keep the rotational transform angle on the magnetic axis t(0) finite (t(0) = 0 in l = 3 systems) from the viewpoint of low axis shift for finite β plasma and good confinement in the central core region. To reduce the aspect ratio without lowering t(0), the pitch of helical winding $\gamma = ma_h/lR_o$, where m, a_h and R_o are the toroidal period number of helical field, minor radius of helical winding and major radius of the torus, is around 1.25 which is lower than the values of H-E, ATF-1 device.

(2) Pitch modulation of helical winding is also employed for the formation of clean and large magnetic surface without the bifurcation in a low aspect ratio helical system. According to Cary-Hanson's theory, the modulation includes multi-harmonic helical fields for the ideal case, but CHS device uses a simple winding law $\theta = (m/l)\phi + \alpha^* \sin(m/l)\phi$ (here θ, ϕ and α^* are poloidal and toroidal angle and the constant value of the pitch modulation factor) to build a real experimental device with a high accuracy. α^* is selected 0.3 ($\sim a_h/R_o$). The positive α^* is effective not only to form clean and large magnetic surfaces but also to reduce the vertical fields induced by helical windings by a factor 2/3.

(3) CHS device is also equipped with the main vertical coils and the additional coils called SF whose role is shaping the averaged magnetic surface by controlling the component of the quadrapole fields. The major parameters of CHS are listed in Table 1. The top view of the device is shown in Fig.1. The magnetic surfaces at different toroidal angle, the radial profile of the rotational transform t(r) and the well depth are shown in Fig.2.

MHS studies are also carried out for CHS configuration by using H-APPOLO code, which uses an averaging method, for the equilibrium/ballooning stability and H-ERATO code for stability. The β value is not limited by the stability but is determined by the destruction of equilibrium in a fat helical torus such as CHS. One example of computer results is shown in Fig.3 which indicates the magnetic axis shifts as a function of the averaged β for three different fixed vertical fields. MHD equilibrium calculation for CHS carried out by different codes such as VMEC for NEAR (ORNL) presented consistent results with those in Fig.3. The maximum β is estimated to be around 5-6 %.

Confinement times are also evaluated by various methods such as the point model of neo-classical transport, 1-D transport WHIST code by ORNL people and the empilical scaling obtained by H-E group. The energy confinement time is 3-10 ms for the plasma parameter of n_e = 1-5 x 10^{13}/cc and T_e = 500-1000 eV. The role of ambipolar electric field is found to be extremely important for plasma confinement in a low aspect ratio helical system.

III. The Experimental Program

(1) After the device construction, ECH of 18 GHz/30 kW (B = 0.64 T) and 28 GHz/200 kW/75 ms (B = 0.5 and 1.0 T) are tried to study the basic confinement characteristic of CHS device. The RF plasma heating is also tried to produce a high dense plasma ($n_e \geq 10^{13}$/cc) in various magnetic field strength (B = 0.3-1.5 T). The development of RF and production heating makes it possible the B dependence of confinement, high β studies in a low magnetic field case, and preparation of target plasmas for a neutral beam injection.

(2) In 2nd phase, high power NBI heating (30-40 keV, 3-4 MW) and high power ICRF are planned to study the confinement of a finite β, high temperature plasma. Higher frequency ECH (60 GHz/200 kW/100 ms) is also carried out in this stage.

(3) CHS device will be up-graded to be operated at B $\sim$ 2T by changing the power supply system of coils.

(4) The helical windings (l = 2, m = 8) of CHS can be operated at different coil currents, so the helical axis like configuration can be studied in the later stage of the experimental program.

Table 1 Major parameters of C.H.S

Major radius R	1.0m
Helical coil radius a_h	0.313 m
Avarage plasma radius a_p	0.2 m
Plasma aspect ratio A_p	5
Multipolarity l	2
Number of field period m	8
Pitch parameter	1.25
Pitch modulation factor	0.3
Field strength on axis B	1.5T-2.0T
Central transform	0.33
Edge transform	0.8-1.0
Pulse length	2s at 1.5T
Access port diameter	30 cm,50cmx38cm
Neutral beam power	3-4MW/40keV/1s
ECH	30 KW/18GH_z/CW
	200KW/28GH_z/75ms
	200KW/60GH_z/100ms
ICRF	500KW/6-28MH_z/10ms
	2MW/20-40MH_z/30ms

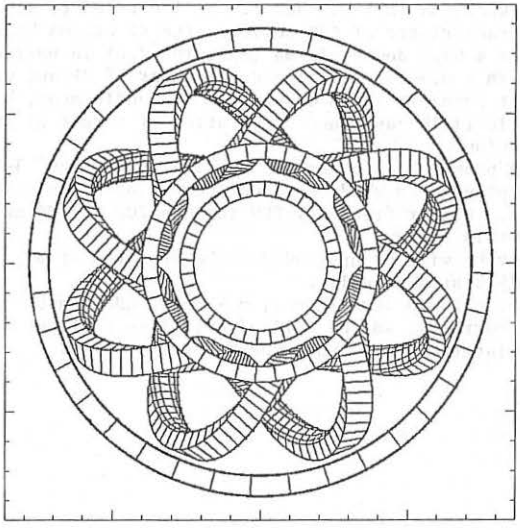

Fig.1 Top view of CHS device.

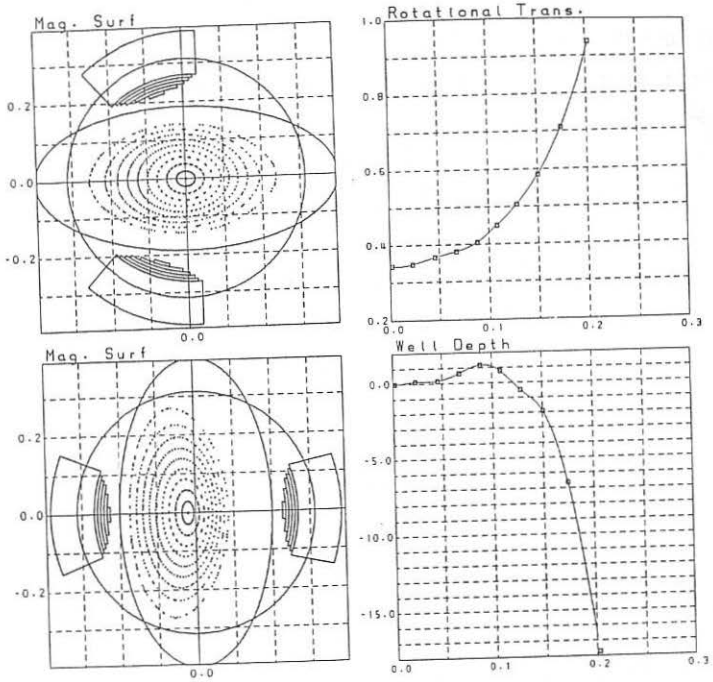

Fig.2 Magnetic surfaces and vaccum field characteristics.

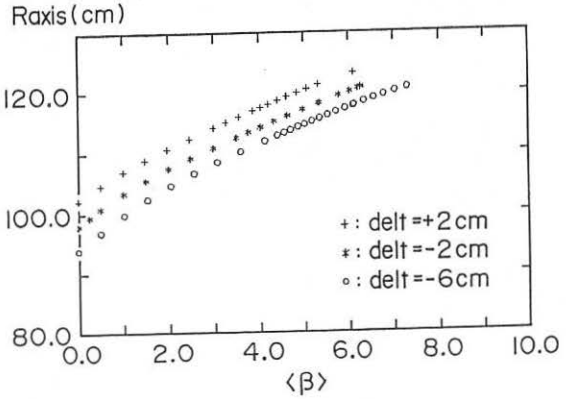

Fig.3 Positions of the magnetic axis as a function of ⟨β⟩.

ABSTRACT

Matveeva E. A., Pustovitov V. D.

EFFECT OF THE PLASMA ELONGATION ON EQUILIBRIUM IN STELLARATORS

In this paper the effect of the boundary shape of plasma on the β -value, the geometry of internal magnetic surfaces and the rotational transform profile $\mu(a)$ in odinary stellarators (with planar circular axis) is investigated. Averaged magnetic surfaces are described by three parameters- toroidal shift Δ , elongation K and triangularity δ . The values of K and Δ on the plasma boundary are specified as initial data. Two-dimensional equilibrium equation is solved numerically using the method of electrodynamic moments.

It is shown that in stellarators with shear elongation of the averaged boundary gives rise to significant increase of the ellipticity of the internal magnetic surfaces, and, correspondingly, to the considerable increase of β_{eq} (2÷2,5 times for rather moderate $K_\ell \lesssim 1{,}3$). In stellarators without shear this effect is much weaker. The dependence of β_{eq} on K_ℓ is the same as for the tokamak with the uniform current density:

$$\beta_{eq}(K_\ell)/\beta_{eq}(1) = \left(3K_\ell^2+1\right)\cdot\left(\frac{K_\ell}{K_\ell^2+1}\right)^2 .$$

In this work analitical dependence of $\mu(a)$ on geometric parameters K and Δ has been derived:

$$\mu(a) = \frac{2K}{K^2+1}\left[\mu_0 + \frac{\mu_\ell-\mu_0}{a^2}\left(a^2\frac{K^2+1}{2}+2\Delta^2\right)\right]\times \quad (1)$$

$$\times\left(1-\frac{3K^2+1}{2(K^2+1)}\frac{\Delta'^2}{2}\right).$$

It follows that the μ -profile control in stellarators with shear is in principal possible by elongating of the averaged magnetic surfaces only. From (1) it is also clear that in shearless stellarators with non-zero β negative shear region always exists and, besides, $\mu(a)$ strongly depends upon pressure distribution $p(a)$ (through Δ'). Formula (1) , obtained in $J''=const$ approximation , is in good qualitative agreement with calculated μ -profile.

HIGH-β EQUILIBRIUM IN A STELLARATOR

L.M.Kovrizhnykh, S.V.Shchepetov

General Physics Institute, USSR Academy of Sciences

D.P.Kostomarov, D.Yu.Sychugov

Moscow State University

As a rule, in analyzing plasma equilibrium in magnetic confinement systems, it is not apriori clear, what is the topology of the magnetic surfaces. The presence of a finite pressure or the currents flowing in the plasma, in particular, lead to the appearence of magnetic islands or separatrix. Here the problem of stellarator equilibrium is numerically solved and the topology of magnetic islands is studied. The case of fixed total current flowing in the plasma is considered as well as that of stationary plasma equilibrium in a stellarator with a zero-current, flowing through the cross section of each magnetic surface. Analytical estimations are given.

Using the system of averaged MHD equations, which reduces the problem to study axisymmetric case [1], it is easy to obtain the equation for the poloidal flux of a magnetic field Ψ :

$$-\Delta^*(\psi-\psi^*)\equiv\left\{-\frac{\partial}{\partial z}\frac{1}{z}\frac{\partial}{\partial z}-\frac{\partial^2}{\partial z^2}\right\}(\psi-\psi^*)=\left[z^2\frac{dP}{d\psi}+\frac{1}{2}\frac{dI^2(\psi)}{d\psi}\left(1+\frac{B_s^*}{B_0}\right)\right]=z\,J_s \qquad (1)$$

where p is the plasma pressure, $I(\psi)$ is the poloidal current, B_0- is the longitudinal magnetic field at the axis of the system. The dependence of $\psi^*(r,z)$ and $B_s^*(r,z)$ functions is governed by the type of helical fields confining the plasma and we shall consider it to be given in our case. In numerical calculations we use the Cartesian coordinate system (r,s,z) where s is the angular coordinate along the axis of the torus. Later on we shall consider that at p=0, J_s=0 level lines in the cross-section s = const are concentric circles, at the same time $\psi^*=B_0\int_0^\rho \rho\iota^*d\rho$, where ι^* is the rotational transform produced by helical windings, $B_s^*/B_0=-NR_0^{-2}\int_0^\rho(\iota^*\rho^4)'\rho^{-2}d\rho$, N is the period number of helical winding, ι^* is represented in a form:

$$\iota^*=\sum_{k=1}C_k x^{2k-2},\quad x=\rho/\rho_0,\quad C_k>0.$$

Here ρ_0 is the minor radius of magnetic surface, $\rho=\sqrt{(z-R_0)^2+z^2}$.

For the sake of certainty we shall consider later on that plasma column is bounded by an ideally conducting shell with a major radius R_0 and minor ρ_0 . In numerical calculations we used the L-2M stellarator parameters (General Physics Inst.)[2]:
$\delta = \rho_0/R_0 = 1/6$, $C_1 = 2C_2 = 2C_3/5 = 0.22$, $C_{k>3} = 0$, $N = 4$.

At $p' \sim$ const $I^{2\prime}(\psi) \sim \psi^n$, n=0,1 Eq.(1) may be solved analytically the toroidicity being arbitrary. Here we shall limit ourselves to the case $B_s^*/B_0 \ll 1$ that seems to be optimal for reaching maximum β [3]:

Let us name the properties of the solution to Eq.(1) at n=0:
1) when the current flowing through the crosssection of the plasma column is fixed and nonnegative, Ψ cease to be a non-negative function at a certain value of $\beta_{max} = 2p_{max}/B_0^2 \equiv \beta_{cr}$. This value of the parameter β is the maximum one since $\Psi<0$ corresponds to a physically meaningless negative pressure;
2) when $C_{1,2} \neq 0$, $C_{k>2} = 0$ at $\Psi \geq 0$ the system has a single axis;
3) when $C_3 \neq 0$ the number of magnetic axes may vary depending on the value of β . At low β values, the configuration with a single axis is realized, while β value grows the configuration with three axes appear - two elliptical axes and one hyperbolic axis (See Fig.1);
4) when t^* is growing arbitrary function of x the number of axes does not exeed three, at an arbitrary β and $\Psi \geq 0$.

Ommiting straightforward algebra let us formulate the following properties of solution to Eq.(1) at n = 1 :
1) non-negative solution for Ψ exist at $0 \leq \beta_{max} \leq \infty$;
2) when $C_1 \neq 0$, $C_{k>1} = 0$, that corresponds to a shearless stellarator, the magnetic configuration has a single axis;
3) in a stellarator with large shear, magnetic islands may appear and the number of magnetic axes does not exeed three;
4) when β value continue to grow, the magnetic islands may disappear due to the decrease of Ψ value on the inner circuit of the torus.

Now let us consider a stellarator with zero current flowing through the cross-section of each magnetic surface. We shall show that under this condition the solution to Eq.(1) cannot have a local minimum surrounded by a local structure of smooth or

piecewise-smooth surfaces, assuming $-\Delta^* \psi^* \equiv g(r,z) > 0$. Suppose by contradiction that there is a local minimum at a certain point M in the inner region, surrounded by closed level lines ψ = const. For the level lines located sufficiently close to the point M, the inequality $\frac{\partial \psi}{\partial n_0} \leq 0$ is valid , where n_0 is the inner normal to the level line. In a currentless regime, integrating Eq.(1) over the region Ω_ε bounded by one of these level lines, and transforming the left-hand side according to the Hauss-Ostrogradskii formula we come to the contradiction:

$$0 \geq \int_{\partial\Omega_\varepsilon} \frac{1}{r} \frac{\partial \psi}{\partial n_0} dl = \iint_{\Omega_\varepsilon} g(r,z) r^{-1} dS > 0$$

The maximum possible number of axes in the case of completely currentless stellarator is, thus, equal to two.

The numerical calculations show that for n = 1 the second magnetic axis is formed at very high pressures $\beta_{max} \sim 2\varepsilon^2\delta$, which are unlikely to be of practical interest.

The lower value of the parameter $\beta_{max} = \hat{\beta}$, at which the system has the second axis in the inner region, is obtained for the pressure profiles, whose gradient maximum is reached at low (ψ/ψ_{max}) , that may be explained as follows. Since the finite pressure causes the shift of the magnetic surfaces, aligned with the major radius increase, and the value of poloidal flux on the inner circumference decreases the maximum value of the Pfirsh-Schluter, which is negative there, is located in the region, where confining field $\vec{B}_p^* = [\vec{\nabla}\psi^* \times \vec{e}_\varphi] r^{-1}$ is small.

The discussion above is illustrated by Figs. 2 a,b which present the calculation results for the pressure profiles:

$$p = p_{max} \int_0^y F(y)dy \Big/ \int_0^1 F(y)dy, \quad F(y) = \exp[-(y-y_0)^2/\delta], \quad y = \psi/\psi_{max}$$

the maximum of pressure gradient is located at $y = y_0$, $\delta = 0.1$. The minimal value of $\hat{\beta}$ parameter at which the system forms an additional axis is reached at $y_0 \sim 0.2$. The calculations show the plasma to be stable against the interchange modes in the vicinity of a zeropoint of a poloidal magnetic field.

---

1. L.M.Kovrizhnykh and S.V.Shchepetov, Fiz.Plazmy 6, 976 (1980) [Sov.J.Plasma Phys. 6, 533 (1980)] .

2. I.S.Danilkin, O.I.Fedyanin, I.S.Shpigel, L.M.Kovrizhnykh, in: Proc. US-USSR Topical Meeting: Magnetic Configurations, Equilibrium and Stability of Stellarators, 1, Rep.1 (1986).
3. L.M.Kovrizhnykh, S.V.Shchepetov, Usp, Fiz. Nauk 148,637(1986), [Sov. Phys. Usp. 29, 343 (1986)] .

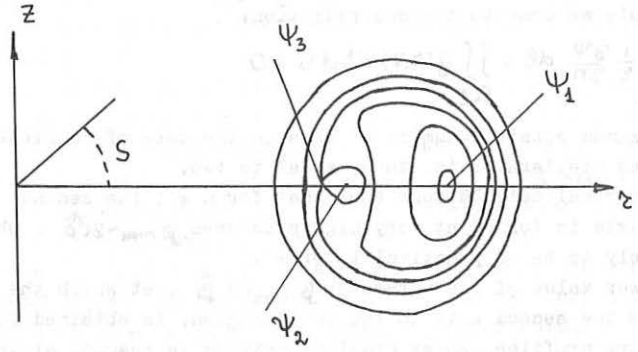

Fig.1. The structure with a maximum Ψ_1 , minimum Ψ_2 and saddle point Ψ_3 .

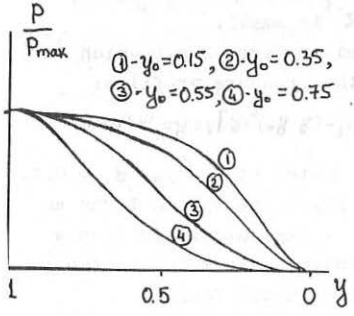

Fig.2a.

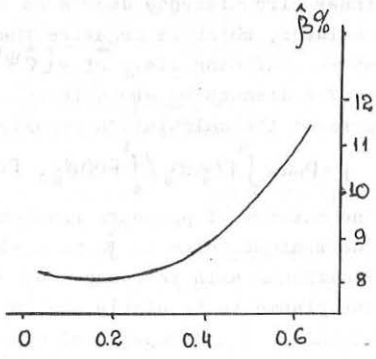

Fig.2b.

ESTIMATION OF PRESSURE RADIAL PROFILE AND ENERGY CONFINEMENT TIME IN STELLARATOR-REACTOR WITH THE LARGE SHEAR

A.V.Komin, A.B.Mineev
D.V.Efremov Scientific Research Institute of
Electrophysical Apparatus, Leningrad

I.S.Danilkin, L.M.Kovrizhnykh, S.V.Shchepetov
General Physics Institute of the USSR
Academy of Sciences, Moscow

Abstract

Method /1/ of estimation of the energy confinement time τ_E in tokamaks has been applied to describe the τ_E behaviour and pressure profile in a large shear stellarator.

Approximations for finite beta plasma displacement in stellarator have been given, which correspond to the data of other works.

The MHD plasma stability criterion /2/ in stellarators has been analyzed. When the plasma pressure increases, the plasma region on periphery, where pressure profile is defined by stability criterion, decreases. This situation allows to conclude that in stellarators, unlike tokamaks /1/ there must not be essential confinement degradation due to plasma instability.

The probability of energy confinement improvement in low collisionality region of stellarator has been studied. It has been shown that if radial profiles of particle and energy sources coincide within complete neoclassical system of equations /3/, the essential improvement of confinement is possible.

/1/ J.W.Connor, J.B.Taylor, M.F.Turner Nucl. Fusion v.24, no.5, p.642, 1984.

/2/ L.M.Kovrizhnykh, S.V.Shchepetov Uspekhi Fiz. Nauk, v.148, no.4, p.637, 1986.

/3/ L.M.Kovrizhnykh Nucl. Fusion v.24, no.4, p.435, 1984.

MODULAR STELLARATORS WITH IMPROVED CONFINEMENT PROPERTIES

E. Harmeyer, F. Herrnegger, J. Kisslinger, A. Montvai*, F. Rau , and H. Wobig

Max-Planck Institut für Plasmaphysik, D-8046 Garching, FRG, EURATOM-Association.
* Guest from: Central Research Institute for Physics, H-1525 Budapest, Hungary.

Abstract *Vacuum field properties of stellarators with modular coils are compared in order to select the configuration with optimum confinement, small bootstrap current, and prospects to achieve a high beta value.*

In an effort to select an optimized configuration for application to Wendelstein VII-X, the next step of the Garching stellarator program, vacuum field properties of three types of stellarators with modular coils and reduced secondary currents and a modular Heliac system are investigated:

(1) : a system W VII-X-1D with 6 elliptically shaped coils in each of the five field periods, otherwise similar to that of the forthcoming Garching Advanced Stellarator Experiment Wendelstein VII-AS;
(2) : a Bean-shaped Advanced Stellarator configuration BSX derived from item (1), with some indentation of the flux surfaces at particular toroidal positions, realized by 9 elliptical coils per field period and otherwise similar to a system described in /1/;
(3) : several Helias systems with 4 to 6 field periods, HS4, HS5 and HS6, with topologies similar to those published in /2/ or /3/ , realized by 10 to 12 coils per field period;
(4) : a modular Heliac with 5 field periods similar to those published in /4/.

These types of modular stellarator configurations were discussed in a recent 'Workshop on Wendelstein VII-X' /5/. Examples of coil shapes and magnetic vacuum fields are given in the five columns of Fig. 1. The coils of W VII-X-1D and BSX 5-2 are centered along planar curves $R(\varphi) = R_o\,(1 + \delta cos(5\varphi))$, with $R_o = 5\,m$ and $\delta = 0.016$ and 0.075, respectively. The coil bores have elliptical minor cross section. This would ease the maintenance of a future reactor. Indeed, W VII-X-1D is a downgraded version of ASRA6C, the reference configuration of a recent study /6/ of critical issues of Advanced Stellarator reactors. The Helias configurations studied so far require coil contours matched to the shape of outer flux surfaces. In the modular Heliac identical coil shapes should be possible. The coils for the Helias (Heliac) systems are arranged along spatial curves with moderate (large) values for the vertical excursion and coil tilt. Consequently, the magnetic axes follow also spatial curves, whereas W VII-X-1D and BSX have nearly planar magnetic axes.

A typical dependence of the electromagnetic forces in such a coil systems is visualized by the effective force F_{res} shown as arrows in the top part of Fig. 1. These forces are largest near the 'corners' of the coil systems, they point radially outwards in BSX 5-2 at the middle of the field period, and they are spiralling in the Heliac. Other engineering aspects of the four types of stellarators are also investigated, like the support of local electromagnetic forces and the resulting stresses and strains. Reinforcement of the coils is required, by some coil housing and by intercoil structural elements. The stored magnetic energies amount between 0.3 and $1\,GJ$ at a field $B_o = 4\,T$ on axis; the maximum fields at the coils are below $7.5\,T$.

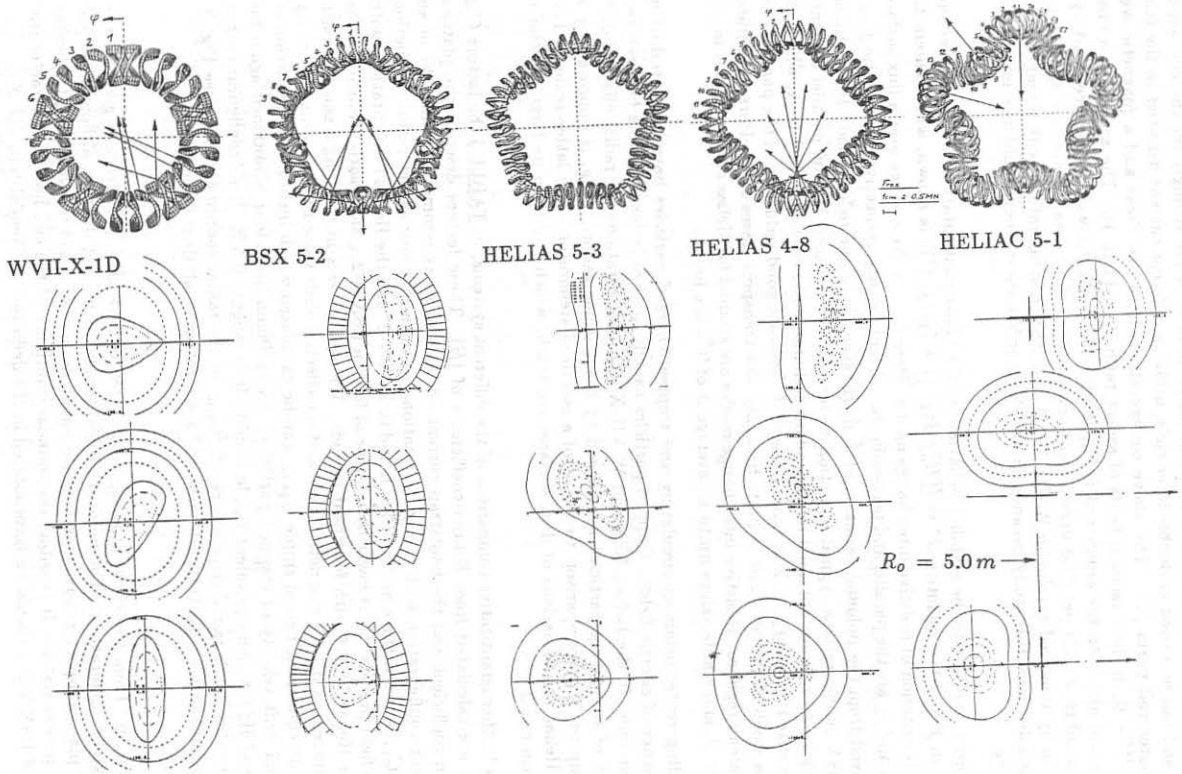

Fig. 1 : Top view on the coil systems, and coil cross sections with magnetic flux surfaces shown at three typical positions along a field period.

The rotational transform ι of modular stellarators depends strongly on the coil aspect ratio and can be varied in double layer coils, utilizing different current densities in the inner and outer coil parts /7/. The above configurations have low shear and a magnetic well, $\Delta V'/V' < 0$, in their vacuum fields of aspect ratio $A = 11$ to 16. The aspect ratio raises with ι and also with the number of field periods. The magnetic well can be deepened by a large number of coils per field period (on the expense of the access between coils, however), and also by a lowered ι-value in W VII–X–1D and BSX. Configurations with a magnetic hill are excluded from this study because, at vanishing or low shear, they would lack interchange stability.

In order to estimate the stability behaviour of the above configurations from their vacuum fields, in Fig. 2 the quantity $J^* = \langle (B_o^2/B^2) \cdot (1 + (j_\parallel/j_\perp)^2) \rangle$ is shown, which enters the stability criterion of resistive interchange modes. Here $\langle \ldots \rangle$ is the average over a flux surface, and $j_\parallel$ and $j_\perp$ are the parallel and perpendicular current density, respectively. The ratio $j_\parallel/j_\perp$ is derived from the poloidal variation of $\int dl/B$ taken along one field period. In the Helias and BSX configurations typical reduction factors of ≈ 3 are seen for the parallel currents, as compared to values obtained in a standard stellarator like Wendelstein VII–A, which are characterized by $|j_\parallel/j_\perp| \sim 2/\iota$. Low values of J^* indicate good reduction of the parallel currents, a small Shafranov–shift at finite beta, and low transport losses in the Pfirsch–Schlüter and plateau regimes. Resistive interchange modes are studied for Helias configurations in /8/ at finite β, and stable values up to an average β of 9 % are found.

Guiding center orbits of circulating and trapped charged particles have been studied in the absence of electric fields. Trapped particles usually are lost in local mirrors between two adjacent coils. In the Helias, BSX and W VII–X–1D configurations the radial offset of drift surfaces of circulating particles normalized by the Larmor radius, Δ/ρ, is improved by a factor up to 3, in comparison to values of a standard stellarator. The latter scale $\sim 1/\iota$. In the Heliac the deviations of drift surfaces are small, which is due to its large rotational transform $\iota \approx 2$.

For a further quantitative comparison of the different systems, in TABLE I the factors C_{pl} and C_b are calculated from Fourier-coefficients of $|B|$. These factors describe the plateau diffusion coefficient and the bootstrap current normalized to axisymmetric values /9/ of an equivalent configuration with the same rotational transform ι and aspect ratio. Reduction factors C_{pl} between three and four are found in BSX 5–2 and the Helias configurations with 4 and 5 field periods; C_b is lower by a factor of four in BSX 5–2 , and nearly vanishes in the modular Helias HS4–8 with four field periods. Transport losses in the long mean free path regime increase with the magnetic ripple and the effective drift velocity. Following the theory of /10/ an equivalent helical ripple $\epsilon_{equiv.}$ can be calculated which includes the reduction of the radial drift velocity of trapped particles. An optimum behaviour is obtained again for the case of HS4–8. An equivalent ripple amplitude is roughly 0.5 %. This configuration has a considerably small radial dependence of B_{min} on the radial coordinate r_{eff}, see Fig. 3, which implies that deeply trapped particles have a rather small drift velocity.

Conclusion : From the above studies, summarized in TABLE I, preference is given to the Helias type configurations. The number of field periods is not yet definite, although the low coil and plasma aspect ratios, as well as the small value of C_{pl} and the vanishing C_b favour the four period system. If possible, the toroidal invariance of the coil bores, a characteristic feature of BSX 5–2 , should be incorporated in the definition of Wendelstein VII–X.

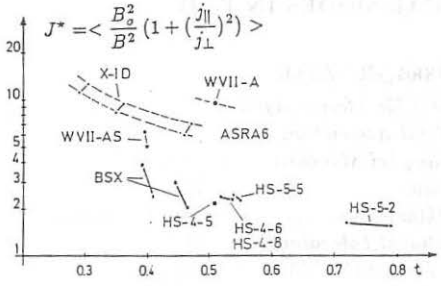

Fig. 2 : Dependence of J^* on the rotational transform ι for modular systems with reduced secondary currents.

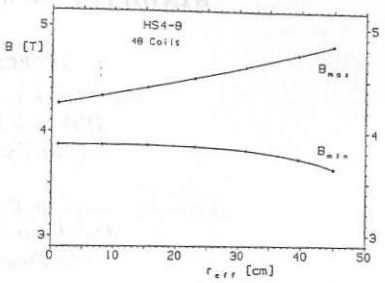

Fig. 3 : Dependence of minimum and maximum induction B_{min} , B_{max} on the effective minor radius for HS4–8.

TABLE I: Characteristics of different WVII-X approaches.
Major radius $R_o = 5.0\,m$, magnetic induction $B_o = 4.0\,T$

	$r_p[m]$	$r_c[m]$	ι_o	$\Delta V'/V'[\%]$	J^*	Δ/ρ	C_{pl}	C_b
WVII-X-1D	0.45	1.22	0.45	-1.7	7.	1.7-2.4	0.75	0.55
BSX 5-1	0.40	0.90	0.41	-0.1	3.			
BSX 5-2	0.30 +)	0.89	0.49	-0.1	2.3	0.3-0.9	0.22-0.3	-0.25
HELIAS 4-1	0.44			-1.0	2.6	0.3-1.0		
HELIAS 4-5	0.44	0.80	0.51	-0.4	2.2			
HELIAS 4-8	0.45	0.90	0.55	-0.7	2.4		0.27-0.3	≈ 0
HELIAS 5-3	0.38	0.72	0.72	-0.4	1.6	< 0.6	0.3-0.35	-1.2
HELIAS 6-1	0.34		1.03	-0.1	1.3	< 0.4	0.61-0.8	-2.8
HELIAC 5-1	0.45	0.85	1.99	-0.1	2.5	0.2-1.0	2.4-2.5	-3.3

+) determined by preliminary vacuum tank, separatrix $r_s = 0.38\,m$
r_p , r_c : minor plasma and coil radius, respectively; ι_o: rotational transform on axis

References :

/1/ F. Herrnegger, F. Rau, 13^{th} Eur. Conf. Schliersee, 10 C/I, 307 (1986).
/2/ J. Nührenberg, R. Zille, Physics Letters 114A, 129 (1986).
/3/ J. Nührenberg et al., 8^{th} Eur. Conf. Comp. Phys., Eibsee, 10 D, 57 (1986).
/4/ J. Kisslinger et al., 12^{th} Eur. Conf. Budapest, 9 F/I, 449 (1985).
/5/ Workshop on Wendelstein VII–X , Schloss Ringberg, FRG, March 1987, EURATOM Report EUR 11058 EN, to be published (1987).
/6/ G. Böhme et al., Studies of a Modular Advanced Stellarator Reactor ASRA6C, IPP Garching Report IPP 2/285, to be published (1987).
/7/ E. Harmeyer et al., 14^{th} Symp. Fus. Techn., Avignon, France, **2**, 1631 (1986).
/8/ W. Dommaschk et al., 11^{th} IAEA Conf. Kyoto, paper D-I-3 (1986).
/9/ E. R. Solano, K.C. Shaing, Phys. Fluids **30**, 462 (1987).
/10/ K.C. Shaing, S.A. Hokin, Phys. Fluids **26**, 2136 (1983).

STABILITY OF LOCAL MODES IN TJ-II

J. NÜHRENBERG, R. ZILLE
Max-Planck-Institut für Plasmaphysik
IPP-EURATOM Association
D-8046 Garching bei München
and
S.P. HIRSHMAN
Oak Ridge National Laboratory
Oak Ridge, TN 37831/USA

The TJ-II four-period heliac [1] derives its flexibility largely from the replacement of an axisymmetric toroidal heliac current [2] by a combination of this current with a helix-like one twisted around it [3]. Two key parameters, the rotational transform and the magnetic well, can be controlled in this way. In this paper, various TJ-II configurations are analyzed with respect to their local mode stability properties [4], only resistive interchange stability results being described because they are very close to Mercier stability results for heliacs.

Vacuum field calculations approximating TJ-II configurations are performed with fixed TF coil line currents, fixed VF coil line currents, and various circular-coil (cc) as well as helical-coil (hc) line currents. A selection of configurations from the TJ-II operational space is obtained with the following prescription for the cc and hc currents:

$$I_{hc}\ [\mathrm{kA}] = -2.1(I_{cc}\ [\mathrm{kA}] + 257.2).$$

Figure 1 shows configurations of this type; the rotational transform per period ι_p is in the range $\frac{1}{4} \lesssim \iota_p \lesssim \frac{1}{2}$; the magnetic well W is given by $0 \lesssim W \lesssim 0.06$; deep wells and large rotational transform occur simultaneously. For these configurations, magnetic surfaces inside but close to the boundary of the confinement region are selected as plasma boundary for the VMEC fixed-boundary 3D code [5]. Such a surface is Fourier analyzed in a form suitable as input for VMEC. Figure 1 shows these boundaries which approximate the original magnetic surfaces sufficiently well. Improvement of the representation is still necessary for the very indented case.

Case III is described in some detail. The currents $(I_{cc}, I_{hc}) = -(200, 120)$ kA result in ι_0 (at the magnetic axis) $= 1.58$, ι_1 (at the boundary) $= 1.592$. The boundary is chosen such that $V'' \approx 0$, and the overall magnetic well is $W \approx 0.03$. This boundary lies just inside the $\iota_p = \frac{2}{5}$ resonance. Use of the VMEC code with approximately 10^2 Fourier amplitudes and 25 radial grid points yields $\iota_0 \approx 1.63$, $\iota_{min} \approx 1.58$, $\iota_1 \approx 1.598$, and $W \approx 0.038$ for the $\beta = 0$ case. While these values are fairly accurate, the fictitious increase in twist near the magnetic axis artificially introduces the $\frac{2}{5}$ resonance. Calculation of a finite β equilibrium with a bell-shaped pressure profile, which is close to the optimum (for stability) because of $V'' = 0$ at the boundary,

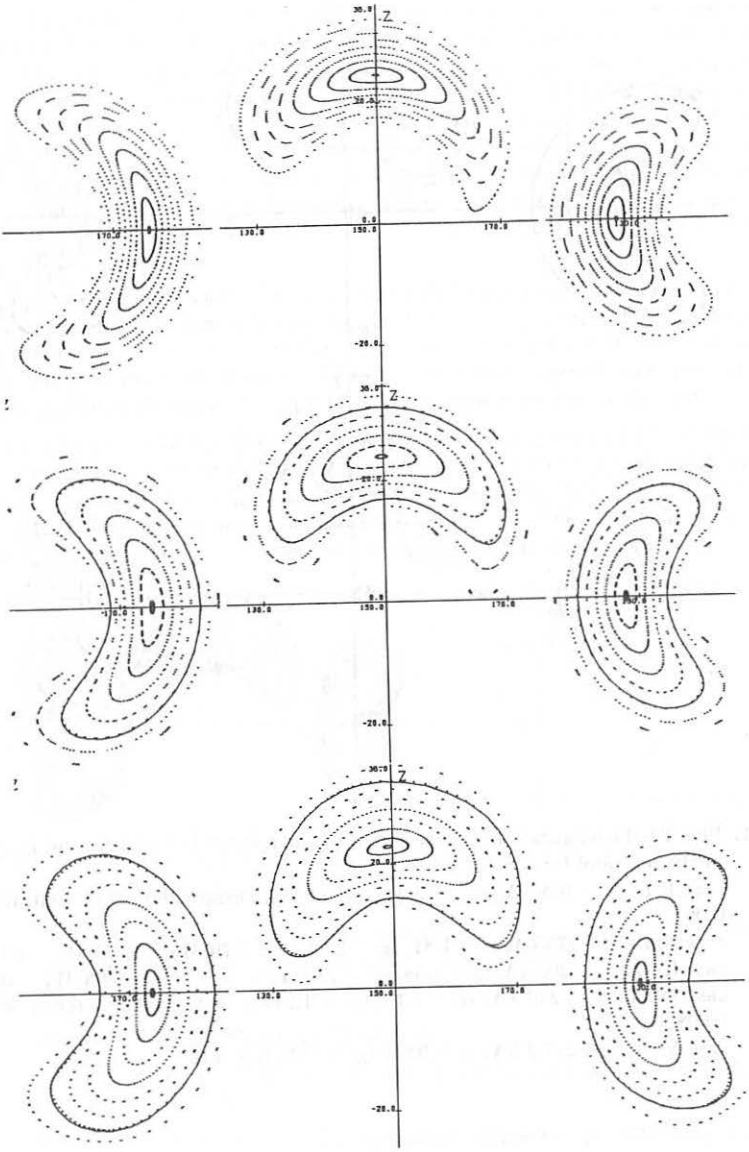
Z
Z
Z

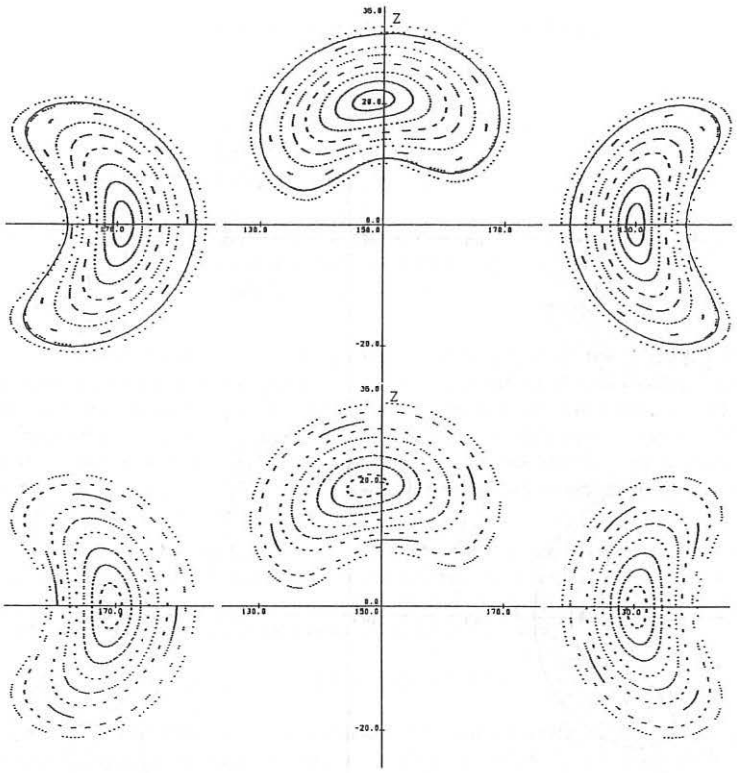

Fig.1: Five TJ-II configurations characterized by the relation between I_{hc} and I_{cc} given in the text and for
case I: $I_{cc} = -163$ kA, $\iota_0 = 1.90$, ι_E (last flux surface shown) $= 1.90$, $W_E = 0.064$,
case II: $I_{cc} = -175$ kA, $\iota_0 = 1.81$, $\iota_E = 1.82$, $\iota_1 = 1.79$, $W_E = 0.05$, $W_1 = 0.036$,
case III: $I_{cc} = -200$ kA, $\iota_0 = 1.58$, $\iota_E = 1.61$, $\iota_1 = 1.59$, $W_E = 0.03$, $W_1 = 0.03$,
case IV: $I_{cc} = -240$ kA, $\iota_0 = 1.15$, $\iota_E = 1.24$, $\iota_1 = 1.22$, $W_E = 0.006$, $W_1 = 0.008$,
case V: $I_{cc} = -257.2$ kA, $\iota_0 = 0.92$, $\iota_E = 1.05$, $W_E \approx 0$.

yields a stable equilibrium at $\langle\beta\rangle = 0.01$. At this value of β the change in rotational transform is negligible; $\langle j_\parallel^2/j_\perp^2\rangle \approx 2$ at $\iota_p = \iota_{min}$, where the $\frac{2}{5}$ resonance is not important, and becomes large at the boundary owing to this resonance. At $\langle\beta\rangle = 0.015$ the stability condition becomes approximately marginal; at $\langle\beta\rangle = 0.02$ the equilibrium is unstable over most of the plasma cross-section. If the resonant contribution to the parallel current density is neglected, i.e. only the non-resonant part of the parallel current density drives the interchange instability, the equilibrium is stable. It has been verified that this behaviour leads indeed to stability at $\langle\beta\rangle \approx 0.02$, with resonances up to order 10 being taken into account, if the configuration is carefully adjusted between $\iota_p = \frac{3}{8}$ and $\iota_p = \frac{2}{5}$.

The results for the other cases shown in Fig. 1 exhibit the same basic features. Case IV, for example, avoids low-order resonances, but $\iota_p = \frac{3}{10}$ occurs. Without taking this resonance into account, the stability boundary is $\langle\beta\rangle \approx 0.01$, with this resonance slightly lower. As expected, these results verify that deeper magnetic wells and larger transforms yield larger stable β values if low-order resonances can be avoided.

A sequence of TJ-II-like equilibria is defined as follows. Suppression of small Fourier amplitudes of the boundary and symmetrization of those which are non-vanishing in helical symmetry yields a neighbouring boundary (see Fig.2). With the aspect ratio of the period fixed, the number of periods N can be used to obtain the limit of helical symmetry by taking $N \to \infty$. Figure 3 shows β-values obtained in this way.

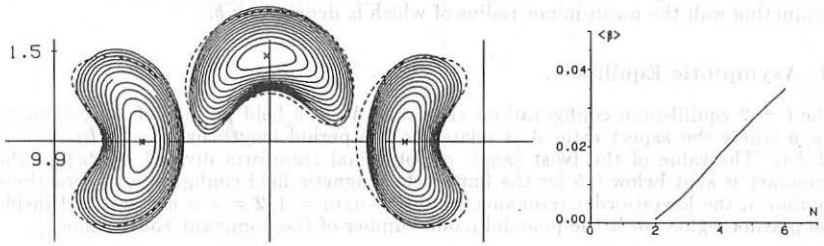

Fig.2: Flux surfaces of a TJ-II and a symmetrized TJ-II configuration.

Fig.3: β limit as a function of the number of periods.

[1] A. Perea, J.L. Alvarez Rivas et al., 12th Eur. Conf. on Contr. Fusion and Pl. Phys., Budapest 1985, ECA Vol. 9F, Part I, 433.

[2] S. Yoshikawa, Nucl. Fusion **23** (1983) 667.

[3] J.H. Harris et al., Nucl. Fusion **25** (1985) 623.

[4] J. Nührenberg, R. Zille, 5th Int. Workshop on Stellarators, Ringberg 1984, EUR9618 EN, Vol. I, 339.

[5] S.P. Hirshman, W.I. van Rij, P. Merkel, Comput. Phys. Comm. **43** (1986) 143.

FIXED- AND FREE-BOUNDARY $n \geq 1$ MODES IN TOROIDAL $l = 2$ STELLARATORS

F. HERRNEGGER
Max-Planck-Institut für Plasmaphysik
IPP-EURATOM Association
D-8046 Garching bei München

1. Introduction.

The magnetohydrodynamic equilibrium and stability properties of toroidal $l = 2$ stellarator configurations of large aspect ratio A ($A = R_T/a = 10$ to 20 as for the WENDELSTEIN VII-A device, R_T is the major torus radius and a the mean minor plasma radius) are accessible to the asymptotic stellarator expansion procedure STEP [1,2,3]. So this is an adequate tool to study some characteristic equilibrium and stability properties of stellarator configurations without longitudinal net-current, which also apply to Advanced Stellarators [4]. Results of a mode analysis of Heliotron-E configurations using the three-dimensional BETA- code are given in Ref.5, and in Ref.6 ideal and resistive $n = 1$ modes are studied for that configurations based on the average MHD equations. In the present paper a classification of unstable free-boundary modes occurring in toroidal $l = 2$ stellarators is given. The normalized eigenvalues of fixed- and free-boundary modes with mode numbers $n = 1, 2, 3, ..$ in toroidal direction and various radial node numbers of the eigenfunctions are given as functions of the position of an electrically conducting wall the mean minor radius of which is denoted by b.

2. Asymptotic Equilibria.

The $l = 2$ equilibrium configurations consist of $M = 5$ field periods of period length L_P/a where the aspect ratio A is related to the period length by $A = ML_P/2\pi a = M/ha$. The value of the twist (angle of rotational transform divided by 2π) at the boundary is kept below 0.5 for the finite-beta magnetic field configurations. For these equilibria, the lowest-order resonance condition $n/m = 1/2 = \iota$ is not satisfied inside the plasma region (m is the poloidal mode number of the dominant Fourier mode).

The vacuum magnetic field is given by $\vec{B} = B_0[\vec{e}_z + (\delta/h)\nabla I_2(hr)\ sin(2\theta - hz)]$ in the pseudo-cylindrical coordinate system (r, θ, z), where the Bessel function $I_2(hr)$ appears in the solution of the Laplace equation for the straight system (Bessel model); δ describes the amplitude of the helical $l = 2$ field. The asymptotic value of the twist on magnetic axis is given by $\iota = M\delta^2/16$ for the vacuum field. The ι-profile of the vacuum field as function of the mean minor radius r of the magnetic surfaces is approximately given by $\iota(r) \approx \iota_0[1 + (hr)^2/2 + 7(hr)^4/96]$. At finite β, the ι-profile is changed as shown in Fig.1. The local shear $r\iota'/\iota$ ($\approx (hr)^2$ in leading order) of these configurations is rather small compared to Heliotron-E configurations because of the long period length. The pressure profile $p = p_0(1 - \psi) \approx p_0(1 - (r/a)^2)$ is approximately a parabolic function in r (ψ is the normalized poloidal flux). The aspect ratio is $A \approx 7.7$.

Figure 1 shows the twist ι and the normalized specific volume $(V' - V_0')/V_0'$ as functions of r/a and $(r/a)^2$, respectively, for two different β-values and vanishing longitudinal net current. The corresponding vacuum fields have a large average magnetic hill meaning that $(V' - V_0')/V_0' > 0$. By superimposing $l = 3$ fields with the same period length

L_P or half of that, vacuum fields with a magnetic well can be obtained having more favorable stability properties [7].

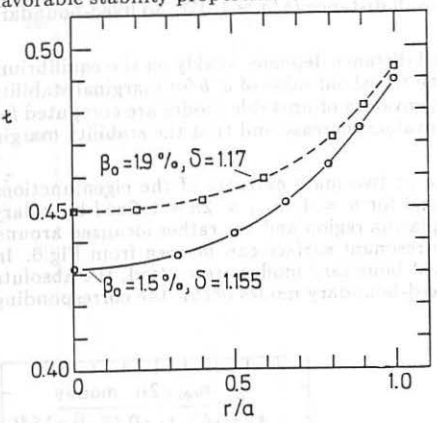

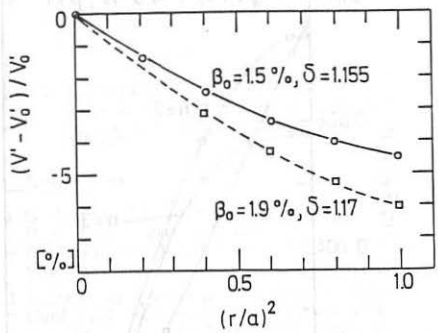

Fig.1. Twist and normalized specific volume $(V'-V_0')/V_0'$ as functions of r/a and $(r/a)^2$, respectively ($A \approx 7.7$).

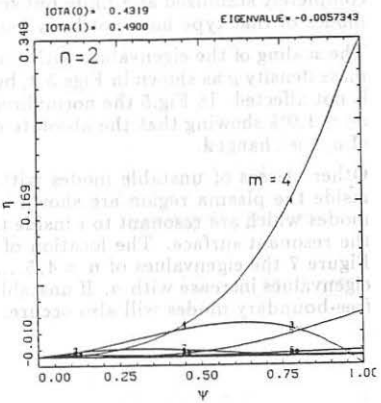

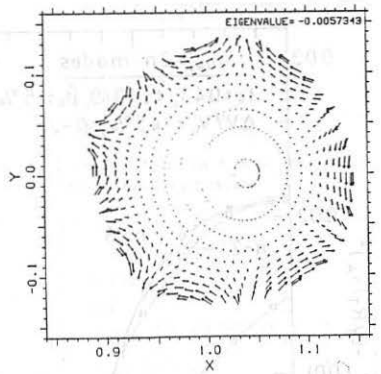

Fig.2. Eigenfunction and displacement vector of a free-boundary $n = 2$ mode with one maximum ($\iota_0 = 0.43, \iota_b = 0.49$).

3. Stability Results.

For all stability computations the equilibrium mass density ρ is assumed to be $\rho \sim \sqrt{p}$ except for the results in Fig.4. The eigenfunction η of a free-boundary $n = 2, m_{res} = 4$ mode is shown in Fig.2 as function of ψ together with the corresponding displacement vector. The eigenfunction assumes its maximum at the boundary. The equilibrium configurations have been chosen so that the $n = 1, 2, 3$ and $m_{res} = 2n$ $(n/m_{res} = 1/2)$ modes are not resonant to ι inside the plasma region. As shown in Fig.3, the free-

boundary $n = 1, 2, 3$ ($m_{res} = 2n$) modes are unstable if the conducting wall is at infinity ($a/b = 0$); as the wall approaches the plasma boundary ($a/b > 0$), these modes are completely stabilized at a finite but small wall distance ($b/a \approx 1.05$). So fixed-boundary modes of that type have not been found.

The scaling of the eigenvalues with the wall distance depends weakly on the equilibrium mass density ρ as shown in Figs.3,4, but the threshold value of a/b for marginal stability is not affected. In Fig.5 the normalized eigenvalues of unstable modes are computed for $\beta_0 = 1.9\%$ showing that the absolute eigenvalues increase and that the stability margin of a/b is changed.

Other classes of unstable modes with one or two main extrema of the eigenfunctions inside the plasma region are shown in Fig.6 for $n = 4, m_{res} = 2n + 1$ fixed-boundary modes which are resonant to ι inside the plasma region and are rather localized around the resonant surface. The location of the resonant surface can be seen from Fig.6. In Figure 7 the eigenvalues of $n = 4, 5, \ldots$ fixed boundary modes are plotted, the absolute eigenvalues increase with n. If unstable fixed-boundary modes occur, the corresponding free-boundary modes will also occure.

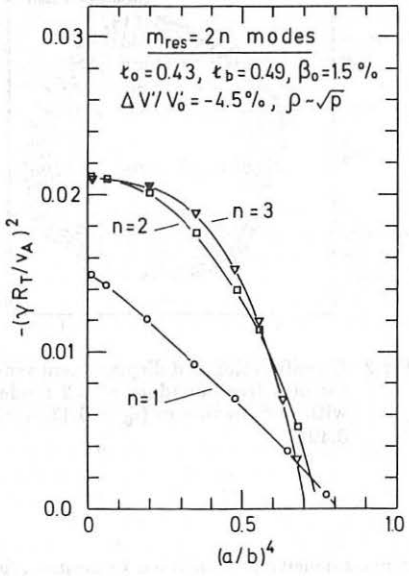

Fig.3. Eigenvalues as functions of $(a/b)^4$ for $n = 1, 2, 3$ free-boundary modes.

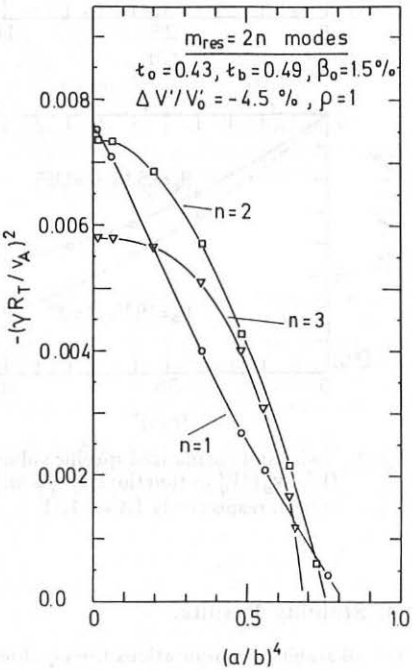

Fig.4. Eigenvalues as functions of $(a/b)^4$ for $n = 1, 2, 3$ free-boundary modes ($\rho = 1$).

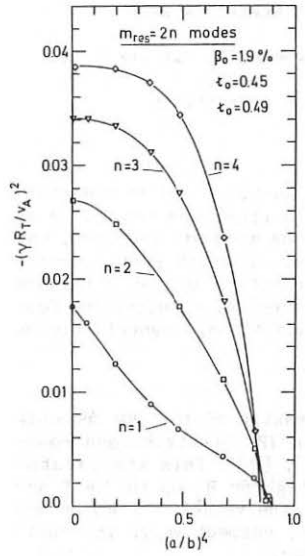

Fig.5. Eigenvalues as functions of $(a/b)^4$ for $n = 1, 2, 3, 4$ modes with $m_{res} = 2n$ ($\beta_0 = 1.9\%$).

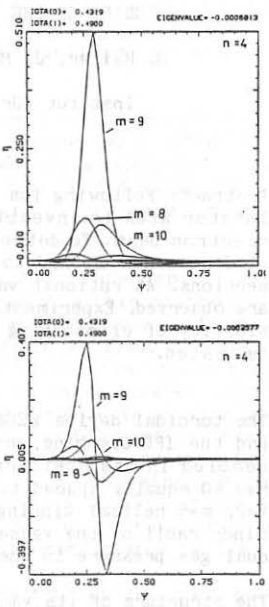

Fig.6. Eigenfunctions of $n = 4$, $m_{res} = 9$ fixed-boundary modes

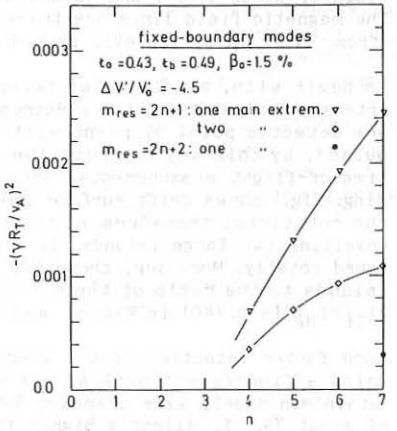

Fig.7. Eigenvalues as functions of n for fixed-boundary modes with $m_{res} = 2n+1$ and $m_{res} = 2n + 2$.

4. References

1 G. Anania, J.L. Johnson, and K.E. Weimer, Phys. Fluids **26** (1983) 2210.
G. Anania and J.L. Johnson, Phys. Fluids **26** (1983) 3070.

2 F. Herrnegger and J.L. Johnson, 12th Europ. Conf. on Controlled Fusion and Plasma Physics (2-6 Sept. 1985, Budapest, Hung.), Vol. **9F**, Pt. I, p.409 (Europ. Phys. Soc., L. Pócs and A. Montvai, Edts., Budapest 1985).
F. Herrnegger, 8th Europhys. Conf. Comput. Phys. Computing in Plasma Physics, Vol. **10D**, p.153 (Europ. Phys. Soc., May 1986, Eibsee, Germany).

3 F. Herrnegger, J.L. Johnson, and P. Merkel, J. Comput.Physics **66** (1986) 445.

4 A. Schlüter, Nucl. Instruments & Methods in Physics Research **207** (1983) 139.

5 M. Wakatani, K. Ichiguchi; F. Bauer, O. Betancourt, P.R. Garabedian, Nucl. Fusion **26** (1986) 1359.

6 B.A. Carreras, L. Garcia, and V.E. Lynch, Phys. Fluids **29** (1986) 3356.

7 F. Herrnegger, to be published.

STUDIES OF THE MAGNETIC SURFACES IN THE STELLARATOR WEGA

H. Hailer, J. Massig, F. Schuler, K. Schwörer, H. Zwicker

Institut für Plasmaforschung, Universität Stuttgart
D-7000 Stuttgart 80, FRG

Abstract: Following its reassembly, the vacuum magnetic field of the stellarator WEGA is investigated. The magnetic field lines are traced by an electron beam. To detect the electron beam various methods are used, including a new method to take high-quality pictures of drift surface cross sections. At rational values of the rotational transform magnetic islands are observed. Experimental data are compared to numerical results. The feasibility of eliminating the magnetic islands by additional magnetic fields is tested.

The toroidal device WEGA, formerly a joint undertaking of the CEN Grenoble and the IPP Garching, has been transferred to the IPF Stuttgart and reassembled in its stellarator version (see e.g. [1], [2]). This stellarator has 40 equally spaced toroidal field coils allowing for B_o up to 1.4 T and ℓ=2, m=5 helical windings mounted on the shell of the vessel. The major and minor radii of the vessel are R_o=0.72m and a=0.19m, respectively. The residual gas pressure in the torus is about 2×10^{-7} mbar.

The structure of its vacuum magnetic field is investigated experimentally, feeding the toroidal field coils and the helix windings independently by highly stabilized power supplies (better than 10^{-4}) producing a magnetic field of about 0.06 T and values of the rotational transform up to $\iota \approx 0.6$. The magnetic field lines are traced by means of a low-energy electron beam (from 30 eV up to 120 eV), pulsed or dc, using various detection methods.

To begin with, a well known technique was used ([3], [4], [5], [6]): The intersection points of the electron beam with a meridional (poloidal) plane are detected point by point with an electric point probe. If the beam is pulsed, by this way the rotational transform can be evaluated, too, via time-of-flight measurements. This method is accurate but very time consuming. Fig.1 shows drift surface cross sections mapped this way at values of the rotational transform ι_o slightly below 1/2 (1a) and next to 1/2 (1b), unveiling two large islands. In Fig.1b the inner closed surfaces have vanished totally. Moreover, these two pictures indicate the sensitivity of the islands to the ratio of the toroidal field current to the helix current (I_{TF}/I_{HF} is 0.4401 in Fig.1a and 0.4373 in Fig.1b).

Much faster detection of the electron beam transit points is achieved by using a fluorescent mesh as has been done in HELIOTRON E [7]. Our mesh (stainless steel, wire diameter 0.8 mm, spacing 5.8 mm) has a transparency of about 74.3 %, slightly higher than that used in HELIOTRON E. This value prooved to be much too low, resulting in a rapid decrease of the beam intensity at consecutive transits and leaving, for example, after 100 transits a relative beam intensity of only 1.3×10^{-13}. Fig.3 shows two ex-

amples for this method, a nearly elliptic drift surface at $\iota_0 \approx 0.118$ (3a) and islands at $\iota_0 \approx 1/2$ (3b). Only small parts of the two islands can be identified because of overradiation at the first transits and rapid decrease of beam intensity.

Calculations of electron trajectories indicate that some 50 to 200 beam transits are needed to identify magnetic islands properly. If after 100 transits a remaining beam intensity of only 1 % seems to be acceptable, the average transparency of the mesh has to be higher than 95.5 % resulting in a wire diameter of less than 0.11 mm at 5 mm spacing giving a rather poor spatial resolution.

Optimum spatial resolution as well as minimum beam interception are achieved by moving a linear fluorescent detector, e.g. a thin coated rod, across the beam path, while imaging this detector on a photographic film or on the target of an electronic camera and exposing for at least one sweep time. This is a fast method producing high-quality pictures of electron drift surface cross sections (Poincaré plots), and it is especially suited for the detection of magnetic islands. Multiple exposures with varying positions of the electron gun, practicable because of the high spatial resolution, give pictures of groups of adjacent drift surfaces, and thus fast surveys of actual magnetic field configurations can be obtained. Fig.4 displays results obtained by this method. Fig.4a ($\iota_0 \approx 0.118$) and Fig.4b ($\iota_0 \approx 1/2$) correspond to the neighbouring Fig.3a and 3b taken by the fluorescent mesh. In addition, Fig.4c shows island formation at $\iota_0 \approx 1/3$.

Parallel to the measurements electron guiding centre trajectories have been calculated using an up-to-date version of the GOURDON code [8]. The drift surface plots of Fig.2 are obtained for the experimental parameters of Fig. 1a, i.e. toroidal field current $I_{TF} = 404.5$ A, helical field current $I_{HF} = 919.1$ A, electron energy $E = 30$ eV, $E_\perp \approx 1$ eV, and assuming a displacement of 1.5 mm between the main axes of the helix and of the toroidal field coil arrangement to be the only perturbation. Size and direction of this displacement have been deduced from geometrical as well as magnetic field measurements. The good agreement between the measured (Fig.1a) and the calculated (Fig.2a) drift surfaces, although the contours of the islands are highly sensitive to the parameters, indicates that the islands shown are predominantly caused by this displacement. Fig.2b shows the same drift surfaces at the position of the fluorescent detectors, thus corresponding to Fig.3b and Fig.4b.

This helix displacement has not yet been corrected, in order to continue studying its effects and to check the feasibility of compensating such defects by additional magnetic coils. A substantial reduction of the size of the islands has already been achieved.

References

[1] R. Fritsch et al., 9th SOFT, Garmisch-Partenkirchen, 1976, p. 287
[2] F. Söldner et al., 9th Europ. Conf. on Contr. Fus. and Pl. Phys., Oxford, 1979, Paper A2.5
[3] E. Berkl et al., 3rd IAEA Conf. on Pl. Phys. and Contr. Nucl. Fus., Novosibirsk, 1968, Vol. 1, p. 513

[4] E. Berkl et al., Report IPP 2/69, IPP Garching, 1968
[5] R.M. Sinclair et al., Rev. Scientific Instr. 41/11 (1970) 1552
[6] H.J. Jäckel et al., Report IPP 2/231, IPP Garching, 1976
[7] R. Takahashi et al., Int. Stellarator / Heliotron Workshop, Kyoto, 1986
[8] C. Gourdon et al., 3rd IAEA Conf. on Pl. Phys. and Contr. Nucl. Fus., Novosibirsk, 1986, Vol. 1, p. 847

Pictures: The scales of all pictures are equal. Relative to the position of the electron gun the toroidal position of the fluorescent detectors is $\varphi_F = 1/2 \times 2\pi$ and the position of the point probe is $\varphi_p = 4/5 \times 2\pi$.

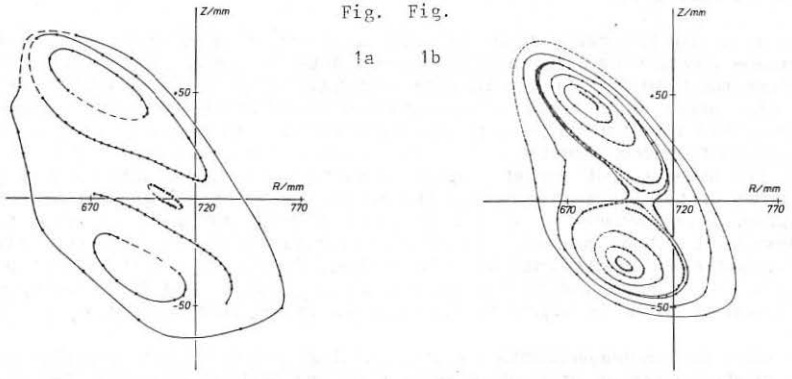

Fig. 1a Fig. 1b

Fig.1: Electron drift surfaces at $\iota = 1/2$ mapped by means of a point probe
Parameters: I_{HF} = 919.1 A, E = 30 eV and a) I_{TF} = 404.5 A, b) I_{TF} = 401.9 A

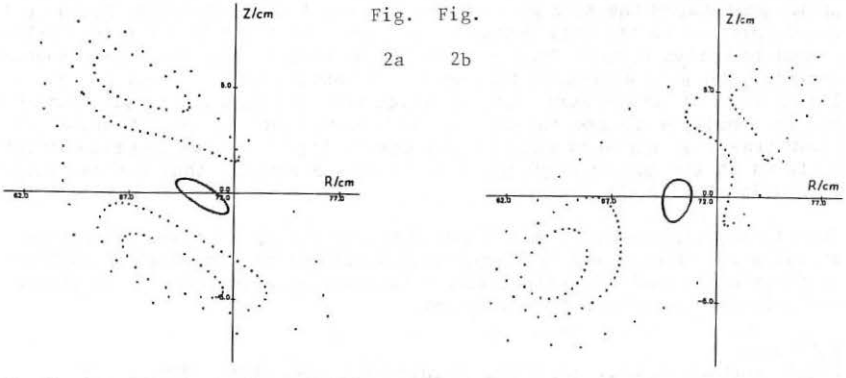

Fig. 2a Fig. 2b

Fig.2: Calculated electron drift surface cross sections. Parameters correspond to Fig.1a. a) Cross sections at the position of the point probe to be compared to Fig.1a, b) Cross sections at the position of the fluorescent detectors to be compared to Fig.3b and Fig.4b.

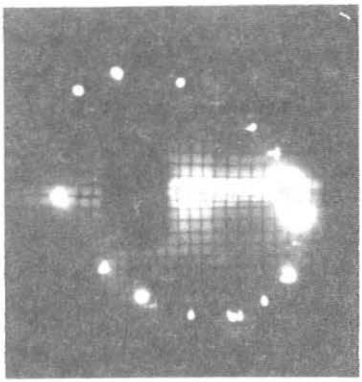

Fig. 3a

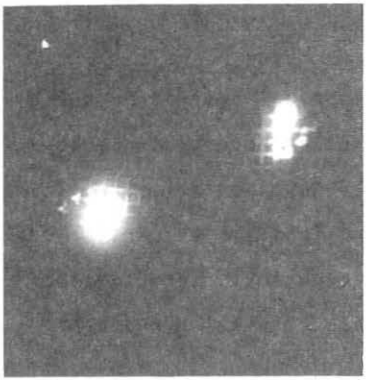

3b

Fig. 4a

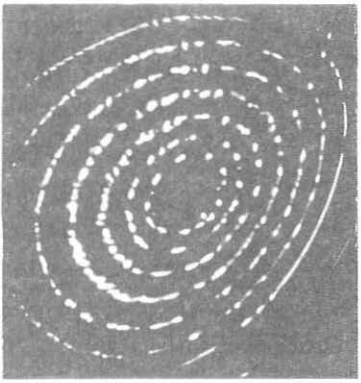

4b

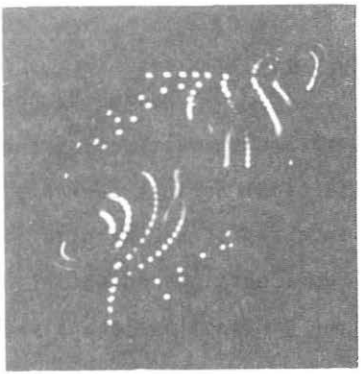

4c

Electron drift surface cross sections made visible by a

Fig.3: fluorescent mesh

Fig.4: moved fluorescent rod

where a) $t_o = 0.118$
b) $t_o = 1/2$
c) $t_o = 1/3$

TOROIDAL HELICAL FIELDS

M.Y. Kucinski and I.L. Caldas
Instituto de Física, Universidade de São Paulo
C.P. 20516, 01498 São Paulo,SP, Brazil

ABSTRACT

Using the conventional toroidal coordinate system Laplace's equation for the magnetic scalar potential due to toroidal helical currents is solved. The potential is written as a sum of an infinite series of functions. Each partial sum represents the potential within some accuracy. The effect of the winding law is analysed in the case of small curvature.

V.D. PUSTOVITOV.

THEORY OF EQUILIBRIUM CURRENTS IN STELLARATORS

I.V. Kurchatov Institute of Atomic Energy, Moscow, USSR

It is shown in this report that equilibrium currents in stellarators are very sensitive to the changes in the inner geometry of plasma column. Observed in experiments on Uragan stellarators second cosine harmonic of longitudinal current density can be connected with the plasma toroidal shift due to finite pressure. This shift and more effectively - ellipticity of the magnetic surfaces determine the longitudinal current generated during fast heating of a plasma. Analitical expressions of this current through plasma geometrical characteristics are derived. Effect of current generation is the display of strong dependence of rotational transform in stellarators on the form and reciprocal positions of magnetic surfaces. Formulae derived in this report explain the essence of this dependence.

FIRST AUTHOR ALPHABETICAL INDEX